Universidade Federal do Rio de Janeiro
Centro de Ciências Matemáticas e da Natureza
Observatório do Valongo
Programa de Pós Graduação em Astronomia

Formation, Destruction and Identification of Complex Organic Molecules (COMs) in Circumstellar Environments

Heidy Mayerly Quitián Lara

Rio de Janeiro
April, 2020

Formation, Destruction and Identification of Complex Organic Molecules (COMs) in Circumstellar Environments

Heidy Mayerly Quitián Lara

Tese de Doutorado submetida ao Programa de Pós Graduação em Astronomia, Observatório do Valongo, da Universidade Federal do Rio de Janeiro, como parte dos requisitos necessários à obtenção do título de Doutora em Ciências (Astronomia).

Orientadores:
Heloisa Maria Boechat-Roberty
Bertrand Lefloch

Rio de Janeiro
April, 2020

CIP - Catalogação na Publicação

QQ8f

Quitián Lara, Heidy Mayerly
Formation, Destruction and Identification of Complex Organic Molecules (COMs) in Circumstellar Environments / Heidy Mayerly Quitián Lara. -- Rio de Janeiro, 2020.
385 f.

Orientadora: Heloisa Maria Boechat-Roberty.
Coorientador: Bertrand Lefloch.
Tese (doutorado) - Universidade Federal do Rio de Janeiro, Observatório do Valongo, Programa de Pós Graduação em Astronomia, 2020.

1. Astroquímica. 2. Espectrometria de massas. 3. Radioastronomia. 4. Moleculas. 5. Meio interestelar. I. Boechat-Roberty, Heloisa Maria, orient. II. Lefloch, Bertrand, coorient. III. Título.

Elaborado pelo Sistema de Geração Automática da UFRJ com os dados fornecidos pelo(a) autor(a), sob a responsabilidade de Miguel Romeu Amorim Neto - CRB-7/6283.

Formation, Destruction and Identification of Complex Organic Molecules (COMs) in Circumstellar Environments

Heidy Mayerly Quitian Lara

Dr.ª Heloísa Maria Castro Boechat (Orientadora)
Dr. Bertrand Lefloch (Coorientador)

Tese de Doutorado submetida ao Programa de Pós-Graduação em Astronomia, Observatório do Valongo, da Universidade Federal do Rio de Janeiro - UFRJ, como parte dos requisitos necessários à obtenção do título de Doutora em Ciências - Astronomia.

Aprovada por:

Presidente, Dr.ª Heloísa Maria Castro Boechat (Orientadora) – OV/UFRJ

Dr. Bertrand Lefloch – (Coorientador) – IPAG/UGA

Dr. Jacques Raymond Daniel Lepine – (Avaliador Externo) – IAG/USP

Dr. Fábio de Almeida Ribeiro – (Avaliador Externo) – IFRJ

Diana Paula Pinho de Andrade – (Avaliadora Interna) – OV/UFRJ

Dr. Edgar Fabian Mendoza Rodriguez – (Avaliador Interno) – OV/UFRJ

Esta defesa realizou-se através de videoconferência, completamente remota, em conformidade com a Resolução do CEPG n.º 1 de 16 de março de 2020.

Defesa lavrada em ata: n.º 19/20

Abril de 2020

This study was financed in part by the Coordenação de Aperfeiçoamento de Pessoal de Nível Superior - Brasil (CAPES) - Finance Code 001.

A mi Nonita y a mi Padre... Con todo el corazón.

Acknowledgements

To Professor Heloisa M. Boechat for her guidance and willingness to share knowledge. The opportunity to work with her is one of the most beautiful experiences of my work at the Observatório do Valongo. Sincerely, thank you very much.

To Professor Bertrand Lefloch for his guidance and support, as well as for helping me to observe the molecular universe. This was a fantastic experience.

To Professor Claudine Kahane, of the Institut de Planétologie et d' Astrophysique de Grenoble, for her help and her great disposition in the identification survey of IRAS 4A.

To Professor Wania Wolff, of the Instituto de Física - UFRJ, for kindly providing some of the experimental data presented in this PhD thesis, as well as for her support in the data reducing process.

To Professors Asunción Fuente and José Cernicharo, as well as to the entire NANOCOSMOS team, for their valuable contributions to my academic development.

To Professor Fabio Ribeiro, of the Instituto de Química - IFRJ, the Professors Maria Luiza Rocco, Marco Antonio Chaer Nascimento and Ricardo Rodrigues of the Instituto de Química - UFRJ, as well as Professor Diana Andrade of the Observatório do Valongo, thank you very much for all your support and advice.

To the members of the PhD committee and the administrative staff of the Observatório do Valongo, thank you for your support and dedication for conducting this PhD defense by videoconference in a pandemic scenario. May Science be the star that guides humanity in this dark period.

To the Professors and colleagues of Observatório do Valongo, thank you for sharing experiences and demonstrating that despite the difficulties it is amazing to look to the sky. Thank you for strengthening my decision to become an Astronomer.

To my wonderful husband Felipe Fantuzzi, who besides being my best friend is an excellent colleague. Thank you for believing in me and for giving me so much love every day.

To my mom Gloria Lara and my Colombian-Brazilian family: Cesar, Javier, Fernando, Marilene, Claudia, Lucca, Bonifacius and Nymeria. Your support is essential for me to continue. You are a source of infinite love. I could not have arrived here without each of you. I love you.

To Cynthia, Rene, Fellipe and Ricardo, thank you for the good conversations, dinners, drinks and get-togethers, and for always motivating me to carry on.

To my best friends and colleagues, Sergio, Mario, Lelys and Daniel, for their eternal willingness to listen and elevate the soul, they always know what to say at the right times.

My magic quark, always...

Resumo

Formation, Destruction and Identification of Complex Organic Molecules (COMs) in Circumstellar Environments

Heidy Mayerly Quitián Lara

Orientadores: Heloisa Maria Boechat-Roberty e Bertrand Lefloch

Resumo da Tese de Doutorado submetida ao Programa de Pós Graduação em Astronomia, Observatório do Valongo, da Universidade Federal do Rio de Janeiro (UFRJ), como parte dos requisitos necessários à obtenção do título de Doutora em Ciências (Astronomia).

O Universo é rico em complexidade química e molecular. Até o momento, mais de 200 moléculas foram detectadas em regiões interestelares e circunstelares incluindo objetos protoestelares e nebulosas planetárias (PNe), sendo mais de 60 observadas em objetos extragalácticos. Estudos sobre os mecanismos de formação, destruição de moléculas, assim como a identificação de moléculas em espectros observacionais, são fundamentais para a compreensão da química em ambientes astrofísicos. Neste trabalho, foram utilizadas técnicas experimentais e observacionais para a descrição química de distintos objetos astrofísicos nos quais moléculas orgânicas complexas (COMs) e hidrocarbonetos policíclicos aromáticos (PAHs) estão presentes. Experimentalmente, estudou-se a formação e destruição de moléculas derivadas do benzeno (C_6H_6), unidade básica de PAHs, através da interação de fótons na faixa dos raios X com moléculas na fase gasosa empregando a espectrometria de massas por tempo de voo (MS-TOF), simulando assim os processos que ocorrem nas regiões de fotodissociação (PDRs) de PNe. Analisamos as moléculas: C_6H_6, naftaleno ($C_{10}H_8$), bifenila ($C_{12}H_{10}$) e ciclohexano (C_6H_{12}), esta última como unidade básica de PAHs super- hidrogenados (Hn-PAHs). Adicionalmente, estudou-se os efeitos de protonação e desprotonação de anéis benzênicos destas moléculas na fase condensada a partir da técnica de dessorção iônica estimulada por elétrons (ESID) de análogos de gelos astrofísicos. Os gelos foram preparados a partir de amostras puras de C_6H_6, C_6H_{12} e clorobenzeno (C_6H_5Cl), assim como a partir de uma solução de fenol (C_6H_5OH). Para o C_6H_{12} em fase gasosa, os resultados evidenciam a maior tendência à dissociação do mesmo em comparação com o benzeno, associada à diminuição da energia de ligação do esqueleto carbônico após a hidrogenação. Por outro lado, a alta seção de choque de fotoabsorção do benzeno em energias próximas à ressonância de camada interna (C1s) faz com que a eficiência de dissociação da molécula seja maior do que a do ciclohexano. Os resultados sugerem que um efeito similar é experimentado por PAHs em ambientes ricos em raios-X, como na PDR da NGC 7027, de forma que sua hidrogenação possa atuar como um mecanismo de proteção como consequência da diminuição da seção de choque de fotoabsorção. Para a bifenila, identificou-se os principais fragmentos mono-(A^+) e duplamente (A^{2+}) carregados formados pela fotoionização dissociativa nas energias de 275 e 310 eV, e determinou-se os respectivos percentuais de produção iônica (PIYs). A partir desses valores, estimou-se os tempos de meia-vida da bifenila em quatro PNe nos quais emissões de PAHs estão presentes: NGC 7027, BD+30^{o}3639, NGC 5315 e NGC 40. Nos estudos em fase condensada, foi observada uma tendência à hidrogenação dos anéis aromáticos devido a interação com elétrons na faixa do keV, assim como uma rota competitiva para a desprotonação destes compostos. Estes resultados sugerem possíveis caminhos de formação de PAHs com fragmentos alifáticos, bem como Hn-PAHs, na superfície congelada de grãos de poeira em regiões frias do meio circunstelar. Na parte observacional deste trabalho, realizou-se uma análise abrangente da composição molecular do objeto protoestelar de classe 0 IRAS 4A a partir de dados obtidos pelo radiotelescópio IRAM 30m. Foram identificadas 92 espécies moleculares e catalogou-se

1456 frequências rotacionais, incluindo perfis finos e largos, por meio da análise do conteúdo molecular do IRAS 4A. Os resultados mostram que a IRAS 4A é dominada por moléculas simples contendo carbono, nitrogênio, oxigênio, enxofre e silício. Também identificou-se COMs como CH_3OH, CH_3CHO e CH_3COCH_3, sendo que as mais abundantes são as que contêm oxigênio na estrutura. Com base nos resultados, foi possível identificar três componentes de temperatura de excitação, associadas a distintas regiões da fonte, e estimar a densidade colunar de cada uma das moléculas com relação ao H_2, tanto na envoltória protoestelar como no jato bipolar associado à protoestrela.

palavras chave: *Astroquímica, Radiastronomía, Moléculas, Espectrometría de massas, Protoestrelas*

Rio de Janeiro
Abril de 2020

Abstract

Formation, Destruction and Identification of Complex Organic Molecules (COMs) in Circumstellar Environments

Heidy Mayerly Quitián Lara

Orientadores: Heloisa Maria Boechat-Roberty and Bertrand Lefloch

Abstract da Tese de Doutorado submetida ao Programa de Pós Graduação em Astronomia, Observatório do Valongo, da Universidade Federal do Rio de Janeiro (UFRJ), como parte dos requisitos necessários à obtenção do título de Doutora em Ciências (Astronomia).

The universe is rich in chemical and molecular complexity. To date, more than 200 molecules have been detected in interstellar and circumstellar regions including protostellar objects and planetary nebulae (PNe), with more than 60 observed in extragalactic objects. Studies on the mechanisms of formation, destruction of molecules, as well as the identification of molecules in observational spectra, are fundamental for the understanding of chemistry in astrophysical environments. In this work, experimental and observational techniques were used for the chemical description of different astrophysical objects in which complex organic molecules (COMs) and polycyclic aromatic hydrocarbons (PAHs) are present. Experimentally, the formation and destruction of molecules derived from benzene (C_6H_6), the basic unit of PAHs, were studied through the interaction of photons in the X-ray range with molecules in the gas phase employing time-of-flight mass spectrometry (MS-TOF), thus simulating the processes that occur in the PNe photodissociation regions (PDRs). We analyzed the following molecules: C_6H_6, naphthalene ($C_{10}H_8$), biphenyl ($C_{12}H_{10}$) and cyclohexane (C_6H_{12}), the latter being the basic unit of super-hydrogenated PAHs (H_n-PAHs). Additionally, we studied the protonation and deprotonation effects of benzene rings of these molecules in the condensed phase by the Electron Stimulated Ion Desorption technique (ESID) of astrophysical ice analogs. The ice was prepared from pure samples of C_6H_6, C_6H_{12} and chlorobenzene (C_6H_5Cl), as well as from a phenol solution (C_6H_5OH). For C_6H_{12} in gas phase, the results show a greater tendency to dissociate it compared to benzene, associated with the reduction of the carbon backbone binding energy after hydrogenation. On the other hand, the photoabsorption cross section of benzene t energies close to the inner shell resonance (C1s) is larger than the one of cyclohexane, which ultimately leads to a higher efficiency of dissociation for the aromatic molecule. The results suggest that a similar effect is experienced by PAHs in X-ray rich environments, such as the NGC 7027 PDR, so that their hydrogenation may act as a protective mechanism as a consequence of decreasing the photoabsorption cross section. For the biphenyl molecule, the major mono-(A^+) and double (A^{2+}) charged fragments formed by dissociative photoionization at the energies of 275 and 310 eV were identified. Also its ionic production percentages (PIYs) were determined. From these values, the biphenyl half-life times were estimated in four PNe in which PAHs emissions are present: NGC 7027, BD+30^{o}3639, NGC 5315 and NGC 40. In the condensed phase experiments, we observe hydrogenation of aromatic rings due to interaction with electrons in the keV range, as well as a competitive route for deprotonation of these molecules. These results suggest possible pathways of PAH formation with aliphatic fragments, as well as H_n-PAHs, on the frozen surface of dust grains in cold regions of the circumstellar environment. In the observational part of this work, a survey analysis of the molecular composition of the Class 0 protostellar object IRAS 4A was performed from data obtained by the IRAM 30m radiotelescope. Ninety-two molecular species were identified and cataloged with 1456 rotational frequencies, including narrow and wide profiles, by analyzing the molecular content of IRAS 4A. The

results show that IRAS 4A is dominated by simple molecules containing carbon, nitrogen, oxygen, sulfur and silicon. We also identified COMs such as CH_3OH, CH_3CHO and CH_3COCH_3, the most abundant ones containing oxygen in the structure. Based on our results, we could identify three excitation temperature components, associated with different regions of the source, and estimate the column density of each molecule with respect to H_2, both in the protostellar envelope and in the bipolar jet associated with the protostar.

keywords: *Astrochemistry, Radiastronomy, Molecules, Mass Spectrometry, Protostars*

Rio de Janeiro
April, 2020

List of Figures

List of Tables

Abbreviations

AGB : Asymptotic Giant Branch

AGN : Active Galactic Nuclei

ALMA : Atacama Large Millimeter Array

ASAI : Astrochemical Surveys At IRAM

AU : Astronomical Unit

BE : Bonnor-Ebert

BO : Born-Oppenheimer

CASSIS : Centre d'Analyse Scientifique de Spectres Instrumentaux et Synthétiques

CCSD: Coupled-Cluster Singles and Doubles

CCSD(T): Coupled-Cluster Singles and Doubles plus Perturbative Triples

CDMS : Cologne Database for Molecular Spectroscopy

COM : Complex Organic Molecules

cr : Cosmic Ray

CSM : Circumstellar Medium

Dec : Declination

DFT: Density Functional Theory

EMIR : Eight MIxer Receiver

ESID : Electron Stimulated Ion Desorption

FFTS : Fast Fourier Transform Spectrometers

FUV : Far Ultraviolet

GMC : Giant Molecular Cloud

HAeBe : Herbig Ae/Be Stars

HERA : Heterodyne Receiver Array

HH : Herbig–Haro

H_n-PAH : Hydrogenated Polycyclic Aromatic Hydrocarbons

HOMO : Highest Occupied Molecular Orbital

HR : Hertzsprung-Russell

HST : Hubble Space Telescope

IP : Ionization Potential

IR : Infrared

IRAM : Institut de Radioastronomie Millimétrique

IRAS : Infrared Astronomical Satellite

ISM : Interestellar Medium

ISO : Infrared Space Observatory

JPL : Jet Propulsion Lab

LaQuiS : Laboratório de Química de Superficies LINER : Low-Ionization Nuclear Emission-line Region

LO : Local Oscillator

LNLS : Brazilian Synchrotron Light Source Laboratory

LSB : Lower SideBand

LTE : Local Thermodynamic Equilibrium

LUMO : Lowest Unoccupied Molecular Orbital

MCP : Micro-Channel Plate

mid-IR : Middle Infrared

MK : Morgan-Keenan

MO : Molecular Orbital

MS : Mass Spectrometry

NGC : New General Catalogue

NIST : National Institute of Standards and Technology

PAH : Polycyclic Aromatic Hydrocarbons

PDR : Photodissociation Region

PE : Photoelectron

PEPICO : Photoelectron Photoion Coincidences

PEPIPICO : Photoelectron Photoion Photoion Coincidences

PI : Photoion

PIY : Partial Ion Yield

PMS : Pre-Main-Sequence

PN : Planetary Nebula

PNe : Planetary Nebulae

Ra : Right Ascension

RGA : Residual Gas Analyzer

rms : Root Mean Square

ROSAT : Röntgen Satellite

SED : Spectral Energy Distribution

SGM : Spherical Grating Monochromator

Sy1 : Seyfert 1

Sy2 : Seyfert 2

TDC : Time-to-Digital Converter

TGM : Toroidal Grating Monochromator

TOF : Time of Flight

TTS : T-Tauri Star

ULIRG : Ultra-Luminous IR Galaxy

ULX : Ultra-luminous X-ray

USB : Upper Sideband

UV : Ultraviolet

VLA : Very Large Array

VUV : Vacum Ultraviolet

WC : Wolf-Rayet C-rich

WCCC : Warm Carbon-Chain Chemistry

WO : Wolf-Rayet O-rich

XRD : X-ray Dominated Regions

YSO : Young Stellar Object

ZAMS : Zero-Age-Main-Sequence

ZPE : Zero-Point Energy

Contents

Chapter 1

Introduction

1.1 Astrophysical Environments: Interstellar and Circumstellar Media

At the end of the 18^{th} century, Caroline and William Herschel (Fig. 1.1) were the first to observe dark regions in the celestial sphere, which they called *holes in the sky*. Such observations led them to propose the existence of empty regions without stars in the galaxy (Steinicke, 2016). We now know that these *holes* are actually molecular clouds, which constitute the starting point of the processes of molecular, stellar and planetary formation in the galaxies. Stars, indeed, are the atoms of the universe (McKee and Ostriker, 2007). And as the geometries and electron densities of molecules heavily depend on the nature of the atoms that make them, a similar relationship is also observed between stars and galaxies. In this chapter, we will briefly describe the stages of formation of young stellar objects of solar masses, their main characteristics and the processes that lead to the formation of planetary nebulae at the final stage of the stellar evolution.

1.1.1 Star Formation and Young Stellar Objects

Stars are formed in supersonic self-gravitating turbulent molecular clouds (Burkhart, 2018). Such objects can be considered as the link between galaxy evolution, planet formation and astrobiology (Chyba and Hand, 2005; McKee and Ostriker, 2007; Krumholz, 2014; Burkhart, 2018). In spite of the huge amount of theoretical and observational data related to star formation obtained in the last decades, a full understanding of such process is still matter of debate. This also includes the role of

Figure 1.1: Caroline and William Herschel. Adapted from Steinicke (2016).

turbulence, as there is evidence for its dissipation in many prestellar low-mass cores. Moreover, if gravitation alone was responsible for star formation, interstellar clouds with density ρ_0 would collapse to form stars on a free-fall time, t_{ff}. For a uniform spherical gas cloud, the dynamics of the gravitational collapse can be described by the following equation:

$$F = ma = \frac{GMm}{r^2} \tag{1.1}$$

where m is the element of mass, M is the entire mass of the cloud with r radius, and G is the gravitational constant. By applying the conservation of energy law, the kinetic energy of m is equal to the change in the gravitational potential energy:

$$\frac{1}{2}mv^2 = GMm\left[\frac{1}{r} - \frac{1}{r_0}\right] \tag{1.2}$$

where r_0 is the initial radius of the cloud. The velocity of collapse is then given by:

$$v = \sqrt{2GM\left[\frac{1}{r} - \frac{1}{r_0}\right]} \tag{1.3}$$

For a uniform spherical gas cloud, M is given by:

$$M = \frac{4}{3}\pi r^3 \rho_0 \tag{1.4}$$

By replacing eq. 1.4 in eq. 1.3, we obtain the following expression:

$$v = \sqrt{\frac{8\pi}{3} G\rho_0 r_0^2 \left[\frac{r_0}{r} - 1\right]} \tag{1.5}$$

Since

$$v = \frac{\mathrm{d}r}{\mathrm{d}t} \tag{1.6}$$

the free-fall time t_{ff} is given by:

$$t_{ff} = \int \mathrm{d}t = \left(\frac{8\pi}{3} G\rho_0 r_0^2\right)^{-1/2} \int_{r_0}^{0} \left[\frac{r_0}{r} - 1\right]^{-1/2} \mathrm{d}r \tag{1.7}$$

where integration of eq. 1.7 is from r_0 to zero. This gives:

$$t_{ff} = \sqrt{\frac{3\pi}{32 G\rho}} \tag{1.8}$$

However, distinct phenomena contribute to counteract gravity and influence the overall dynamics of the star-forming regions. Such effects include magnetic fields, supersonic turbulence (Shu et al., 1987a), jet/outflow feedback (Federrath, 2015), and cloud rotation. As a consequence, the timescales of star formation are significantly longer than the ones expected considering t_{ff}. In other words, star formation is a very inefficient process, as exemplified in Fig. 1.2. In the following section, we will describe the basic physical principles that underlie star formation.

1.1.1.1 Basic Principles: Turbulence, Self-Gravity and Magnetic Fields

In the context of star formation, **turbulence** can be defined as the irregular and random state of motion of the gas flow in clouds. Most of terrestrial applications deal with incompressible turbulence, where density remains almost constant as a consequence of the subsonic nature of root-mean-square velocities, v_{rms}. In this perspective, the dissipation of energy occurs predominantly in the smallest vortices, at a rate given by (Mac Low and Klessen, 2004):

$$\dot{E} = \frac{\mathrm{d}E}{\mathrm{d}t} = \frac{\eta v^3}{L} \tag{1.9}$$

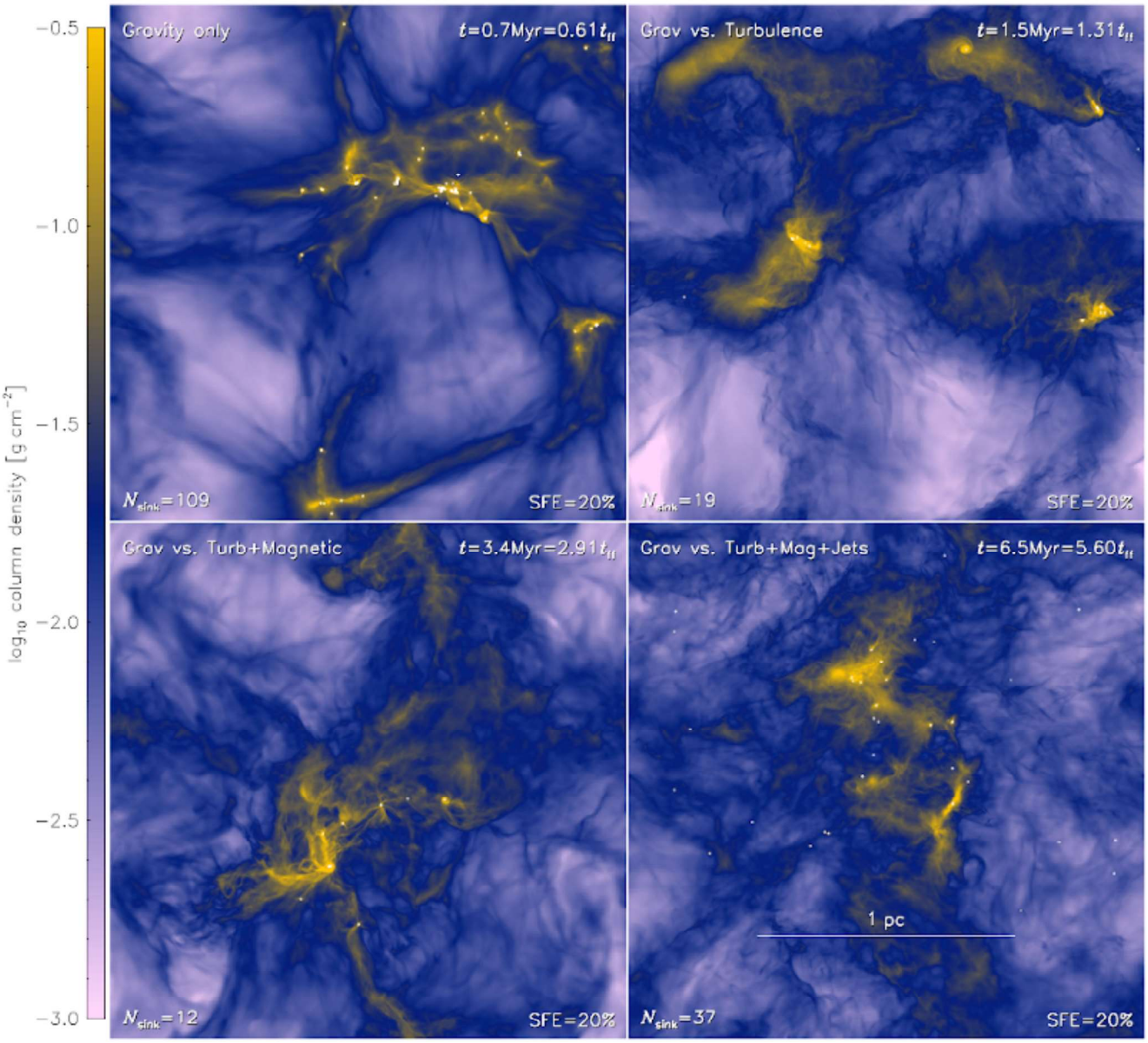

Figure 1.2: Simulated column density projections of star formation considering different physical scenarios. The inclusion of turbulence and magnetic effects significantly increases the time for which a realistic star formation efficiency (SFE) of 20% is obtained, revealing that such effects are responsible for making the star formation process very inefficient. Credits: Federrath (2015).

where L is the integral length scale and η is a constant determined empirically. Gas flows in the interstellar medium, on the other hand, are supersonic, highly compressible and not uniform, coming mainly from blast waves and other inhomogeneous processes (Mac Low and Klessen, 2004). As a consequence, strong density perturbations are observed. In supersonic turbulence, shock waves can transfer energy between widely separated scales, removing the local nature observed for incompressible turbulence (Mac Low and Klessen, 2004). In fact, turbulence is responsible for much of

the complex and filamentary density structure observed in molecular clouds, and its effect can even trigger gravitational collapse due to the creation of dense regions (Bonnell et al., 2003; Hennebelle and Falgarone, 2012). However, the creation of such regions driven by supersonic turbulence is not an effective process, and its overall effect is that of suppressing star formation in regions when the total turbulent kinetic energy exceeds the total gravitational energy (Padoan and Nordlund, 2011). The ratio between both energy terms can be obtained by the virial parameter, α_{vir}, as introduced by Bertoldi and McKee (1992):

$$\alpha_{vir} = \frac{5v_{rms}^2 R}{GM} \tag{1.10}$$

Self-gravity can be defined as the process by which each individual component of a large object is kept together by the combined gravity of the whole entity. This effect plays a very important role in the final stages of star formation, where the star-disk system is formed from the collapse of dense cores inside molecular clouds (Di Francesco et al., 2006). For earlier times, simulations without the inclusion of such effect suggest that turbulence alone is sufficient to create a mass distribution profile that resembles stellar initial mass function (Padoan and Nordlund, 2002). This was further refuted by Goodman et al. (2009), which used a tree-diagram analysis to show that self-gravity acts at multiple length scales, being also critical to the earliest phases of star formation.

The simplest case of a self-graviting cloud is a static isothermal cloud with no magnetic field. The largest mass that such system, embebbed in a medium with a gas pressure p_0, could have to still remain in hydrostactic equilibrium is given by the Bonnor-Ebert mass, M_{BE} (Ebert, 1955; Bonnar, 1956):

$$M_{BE} = \frac{225}{32\sqrt{5\pi}} \times \frac{c_s^4}{(aG)^{3/2}} \times \frac{1}{\sqrt{p_0}} \tag{1.11}$$

where c_s is the isothermal sound speed and a is a dimensionless constant that varies with the density distribution of the molecular cloud. For a uniform mass density, $a = 1$. If the mass of the cloud is greater than M_{BE}, than the system inevitably will undergo gravitational collapse, leading then to the formation of a protostar (Draine, 2011).

The structure and evolution of the molecular cloud is also affected by **magnetic fields**. The importance of magnetic effects to cloud structure is determined by obtaining m_ϕ, which is the ratio of the cloud mass M to the magnetic critical mass M_ϕ:

$$m_\phi = \frac{M}{M_\phi} \tag{1.12}$$

where, for a cold cloud in magnetostatic equilibrium, M_ϕ is given by (McKee et al., 1993):

$$M_\phi = c_\phi \frac{\phi}{\sqrt{G}} \tag{1.13}$$

where ϕ is the magnetic flux threading the cloud and c_ϕ is a numerical coefficient that depends on the internal distribution of density and magnetic fields. If $M > M_\phi$, the cloud is of a magnetically supercritical type, and magnetic fields are not able to prevent gravitational collapse. On the other hand, in magnetically subcritical clouds ($M < M_\phi$), gravitational collapse is not possible.

It is believed that the interstellar medium is strongly magnetized (Nejad-Asghar, 2007). However, the stars are not. As a consequence, the mass-to-flux ratio increases dramatically during star formation. Such ratio can be increased by two distinct mechanisms: flows along magnetic fields and ambipolar diffusion (decoupling of neutral particles from plasma), where mass distribution is affected by the magnetic flux tube (Mouschovias, 1991). For regions of the molecular cloud in which the gas is shielded from the interstellar radiation field and ionization is caused by cosmic rays, the ambipolar diffusion times are around 10 times higher than the free-fall time, t_{ff}, without turbulence effects (McKee and Ostriker, 2007). However, for a gas ionized by far ultraviolet (FUV) radiation from stars, which accounts for most of the mass of a giant molecular cloud (GMC), the ambipolar diffusion time is much longer. As a consequence, suppression of spontaneous star formation in the outer layers of GMCs is expected (quasi-static scenario, Shu et al. 1987b). This effect was further confirmed both in the L1630 region of Orion (Li et al., 1997) and in Taurus (Onishi et al., 1998).

1.1.1.2 Low-Mass Star Formation

Prior to the formation of the protostar, there is a central region in the cloud where the expanding thermal energy is counteracted by gravity. The radius of such region is called Jeans' length, λ_J, and is given by (Jeans, 1902):

$$\lambda_J = \sqrt{\frac{15 k_B T}{4\pi G m_p \mu \rho}} \tag{1.14}$$

where k_B is the Boltzmann constant; T, ρ and μ are, respectively, the temperature, density, and mass per particle of the cloud; and m_p is the mass of a proton.

A marginally unstable core starts collapsing near the outer radius of the Jeans' length. The collapse wave is then accelerated and propagated inwards. When the protostar is formed, the corresponding infall rate is given by (Shu, 1977; McKee and Ostriker, 2007):

$$\dot{m}_{in} = \frac{\mathrm{d}m_{in}}{\mathrm{d}t} = \phi_{in}\frac{c_s^3}{G} \tag{1.15}$$

where c_s is the sound speed of the gas and ϕ_{in} is a numerical factor ≥ 1. The cores that form low-mass stars have density profiles similar to the ones of Bonnor-Ebert gas spheres, as suggested by observations (Motte and André, 2001; Kirk et al., 2005). In the innermost regions of the collapsing core, the opacity becomes large enough so that the gas switches from approximately isothermal to adiabatic behavior (McKee and Ostriker, 2007). Once the gas is hot enough to dissociate H_2, a second collapse occurs and the protostar is finally formed.

Once a protostar is formed by gravitational collapse of a core, it can continue to grow by accretion of the nearby gas. If the star is moving through the ambient medium at a velocity of $v_0 = \mathcal{M}_0 c_s$, where $\mathcal{M}_0$ is the Mach number, the characteristic radius from which the star accretes is known as the Bondi-Hoyle radius, R_{BH}, which is given by:

$$R_{BH} = \frac{Gm_*}{(1+\mathcal{M}_0^2)c_s^2} \tag{1.16}$$

where m_* is the mass of the protostar. The accretion rate is then defined as:

$$\dot{M}_{BH} = \frac{\mathrm{d}M_{BH}}{\mathrm{d}t} = 4\pi\phi_{BH}R_{BH}^2\rho c_s(1+\mathcal{M}_0^2)^{1/2} = 4\pi\phi_{BH}\frac{\rho G^2 m_*^2}{(1+\mathcal{M}_0^2)^{3/2}c_s^2} \tag{1.17}$$

where ϕ_{BH} is a number ~ 1 that fluctuates due to flow instabilities (Ruffert and Arnett, 1994).

It is possible to classify the stages of the growth of protostars using observations of the mass distribution surrounding the protostar, the velocity distribution of the circumnuclear gas, and the non-stellar radiative flux (McKee and Ostriker, 2007). Furthermore, by modelling the spectral energy distribution (SED) of the continuum, mass and temperature distribution can also be inferred. The SED of protostars are divided into four classes, representing distinct evolutionary stages of the object. These stages are called Class 0, Class I, Class II and Class III (Fig. 1.3). Classes I-III were introduced by Lada (1987), while Class 0 protostars were firstly described by Andre et al. (1993). For a comprehensive review of the evolutionary stages of protostars, see André et al. (2000). A schematic diagram of the protostellar evolutionary stages is shown in Fig. 1.4.

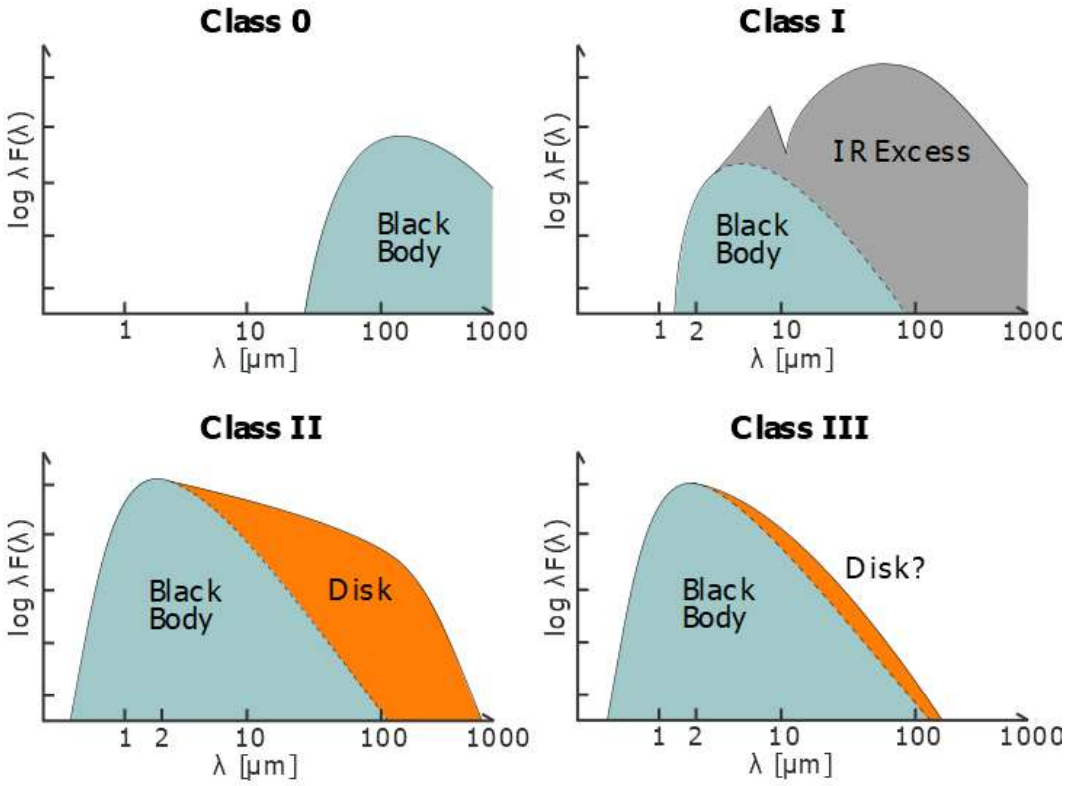

Figure 1.3: Spectral Energy Distribution (SED) of the different protostellar stages. Adapted from Persson (2014).

The classification of protostars, based on the slope of the spectral energy distribution (SED) measured at 2.2 and 10-25 μm (Wilking et al., 1989), is characterized by an α spectral index defined as:

$$\alpha_{ir} = \frac{-dlog\,(\lambda F_\lambda)}{dlog\lambda} \tag{1.18}$$

where F_λ is the flux density.

Class 0 protostars (Fig. 1.3 top left) are the youngest class of protostellar sources currently identified. They are in a highly active accretion phase with a deeply embedded central object surrounded by significant amounts of circumstellar material ($\geq 0.5 M_\odot$). Continuum emission of these objects is extremely weak at optical and near-IR wavelengths (undetectable at $\lambda < 10$ μm in the 90s), but they display significant luminosity in the submillimeter domain (L_{smm}) with respect to the bolometric luminosity, L_{bol}, $L_{smm}/L_{bol} > 0.5\%$. Sources with these properties show $M_{envelope} \geq M_*$ (Andre et al., 1993; Palla, 1996; McKee and Ostriker, 2007).

Class I protostars (Fig. 1.3 top right) are sources with $\alpha_{ir} > 0$, indicating an increase in the

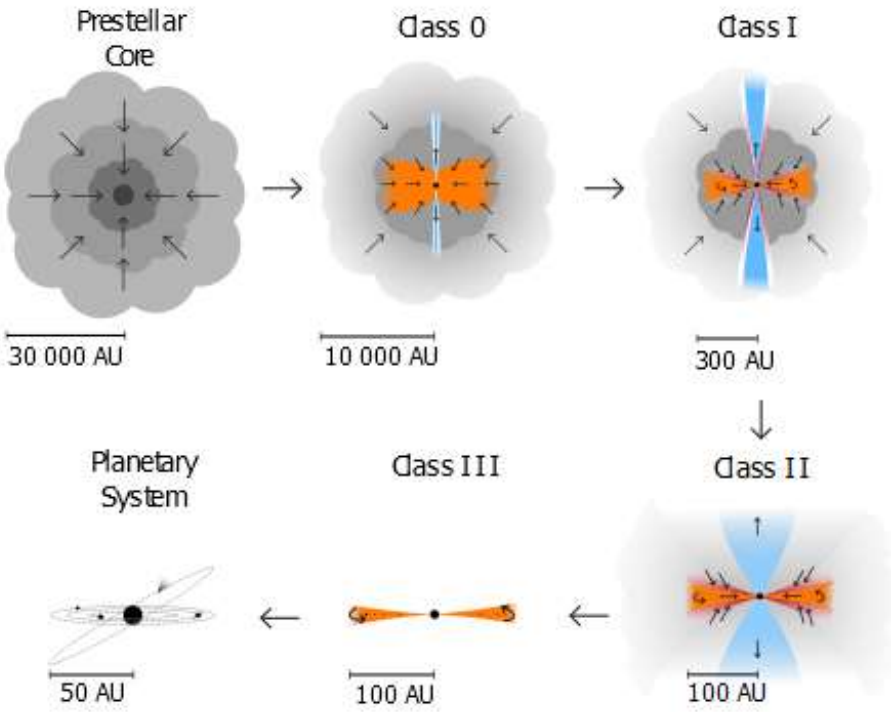

Figure 1.4: Protostellar evolutionary stages: from prestellar core to planetary system. Adapted from Persson (2014).

SED up to $\lambda = 100$ μm. It presents an IR excess and the SED is much broader than that of a single temperature blackbody. Class I sources are thought to represent protostars in a less active accretion stage than Class 0 protostars surrounded by luminous disks with radii of $\sim$100 AU. They can also show infalling processes and extended envelopes with sizes of $\sim 10^4$ AU (Palla, 1996; McKee and Ostriker, 2007).

Class II protostars (Fig. 1.3 bottom right) are sources with $-2 < \alpha_{ir} < 0$. Their SEDs fall at longer wavelengths but continue to be broadened by the presence of a significant amount of circumstellar dust. A Class II object is thought to evolve from a Class I source by clearing of the circumstellar envelope, maybe because of stellar wind effects (see Fuente et al. 2002). Class II sources contain classical T-Tauri (TTS) and Herbig Ae/Be (HAeBe) stars surrounded by a geometrically thin and optically thick circumstellar disk of radius $\sim$100 AU (Palla, 1996; McKee and Ostriker, 2007).

Class III (Fig. 1.3 bottom right) are sources with α_{ir} < -2. Their SED is similar than that of a normal and reddened stellar photosphere without IR excess, indicating the disappearance of circumstellar disks and envelopes. Class III sources are thought to be on the way from Class II sources to main sequence stars. The presence of weak TTS lines (typically $\alpha_{ir} < 1.5$) indicates that these objects

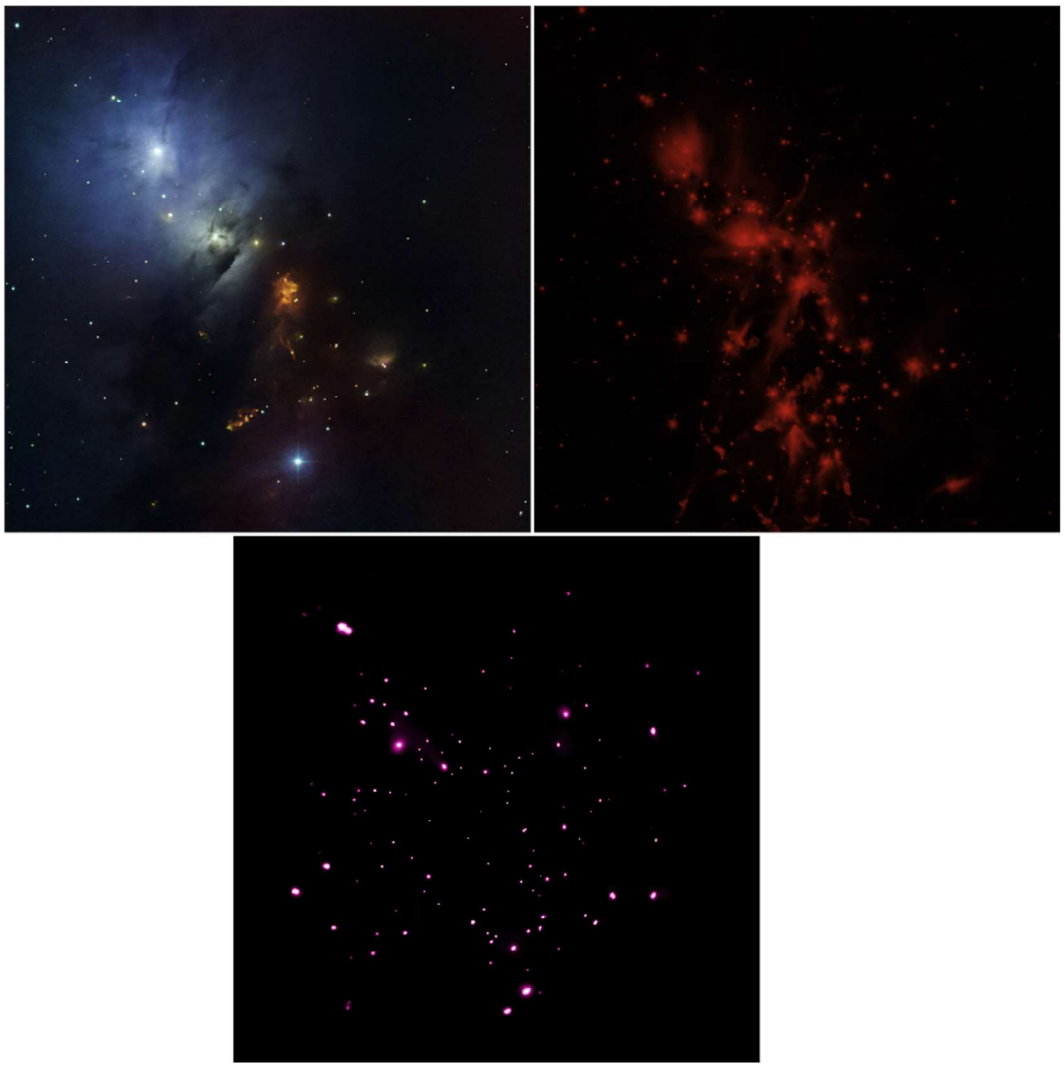

Figure 1.5: The molecular cloud NGC 1333 visualized in the optical (top left), infrared (top right) and X-ray (bottom) ranges. Credits: Optical: DSS, NOAO, AURA and NSF; Infrared: NASA and JPL-Caltech; X-ray: NASA, CXC, SAO and S. Wolk et al.

are pre-main-sequence (PMS) stars that are no longer accreting significant amounts of matter (Palla, 1996; McKee and Ostriker, 2007).

1.1.1.3 The Star Forming Region NGC 1333

NGC 1333 (Fig. 1.5) is a young star forming region located at $\sim$ 260 pc (Schlafly et al., 2014) on the western edge of the Perseus molecular complex (Ra= $03^h28^m55.2^s$, Dec=+31^o22'12"). This region is one of the most active star forming clouds in the solar neighborhood (Walawender et al., 2008). It formed a first generation of young pre-main sequence stars, distributed in a cluster at the center of the cloud (Lada et al., 1993). Its stars are thought to have an average age of 1–2 Myr (Bally

et al., 2008). A new generation of stars is currently forming in the parental cloud, as testified by the presence of several Class 0 and Class I protostars (Langer et al., 1996; Lefloch et al., 1998; Sandell and Knee, 2001; Sadavoy et al., 2014). Inside the cloud, few of the cluster members are easily visible in the optical range. The first infrared mapping of NGC 1333 was made by Strom et al. (1974), which also observed that the region hosts numerous Herbig–Haro (HH) objects. Later, Plunkett et al. (2013) obtained images in the 4.5 μm with the Spitzer Space Telescope, and revealed many outflows coming from young stars.

Systematic observational studies of the chemical composition of protostellar cores have identificed two main chemical classes (see e.g. Lefloch et al. 2018):

Hot Corinos (Ceccarelli et al., 2017) – only a few sources, such as NGC 1333 IRAS 4A, NGC 1333 IRAS 4B and NGC 1333 IRAS 2, were identified as hot corinos for presenting abundant oxygenated molecular species. In a similar manner, other sources, such as Serpens SMM1, Serpens SMM4, and HH212, are also classified as hot corinos. (Cazaux et al., 2003; Bottinelli et al., 2004; Sakai et al., 2006; Öberg et al., 2011; Codella et al., 2016). Hot corinos are also detected towards intermediate-mass protostellar cores (Ospina-Zamudio et al., 2018).

WCCC Sources – objects with an abundant content in polyynic hydrocarbon species, such as L1527, L1157-MM IRAS 15398-3359, and TMC-1A, are classified as chemical objects of the warm carbon-chain chemistry, WCCC (Sakai et al., 2008, 2014; Lefloch et al., 2018).

Recent studies (Sakai et al., 2009; Oya et al., 2017) show that a few protostellar sources actually display the chemical signatures of both classes. It is not completely clear, however, whether the complex organic molecules (COM) emission arises from the thermal evaporation of grain mantle ices, or is caused by other processes, like e.g. shocks.

A systematic study by Higuchi et al. (2018) led to identify a large number of hot corinos and WCCC sources in the Perseus molecular cloud complex. However, full characterization of the chemical properties of these sources is pending. It is, however, the first step in order to understand the origin and the evolution of the molecular species present in the envelope, a fraction of which will be transferred to the disk in which planets will eventually form.

In this PhD thesis, the protostellar object NGC1333 IRAS 4A was studied through observations made with the IRAM 30m radiotelescope. The main characteristics of this source are briefly described in the next section.

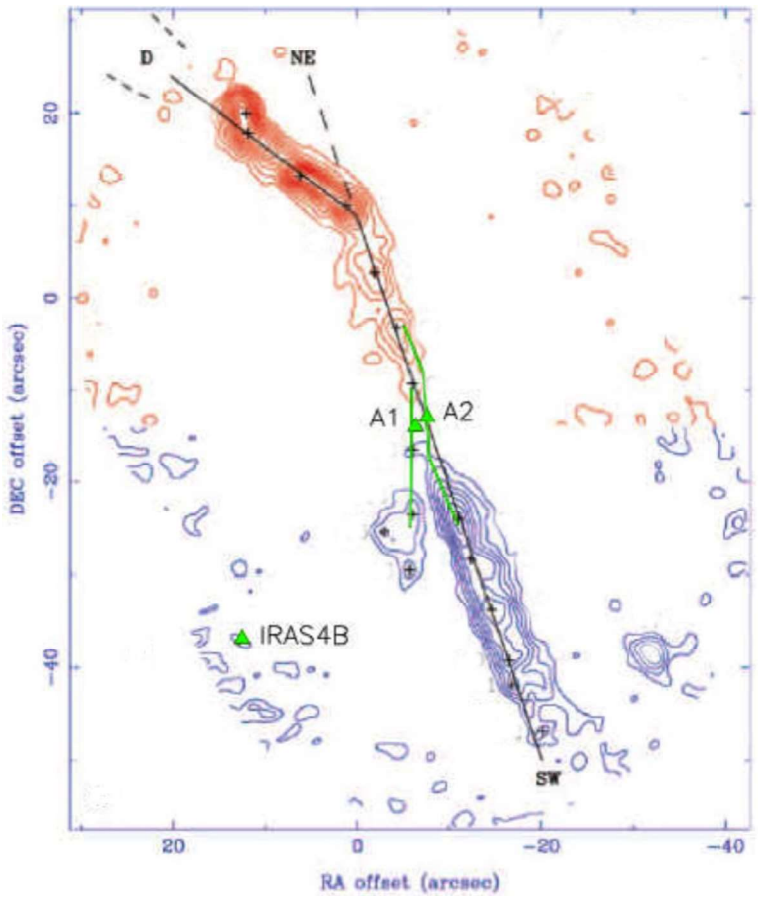

Figure 1.6: NGC 1333 IRAS 4A region. In the image: Very Large Array (VLA) SiO(1-0) map (red and blue contours) is shown in comparison with the proposed propagation directions of the A1 and A2 jets (green solid lines). The positions of IRAS 4A1, IRAS 4A2 and IRAS 4B are marked with green triangles. Taken from Santangelo et al. (2015).

1.1.1.4 The Class 0 protostellar core IRAS 4A

NGC 1333 IRAS 4A is a protostellar binary system located in the Perseus molecular complex at ∼260 pc (Schlafly et al., 2014). IRAS 4A harbours two compact protostellar sources, embedded in an extended, dense envelope. Its two components, IRAS 4A1 and IRAS 4A2, have a separation of about 1.8 arcsec (∼ 420 - 527 AU) (Lefloch et al., 2018; Sahu et al., 2019), with IRAS 4A1 being brighter than IRAS 4A2 in the continuum. Each of them powers a molecular jet, confirming their protostellar nature (Santangelo et al., 2015; Taquet et al., 2015; López-Sepulcre et al., 2017).

The luminosity (including the two components) and envelope mass of IRAS 4A are 9.1 $L_{\odot}$ and 5.6 $M_{\odot}$, respectively (Karska et al., 2013; Sahu et al., 2019). The IRAS 4A system is associated with a large-scale (a few arcminutes) bipolar molecular outflow (Santangelo et al., 2014). Santangelo et al. (2015) showed that the large-scale outflow emission is driven by the component A2 (Fig. 1.6). Ob-

servations made with the IRAM 30m radiotelescope revealed that IRAS 4A2 is a hot corino, merely the second object classified as such (the first observed hot corino was IRAS 16293-2422, Bottinelli et al. 2007; López-Sepulcre et al. 2017. Recent studies published by Santangelo et al. (2015) and López-Sepulcre et al. (2017) confirmed that IRAS 4A2 is a hot corino protostar, as evidenced by the detection of COMs such as dimethyl ether (CH_3OCH_3), ethyl cyanide (C_2H_5CN), and glycolaldehyde (CH_2OHCHO). Furthermore, molecular isotopologues, such as heavy-oxygen water ($H_2^{18}O$), were detected in this source. Interestingly, COM emission in the millimeter domain is not detected towards IRAS 4A1. Such a chemical differentiation is not unique among the multiple systems investigated so far (see e.g. Ospina-Zamudio et al. 2018, 2019), and its origin is strongly debated.

Recently, a systematic survey of the molecular line emission towards IRAS 4A led to the identification of more than 40 molecular species (Lefloch et al., 2018). Such species are oxygen-bearing, sulfur-bearing, carbon-bearing and nitrogen-bearing type molecules, being the chemical composition of the source dominated by oxygen-bearing species. Identifications were made as part of the ASAI large program in the 3mm spectral range using the IRAM 30m telescope (see Chapter 3). This work establishes the starting point for the results presented in Chapter 8, which also includes an extended survey of the source in 1, 2 and 3mm.

In the next section, we discuss the evolutionary stages of low-mass stars.

1.1.2 Stars and Evolved Objects: AGBs and Planetary Nebulae

1.1.2.1 Herzprung-Russel Diagram

The first phase of stellar evolution is known as pre-main-sequence or PMS. As mentioned in the previous sections, large molecular clouds, mainly constituted by gas (H) and dust grains (silicates, graphites, etc.), contract isotropically to form a protostellar object. As a consequence, the huge release of gravitational potential energy heats the interior such object, producing great luminosity. When the onset of nuclear fusion in protostellar objects takes place, a star is finally formed. The Zero Age Main Sequence (ZAMS) object, or star, enters the main sequence and begins its evolutionary path following a trajectory described by the Hertzsprung-Russell (HR) diagram (Fig. 1.8).

The relationship between luminosity (absolute magnitude) and surface temperature (or spectral class) of a star, described in the HR diagram, is directly proportional to the stellar mass (Longair, 1994; Carroll and Ostlie, 2007). In the emission spectrum, the intensity of the spectral line indicates the chemical abundance (elements and molecules) present in the stellar photosphere, as well as the

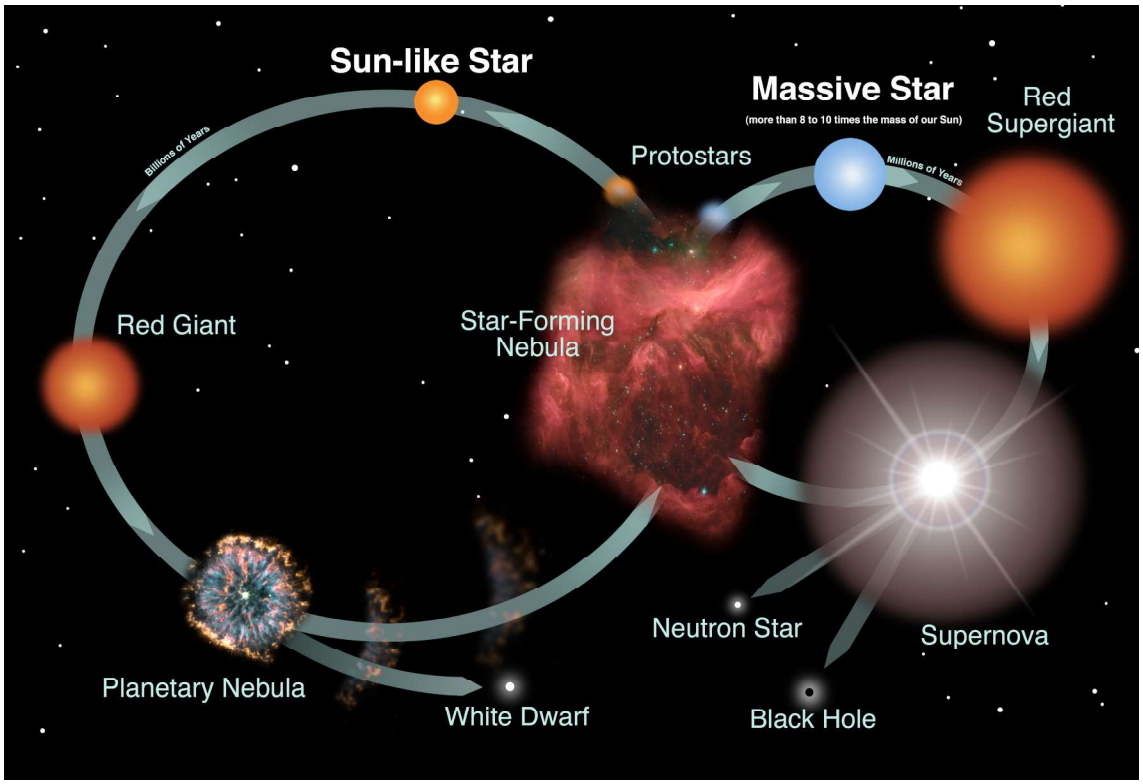

Figure 1.7: Cycle of formation of sun-like and massive stars. Credits: NASA.

ionization states provide a measure directly proportional to the temperature (Carroll and Ostlie, 2007).

Most stars are classified by the Morgan-Keenan system (MK). This system uses the O, B, A, F, G, K and M letters to separate the stars according to their temperature, mass and spectral characteristics. In this sequence, hottest and heavy stars are of the O-type while coldest and low-mass stars are of the M-type. Each class (O to M) is subdivided using a numerical digit, with zero being the hottest and 9 being the coldest. Currently, new classes have been incorporated for other stars and objects similar to stars that do not fit the classical system, such as class D for white dwarfs and classes S and C for carbon stars (Karttunen et al., 2003; Henning, 2010).

All stars that achieve thermonuclear equilibrium reactions in the ZAMS stage enter the main sequence, but differ in its evolutionary pathways. By establishing the stellar mass as a differentiating factor, the energy transport processes and production mechanisms vary from one class to another. Therefore, low-mass stars ($M_* < 1.2\ M_\odot$) evolve to become brighter and more blue, as more massive stars evolve into a brighter state with a decrease in temperature, except during the very fast overall contraction phase (Gallart et al., 2005).

Fig. 1.8 shows that most of the stars occupy the region in the diagram along the main sequence. Main sequence is the evolutionary stage in which the energy released by the burning of hydrogen in

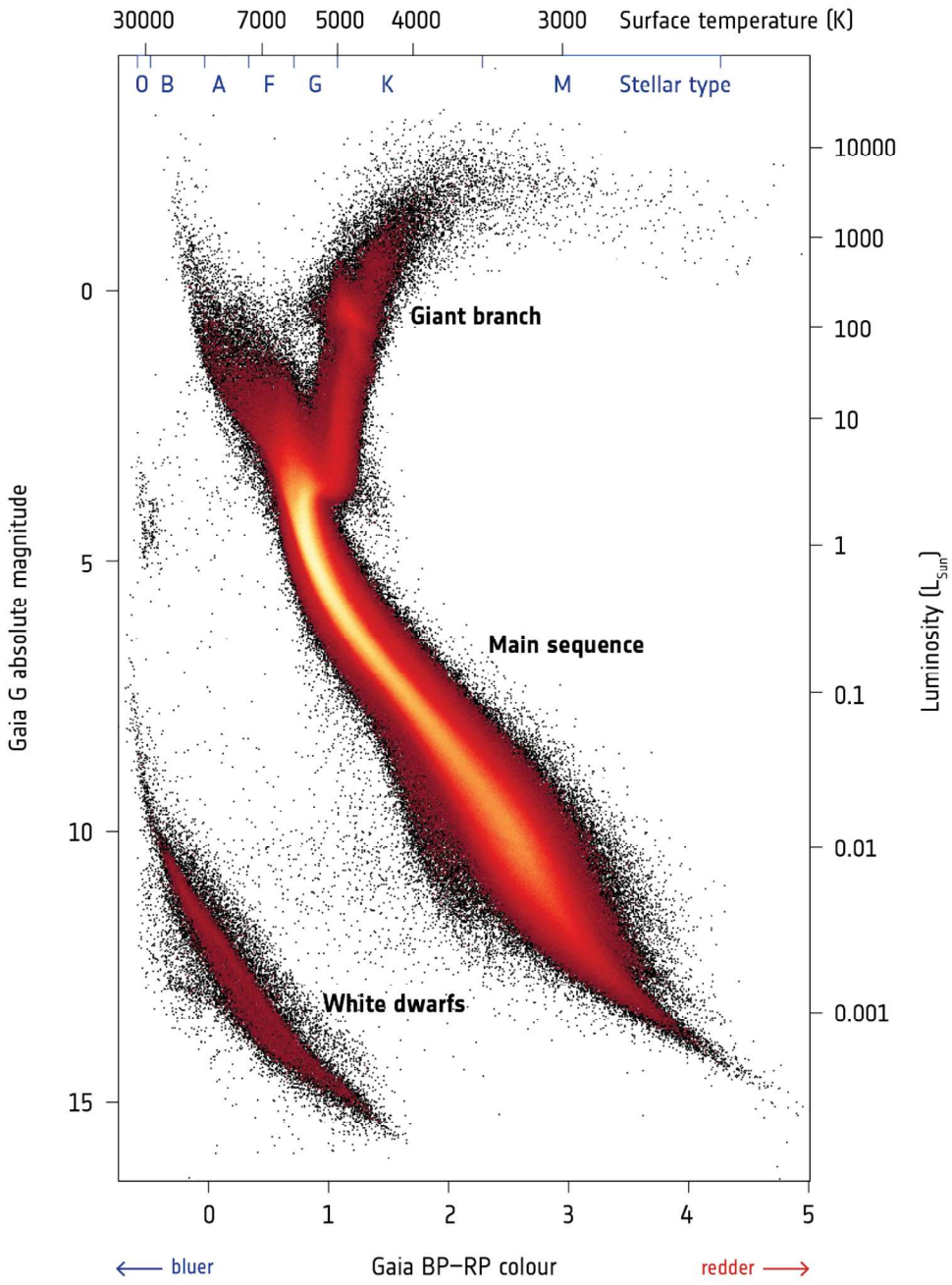

Figure 1.8: Hertzsprung-Russell diagram, obtained by a selection of stars in Gaia's second release catalogue. Credits: ESA, Gaia and DPAC.

the stellar core is the only source of energy (mainly proton-proton chain and CNO cycle). During this stage, the star is in stable equilibrium, and its structure changes only because its chemical composition is gradually altered by the nuclear reactions. Thus, the evolution takes place on a nuclear time scale, which means that the main sequence phase is the longest part of the life of a star. The main sequence phase ends when hydrogen is exhausted at the nucleus. The giant phase star then settles in a state in

which hydrogen is burning in a shell surrounding a helium core. This transition takes place gradually in lower and intermediate mass stars ($M_* < 2.3\ M_\odot$), giving rise to the Subgiant Branch in the HR diagram, while the upper main-sequence stars make a rapid jump at this point (Karttunen et al., 2003).

The evolution that follows core helium burning depends significantly on the stellar mass (Karttunen et al., 2003). It determines how high the central temperature can become and also the degree of degeneracy, when heavier nuclear fuels are ignited. When the central helium supply is exhausted, helium will continue to burn in a shell, while the hydrogen burning shell is extinguished. In the HR diagram the star will move towards lower effective temperature and higher luminosity. This phase is quite similar to the previous red giant phase of low-mass stars, although the temperatures are slightly hotter. For this reason it is known as the asymptotic giant branch, AGB (Fig. 1.8). After the early phase, when the helium shell catches up with the extinguished hydrogen shell, the AGB star enters what is known as the thermally pulsing phase, with hydrogen and helium shells burning in an alternate fashion. A configuration with two burning shells is unstable, and in this phase the stellar material may become mixed or matter may be ejected into space in a shell, like that of a planetary nebula (Karttunen et al., 2003).

Planetary nebulae (PNe) are atomic and molecular gas shells – both neutral and ionized – around small hot stars. Instabilities developed in the helium burning stage leads to stellar pulsations with a high rate of mass loss and eventually a violent expulsion from the stellar atmosphere. In the latter case, a gas shell expanding at 20–30 km s^{-1} will be formed around the core of the original star, whose temperatures reach 5×10^4 to 1×10^5 K. The expanding gas in a planetary nebula is mainly ionized by the ultraviolet radiation of the central star. Typically, the spectrum of a PNe contains many of the same bright emission lines as those of an HII region, as well as emission from grains and molecules, such as polycyclic aromatic hydrocarbons (PAH), which are formed in the AGB phase (Gallart et al., 2005; Karttunen et al., 2003).

1.1.2.2 Planetary Nebula I: BD+30^{o}3639

BD+30^{o}3639 (Fig. 1.9) or Campbell's star, is a young planetary nebula (PN), with an estimated dynamical age of 800 yr (Li et al., 2002; Freeman and Kastner, 2016). It is located at a distance of 1.2 kpc (Li et al., 2002; Yu et al., 2009) in the direction of the constellation of Cygnus (Ra= $19^h34^m45.2^s$, Dec= $+30^o30'58.9$"). This object was observed many times with different telescopes and surveys. In fact, BD+30^{o}3639 is one of the first sources together with NGC 7027 where the emission bands

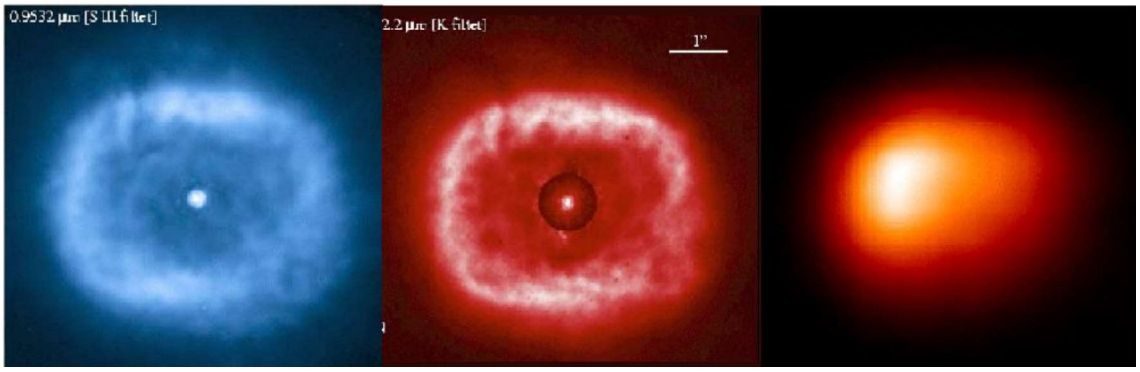

Figure 1.9: The BD+30^{o}3639 planetary nebula. Credits: optical (left): NASA and J. Harrington et al.; infrared (middle): UH, IoA and Gemini; X-ray (right): NASA, RIT, and Kastner et al.

attributed to polycyclic aromatic hydrocarbons (PAHs) in the IR were identified (Allamandola et al., 1989; Bernard et al., 1994; Tielens, 2008; Yang et al., 2017a). The first identifications in the middle infrared (mid-IR) of bands attributed to PAHs at 3.3 3.4 5.7 6.2 7.7 8.6 and 11.6 μm were done from observations of this source made by the telescope Mount Lemmon Arizona (Allamandola et al., 1989) and the CFH Telescope in Hawaii (Bernard et al., 1994). Later, the Infrared Space Observatory (ISO) confirmed that the dust emission features of BD+30^{o}3639 can be attributed to PAHs mixed to carbonaceous and silicate dust, which are all spatially coincident (Persi et al. 1999, see Fig. 1.9, middle panel). Matsumoto et al. (2008), using 8.8, 9.7, 10.5, 11.7, 12.4 μm medium band filters and 8.6, 11.2, and 12.8 μm narrow band filters, revealed a rectangle structure, boxier than previously observed in the mid-IR. These features allowed estimations of the dynamical age for the silicate dust shell to be 4300$\pm$740 yr and the age of the amorphous carbon shell to be 2800$\pm$580 yr (Guzman-Ramirez et al., 2015). These ages suggest that it took $\sim$1500 yr for the central object to make the transition from a Wolf-Rayet O-rich (WO) to a Wolf-Rayet C-rich (WC) star. The analysis by Guzman-Ramirez et al. (2015) also suggests that, while the age of the ionized nebula is $\sim 10^3$ yr, the dusty components were ejected more than twice as long ago (Freeman and Kastner, 2016).

After its first detection using the Röntgen Satellite (ROSAT), BD+30^{o}3639 has been known as the X-ray-brightest PN. From inside its $\sim$4" diameter optical shell (Fig. 1.9, left panel), the central star of BD+30^{o}3639 shows an extended emission (Fig. 1.9, right panel) in soft X-rays (Kastner et al., 2001; Murashima et al., 2006; Yu et al., 2009) with a luminosity of 8.60×10^{32} erg s^{-1} (Yu et al., 2009) and a column density of $N_H = 2.4 \times 10^{21}$ cm^2 (Yu et al., 2009). The X-ray emitting plasma presents high abundance ratios of elements such as Ne and K – different than solar abundances – and a broad spectral band, probably attributed to a blend of C, N, and O lines, subsequently detected with

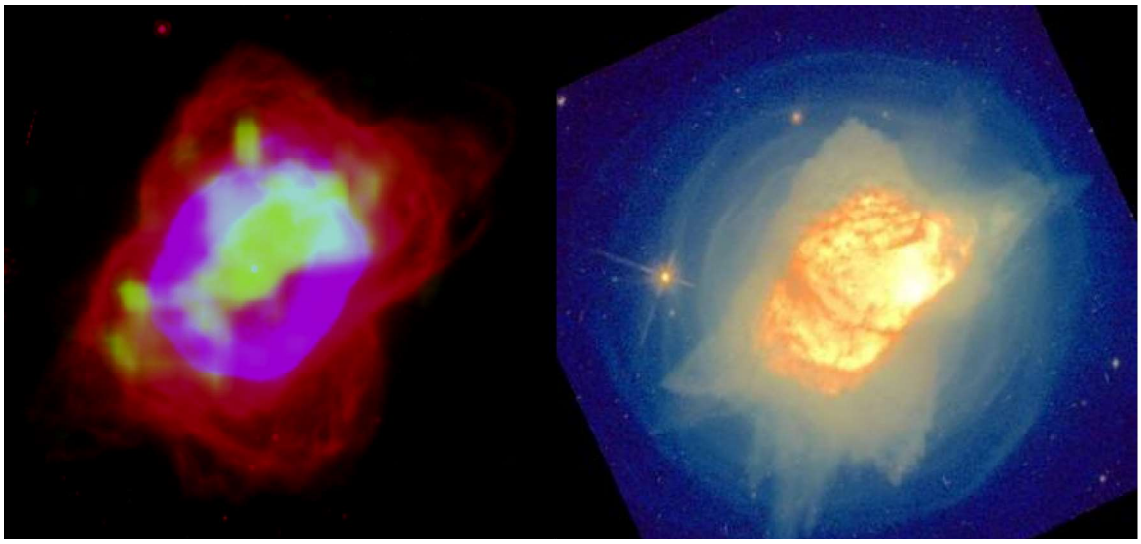

Figure 1.10: The NGC 7027 planetary nebula. Left: Chandra X-ray image (green) is overlaid on the Hubble infrared image (red and blue). Credits: IR: NASA and STScI; X-ray: NASA, RIT and J.Kastner et al. Right: Hubble optical image. Credits: NASA and STScI.

Chandra (Kastner et al., 2001; Guerrero et al., 2000; Maness et al., 2003; Murashima et al., 2006).

1.1.2.3 Planetary Nebula II: NGC 7027

NGC 7027 is a young carbon-rich planetary nebula located in the Cygnus constellation at a distance of 880 pc (Ra= $21^h7^m1.7^s$, Dec= $+42^o14'11''$)(Masson, 1986; Latter et al., 2000; Bernard-Salas et al., 2001; Kastner et al., 2001; Hasegawa and Kwok, 2001, 2003; Wesson et al., 2010). It has a differentiated structure with an ionized elliptical envelope lying at the center of an extended molecular envelope. Intense lines of highly ionized Ne atom were observed in infrared spectra obtained by ISO-SWS of NGC 7027 (Bernard-Salas et al., 2001) and in X-ray spectra taken by the Chandra X-Ray Observatory (Kastner et al., 2001). At the interface between the cold molecular region and the ionized front, there is the photodissociation region (PDR) where chemistry is controlled by the penetrating UV and X-rays photons from the central star (Lau et al., 2016; Latter et al., 2000).

The morphology of NGC 7027 (Fig. 1.10) presents three outflows in the HII region interacting with the outermost regions (Cox et al., 1997; Santander-García et al., 2012; Lau et al., 2016). The variations in the radiative flux of the object provide a non-equivalent mixture of chemical species within the outer layers, thus providing environments with different characteristics within the same nebula (Arnoult et al., 2000). Consequently, it stimulates the formation and destruction of a wide variety of molecular species detected in both neutral and ionized states, such as: H_2, CO, CH_3^+, CH_2^+,

CH^+, c-C_3H_2, PAHs, and aliphatic hydrocarbons (Hasegawa et al., 2000; Hasegawa and Kwok, 2001; Lau et al., 2016).

The physical properties of the central star, a very hot white dwarf with a temperature around 2×10^5 K and an estimated luminosity of 7700 $L_\odot$ (Latter et al., 2000), promote a chemically rich medium. This implies that different reaction mechanisms could be taking place, both in the gas phase and on the surface of grains. Ultimately, such environment could uphold the formation of complex ions and organic molecules, among them PAHs (Herbst and van Dishoeck, 2009).

1.1.2.4 Planetary Nebula III: NGC 5315

NGC 5315 is a planetary nebula with a Wolf-Rayet C-rich type central star with a temperature around 2×10^6 K (Montez Jr. et al., 2015; Kastner et al., 2008). It is located at a distance of 2.5 kpc in the constellation Circinus (Ra= $13^h53^m56.9^s$, Dec= -66^{o}30$'$50.9", Marcolino et al. 2007; Kastner et al. 2008; Ali et al. 2015, with a dynamic age of around 1000 yr (Ali et al., 2015). NGC 5315 has an X-ray emission profile with a luminosity of 2.6×10^{32} erg s^{-1} and a column density of $N_H = 2.29 \times 10^{21}$ cm^2 (Kastner et al., 2008). The source also shows a compact multipolar (4" in the optical range) morphology, with PAH features identified with the PHOTo-polarimeter of the Infrared Space Observatory (ISO-PHOT, Kastner et al. 2008; Marcolino et al. 2007; Monteiro and Falceta-Gonçalves 2011; Szczerba et al. 2001).

Estimations from observations point that the X-ray emission of NGC 5315 comes from a compact and delineated central cavity of $\sim$1" radius (Fig. 1.11), revealing that this object is one of the most luminous "hot bubble" X-ray sources detected (Kastner et al., 2008).

1.1.2.5 Planetary Nebula IV: NGC 40

NGC 40 was discovered by William Herschel in 1788, and is also known as *Bow-Tie Nebula* and *Caldwell 2*. It is located in the northern part of the Cepheus constellation at a distance of 1.1 kpc (Ra= $00^h13^m1.01^s$, Dec= +72^{o}31$'$19.1"). With a dynamical age of 4000 yr (Monteiro and Falceta-Gonçalves, 2011; Ali et al., 2015; Freeman and Kastner, 2016), NGC 40 is a well-studied object, classified as a low-excitation PN. The central star of NGC 40 is a WC-type. Several imaging studies revealed a bright (slightly elliptical) core, a large halo, and filamentary structures (Monteiro and Falceta-Gonçalves, 2011). The source presents a broad PAH feature at 11.3 μm observed by ISO (Delgado-Inglada and Rodríguez, 2014) and emission in soft X-rays with a luminosity of 4.0×10^{31}

Figure 1.11: The NGC 5315 planetary nebula. Hubble Optical Image, credits: NASA,ESA,STScI,AURA and The Hubble Heritage Team.

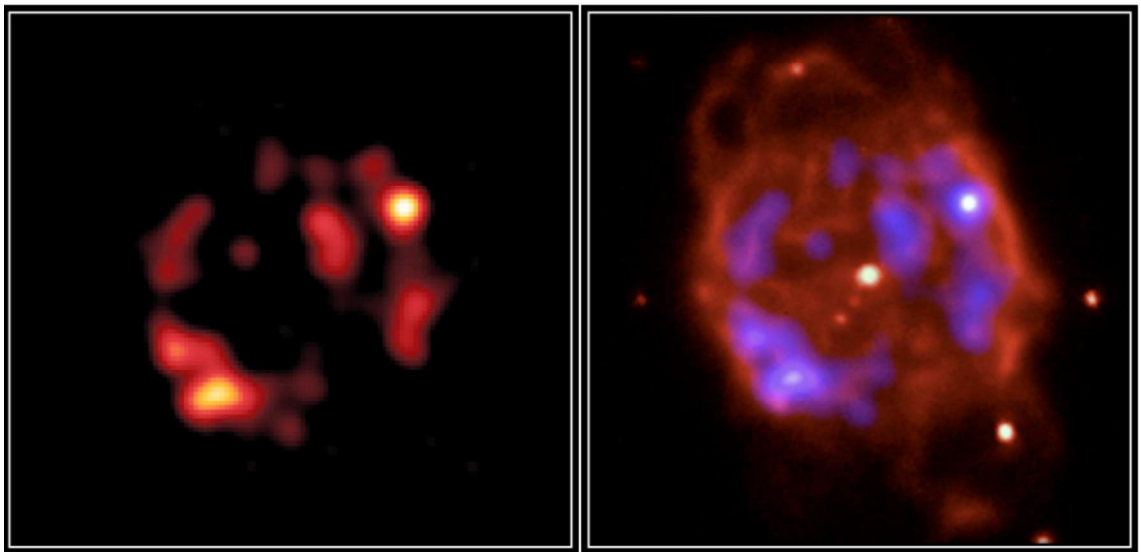

Figure 1.12: The NGC 40 planetary nebula. Left: Image in the X-rays taken from the Chandra telescope. Right: Composite image with X-ray (blue) and NOAO Optical (red). Credits: X-ray: NASA, CXC, RIT and J.Kastner and R.Montez.; Optical: NSF, AURA, NOAO and WIYN.

erg s^{-1} (Kastner et al., 2008) and column density of $N_H = 2.2 \times 10^{21}$ cm^2 (Montez Jr. et al., 2015).

Having 40" of diameter in the optical images, NGC 40 appears as a brightened shell, with a bright rim that is interrupted by fainter protrusions to the north-northeast and south-southwest (Monteiro and

Falceta-Gonçalves, 2011). The detection of soft X-rays in the range of 0.3–1.0 keV energy reveals that the emission in the NGC 40 arises from an annular region (Fig. 1.12-left) around the central star, following the same overall surface brightness distribution as the ones in the optical and near-infrared. Fig. 1.12-right shows an X-ray (blue)/optical (red) image of the hot gas around the central star of NGC 40 (Monteiro and Falceta-Gonçalves, 2011; Montez and Kastner, 2018).

NGC 5315 and NGC 40 are planetary nebulae included in the Cycle 5 of Chandra observations (Montez Jr. et al., 2015; Kastner et al., 2008).

1.2 Chemical Composition of Interstellar and Circumstellar Media

In the Universe, chemistry begins with primordial nucleosynthesis and continues in the stars. The formation of cosmic dust is generally associated with the most evolved stages of the stars (AGB phase). With some exceptions, the elements of the photosphere of the stars reflect the pattern of the abundances present in the parent cloud, but during the stages subsequent to the main sequence, variations in these abundances may occur for two mainly reasons (Henning, 2010):

I. In low- and intermediate-mass stars, convective mixing between the nuclear burning interior and the stellar photosphere carries some quantities of the freshly synthesized heavy nuclei and small molecules from the centre to the surface. In rapidly rotating hot stars some mixing from the central region to the photosphere occurs by circulation currents.

II. The dust formed in highly evolved stars has a composition considerably more enriched than standard cosmic element abundance.

These two situations are important for the enrichment of both the interstellar and circumstellar media, the winds associated with the stars provide the necessary material for the formation of refractory grains. These grains will be the seed for the formation of a wide variety of chemical species, formed by the synthetic routes in condensed phase on the grain surface and/or directly in the gas phase.

1.2.1 Gas Phase Chemical Reactions

Gas phase collisions are fundamental to the physics and chemistry of the interstellar medium (Draine, 2011). Collisions excite atoms and molecules, eventually resulting in emission of photons

from the ISM. They are also responsible for chemical reactions, including both formation and destruction of chemical species.

Chemical processes in the gas phase begin when the molecular hydrogen, H_2, is released into the interstellar medium. Inside dense molecular cores, the temperature is low enough ($T_{gas} \approx T_{grain} \approx$ 10 K) and the density high enough that exothermic reactions are favored. The only possible reactions in practice are those with low activation energies between reagents and products. Reactions involving ions and neutral species (Table 1.1, ion-neutral reactions) often obey this restriction and dominate the chemistry in these astrophysical environments (Herbst and van Dishoeck, 2009). However, there are other types of reactions that can be carried out in the gas phase. The different types of possible reactions in the interstellar medium are summarized in Table 1.1.

Neutral-neutral reactions. The reaction between two neutral species can be formally written as:

$$A + B \xrightarrow{k} C + D \tag{1.19}$$

where A and B are the reactants, while C and D are the products. We can calculate the reaction rate Γ by the following equation:

$$\Gamma = \frac{d[C]}{dt} = -\frac{d[A]}{dt} = k n_A n_B \tag{1.20}$$

where [A], [B] and [C] are the concentrations of species A, B and C, respectively; k is the kinetic coefficient (cm^{-3} s^{-1}); and n_R is the numerical density of the reagents. The kinetic coefficient k is specific for each reaction. In this case, for a second order reaction (two reagents are involved), the reaction rate Γ is proportional to the product of the concentrations (numerical densities) of the two species (Tielens, 2005; Draine, 2011).

Photon-induced processes. The interaction of the interstellar radiation field with molecular species can lead to the photoionization and/or the photodissociation of the latter. This process is modelled by the following reaction:

$$AB + h\nu \xrightarrow{k} A + B \tag{1.21}$$

and their reaction rate Γ and kinetic coefficient k have the following relation:

$$\Gamma = \frac{d[A]}{dt} = -\frac{d[AB]}{dt} = k n_{AB} \tag{1.22}$$

Table 1.1: Examples of selected gas phase reactions. Adapted from Smith (2011).

Type of mechanism	Example
Gas-grain	$H + H + grain \rightarrow H_2 + grain$
Cosmic-rays	$H_2 + cr \rightarrow {H_2}^+ + e^-$
Cation-neutral	${H_2}^+ + H_2 \rightarrow {H_3}^+ + H$
Anion-neutral	$C^- + NO \rightarrow CN^- + O$
Radiative associations (ion)	$C^+ + H_2 \rightarrow {CH_2}^+ + h\nu$
Associative detachment	$C^- + H_2 \rightarrow CH_2 + e^-$
Chemi-ionization	$O + CH \rightarrow HCO^+ + e^-$
Neutral-neutral reactions	$C + C_2H_2 \rightarrow C_3H + H$
Radiative association (neutral)	$C + H_2 \rightarrow CH_2 + h\nu$
Dissociative recombination	$N_2H^+ + e^- \rightarrow N_2 + H$
Radiative recombination	$H_2CO^+ + e^- \rightarrow H_2CO + h\nu$
Anion-cation recombination	$HCO^+ + H^- \rightarrow H_2 + CO$
Electron attachment	$C_6H + e^- \rightarrow C_6H^- + h\nu$
External photo-processes[a]	$C_3N + h\nu \rightarrow C_2 + CN$
Internal photo-processes[b]	$CO + h\nu \rightarrow C + O$

[a] External photo-processes are those induced by the interstellar radiation field.

[b] Internal photo-processes are induced by radiation generated in dark clouds by the interaction of molecules, especially H_2, with cosmic rays.

The kinetic coefficient k (s^{-1}) represents the number of photoionized or photodissociated molecules per second. This value depends on the photon flux in the astrophysical source and other parameters, such as the cross-section of the each species (see Chapter 2). However, it is necessary to take into account the attenuation flux due to the presence of interstellar grains and dust. Therefore, for UV photoionization reactions, we can calculate the kinetic coefficient as:

$$k = \alpha e^{-\gamma A_V} \tag{1.23}$$

where α represents the rate without UV attenuation, A_V is the extinction coefficient in the optical range and γ is the factor that describes attenuation by UV photoabsorption in interstellar grains and dust.

Cosmic-Ray ionization. In dense ISM regions, cations are formed mainly by cosmic-ray bombardment and are modified by secondary reactions. ${H_2}^+$ ions react rapidly with H_2 to produce ${H_3}^+$. Because H_2 has a rather low proton affinity, ${H_3}^+$ is the hydrogen-bearing moiety that most effectively reacts with other species, notably C, O and N, in the following manner (Smith, 2011):

$$H_2 + cr \rightarrow {H_2}^+ + e^- \tag{1.24a}$$

$$H_2{}^+ + H_2 \rightarrow H_3{}^+ + H \tag{1.24b}$$

$$H_3{}^+ + X \rightarrow H_2 + XH^+ \tag{1.24c}$$

where X can be atoms or even molecules, such as CO. For the ionization of H_2 molecules into dense regions, the cosmic-ray flux should have a rate of $t \sim 1-5 \times 10^{-17}$ s^{-1}. In addition to ionization, cosmic-rays can also lead to the formation of UV photons from a mechanism in which the secondary electrons excite H_2, and the photon is subsequently emitted by relaxation processes. These secondary photons are a source of ionization and destruction of molecules despite high visual extinction (Herbst and van Dishoeck, 2009; Smith, 2011).

Molecular species formed from ion-neutral reactions tend to be unsaturated because hydrogenation reactions have a high energy barrier. For example, in the gas phase, the transfer of H in $C_nH_m^+$ hydrocarbon chains with n > 3 cannot produce ions with m > 2. In addition, once the molecular cations are formed, the processes of dissociative recombination, such as $C_nH_2{}^+ + e^- \rightarrow C_nH^+ + H$, produce neutral fragments that tend to be more unsaturated than the original ionic structure (Smith, 2011). Therefore, ion-neutral reactions with C^+, C or C_2H_2 and neutral-neutral reactions with carbon insertion in molecular clouds produce long and unsaturated (polyynic) carbon chains, such as C_4H, C_6H and C_8H (Sun et al., 2015). H transfer reactions between molecular ions of the type $X^+ + H_2 \rightarrow XH^+ + H$, or even hydrogenation reactions, are endothermic and, therefore, they are not favored at low temperatures (Herbst and van Dishoeck, 2009; Smith, 2011). Consequently, this type of reaction requires the presence of catalytic environments to reduce the excitation barriers, such as ices or grain surfaces.

1.2.2 Condensed Phase Chemical Reactions

At temperatures low enough, atoms and molecules tend to freeze out from the gas phase onto dust grains. The freeze-out temperature is directly related to the binding energy of the molecular species with the grain surface. In practice, CO freeze out occurs below 20K, whereas H_2O freeze out already at 100K. Sublimation at 10K can only occur efficiently for weakly bound species, such as H, H_2 and He. The accretion of atoms and molecules on a solid surface can occur through two distinct processes (Herbst and van Dishoeck, 2009): physisorption (involving van der Waals forces) and chemisorption

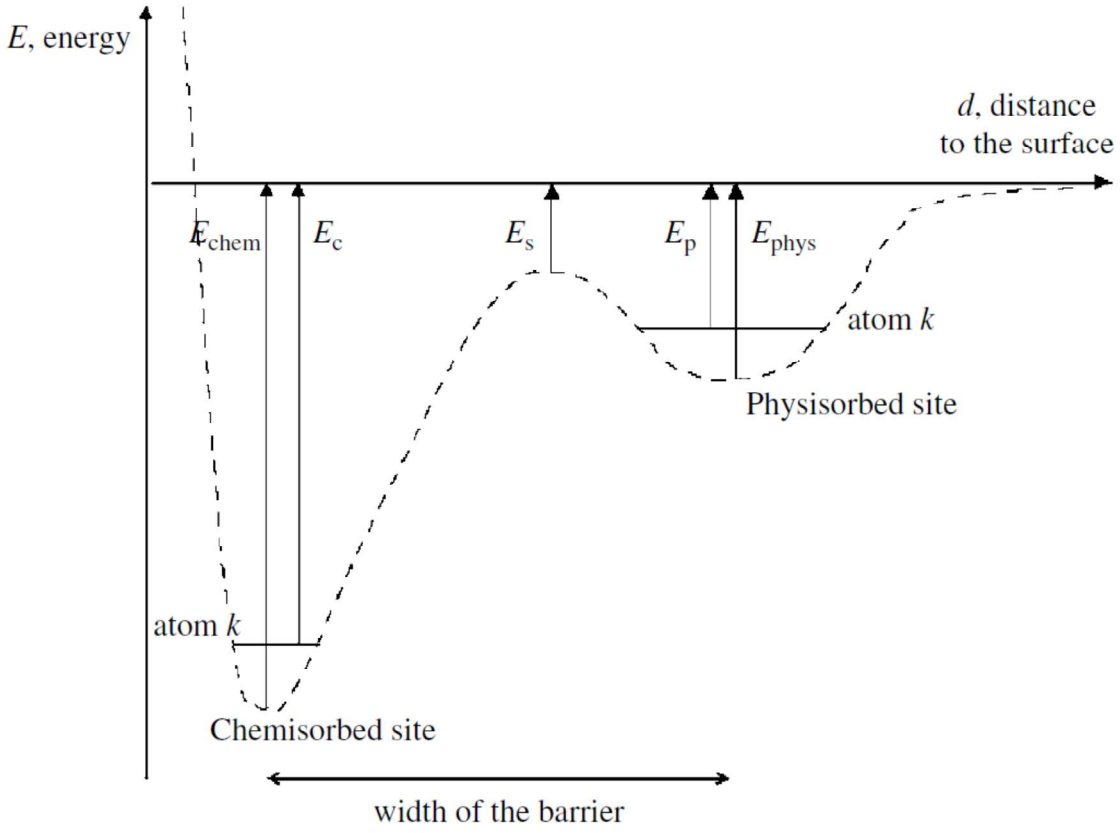

Figure 1.13: Scheme of the adsorbate-surface interaction. The physisorbed site is due to van der Waals interactions (binding energy: E_{phys}). The chemisorbed site involves valence shell interaction (binding energy: E_{chem}). The actual binding energies E_p and E_c take the zero-point energy into account. The two bonding sites are separated by a saddle point with energy E_s. Taken from Tielens (2005).

(through valence shell interactions). A gas phase species approaching a surface will feel at a large distance a weak attraction due to van der Waals forces. These are due to mutually induced dipole moments in the electron shells of the gas phase species and the atoms in the surface. At short range, forces associated with the overlap of the wave functions of the approaching species and the surface atoms lead to much stronger binding (Tielens, 2005).

The interaction potential depends not only on the distance to the surface but also on the location on the surface. For example, on a perfect surface (crystal) the process experiments a regular variation of the potential energy across the material surface with an array of wells evenly spaced in between the surface atoms (Fig. 1.13). In an irregular material, this regularity is lost, and the reaction curve resembles a mountainous configuration with peaks associated with the surface atoms and valleys representing the physisorbed and the chemisorbed wells.

When adsorbed species (adsorbate) accumulate on the surface of an interstellar grain or dust, processes or reactions are stimulated, thus forming astrophysical ices (Herbst and van Dishoeck, 2009).

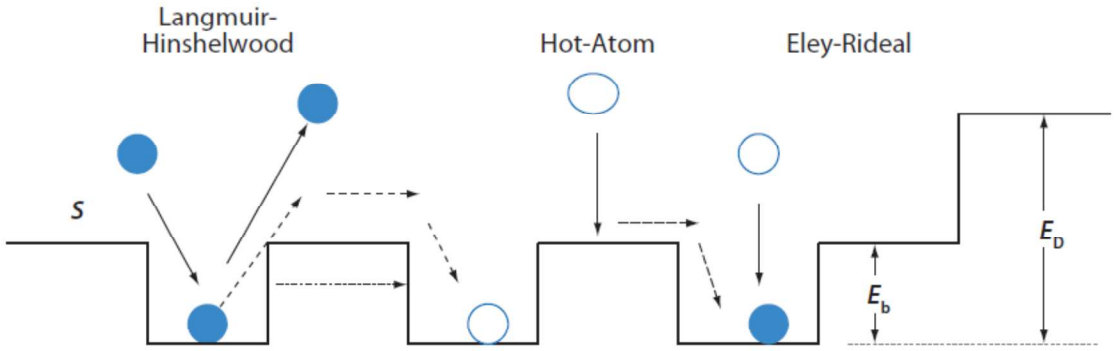

Figure 1.14: Scheme of some mechanisms for surface reactions on a regular grain surface. S is the sticking efficiency of a gas phase species, E_D is the binding, or desorption, energy of the adsorbate to the surface, and E_b is the barrier from one site to an adjacent one. Taken from Herbst and van Dishoeck (2009).

The exact processes responsible for the formation of molecular species on dust grain are subject of intense theoretical work and modelling and laboratory experiments. Recent works (Wakelam et al., 2010; Cuppen et al., 2017) stress the difference of reactivity between the surface layers and the bulk of the grain mantles. In these substrates (ice) the main physisorption reaction mechanisms on the surface are: diffusive, or Langmuir-Hinshelwood mechanism; the hot-atom mechanism; and the Eley-Rideal mechanism. All of them are represented in the scheme of Fig. 1.14, where the processes are assumed to happen on a regular surface with a periodic potential. In this model surface, accretion occurs onto the binding sites, which are regions of potential minimum energy, and are given by the sticking efficiency, S. On the other hand, desorption can occur if the desorption energy, E_D, is reached, either by sublimation (thermal evaporation) of by non-thermal processes. In the Langmuir-Hinshelwood mechanism, diffusion is obtained by tunneling over the barrier E_b between binding sites. Once located in the same minimum, absorbates can react by sticking together, with the excess energy being absorbed by the grain. In the hot-atom mechanism, a gas phase species lands on a surface acquiring an increase in kinetic energy before its thermalization, favoring the collisions of the species with the adsorbate (Tielens, 2005; Herbst and van Dishoeck, 2009). Finally, in the Eley-Rideal mechanism physisorption is produced by the interaction of a gas phase species that lands on an adsorbate and reacts with it.

Unlike the highly unsaturated molecules produced in the gas, species formed on the surface of the ice are saturated. The Langmuir-Hinshelwood mechanism describes the process where the activation barriers are low. Therefore, the atomic hydrogen of the gas accumulates on the surface and diffuses rapidly, acting as a very efficient reagent on ice surfaces. In the different astrophysical environments

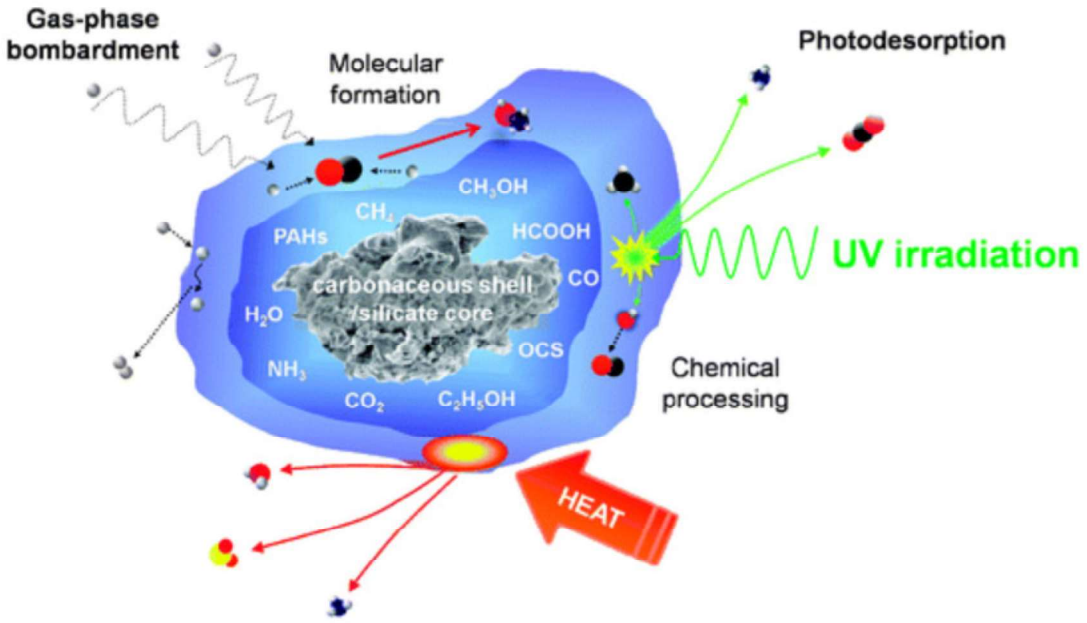

Figure 1.15: Schematic picture of interstellar ice processing. The hydrogenated species labelled within the inner layer are formed by Langmuir-Hinshelwood mechanism. Some of the main constituents usually detected in interstellar ice analogues are also depicted. Adapted from Burke and Brown (2010).

(comets, asteroids, clouds, etc.), water ices are the most abundant. These ices are produced by the sequential hydrogenation of O atoms accreted on the surface of a grain: $O \rightarrow OH \rightarrow H_2O$. This reaction is just an example of hydrogenation processes that can become much more complex (Fig. 1.15). For example, the formation of ammonia (NH_3), methane (CH_4), and methanol (CH_3OH), as well as the hydrogenation of polycyclic aromatic hydrocarbon species (PAHs), are described by the Langmuir-Hinshelwood mechanism (Henning, 2010; Herbst and van Dishoeck, 2009; Tielens, 2005).

In the more diffuse phases of the ISM, the grain-surface chemistry and ice-mantle processing are limited due to the unshielding of UV radiation, which drives photodesorption of adsorbed molecules (Tielens, 2005). On the other hand, in dense cloud cores, which are shielded from UV photons, the composition of the accreting gas dictates the fate of the condensed phase reaction network. In such regions, hydrogen is mainly in the molecular form (H_2), but cosmic-ray ionization is responsible for introducing a low level of atomic hydrogen. Assuming that each cosmic-ray ionization of H_2 eventually delivers two H atoms through accretion onto grains, the numerical density of H, n(H), is given by:

$$n(\mathrm{H}) = \frac{2.3\zeta_{cr} n(\mathrm{H_2})}{k_d} \simeq 2\ \mathrm{cm^{-3}} \tag{1.25}$$

where ζ_{cr} is the ionization rate by cosmic rays and k_d is the accretion rate, which is estimated as $3 \times 10^{-17} n$ s^{-1} independent of the environment density. Given that oxygen will predominantly exist in the atomic form, carbon as CO and N as N_2, the composition of the ice sheets is largely determined by the reaction between H, O and CO, with traces of C and N. The abundance of H dominates these environments, consequently the abundance of hydrogenated species will be high (Tielens, 2005; Burke and Brown, 2010).

1.2.3 Complex Organic Molecules (COMs)

Laboratory experiments suggest that the UV and the cosmic ray irradiation of H_2O interstellar ices could play an important role in the formation of more complex species (Burke and Brown, 2010). Atomic carbon can be hydrogenated on grain surfaces through sequential atomic H incorporation, which is an important formation pathway of interstellar hydrocarbons. Hydrocarbon radicals in this route can react with atomic O and N to form organic molecules with heteroatoms, such as CH_3OH and HCN. In the ISM, atomic C is only abundant during the first diffuse phases of a cloud – after that most of the accreted carbon in molecular clouds is in the form of CO and its reaction with H proceeds efficiently. The radicals formation from HCO leads to the formation of other C-bearing species that can react with atomic C, N, or O. (Fig. 1.16) show various ways where CO can efficiently be converted into complex organic species (Tielens, 2005).

Gas phase pathways have also been proposed for the formation of COMs in star forming regions, both in hot cores and in hot corinos and shock regions (Herbst and van Dishoeck, 2009). Determination of the relative efficiencies of distinct proposed pathways (Kaiser et al., 2015; Öberg, 2016; Biczysko et al., 2018), as well as the identification of the most stable isomers of a given molecular formula (Lattelais et al., 2009), requires a large effort from chemists. Most likely, the processes at work depend on the actual physical conditions (density, temperature) in the astrophysical objects of study.

1.2.4 Deuteration

It is important to mention that in young stellar objects there may be a high rate of deuterated species (Marcelino et al., 2005; Roueff et al., 2005; Ceccarelli et al., 2007; Emprechtinger et al., 2009; Ceccarelli et al., 2014; Vastel et al., 2014; Codella et al., 2012; Lefloch et al., 2018). The formation of deuterated species on grain surfaces largely follows from the reaction of accreted atomic D. After

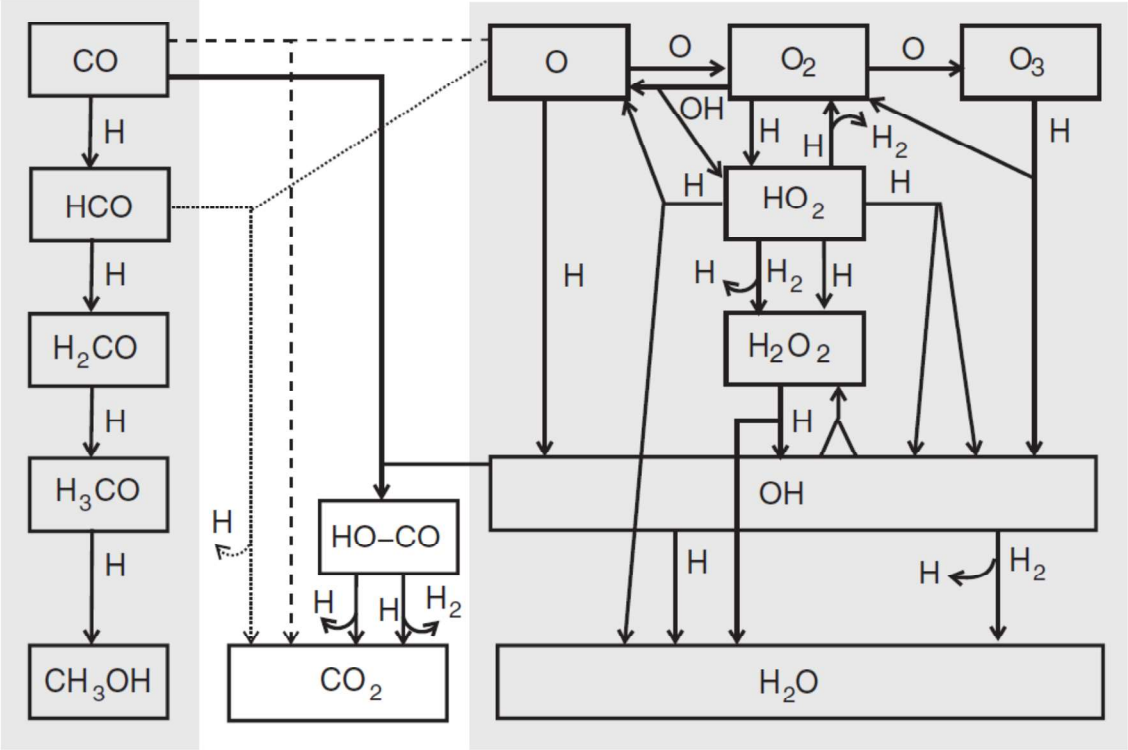

Figure 1.16: Scheme of the reaction pathway of hydrogenation and oxidation of CO on grain surfaces. Adapted from Tielens (2005).

accretion, the chemistry of atomic D on grain surfaces is very similar to that of atomic H. In ices, atomic D is quickly distributed over the surface, and compared to atomic H, deuterium reactions have lower activation energies. Thus, any species that can be hydrogenated on a grain surface can also be deuterated (Linnartz et al., 2011).

1.2.5 Polycyclic Aromatic Hydrocarbons (PAHs)

Polycyclic aromatic hydrocarbons (PAHs, Fig. 1.17) are molecular archetypes that can be classified according to the number of fused benzene (C_6H_6) rings that make up the base structure (Scott, 2015). Neutral and ionized PAHs are detected in astronomical sources through emission bands in the infrared (IR) wavelength range, due to the corresponding molecular vibrations. (Peeters et al., 2002; Tielens, 2008). The main vibrational features of PAHs (Fig. 1.18) comprise the C–H (3.3 μm), C=C (6.2 μm) and C–C (7.7 μm) bond stretching modes, as well as the in-plane (8.6 μm) and out-of-plane (11.3 μm) C–H bond bending modes. From the analysis of such IR bands, PAHs have been observed in a diversity of galactic objects, such as planetary nebulae (Waters et al., 1998; Górny et al., 2001; Ohsawa et al., 2012; Guzman-Ramirez et al., 2014), HII regions (Roelfsema et al., 1996;

Peeters et al., 2002), reflection nebulae (Boersma et al., 2014; Ricca et al., 2018), protoplanetary disks (Ressler and Barsony, 2003; Maaskant et al., 2014; Schworer et al., 2017; Seok and Li, 2017; Taha et al., 2018), among others. PAH IR features contribute to about 10% of the ISM luminosity in the 1-1000 μm range, accounting for a large fraction of the elemental C in star-forming galaxies (Lagache et al., 2004). In addition, their luminosities are well correlated with star formation rates (Peeters et al., 2004; Stierwalt et al., 2014; Alonso-Herrero et al., 2014; Esparza-Arredondo et al., 2018). In view of such remarkable characteristics, continuing research on the formation and stability of PAHs has a key relevance to astrochemistry.

In addition to galactic sources, PAHs have also been observed in a variety of extragalactic objects, such as HII regions in the Magellanic Clouds (Li and Draine, 2002; Vermeij et al., 2002; Oey et al., 2017), local dusty elliptical galaxies (Kaneda et al., 2008), starburst galaxies (Brandl et al., 2006), submillimeter galaxies (SMGs) (Menéndez-Delmestre et al., 2009), ultra-luminous IR galaxies (ULIRGs) (Desai et al., 2007) and in the circumnuclear regions of Active Galactic Nuclei (AGNs) (Lutz et al., 1998; O'Dowd et al., 2009; Tommasin et al., 2010; Sales et al., 2013; Esquej et al., 2013; Alonso-Herrero et al., 2016). Concerning the latter objects, PAHs have been identified in both Seyfert 1 and Seyfert 2 galaxies (Mazzarella et al., 1994; Deo et al., 2007; Diamond-Stanic and Rieke, 2010; Sales et al., 2013), in low-ionization nuclear emission-line regions (LINERs) (Sturm et al., 2006) and obscured quasars (Martinez-Sansigre et al., 2008).

The most accepted mechanism for the formation of benzene molecule, building block of PAHs, in circumstellar environments is from polymerization of the acetylene molecule (C_2H_2, Fig. 1.19) (Woods et al., 2003). PAH formation pathways are carried out starting from the previous reaction, followed by polymerization from the phenyl ion (ionized benzene, Fig. 1.20, Frenklach and Feigelson 1989; Cherchneff et al. 1992; Carelli et al. 2011; Jones et al. 2011).

Frequently, PAH infrared features are accompanied by bands at 3.4 and 6.9 μm (Zhang and Kwok, 2014), characteristic of C-H and C-C aliphatic bonds. These bands are emitted by hydrogenated PAHs (H_n-PAHs) and by species of PAHs with aliphatic side groups observed in many sources, such as HII regions, interstellar (ISM) and circumstellar mediums (CSM), planetary nebulae (PNe) and galaxies (Tielens, 2008; Li and Draine, 2012; Sandford et al., 2013; Hsia et al., 2016; Simonian and Martini, 2017; Yang et al., 2017b). For example, in the infrared spectra of the well studied planetary nebula NGC 7027, the emission feature 3.3 μm is much more intense than 3.4 μm. The difference between the profile of both bands can be attributed to distinct factors, such as the relative abundances of the

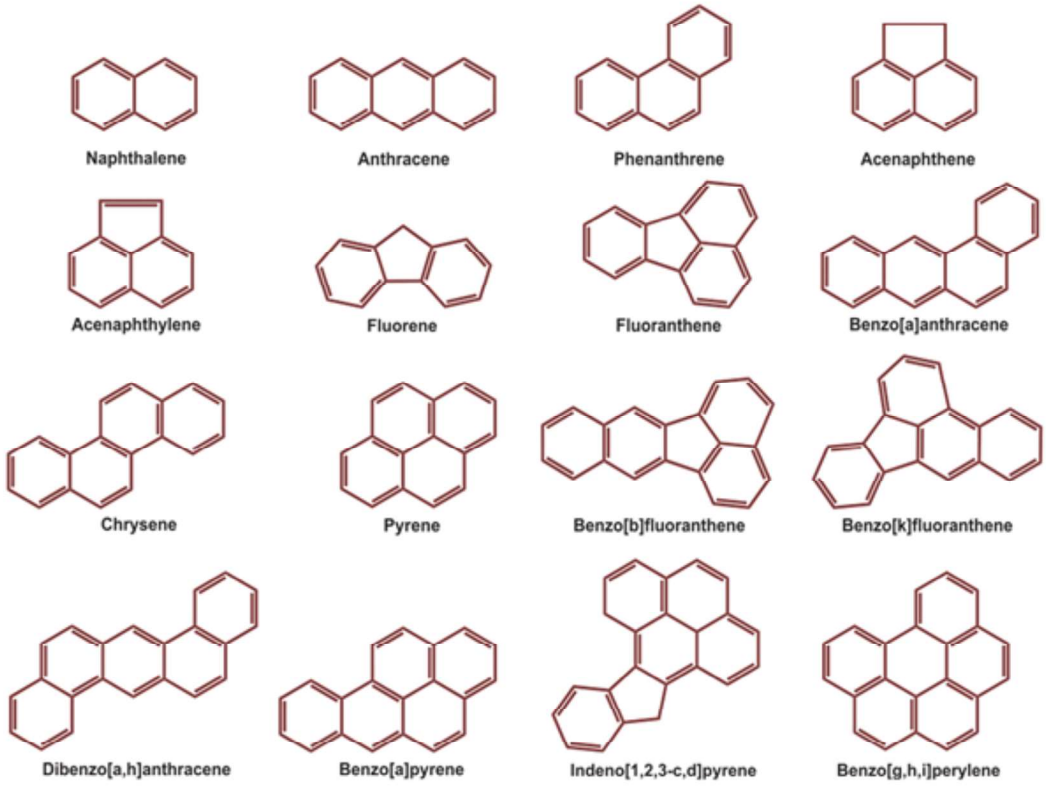

Figure 1.17: Scheme of molecular structure of some representative polycyclic aromatic hydrocarbon molecules. Adapted from Tielens (2005).

aromatic and aliphatic compounds (Tielens, 2008), differences in the oscillator strength values of each transition (Yang et al., 2017b), the average size of the PAH carbon backbone (Le Page et al., 2003; Montillaud et al., 2013), and the evolution stage of the object (Sandford et al., 2013; Steglich et al., 2013).

Currently, the stability of H_n-PAHs and their role as catalysts in the formation of H_2 in different astrophysical environments are of special interest in astrophysics and astrochemistry, and the subject of an intense debate (Reitsma et al., 2014; Gatchell et al., 2015; Cazaux et al., 2016; Wolf et al., 2016). Le Page et al. (2003) studied the hydrogenation and charge state of PAHs in diffuse clouds, and concluded that the size of the PAH influences the stability of highly hydrogenated species. More recently, it was shown that the hydrogenation of the coronene cation, $C_{24}H_{12}^{+\cdot}$, follows a site-selective sequence, leading to the appearance of magic numbers of attached hydrogen atoms (Cazaux et al., 2016). Besides, Reitsma et al. (2014) verified that although the carbon backbone of a super-hydrogenated PAH is locally weakened, its deexcitation by H loss protects the PAH from fragmentation. These findings suggest that the addition of peripheral hydrogen atoms in PAHs could impart a greater stability

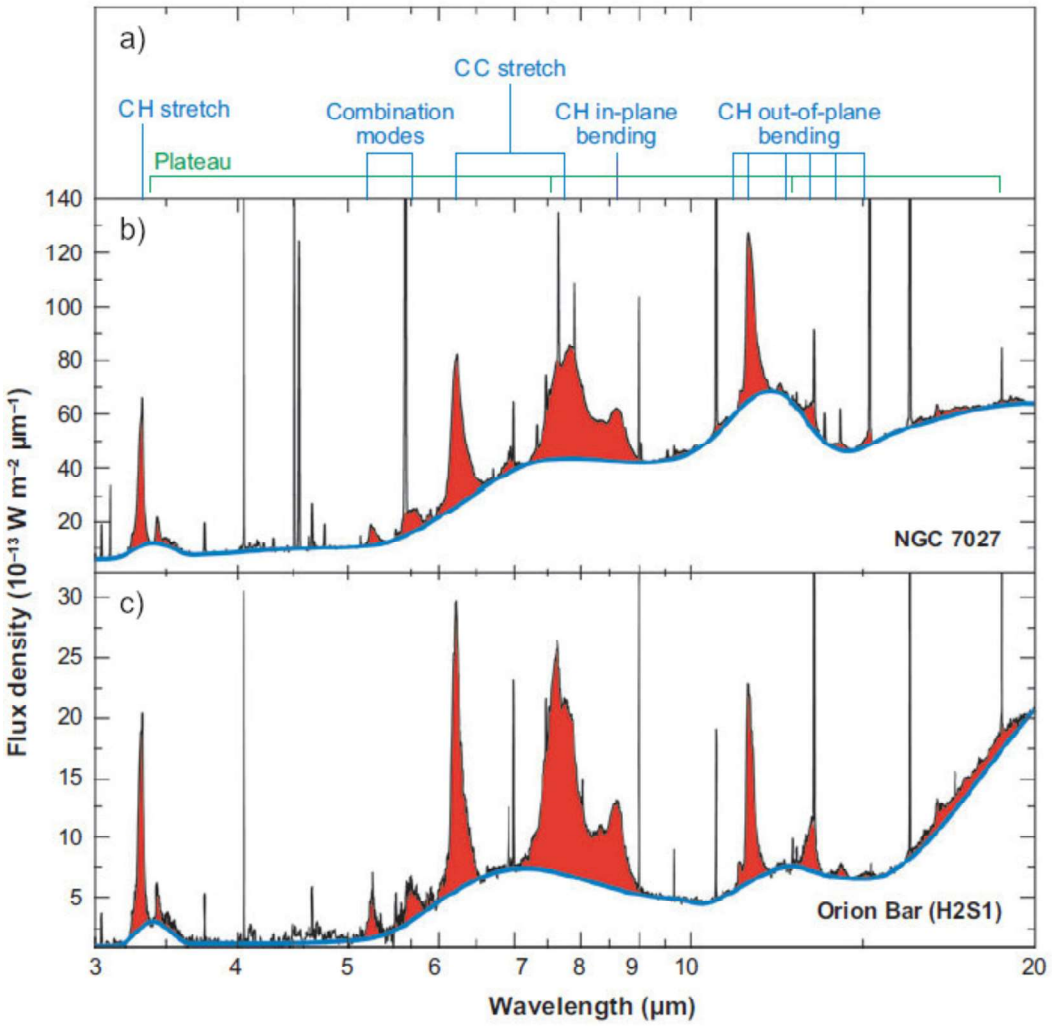

Figure 1.18: a) Label of the vibrational modes of polycyclic aromatic hydrocarbon molecules. b-c) The mid-infrared spectrum of the photodissociation region in the planetary nebula NGC 7027 (b) and in the Orion Bar (c). Adapted from Tielens (2005).

to these molecules in interstellar and circumstellar photodissociation regions (PDR). Gatchell et al. (2015) and Wolf et al. (2016), however, have shown that carbon backbone fragmentation was actually increased in collision and photoinduced experiments with super- and fully-hydrogenated pyrene cations ($C_{16}H_n^+$). Their results, therefore, point out to a failure of the hydrogenation protection mechanism, at least for small H_n-PAHs.

The results obtained in the study of molecular units of PAHs and H_n-PAHs in selected astrophysical environments are discussed in detail in Chapters 4 to 6.

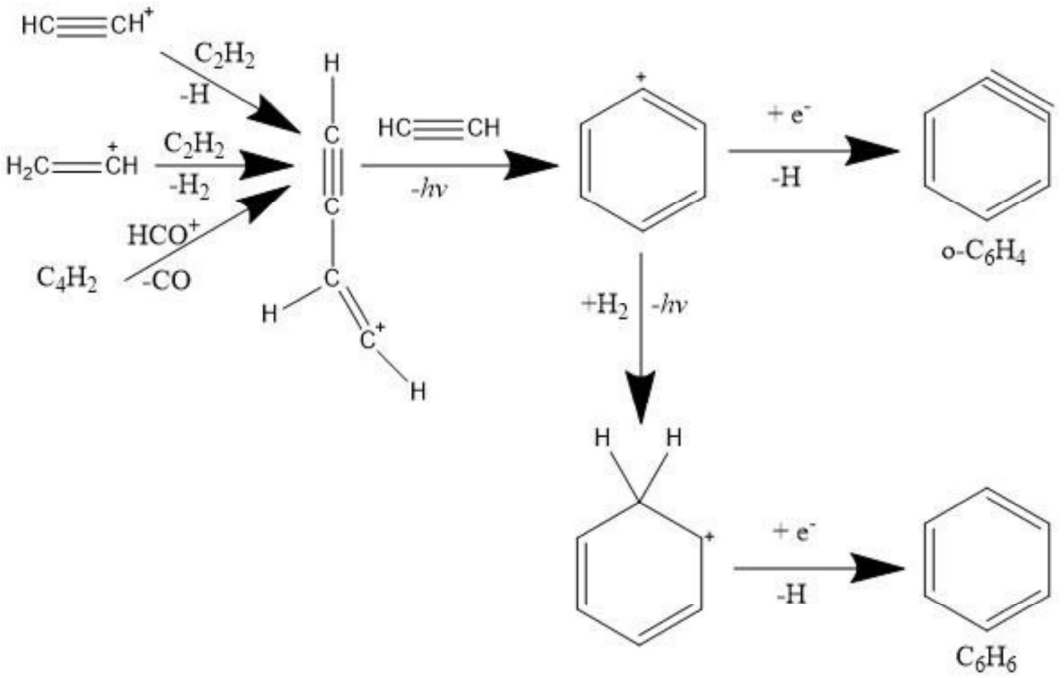

Figure 1.19: Scheme of Benzene formation path in circumstellar environments. Adapted from Woods et al. (2003).

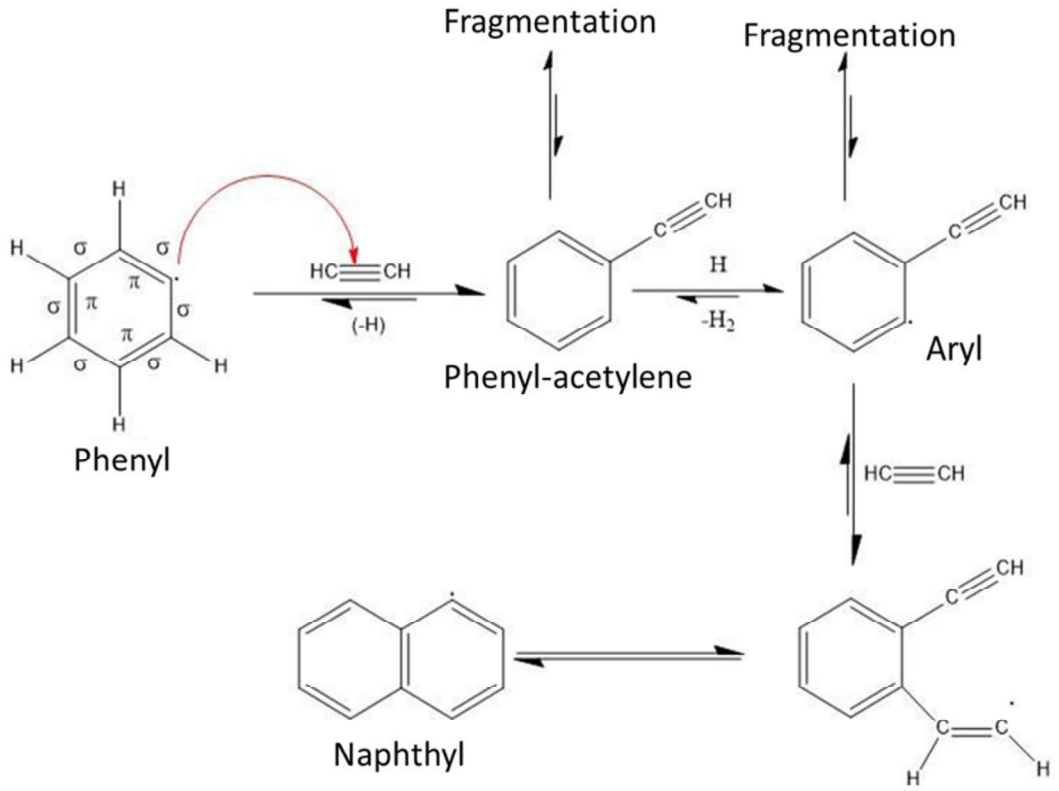

Figure 1.20: Scheme of PAHs formation path of through the reaction between the phenyl ion and acetylene. Adapted from Carelli et al. (2011); Cherchneff et al. (1992).

Chapter 2

Interaction of Radiation with Matter

Astrochemistry (or Molecular Astrophysics) is a young branch in the field of Astrophysics. Its primary goal is to understand the nature of chemical complexity, the existence of molecules, as well as their routes of formation and destruction, in distinct astrophysical environments. It secondary goal is to use the properties of the molecular emission to probe the physical and chemical properties of the objects of study. To do so, Astrochemistry relies on a multi-disciplinary approach combining astronomical observations, modelling, theory and laboratory experiments. In this perspective, the search for molecules is conducted by means of observations in different wavelength ranges of the electromagnetic spectrum. Photons emitted by rotational, vibrational and electronic transitions are observed at microwave and radio, Infrared and Ultraviolet (UV) and X-rays respectively. In this chapter, we will discuss the general concepts of the interaction of radiation with matter, and then focus on the most relevant types of spectroscopy for the development of this PhD thesis: rotational and X-ray spectroscopy.

2.1 General Concepts

2.1.1 The Electromagnetic Spectrum

Electromagnetic waves are produced by the oscillation of electric and magnetic fields in space and time over ranges of frequencies ν (Hz), or wavelengths λ (nm). They propagate in the free space with the speed of light, c, and transport electromagnetic radiation through the universe. The electromagnetic spectrum is the set of all possible frequencies at which this radiation is propagated. The frequency and wavelength of the electromagnetic radiation are related by the following equation:

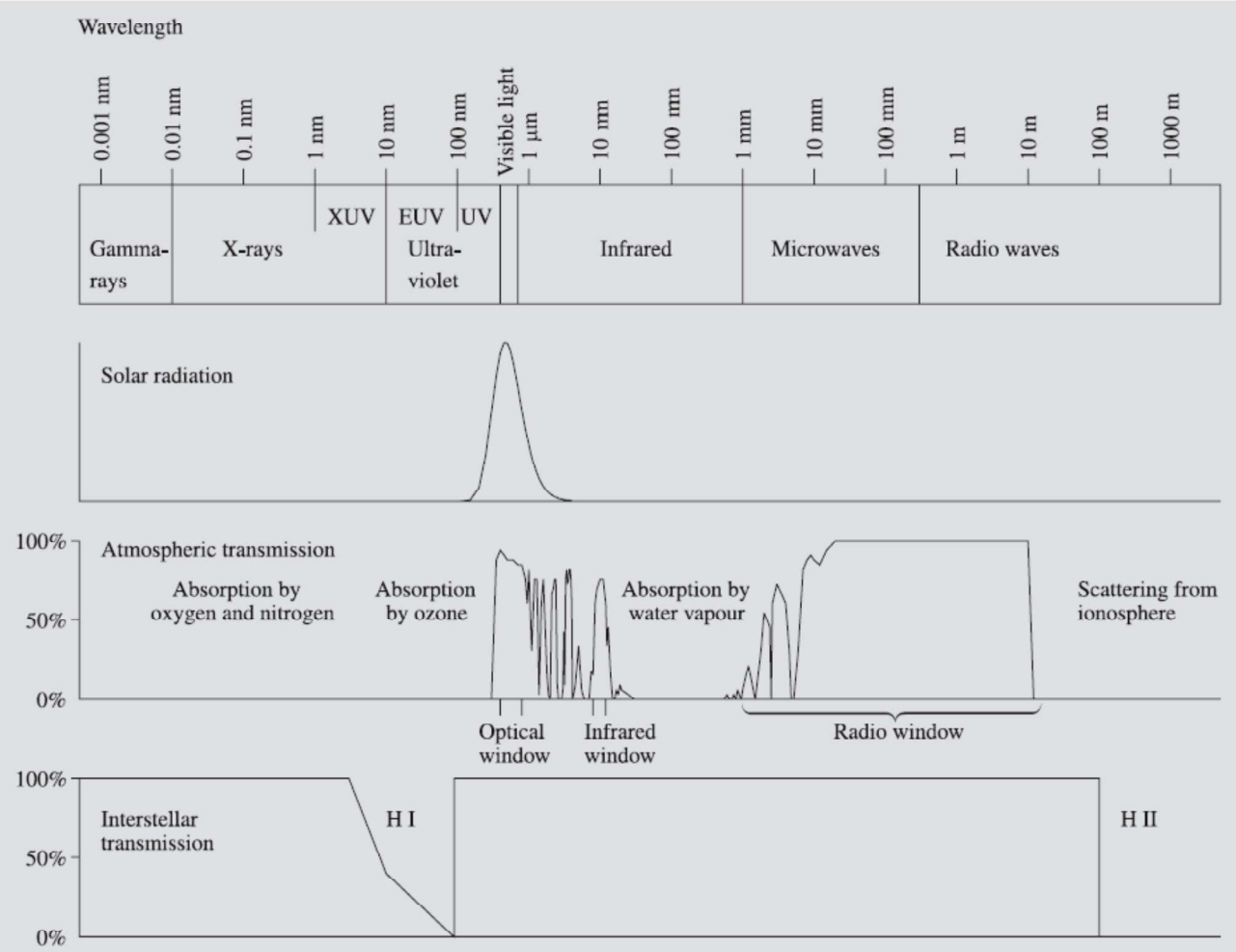

Figure 2.1: Spectrum of electromagnetic radiation and the transparency of the atmosphere at different wavelengths. Taken from Karttunen et al. (2003).

$$\lambda\nu = c \tag{2.1}$$

The photon energy is given by $E = h\nu$ (ergs or eV), where h is the Planck constant (6.625×10^{-27} erg s). The analysis of the molecular transitions provides important information about the temperature of emitting source, $T = E/k_B$, where k_B is the Boltzmann constant ($1.38\times\ 10^{-16}$ erg K^{-1}).

Fig. 2.1 presents the electromagnetic spectrum divided into wavelength ranges (at the top) showing: the Solar radiation spectrum in the visible wavelengths only; the percentage of atmospheric transmission due to the photoabsorption by the molecules such as O_2, N_2, ozone (O_3), water vapour; and the interstellar transmission due to the H atom.

The electromagnetic spectrum, from the shortest gamma rays to long radio waves, is used for astronomical observations (Karttunen et al., 2003). However, some wavelength ranges are absorbed

by the atmosphere (Fig. 2.1). Historically, the most important transparent window lies in the optical range, between 300 and 800 nm. The optical radiation is, however, partially attenuated by atmospheric molecules and dust as a result of scattering effects. The optical interval coincides with the region where the human eye is sensitive to elelectromagnetic radiation (400–700 nm). For $\lambda < 300$ nm, absorption by the atmospheric ozone prevents radiation from reaching the surface of the Earth. In fact, the atmospheric ozone layer protects the Earth from harmful UV radiation. For even shorter values of λ, the main absorbers are O_2, N_2, O_3 and some atoms. For $\lambda > 800$ nm, in the near-infrared region, the atmosphere is fairly transparent up to 10 μm, except for some absorption lines due to the presence of atmospheric water and O_2. All wavelengths between 20 μm and 1 mm are totally absorbed at ground level, mainly because of absorption by the water line emission. The bulk of water vapour in the atmosphere is located in the first two kilometers above the ground. For that reason, some atmospheric windows offer a reasonably high transparency under dry (and cold) conditions, permitting observations up to about 1 THz from high-altitude sites like Sierra Nevada (3000m; Spain), Mauna Kea (4000m; Hawaii), Atacama (5000m; Chile), from Earth. Last, for $\lambda > 1$ mm, there is a transparent window, called the *radio window*, which extends up to 20 m. At longer values of λ (typically a few MHz, as it depends on the day/night solar activity) the radiation is reflected by the ionosphere.

2.1.2 Radiative Flux and Luminosity

In order to know the flux emitted by astronomical objects, we need to define the amount of energy dE per unit of time, area dA, solid angle $d\Omega = \sin\theta\ d\theta\ d\phi$ and frequency $d\nu$, which is given by (Rybicki and Lightman, 1985):

$$dE = I_\nu\, dA\, dt\, d\Omega\, d\nu \tag{2.2}$$

where I_ν (ergs s^{-1} cm^{-2} $ster^{-1}$ Hz^{-1}) is the **specific intensity**. Integrating I_ν over the total solid angle subtended by the source, we get the flux per unit of frequency F_ν (erg $s^{-1}cm^{-2}$) that depends on the direction in relation of the normal to the surface (Fig. 2.2):

$$F_\nu = \int I_\nu cos\Theta d\Omega \tag{2.3}$$

The luminosity L (ergs s^{-1}) is the electromagnetic power emitted by an object, or the flux inte-

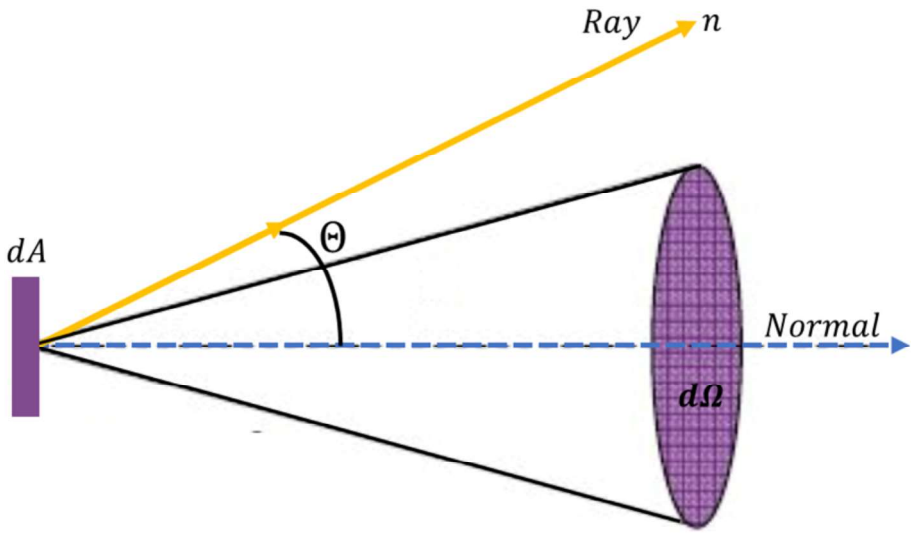

Figure 2.2: Scheme of the geometry for n direction incident ray. Adapted from Rybicki and Lightman (1985).

grated in its area and in each frequency range. For example, the X-ray luminosity value L_X is obtained by the integration of the flux F_X in this frequency (or photon energy) range. If the flux radiated by an object is integrated over all wavelengths, we have the bolometric luminosity, L_{bol}.

Therefore, by knowing the luminosity it is possible to determine the flux as a function of the distance r from the object by the following relation:

$$F_\nu = \frac{L_\nu}{4\pi r^2} \tag{2.4}$$

2.1.3 The Beer-Lambert Law

The Beer-Lambert law is an empirical law that determines how the radiation is absorbed by a gaseous medium due to the presence of atoms and molecules. The initial intensity of the radiation I_0 or the photon flux (number of photons cm^{-2} s^{-1}), in a given wavelength (λ) that enters in a cylinder of length L, is absorbed by the constituents of the medium, emerging from the opposite side with a reduced number of photons I given by:

$$I = I_0 e^{-\tau} \tag{2.5}$$

where τ is the dimensionless optical depth, given by:

$$\tau = \int_0^L k\rho dl \tag{2.6}$$

where k is the absorption coefficient (cm^2 g^{-1}), ρ is the mass density (g cm^{-3}) and L (cm) is the distance traveled by the light.

This work deals with formation and destruction of molecules in astrophysical environments of extremely low densities. Therefore, it is necessary to know the probability, or cross section, of molecules absorbing photons in a given wavelength to make molecular transition. In this perspective, we can also write τ as:

$$\tau = \sigma_{ph-abs} nL \tag{2.7}$$

where σ_{ph-abs} is the photoabsorption cross section (cm^2) as a function of λ and n is the numerical density (cm^{-3}). Integrating n in L we obtain the column density (cm^{-2}), $N = nL$.

Although scattering of radiation can also occur, the dominant radiation extinction process is due to light absorption. However, the radiation energy needs to be the same as the energy gap between quantum states of the molecule for the absorption to occur, while the scattering process can occur at all wavelengths with distinct degrees of efficiency.

2.1.4 Natural linewidth and the Doppler Effect

The line profiles of transitions between two energy levels are not exactly sharp. They have an intrinsic width and shape, which also reveal information about the local environment of the absorbing material. The line profile of an atomic or molecular transition has contribution mainly from three distinct effects. First, energy transitions have a natural linewidth, which is associated with their lifetime. Second, the presence of nearby molecules perturb the position of the energy levels due to an effect known as pressure broadening. This effect may be irrelevant in the interstellar medium, but become more important when molecules are, for example, in planetary atmospheres. Finally, some of the molecules in a gas cloud may be moving towards the observer, while others are moving away in the line of sight. This effect is known as Doppler broadening, and also contributes for the overall linewidth of the energy transition.

The natural linewidth is related to the lifetime, t, of the upper state of a spontaneous transition.

Faster transitions have shorter lifetimes, while slower transitions have longer lifetimes. All transitions are naturally broadened due to the existence of the uncertainty principle, which is a fundamental effect in quantum mechanics:

$$\Delta E \Delta t \geq \hbar \tag{2.8}$$

As for the Doppler shifting, this arises because of the Doppler effect, which is an apparent shift in frequency or wavelength of a transition, that is observed in all objects, due to the relative movement between the source and the observer. A transition is called redshifted when the source is moving away from the observer, so the transition is shifted to a longer wavelength. On the other hand, a transition is called blueshifted if the source is moving towards the observer, so the transition is shifted to a shorter wavelength.

The shift in the wavelength due to the relative velocity between the source and the observer is given by:

$$\frac{\Delta\lambda}{\lambda} = \frac{v_{source}}{c} \tag{2.9}$$

where λ is the wavelength of the transition, v_{source} is the relative velocity of the source and c is the speed of light.

In a gas sample, the effect of the Doppler shift related to the movement of the molecules in the sample creates a Gaussian line shape with a linewidth given by:

$$\delta\lambda = \frac{2\lambda}{c}\left(\frac{2k_B T ln2}{m}\right)^{1/2} \tag{2.10}$$

where k_B is the Boltzmann constant, T is the local temperature and m is the mass of the molecule.

2.2 Rotational Spectroscopy

2.2.1 Molecular Rotation in the Rigid Rotor Approximation

In order to describe molecular rotation, first we need to define moment of inertia, I. This quantity, as defined by Encyclopedia Britannica, is a "*quantitative measure of the rotational inertia of a body–i.e., the opposition that the body exhibits to having its speed of rotation about an axis altered by*

the application of a torque (turning force)". In a molecule, the moment of inertia about an arbitrary axis q set in the molecule is given by:

$$I_q = \sum_i m_i x_i(q) \tag{2.11}$$

where $x_i(q)$ is the perpendicular distance of the atom i with mass m_i from the axis q. Let us consider a diatomic molecule with bond length R and atomic masses m_A and m_B, and that it behaves as a rigid rotor. The moment of inertia, I, of such a molecule is given by:

$$I = \mu R^2 \tag{2.12}$$

where μ is the reduced mass of the molecule:

$$\mu = \frac{1}{m_A} + \frac{1}{m_B} \tag{2.13}$$

For polyatomic molecules, the expression of the moment of inertia can be more complex (see Fig. 2.3).

If the diatomic molecule is composed of heavy atoms which are far from the center of mass, it will have a large moment of inertia and, therefore, will accelerate slowly when subjected to a torque τ:

$$\frac{\mathrm{d}\omega}{\mathrm{d}t} = \frac{\tau}{I} \tag{2.14}$$

where ω is the angular velocity.

Now let us define the Hamiltonian operator, which corresponds to the sum of the kinetic and potential energies for all particles in the system:

$$\mathscr{H} = \widehat{T} + \widehat{V} \tag{2.15}$$

where $\widehat{T}$ and $\widehat{V}$ are the kinetic and potential operators, respectively. The kinetic energy of rotation of a body of moment of inertia I_q with respect to the axis q is given by:

$$T = \frac{1}{2} \sum_q I_q \omega_q^2 = \sum_q \frac{J_q^2}{2I_q} \tag{2.16}$$

1. *Diatomic molecules*

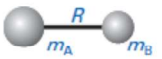

$$I = \mu R^2 \quad \mu = \frac{m_A m_B}{m}$$

2. *Triatomic linear rotors*

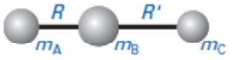

$$I = m_A R^2 + m_C R'^2 - \frac{(m_A R - m_C R')^2}{m}$$

$$I = 2m_A R^2$$

3. *Symmetric rotors*

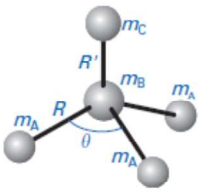

$$I_\parallel = 2m_A(1-\cos\theta)R^2$$

$$I_\perp = m_A(1-\cos\theta)R^2 + \frac{m_A}{m}(m_B+m_C)(1+2\cos\theta)R^2$$

$$+\frac{m_C}{m}\left\{(3m_A+m_B)R' + 6m_A R[\tfrac{1}{3}(1+2\cos\theta)]^{1/2}\right\}R'$$

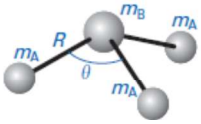

$$I_\parallel = 2m_A(1-\cos\theta)R^2$$

$$I_\perp = m_A(1-\cos\theta)R^2 + \frac{m_A m_B}{m}(1+2\cos\theta)R^2$$

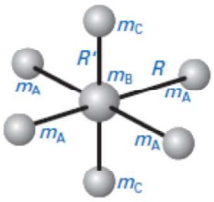

$$I_\parallel = 4m_A R^2$$

$$I_\perp = 2m_A R^2 + 2m_C R'^2$$

4. *Spherical rotors*

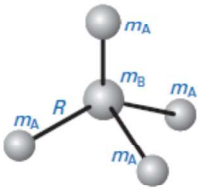

$$I = \tfrac{8}{3}m_A R^2$$

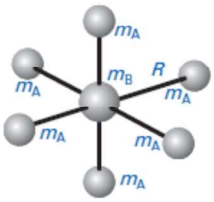

$$I = 4m_A R^2$$

Figure 2.3: Moments of inertia of diatomic and selected triatomic and polyatomic molecules. Adapted from Atkins and Friedman (2005).

where ω_q^2 is the angular frequency with respect to the axis q and J_q is the angular momentum around axis q.

The kinetic energy of rotation operator, then, is given by:

$$\hat{T} = \sum_q \frac{\hat{J}_q^2}{2I_q} \tag{2.17}$$

where $\hat{J}_q$ is the q-component of the angular moment operator $\hat{J}$, whose square, $\hat{J}^2$, is given by:

$$\hat{J}^2 = \sum_q \hat{J}_q^2 \tag{2.18}$$

The potential energy does not contribute to the free rotation. Therefore, in this case:

$$\hat{V} = 0 \tag{2.19}$$

By replacing eqs. 2.17 and 2.19 in eq. 2.15, and letting q be the *molecule-fixed* coordinates x, y and z, we obtain:

$$\mathscr{H} = \mathscr{H}_{rot} = \frac{\hat{J}_x^2}{2I_x} + \frac{\hat{J}_y^2}{2I_y} + \frac{\hat{J}_z^2}{2I_z} \tag{2.20}$$

The respective J^2 operator is, then:

$$\hat{J}^2 = \hat{J}_x^2 + \hat{J}_y^2 + \hat{J}_z^2 \tag{2.21}$$

Let Ψ be the wave function that contains all information of the molecular system. The eigenvalue equation derived from the application of $\mathscr{H}_{rot}$ on Ψ is:

$$\mathscr{H}_{rot}\Psi = E_{rot}\Psi \tag{2.22}$$

where E_{rot} are the eigenvalues of the rotational Hamiltonian, and represent the quantized rotational energy levels.

At this point, it is useful to describe the commutation relations of $\hat{J}$ using the *laboratory-fixed* coordinates X, Y and Z. First, $\hat{J}^2$ commutes with the components of $\hat{J}$:

$$\left[\hat{J}^2, \hat{J}_X\right] = \hat{J}^2\hat{J}_X - \hat{J}_X\hat{J}^2 = 0 \tag{2.23a}$$

$$\left[\hat{J}^2, \hat{J}_Y\right] = \hat{J}^2\hat{J}_Y - \hat{J}_Y\hat{J}^2 = 0 \tag{2.23b}$$

$$\left[\hat{J}^2, \hat{J}_Z\right] = \hat{J}^2\hat{J}_Z - \hat{J}_Z\hat{J}^2 = 0 \tag{2.23c}$$

On the other hand, the q-components of $\hat{J}$ do not commute among themselves. Alternatively, in atomic units, they satisfy the following commutation relations:

$$\left[\hat{J}_X, \hat{J}_Y\right] = i\hat{J}_Z \tag{2.24a}$$

$$\left[\hat{J}_Y, \hat{J}_Z\right] = i\hat{J}_X \tag{2.24b}$$

$$\left[\hat{J}_Z, \hat{J}_X\right] = i\hat{J}_Y \tag{2.24c}$$

This shows that only $\hat{J}^2$ and one of the components (usually chosen as $\hat{J}_Z$) share a common set of eigenfunctions ψ, which in Dirac notation are designated as $|J,M\rangle$. Starting from the commutation rules, it is possible to obtain the following eigenvalue equations for $\hat{J}^2$ and $\hat{J}_Z$:

$$\hat{J}^2 |J,M\rangle = J(J+1)\,|J,M\rangle \tag{2.25a}$$

$$\hat{J}_Z |J,M\rangle = M\,|J,M\rangle \tag{2.25b}$$

where the quantum number J is a non-negative integer and the quantum number M takes all integer values between ($M = J$), ($M = J-1$), ($M = J-2$), ..., ($M = -J$). In the J,M representation, the eigenvalues of $\hat{J}^2$ and $\hat{J}_Z$ are, respectively:

$$\langle J,M|\hat{J}^2|J,M\rangle = J(J+1) \tag{2.26a}$$

$$\langle J,M|\hat{J}_Z|J,M\rangle = M \tag{2.26b}$$

Let us consider now a symmetric top rotor, which is a rigid body containing two identical moment of inertia, and a third one different. Examples of such molecules are NH_3, CH_3Cl, CH_3CCH and C_6H_6. The z component of the angular momentum, $\hat{J}_z$, in a *molecule-fixed* coordinate system also commutes with $\hat{J}^2$. Thus, $\hat{J}^2$, $\hat{J}_Z$ and $\hat{J}_z$ have a common set of eigenfunctions, which in Dirac notation

is written as $|J,K,M\rangle$. The eigenvalues of $\hat{J^2}$, $\hat{J_Z}$ and $\hat{J_z}$ are then:

$$\langle J,K,M|\hat{J^2}|J,K,M\rangle = J\left(J+1\right) \tag{2.27a}$$

$$\langle J,K,M|\hat{J_z}|J,K,M\rangle = K \tag{2.27b}$$

$$\langle J,K,M|\hat{J_Z}|J,K,M\rangle = M \tag{2.27c}$$

with K, as M, taking all integer values between $(K=J)$, $(K=J-1)$, $(K=J-2)$, ..., $(K=-J)$. The Hamiltonian for a symmetric top rotor is expressed by taking eq. 2.20 and making $I_x = I_y$:

$$\mathscr{H}_{rot} = \frac{\hat{J^2}}{2I_x} + \left(\frac{1}{2I_z} - \frac{1}{2I_x}\right)\hat{J_z^2} \tag{2.28}$$

The eigenvalues of the rotational Hamiltonian of eq. 2.28 are given by:

$$E_{rot} = E_{J,K} = \langle J,K,M|H_{rot}|J,K,M\rangle = \frac{1}{2}\left[\frac{J(J+1)}{I_x} + \left(\frac{1}{I_z} - \frac{1}{I_x}\right)K^2\right] \tag{2.29}$$

By introducing the rotational constants A, B and C:

$$A = \frac{1}{2I_z} \tag{2.30a}$$

$$B = \frac{1}{2I_x} \tag{2.30b}$$

$$C = \frac{1}{2I_y} \tag{2.30c}$$

Eq. 2.29 can be rewritten and simplified to as:

$$E_{J,K} = BJ(J+1) + (A-B)K^2 \tag{2.31}$$

for a prolate (American football-like) top ($A > B = C$), or to

$$E_{J,K} = BJ(J+1) + (C-B)K^2 \tag{2.32}$$

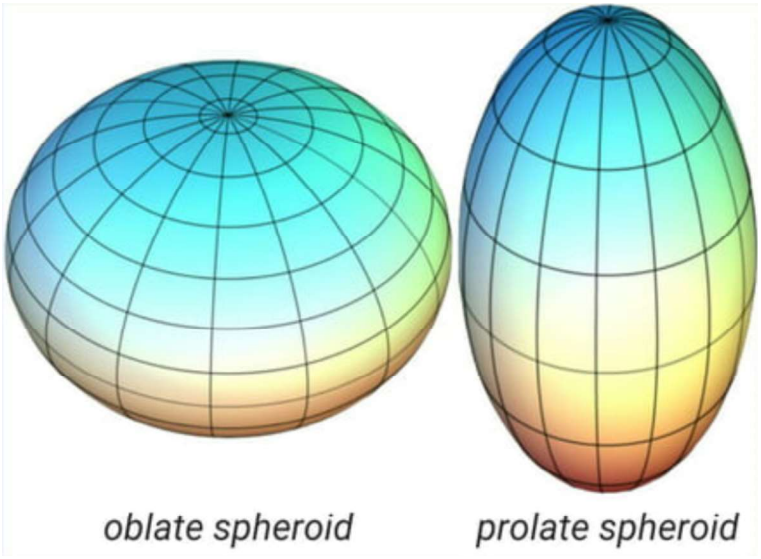

Figure 2.4: Schematic figure containing oblate- and prolate-type symmetric top rotors.

for an oblate (pancake-like) top ($A = B > C$).

For a linear rigid-rotor, as $I_z = 0$ and $I_x = I_y = I$, eq. 2.31 is further simplified to:

$$E_J = BJ(J+1) \tag{2.33}$$

Molecules belonging to this class are all diatomic and linear polyatomic , such as CO_2, C_2H_2 and interstellar polyynic chains. A similar energy expression is also observed for spherical rotors, in which all three moments of inertia are equal. Examples of molecules pertaining to this class are CH_4, SF_6 and C_{60}.

From eq. 2.33 and taking the transitions from $J = 0 \rightarrow J = 1$; $J = 1 \rightarrow J = 2$; etc., it is possible to see that the difference between the energy levels is given by:

$$\nu = 2B(J+1) \tag{2.34}$$

and the separation between the levels is:

$$\Delta\nu = 2B \tag{2.35}$$

Given that B is of the order of 30 GHz for small molecules (Shaw, 2007), these rotational transitions are in the middle of the microwave region. By determining the spacing of the energy levels, one can also determine the rotational constant, the moment of inertia and, finally, the bond length. In

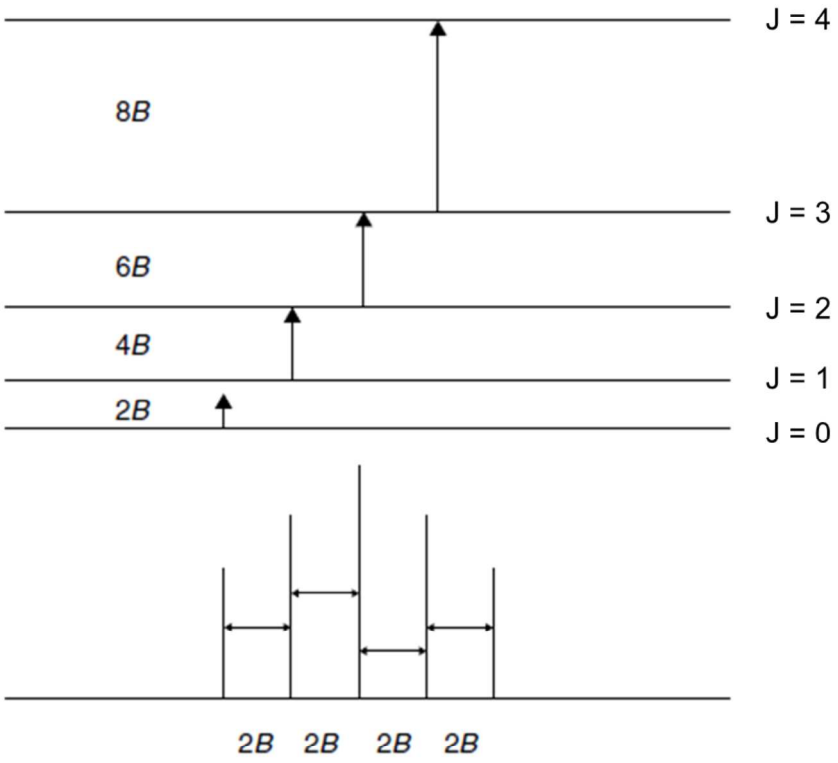

Figure 2.5: The energy level diagram for a rotational spectrum. Adapted from Shaw (2007).

fact, gas-phase microwave spectroscopy is a very powerful technique for measuring bond lengths.

Fig. 2.5 shows a general scheme of the microwave spectrum. Transitions from $(J = n)$ to $(J = n+1)$ are labeled as transitions from the R-branch, with $R(n) = n \rightarrow n+1$, while transitions from $(J = n+1)$ to $(J = n)$ are labeled as transitions from the P-branch, with $P(n+1) = n+1 \rightarrow n$.

Fig. 2.6 shows the simulated rotational spectrum of the CO molecule at 40K. The lines in the spectrum are regularly spaced, a feature called as rotational progression. For transitions involving low J numbers, the separation between the energy levels is given by $2B$ and is $\sim$ 115 GHz for CO. This is not exactly true for high J values because for these cases the rigid rotor approximation is no longer valid, as *centrifugal distortion* takes place. Furthermore, the intensity of the $R(n)$ transitions depend on the temperature, and for T = 40K $R(4)$ shows the greatest intensity. The relative intensities of the rotational transitions, therefore, can be used to identify the temperature of the surroundings of the molecule, assuming that a *local thermal equilibrium* is valid. In the next sections, *centrifugal distortion* and *local thermal equilibrium* will be described.

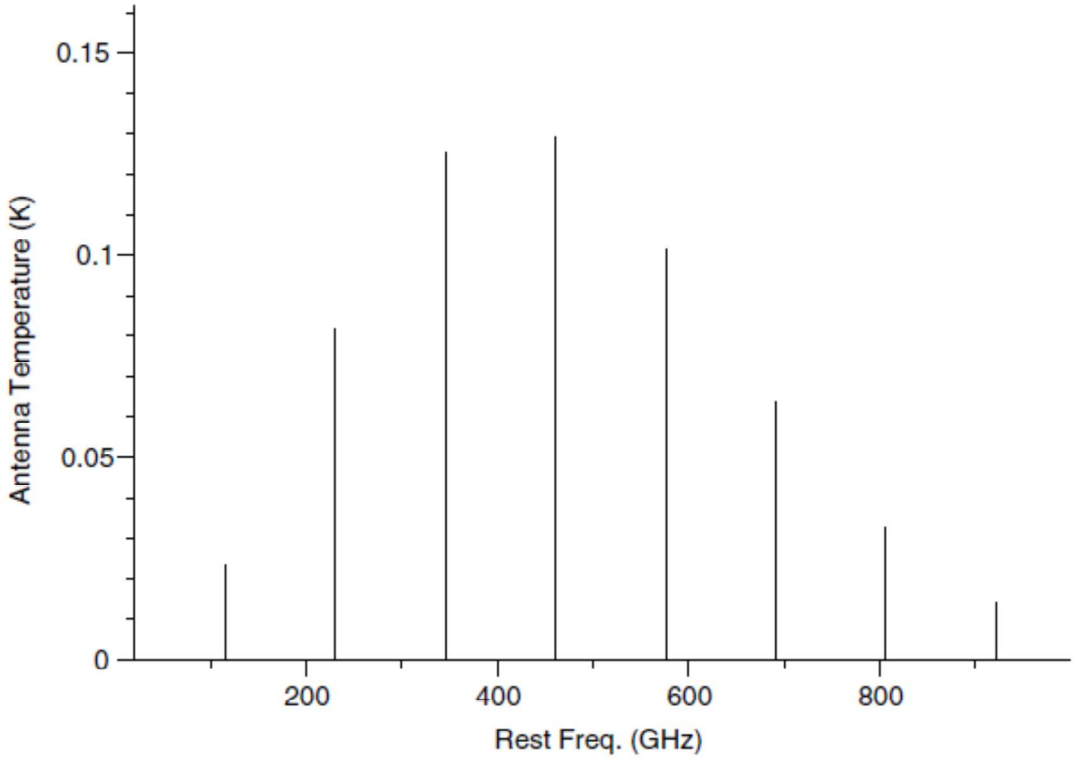

Figure 2.6: Simulated spectrum of CO with a rotational temperature of 40 K.Adapted from Shaw (2007).

2.2.2 Centrifugal Distortion

As mentioned before, treating a molecule as a rigid rotor is only an approximation. As the degree of rotational excitation is increased, the molecule experiences a centrifugal force that increases the bond lengths and, consequently, the moment of inertia. This effect is known as centrifugal distortion, and as a consequence the rotational constants are lowered. Therefore, the energy levels for high J values are closer than expected from the rigid rotor approximation.

A convenient way of treating the effect of centrifugal distortion on the rotational spectra is obtained by using perturbation theory (Puzzarini et al., 2010). In this treatment, the rotational Hamiltonian is expressed as:

$$\mathscr{H}_{rot} = \mathscr{H}^0_{rot} + \mathscr{H}'_{dist} \tag{2.36}$$

where $\mathscr{H}^0_{rot}$ is the zero-order Hamiltonian given in eq. 2.20 and $\mathscr{H}'_{dist}$ is the perturbation operator that describes centrifugal distortion, which for a symmetric top rotor can be written as:

$$\mathscr{H}'_{dist} = -D_J \hat{J}^4 - D_{JK} \hat{J}^2 \hat{J}_z^2 - D_K \hat{J}_z^4 \tag{2.37}$$

where D_J, D_{JK} and D_K are quartic centrifugal distortion constants. The corresponding energy correction is given by:

$$E'_{dist} = -\left[D_J J^2 (J+1)^2 + D_{JK} J (J+1) K^2 + D_K K^4\right] \tag{2.38}$$

For a linear molecule, eq. 2.37 is simplified to:

$$\mathscr{H}'_{dist} = -D_J \hat{J}^4 \tag{2.39}$$

and the corresponding energy correction is:

$$E'_{dist} = -D_J J^2 (J+1)^2 \tag{2.40}$$

For a diatomic molecule, D_J in SI units is given by:

$$D_J = \frac{\hbar^3}{4\pi k c \mu^2 R_0^6} \tag{2.41}$$

where $\hbar$ is the reduced Planck constant, k is the force constant of the bond, μ is the reduced mass of the molecule, c is the speed of light and R_0 is the equilibrium bond length of the molecule.

2.2.3 Rotational Selection Rules

In order to obtain the selection rules for rotational transitions, we first need to consider that the nuclei movement can be decoupled from the electron movement, which is known as the Born-Oppenheimer approximation (Atkins and Friedman, 2005). Presuming that the vibrations of the molecule are much faster than the rotations, it is also possible to separate both motions. Without going into much detail, rotational transitions are induced by the interaction of molecular electric-dipole components with the electric components of the radiation field. From that, we can immediately conclude that only polar molecules can have a pure rotational spectrum (Atkins and Friedman, 2005). The selection rules for polar linear rotors are:

$$\Delta J = 0, \pm 1, \quad \Delta M = 0, \pm 1 \tag{2.42}$$

For polar symmetric rotors there is one additional selection rule:

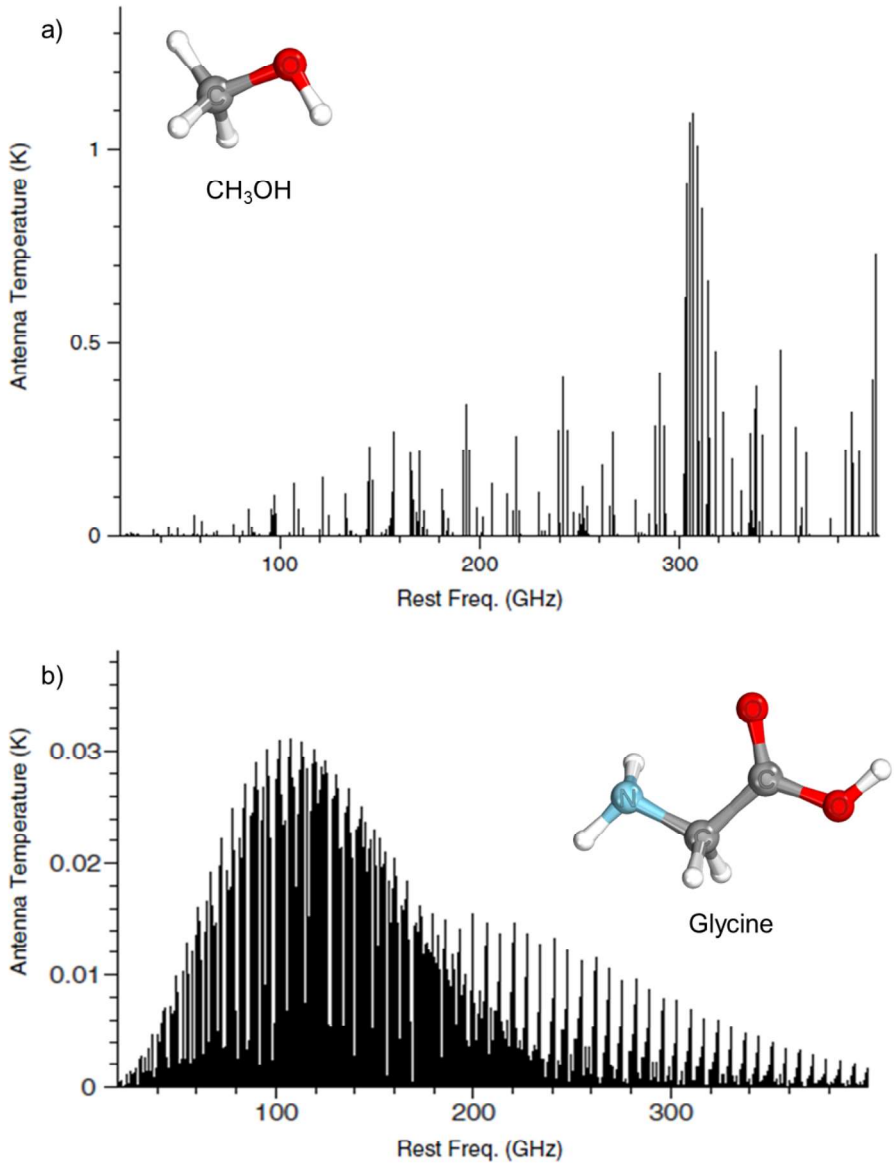

Figure 2.7: Simulated rotational spectrum of a) CH_3OH and b) glycine. Adapted from Shaw (2007).

$$\Delta K = 0 \tag{2.43}$$

Spherical rotors do not have permanent dipole moments and, therefore, do not show pure rotational transitions. An homonuclear molecule such as H_2 therefore does not display pure dipolar electric, rotational transitions. Note however that quadrupolar electric transitions are still possible though, and are observed. They follow different selections rules ($\Delta J = 0, \pm 2$) and the line intensity is much lower.

Centrifugal distortion and the progression of the transitions related to the quantum numbers J, M

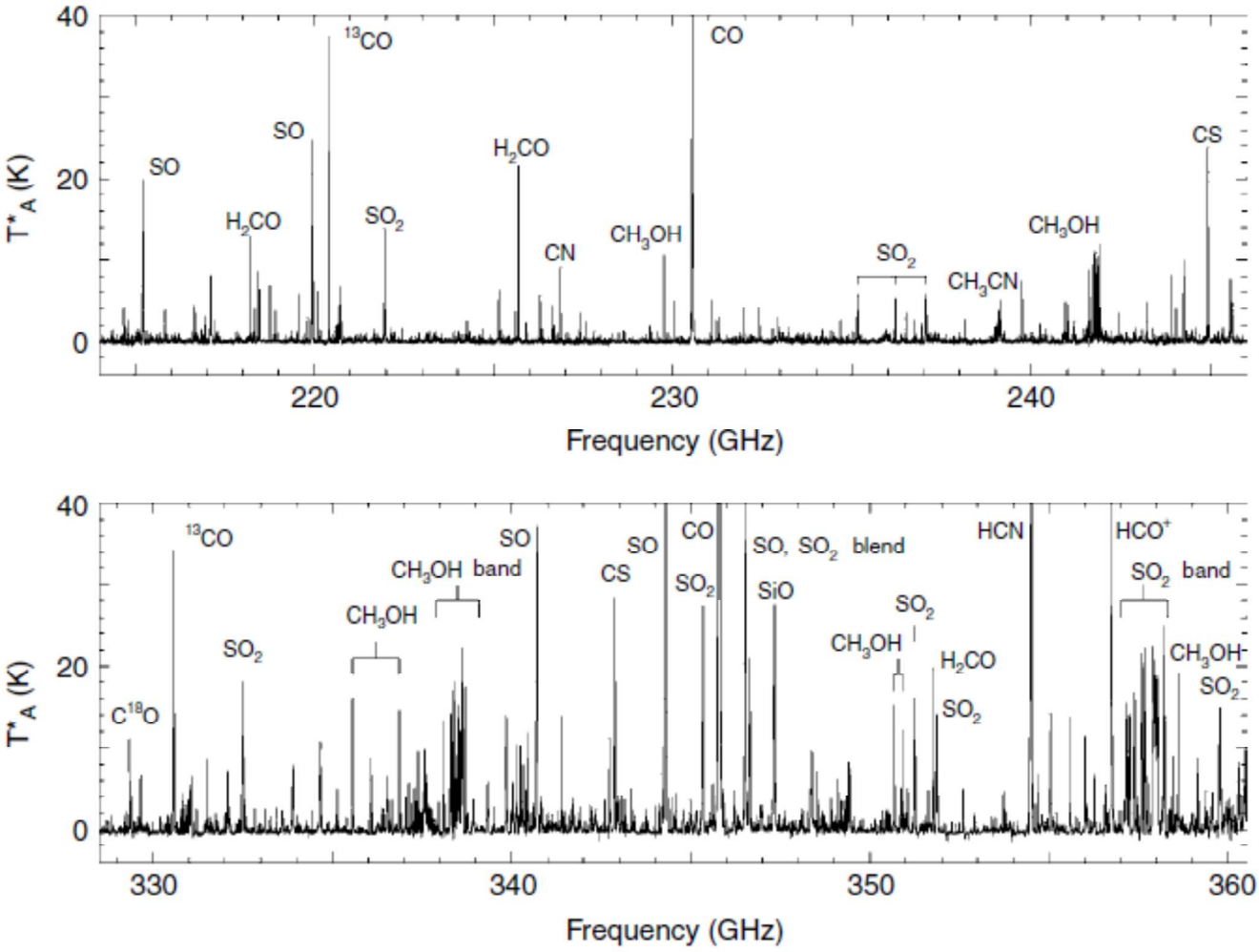

Figure 2.8: The microwave spectrum of the Orion nebula. Adapted from Shaw (2007).

and K give rise to complicated rotational spectra, as the ones exemplified in Fig. 2.7. The identification of complex molecules through its rotational spectrum is, therefore, non-trivial.

The microwave identification of interstellar molecules is a very complicated task due to the presence of many molecules in the field of view in astronomical observations. The observed spectrum is then a complicated mixture of allowed rotational transitions, as exemplified in Fig. 2.8.

A number of aspects should be considered for assigning rotational spectral lines, such as (Shaw, 2007):

- Doppler shift correction for the molecules;
- Determination of lines within the rotational progression;
- Molecules should be present in distinct environments within the source;
- Distinct isotopologues should be considered.

2.2.4 Radiative Transfer and the Local Thermal Equilibrium

As mentioned before, the relative intensities of the rotational transitions depend on the temperature,and also on the gas density of the main collider, usually H_2. Rotational energy levels within a molecule are populated depending on the availability of energy from collision with other molecules. In fact, molecular collision is related to the kinetic definition of temperature, and while collisions dominate the energy exchange between levels, through excitation and de-excitation processes, it is said that the system has local thermal equilibrium (LTE). The ratio between the population n_i of the state i and the population n_j of the state j is then given by the Boltzmann Law:

$$\frac{n_i}{n_j} = \frac{g_i}{g_j} \times exp\left(-\frac{\Delta E}{k_B T}\right) \tag{2.44}$$

where g_i and g_j are the degeneracies of the states i and j, respectively; ΔE is the difference between the energy levels, k_B is the Boltzmann constant and T is the temperature.

In LTE regime, the photon energy absorbed by the molecule is distributed across other molecules by collisions before it is re-radiated by emission. The intensities of emitted and absorbed radiation are not independent. A convenient way on describing the interaction of radiation with matter by the emission and absorption of photons is given by the Einstein coefficients.

Let us consider a gas of atoms containing discrete energy levels E_u and E_l. A system in the excited state E_u returns spontaneously to the lower level E_l with a probability given by A_{ul}. If n_u is the density of the state u, the quantity $n_u A_{ul}$ is the number of spontaneous decays per second in a unit volume.

Now consider that the average energy density of the radiation field is given by:

$$\bar{U} = \frac{4\pi \bar{I}}{c} \tag{2.45}$$

where $\bar{I}$ is the average radiation intensity. The probability of the absorption of a photon of that field is $B_{lu}\bar{U}$, and the number of absorbed photons is $n_l B_{lu}\bar{U}$. In order to derive Planck's law, another emission process is necessary: $n_u B_{ul}\bar{U}$, namely the stimulated emission. If the system is in stationary state, the number of absorbed and emitted photons must be equal, leading to the following relation:

$$\underbrace{n_u A_{ul} + n_u B_{ul}\bar{U}}_{emission} = \underbrace{n_l B_{lu}\bar{U}}_{absorption} \tag{2.46}$$

where A_{ul}, B_{ul} and B_{lu} are the Einstein coefficients, and must obey the following rules:

$$g_l B_{lu} = g_u B_{ul} \tag{2.47a}$$

$$A_{ul} = \frac{8\pi h\nu^3}{c^3} B_{ul} \tag{2.47b}$$

where g_l and g_u are the degeneracies of the lower and higher energy levels, respectively. A complete description of the radiative transfer equations can be found in Elitzur (1992); Vastel (2016).

2.3 X-Ray Spectroscopy

2.3.1 Inner-shell Excitation

In this section, we present some fundamental aspects regarding the theory of inner shell excitation and the calculation or the experimental determination of X-ray absorption spectra (Stöhr, 1992). For that purpose, we will start by defining X-ray photoabsorption cross section as a function of the photon energy E, $\sigma_{ph-abs}(E)$, which is given by:

$$\sigma_{ph-abs}(E) = \frac{n_e}{n_p} \times A \tag{2.48}$$

where n_e is the number of excited core electrons per unit of time, n_p is the number of incident photons per unit of time and A is the effective area of the system. The photoabsorption cross section, therefore, has the dimension of cm^2. Similarly, σ_{ph-abs} can also be described by the following equation:

$$\sigma_{ph-abs}(E) = \frac{\Gamma_{i\to f}}{F_X(E)} \tag{2.49}$$

where $\Gamma_{i\to f}$ is the transition probability per unit of time, also known as transition rate, and $F_X(E)$ is the X-ray photon flux per unit of time per unit of area. The transition rate can be obtained by the Fermi's golden rule, which describes such quantity from an initial state i to a final state f as a result of a weak perturbation $\mathscr{H}'$. If $\mathscr{H}'$ is an harmonic perturbation, the transition rate is essentially constant, and is given by:

$$\Gamma_{i\to f} = \frac{2\pi}{\hbar} \left|\langle f \left| \mathscr{H}' \right| i \rangle\right|^2 \rho(E_f) \tag{2.50}$$

where $\langle f|\mathscr{H}'|i\rangle$ is the matrix element of the perturbation between the final and initial states and $\rho(E_f)$ is the density of states at the energy E_f. A transition between different states with energies E_i and E_f is equal to a photon with energy $\hbar\omega$ being absorbed or emitted.

For a K-shell excitation, $\Gamma_{i\to f}$ is the number of electrons excited per unit of time from the 1s shell to a final state $|f\rangle$, which can be a bound or a continuum state. The photoionization occurs if $|f\rangle$ is related to a continuum state leading to the release of a free electron, called photoelectron.

For a plane electromagnetic wave with angular frequency ω $(= 2\pi\nu)$, vector potential $\boldsymbol{A}$ and electric field vector $\boldsymbol{E}$, F_{ph} is given by the following equation:

$$F_{ph} = \frac{A_0^2\omega}{8\pi\hbar c} = \frac{E_0^2 c}{8\pi\hbar\omega} \tag{2.51}$$

where A_0 and E_0 are the amplitudes of $\boldsymbol{A}$ and $\boldsymbol{E}$, respectively. If $\Gamma_{i\to f}$ is the result of the interaction of spinless particles of charge $-e$ and mass m with the electromagnetic wave described in eq. 2.51, the harmonic perturbation $\mathscr{H}'$ is given by:

$$\mathscr{H}' = \frac{e}{mc}\boldsymbol{A}\cdot\boldsymbol{p} \tag{2.52}$$

where $\boldsymbol{p}$ is the sum of the linear momentum operators of the electrons:

$$\boldsymbol{p} = \sum_i \boldsymbol{p}_i \tag{2.53}$$

By substituting eqs. 2.50, 2.51 and 2.52 into eq. 2.49, and after some mathematical manipulation, we obtain the following expression for $\sigma_{ph\text{–}abs}$:

$$\sigma_{ph\text{–}abs} = \frac{4\pi^2\hbar^2}{m^2}\frac{e^2}{\hbar c}\frac{1}{\hbar\omega}\left|\langle f|\boldsymbol{e}\cdot\boldsymbol{p}|i\rangle\right|^2\rho(E_f) \tag{2.54}$$

where $\boldsymbol{e}$ is the unit vector of the plane electromagnetic wave.

Let us now define the optical oscillator strength, f, which is related to the X-ray photoabsorption cross section by the following equation:

$$\sigma_{ph\text{–}abs} = C\frac{\mathrm{d}f}{\mathrm{d}E} = \frac{2\pi e^2\hbar}{mc}\frac{\mathrm{d}f}{\mathrm{d}E} \tag{2.55}$$

where C is the constant 1.0976×10^{-16} cm^2 eV and df/dE is the differential oscillator strength per photon energy. The oscillator strength measures the intensity of an energy resonance, and since f

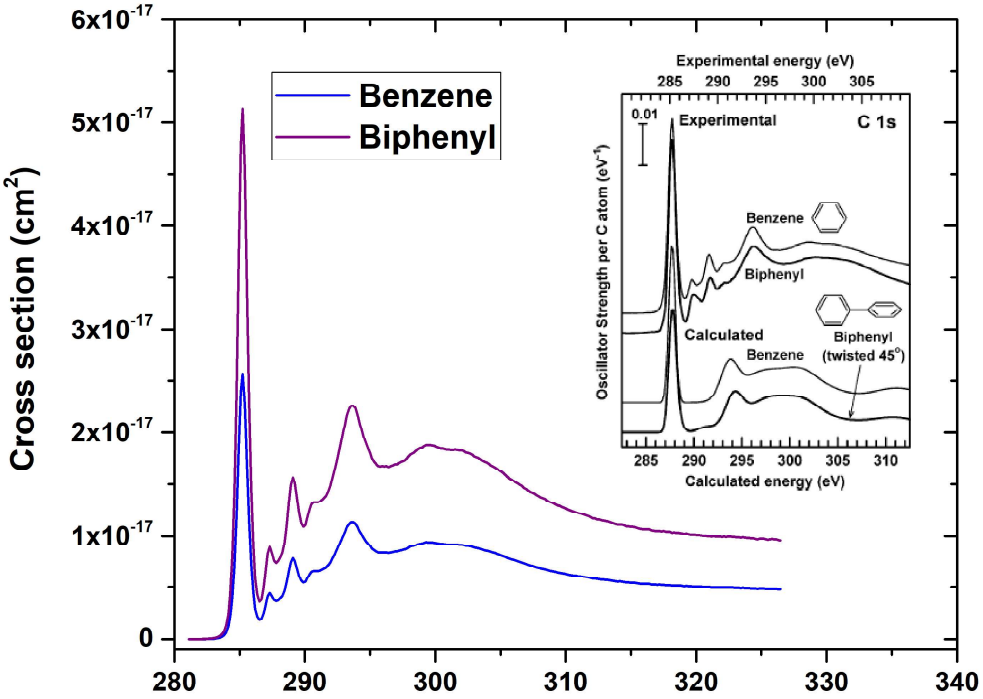

Figure 2.9: Absolute photoabsorption cross sections of benzene (Hitchcock et al., 1987) and biphenyl (this work, see Chapter 5) as a function of the photon energy E (eV) around the C1s resonances. The inserted figure shows the comparison of experimental and calculated oscillator strengths. Adapted from (Wang et al., 2005).

for bound state transitions is given by:

$$f = \frac{2}{m\hbar\omega} |\langle f | \boldsymbol{e} \cdot \boldsymbol{p} | i \rangle|^2 \tag{2.56}$$

the calculated oscillator strengths can be converted to cross sections by integrating eq. 2.55 and introducing the energy density $\rho(E_b)$:

$$\sigma_{ph-abs} = \frac{2\pi e^2 \hbar}{mc} f \rho(E_b) \tag{2.57}$$

where $\rho(E_b)$ is the density of final states with the bound state energy. At the ionization potential (IP):

$$\rho(E_b) = \rho(E_f) \tag{2.58}$$

and, therefore, eq. 2.54 is equal to eq. 2.57. By plotting the X-ray absorption cross section as a function of the photon energy (Fig.2.9), the height of a bound state resonance peak is given by σ_{ph-abs}, and the area of the peak is equal to the oscillator strength. The total oscillator strength for

the electronic excitation of an atom or molecule is equal to the number of electrons N pertaining to the atom or molecule:

$$\underbrace{\sum_n f_n}_{\text{bound states}} + \underbrace{\int_{IP}^{\infty} \frac{\mathrm{d}f(E)}{\mathrm{d}E} dE}_{\text{continuum states}} = N \tag{2.59}$$

which is known as the Thomas-Reiche-Kuhn sum rule.

Finally, another important feature of the resonance peak in the cross section versus energy plot is its full-width at half-maximum, FWHM. This quantity is related to the lifetime of the final state, τ, which can be separated into two contributions:

$$\frac{1}{\tau} = \frac{1}{\tau_e} + \frac{1}{\tau_h} \tag{2.60}$$

where τ_e is the lifetime of the excited electron within the molecular potential and τ_h is the lifetime of the inner-shell hole state. Using high resolution X-ray absorption spectra, it is possible to estimate the core hole lifetime τ_h from the measured FWHM of a bound state resonance, since for such transitions $\tau_e = \infty$. For low-Z atoms, the characteristic lifetime of the K-shell excitation is in the range of $10^{-15} - 10^{-14}$ s. This value is around two orders of magnitude slower than a typical continuum resonance, which is dictated by the lifetime of the resonantly trapped electron and is usually in the $10^{-17} - 10^{-16}$ s range.

2.3.2 The K-shell spectra of molecules

The K-shell spectra of atoms and molecules are composed of a variety of resonances which correspond to electronic transitions of a K-shell electron to states near the vacuum level (E_v), whose excitation energies are close to the ionization potential. Fig. 2.10 shows a schematic representation of the effective molecular potential and the different types of final states for an atom (left) and for a diatomic molecule (right). A closed shell atom in its ground state shows a huge amount of empty Rydberg states just below E_v, and a continuum of empty states above E_v. The same profile is observed for core-excited atoms, in a way that the expected K-shell excitation spectrum resembles the top left panel of Fig. 2.10. For a diatomic molecule, Rydberg states are also present below E_v, and a continuum of empty states above E_v. The lowest unoccupied molecular orbital (LUMO) of a diatomic

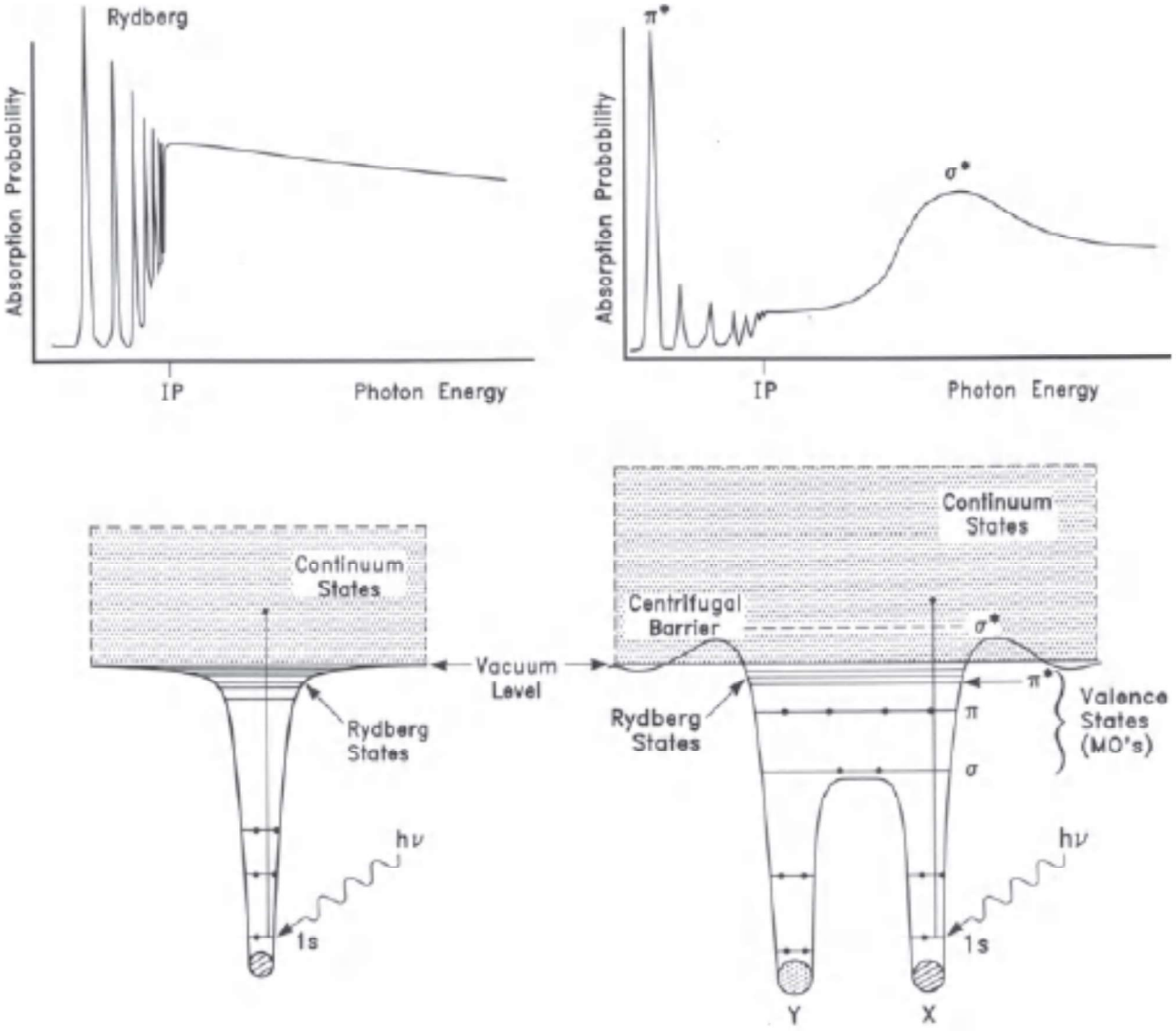

Figure 2.10: Scheme of the effective energy potentials (bottom) and the K-shell spectra (top) of atoms (left) and diatomic molecules (right). See text for details. Taken from Stöhr (1992).

molecule is usually of π symmetry, with σ symmetry unoccupied orbitals being higher in energy. Such orbitals are designed as π^* and σ^* (the asterisk indicates unfilled MO). Due to electron-hole Coulomb interaction, the π^* state falls below E_v, leading to the energy level diagram depicted in the bottom right panel of Fig. 2.10.

We will now discuss the main features that appear in the K-shell spectra of molecules. These are: **π^* resonances**; **Rydberg (or mixed Valence-Rydberg) resonances**; **σ^* shape resonances**; and **multi-electron features**.

As the name suggests, **π^* resonances** are only observed for molecules with π bonding. They are

usually the lowest energy resonance structure in the K-shell spectrum, and its energy position falls below the 1s ionization potential. For a given atom pair, the intensity of the π^* resonance changes with the bond order between the atoms. Taking the C–O bond, for example, the intensity of the π^* resonance decreases by a factor of 2.3 at the C K-edge and by a factor of 1.3 at the O K-edge between the triply-bonded CO and $H_2C{=}O$ (Hitchcock and Brion, 1980b,a). This also reveals that, at the C K-edge, the π^* resonance loses oscillator strength to the resonances associated with C–H bonds.

Between the π^* resonance and the ionization potential, several sharp but weak resonances can be observed. These features correspond to excitations from the 1s electron to Rydberg orbitals, and then correspond to **Rydberg resonances**. If hydrogen atoms are present in the molecule, these transitions can also be related to a mixture of Rydberg and hydrogen-derived antibonding orbitals bearing the same symmetry. These features then merge into a continuous feature at about 2 eV below the ionization potential.

For some molecules, above the 1s ionization potential it is possible to observe broad resonance features, which are known as σ^* **shape resonances**. Such transitions are related to the stabilization of the excited state against immediate decay due to the presence of an energy barrier that arise from the centrifugal part of the potential. This barrier separates the inner potential well of the molecule from a shallower outer potential well (see Fig. 2.10).

Finally, it is important to mention that all electronic excitations are multi-electron in nature. This points that some transitions involve the participation of "passive" electrons. The sudden creation of the core-hole potential as the result of the "active" electron absorbing an X-ray photon may induce excitation to a secondary "passive" electron. This leads to **multi-electron features** in the X-ray absorption spectrum, which are generally separated into *shake-up* processes when the excited state is a bound state, and *shake-off* processes when the passive electron is excited to a continuum state.

Chapter 3

Objectives and Methods

3.1 Objectives

Eighty-three years have passed since the first interstellar molecule (CH) was identified (Swings and Rosenfeld, 1937) – and now there is no doubt that we live in a molecular universe (Tielens, 2013). In the recent years, more than 200 molecules have been identified in the Universe, particularly in the interstellar medium and in the circumstellar envelopes of evolved stars. Simple and "complex" molecules, up to 13 atoms, both inorganic and organic, as well as fullerenes (C_{60} and C_{70}), are present. The study of viable mechanisms of formation and destruction of chemical species, as well as the identification of the molecular content in astrophysical objects, is completely necessary. The general goals of this PhD thesis are enumerated as follows:

1. Application of experimental techniques (gas and condensed phase) to study the formation and destruction of complex organic molecules in laboratory-simulated circumstellar environments.

2. Identification of the molecular (and ionic) content in star formation environments through radio observations.

In this chapter, we show a brief description of the methods; the main characteristics of the equipment (experimental and observational); data reduction techniques; and spectral analysis.

3.2 Experimental Methods

3.2.1 Gas Phase Experiments

3.2.1.1 The Experimental Setup

The gas phase photon measurements were performed at the Brazilian Synchrotron Light Source Laboratory (LNLS) using UV and soft X-ray photons selected by the Toroidal Grating Monochromator (TGM) and the Spherical Grating Monochromator (SGM) beamlines at energies from 10.0 to 310.0 eV (Fig. 3.1).

The synchrotron radiation is generated by electrons with relativistic velocities $u \rightarrow c$ orbiting around a magnetic field B. In this process, the electrons lose energy by emitting photons tangent to the orbit. The electron energies E are given by:

$$E = m_0 c^2 \gamma \tag{3.1}$$

where m_0 is the resting mass of the electron and γ is given by the following expression:

$$\gamma = \frac{1}{\sqrt{1 - \frac{u^2}{c^2}}} \tag{3.2}$$

The emission of photons by synchrotron process is characterized by a pulsating beam distributed in a light cone of solid angle $\Omega = \gamma^{-1}$, always tangent to the orbit of the electrons. In the LNLS facilities, photons are made available in beamlines that surround the electron storage ring (Fig. 3.1). These beamlines are equipped with monochromators, diffraction grids and crystals, ensuring greater control, better selection and performance of the radiation energy range required for each experiment.

In the present thesis work we use photons from the TGM and SGM beamlines at energies around the inner carbon K-shell to induce the processes of absorption, excitation, ionization and dissociation in benzene (C_6H_6), cyclohexane (C_6H_{12}) and biphenyl ($C_{12}H_{10}$) molecules. The study of the interaction of photon beam with molecular beam is done inside an ultra-high vacuum chamber installed at the end of the beamline.

Fig. 3.2) shows a schematic diagram of the experimental set up inside the vacuum chamber with the time-of-flight mass spectrometer (TOF-MS). The ions that are formed by ejection of an electron after the interaction of the molecule with a photon, or produced from the fragmentation of the parent ion, are directed and accelerated by the electric extraction field and focused by an electrostatic lens.

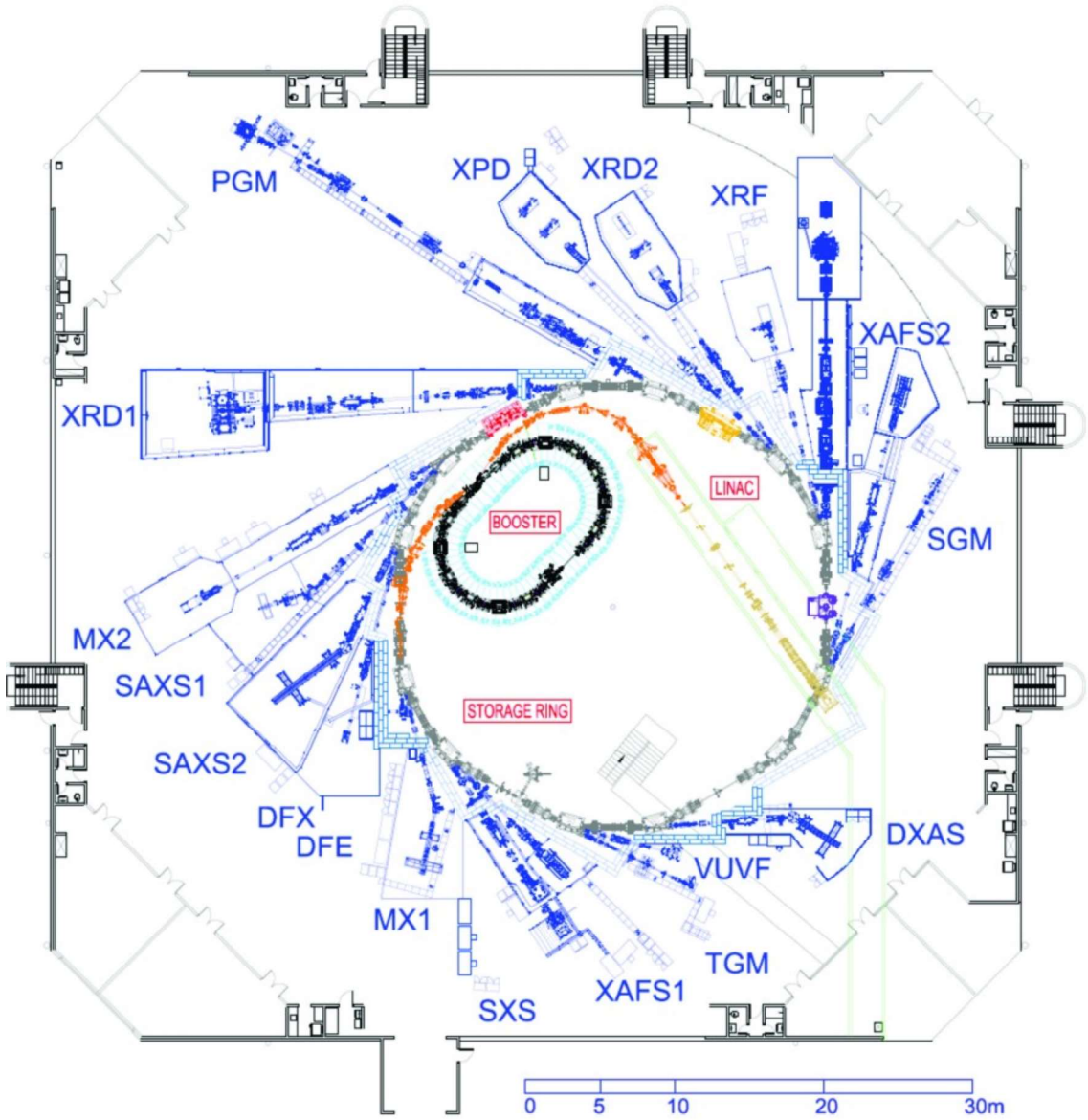

Figure 3.1: Scheme of the beamlines of the Brazilian Synchrotron Light Source Laboratory (LNLS) facilities.

After such processes, the ions enter a field-free drift tube (or time-of-flight tube) with 297 mm long until reaching the detector.

3.2.1.2 The Time-Of-Flight Equations

The ions that reach the detector are discriminated by their mass-to-charge (m/q) ratio. Lighter ions are faster than heavier ions, and the time-of-flight (TOF) of each ion can be determined using the Wiley-McLaren set of equations (Wiley and McLaren, 1955):

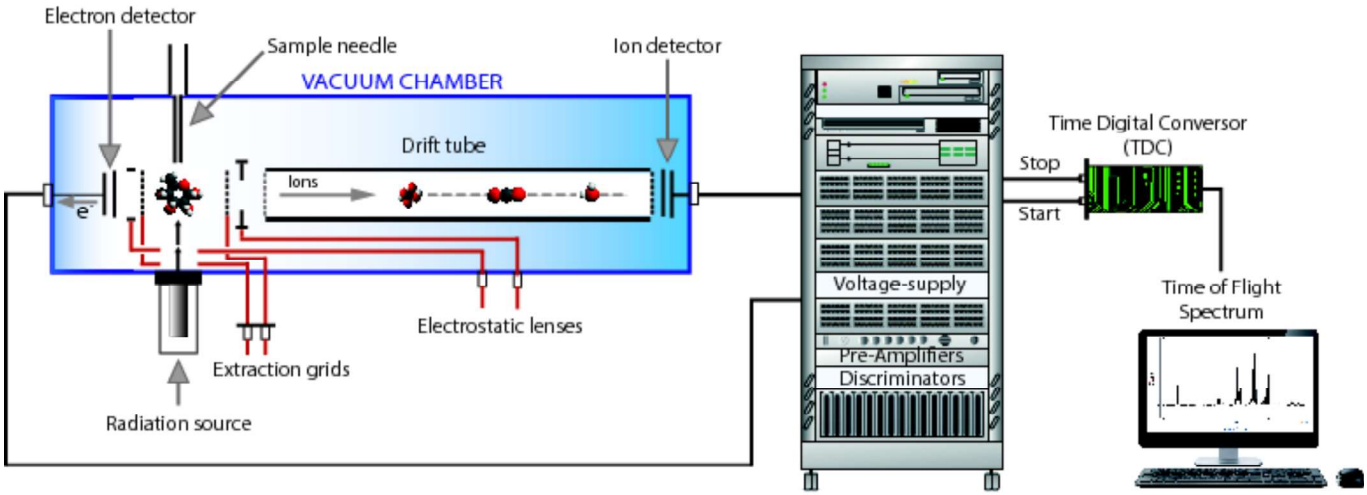

Figure 3.2: Schematic diagram of the experimental set up inside the vacuum chamber with time-of-flight mass spectrometer (TOF-MS), also showing the rack with associated electronic components.

$$TOF = \underbrace{t_1}_{extraction} + \underbrace{t_2}_{drift} + \underbrace{t_3}_{detection} \tag{3.3}$$

where TOF is determined by the sum of the three components. In equation 3.3, t_1 is the time corresponding to the acceleration of the ion in the extraction grid; t_2 is the time of the ion inside the drift tube; and t_3 is the response time of the acquisition (detection) system. The term t_1 can be obtained by applying Newton's third law to the electrostatic force experienced by an ion of charge q induced by an electric field E:

$$F = qE = ma \tag{3.4}$$

The ion acceleration a is then expressed as:

$$a = E\frac{q}{m} \tag{3.5}$$

By knowing that a is the first derivative of the velocity over time:

$$a = \frac{dv}{dt} \tag{3.6}$$

$$v = \int adt = \int E\frac{q}{m}dt \tag{3.7}$$

And, therefore:

$$v_1 = v_0 + \frac{qEt_1}{m} \tag{3.8}$$

which leads to the following equation for the extraction time t_1:

$$t_1 = \frac{v_1 - v_0}{E}\left(\frac{m}{q}\right) \tag{3.9}$$

where v_0 and v_1 are the initial and final velocities in the extraction grid, respectively.

For the drift region, the velocity of the ions (v_{drift}) is obtained by applying the energy conservation law. In this case, the kinetic energy K is equal to the electrostatic potential energy U obtained by the particle as a consequence of the difference of potential ($V_1 - V_2$) between the extraction grid and the drift tube grid.

$$K = \frac{1}{2}mv_{drift}^2 \tag{3.10a}$$

$$U = q(V_1 - V_2) \tag{3.10b}$$

$$K = U \tag{3.10c}$$

$$\frac{1}{2}mv_{drift}^2 = q(V_1 - V_2) \tag{3.10d}$$

Therefore:

$$v_{drift} = \sqrt{2(V_1 - V_2)\frac{q}{m}} \tag{3.11}$$

The time of the ion in the drift region, t_2, is obtained by the following set of equations:

$$v_{drift} = \frac{\mathrm{d}x_{drift}}{\mathrm{d}t} \tag{3.12a}$$

$$\int dt = \int \left[2(V_1 - V_2)\frac{q}{m}\right]^{1/2} dx_{drift} \tag{3.12b}$$

Therefore:

$$t_2 = \frac{x_{drift}}{\sqrt{2(V_1 - V_2)}} \times \sqrt{\frac{m}{q}} \tag{3.13}$$

where x_{drift} is the length of the drift tube. By inspecting equation 3.13, it is possible to see that ions are progressively separated in groups according to their m/q relation as they trespass the field-free drift region between the extraction zone and the detector.

The times t_1 and t_3 in equation 3.3 are negligible compared to t_2. Therefore, TOF is approximately equal to t_2. As the difference of potential and the drift tube length are constant, we can approximate t_2 as:

$$t_2 = A\sqrt{\frac{m}{q}} \tag{3.14}$$

More details on the TOF equations can be seen in Guilhaus (1995).

3.2.1.3 Photoelectron Photoion Coincidence techniques (PEPICO, PEPIPICO and the Partial Ion Coincidence Yield)

In the experiments, a uniform electric field was used to extract in opposite directions the photoelectrons (PE) and photoions (PI) produced by the interaction of the beam with the sample. The positive ionic charged species were accelerated and focused into a field-free drift time-of-flight tube towards a micro-channel plate (MCP) detector disposed in a chevron configuration. The detection of one of the photoelectrons by a second MCP detector provides the start signal, while the stop signals are given by the detection of the photoions by a multi-hit fast time-to-digital converter (TDC) unit. Thus, standard time-of-flight spectra were obtained using the photoelectron-photoion coincidence (PEPICO) technique. The PEPICO spectrum can be considered as a single event mass spectrum. By setting up the voltage of the collimating lens, it is possible to operate the spectrometer in a highly discriminating condition, detecting only ions ejected along the spectrometer axis and providing an easy and accurate method for the determination of the kinetic energy release (Maciel et al., 1997). An example of PEPICO spectrum is shown in Fig. 3.3.

Photoionization of a prototypical molecule AB (Lindon et al., 2016) takes place by both direct ionization (eq. 3.15a) and autoionization (eq. 3.15b):

$$\mathrm{AB} + \mathrm{h}\nu \rightarrow \mathrm{AB}^{+\cdot} + \mathrm{e}^{-} \tag{3.15a}$$

$$\mathrm{AB} + \mathrm{h}\nu \rightarrow \mathrm{AB}^{*} \rightarrow \mathrm{AB}^{+} + \mathrm{e}^{-} \tag{3.15b}$$

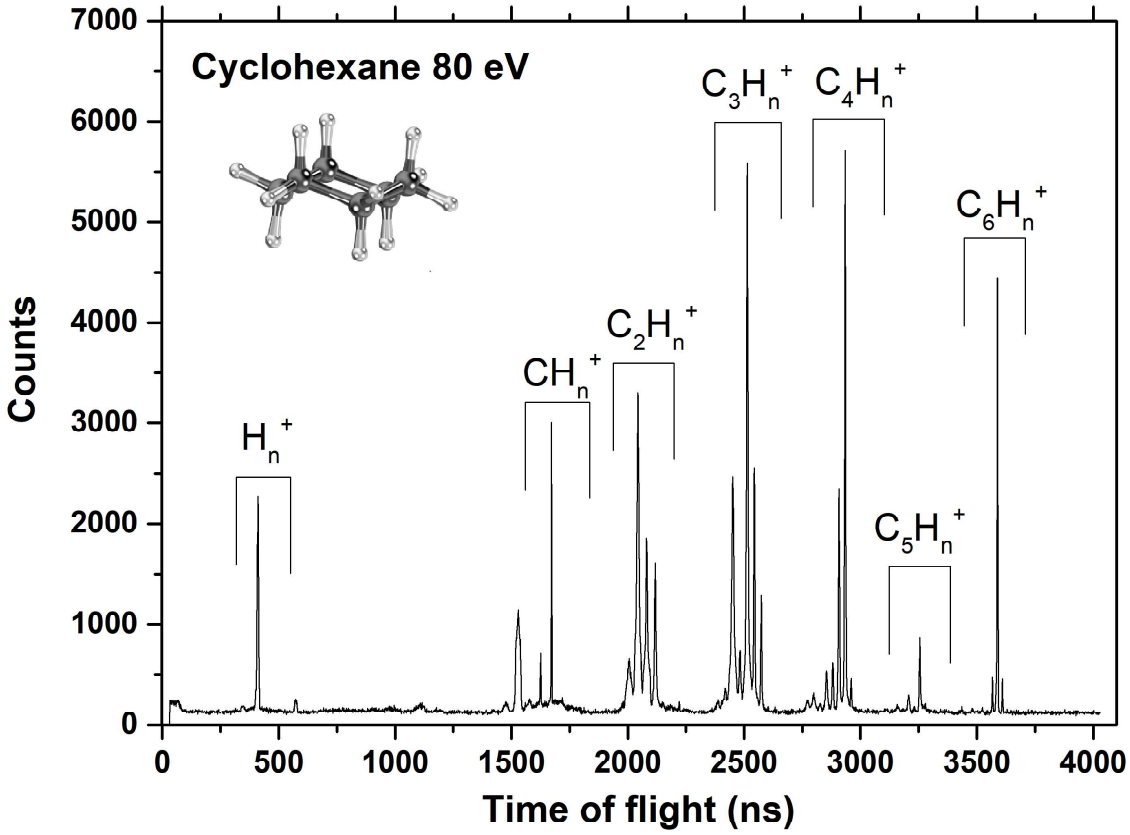

Figure 3.3: Example of photoelectron-photoion coincidence (PEPICO) spectrum. Taken from Quitián-Lara (2016).

These processes account for non-dissociative photoionization. Additionally, the molecular ion AB^+ can undergo dissociation, in a process namely dissociative photoionization, or photodissociation:

$$AB^+ \rightarrow A^+ + B \tag{3.16}$$

In the photodissociation process, the molecular ion is broken, leading to the formation of a detectable positive fragment A^+, an undetectable neutral fragment (B) and a photoelectron. For a complex molecule, distinct fragmentation channels from the molecular ion are possible. This leads consequently to a mass spectrum with several peaks, each one related to a particular ionic fragment with a specific mass-to-charge ratio.

For core-shell photoionization (Fig. 3.4), there is a third way in which the molecule can undergo fragmentation. This is called the Auger process, and it happens when a secondary (or Auger) electron is ejected as a consequence of the core-shell ionization, leading to a doubly-charged species:

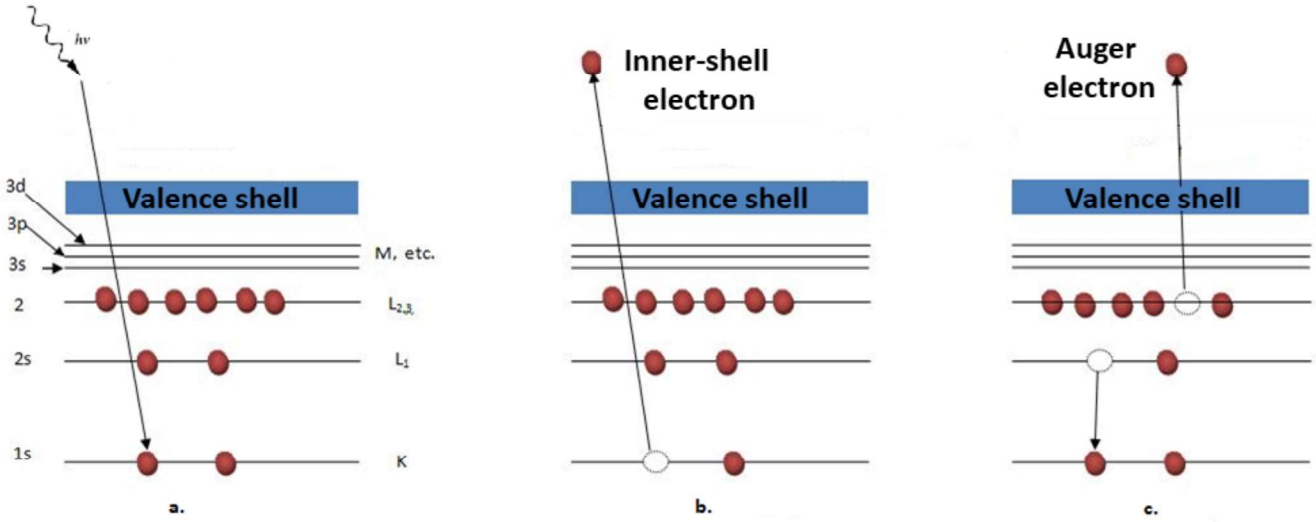

Figure 3.4: Schematic representation of the excitation and ionization processes in the inner shell. a) Photoabsorption. b) Photoionization. c) Emission of an Auger electron. Taken from Quitián-Lara (2016).

$$(AB^{+})^{*} \xrightarrow{Auger} AB^{++} + e^{-} \tag{3.17}$$

In this case, the emission of the second electron is due to the decay of an external electron that occupy the empty level generated in the first ionization.

The doubly-charged species can undergo dissociation through distinct dissociation pathways, involving two-body (AB), three-body (ABC) and even four-body (ABCD) mechanisms. A powerful approach for studying the fragmentation due to Auger processes is the PhotoElectron-PhotoIon-PhotoIon coincidence (PEPIPICO, Fig. 3.5, Eland 1987).

The processes up to four-body mechanisms that can be studied through the PEPIPICO technique are depicted below (Arion, 2008).

1. Two-Body Dissociation

The simplest scenario of a PEPIPICO fragmentation mechanism is the two-body process, which results from the fission of two fragment ions from a doubly-charged species AB^{++}:

$$AB^{++} \rightarrow A^{+} + B^{+} \tag{3.18}$$

2. Three-Body Mechanisms

In three-body mechanisms, apart from the two charged fragments, the emission of one additional neutral species from a doubly-charged ABC species also occur. Such dissociation can happen in three

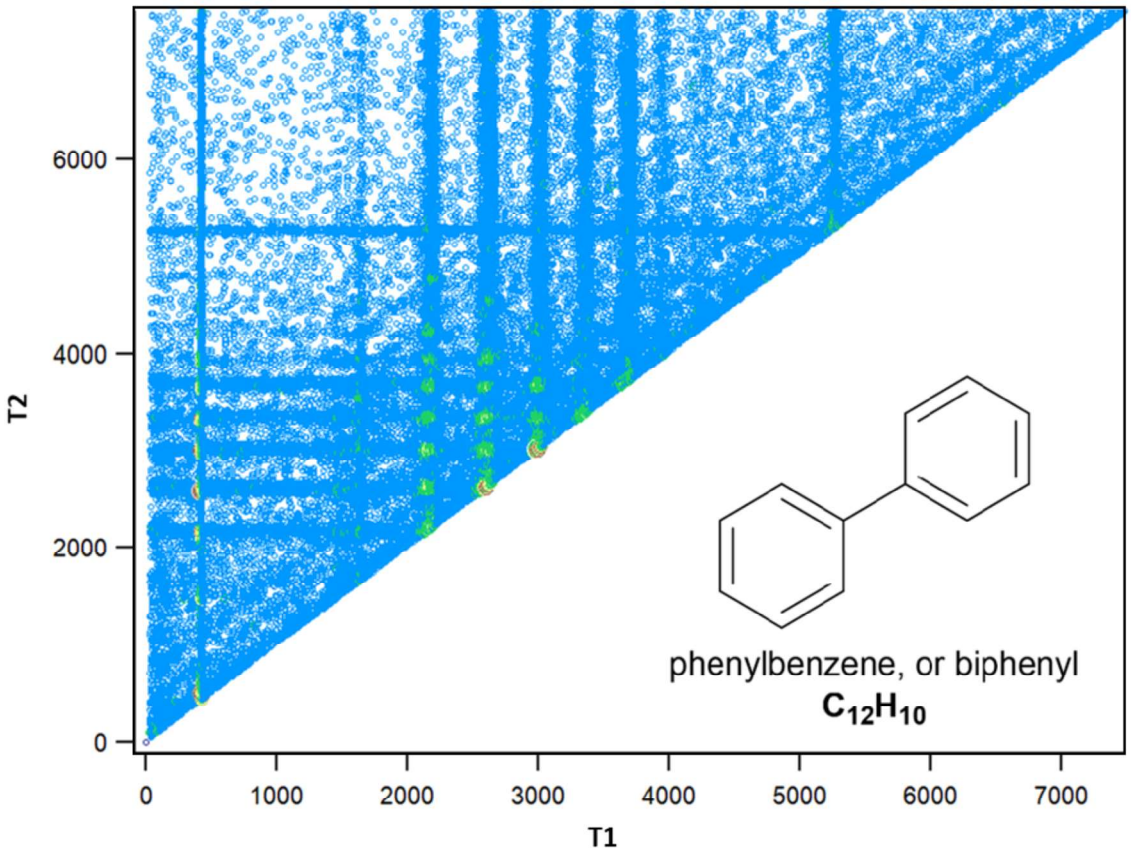

Figure 3.5: Example of photoelectron-photoion-photoion coincidence (PEPIPICO) spectrum.

distinct ways, namely:

2a. Concerted Three-Body Dissociation

$$ABC^{++} \rightarrow A^{+} + B^{+} + C \tag{3.19}$$

2b. Three-Body Deferred Charge Separation

$$ABC^{++} \rightarrow AB^{++} + C \tag{3.20a}$$

$$AB^{++} \rightarrow A^{+} + B^{+} \tag{3.20b}$$

2c. Three-Body Secondary Decay

$$ABC^{++} \rightarrow A^{+} + BC^{+} \tag{3.21a}$$

$$BC^{+} \rightarrow B^{+} + C \tag{3.21b}$$

3. Four-body mechanisms

In four-body mechanisms, two neutral species are formed from the dissociation of the doubly-charged $ABCD^{++}$ species. This can occur in four distinct ways, namely:

3a. Concerted Four-Body Dissociation

$$ABCD^{++} \rightarrow A + B^{+} + C^{+} + D \tag{3.22}$$

3b. Four-Body Deferred Charge Separation

$$ABCD^{++} \rightarrow ABC^{++} + D \tag{3.23a}$$

$$ABC^{++} \rightarrow AB^{++} + C \tag{3.23b}$$

$$AB^{++} \rightarrow A^{+} + B^{+} \tag{3.23c}$$

3c. Four-Body Secondary Decay after a Deferred Charge Separation

$$ABCD^{++} \rightarrow ABC^{++} + D \tag{3.24a}$$

$$ABC^{++} \rightarrow A^{+} + BC^{+} \tag{3.24b}$$

$$BC^{+} \rightarrow B^{+} + C \tag{3.24c}$$

3d. Four-body Secondary Decay in Competition

$$ABCD^{++} \rightarrow AB^{+} + CD^{+} \tag{3.25a}$$

$$AB^{+} \rightarrow A + B^{+} \tag{3.25b}$$

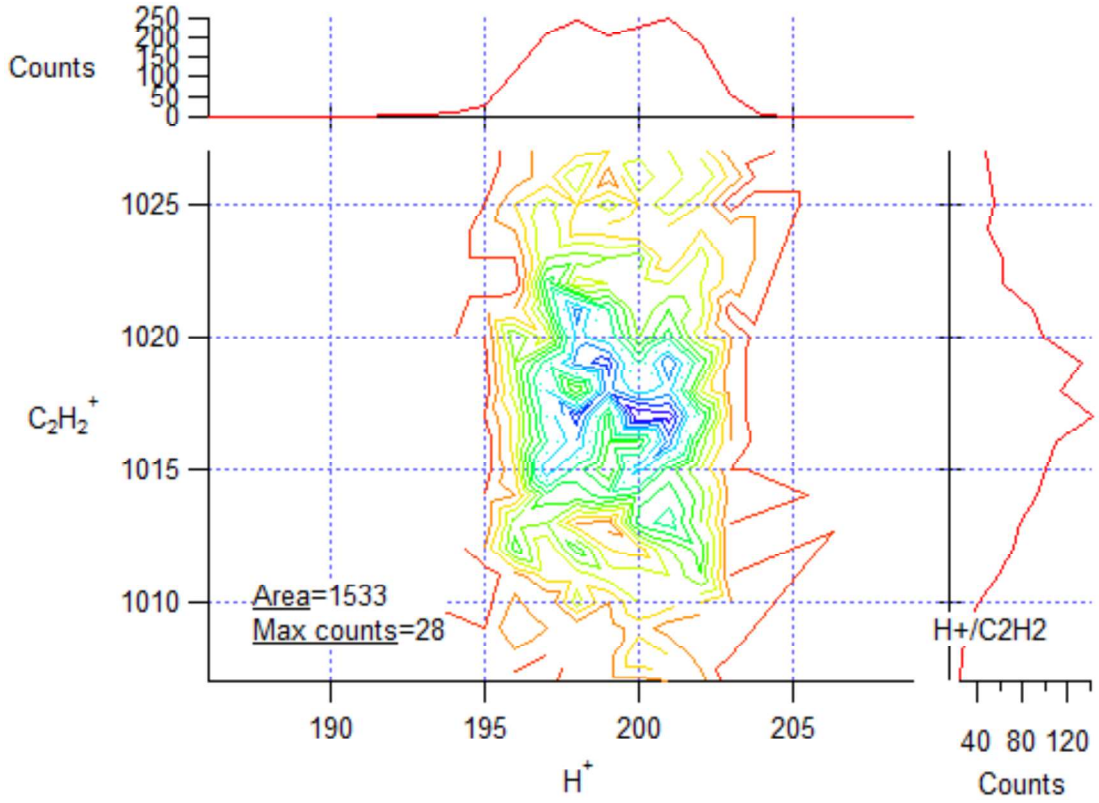

Figure 3.6: Example of the contour map extracted from (PEPIPICO) spectrum. Adapted from Quitián-Lara (2016).

$$CD^+ \rightarrow C^+ + D \tag{3.25c}$$

All information provided by a PEPIPICO spectrum is identified by two-dimensional projections (Fig. 3.5). The 2D spectrum shows the signal intensity (counts) as a function of the time-of-flight of each ion (t_1 and t_2). However, it is necessary to map the two-dimensional projections to extract numerical parameters from both the original figure and the projections (Fig. 3.6).

The production of ionic fragments is determined by using a multiple Gaussian functions fitting for obtaining the area of the peaks and the Partial Ion Yield (Fig. 3.7, $PIY(\%)$), of each fragment-ion, which is then obtained by the following equation:

$$PIY(\%) = \left[\frac{A_i^+}{\sum A_i^+}\right] \times 100 \tag{3.26}$$

where A_i^+ is the area of each ion i and $\sum A_i^+$ is the sum of the areas of all peaks in the spectrum. The uncertainties of the partial yields are estimated around 10%.

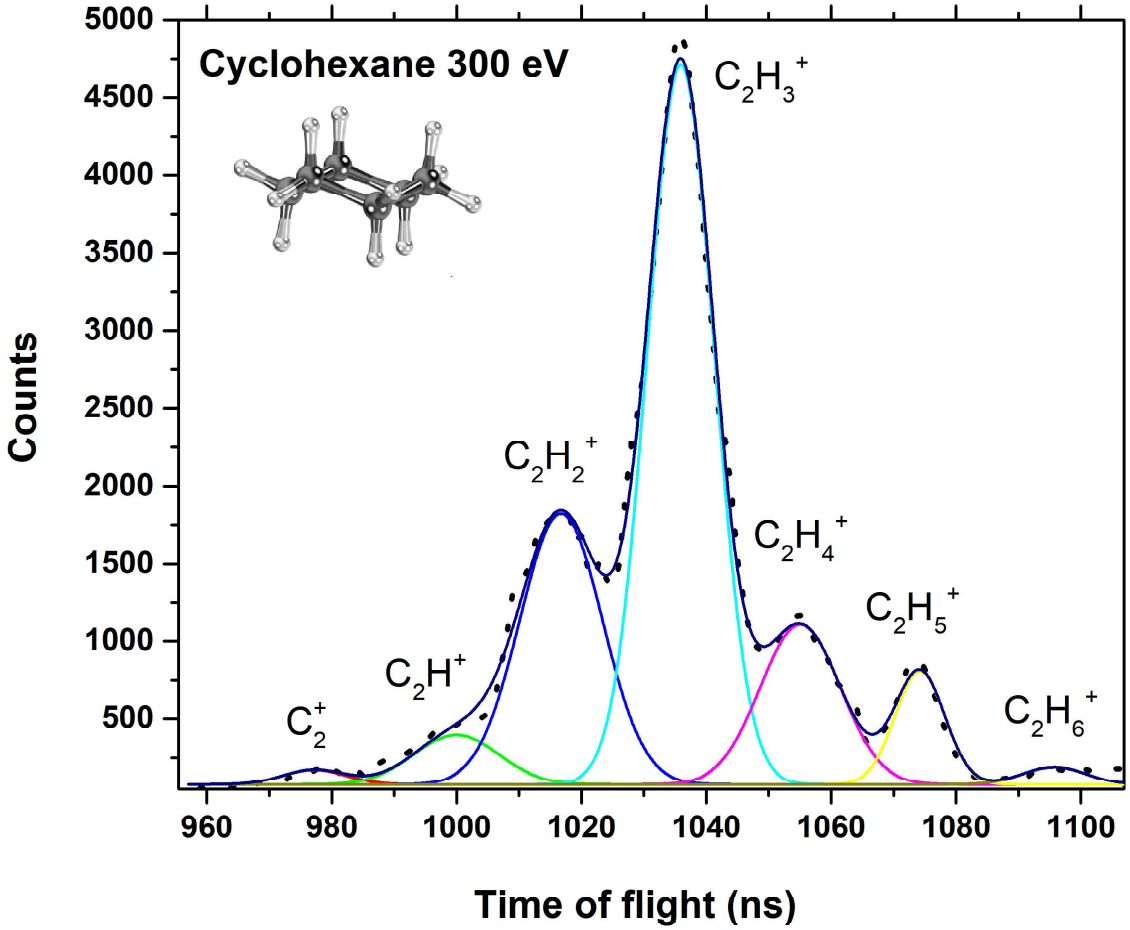

Figure 3.7: Example of the multiple gaussian fitting from PEPICO spectrum. Adapted from Quitián-Lara (2016).

3.2.1.4 Photoionization and Photodissociation Cross Sections

Assuming that the fluorescence yield is negligible in the X-ray photon energy range due to the low atomic number of carbon (Chen et al., 1981), and that all absorbed photons lead to non-dissociative ionization (σ_{ph-i}) or dissociative ionization (σ_{ph-d}) processes, σ_{ph-abs} can be divided into two distinct contributions:

$$\sigma_{ph-abs} = \sigma_{ph-i} + \sigma_{ph-d}, \tag{3.27}$$

where σ_{ph-d} accounts for all processes in which the ionization induced by the absorption of X-ray photons leads to dissociation.

On the other hand, the non-dissociative photoionization cross section (σ_{ph-i}) can be discriminated in two terms, depending on the degree of ionization:

$$\sigma_{ph-i} = \sigma^{+}_{ph-i} + \sigma^{q+}_{ph-i} \tag{3.28}$$

where σ^{+}_{ph-i} represents the process in which only the singly-charged parent ion is produced, while σ^{q+}_{ph-i} accounts for non-dissociative multiple ionization processes.

The σ_{ph-d}, σ^{+}_{ph-i} and σ^{q+}_{ph-i} values can be obtained by multiplying σ_{ph-abs} by the appropriate *PIY* values, as shown in the following equations:

$$\sigma^{+}_{ph-i} = \sigma_{ph-abs}\left(\frac{PIY_{M^+}}{100}\right), \tag{3.29a}$$

$$\sigma^{q+}_{ph-i} = \sigma_{ph-abs}\left(\sum_{q=2}^{q_{max}} \frac{PIY_{M^{q+}}}{100}\right), \tag{3.29b}$$

$$\sigma_{ph-d} = \sigma_{ph-abs}\left(1 - \frac{PIY_{M^+}}{100} - \sum_{q=2}^{q_{max}} \frac{PIY_{M^{q+}}}{100}\right), \tag{3.29c}$$

where PIY_{M^+} is the partial ion yield value related to the singly-charged parent ion, $PIY_{M^{q+}}$ is related to the production of the parent ion of mass M in its charge state $q > 1$ and q_{max} is the maximum charge state for which the multiple ionization process is observed. The *PIY*s of singly- and multiply-charged isotopologues were also taken into account in the calculation of the σ^{+}_{ph-i} and σ^{q+}_{ph-i} cross sections, respectively.The full description of the determination of absolute cross sections can be found elsewhere (Pilling et al., 2006; Fantuzzi et al., 2011; Monfredini et al., 2019).

3.2.1.5 Photodissociation Rates and the Half-life of Molecules

The determination of σ_{ph-d} values is of significant importance for estimating the molecular abundance in both interstellar and circumstellar environments. The decreasing of the abundance of a given molecule subjected to a radiation field in the photon energy range $E_2 - E_1$ inside a gaseous dusty cloud can be written as (Cottin et al., 2003; Boechat-Roberty et al., 2009a):

$$-\frac{dN}{dt} = N k_{phd} \tag{3.30}$$

where N is the column density (cm^{-2}) and k_{ph-d} is the photodissociation rate (s^{-1}), given by:

$$k_{ph-d} = \int_{E_1}^{E_2} \sigma_{ph-d}(E) F_X(E) dE \tag{3.31}$$

where $\sigma_{ph-d}(E)$ is the photodissociation cross section (cm^2) and $F_X(E)$ is the photon flux (photons cm^{-2} $eV^{-1}s^{-1}$), both as a function of the photon energy $E = h\nu$.

Therefore, it is possible to determine the half-life of a given molecule by the following equation (Andrade et al., 2010):

$$t_{1/2} = \frac{ln2}{k_{phd}} \tag{3.32}$$

In addition, we can also determine the photoionization rate, k_{phi}, given by:

$$k_{ph-i} = \int_{E_1}^{E_2} \sigma_{ph-i}(E) F_x(E) dE \tag{3.33}$$

where $\sigma_{phi}(E)$ (cm^2) is the photoionization cross section.

3.2.2 Condensed Phase Experiments

The condensed phase experiments with astrophysical ice analogues were carried out at the Laboratório de Química de Superfícies (LaQuiS) of the Federal University of Rio de Janeiro. The electron-stimulated ion desorption technique (ESID, Ramsier and Yates 1991) was used to study desorbed cations of pure samples of benzene (C_6H_6), cyclohexane (C_6H_{12}), chlorobenzene (C_6H_5Cl) and a solution of phenol (C_6H_5OH) in methanol (CH_3OH) at 89%. The samples were condensed on a steel substrate at 125 K and bombarded by a pulsed electron beam. The positive ions desorbed from the surface ice were analyzed by time-of-flight mass spectrometry (TOF-MS).

The experimental setup consists of an ultra-high vacuum chamber that operates at 1.0×10^{-9} mbar pressure. Integrated to the chamber, a manipulator allows a fine adjustment of the positioning of the sample holder in XYZ. The ionizing source is an electron gun (Kimball Physics, ELG-2). Coupled to the system, we have a residual gas analyzer (RGA), a time-of-flight mass spectrometer (TOF-MS) and a system of cooling by continuous circulation of liquid nitrogen. The experimental setup diagram can be seen in the Figure 3.8.

The injection process of the individual samples consists of a previous degassing through several cycles of freezing-pump-thaw before its admission to the inside of the chamber. Into the chamber,

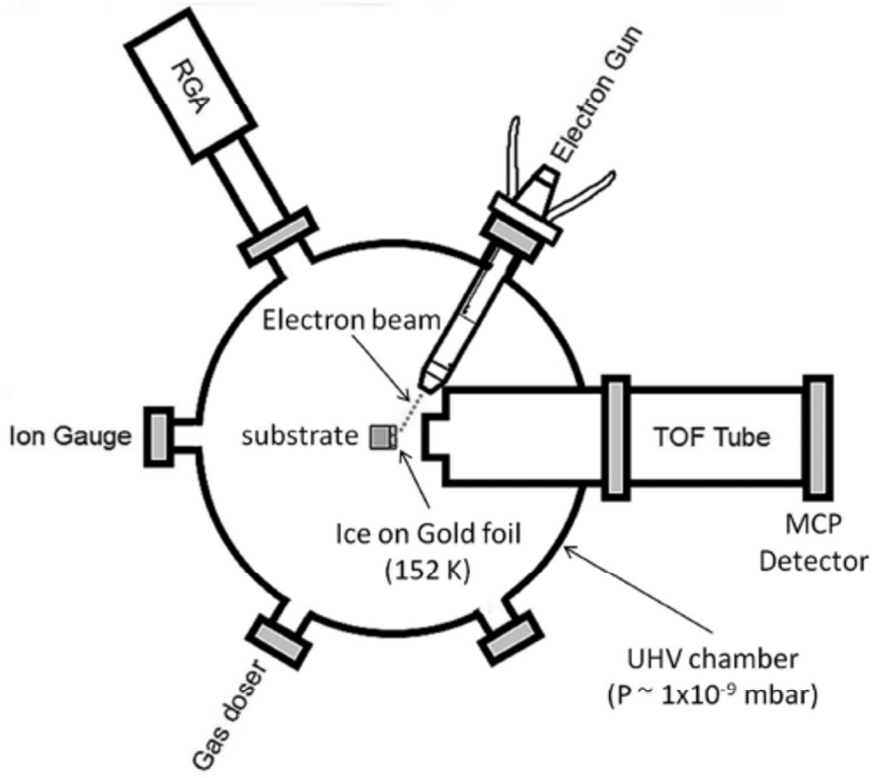

Figure 3.8: Experimental setup of the condensed phase experiments. Adapted from Ribeiro et al. (2014).

the vaporized sample is monitored by the RGA while the ice analog is grown by direct condensation of the samples on steel substrate cooled at 125K.

The TOF-MS is composed of an electrostatic extraction system, collimator lenses, a drift tube of 25 cm of length and two micro-channel plate detectors (MCP) in chevron configuration. The desorbed cations are extracted by a constant electrical potential (+1900 V) applied to the sample. Before reaching the MCP detector, the positive ion beam drifts through three metal grids (nominal transmission of 90%). The inlet grid of the TOF tube is grounded and positioned at 10 mm from the sample surface.

Externally, a Hewlett-Packard pulse generator (HP 8116A) is responsible for starting and pulsing the electron beam with a pulse time of 20 ns at 80 kHz of repetition frequency. Therefore, for the arrival of ions, the external pulse generator participates in the start process of the signal from the time-to-digital converter device (TDC), counting the signals within a 12.5 μs period. More details about the experimental setup are available in Ribeiro et al. (2014, 2015).

The signal analysis of the time-of-flight spectra was performed based on the same principle described in the previous section. The ionic yield (Y_i) of the desorbed fragments to gas phase were

determined to applying the following equation:

$$Y_i = \frac{A_i}{N_{pulses}\left(\frac{n_{e^-}}{pulses}\right)} \tag{3.34}$$

where A_i is the area obtained by a Gaussian fit from each desorbed cation, N_{pulses} is the number of start signals of the electron gun determined by the TDC device (1.2×10^8 pulses) and n_{e^-} is the number of electrons incident at the electron beam from each start signal. The n_{e^-} value is obtained by multiplying the incident current of the electron beam by the pulse period and dividing it by the electron charge. In this case the value of the current is 6.7 nA, resulting in 5.23×10^5 incident electrons.

3.3 Radioastronomical Line Observations

3.3.1 IRAM 30m Radiotelescope

The IRAM 30m radio telescope (Fig. 3.9) is operated by the French-German-Spanish Institute for Millimeter Radio Astronomy (IRAM). It is located near Pico Veleta at an altitude of 2870 m in the mountains of Sierra Nevada, Spain. It is the most sensitive single-dish telescope in the world that observes the millimeter windows of the electromagnetic spectrum.

The structure of the radio telescope is composed of a 30m reflective paraboloid surface with a surface accuracy of 0.08 mm and a pointing accuracy better than 2 arc seconds. The primary surface is formed by the micrometric junction of 420 aluminum panels on a solid steel structure supported by a concrete base that allows an alt-azimuth pointing (Baars et al., 1994).

3.3.2 Receivers

The frontend of the IRAM 30m radiotelescope offers three possible types of receivers: EMIR, HERA and NIKA2. The EMIR spectral line receivers (Eight Mixer Receiver) operate in the atmospheric windows at 3mm, 2, 1.3 and 0.9 mm, between 72GHz and 360 GHz. Each spectral window is covered by a dedicated receiver, designated as E090, E150, E230 and E330 according to their approximate center frequencies in GHz. The Heterodyne Receiver Array (HERA) consists of 9 dual-polarization pixels arranged in the form of a center-filled square separated by 24 arcs. Finally, NIKA2

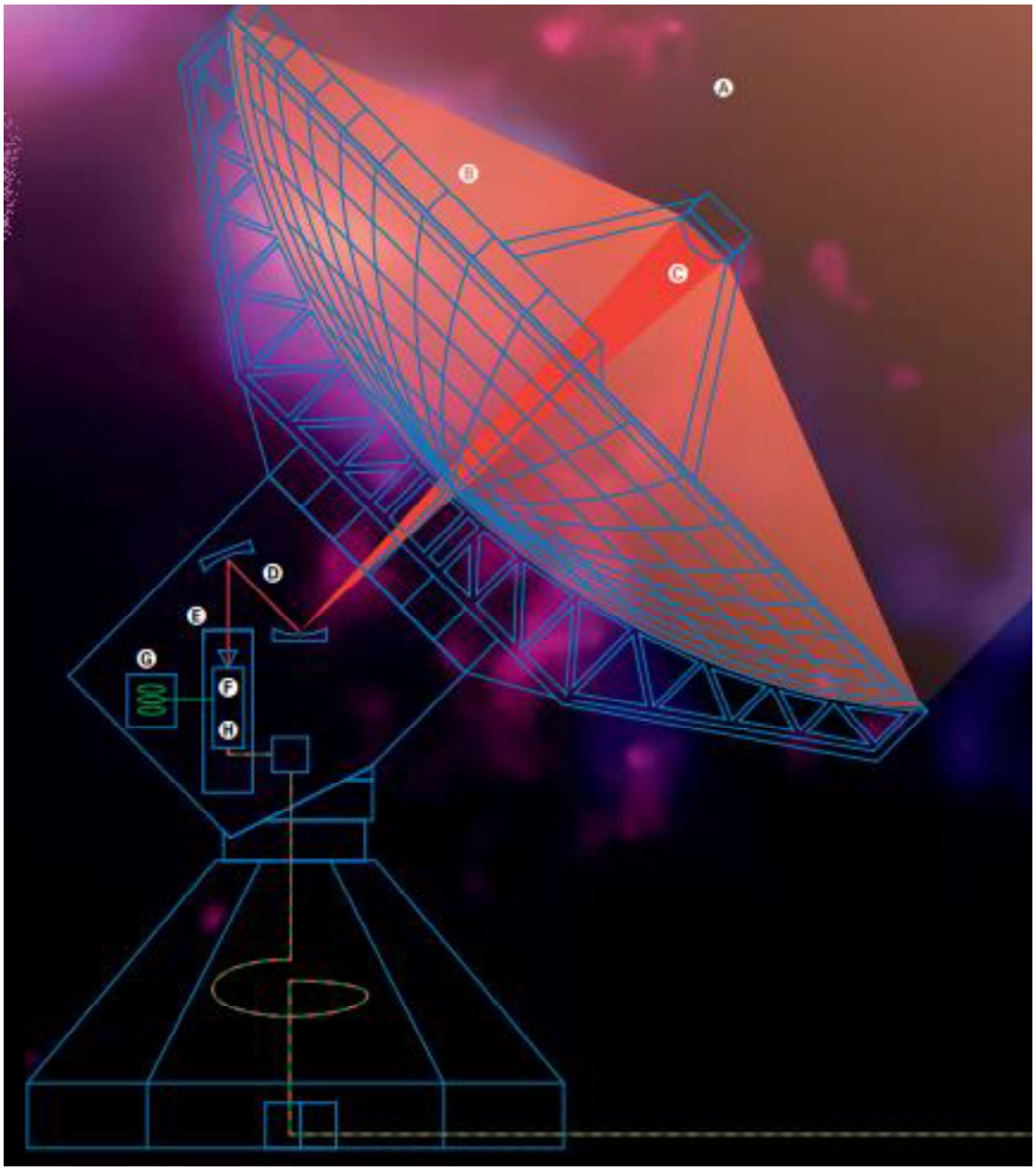

Figure 3.9: IRAM 30m Radio Telescope cross section on concrete pedestal (A) Path traveled from the object signal to the 30m primary reflective surface (B). Signal reflected in the secondary mirror (C) and directed to the tertiary mirror (D). The focused signal contacts local receivers, amplifiers, and oscillator (E, G, and H) contained in an insulated box cooled with a liquid nitrogen cryostat. Adapted from the doctoral thesis of Mendoza (2014)

is a dual band camera that comprises three arrays of Kinetic Inductance Detectors that operates simultaneously at wavelengths of 1 and 2 mm (Kramer, 2018).

The spectral line survey of IRAS 4A was carried out over six semesters from September 2012 to March 2015, as part of the Large Program ASAI (Lefloch et al., 2018) with the IRAM 30m telescope. The observations of the band 72-80 GHz were obtained in January 2016. The broad-band EMIR receivers E090, E150 and E230 were used to cover the three spectral windows at 3mm, 2mm and 1.3mm. They were connected to the Fast Fourier Transform Spectrometers (FTS) in its low (200 kHz) spectral resolution mode. The observations at 3mm (72–116 GHz) and 2mm (126–174 GHz) bands were carried out simultaneously. The 1mm (200-276 GHz) band was covered observing both the lower sideband (LSB) and the upper sideband (USB) simultaneously. The frequency of the local oscillator (LO) was regularly shifted by a fixed amount of 50 MHz, in order to allow easy identification of lines from the image and signal bands in the spectrum.

3.3.3 Observing technique

The radiation from the astronomical sources is often only a small fraction of the total radiation collected by the antenna receivers (Reichertz et al., 2001), which includes the contribution of the atmosphere, which is time variable. A common method is to collect and then subtract the emission of the atmosphere to the signal received "on source". This procedure is obtained by "switching" the pointing direction of the telescope (main-beam) in the sky between the astronomical source and a nearby position, supposed to be (astronomically) emission free. This new position contains approximately the same total power in the main lobe of the antenna but does not contain the source. The spatial and temporal emission fluctuations are canceled after source sensitive detection, provided that the broadband emission from sky, ground or continuum sources are similar at both positions (Wilson et al., 2009).

With this method it is possible to reduce very efficiently the contribution of the sidelobes of the antenna and atmospheric fluctuations. It is highly effective if baseline waves are a problem. For compact sources, a variant of this method is the wobbler switching, very useful for the noise suppression (Wilson et al., 2009; Wilson, 2013). One common method to minimize instability effects consists in using of a rapidly wobbling of the secondary mirror which alternatively points the telescope beam to an adjacent position on the sky.

Most of the observations were carried out using the so-called Wobbler Switching mode with a

nutating subreflector, in order to ensure very flat baselines. This is at the cost of a nearby reference position, 3 arcmin from the protostellar core, and whose location with respect to the protostar varies with time. It turned out that, for abundant molecular species their emission is extended enough to be non-negligible towards the reference position. This affects mainly CO and ^{13}CO. For that reason, the observations of the 112–116 GHz band were carried out in Position Switching mode, adopting a reference position fixed with respect to the protostellar core, which was checked to be almost free of line emission.

The observations were calibrated by monitoring regularly (every 10 to 15 min) the atmospheric transmission. At the IRAM 30m telescope, the intensities measured by the receivers are expressed in units of antenna temperature T_A^*, corrected for atmospheric attenuation and sky coupling. The conversion from instrumental count units to T_A^* is performed using the standard chopper-wheel method (Kutner and Ulich, 1981). More details about the calibration procedures at the IRAM 30m telecope can be found in the report of Kramer (1997, 2018). The instrumental uncertainties at the IRAM 30m are typically 10%, 15% and 20% for lines at 3mm, 2mm and 1mm, respectively (Lefloch et al., 2018).

For the subsequent line analysis and radiative transfer modelling, flux intensities were expressed in units of main-beam antenna temperature T_{MB}, adopting the values of Forward efficiency F_{eff} and Beam efficiency B_{eff} tabulated by the IRAM observatory.

3.3.4 Data reduction

As explained in Lefloch et al. (2018), the data reduction was performed using the GILDAS/CLASS software developed at IRAM. A simple flat baseline was first subtracted to each spectrum. We discarded spectra with a very high noise or obvious calibration problems. From comparing every scan with their (50 MHz LO) frequency shifted counterpart, spurious signals from the image band could be identified and removed. The resulting scans were then averaged in order to produce the final spectral bands. Overall, we could obtain an excellent sensitivity in all three millimeter bands, with a final rms in the range 2mK to 5mK per interval of 1 km/s, depending on the frequency.

3.3.5 Line identification

We used the CASSIS software (Vastel et al., 2015) to identify the molecular line content, which is based on the Cologne Database for Molecular Spectroscopy (CDMS) and Jet Propulsion Lab (JPL) databases. We considered all the lines detected with an intensity higher than 3σ. We examine in this

thesis the molecular content based on the molecular line identification performed in the three bands of the line survey.

In order to derive significant information on the molecules observed in the source, such as the excitation temperature and the column density with respect to H_2, we obtained the rotational diagram of each species. This term refers to a plot of the column density per statistical weight of a number of molecular energy levels, as a function of their energy above the ground state (see Goldsmith and Langer 1999). In a local thermodynamic equilibrium (LTE) regime, it corresponds to a Boltzmann distribution, for which a plot of the natural logarithm of N_u/g_u versus E_u/k_B yields a straight line with a slope of $1/T_{rot}$:

$$ln\frac{N_u}{g_u} = ln\frac{N_{tot}}{Q(T_{rot})} - \frac{E_u}{k_B T_{rot}} \tag{3.35}$$

where N_u is the population of molecules in the energy level u, g_u is the statistical weight of u, N_{tot} is the total population of molecules, $Q(T_{rot})$ and T_{rot} are respectively the rotational partition function and the rotational temperature of the molecule, E_u is the energy of the level u and k_B is the Boltzmann constant. A rotational diagram can be useful to determine whether the emission is optically thick or thin, whether the level populations are described by LTE, and to determine what temperature describes the population distribution in the event that LTE applies (Vastel et al., 2015).

Chapter 4

Experimental Results I: Cyclohexane (Gas Phase)

4.1 Hydrogenated Benzene and Super-Hydrogenated PAHs

As discussed in more detail in Chapter. 1, polycyclic aromatic hydrocarbons (PAHs) are molecular archetypes that can be classified according to the number of fused benzene (C_6H_6) rings that make up the base structure (Scott, 2015). These molecules are identified by spectral features due to stretching and bending vibrations (Allamandola et al., 1989; Peeters et al., 2002; Yang et al., 2017b). Frequently, such features are accompanied by bands at 3.4 and 6.9 μm, characteristic of C–H and C–C aliphatic bonds (Zhang and Kwok, 2014) and emitted by hydrogenated PAHs, H_n-PAHs (Zhang and Kwok, 2014).

The stability of H_n-PAHs and their role as catalysts in the formation of H_2 in different astrophysical environments are of special interest in astrophysics and astrochemistry, and the subject of an intense debate (Reitsma et al., 2014; Gatchell et al., 2015; Cazaux et al., 2016; Wolf et al., 2016). Le Page et al. (2003) studied the hydrogenation and charge state of PAHs in diffuse clouds, and concluded that the size of the PAH influences the stability of highly hydrogenated species. More recently, it was shown that the hydrogenation of the coronene cation, $C_{24}H_{12}^{+\cdot}$, follows a site-selective sequence, leading to the appearance of magic numbers of attached hydrogen atoms (Cazaux et al., 2016). Besides, Reitsma et al. (2014) verified that although the carbon backbone of a super-hydrogenated PAH is locally weakened, its deexcitation by H loss protects the PAH from fragmentation.

Some studies pointed that the addition of peripheral hydrogen atoms in PAHs could impart a

greater stability to these molecules in interstellar and circumstellar photodissociation regions (PDR). Gatchell et al. (2015) and Wolf et al. (2016), however, have shown that carbon backbone fragmentation was actually increased in collision and photoinduced experiments with super- and fully-hydrogenated pyrene cations ($C_{16}H_n^+$). Their results, therefore, point out to a failure of the hydrogenation protection mechanism, at least for small H_n-PAHs.

There is still no consensus in the literature about the role of peripheral H atoms to the photostability of H_n-PAHs. While there are some evidences that the addition of peripheral hydrogen atoms in PAHs could impart a greater stability to these molecules in interstellar and circumstellar PDRs (Reitsma et al., 2014), other studies suggest that the carbon backbone fragmentation increases significantly in super- and fully-hidrogenated PAHs of small size (Gatchell et al., 2015; Wolf et al., 2016). In any case, some of the electronic and structural properties of such macromolecules are expected to be already present in their smallest units. Benzene, the basic building block of a PAH, is composed of an aromatic ring with sp^2-type carbon atoms occupying the vertices of a regular hexagon (Martín and Scott, 2015). It is one of the most studied systems in chemistry, due to its several remarkable structural, electronic and reactivity properties (Cardozo et al., 2014; Papadakis and Ottosson, 2015). In opposition to alkenes and acyclic polyenes, the first hydrogenation step of benzene in its ground state is endothermic, which is attributed to aromaticity loss (Papadakis et al., 2016). In fact, the partial hydrogenation of benzene is not favored from the thermodynamic point of view, and the development of catalysts and processes to account for this transformation is still the focus of scientific inquiry (Foppa and Dupont, 2015). The complete hydrogenation of C_6H_6 (Figure 4.1) is accompanied by a change in the type of the C atoms (from sp^2 to sp^3-type), as all π electrons of the valence space are now being used to form the new C-H σ bonds. This process is exothermic by 208 kJ mol^{-1} (Carey and Sundberg, 2007), and ultimately leads to the formation of the cyclohexane (C_6H_{12}) molecule.

4.2 The Cyclohexane (C_6H_{12}) Molecule

The fully-hydrogenated counterpart of benzene, cyclohexane (C_6H_{12}, see Fig. 4.1), is an aliphatic organic molecule of the cycloalkane group. It is formed by covalent σ bonds of six sp^3-type C atoms and twelve H peripheral atoms. Due to the nature of the sp^3-type orbitals, C_6H_{12} does not form a planar hexagonal structure. The three-dimensional potential energy surface and the conformational analysis of the neutral C_6H_{12} molecule have been the focus of several studies, such as the ones

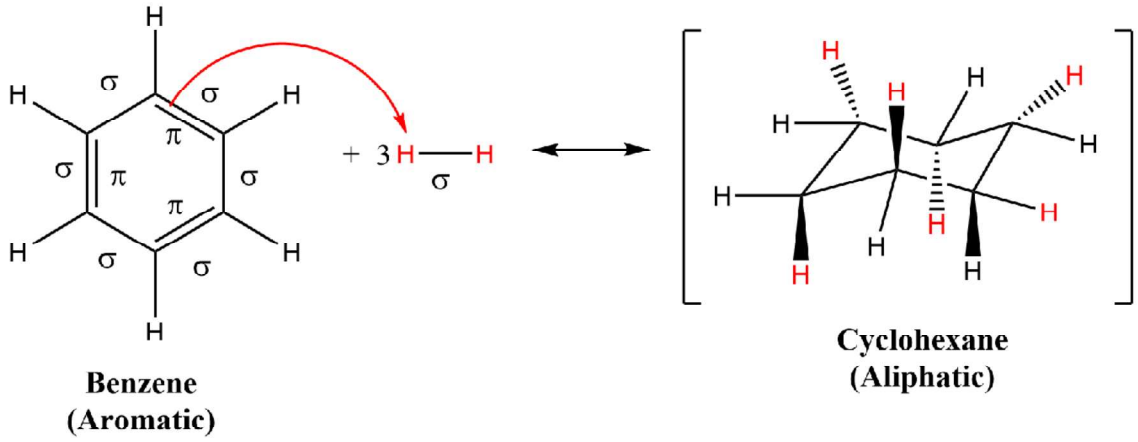

Figure 4.1: Schematic diagram of the complete hydrogenation reaction of benzene.

developed by Leventis et al. (1997) and Kakhiani et al. (2009). To summarize, there are two potential energy minima for the most stable conformer, which is the chair structure of D_{3d} symmetry (see Figure 4.2). These minima can interconvert through six different metastable twist-boat structures of D_2 symmetry. The interconversion between one of the chair conformers and each of the twist-boat structures follow through either of two transition states: one of C_2 symmetry and the other of C_1 symmetry, usually identified as a half-chair conformer. Finally, two twist-boat conformers are connected via a boat transition-state structure of C_{2v} symmetry. A simplified version of such transformations is also depicted in Fig. 4.2.

In this chapter, we study the stability of cyclohexane (C_6H_{12}) to ionizing and dissociative effects of UV and X-ray radiation. From the experimental data, we determined the main fragmentation pathways, as well as the photoionization and photodissociation cross sections of C_6H_{12}. We briefly describe the geometries of singly-charged C_6H_{12} species, and the consequences of generating such species from the ionization of cyclohexane in the ISM. From the photon flux in the photodissociation region of the planetary nebula NGC 7027, we contrast the stability and survival rates of cyclohexane and benzene (C_6H_6) in this carbon-rich object (Bernard-Salas et al., 2001; Bernard-Salas and Tielens, 2005; Wesson et al., 2010). Whenever possible, we extrapolate our results to the chemistry of PAHs and H_n-PAHs in circumstellar environments. It is worth mentioning that bands related to the mentioned polycyclic molecules have already been detected in NGC 7027 (Bernard-Salas et al., 2001; Goicoechea et al., 2004; Boersma et al., 2009; Tielens, 2008; Lau et al., 2016), thus providing an appropriate astrophysical environment for such analysis.

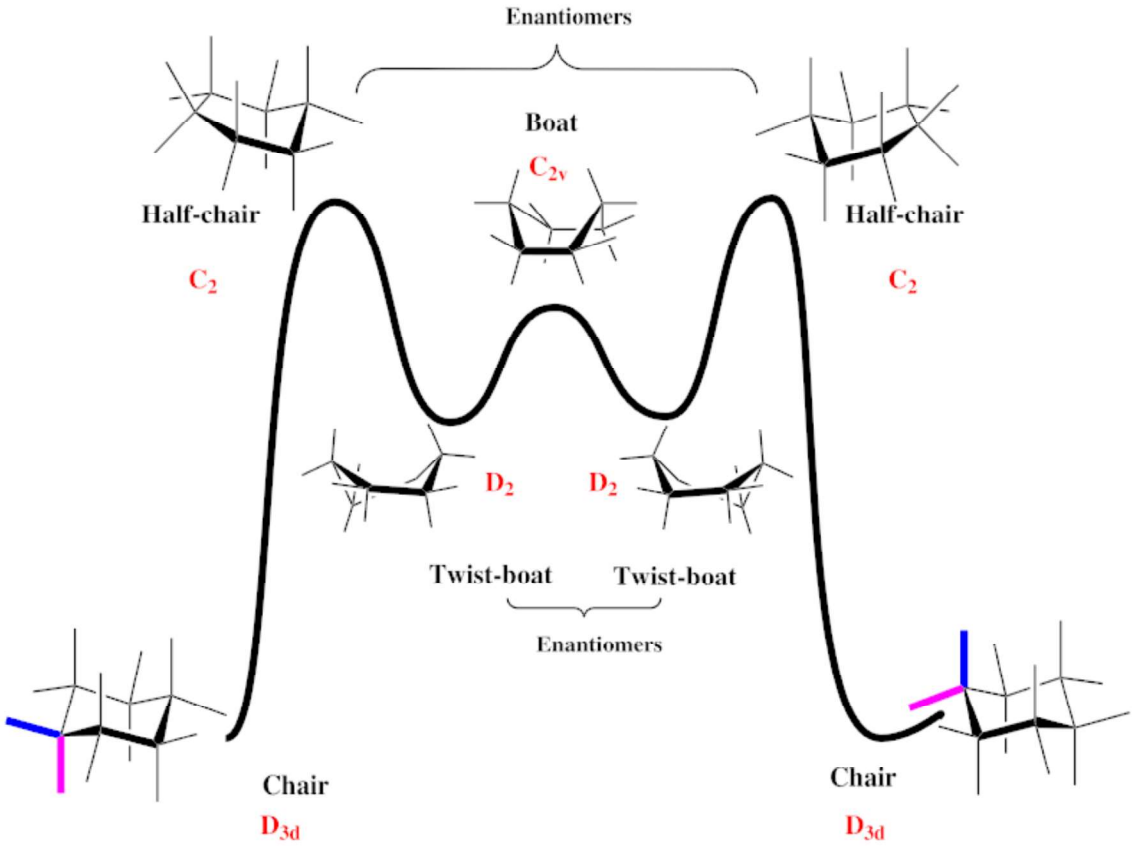

Figure 4.2: Simplified potential energy surface of cyclohexane. Adapted from Rzepa (2012).

Table 4.1: Partial Ion Yield, *PIY* (%), as a function of the photon energy in the UV region (10-16 eV). Only the fragments with intensity greater than 1% were shown, except the ions $H_2^{+\cdot}$ and H_3^+.

m/q	Attribution	*PIY* ($\geq$ 1%), per energy (eV)					
		10.8	11.4	12.4	13	14	16
28	$C_2H_4^{+\cdot}$	-	-	-	-	-	1.4
41	$C_3H_5^+$	-	-	-	-	-	10.9
42	$C_3H_6^{+\cdot}$	-	-	4.5	6.3	9.1	12.7
43	$C_3H_7^+$	-	-	1.9	3.2	5.1	5.2
55	$C_4H_7^+$	-	-	3.0	4.0	5.4	9.0
56	$C_4H_8^{+\cdot}$	-	-	22.7	29.5	34.1	29.8
57	$C_4H_9^+$	-	-	1.9	1.9	2.2	1.9
69	$C_5H_9^+$	-	-	5.9	6.7	9.0	5.1
83	$C_6H_{11}^+$	-	-	-	2.2	1.7	1.6
84	$C_6H_{12}^{+\cdot}$	93.8	93.9	53.4	41.9	27.2	18.4
85	$^{13}CC_5H_{12}^{+\cdot}$	6.2	6.1	2.8	2.4	1.5	1.2

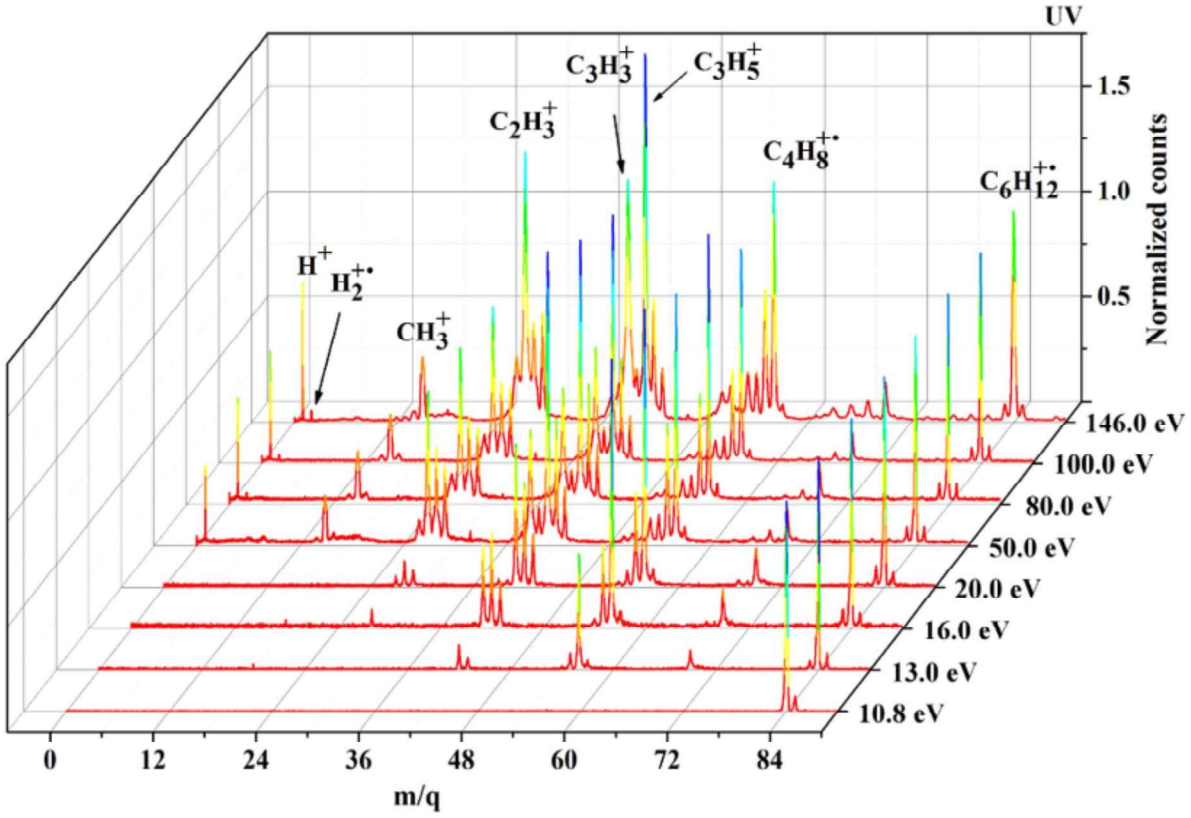

Figure 4.3: Selected mass spectra of the cyclohexane molecule recorded at UV (10-146 eV). The color variation indicates differences in the intensity of the peaks. For each energy the counts are normalized with respect to that of the parent ion, $C_6H_{12}^{+\cdot}$.

4.3 Ionization and Fragmentation of Cyclohexane

4.3.1 Ultraviolet (UV)

The UV results were thoroughly described in Quitián-Lara (2016). For contextualization with the X-ray results, a brief discussion is also given herein.

Fig. 4.3 shows the production of $C_6H_{12}^{+\cdot}$ as a function of the photon energy in the UV range (10.8 eV to 200.0 eV). For energies close to the first Ionization Potential (IP) of cyclohexane (9.8 eV, as determined by Dewar and Worley 1969), the photodissociation process is poorly activated. The *PIY* value of the parent ion decreases by a factor of almost 9 in the UV range, remaining only 4.5% at 200.0 eV.

A significant production of $C_4H_8^{+\cdot}$ is observed when the production of $C_6H_{12}^{+\cdot}$ starts to drop fast at around 12.4 eV (see Figure 4.3). That is, the original molecular ion breaks up through the loss of a neutral ethylene (C_2H_4) unit. The loss of only hydrogen atoms from the parent ion ($C_6H_n^+$, n=1-

Table 4.2: Partial Ion Yield, *PIY* (%), as a function of the photon energy in the UV region (20-200 eV). Only the fragments with intensity greater than 1% were shown, except the ions $H_2^{+\cdot}$ and H_3^+.

m/q	Attribution	*PIY* ($\geq$ 1%), per energy (eV)					
		20	50	80	100	146	200.0
1	H^+	-	4.2	4.7	5	3.9	4.4
2	$H_2^{+\cdot}$	-	0.2	0.3	0.4	0.3	0.4
3	H_3^+	-	-	0	0.1	0	0.1
15	CH_3^+	-	6.0	5.9	5.9	4.1	4.2
26	$C_2H_2^{+\cdot}$	-	-	1.9	2.7	4.1	4.7
27	$C_2H_3^+$	-	10.8	10.9	12.9	14	12.7
28	$C_2H_4^{+\cdot}$	2.7	7	5	6.5	4	3.8
29	$C_2H_5^+$	1.6	3.6	4.2	5.1	3.2	4.2
38	$C_3H_2^{+\cdot}$	-	-	-	-	2.4	2.2
39	$C_3H_3^+$	-	8.9	9.0	7.6	11.5	12.9
40	$C_3H_4^{+\cdot}$	-	1.9	1.6	2.1	2.2	2.9
41	$C_3H_5^+$	15.1	15.5	16.4	12.7	14.4	11.5
42	$C_3H_6^{+\cdot}$	9.4	4.8	4.3	6.4	3.7	3.1
43	$C_3H_7^+$	4.7	2.1	1.9	2.7	1.6	1.2
50	$C_4H_2^{+\cdot}$	-	-	-	-	1.4	1.2
51	$C_4H_3^+$	-	-	-	-	1.6	1.6
53	$C_4H_5^+$	-	1.5	1.3	1.1	1.7	1.8
54	$C_4H_6^{+\cdot}$	1.3	1.4	1.1	1.1	1.4	1.4
55	$C_4H_7^+$	9.6	5.5	4.9	4.2	3.6	3.4
56	$C_4H_8^{+\cdot}$	26.8	10	11.2	9.8	5.5	6.0
57	$C_4H_9^+$	1.7	-	-	-	-	-
69	$C_5H_9^+$	4.0	1.7	1.1	1.3	-	-
83	$C_6H_{11}^+$	1.4	-	-	-	-	-
84	$C_6H_{12}^{+\cdot}$	17.4	7.1	5.3	5.5	4.6	4.5
85	$^{13}CC_5H_{12}^{+\cdot}$	1.0	-	-	-	-	-

8) as well the loss of one carbon atom ($C_5H_n^+$, n=1-8) are inhibited, as observed by their low relative amounts (see Tables 4.1 and 4.2). The production of $C_4H_8^{+\cdot}$ reaches a maximum value (34.1%) at 14.0 eV and then it starts to decrease, reaching 26.8% at 20.0 eV. In this energy range, the production of $C_4H_7^+$ more than double, from 4% to 9%. This indicates that part of the closed-shell $C_4H_7^+$ production comes through the loss of a hydrogen atom from the open-shell $C_4H_8^{+\cdot}$ radical cation system. Other significant ions produced in the 14.0 eV to 20.0 eV energy range are the $C_5H_9^+$ (M^+–$CH_3^{\cdot}$), $C_3H_6^{+\cdot}$ (M^+–C_3H_6) and $C_3H_5^+$ species.

At 100.0 eV, the production of ions from the ethyl ($C_2H_n^+$), methyl (CH_n^+) and hydrogen (H_n^+) groups begins to increase. The most produced ion is the $C_3H_5^+$ species, followed by $C_2H_3^+$ (M^+–$C_4H_9^{\cdot}$) and $C_4H_8^{+\cdot}$. The production of the cyclopropenyl molecule $C_3H_3^+$ becomes significant at 100.0

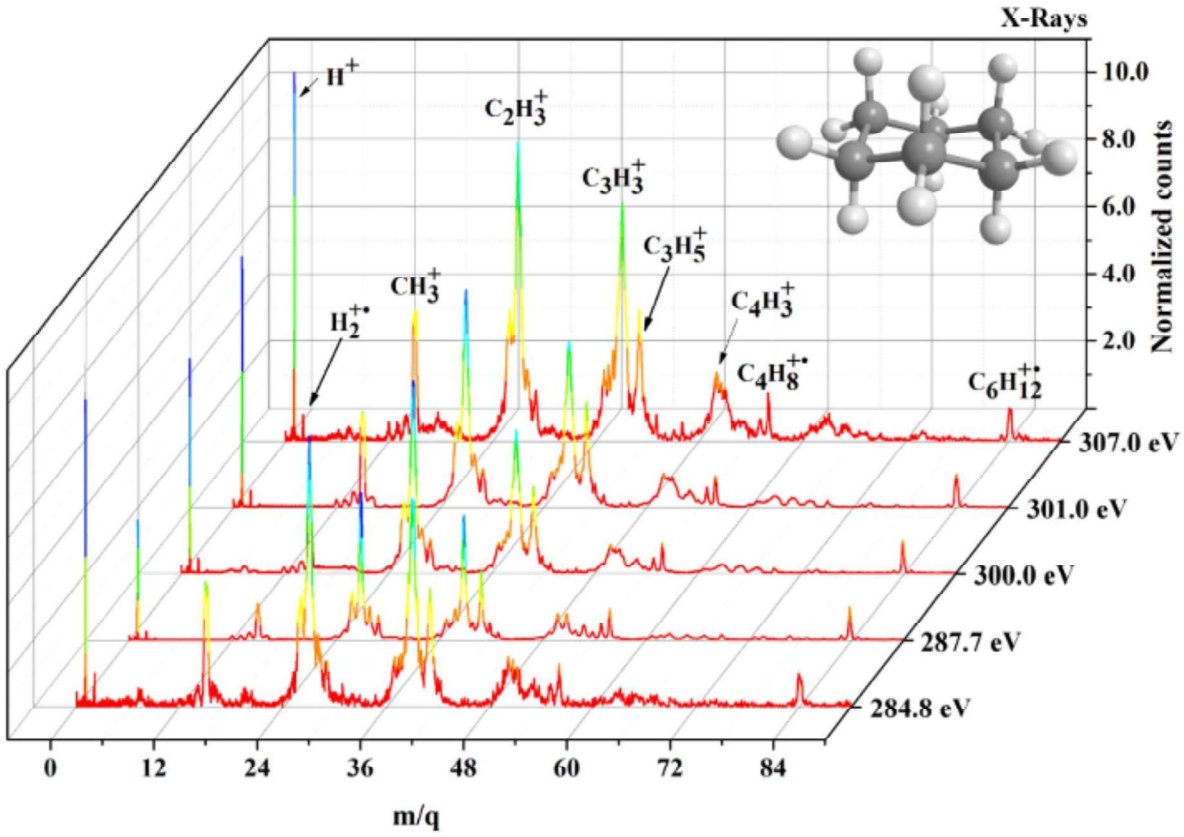

Figure 4.4: Selected mass spectra of the cyclohexane molecule recorded at soft X-ray photons (280-307 eV). The color variation indicates differences in the intensity of the peaks. For each energy the counts are normalized with respect to that of the parent ion, $C_6H_{12}^{+\cdot}$.

eV and at 200.0 eV this species is the most produced one.

By comparing the present results with the *PIY* of the literature data of the National Institute of Standards and Technology (NIST, Johnson III 2013), we verified that the fragmentation pattern at 70 eV electron energy resembles already the one induced by photons of 16 eV. It is also interesting to note that at the electron impact of 70 eV (or photon impact of 16 eV) the abundance of the aromatic ring parent ion is twice that of the cyclohexane parent ion.

4.3.2 X-Rays

The fragmentation pattern observed in the soft X-ray region around the C1s resonance energy is significantly different from that measured in the UV region. From 284.8 eV to 307.0 eV, more than 90% of the ion yield comes from the light fragment ions contribution, from the CH_n^+ (and H_n^+) to $C_3H_n^+$ groups. The parent ion production ranges (see Figure 4.5 for comparison) from merely 0.6% (307.0 eV) to 1.4% at the C1s resonance energy (287.7 eV). This profile contrasts reasonably with

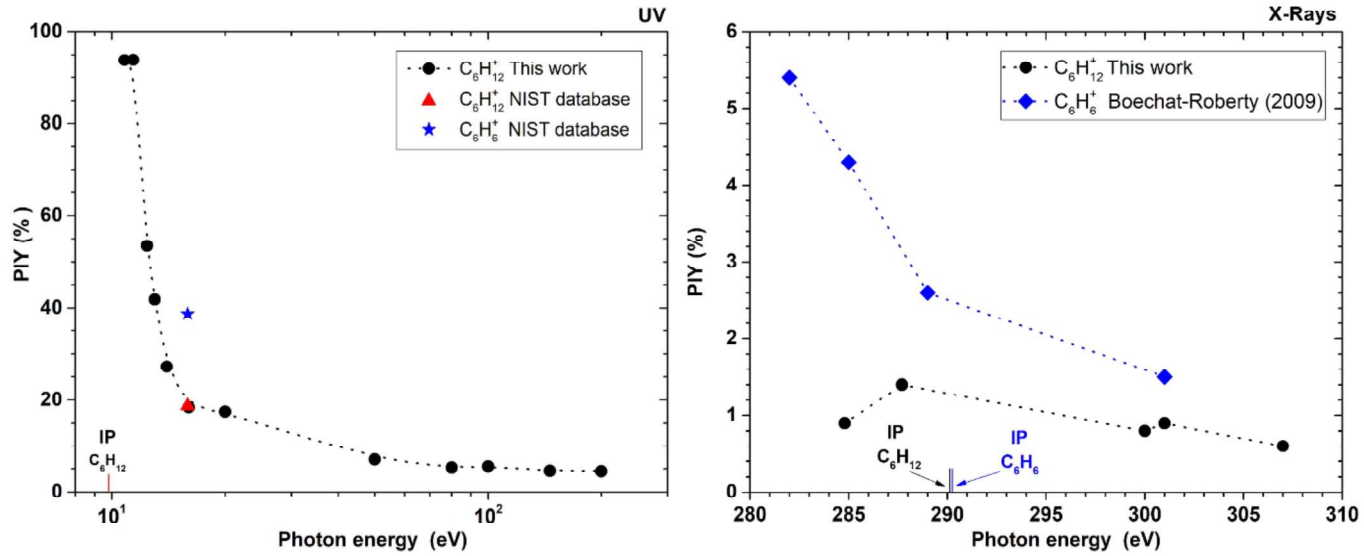

Figure 4.5: Production (Partial Ion Yield, *PIY*) of $C_6H_{12}^{+\cdot}$ as a function of the photon energy. Left in the UV range: the red triangle and the blue star indicate the values of $C_6H_{12}^{+\cdot}$ and $C_6H_6^{+\cdot}$ respectively, both obtained from the NIST database (Johnson III, 2013). Right in the X-rays range: comparison of the yields of ionized cyclohexane with ionized benzene (blue dots taken from Boechat-Roberty et al. 2009a). The ionization energies of cyclohexane (290.12 eV) and benzene (290.24 eV) are also indicated (Kolczewski et al., 2006).

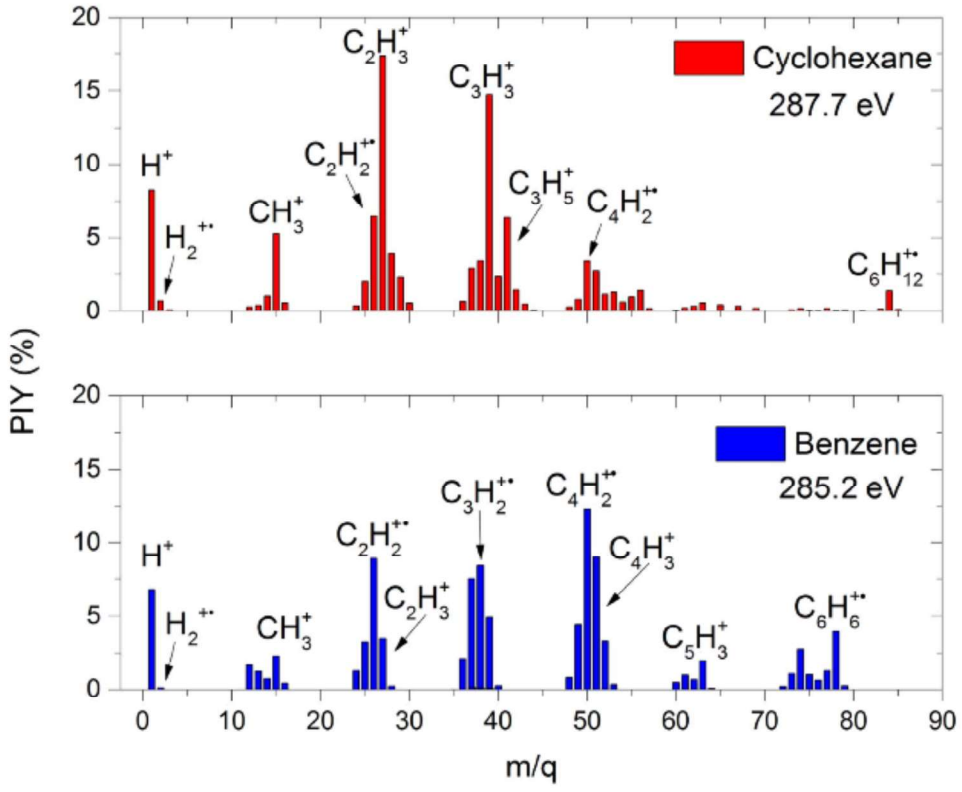

Figure 4.6: Comparison between the mass spectra of cyclohexane (red) and benzene (blue) at the respective C1s resonance energies.

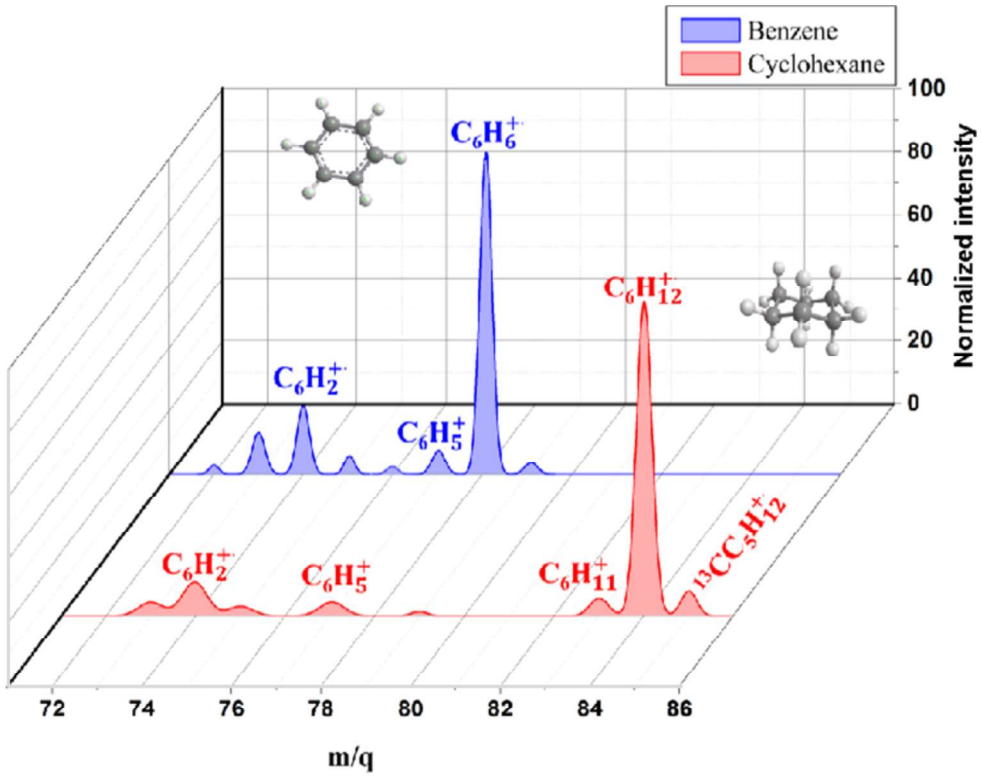

Figure 4.7: Normalized abundances of the $C_6H_n^+$ group produced by the fragmentation of cyclohexane and benzene at 301.0 eV.

the one presented by the parent ion of benzene, for which a production of 5.4% was observed at 282.4 eV, a value more than five times larger than the average production of the parent ion of cyclohexane at the C1s edge. These values reveal a higher propensity of cyclohexane to photodissociate after absorbing a soft X-ray photon in the C1s edge. This tendency is related to the higher molecular rigidity of benzene and its parent ion, in comparison to cyclohexane and its ionization product. By far, the most relevant fragments produced by the photodissociation of cyclohexane are $C_3H_3^+$ and $C_2H_3^+$, related to cyclopropenyl cation (Zhao et al., 2014) and protonated acetylene (Glassgold et al., 1992), respectively.

Figure 4.6 shows the comparison of the different ions resulting from the fragmentation of benzene and cyclohexane at the C1s resonance energy. By analyzing the production of the parent ion and other $C_6H_n^+$ species, it is possible to see that the main difference between benzene and cyclohexane is that the backbone fragmentation is significantly more pronounced in the latter. This result evidences that the hydrogenated benzene molecule shows, after X-ray photoionization, a higher tendency of dissociation than its aromatic counterpart. Consequently, a high production of ions pertaining to the CH_n^+, $C_2H_n^+$ and $C_3H_n^+$ groups is observed for cyclohexane. In fact, the formation of CH_3^+, $C_2H_3^+$ and $C_3H_3^+$

Table 4.3: Partial Ion Yield, *PIY* (%), as a function of the photon energy around C 1s resonance in the soft X-rays region. Only the ionic fragments with intensity greater than 1% were shown, except the H_2^+, H_3^+ and parent ion $C_6H_{12}^{+\cdot}$.

m/q	Attribution	*PIY* ($\geq$ 1%), per energy (eV)				
		284.8	287.7	300.0	301.0	307.0
1	H^+	10.0	8.2	9.2	9.5	9.3
2	$H_2^{+\cdot}$	0.8	0.7	0.7	0.7	0.6
3	H_3^+	0.1	0.1	0.1	0.1	0.1
14	$CH_2^{+\cdot}$	1.2	1.0	1.4	1.2	1.2
15	CH_3^+	8.5	5.3	8.2	7.8	7.5
26	$C_2H_2^{+\cdot}$	7.4	6.5	8.3	8.5	8.0
27	$C_2H_3^+$	18.6	17.4	17.8	17.5	16.1
28	$C_2H_4^{+\cdot}$	4.2	3.9	4.8	4.2	3.9
29	$C_2H_5^+$	2.9	2.3	2.1	2.5	2.1
37	C_3H^+	2.4	2.9	2.7	2.4	3.4
38	$C_3H_2^{+\cdot}$	5.3	3.4	3.5	3.1	4.2
39	$C_3H_3^+$	12.4	14.8	12.8	14.2	12.5
40	$C_3H_4^{+\cdot}$	2.9	2.4	1.8	1.6	2.0
41	$C_3H_5^+$	5.7	6.4	6.2	6.7	5.2
42	$C_3H_6^{+\cdot}$	-	1.5	1.1	1.1	1.2
50	$C_4H_2^{+\cdot}$	2.5	3.4	2.6	2.4	3.4
51	$C_4H_3^+$	1.8	2.7	2.2	2.4	2.3
53	$C_4H_5^+$	1.1	1.3	1.2	1.4	-
63	$C_5H_3^+$	-	-	1.0	1.0	1.5
84	$C_6H_{12}^{+\cdot}$	0.9	1.4	0.8	0.9	0.6

are particularly high for C_6H_{12} compared to aromatic systems, such as benzene (Boechat-Roberty et al., 2009a) and toluene (C_7H_8, Monfredini et al. 2016). On the other hand, the fragmentation of benzene into the ionic species $C_4H_n^+$ to $C_6H_n^+$ is significantly more pronounced. Concerning the H_n series, the H^+ production is relatively the same for both species. In turn, $H_2^{+\cdot}$ and H_3^+ are much more efficiently produced from the break up of the aliphatic structure than from benzene.

A comparison between the fragmentation pattern of benzene and cyclohexane around the parent ion m/q value at 301 eV photon impact is shown in Figure 4.7. For benzene, all C_6H_n cations were observed, and the most abundant ions are the C_6H^+, $C_6H_2^{+\cdot}$, $C_6H_5^+$ and $C_6H_6^{+\cdot}$. For cyclohexane, the results are quite different. Several of the C_6H_n cations were absent, such as $C_6H_4^{+\cdot}$, $C_6H_6^{+\cdot}$, $C_6H_8^{+\cdot}$, $C_6H_9^+$ and $C_6H_{10}^{+\cdot}$. These results indicate that stable C_6H_n ionic structures are not directly achievable from the molecular rearrangement of cyclohexane after ionization. The most relevant C_6H_n ions produced by photodissociation of C_6H_{12} are $C_6H_2^{+\cdot}$ and $C_6H_5^+$ and $C_6H_{11}^+$.

4.4 The C_6H_{12} Molecular Ion

Structural and spectroscopic properties of the singly charged cyclohexane radical cation, $C_6H_{12}^{+\cdot}$, and similar cycloalkane cations have been exhaustively studied by both Ion Cyclotron Resonance (ICR) techniques (Dunbar, 1984) and collisional activation measurements (Borchers et al., 1977). Dunbar (1976) has shown that strong optical absorptions in the visible region could be observed for gas-phase radical cations of saturated hydrocarbons. In contrast, radical cations originated from linear alkenes present weak visible absorptions and strong UV peaks. For cyclohexane and larger cycloalkane rings, the optical spectrum is similar to *n*-alkanes, which indicates that they retain their ring structures upon ionization. A profile similar to alkenes is observed for cyclopentane (C_5H_{10}) and smaller cycloalkane rings, indicating that a ring-opening isomerization occurs in these radical ions prior to fragmentation (Benz and Dunbar, 1979).

The ring opening mechanisms for the cyclopentane and cyclohexane radical cations have been studied by van der Hart (2001) using *ab initio* calculations. The author showed that the ring opening barrier heights in both cases are comparable, being significantly lower than the ionization energies. Although these results could not explain the ICR experimental results, they suggest that open-chain radical cations are accessible by the photoionization of neutral cyclohexane. Moreover, it was also shown by van der Hart (2001) that some of the acyclic $C_6H_{12}^{+\cdot}$ radical cations are thermodynamically more stable than six- or five-membered rings. Since there was no previous information about which isomer represents the ground state of the parent ion of cyclohexane, a careful computational analysis was made by our collaborators in order to identify the most stable isomers. These results were recently published (Fantuzzi et al., 2019) and, since they are relevant for the discussion of this chapter, they will be briefly discussed.

Fig. 4.8 (top panel) shows all acyclic $C_6H_{12}{}^{+\cdot}$ structures obtained by Fantuzzi et al. (2019), as well as their respective enthalpy values at 298 K, ΔH_{298}. The enthalpies of their optimized neutral analogs are also shown in Fig. 4.8 for comparison. The global minimum energy structure ($\mathbf{1}^{+\cdot}$) at the coupled cluster (CCSD(T)/cc-pVTZ//M06-2X/cc-pVTZ(-f)) level of theory is the tetramethylethylene radical cation. The main geometrical features of $\mathbf{1}^{+\cdot}$ are a central C–C bond length of 1.420 Å – an intermediate value between typical single and double bonds – and a CCCC torsional angle of $\sim 13^\circ$ between any two vicinal methyl groups. For comparison, these values are, respectively, 1.348(1) Å and below 1° for neutral tetramethylethylene, as taken from low-temperature crystal X-ray determination (Boese et al., 1992). The presence of such alkyl groups aids in the stabilization of the one-electron π bond of

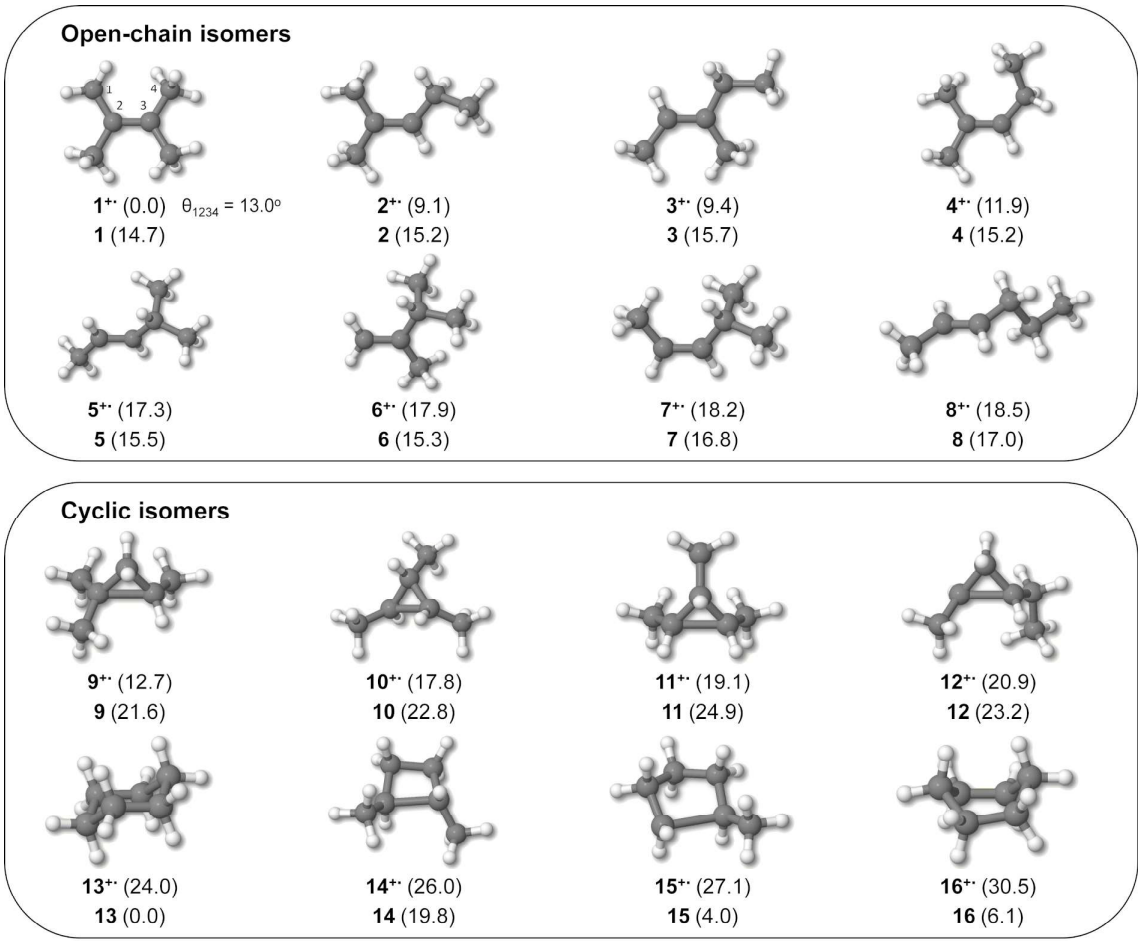

Figure 4.8: Optimized structures of the acyclic (top panel) and cyclic (bottom panel) $C_6H_{12}^{+\cdot}$ radical cations obtained by us (Fantuzzi et al., 2019). The values in parentheses are the relative enthalpy at 298 K (ΔH_{298}, kcal.mol^{-1}) calculated at the CCSD(T)/cc-pVTZ//M06-2X/cc-pVTZ(-f) level of theory, with respect to the global minimum energy isomer ($\mathbf{1}^{+\cdot}$). The ΔH_{298} values of the respective optimized neutral species are also shown for comparison. The global minimum for neutral C_6H_{12} is cyclohexane in the chair conformation (**13**). For $\mathbf{1}^{+\cdot}$, we also include the CCCC torsional angle, θ_{1234}. Taken from Fantuzzi et al. (2019).

$\mathbf{1}^{+\cdot}$, and ultimately could be responsible for making this structure the global minimum of $C_6H_{12}^{+\cdot}$. In fact, this is the only structure among the ones studied in which the one-electron π bonding involves only tertiary carbon atoms. In contrast, the neutral tetramethylene molecule is 14.7 kcal mol^{-1} less stable than the cyclohexane in the chair conformation (**13**), the global minimum energy structure of C_6H_{12}.

The first singly-charged low-lying isomer ($\mathbf{2}^{+\cdot}$, $\Delta H_{298} = 9.1$ kcal mol^{-1}) is the 2-methyl-2-pentene radical cation. It is slightly more stable than the singly charged 3-methyl-2-pentene species ($\mathbf{3}^{+\cdot}$, $\Delta H_{298} = 9.4$ kcal mol^{-1}), and 2.8 kcal mol^{-1} below in enthalpy with respect to its conformer $\mathbf{4}^{+\cdot}$ ($\Delta H_{298} = 11.9$ kcal mol^{-1}). The lower thermodynamic stability of structures $\mathbf{2}^{+\cdot}$-$\mathbf{4}^{+\cdot}$ in comparison to $\mathbf{1}^{+\cdot}$ can be attributed to the lower substitution level of the radical cations, for which the one-electron

π bonds are formed by a tertiary and a secondary carbon atom.

The next set of acyclic low-lying isomers ($\mathbf{5}^{+\cdot}$-$\mathbf{8}^{+\cdot}$) are more than 17 kcal mol^{-1} less stable than $\mathbf{1}^{+\cdot}$, and just slightly different in energy among each other. While in the singly charged structures $\mathbf{5}^{+\cdot}$ (*trans*-4-methyl-2-pentene radical cation, $\Delta H_{298} = 17.3$ kcal mol^{-1}), $\mathbf{7}^{+\cdot}$ (*cis*-4-methyl-2-pentene radical cation, $\Delta H_{298} = 18.2$ kcal mol^{-1}) and $\mathbf{8}^{+\cdot}$ (2-hexene radical cation, $\Delta H_{298} = 18.5$ kcal mol^{-1}) the one-electron π bonds are formed by two secondary carbon atoms, in $\mathbf{6}^{+\cdot}$ (2,3-dimethyl-1-butene radical cation, $\Delta H_{298} = 17.9$ kcal mol^{-1}) such bonding motif is found for a primary and a tertiary carbon atom. These results support the idea that the substitution level on the carbon atoms influences the stability of the one-electron π bonding in hydrocarbon radical cations.

In addition to the acyclic radical cation structures that bear relation to linear and branched neutral alkenes, we have found low-lying cyclic structures containing from three- to six-membered rings. These structures are shown in the bottom panel of Figure 4.8. The isomers $\mathbf{13}^{+\cdot}$ ($\Delta H_{298} = 24.0$ kcal mol^{-1}) and $\mathbf{16}^{+\cdot}$ ($\Delta H_{298} = 30.5$ kcal mol^{-1}) are related, respectively, to the chair and twist-boat structures of neutral cyclohexane. However, due to Jahn-Teller instability, both ionic species are less symmetric than their neutral counterparts. In fact, Electronic Paramagnetic Resonance (EPR) studies on the radical cation of cyclohexane have shown that the chair structure distorts to a C_{2h} symmetry ^2A_g ground state with two elongated C–C bonds in low-temperature solid matrices (Shiotani et al., 1991). According to our results, the elongated bond lengths in the optimized twist-boat $C_6H_{12}{}^{+\cdot}$ are 1.625 Å. Although greater than the average C–C single bond, this distance is significantly smaller than the ones obtained for alkyl-stabilized species. Moreover, these six-membered rings are among the least stable cyclic isomers obtained by us (Fantuzzi et al., 2019), a dramatic change in comparison to the relative energies of their neutral structures. In opposition to the stability trend among neutral C_6H_{12}, branched three-membered rings are the most stable cycloalkanes. Structure $\mathbf{9}^{+\cdot}$ ($\Delta H_{298} = 12.7$ kcal mol^{-1}) is the 1,1,2-trimethylcyclopropane radical cation, which is 11.3 kcal mol^{-1} more stable than the singly-charged chair-like cyclohexane. From the structural point of view, the most interesting feature of $\mathbf{9}^{+\cdot}$ is the presence of an elongated C^1–C^2 bond of 1.906 Å. Such elongation suggests the presence of a one-electron sigma bond, which is stabilized by the methyl substituents. In fact, $\mathbf{9}^{+\cdot}$ is the only isomer among the cycloalkane radical cations studied herein in which such elongated bond involves a tertiary and a quaternary carbon atom, which may explain its relatively high stability. In the case of isomers $\mathbf{10}^{+\cdot}$ ($\Delta H_{298} = 17.8$ kcal mol^{-1}), $\mathbf{11}^{+\cdot}$ ($\Delta H_{298} = 19.1$ kcal mol^{-1}) and $\mathbf{12}^{+\cdot}$ ($\Delta H_{298} = 20.9$ kcal mol^{-1}), the elongated bond involves two tertiary carbon atoms, and the enthalpy

values differ by approximately 3 kcal mol^{-1}. The C_3 ring backbone of these isomers resembles the trimethylene cyclopropane radical cation as described in the works of Roth (1987, 1992). The authors also discussed the existence of a π complex $C_3H_6^{+\cdot}$ structure in which two C–C bonds are lengthened and the third one shortened. Substitution on the C_3 ring leads to the predominance of the trimethylene case over the latter and no π complex structure for the distinct singly-charged trimethylcyclopropane isomers was found.

Isomer $\mathbf{14}^{+\cdot}$ ($\Delta H_{298} = 26.0$ kcal mol^{-1}) is the 1,2-dimethylcyclobutane radical cation. In this case, the elongated C–C bond distance is 1.964 Å, and, as in $\mathbf{10}^{+\cdot}$-$\mathbf{12}^{+\cdot}$, it involves two tertiary carbon atoms. Among the $C_6H_{12}^{+\cdot}$ isomers, $\mathbf{15}^{+\cdot}$ (methylcyclopentane radical cation, $\Delta H_{298} = 27.1$ kcal mol^{-1}) has the longest C–C bond: 2.150 Å. Its high enthalpy value can be attributed to the fact that only one methyl group is stabilizing the one-electron sigma bond, which involves a tertiary and a secondary carbon atom.

In summary, the computational results point that the global minimum of the C_6H_{12} radical cation ($\mathbf{1}^{+\cdot}$) is a highly branched structure. The first alkyl branched molecule detected in the interstellar medium was the isopropyl-cyanide (*i*-C_3H_7CN) species, in a study developed by Belloche et al. (2014). The present results suggest that, in a PDR region, the photoionization of C_6H_{12} could induce the formation of the mentioned highly branched radical cation. Since methyl substituents help in the stabilization of carbocations and radical centers, it is expected that the molecular rearrangement that follows the photoionization process of both cyclic and open chain hydrocarbons could lead to an enhancement of branched molecules in PDR regions.

4.5 Absolute Photoionization and Photodissociation Cross Sections

Before going into details on the determination of the photoionization and photodissociation cross sections, it is interesting to compare the absolute X-ray photoabsorption cross sections of benzene and its hydrogenated analogues, as shown in Figure 4.9. A strong photoabsorption peak is observed for benzene at 285.2 eV, with a maximum value of 2.6×10^{-17} cm^2. This feature is attributed to a K-shell transition from a C1s orbital to the lowest unnocupied π^* orbital of e_{2u} symmetry (Horsley et al., 1985). The shape of this transition, together with additional features in the K-shell spectra related to the splitting of π^* and σ^* resonances, has been used to prove the aromatic character of

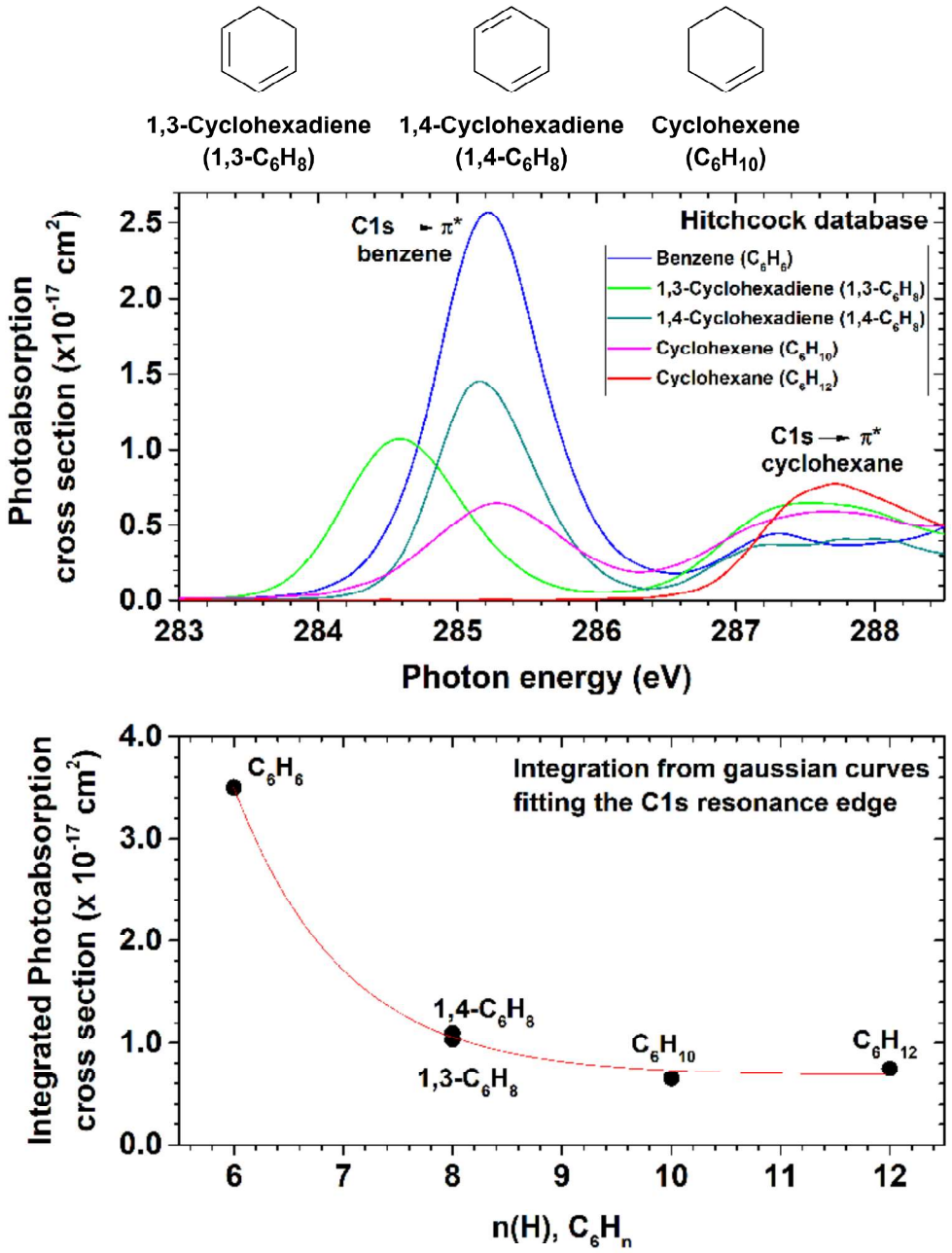

Figure 4.9: Absolute photoabsorption cross sections as a function of the number of H atom. Top: benzene (C_6H_6, blue), 1,3-cyclohexadiene (C_6H_8, green), 1,4-cyclohexadiene (C_6H_8, dark cyan), cyclohexene (C_6H_{10}, pink) and cyclohexane (C_6H_{12}, red), adapted from the Hitchcock database (Hitchcock et al., 1986, 1987; Hitchcock and Rühl, 1989; Hitchcock and Mancini, 1994). Bottom: comparison between the areas of the C1s$\rightarrow \pi^*$ resonance bands after a Gaussian fitting procedure. The red line is an adjusted exponential decay curve, with a coefficient of determination $R^2 = 0.9978$.

heterocyclic rings (Stöhr, 1992), such as borazine (Doering et al., 1986). A second peak (287.2 eV, 4.4×10^{-18} cm^2) is also observed for benzene in Figure 4.9, which is assigned to a transition to a 3p Rydberg orbital (Horsley et al., 1985).

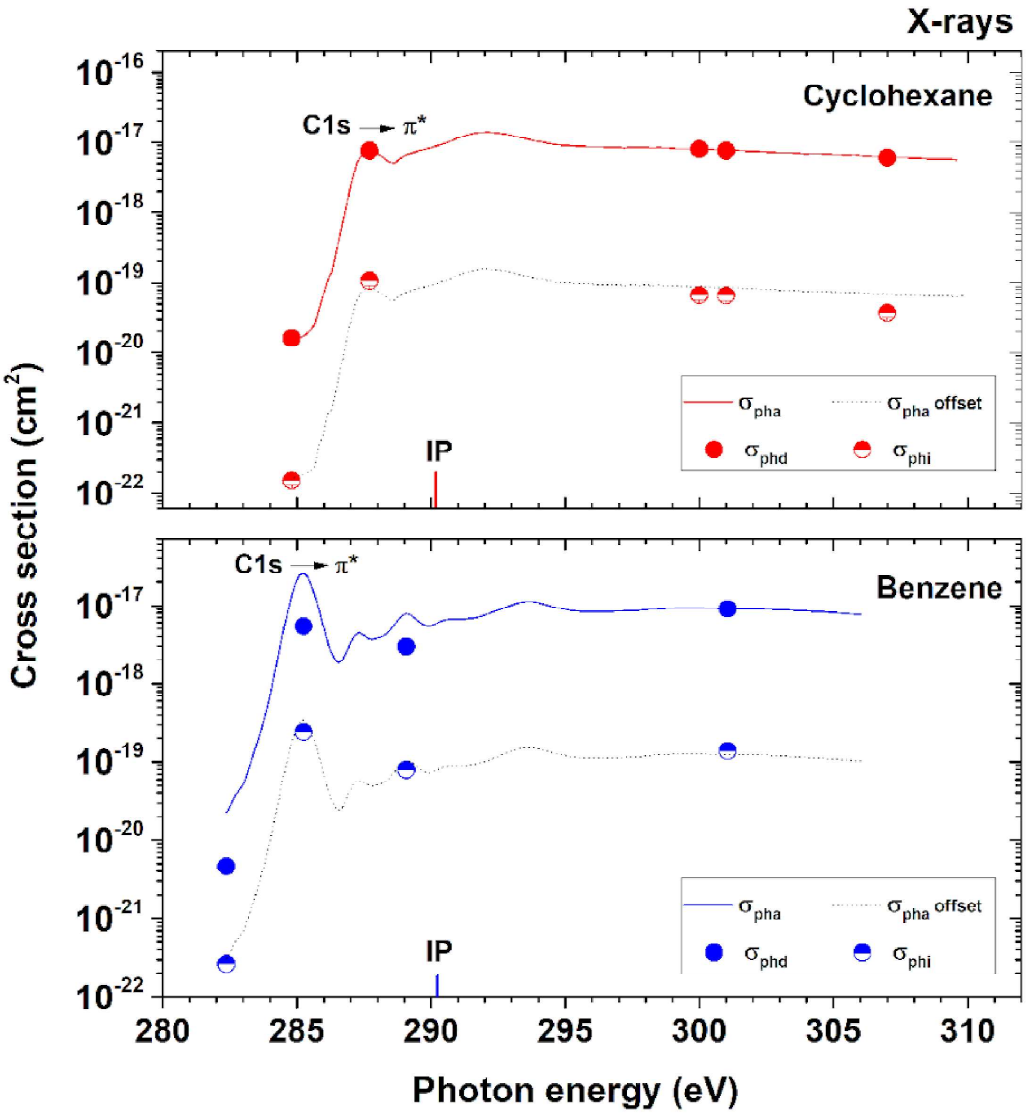

Figure 4.10: Dissociative ionization (photodissociation) σ_{phd} (filled circle), non-dissociative single ionization (photoionization) σ_{phi} (half-filled circle) and absolute photoabsorption, σ_{pha} (solid line), cross sections as a function of the X-rays energies. Top: cyclohexane (red); bottom: benzene (blue). The dotted lines are an offset of the photoabsorption cross section, only to guide the eyes. The photoabsorption cross section values are obtained from Hitchcock et al. (1987) and Hitchcock et al. (1986) for benzene and cyclohexane, respectively. See details in text.

The increase in the number of hydrogen atoms from benzene (C_6H_6) to the isomers 1,3- and 1,4-hexadiene (C_6H_8) is followed by a significant decrease in the photoabsorption cross section values at the respective C1s$\rightarrow \pi^*$ resonance energies. This trend is also observed for the more hydrogenated six-membered ring molecules, cyclohexene (C_6H_{10}) and cyclohexane (C_6H_{12}). In the case of the latter, besides the reduction in the cross section value, there is also a significant displacement of the resonance energy to a higher photon energy value from 285.2 eV to 287.7 eV (Figure 4.9-top). The absence of a peak around 285 eV comes from the fact that there is no sp^2-like atom in cyclohex-

ane, and the feature in 287.7 eV is attributed to a transition to the $4a_1\pi^*$ (CH_2) orbital (Hitchcock et al., 1986), whose maximum value is 7.7×10^{-18} cm^2. By fitting the C1s$\rightarrow \pi^*$ resonance bands with Gaussian functions and integrating, an exponential decay profile between the integrated photoabsorption cross sections and the number of hydrogen atoms in the C_6H_n molecules is observed. The fluorescence yield can be assumed as negligible, due to the low C atomic number (Chen et al., 1981). Moreover, since typical K-shell core hole lifetimes of light elements are in the femtosecond range (Drescher et al., 2002), and therefore some orders of magnitude faster than a vibrational period, it is possible to conclude that photorelaxation of the neutral molecule by internal conversion and energy redistribution into vibrational modes, such as the one described by cationic excited states of PAHs (Marciniak et al., 2015), is also negligible. Finally, given the fact that these core hole states are embedded in the electronic continua of ionic states (Carravetta et al., 1988), we can conclude that the only relaxation channels of such metastable highly excited states are photoionization and photodissociation processes. Therefore, the high photoabsorption cross section of benzene in comparison to cyclohexane could also impart a higher photodissociation rate, depending on the intensity of the photon flux at the C1s resonance edge of benzene.

The absolute cross sections of cyclohexane and benzene at the C1s edge are shown in Figure 4.10 and Table 4.4. The photoabsorption cross-section value of cyclohexane at the C1s resonance energy, 7.7×10^{-18} cm^2 (Hitchcock et al., 1986), is about half of the benzene one, which is 2.6×10^{-17} cm^2 (Hitchcock et al., 1987). Since a stronger photoabsorption leads to higher photoionization and photodissociation cross sections, the addition of peripheral hydrogen atoms to the aromatic moiety could afford a greater stability against X-ray dissociation. These values are used to determine the survival rates of both molecules in the PDR of the planetary nebula NGC 7027, which are discussed in the following section.

4.6 Survival of Cyclohexane in the PDR of the Planetary Nebula NGC 7027

NGC 7027 is a young carbon-rich planetary nebula, as already discussed in 1. Fig.4.11 shows a schematic diagram of the geometric regions of NGC 7027 composed by superimposing visible and infrared images obtained by Hubble Space Telescope (HST) (Latter et al., 2000). The figure also indicates the main regions of the nebula (HII region, photodissociation region or neutral shell and

Table 4.4: Absolute photoabsorption (σ_{pha}), photodissociation (σ_{phd}) and photoionization (σ_{phi}) cross sections of cyclohexane and benzene. The σ_{pha} values are obtained from Hitchcock et al. (1986) and Hitchcock et al. (1987). The † symbol indicates the C1s resonance energies.

Energy (eV)	σ_{pha} (cm^2)	σ_{phd} (cm^2)	σ_{phi} (cm^2)
Cyclohexane			
284.8	1.6×10^{-20}	1.6×10^{-20}	1.5×10^{-22}
287.7†	7.7×10^{-18}	7.6×10^{-18}	1.1×10^{-19}
300.0	8.1×10^{-18}	8.0×10^{-18}	6.6×10^{-20}
301.0	7.7×10^{-18}	7.6×10^{-18}	6.6×10^{-20}
Benzene			
282.4	2.3×10^{-20}	2.2×10^{-20}	1.2×10^{-21}
285.2†	2.6×10^{-17}	2.5×10^{-17}	1.1×10^{-18}
289.1	7.8×10^{-18}	7.6×10^{-18}	2.0×10^{-19}
301.0	9.2×10^{-18}	9.0×10^{-18}	1.4×10^{-19}

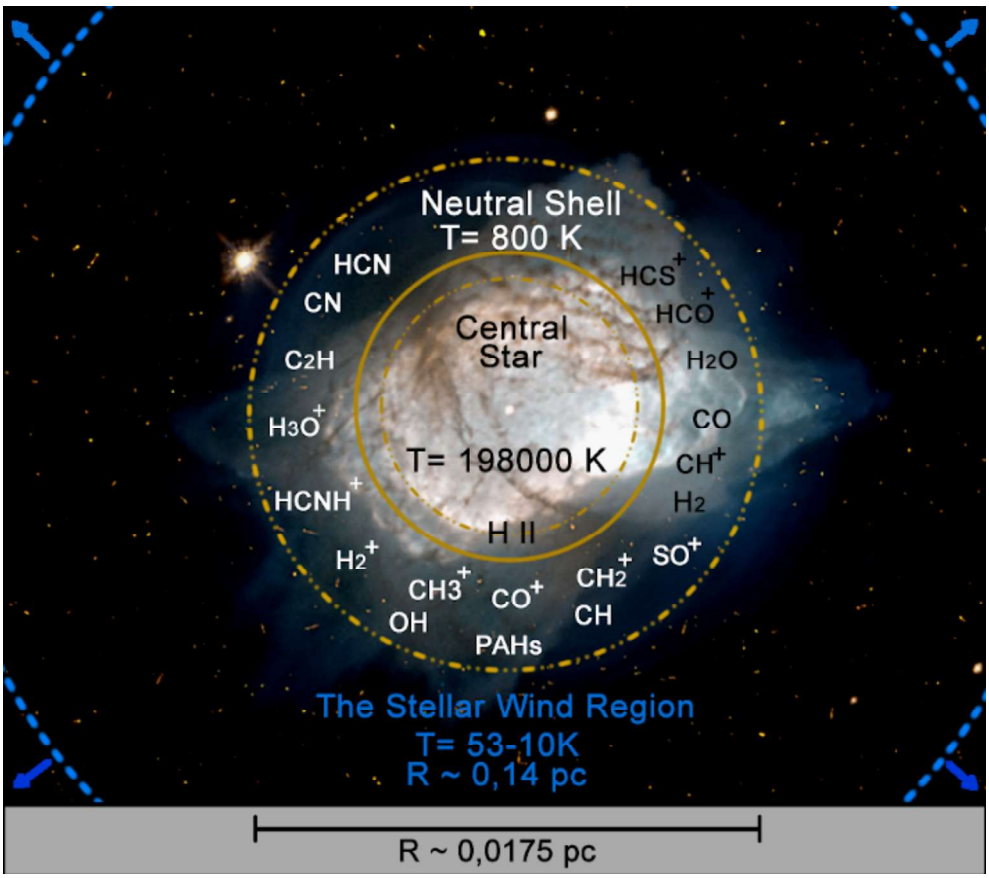

Figure 4.11: Schematic diagram of the geometric regions of NGC 7027, image from (Latter et al., 2000) and regions adapted from (Hasegawa et al., 2000).

the wind region), including some of the molecules and ions observed in the photodissociation region. Physical values and quantities are approximate, adapted from (Hasegawa et al., 2000).

The central star promotes a chemically rich medium. This implies that different reaction mecha-

nisms could be taking place, both in the gas phase and on the surface of grains. Ultimately, such an environment could uphold the formation of complex ions and organic molecules, among them PAHs (Herbst and van Dishoeck, 2009).

In order to know the X-ray photon flux (F_X) values in the PDR of NGC 7027 we used the equations:

$$F_X = \frac{L_X}{4\pi r^2 h\nu} e^{-\tau_x} \tag{4.1}$$

where 7.0×10^{31} erg s^{-1} is the integrated X-ray luminosity from 0.2 to 2.5 keV, reported by (Montez and Kastner, 2018), r = 5.21x10^{16} cm is the distance from the central star to a position inside the PDR (Agúndez et al., 2010) and τ_X is the X-ray optical depth, given by Deguchi et al. (1990):

$$\tau_X = \alpha\tau_d \left(\frac{E}{0.6\,\mathrm{keV}}\right)^{-2.67} \tag{4.2a}$$

$$\tau_d = 4.6x10^{-21} N_{\mathrm{H_2}} \tag{4.2b}$$

which accounts for the absorption due to materials on the envelope along a radius. In eqs. 4.2a and 4.2b, τ_d is the UV optical depth of dust grains at 1000 Å, proposed by Morris and Jura (1983), the factor α = 0.054 for energies below 0.6 keV, and $N_{\mathrm{H_2}}$ is the column density of H_2 for which we adopted the value of 1.3x10^{21} cm^{-2} obtained by Agúndez et al. (2010). The energy 0.6 keV corresponds to the oxygen O1s absorption edge (Deguchi et al., 1990).

Figure 4.12 shows the X-ray optical depth in the PDR of NGC 7027, its photon flux with and without the attenuation and the estimated half-life times of cyclohexane and benzene in this object. The X-ray optical depth ranges from 2.4 (282.0 eV) to 0.3 (600.0 eV), which shows that the object is essentially transparent for energies above the O1s resonance energy. In the vicinity of the C1s resonance energies, the attenuated photon flux values range from 7.4×10^5 cm^{-2}s^{-1}eV^{-1} to 1.1×10^6 cm^{-2}s^{-1}eV^{-1}. Although the maximum X-ray attenuated photon flux is not located in the C1s edge, the photoabsorption cross sections significantly decay after the inner shell excitation energies (Sakamoto et al., 2010). Therefore, the half-life times obtained in this chapter are a good estimation of the X-ray survival rates of the molecules in NGC 7027.

We estimate that the half-life time of cyclohexane is 3.5×10^3 years in the C1s resonance energy (287.7 eV, see Table 4.5), more than three times higher than the half-life of benzene at 285.2 eV

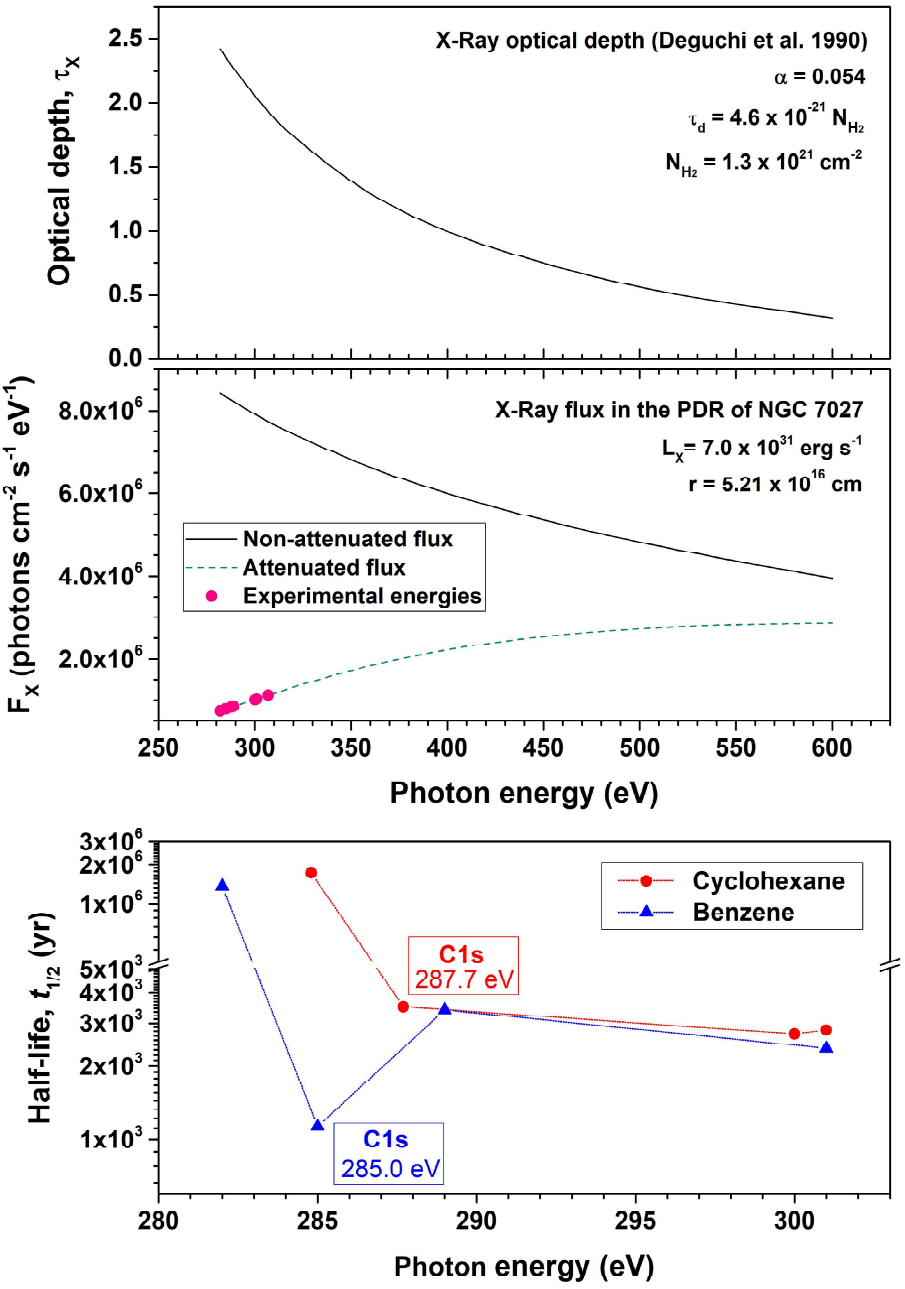

Figure 4.12: Top: X-ray optical depth, τ_X, in the photon energy range from 280 to 600 eV. Middle: X-ray photon flux, $F_X(E)$, with and without attenuation in the same photon energy range, arriving to the PDR of the planetary nebula NGC 7027 in a position r from the central star of 5.21x10^{16} cm. The pink circles indicate the energies studied herein. Bottom: Half-life times, $t_{1/2}$, of C_6H_{12} (red circles) and C_6H_6 (blue triangles) at energies around the C1s resonance of each molecule (lines are included to guide the eye).

(1.1×10^3 years). This large distinction is directly related to differences in the photoabsorption cross sections of both molecules at the mentioned energies (7.7×10^{-18} cm^2 for cyclohexane and 2.6×10^{-17} cm^2 for benzene). On the other hand, in the vicinity of the C1s resonance energy, the survival of both molecules is practically the same. By integrating the half-life time curves of both molecules and

Table 4.5: Photodissociation k_{phd} and photoionization rates k_{phi}, as well as the half-lives, $t_{1/2}$, of cyclohexane and benzene under X-ray photon fluxes, F_X (E), in NGC 7027. The † symbol indicates the C1s resonance energies.

Energy (eV)	$F_X(E)$ ($cm^{-2}s^{-1}$)	k_{phd} (s^{-1})	k_{phi} (s^{-1})	$t_{1/2}$ (yr)
Cyclohexane				
284.8	7.9×10^{5}	1.3×10^{-14}	1.2×10^{-16}	1.7×10^{6}
287.7†	8.3×10^{5}	6.3×10^{-12}	8.9×10^{-14}	3.5×10^{3}
300.0	1.0×10^{6}	8.1×10^{-12}	6.7×10^{-14}	2.7×10^{3}
301.0	1.0×10^{6}	7.8×10^{-12}	6.8×10^{-14}	2.8×10^{3}
Benzene				
282.4	7.5×10^{5}	1.6×10^{-14}	9.2×10^{-16}	1.4×10^{6}
285.2†	7.9×10^{5}	1.9×10^{-11}	8.7×10^{-13}	1.1×10^{3}
289.1	8.5×10^{5}	6.5×10^{-12}	1.7×10^{-13}	3.4×10^{3}
301.0	1.0×10^{6}	9.3×10^{-12}	1.4×10^{-13}	2.4×10^{3}

comparing the areas, it is possible to see that the survival of cyclohexane in the C1s edge is $\sim 20\%$ higher than that of benzene. Since the abundances of interstellar molecules depend on both their formation and destruction rates, we suggest that the richness of interstellar benzene in comparison to its fully hydrogenated counterpart comes from more effective mechanisms of formation, such as the one described by Jones et al. (2011). This result indicates, therefore, that the addition of peripheral atoms in the basic PAH unit could impart a greater X-ray stability in photodissociation regions.

At this point, it is important to make a comparative analysis of the findings discussed in the last paragraph with the ones presented in Figs. 4.6 and 4.7, as they could be naïvely interpreted as contradictory. From the figures, it is shown that the backbone fragmentation of cyclohexane is significantly more pronounced than the one of benzene. This means that once photoabsorption has taken place, the fully hydrogenated molecule is more likely to photodetach its carbon skeleton. In other words, the survival probability of cyclohexane is smaller than that of benzene after the photoabsorption process. However, the benzene molecule has a strong absorption feature at the C1s edge (see Figure 4.9). This feature disappears entirely when additional hydrogen atoms are inserted into the carbon backbone. Consequently, the photoabsorption cross section of benzene is larger than cyclohexane, which ultimately leads to a higher efficiency of dissociation for the aromatic molecule. The protective effect of additional hydrogen atoms is, therefore, related to a damping out process of the strong absorption feature of benzene. The extrapolation of such finding to PAHs of high molecular mass will be discussed in the next subsection.

4.7 Survival of Super-Hydrogenated PAHs in PDRs

In previous subsections we shown that, after an X-ray photoabsorption process, the cyclohexane molecule is almost entirely dissociated, as the average partial ion yield of $C_6H_{12}^{+\cdot}$ is around 1%. The carbon backbone rigidity of benzene, on the other hand, is responsible for keeping the partial ion yield values around 5% at the C1s resonance energy. In fact, only after a double ionization process the six-membered ring is surpassed by a different structure as the global minimum. In this case, it acquires a pentagonal-pyramidal carbon arrangement (Jašík et al., 2014; Fantuzzi et al., 2017a). As the carbon backbone size increases, the resistance of super-hydrogenated PAHs towards dissociation is also expected to increase. The fragmentation of perhydropyrene ($C_{16}H_{26}$) will still be greater than the one of pyrene ($C_{16}H_{10}$), as the collision experiments developed by Gatchell et al. (2015) suggest, but not so pronounced as the one of C_6H_{12}. However, by increasing even more the number of carbon atoms, the fragmentation of the carbon backbone in an H_n-PAH could be reduced to a secondary process, being exceeded by hydrogen elimination to ultimately form a PAH ion, as suggested by Reitsma et al. (2014) in experiments with coronene ($C_{24}H_{12}$). In this scenario, the excess of peripheral H atoms acts as a protection mechanism for the PAH structure.

Parallel to the mechanism proposed by Reitsma et al. (2014), an auxiliary photostabilization mechanism could be present in super-hydrogenated PAHs. The strong photoabsorption cross section of the C1s$\rightarrow \pi^*$ resonance energy of benzene (2.6×10^{-17} cm^2) is more than three times higher than the one of cyclohexane (7.7×10^{-18} cm^2). This is a common feature of aromatic molecules, as shown in Figure 4.12, and is expected to be present in the X-ray photoabsorption spectra of PAHs. In comparison, adamantane ($C_{10}H_{16}$), a polycyclic fully-hydrogenated non-aromatic hydrocarbon, does not have such feature. In fact, the spectral profile of adamantane shows several resemblances to the one of cyclohexane, as so its dissociative ionization (Candian et al., 2018). In this perspective, we suggest that an auxiliary protection mechanism could exist in super-hydrogenated PAHs. By decreasing the X-ray photoabsorption cross section, an H_n-PAH molecule will also have a smaller photodissociation cross section, which ultimately enhances its photostability in PDR regions. This mechanism, to the best of our knowledge, proposed for the first time in the literature, should contribute to explaining the existence of hydrogenated PAHs in interstellar and circumstellar media. The importance of such mechanism in comparison to the one described by Reitsma et al. (2014) will be the focus of a future study.

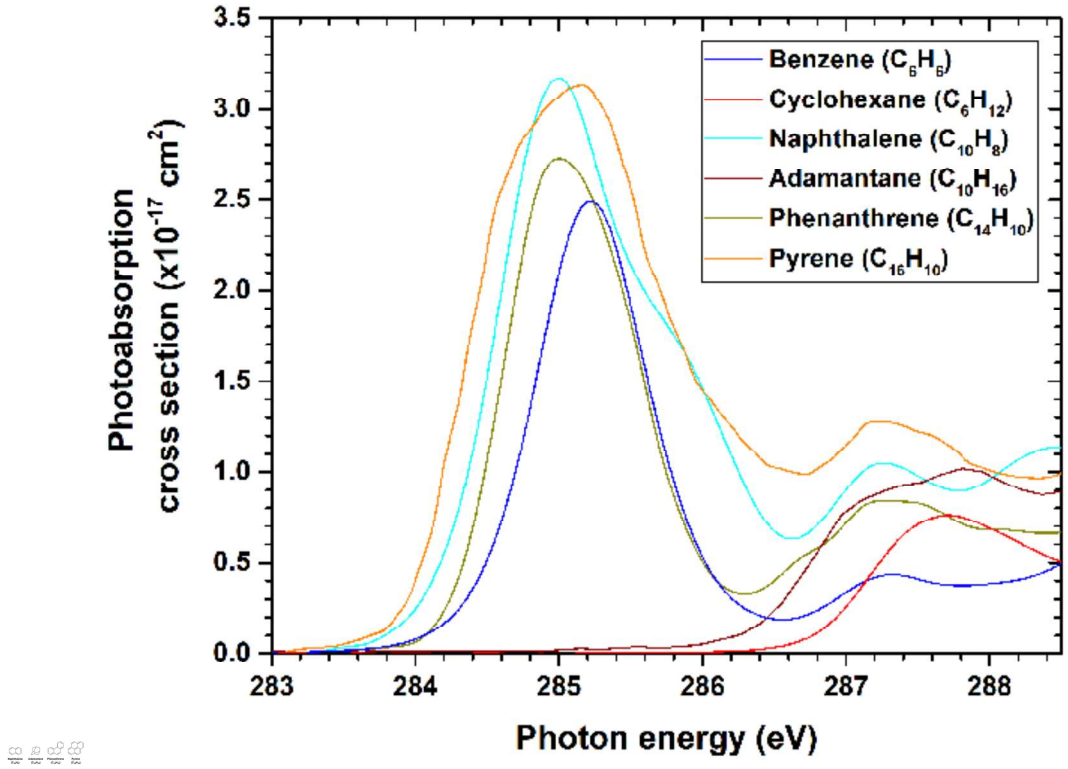

Figure 4.13: Absolute photoabsorption cross sections of benzene (C_6H_6, blue), cyclohexane (C_6H_{12}, red) naphthalene ($C_{10}H_8$, cyan), adamantane ($C_{10}H_{16}$, wine), phenanthrene ($C_{14}H_{10}$, pink) and pyrene ($C_{16}H_{10}$, orange), adapted from the Hitchcock database (Hitchcock and Mancini, 1994).

Chapter 5

Experimental Results II: Biphenyl (Gas Phase)

5.1 The Biphenyl Molecule

Biphenyl ($C_{12}H_{10}$, or phenylbenzene, see Figure 5.1) is an aromatic molecule composed of two phenyl ($C_6H_5^{\cdot}$) radical groups connected by a C–C sigma bond. Despite its apparent simplicity, the molecule has received significant attention in the last decades due to its fundamental, environmental and technological properties. It is the main precursor of polychlorinated biphenyls (PCBs), a toxic and complex mixture of Cl-containing biphenyl derivatives/congeners whose stability towards thermal and biochemical degradation led to its worldwide accumulation after ubiquitous industrial use (Safe, 1994; Kania-Korwel et al., 2004; Faroon and Ruiz, 2016). Biphenyl is also used as a model for the conducting polymer poly(*p*-phenylene), PPP (Berresheim et al., 1999), playing a central role in the development of molecular electronic devices (Baldo et al., 1999; Jia et al., 2005; Holman et al., 2005; Venkataraman et al., 2006), tridimensional dendrimers (Lo et al., 2003, 2008; Stoltzfus et al., 2018) and macrocycles (Korich et al., 2014). However, the reactivity and electronic properties of biphenyl and substituted biphenyl compounds depend significantly on the torsional angle (ϕ) between the two phenyl rings (Pacios and Gómez, 2006). While in the gas phase ϕ is around 44° as observed by experiments (Suzuki, 1959; Almenningen et al., 1985; Bastiansen and Samdal, 1985) and calculations (Häfelinger and Regelmann, 1987; Tsuzuki and Tanabe, 1991), smaller ϕ values down to almost 0° are observed both in solution and solid state (see, for example, Robertson 1961; Cheng et al. 1972). The origin of the twisted conformation is usually attributed to the interplay between π-conjugation,

Figure 5.1: Molecular structure of biphenyl molecule

which drives the system to a coplanar (ϕ = 0°) structure, and steric repulsion of the hydrogen atoms in *ortho* position, which should favor a perpendicular conformation (ϕ = 90°). The role of sterics, conjugation and hydrogen bonding to the equilibrium structure of biphenyl is still matter of debate (Matta et al., 2003; Poater et al., 2006; Hernández-Trujillo and Matta, 2007; Johansson and Olsen, 2008; Jenkins et al., 2015; Li et al., 2018; Popelier et al., 2019), thus evidencing the challenging nature of the molecule.

Biphenyl is also very interesting from the astrochemical point of view. Although the molecule was not unambiguously detected in the interstellar medium (ISM) up to this date, biphenyl is pointed as an important building block for the formation of polycyclic aromatic hydrocarbons (PAHs), whose infrared emission features are largely present in the spectra of both galactic and extragalactic sources (Tielens, 2008). The synthesis of phenanthrene ($C_{14}H_{10}$) in the circumstellar envelope of Asymptotic Giant Branch (AGB) stars, for instance, could be achieved starting from biphenyl and following the hydrogen-abstraction/acetylene-addition (HACA) mechanism (Yang et al., 2017b). A series of HACA steps with biphenyl also as precursor could lead to the formation of pyrene ($C_{16}H_{10}$), from which systematic ring fusions could trigger the formation of more complex PAHs and two-dimensional graphene-type structures (Zhao et al., 2018). In planetary nebulae, where the relatively high translational temperature (> 1000 K) of molecules enables reactions with entrance barriers, biphenyl could be produced either from a single radical-neutral collision event involving the phenyl radical ($C_6H_5^{\cdot}$) and the benzene (C_6H_6) molecule (Scaiano and Stewart, 1983; Park et al., 1999; Zhang et al., 2008; Shukla et al., 2008, 2011), or from the radical-radical reaction of two $C_6H_5^{\cdot}$ species (Park and Lin, 1997; Tranter et al., 2010; Constantinidis et al., 2015; Zhao et al., 2016). Laboratory experiments of hydrogenated amorphous carbon nanoparticles simulating the deposition conditions of the diffuse ISM revealed the presence of biphenyl together with other aromatic molecules containing benzene

rings linked by distinct bridging groups (Duley and Hu, 2012). The importance of biphenyl and polyphenyl-type molecules as viable precursors of PAHs has motivated theoretical studies on their infrared spectra modeling (Talbi and Chandler, 2012; Martin-Drumel et al., 2014). Furthermore, several studies revealed that the system is a major component of carbonaceous chondrite meteorites (Hayatsu et al., 1977; Basile et al., 1984; Mimura, 1995; Sephton, 2002; Yabuta et al., 2007; Matthewman et al., 2013; Huang et al., 2015; Sephton et al., 2018). Biphenyl was also observed in experiments simulating a prebiotic scenario of icy planetary bodies under reducing primordial atmosphere (Menor-Salván et al., 2008), and in the refractory residues of UV-irradiated ice mixtures of H_2O:benzene and H_2O:NH_3:naphthalene (Materese et al., 2015). Taken together, these studies demonstrate that biphenyl could play an important role in processes relevant to both interstellar and prebiotic chemistry.

In this chapter, we examine the production of singly- and doubly-charged hydrocarbon molecular ions triggered by X-ray photons at energies around the carbon C1s resonance energy on biphenyl, the simplest system composed of phenyl radicals connected by C–C single bonds. The main differences observed for biphenyl in comparison to benzene and naphthalene, the latter composed of two fused benzene rings in a C_{10}-skeleton, are highlighted. We analysed dissociation events that result from single and double photoionization processes. The outcomes of our results to the survival of biphenyl in the context of planetary nebulae are analysed. Since the doubly-charged $C_{12}H_{10}{}^{2+}$ molecule has the same mass-to-charge ratio as the phenylium cation ($C_6H_5{}^+$), we could not discriminate in our experiments the signals that are related to the parent doubly-charged system. However, we could identify a number of fragment ions originated from double coincidence events, and hence from the dissociation of a doubly-charged $C_{12}H_{10}{}^{2+}$ parental species. We therefore applied quantum chemistry calculations in order to map the most stable $C_{12}H_{10}{}^{2+}$ molecular structures and to obtain the thermochemistry of selected fragmentation pathways starting from the biphenyl dication. To the best of our knowledge, this is the first study in which the $C_{12}H_{10}{}^{2+}$ minimum energy landscape is systematically explored.

5.2 Single Ionization and Fragmentation of Biphenyl

Figure 5.2 (top and bottom panels) shows the single coincidence mass spectra of biphenyl ($C_{12}H_{10}$) at 275 and 310 eV. The intensities are normalized with respect to the counts of the $C_{12}H_{10}{}^{+\cdot}$ parental ion. We could easily discriminate distinct groups of peaks, each one related to a distinct $C_mH_n{}^+$ fam-

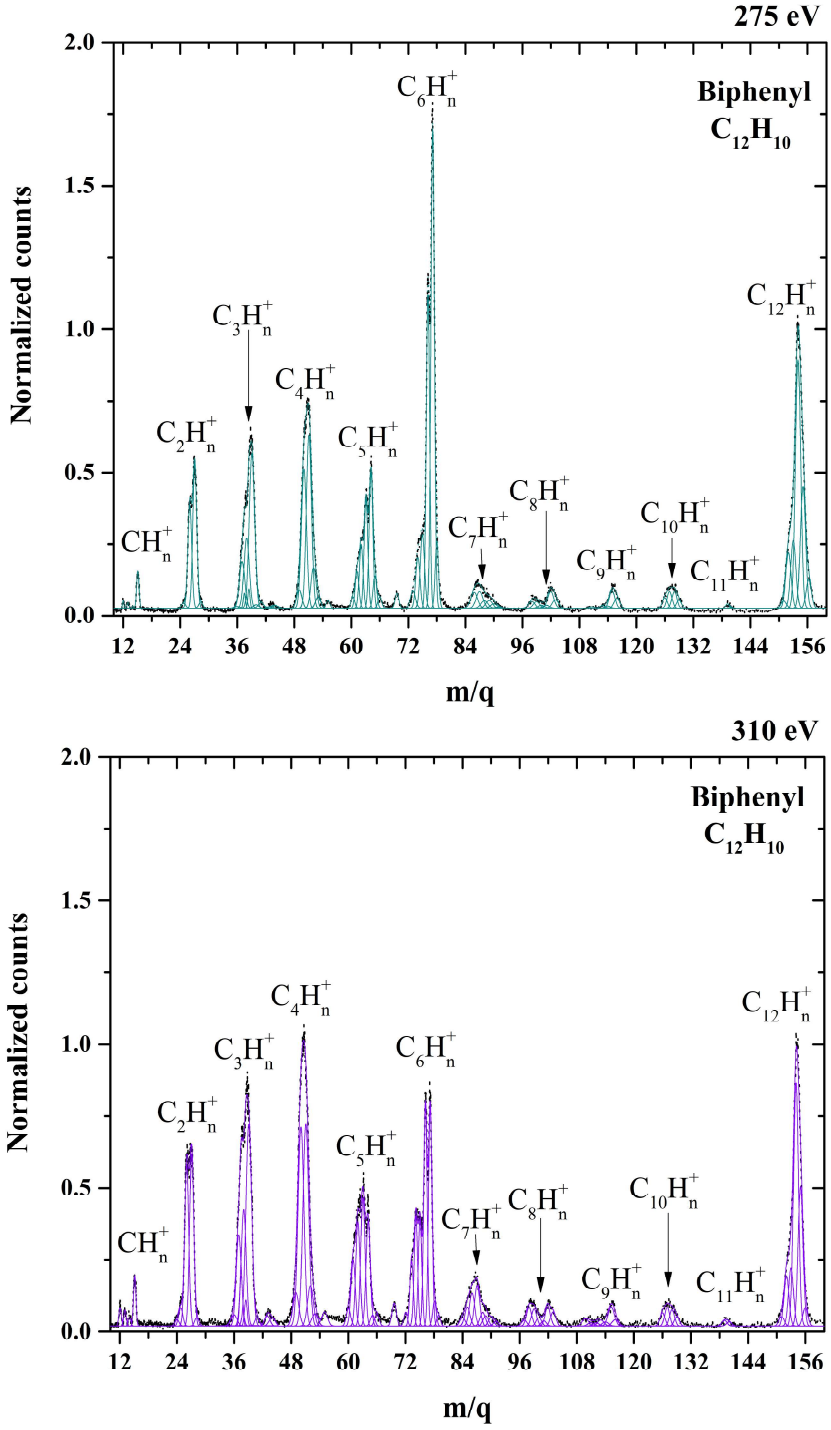

Figure 5.2: Time-of-flight mass spectra in normalized counts of biphenyl at 275 eV (top) and 310 eV (bottom)

ily. In order to quantify the production of each individual ion to the overall mass spectrum, we used a multiple Gaussian function fitting procedure to calculate the Partial Ion Yield, *PIY*.

The *PIY* values are shown in Fig. 5.3 and Table 5.1. For 275 eV, energy below the C1s resonance (285.07 eV, Minkov et al. 2005), the spectrum is dominated by the $C_6H_5^+$ ($[M–C_6H_5]^+$,

m/q = 77) ion signal with $PIY = 12.2\%$. This species is produced directly from the dissociation of the carbon-carbon bond that connects both phenyl moieties, whose bond breakage leads also to the formation of the $C_6H_5^{\cdot}$ radical. The appearance energy of $C_6H_5^+$ was calculated as 21.28 eV by Jochims et al. (1997), and the ion is scarcely produced in the 70 eV photoelectron spectrum (Wallace, 2011). The potential energy surface of $C_6H_5^+$ was thoroughly explored by Peverati et al. (2016). The global minimum energy structure is the aromatic six-membered ring molecule with singlet multiplicity, calculated as 25 to 40 kcal mol^{-1} lower in energy than its triplet counterpart (Hrušák et al., 1997; Nicolaides et al., 1997; Patzer et al., 2010; Peverati et al., 2016). The next singlet $C_6H_5^+$ isomer is the ethynylcyclobutenylium system, lying 26.0 kcal mol^{-1} above the six-membered ring (Peverati et al., 2016). These results strongly suggest, therefore, that the $C_6H_5^+$ molecular ion produced in our experiments retains the aromatic structure. By inspecting the shape of the peak m/q= 77, it was not possible to discriminate any signal coming from the parent dication. However, we do observe a multitude of signals in our PEPIPICO experiments, as well as fractional m/q values in PEPICO spectra, which are characteristic of fragmentation processes starting from a doubly-ionized excited state of the parent molecule. Apart from dissociation, a fraction of the doubly-ionized parent molecules could also undergo electronic relaxation processes and accommodate the excess of positive charge on a rigid, non-dissociated structure. More experiments are necessary in order to investigate the production of $C_{12}H_n$ multiply charged species.

Among the other C_6Hn^+ ions, only $C_6H_4^{+\cdot}$ ($[M–C_6H_6]^{+\cdot}$, m/q = 76) has a *PIY* value greater than 5% at 275 eV ($PIY = 7.4\%$). This species is probably the *ortho*-benzyne cation, in which two adjacent carbon atoms of the six-membered rings are not bonded to hydrogen. By combining DFT and high-level multireferential approaches, Kaiser et al. (2018) revealed that $C_6H_4^{+\cdot}$ has a twisted boat-like geometry with C_2 symmetry. Starting from an ionized biphenyl molecule, the ion could be formed by an initial inter-ring hydrogen migration followed by the cleavage of the central carbon-carbon bond.

The second most prominent ion at 275 eV corresponds to the parental ion $C_{12}H_{10}^{+\cdot}$ ($[M]^{+\cdot}$, m/q = 154), with $PIY = 9.4\%$. Early studies using transient and time-resolved resonance Raman spectroscopy suggested that the structures of both the radical cation and the radical anion of biphenyl have planar or nearly planar structures in solution (Buntinx and Poizat, 1989; Sasaki and Hamaguchi, 1994). A similar conclusion for the isolated radical cation was obtained by Erickson et al. (1995), which determined torsional angles of less than 10° for the $C_{12}H_{10}^{+\cdot}$ species absorbed in distinct solid matrices. As for computational studies, Rubio et al. (1995) performed C_{2h}-symmetry constrained ge-

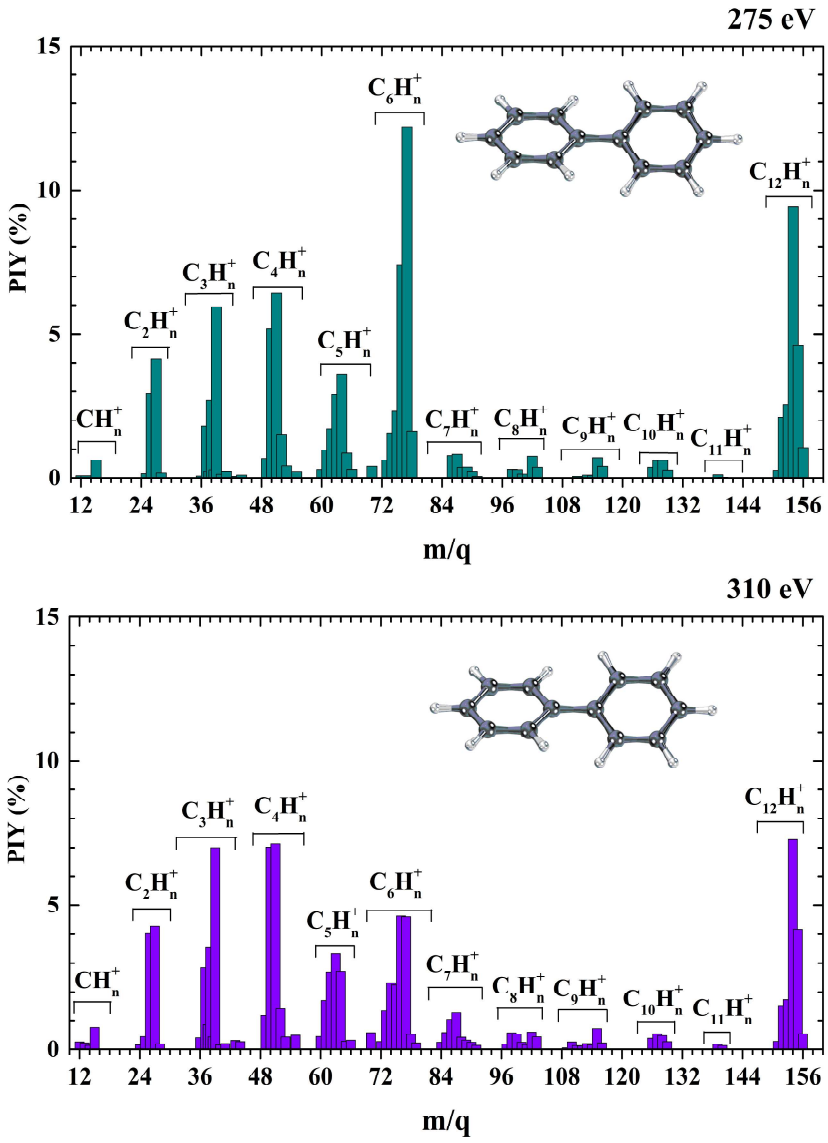

Figure 5.3: Partial ion yield, *PIY* (%), measured at 275 eV (top) and 310 eV (bottom)

ometry optimizations of $C_{12}H_{10}^{+\cdot}$ at the complete active space self-consistent field (CASSCF) level and used the structures as model systems for investigating charge defects in PPP. Further studies employing full geometry optimizations at the DFT level revealed that the $C_{12}H_{10}^{+\cdot}$ radical cation has actually a non-planar structure, with torsional angles ranging from $\phi = 17.5°$ to $\phi = 20.5°$ (Furuya et al., 1998; Arulmozhiraja and Fujii, 2001; Tachikawa and Kawabata, 2003). However, as revealed in this work, the biphenyl structure (**A.3**$^{+\cdot}$) is not the global minimum of the $C_{12}H_{10}^{+\cdot}$ system (see section 3.2), being 19.9 kcal mol^{-1} less stable than the singly-charged acenaphthene ion (**A.1**$^{+\cdot}$). This structure is composed of a naphthalene carbon backbone, with a bridging ethylene group connecting the positions 1 and 8. We therefore expect that the parent ion detected in our experiments underwent

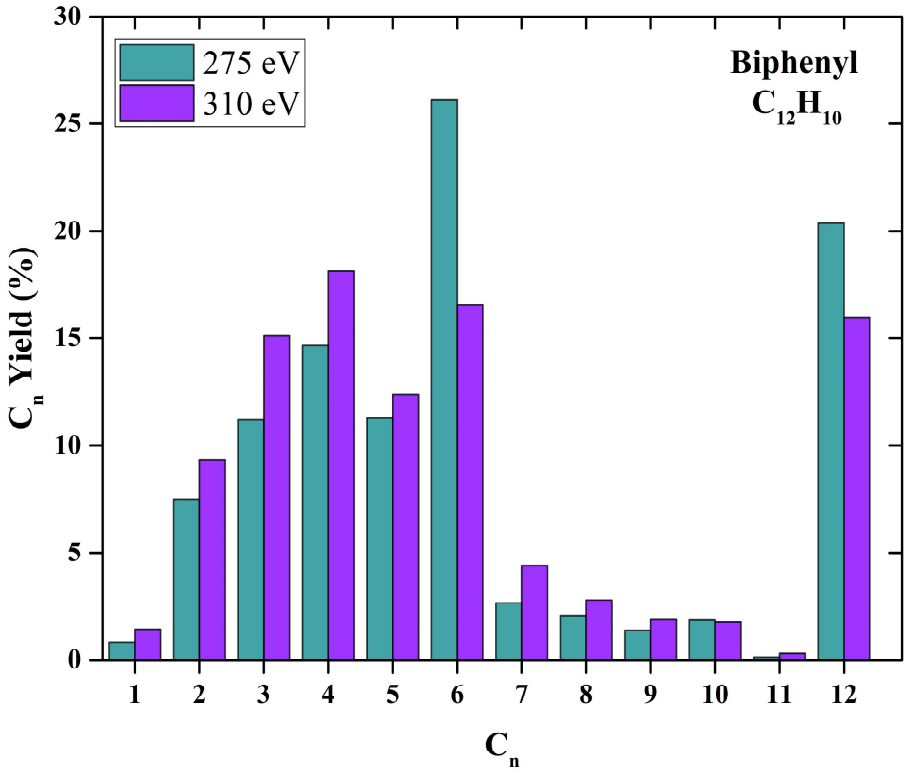

Figure 5.4: Comparison of the production of ionic fragments of carbon backbone families C_n (n=1–12) of biphenyl molecule in 275 and 310 eV.

loss of molecular integrity after isomerization to the global minimum of the $C_{12}H_{10}^{+\cdot}$ system.

Buchanan et al. (1980) generated the acenaphthene radical cation $C_{12}H_{10}^{+\cdot}$ in pure molten antimony trichloride medium, and obtained its electron paramagnetic resonance (EPR) spectrum for the first time. The photodissociation of $C_{12}H_{10}^{+\cdot}$ upon visible and UV radiation was studied by Ekern et al. (1998), revealing that the ion does not isomerize during the process, but loses one or two hydrogen atoms from the ethylene bridge. The latter process gives rise to the acenaphthylene radical cation ($C_{12}H_8^{+\cdot}$), whose spectroscopic and photochemical properties were determined by Banisaukas et al. (2003). Both $C_{12}H_9^+$ (m/q = 153) and $C_{12}H_8^{+\cdot}$ (m/q = 152) ions are also observed in our experiments, and may suggest that they are generated mainly after isomerization of the biphenyl radical cation to the acenaphthene structure. In their experiments, Banisaukas et al. (2003) were able to remove up to four hydrogen atoms from $C_{12}H_{10}^{+\cdot}$, and showed that the two lower-mass ions with m/q = 151 and m/q = 150 are not formed from the dehydrogenation of $C_{12}H_8^{+\cdot}$. While $C_{12}H_7^+$ (m/q = 151) is formed from H_2 loss of $C_{12}H_9^+$, $C_{12}H_6^{+\cdot}$ (m/q = 150) is produced entirely from the single hydrogen loss from $C_{12}H_7^+$. In our experiments, while a small production of $C_{12}H_7^+$ is observed (*PIY* = 2.6% at 275 eV), there is no evidence of the fourth dehydrogenation of the parent ion.

Apart from $[M]^{+\cdot}$, $[M–H_n]^+$ and $[M–C_6H_n]^+$, we can also observe families of molecular ions containing all numbers of backbone carbon atoms from one to twelve, especially $C_4H_n^+$, $C_3H_n^+$ and $C_2H_n^+$. However, among these species, only $C_3H_3^+$ ($[M–C_9H_7]^+$, m/q = 39, $PIY = 6.0\%$), $C_4H_2^{+\cdot}$ ($[M–C_8H_8]^{+\cdot}$, m/q = 50, $PIY = 5.2\%$) and $C_4H_3^+$ ($[M–C_8H_7]^+$, m/q = 51, $PIY = 6.4\%$) have *PIY* values greater than 5% at 275 eV.

The $C_3H_3^+$ species is probably the aromatic cyclopropenyl cation, which is considered a key intermediate for hydrocarbon formation in the ISM (Agúndez and Wakelam, 2013; Zhao et al., 2014). The production of such species from the dissociative photoionization of biphenyl is almost two-fold greater than the one observed for naphthalene at the same incident photon energy of 275 eV (Monfredini et al., 2019), which is probably related to the higher carbon backbone structural rigidity of the latter.

The bottom panel of Figure5.3 shows the *PIY* values at 310 eV. After the C1s resonance energy, we observe a significant decrease in the production of $C_6H_5^+$ and $C_6H_4^{+\cdot}$, whose *PIY* values drop down to 4.6%. While the signal coming from $C_6H_4^{+\cdot}$ at 310 eV is around 60% of the one observed at 275 eV, the $C_6H_5^+$ species is reduced to merely 38% of its previous value. This indicates that both species are more susceptible to further dissociation pathways when the incident photon energy is higher than the C1s resonance energy. As a consequence, fragments with smaller numbers of carbon backbone atoms (from $C_1H_n^+$ to $C_5H_n^+$) are increased, as shown in Fig. 5.4. The $C_3H_3^+$, $C_4H_2^{+\cdot}$ and $C_4H_3^+$ molecular ions, for example, show an increase in their *PIY*s to values above 7%. A similar process, although less pronounced, is observed when comparing the parent ion and smaller fragments. The $C_{12}H_{10}^{+\cdot}$ signal for an incident energy of 310 eV is reduced to $PIY = 7.3\%$, which is followed by an increase in the yield of the carbon backbone families from $C_7H_n^+$ to $C_{11}H_n^+$. The highest *PIY* among ions from these families are the very unsaturated $C_7H_2^{+\cdot}$ ($[M–C_5H_8]^{+\cdot}$, m/q = 86, $PIY = 1.0\%$) and $C_7H_3^+$ ($[M–C_5H_7]^{+\cdot}$, m/q = 87, $PIY = 1.3\%$) systems. The most stable $C_7H_2^{+\cdot}$ species presents a linear polyynic HC_7H open-chain structure (Fulara et al., 1995; Mühlhauser et al., 2003). The global minimum of $C_7H_3^+$, on the other hand, is predicted as a C_4H-substituted cyclopropenyl ring (Chakraborty et al., 2014). Taken together, these results suggest that ring-opening dissociative photoionization pathways are more active for photon energies above the C1s resonance.

Table 5.1: PIY (per cent) of biphenyl, organized per mass-to-charge ratio and photon energy.

m/q	Attribution	PIY (%)		m/q	Attribution	PIY (%)	
		275 eV	310 eV			275 eV	310 eV
1	H^+	1.04	1.20	76	$C_6H_4^+$	7.41	4.62
2	H_2^+	0.02	0.04	77	$C_6H_5^+$	12.19	4.60
12	C^+	0.08	0.27	78	$C_6H_6^+$	1.61	0.52
13	CH^+	0.08	0.23	79	$C_6H_7^+$	–	0.23
14	CH_2^+	0.02	0.13	84	C_7^+	–	0.26
15	CH_3^+	0.62	0.76	85	C_7H^+	–	0.59
24	C_2^+	–	0.15	86	$C_7H_2^+$	0.78	1.04
25	C_2H^+	0.15	0.44	87	$C_7H_3^+$	0.83	1.29
26	$C_2H_2^+$	2.93	4.02	88	$C_7H_4^+$	0.37	0.42
27	$C_2H_3^+$	4.12	4.28	89	$C_7H_5^+$	0.38	0.33
28	$C_2H_4^+$	0.17	0.20	90	$C_7H_6^+$	0.21	0.26
36	C_3^+	0.07	0.41	91	$C_7H_7^+$	0.05	0.13
37	C_3H^+	1.79	2.84	97	C_8H^+	–	0.17
37.5	$C_6H_3^{2+}$	0.23	0.84	98	$C_8H_2^+$	0.31	0.58
38	$C_3H_2^+$	2.69	3.54	99	$C_8H_3^+$	0.30	0.53
38.5	$C_6H_5^{2+}$	0.30	0.43	100	$C_8H_4^+$	0.14	0.26
39	$C_3H_3^+$	5.94	7.00	101	$C_8H_5^+$	0.14	0.15
40	$C_3H_4^+$	0.13	0.14	102	$C_8H_6^+$	0.76	0.61
41	$C_3H_5^+$	0.22	0.22	103	$C_8H_7^+$	0.38	0.44
43	$C_3H_6^+$	0.06	0.31	109	C_9H^+	–	0.05
44	$C_3H_7^+$	0.10	0.28	110	$C_9H_2^+$	0.06	0.27
49	C_4H^+	0.69	1.18	111	$C_9H_3^+$	0.00	0.12
50	$C_4H_2^+$	5.17	7.02	112	$C_9H_4^+$	0.10	0.11
51	$C_4H_3^+$	6.43	7.14	113	$C_9H_5^+$	0.09	0.22
52	$C_4H_4^+$	1.50	1.42	114	$C_9H_6^+$	0.71	0.15
53	$C_4H_5^+$	0.42	0.43	115	$C_9H_7^+$	0.40	0.72
55	$C_4H_6^+$	0.21	0.49	116	$C_9H_8^+$	–	0.23
60	C_5^+	0.31	0.45	126	$C_{10}H_6^+$	0.37	0.39
61	C_5H^+	0.98	1.70	127	$C_{10}H_7^+$	0.60	0.55
62	$C_5H_2^+$	1.71	2.69	128	$C_{10}H_8^+$	0.60	0.48
63	$C_5H_3^+$	2.90	3.31	129	$C_{10}H_9^+$	0.29	0.28
64	$C_5H_4^+$	3.61	2.71	139	$C_{11}H_7^+$	0.11	0.17
65	$C_5H_5^+$	0.86	0.28	140	$C_{11}H_8^+$	0.02	0.12
66	$C_5H_6^+$	0.31	0.32	151	$C_{12}H_7^+$	0.28	0.29
70	$C_5H_{10}^+$	0.41	0.59	152	$C_{12}H_8^+$	2.12	1.51
72	C_6^+	–	0.28	153	$C_{12}H_9^+$	2.56	1.73
73	C_6H^+	0.63	1.35	154	$C_{12}H_{10}^+$	9.40	7.30
74	$C_6H_2^+$	1.55	2.30	155	$^{13}CC_{11}H_{10}^+$	4.61	4.17
75	$C_6H_3^+$	2.32	2.24	156	$^{13}C_2C_{10}H_{10}^+$	1.06	0.55

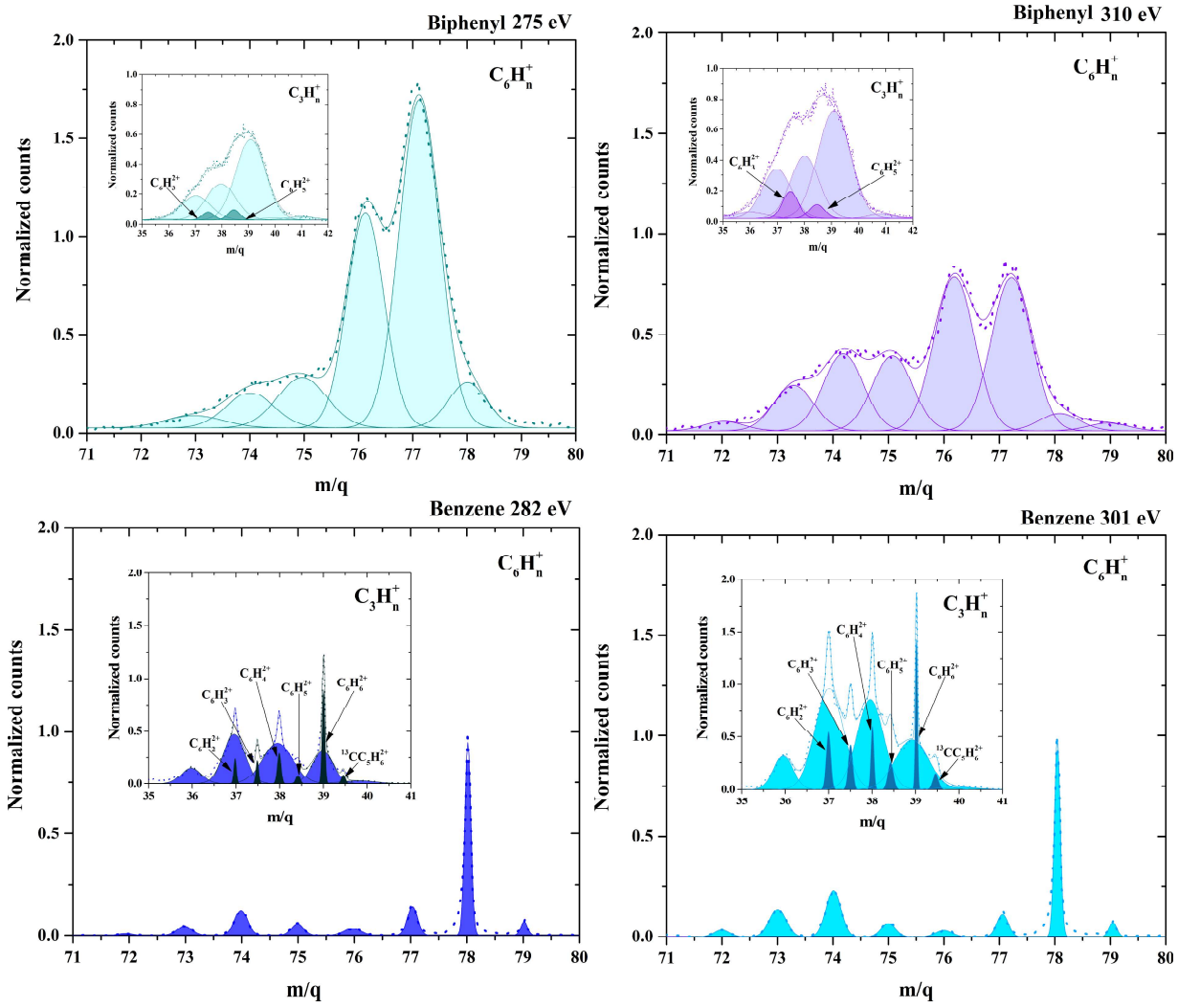

Figure 5.5: Normalized time-of-flight mass spectra of ionic fragments from biphenyl at 275 eV and 310 eV (top) and benzene at 282 eV and 301 eV (bottom) with m/q = 71 – 79. The inserted figures highlight the identification of ionic fragments with 2+ charge: $C_6H_3^{2+}$ (m/q = 37.5) and $C_6H_5^{2+}$ (m/q = 38.5) for biphenyl; from $C_6H_2^{2+}$ (m/q = 37) to $^{13}CC_5H_6^{2+}$ (m/q = 39.5) for benzene.

5.3 Multiply-Charged Ions and Double Coincidence Mass Spectra of Biphenyl

In our experiments with biphenyl (see top panels of Fig. 5.5), we were also able to identify signals containing fractional mass-to-charge ratios related to the doubly-charged ions $C_6H_3^{2+}$ ($[M–C_6H_7]^{2+}$, m/q = 37.5) and $C_6H_5^{2+}$ ($[M–C_6H_5]^{2+}$, m/q = 38.5). The phenyl radical dication $C_6H_5^{2+}$ was computationally studied by Zyubina et al. (2002), and has C_{2v} symmetry and $^2A_2$ electronic state, with spin density delocalized throughout the π space of the six-membered carbon ring. However, to the best of our knowledge, there is no systematic study on the thermodynamic stability of neither $C_6H_5^{2+}$

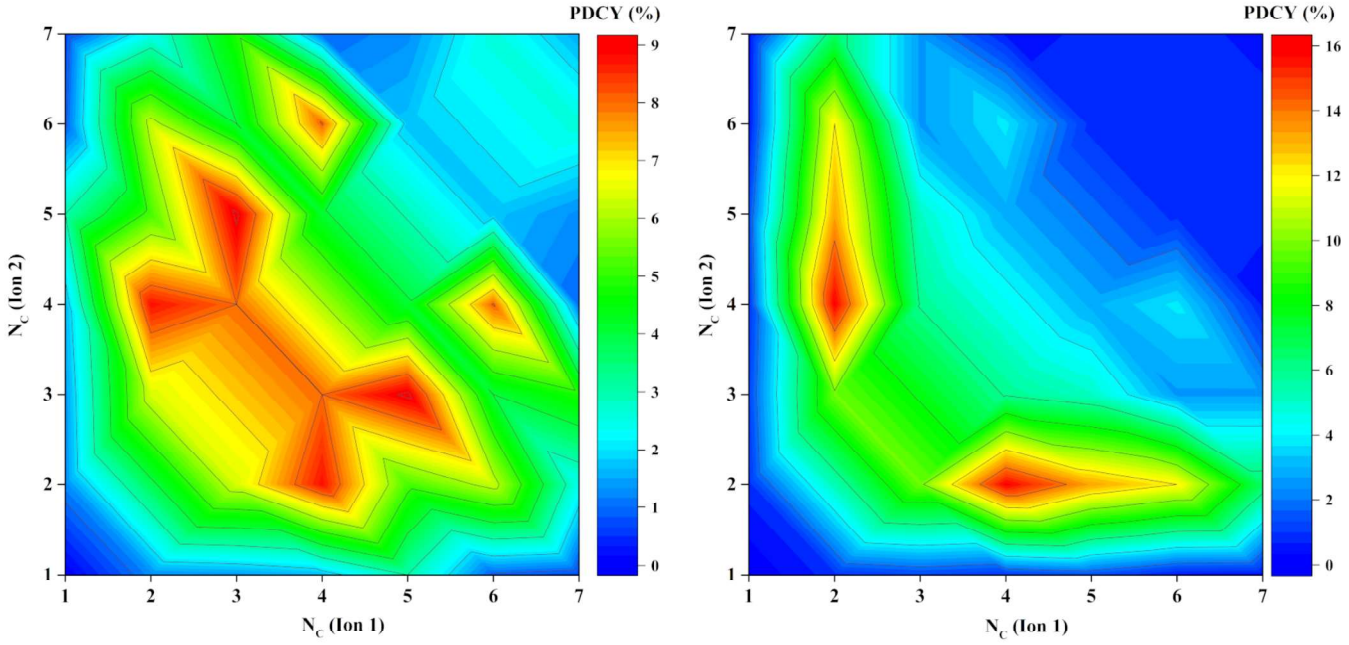

Figure 5.6: Partial Double Coincidence Yield (*PDCY*) contour map obtained from PEPIPICO measurements of biphenyl with respect to the number of carbon atoms (N_C) of each fragment at 275 eV (left panel) and 310 eV (right panel).

nor $C_6H_3^{2+}$ isomers up to this date. The detection of $C_6H_5^{2+}$ reveals that dissociation processes were activated after the formation of a multiply-charged $C_{12}H_{10}$ species, such as $C_{12}H_{10}^{2+}$ or even $C_{12}H_{10}^{3+}$. Starting from the doubly-charged parent dication, the formation of $C_6H_5^{2+}$ would indicate that the carbon-carbon central bond could be cleaved not only leading to homolytic charge separation and formation of two $C_6H_5^+$ species, but also to heterolytic charge separation and formation of the radicals $C_6H_5^{2+}$ and $C_6H_5^{\cdot}$.

The $C_6H_3^{2+}$ and $C_6H_5^{2+}$ radical dications are also observed in similar experiments conducted by us with benzene (see bottom panels of Fig. 5.5) and naphthalene (Monfredini et al., 2019) in the surroundings of their respective C1s resonance energies. For benzene we could actually observe signals coming from $C_6H_n^{2+}$ dications with $2 \leq n \leq 6$. The global minimum energy isomer of $C_6H_6^{2+}$ is the pentagonal pyramidal structure of singlet multiplicity (Hogeveen and Kwant, 1973; Jašík et al., 2014; Malischewski and Seppelt, 2017; Fantuzzi et al., 2017b; Klein et al., 2018). In turn, the most stable $C_6H_4^{2+}$ isomer is the triafulvene dication, where two cyclopropenyl aromatic rings are perpendicularly connected by a single carbon-carbon bond (Lammertsma and Schleyer, 1988). Finally, Burdick et al. (1985) computed potential energy curves for linear HC_6H^{2+} ions, and showed that the dissociation into two C_3H^+ units has the lowest dissociation barrier (5.77 eV). However, to the best of

our knowledge, the minimum energy landscape of $C_6H_2{}^{2+}$ isomers has not been explored up to date. Due to experimental limitations, we could not discriminate if molecular dications with even number of hydrogen atoms are also produced from the dissociative photoionization of biphenyl. However, we believe that the signals of these species are hindered by the counts of the singly-charged ions of the same mass-to-charge ratio. We therefore conclude that more experiments are needed in order to elucidate the formation of other multiply-charged species from biphenyl.

In Fig. 5.6, we compare the production of singly-charged species generated from a photoelectron-photoion-photoion coincidence event for a photon energy before and after the C1s resonance. For that purpose, we plot the Partial Double Coincidence Yield (PDCY) of the species with respect to the number of carbon atoms (N_C) of each fragment. The PDCY is obtained by integrating the counts in the PEPIPICO map of a particular ion-ion coincidence. It indicates the probability of the fragmentation pathway that leads to the respective ions starting from a double photoionization event.

For 275 eV, we show that the main fragmentation channels lead to the formation of [$C_5H_n{}^+$ + $C_3H_m{}^+$] (9.1%), [$C_4H_n{}^+$ + $C_2H_m{}^+$] (8.8%) and [$C_6H_n{}^+$ + $C_4H_m{}^+$] (8.1%). In the first channel, neutral fragments with a total number of four carbon atoms are produced, most probably two C_2H_2 molecules. In turn, the formation of [$C_4H_n{}^+ + C_2H_n{}^+$] in coincidence indicates that half of the carbon content is released as neutral fragments, most probably in the form of benzene (C_6H_6), phenyl ($C_6H_5{}^{\cdot}$) or three C_2H_2 units. Finally, the last channel suggests the liberation of a neutral C_2H_2 fragment.

By increasing the photon energy to 310 eV, a depletion of the [$C_5H_n{}^+ + C_3H_n{}^+$] and the [$C_6H_n{}^+$ + $C_4H_n{}^+$] channels is observed, as the PDCY values decrease to 5.1% and 3.8%, respectively. On the other hand, the PDCY of the [$C_4H_n{}^+ + C_2H_n{}^+$] channel increases to 15.9%, and dominates the double coincidence plot. This result suggests that a separation of the two C_6 rings (with or without hydrogen migration) is the most probable fragmentation process starting from the double photoionization of biphenyl after the C1s resonance. Other relevant pathways involve the formation of [$C_5H_n{}^+ + C_2H_m{}^+$] (13.2%) and [$C_6H_n{}^+ + C_2H_m{}^+$] (12.0%). For the first case, neutral fragments with a total of five carbon atoms are produced, such as cyclopentadiene (C_5H_6), the $C_5H_5{}^{\cdot}$ radical or a combination of neutral species containing C_2 and C_3 backbones. Finally, the [$C_6H_n{}^+$ + $C_2H_m{}^+$] channel is associated with liberation of neutral species containing up to four carbon atoms, most probably two C_2H_2 species.

5.4 Fragmentation pathways of biphenyl dication from computations

In the previous section, we show that the production of [$C_4H_n^+$ + $C_2H_m^+$] from the dissociation of a doubly-charged $C_{12}H_{10}^{2+}$ is the dominant fragmentation route of biphenyl for energies above the C1s resonance energy. This suggests that the carbon-carbon bond that connects both C_6 rings is cleaved after double ionization, with the release of a neutral $C_6H_5^{\cdot}$ or C_6H_6 molecule and a doubly-charged $C_6H_n^{2+}$ ion ($n = 5$ or 4, respectively), which is further dissociated leading to a photoinduced three-body decay process. In order to investigate the energetics of distinct channels related to the mentioned fragmentation mechanism, our theoretical collaborators computed the electronic energy corrected by zero-point energy (E + ZPE) at the DFT (PBE0/def2-TZVP) and coupled-cluster (CCSD(T)-F12/cc-pVTZ//PBE0/def2-TZVP) levels of each one of the channels starting from the doubly-charged biphenyl molecule. The fragment ions were computed for their respective global minima and ground state multiplicities. The differences in energy among the pathways can be used for identifying the thermodyamically preferred dissociation products. The computational results are briefly discussed in this section.

Table 5.2 shows the thermochemistry of selected fragmentation pathways of the biphenyl dication. The most stable pathway, as indicated by both DFT and CCSD calculations, involve the formation of a neutral C_6H_6 and the singly-charged ions $C_4H_2^{+\cdot}$ and $C_2H_2^{+\cdot}$. This indicates that hydrogen migration from one phenyl ring to the other must occur after the double ionization process in order to allow the system to relax through the thermodynamically preferential route. The fragmentation pathway involving release of neutral $C_6H_5^{\cdot}$ and the $C_4H_2^{+\cdot}$ and $C_2H_3^+$ molecular ions is 0.62 eV (at the CCSD(T)-F12 level) higher in energy than the previous one, and is the most stable pathway in which there is no hydrogen migration between the phenyl rings. This route is 0.29 eV less endoergic than the one in which $C_4H_3^{+\cdot}$ is formed together with $C_6H_5^{\cdot}$ and $C_2H_2^{+\cdot}$. With the exception of the pathway leading to C_6H_6 + C_4H^+ + $C_2H_3^+$ (ΔE = 2.11 eV at the CCSD(T)-F12 level), all other fragmentations have ΔE greater than 4 eV in comparison to the least endoergic one. Taken together, our results suggest that photoinduced three-body decay routes after double photoionization of biphenyl contribute predominantly for the production of $C_4H_2^{+\cdot}$, $C_4H_3^+$, $C_2H_2^{+\cdot}$ and $C_2H_3^{+\cdot}$.

Table 5.2: Thermochemistry of selected fragmentation pathways of the biphenyl dication (**B.3**$^{2+}$) at the DFT (PBE0/def2-TZVP) and CCSD(T)-F12/cc-pVTZ//PBE0/def2-TZVP levels.

Fragmentation Pathway	DFT		CCSD(T)-F12	
	E + ZPE (a.u.)	ΔE (eV)	E + ZPE (a.u.)	ΔE (eV)
$C_6H_6 + C_4H_4^{+\cdot} + C_2^{+\cdot}$	-461.48896	6.12	-461.22980	4.89
$C_6H_6 + C_4H_3^{+} + C_2H^{+}$	-461.51992	5.28	-461.23928	4.63
$C_6H_6 + C_4H_2^{+\cdot} + C_2H_2^{+\cdot}$	-461.71395	0.00	-461.40938	0.00
$C_6H_6 + C_4H^{+} + C_2H_3^{+}$	-461.62156	2.51	-461.33185	2.11
$C_6H_6 + C_4^{+\cdot} + C_2H_4^{+\cdot}$	-461.53499	4.87	-461.21010	5.42
$C_6H_5^{\cdot} + C_4H_5^{+} + C_2^{+\cdot}$	-461.44833	7.23	-461.18617	6.07
$C_6H_5^{\cdot} + C_4H_4^{+\cdot} + C_2H^{+}$	-461.45412	7.07	-461.16507	6.65
$C_6H_5^{\cdot} + C_4H_3^{+} + C_2H_2^{+\cdot}$	-461.68397	0.82	-461.37803	0.85
$C_6H_5^{\cdot} + C_4H_2^{+\cdot} + C_2H_3^{+}$	-461.69464	0.53	-461.38657	0.62
$C_6H_5^{\cdot} + C_4H^{+} + C_2H_4^{+\cdot}$	-461.56229	4.13	-461.26143	4.03
$C_6H_5^{\cdot} + C_4^{+\cdot} + C_2H_5^{+}$	-461.50014	5.82	-461.17622	6.34

Table 5.3: Average values of photon flux (F_x), photodissociation rate (k_{ph-d}) and half-life ($t_{1/2}$) of the sources studied in this chapter.

Source	$\langle F_x \rangle$ (photons eV^{-1} cm^{-2} s^{-1})		$\langle k_{ph-d} \rangle$ (s^{-1})		$\langle t_{1/2} \rangle$ (yr)	
	275 eV	310 eV	275 eV	310 eV	275 eV	310 eV
BD+30°3639	2.70×10^{4}	4.62×10^{4}	2.34×10^{-15}	5.39×10^{-13}	2.46×10^{7}	1.07×10^{5}
NGC 7027	1.80×10^{3}	3.47×10^{3}	1.56×10^{-16}	3.80×10^{-14}	3.70×10^{8}	1.52×10^{6}
NGC 5315	9.01×10^{3}	1.50×10^{4}	7.81×10^{-16}	1.75×10^{-13}	7.40×10^{7}	3.30×10^{5}
NGC 40	1.54×10^{3}	2.48×10^{3}	1.33×10^{-16}	2.90×10^{-14}	4.34×10^{8}	1.99×10^{6}

5.5 Absolute Photoionization and Photodissociation Cross Sections of Biphenyl

For the determination of photoionization (σ_{ph-i}) and photodissociation (σ_{ph-d}) cross sections, it is necessary to know the photoabsorption (σ_{ph-abs}) cross section as a function of the photon energy. The C1s spectra of biphenyl and benzene are very similar, as shown by Wang et al. (2005). Therefore, we obtained the σ_{ph-abs} values for the biphenyl molecule at 275 and 310 eV by doubling the photoabsorption cross section of benzene taken from the core excitation database of the Hitchcock Group (Hitchcock et al., 1987; Hitchcock and Mancini, 1994). For 275 eV and 310 eV, the σ_{ph-abs} values of biphenyl are 9.57 x 10^{-20} and 1.26 x 10^{-17} cm^{-2}, respectively.

The procedure for calculating the photoionization and photodissociation cross sections is de-

scribed in chapter 3. For biphenyl, the absolute photodissociation cross sections, σ_{ph-d}, were calculated as 8.67×10^{-20} cm^{-2} at 275 eV and 1.17×10^{-17} cm^{-2} at 310 eV. The absolute single photoionization cross sections, σ^{+}_{ph-i}, on the other hand, are 9.00×10^{-21} cm^{-2} for 275 eV and 9.20×10^{-19} cm^{-2} for 310 eV. In this chapter, the multiple photoionization cross sections are not estimated because they could not be quantified in our experiments, and their identification is only inferred through the PEPIPICO spectra. Therefore, more experiments are necessary in order to quantify the spectral contribution of these species.

5.6 Survival of biphenyl in the PDR of Planetary Nebulae

After obtaining the photoionization and photodissociation cross sections as described in the previous section, we proceed with the analysis of the stability of the biphenyl molecule in the photodissociation region of some astrophysical objects. We selected four planetary nebulae with similar evolutionary states, all of them presenting PAH emission features: BD+30°3639 (Allamandola et al., 1989; Murashima et al., 2006; Zhang et al., 2008; Freeman and Kastner, 2016), NGC 7027 (Tielens, 2008; Freeman and Kastner, 2016; Cruz-Diaz et al., 2019), NGC 5315 (Cohen and Barlow, 2005; Szczerba et al., 2001) and NGC 40 (Delgado-Inglada and Rodríguez, 2014). Such objects were described in detail in Chapter 1.

We calculate the X-ray flux in 275 eV and 310 eV from the luminosity data reported in the literature using the same procedure as the one described in Chapter 4. The X-ray optical depth, τ_X, is obtained from eq. 4.2.

We adopted the following molecular hydrogen column density values: $N_{H_2} = 1.20 \times 10^{21}$ cm^2 for BD+30°3639, $N_{H_2} = 1.15 \times 10^{21}$ cm^2 for NGC 5315 and $N_{H_2} = 1.10 \times 10^{21}$ cm^2 for NGC 40. These values correspond to half of the ones reported in the literature for N_H. For NGC 7027, an H_2 column density of $N_{H_2} = 1.3 \times 10^{21}$ cm^2 was taken from Agúndez et al. (2010). From these values, we calculated the photodissociation and photodissociation rates and the half-life of biphenyl in the four distinct PN sources.

In Figure 5.7 we show the estimated half-life values for the biphenyl molecule in the photodissociation regions of the planetary nebulae BD+30°3639, NGC 7027, NGC 5315 and NGC 40. The average values obtained for the photon fluxes, photodissociation rates and half-lives at 275 eV and 310 eV are shown in Table 5.3. For a photon energy of 275 eV, the half-lives of biphenyl in the plan-

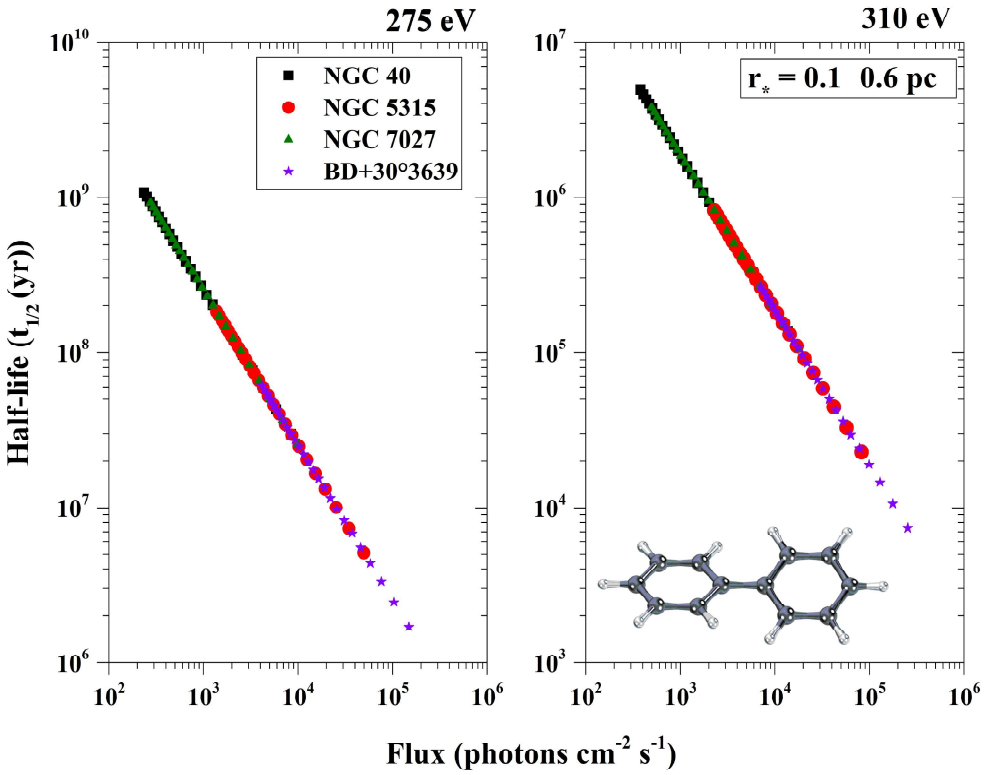

Figure 5.7: Half-life values of the biphenyl molecule after interaction with the X-ray photon flux of the planetary nebulae NGC 40, NGC 5315, NGC 7027 and BD+30°3639. Each data in the figure represents a specific value of distance between 0.1 to 0.6 pc from the central star.

etary nebulae studied herein vary from 2.46×10^7 years to 4.34×10^8 years, while for 310 eV these values span from 1.07×10^5 years to 1.99×10^6 years. The half-lives at 275 eV are similar to the ones estimated for amorphous hydrocarbons and PAHs in the interstellar medium, which are in the range of $2-6 \times 10^8$ years (Jones et al., 2011; Parker et al., 2012). However, they are at least one order of magnitude smaller than the injection timescales (2.5×10^9 years) of carbonaceous materials into the interstellar medium by AGB stars and carbon-rich planetary nebulae (Jones et al., 1994, 1996). Therefore, the attenuation of the X-ray flux due to the presence of grains seems not sufficient to account for the presence of biphenyl and small-sized PAHs in regions with high incidence of ionizing photons. This is in line with previous works, such as Jones et al. (2011), which suggested that density inhomogeneities in both pre- and post-shocked media could protect PAHs and enhance their lifetimes in such hostile environments. Moreover, for hydrogenated and superhydrogenated PAHs, the decrease of the photoabsorption cross sections around the C1s resonance energy due to the removal of the strong C1s$\rightarrow \pi^*$ excitations may also contribute for increasing the lifetimes of such molecules in the PDRs of planetary nebulae (Quitián-Lara et al., 2018), as discussed in Chapter 4. The char-

acteristic infrared emission of PAHs may also have the contribution of aromatic fragments produced from the dissociation of larger PAHs (Micelotta et al., 2011; Monfredini et al., 2019). Taken together, these processes could contribute for the presence of PAH infrared emission features in astrophysical environments bearing high-energy photon fluxes.

Chapter 6

Experimental Results III: PAHs in AGNs

Active Galactic Nuclei (AGNs) are sources of both soft (0.2-2 keV) and tender (2-10 keV) X-ray radiation, and contribute significantly to the extragalactic X-ray background (Comastri et al., 1995; Mushotzky et al., 2000; Lubiński et al., 2016; Hickox and Alexander, 2018). The X-ray emission mechanism is known to be powered by gas accretion on to a central supermassive black hole (Ferrarese and Ford, 2005; Zhang, 2005; Di Matteo et al., 2005; Barai et al., 2012), which is the basis of the standard unification model for AGNs (Antonucci, 1993; Urry and Padovani, 1995) — for a recent review, see Netzer 2015. The combination of a 0.2-10 keV radiation field and the presence of PAHs in the AGN vicinity provides an interesting scenario in which laboratory investigation of molecular photoionization and photodissociation in the X-ray energy range could provide important information.

As mentioned in Chapter 1, PAHs have also been observed in a variety of extragalactic objects, including in the circumnuclear regions of AGNs. The experimental studies of vacuum ultraviolet (VUV) photoionization and photodissociation of PAHs were firstly reported at about thirty years ago by Leach et al. (1989a,b), using time-of-flight mass-spectrometry and photoelectron-photoion coincidence techniques. Jochims et al. (1994, 1996, 1999) have also investigated the VUV photostability of PAHs and methyl-substituted PAHs. In addition, the competition between VUV photoionization, photofragmentation and the photoproduction of dications in the context of interstellar PAH population were discussed by Zhen et al. 2016. Using soft X-ray photons with energies around the C1s$\rightarrow \pi^*$ resonance (285 eV), Reitsma et al. (2014); Reitsma et al. (2015) have investigated the fragmentation of PAH cations. However, there is still a lack of information on the ionization and dissociation of PAHs driven by photons of higher energies, which would be useful in the context of the circumnu-

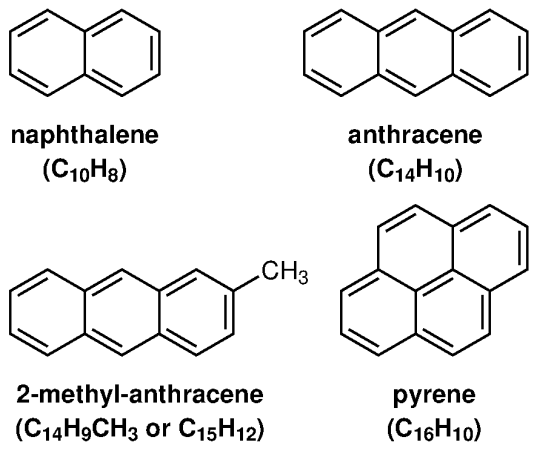

Figure 6.1: The polycyclic aromatic hydrocarbons studied in this work.

clear regions of AGNs. The photochemistry of these regions should be highly affected by a radiation field with 0.2-10 keV photons due to its high penetration power, even through a gas with column densities up to 10^{24} cm^{-2}, such as X-ray dominated regions (XRD, see Usero et al. 2004) .

In this chapter, study the effect of X-ray photon interactions on the photodissociation and photoionization rates of the PAH molecules shown in Fig. 6.1. The experiments were part of a previous PhD thesis (Monfredini, 2015), while the determination of the photoionization and photodissociation cross sections of the molecules depicted in this chapter were developed during the present thesis.

6.1 Photoabsorption, Photoionization and Photodissociation Cross Sections of PAHs at 2500 eV

To the best of our knowledge, there is neither experimental nor theoretical data on the absolute photoabsorption cross section of PAHs at 2500 eV. Even for benzene, which is the building block of PAHs and one of the most emblematic molecular systems, such measurements have only been made up to 800 eV (Rennie et al., 2000).

We obtained the σ_{ph-abs} values of the PAH molecules at 2500 eV by multiplying the photoabsorption cross section of the carbon atom (3.1 x 10^{-21} cm^2), taken from the literature (Henke et al., 1982; Voit, 1992; Henke et al., 1993; Berkowitz, 2002), by the number of C atoms (N_C) that compose the carbon backbone. The dependence of the absolute photoabsorption cross section with respect to the number of carbon atoms in the backbone of the PAH is shown in Figure 6.2 (top) and the σ_{ph-abs} values for the molecules studied herein are presented in Table 6.1. As we can see, the σ_{ph-abs} values

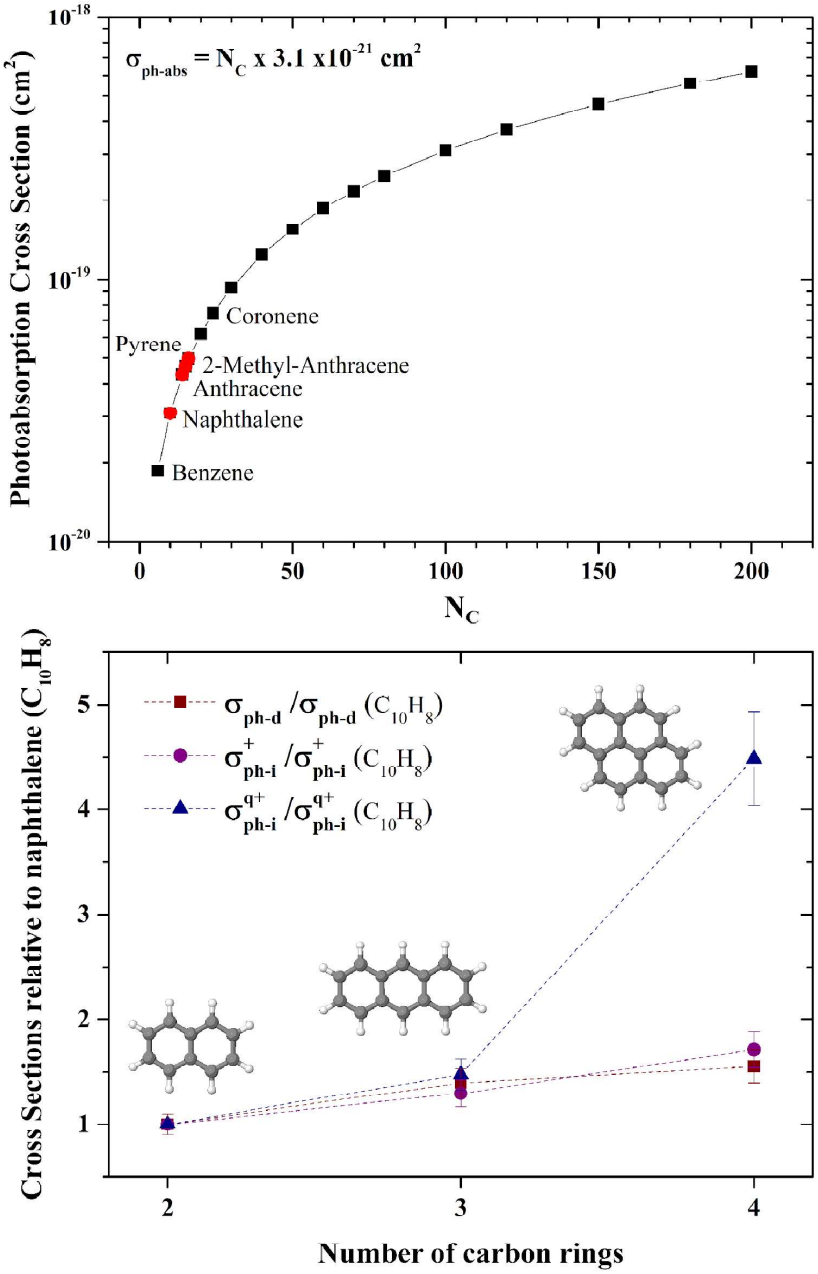

Figure 6.2: Top: Photoabsorption cross section (cm^2) at 2500 eV as a function of the number of carbons (N_C) for each molecule. Bottom: Cross-sections relative to naphthalene as a function of the number of carbon rings.

at 2500 eV do not vary significantly for PAHs with N_C= 10 to 16. On the other hand, the photoabsorption cross section at 2500 eV (3.1x10^{-20} cm^2) for the naphthalene molecule is about two orders of magnitude smaller than at 310 eV (1.05x10^{-17} cm^2). In fact, it is known that low-energy X-ray photons are more easily absorbed than high-energy X-ray photons (Wilms et al., 2000).

The cross sections σ_{ph-abs}, σ_{ph-d}, σ_{ph-i}, σ^{+}_{ph-i} and σ^{q+}_{ph-i} values at 2500 eV for the PAHs studied herein are shown in Table 6.1. It is possible to see that the photodissociation of the carbon backbone

Table 6.1: Cross-sections (cm^2) for photoabsorption (σ_{ph-abs}), photodissociation (σ_{ph-d}), total non-dissociative photoionization (σ_{ph-i}), single photoionization (σ^{+}_{ph-i}) and non-dissociative multiple photoionization (σ^{q+}_{ph-i}) for the following parent PAH molecules: naphthalene ($C_{10}H_8$), anthracene ($C_{14}H_{10}$), 2-methyl-anthracene ($C_{14}H_9CH_3$) and pyrene ($C_{16}H_{10}$), measured at energy of 2500 eV.

Molecule	Cross Section (cm^2)				
	σ_{ph-abs}	σ_{ph-d}	σ_{ph-i}	σ^{+}_{ph-i}	σ^{q+}_{ph-i}
Naphthalene ($C_{10}H_8$)	3.10×10^{-20}	3.05×10^{-20}	5.35×10^{-22}	6.94×10^{-23}	4.66×10^{-22}
Anthracene ($C_{14}H_{10}$)	4.34×10^{-20}	4.26×10^{-20}	7.78×10^{-22}	8.99×10^{-23}	6.88×10^{-22}
2-Methyl-Anthracene ($C_{14}H_9CH_3$)	4.65×10^{-20}	4.59×10^{-20}	6.27×10^{-22}	6.16×10^{-23}	5.66×10^{-22}
Pyrene ($C_{16}H_{10}$)	4.96×10^{-20}	4.74×10^{-20}	2.20×10^{-21}	1.19×10^{-22}	2.09×10^{-21}

(σ_{ph-d}) accounts for the majority of the events that follow photoabsorption. Similarly, the partitioning of σ_{ph-i} into σ^{+}_{ph-i} and σ^{q+}_{ph-i} contributions also follows the trend already observed in the *PIY*s, which indicates a preference of multiple over single non-dissociative photoionization at 2500 eV.

The relative weight of σ^{q+}_{ph-i} with respect to the increase of the number of rings in the carbon backbone can be traced by analyzing the bottom panel of Figure 6.2. The plot shows the ratio between σ_{ph-d}, σ^{+}_{ph-i} and σ^{q+}_{ph-i} and their respective values for naphthalene as the number of carbon rings varies from 2 to 4. While the ratios for σ_{ph-d} and σ^{+}_{ph-i} exhibit a monotonic growth in this range, σ^{q+}_{ph-i} appears to be significantly affected by the increase in the number of carbon rings. This suggests that larger PAHs in X-ray fields can be found in their multiple ionization states. The astrophysical implications of these results to the chemistry of circumnuclear regions of AGNs is discussed in the next section.

6.2 Astrophysical Implications: PAHs in AGNs

6.2.1 Photodissociation of PAHs by X-rays in AGNs

In order to explain the emission of PAHs around AGNs, Voit (1992) proposed that these molecules should be protected by a dense torus surrounding the X-ray source. It is known that the inflowing gas onto a central AGN could form a circumnuclear disk (CND) in which star formation can take place. The CND structure is expected to play an important role in the AGN obscuration, as suggested by starburst disk models (Thompson et al., 2005; Ballantyne, 2008) and high-resolution observations, such as the ones conducted by Izumi et al. (2018). Moreover, Kawakatu and Wada (2008) have shown

Table 6.2: Some properties of the AGN sources studied herein. L_X stands for the X-ray luminosities integrated from 2-10 keV, while $\overline{F}_X$ are the respective average X-ray photon fluxes at 2500 eV ($\tau_x = 4.45$) within distances of 20-80 pc from the Seyfert nucleus.

Source	Type	L_X (eV s^{-1})	$\overline{F}_X$ (photons cm^{-2}s^{-1})
Mrk 279[a]	Sy1	2.48×10^{55}	6.68×10^{8}
Mrk 334[b]	Sy1	1.37×10^{54}	3.68×10^{7}
Mrk 3[b]	Sy2	1.16×10^{55}	3.12×10^{8}
NGC 5728[b]	Sy2	9.42×10^{53}	2.54×10^{7}
NGC 7682[d]	Sy2	3.28×10^{53}	8.82×10^{6}
NGC 1808[c]	Sy2	3.13×10^{51}	8.41×10^{4}

[a] Vasudevan and Fabian (2009) [b] Shu et al. (2007)
[c] Esparza-Arredondo et al. (2018) [d] Gu and Huang (2002)

that the circumnuclear disk might be in coincidence with the putative torus of the standard unification model for AGNs. The authors also predicted that star formation – and consequently PAH emission – is more likely to occur in the outer parts of a 100 pc-size torus. Using 8-m class telescopes and Spitzer, Sales et al. (2013) and Esquej et al. (2014) shortened this distance to around a few pc, with resolution of 26 pc. Additionally, using data from ALMA, Salak et al. (2017) mapped a molecular torus by observing the CO(3-2) and CO(1-0) lines, with a radius of ∼30 pc, around the central X-ray source. These observations might be in coincidence with the PAH emission from Sales et al. (2013).

To the best of our knowledge, the photodissociation of PAHs due to interaction with high energy photons ($E > 1000$ eV) has only been studied by extrapolation from indirect measurements. Such estimates were based on PAH experiments with lower energy photons, up to the VUV range (Leach et al., 1989a,b; Jochims et al., 1994, 1996, 1999), and on the photoabsorption profile of the C atom in a photon energy range up to 30 keV (Henke et al., 1982, 1993). In addition, the interaction of PAHs and their precursors with photons around the C1s$\rightarrow \pi^*$ resonance (285 eV) has been explored by several authors (Rennie et al., 2000; Boechat-Roberty et al., 2009b; Reitsma et al., 2014; Reitsma et al., 2015; Monfredini et al., 2016; Quitián-Lara et al., 2018). However, there is still a lack of data when it comes to investigating the effects of keV photons on these astrophysically relevant molecules.

We applied our experimental data to estimate the stability of PAHs in the circumnuclear regions of six different AGNs (Table 6.2): Mrk 279, Mrk 334, Mrk 3, NGC 5728, NGC 7682, and NGC 1808. These AGNs were taken from the Sales et al. (2010) catalog, and all of them show emission in 8.6 μm, which is due to ionized PAHs (Draine and Li, 2001, 2007; Sales et al., 2010, 2013). The first two entries are Seyfert 1 (Sy1) AGNs, while the others are classified as Seyfert 2 (Sy2). In order to know

the X-ray photon flux, F_X (photons cm^{-2} s^{-1}), at a given distance from the central source of the AGN and for a given photon energy $E = h\nu$, we applied, for each object, the following equation:

$$F_X = \frac{L_X}{4\pi r^2 h\nu} e^{-\tau_x} \tag{6.1}$$

where L_x is the X-ray luminosity (eV s^{-1}) integrated from 2 to 10 keV, r is the distance from the nucleus to a position between 20 to 80 pc inside the dust torus, and τ_x is the X-ray optical depth. Here, the τ_x values were systematically varied from $\tau_x = 0.0$ to $\tau_x = 10.0$ in order to discuss the importance of shielding to the survival of PAHs in AGNs. These values of τ_x can be associated with the respective H_2 column densities by considering the following equation:

$$\tau_x = 2\sigma_H(E) N_{H_2} \tag{6.2}$$

where $\sigma_H(E)$ is the X-ray photoabsorption cross section per H nucleus given by Gorti and Hollenbach (2004):

$$\sigma_H(E) = 1.2 \times 10^{-22} \left(\frac{E}{1\,\mathrm{keV}}\right)^{-2.594} \tag{6.3}$$

In the context of AGNs, the structure and dynamics of the ionic (H II), atomic (H I) and molecular (H_2) gases have been studied by three-dimensional hydrodynamic simulations which include radiative feedback from the central source (Wada, 2012; Wada et al., 2016; Izumi et al., 2018). These studies led to the development of the multi-phase dynamic torus model, in which a combination of dusty outflows, inflows and failed winds give rise to a geometrically thick structure. Dense molecular gases are distributed near the equatorial plane, whereas the atomic gas is more extended along the vertical direction of the disk due to turbulence effects. In our approach, we are considering X-ray obscuration by the mid-plane H_2 column density, which would more effectively protect PAHs from photoprocessing.

Figure 6.3 (top) shows the N_{H_2} values as a function of the X-ray optical depth according to eq. 6.2 ($E = 2.5$ keV). By taking $N_{H_2} = 2.0 \times 10^{23}$ cm^{-2}, which is the upper limit of the H_2 column density for NGC 1808 (Salak et al., 2018), we obtain that $\tau_x \sim 4.45$. Since this value is estimated by considering an optically thick molecular mass, it will be used as a reference scenario for the six AGNs studied herein. In addition to the datapoint related to the work of Salak et al. (2018), we also highlight τ_x values (and their corresponding N_{H_2} estimates) proposed by different authors for distinct

AGN sources. Except for $\tau = 2.7$ (Kara et al., 2017), all other values are higher than the upper limit for N_{H_2} estimated by Salak et al. (2018).

The photoabsorption (k_{ph-abs}), photoionization (k_{ph-i}) and photodissociation (k_{ph-d}) rates (s^{-1}) of each PAH molecule, for a given distance r from the central source, are determined by multiplying the respective cross section, $\sigma_{ph}(E)$, by the photon flux, $F_x(E)$:

$$k_{ph} = \sigma_{ph}(E) F_x(E) \tag{6.4}$$

where k_{ph} represents the rates (k_{ph-abs}, k_{ph-d} or k_{ph-i}) and $\sigma_{ph}(E)$ can be the $\sigma_{ph-abs}(E)$, $\sigma_{ph-d}(E)$ or $\sigma_{ph-i}(E)$. They are determined by using the procedure described in Chapter 3. We obtained these rates, as well as the respective half-lives, for naphthalene, anthracene, 2-methyl-anthracene and pyrene at E = 2500 eV in the AGN sources studied herein, as shown in Figure 6.5.

Figure 6.3 (bottom) shows the half-life estimates of pyrene ($C_{16}H_{10}$) for distances between 20 and 80 pc from the nuclear region of NGC 1808. Each curve represents a different value for the X-ray optical depth ($0.0 \leq \tau_x \leq 10.0$). For comparison, injection timescale estimates (2.5×10^9 yr, see Jones et al. 1994) assuming carbon-rich AGB stars as the primary source of PAHs are also shown. For $\tau_x = 0.0$, the half-lives span from merely 1.8×10^4 to 2.8×10^5 yr, which are at best four orders of magnitude shorter than the PAH injection estimates. This large discrepancy illustrates the importance of shielding effects by the dusty torus in order to account for the survival of PAHs in such X-ray luminous sources. These values are weakly affected if an optically thin dust model is considered. For $\tau_x = 2.7$ ($N_{H_2} = 1.2 \times 10^{23}$ cm^{-2}), the half-life values span from 2.6×10^5 to 4.2×10^6 yr, which are still significantly shorter than the injection times of Jones et al. (1994). This value of τ_x was obtained by Kara et al. (2017) after using a thermal Comptonization model to estimate the corona electron temperature of Ark 564, a narrow-line Seyfert 1 AGN.

The half-life estimates are still unsatisfactory even if τ_x = 4-6 values are considered. For τ_x = 4.45, which is related to the upper limit value of $N_{H_2} = 2 \times 10^{23}$ cm^{-2} for NGC 1808 (Salak et al., 2018), the half-lives are in the range of 1.5×10^6 yr to 2.5×10^7 yr. For $\tau_x = 5.0$ ($N_{H_2} = 2.2 \times 10^{23}$ cm^{-2}), the half-lives span from 2.6×10^6 to 4.2×10^7 yr, while for $\tau_x = 6.0$ ($N_{H_2} = 2.7 \times 10^{23}$ cm^{-2}) they range from 7.1×10^6 to 1.1×10^8 yr. These values of X-ray optical depths are associated with microquasar and AGN coronae. A scattering optical depth value of 5.0, for example, was found for the Comptonizing corona of the microquasar GRS 1915+105 (Ueda et al., 2009), while a $\tau_x = 6.0$ value was used by Kamraj et al. (2018) in conjunction to theoretical constrains from Petrucci et al.

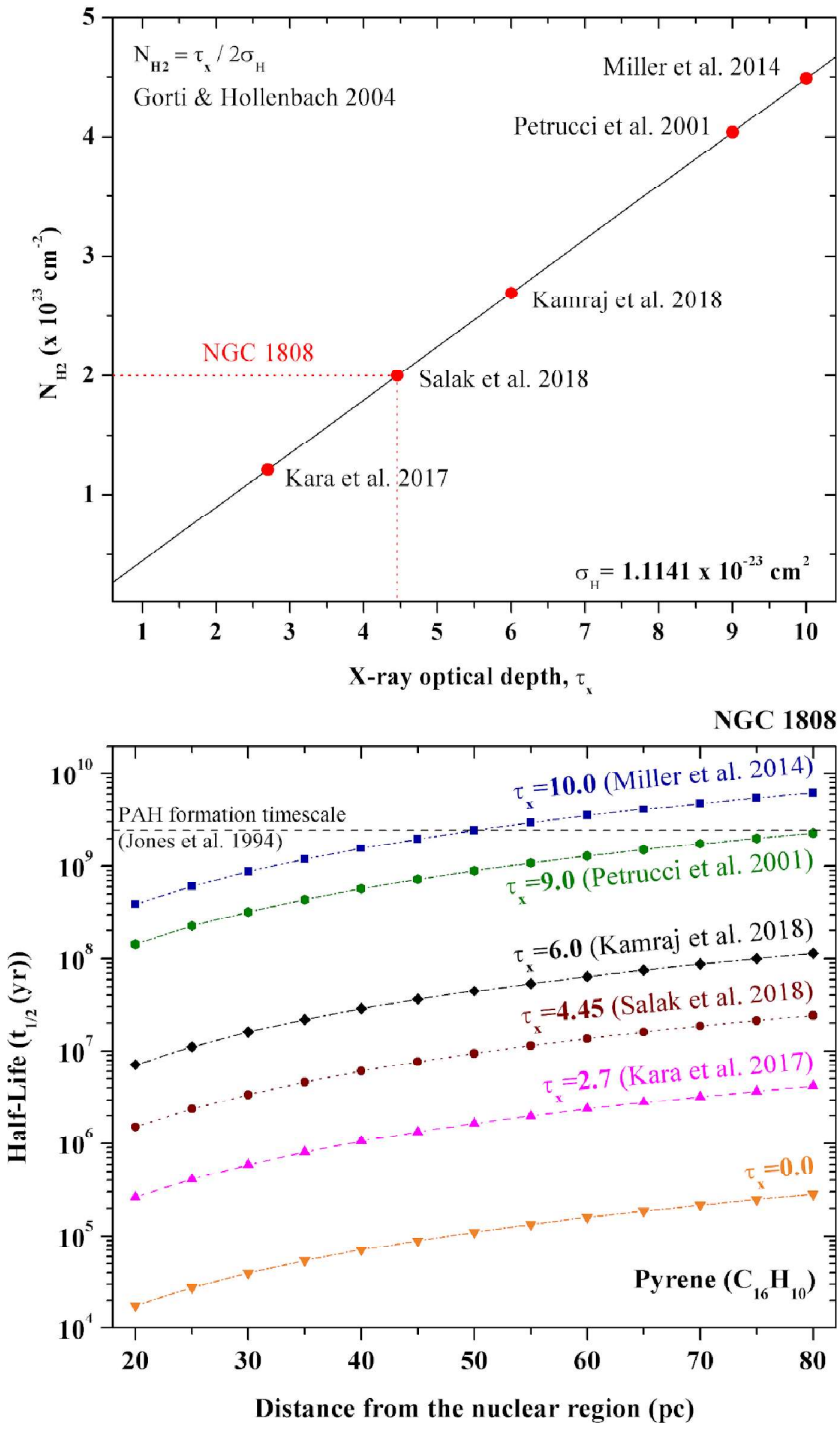

Figure 6.3: Top: Column density of H_2 (black line) as a function of the X-ray optical depth, τ_x ($E = 2.5$ keV, see eq. 6.3). The red datapoints are τ_x values taken from the literature. The datapoint of Salak et al. 2018 is related to the upper limit of N_{H_2} for NGC 1808. Bottom: Half-life of pyrene ($C_{16}H_{10}$) as a function of the distance (pc) from the central source of NGC 1808. Distinct X-ray optical depth values (τ_x) were considered. The horizontal dashed line is the PAH injection timescale estimate of 2.5×10^9 yr (Jones et al., 1994), which is shown for comparison. See text for details.

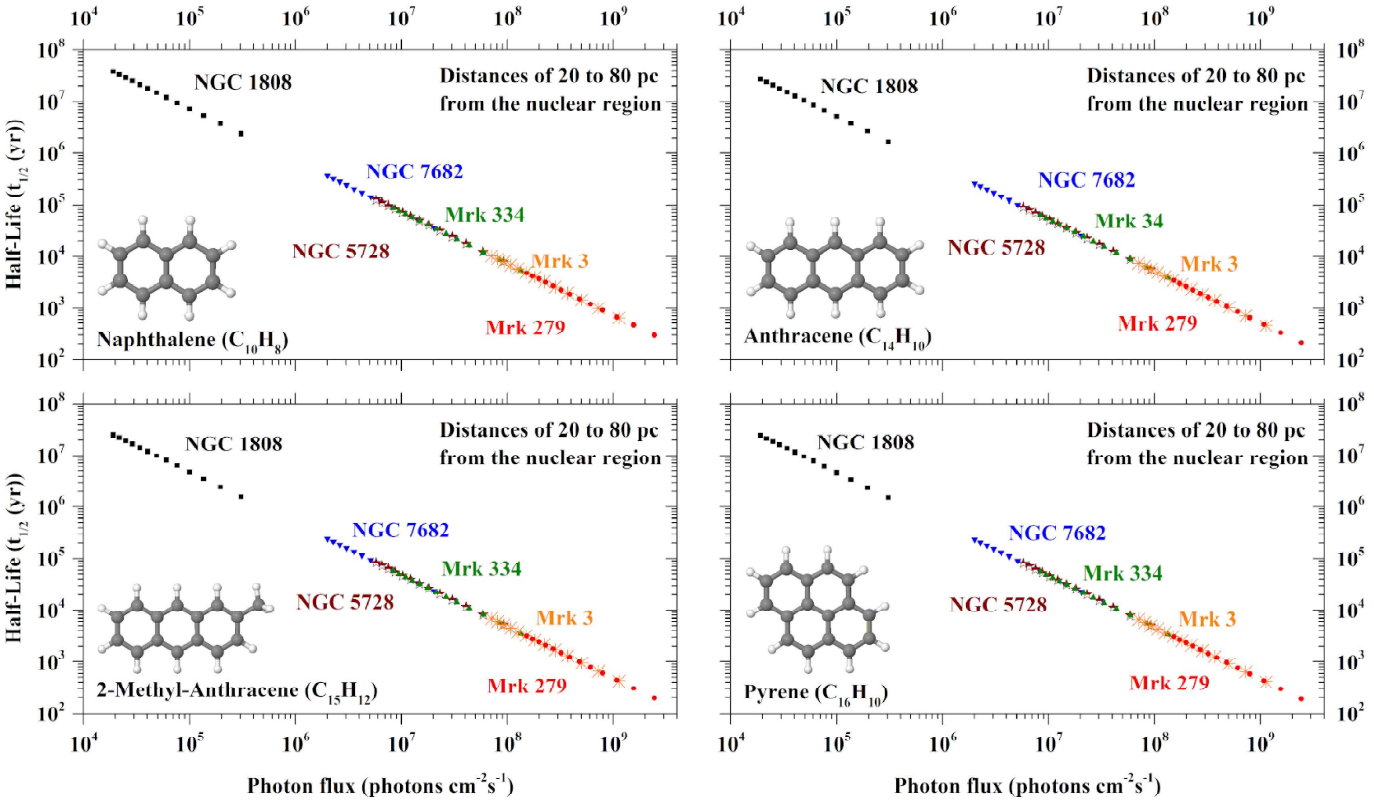

Figure 6.4: Half-life values of the PAH molecules studied herein after interaction with the X-ray radiation field ($\tau_x = 4.45$) of selected AGNs. Each datapoint refers to a specific distance in the 20-80 pc range from the Seyfert nucleus.

(2001) to describe the coronal properties of a sample of *NuSTAR*-observed Seyfert 1 AGNs.

The survival time of pyrene towards the inner region of NGC 1808 is only compared to the PAH injection timescale of Jones et al. (1994) if very high X-ray optical depth values, such as $\tau_x = 9.0$ ($N_{H_2} = 4.0 \times 10^{23}$ cm^{-2}) and $\tau_x = 10.0$ ($N_{H_2} = 4.5 \times 10^{23}$ cm^{-2}), are considered. For $\tau_x = 9.0$, the half-lives vary from 1.4×10^8 to 2.3×10^9 yr, while for $\tau_x = 10.0$ these values span from 3.9×10^8 to 6.2×10^9 yr. Although these high values of τ_x were reported in the literature for some objects, such as the AGN corona of NGC 4151 (Petrucci et al., 2001) and ultra-luminous X-ray sources (ULXs, see Miller et al. 2014), they are overly unrealistic for the purposes of this work. By taking the results of Figure 6.3 altogether, the X-ray shielding mechanism by the torus seems to be insufficient to account for the existence of pyrene and other small-size PAHs in the inner regions of AGNs. In fact, given the large differences in the injection and destruction timescales, our results point out that a more sophisticated interplay between PAHs and dust grains should be considered. In the following paragraphs, we briefly discuss two possible, non-exhaustive, scenarios in which dust grains could aid the production and survival of PAHs in the circumnuclear vicinity of AGN sources. Although

based on experimental and observational findings described by several authors, the feasibility of these processes is, for practical reasons, still speculative. A quantitative assessment of the role of dust in the survival of PAHs is far beyond the scope of this work.

In the first scenario, namely PAH-to-dust adsorption, we suggest that small-size PAHs formed in the circumnuclear environments of AGNs should be adsorbed onto the dust grains, where they could grow or rebuild themselves by chemical reactions driven by thermal- and/or photo-processing. In the gas-phase, these species could be produced, for instance, following barrierless reactions typical of low-temperature chemistry (Jones et al., 2011; Parker et al., 2012; Kaiser et al., 2015; Lee et al., 2019). On the surface of grains, small-size PAHs could undergo molecular growth by bottom-up chemical reactions, such as the ones described by Zhao et al. (2016); Johansson et al. (2018). Top-down routes of PAH formation, including the path depicted by Merino et al. (2014) involving graphitized grain surfaces exposed to atomic hydrogen, may also play a role. Large-size PAHs formed either by bottom-up or top-down processes could be desorbed from the grains and ejected into the gas-phase. Although these species are also subject to carbon backbone dissociation due to interaction with the radiation field, a substantial part of their fragments is expected to exhibit vibrational features typical of aromatic hydrocarbons (Micelotta et al., 2011). Similarly, large fragments of PAHs are detected after the interaction of ions with carbonaceous dust analogues, as recently shown by Pino et al. (2019). As the size of the parent PAH increases, more photon events are necessary in order to dissociate the whole set of fragments featuring the mentioned vibrational modes. As a consequence, the molecular vibrations of such a cascade of fragments would also contribute to the overall IR emission signatures of PAHs detected in AGNs.

Another possible mechanism in which dust grains could contribute to PAH survival, herein mentioned as the PAH-to-dust incorporation mechanism, is the one previously depicted by Postma et al. (2010) to account for the presence of PAHs in supernova ejecta. In this case, small-size PAHs could be incorporated into the growing dust grains, which could function as PAH reservoirs. The detection of PAHs in individual circumsolar graphite grains extracted from meteorites (Bernatowicz et al., 1996; Messenger et al., 1998) provides experimental evidence for the viability of such a process. However, as mentioned before, our results are not able to estimate the relative contribution of the distinct scenarios mentioned herein to the overall mechanism which allows PAHs to survive in the circumnuclear regions of AGNs, and whose explanation is still unknown. In this perspective, more work is needed to shed a light on this question, as well as to evaluate the importance of the PAH-to-dust adsorption

and incorporation processes discussed herein.

In order to compare the half-life results of pyrene in NGC 1808 with the other molecules and AGN sources studied in this work, we obtained $t_{1/2}$ as a function of the photon flux for an X-ray optical depth of $\tau_x = 4.45$. These results are summarized in Figure 6.4. We could not see any significant difference in the half-life values by increasing the size of the carbon backbone. This is probably due to the fact that we spanned only small-size PAH molecules. For medium- and large-size PAHs, although the X-ray photoabsorption cross sections are increased in comparison to the smaller ones (see Figure 6.2, top panel), a large number of dissociation pathways will have, as products, PAHs with a smaller number of carbon atoms. Ultimately, this will contribute to increase the half-life of PAHs in our AGN sources. A similar consideration was done by Micelotta et al. (2011) when assuming that the PAH is destroyed by cosmic rays only if the dissociation is followed by the ejection of at least 1/3 of the initial PAH carbon content.

From Figure 6.4, it is also possible to see that the half-life values are severely affected by the X-ray photon flux experienced by the molecules at a given distance from the central region of the AGN. In spite of considering attenuation of the X-ray radiation field by a dusty torus with moderate optical depth, the lifetime of PAHs spanned values from 10^8 to 10^2 yr. Even in the best-case scenario, the half-life is still shorter than injection timescale estimates of Jones et al. (1994) by a factor of $\sim$20.

The highest $t_{1/2}$ values (10^7-10^8 yr) are obtained for NGC 1808, which also presents the smallest X-ray luminosity (3.13×10^{51} eV s^{-1}, Esparza-Arredondo et al. 2018) among the AGNs studied herein and, consequently, the smallest average X-ray photon flux at 2500 eV (8.41×10^4 photons cm^{-2} s^{-1}). This nearby barred starburst, which is located at a distance of 10.8 Mpc (Tully, 1988), is known to have molecular gas outflow from a compact (r < 200 pc) circumnuclear disk, as well as a 500 pc gaseous ring (Salak et al., 2016). A dynamically driven evolutionary scenario, in which star formation is triggered by the gravitational collapse and cloud-cloud collisions that follow molecular cloud accretion onto this 500 pc ring, was proposed by Salak et al. (2017). More recently, the authors have also identified new dense gas tracer lines, which corroborates the existence of a velocity gradient in the outflow direction (Salak et al., 2018). PAH emission lines were observed in this object even at small distances (26 pc) from the Seyfert nucleus (Sales et al., 2013), for which our half-life values are merely 10^6 yr.

In contrast to NGC 1808, the shortest half-life times ($\sim 10^2$ yr) are obtained for Mrk 279, which presents the highest average X-ray photon flux at 2500 eV (6.68×10^8 photons cm^{-2} s^{-1}). The ab-

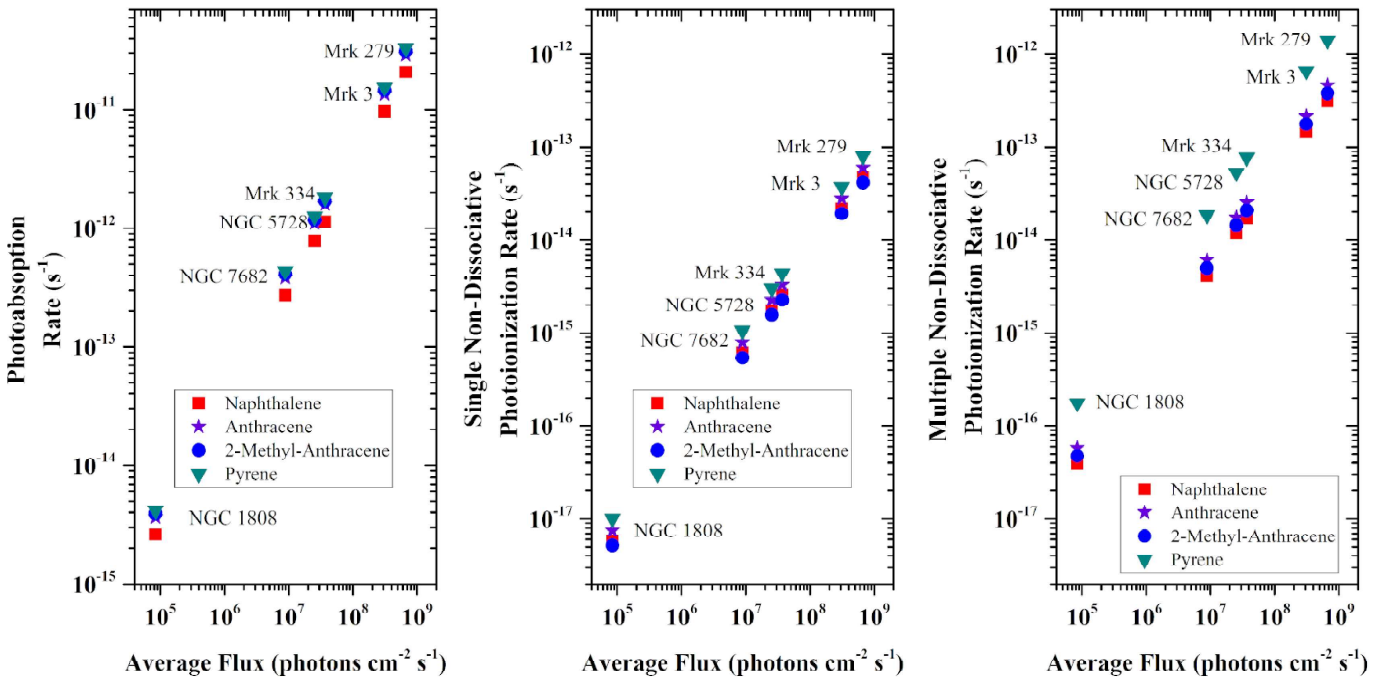

Figure 6.5: Photoabsorption and photoionization rates (s^{-1}) of the PAHs studied herein as a function of the average photon flux $\overline{F}_X$ of the distinct AGN sources. The $\overline{F}_X$ values are taken at 2500 eV ($\tau_x = 4.45$) within distances of 20-80 pc from the Seyfert nucleus.

sorption features of this very luminous Sy1 galaxy, which is located at 128.6 Mpc (Scott et al., 2004), are consistent with the presence of a warm absorber, most likely a dusty torus (Ebrero et al., 2010). Moreover, weak PAH emission features have been independently observed in Mrk 279 by different groups (Santos-Lleó et al., 2001; Sales et al., 2010).

The determined half-lives of PAHs in the remaining AGN sources span from $\sim 10^3$ yr to $\sim 10^6$ yr. Once more, these values suggest that a more complex interplay between PAHs and dust grains should be present in order to account for the survival and detection of PAHs in AGNs.

6.2.2 Multiple Ionization of PAHs in AGNs

The strong X-ray radiation fields that are generated in the central regions of AGNs can easily destroy PAHs, as discussed in the previous section. However, PAHs are substantially formed in such environments, and a conclusive solution for this apparent dichotomy is, to the best of our knowledge, still unknown. In fact, observation of PAH emission in the kpc-scaled circumnuclear vicinity of AGNs have been commonly used to track the presence of star forming activity (Peeters et al., 2004; Stierwalt et al., 2014; Alonso-Herrero et al., 2014; Esparza-Arredondo et al., 2018). This is due to the fact that the UV radiation emitted from young massive O- and B-stars is able to vibrationally

excite PAHs (Peeters et al., 2004). The underlying mechanism was recently studied by Marciniak et al. (2015), which have shown that UV-excited PAHs undergo ultrafast non-adiabatic relaxation through internal conversion processes that couple the electronic and vibrational degrees of freedom. The mid-IR emissions coming from excited PAHs are used as star formation tracers in AGNs because emission from the accretion process contaminates the traditional tracers, such as UV emission, H α and Pa α.

In addition to the destruction pathway, Jensen et al. (2017) have recently shown that the AGN Seyfert nucleus could act as a central excitation source of PAHs within 10-500 pc from the nuclear region. According to their findings, the interaction of shielded PAHs with the radiation field emitted from the AGN can vibrationally excite such molecules, which could undermine the PAH emission as a star forming tracer within the kpc distance range from the central region.

Besides destruction and vibrational excitation, our results point to a third fate of the PAH molecules that are formed within the inner regions of AGNs. Since the removal of two electrons from the aromatic moiety weakens both the C–H bonding and the cohesion of the carbon skeleton, the production of such metastable species could enhance fragmentation by activating Coulomb explosion dissociation pathways (Voit, 1992). This is corroborated by our results with 2500 eV photons, which show a plethora of low-mass fragments in significantly yield when compared to the mass spectra taken at lower photon energies (see Monfredini et al. 2019 for comparison between the mass spectra of naphthalene at 275, 310 and 2500 eV). On the other hand, our results also suggest that the production of stable multiply charged ions increases as a function of N_C. In contrast to doubly charged diatomics, for which metastability is achieved through the formation of strong covalent bonding aided by polarization effects (Fantuzzi et al., 2017b), the charge density in polyatomic species can be distributed through a large number of atoms (Cohen et al., 1988). Therefore, by increasing the carbon backbone of the PAH, it is expected that the respective dication (or even higher order charge states) is more easily stabilized through charge alternation.

Finally, we discuss the possibility of forming multiply charged PAHs in the surroundings of AGNs. Figure 6.5 shows a comparison between the photoabsorption rate (k_{ph-abs}), the single non-dissociative photoionization rate (k^{+}_{ph-i}) and the multiple non-dissociative photoionization rate (k^{q+}_{ph-i}) of the PAHs studied herein in the selected AGN sources. In order to show only one datapoint for each AGN source, we replaced the X-ray photon flux (F_X) of eq. 6.4, which depends on the distance from the central Seyfert nucleus, by the average X-ray photon flux ($\overline{F}_X$) shown in Table 6.2, which

is the average flux within 20-80 pc for each one of the sources. It is possible to see that, irrespective of the source, the k_{ph-i}^{q+} values are significantly greater than the corresponding k_{ph-i}^{+} ones, evidencing the high tendency of these systems to form multiply charged states. In addition, it is possible to see that the multiple non-dissociative photoionization rate of pyrene is remarkably higher than the ones of the other PAHs. These results suggest that stable multiply charged PAHs could be formed in the circumnuclear regions of AGNs.

Neutral and ionized PAHs present large differences in the relative intensities of their resulting IR spectra (Allamandola et al., 1999; Tielens, 2008). However, there is still no evidence for a unambiguous identification between singly and doubly charged PAHs in the ISM (Zhen et al., 2017). The precise determination of the charge state of PAHs is a relevant astrophysical feature, which is also corroborated by our results. Further studies aiming at the spectral signature of these multiply charged species should be developed in the nearby future.

Chapter 7

Experimental Results IV: Condensed Phase

Up to this date, more than 200 molecules have been detected in the interstellar medium (Müller et al., 2018). The presence of large chemical structures (>5 atoms) in these environments illustrates the existence of physical effects and chemical mechanisms that contribute to the formation and stability of different molecular species, in spite of the high UV and X-ray radiation fields (Deguchi et al., 1990; Jones et al., 2011; Micelotta et al., 2010a,b; Reitsma et al., 2014; Öberg, 2016; Quitián-Lara et al., 2018; Monfredini et al., 2019).

In Chapter 1, we reviewed some routes for molecular formation in the interstellar medium. Chemical reactions in condensed phase involving the participation of radicals and neutral molecules play a major role in the formation of complex organic molecules (COMs) in low-temperature environments (Herbst and van Dishoeck, 2009; Tielens, 2005). In this context, radicals are easily formed on the surface of interstellar ices from the interaction with UV photons and other sources of ionization and dissociative radiation (Fig. 7.1, Burke and Brown 2010; Fedoseev et al. 2012). Ions and radical species react quickly with other moieties to form more complex molecules (Garrod et al., 2008; Fedoseev et al., 2012; Öberg, 2016). For example, the hydrogenation of diatomic molecules, such as CO and NO, can lead to the formation of COMs, such as methanol (CH_3OH, (Chuang et al., 2016)), glycolaldehyde (CH_2OHCHO, (Li et al., 2017)), ethyleneglycol ($HOCH_2CH_2OH$, (Li et al., 2017)) and hydroxylamine (NH_2OH), an amino acid precursor (Li et al., 2017; Sorrell, 2001; Congiu et al., 2012). These examples highlight the importance of condensed phase reactions for the formation of complex organic molecules.

In addition to the chemistry of COMs, condensed phase reactions also play an important role in the formation and evolution of PAHs in distinct astrophysical environments. Recent laboratory

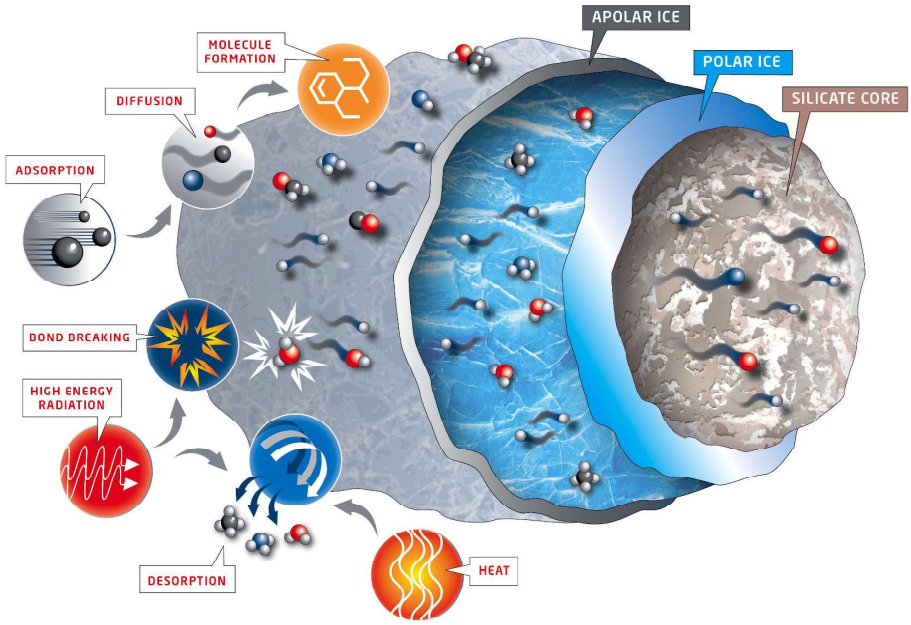

Figure 7.1: Schematic representation of an astrophysical ice and some examples of processes that can occur on its surface. Credits: Center for Space and Habitability (CSH), Universität Bern. *https://www.csh.unibe.ch/services/infographics/index_eng.html*.

simulation experiments show that aromatic molecules, such as benzene (C_6H_6), naphthalene ($C_{10}H_8$) and phenanthrene ($C_{14}H_{10}$), can be efficiently formed from the interaction of acetylene (C_2H_2) ice analogues with cosmic-rays at low temperatures (Abplanalp et al., 2019). Photochemical reactions on astrophysical ice surfaces can lead to saturation of carbon chains and hydrogenation of PAHs (Sorrell, 2001; Henning, 2010; Herbst and van Dishoeck, 2009; Tielens, 2005; Congiu et al., 2012; Chuang et al., 2016; Li et al., 2017). Additionally, laboratory simulations of meteoritic organic globule analogues suggest that such structures are actually the final products in the evolution of carbonaceous matter as a consequence of the coagulation of interstellar PAHs. (Saito and Kimura, 2009). As they are observed in protoplanetary disks (Seok and Li, 2017) and in the ISM, understanding the low-temperature formation and fate of non-substituted PAHs, as well as those of PAHs carrying substituent groups, are of significant importance.

In this chapter, we apply experimental methods to examine the interaction of a high energetic electron beam with benzene (C_6H_6), chlorobenzene (C_6H_5Cl), phenol (C_6H_5OH) and cyclohexane (C_6H_{12}) solid samples, simulating electron-driven chemical transformations that occur on the surface of astrophysical ices. To the present date, only preliminary results are obtained, which are briefly shown in the following sections. The experimental setup is described in Chapter 3. Briefly, the samples were condensed at a temperature of 125 K on a steel substrate and were subjected to ioniza-

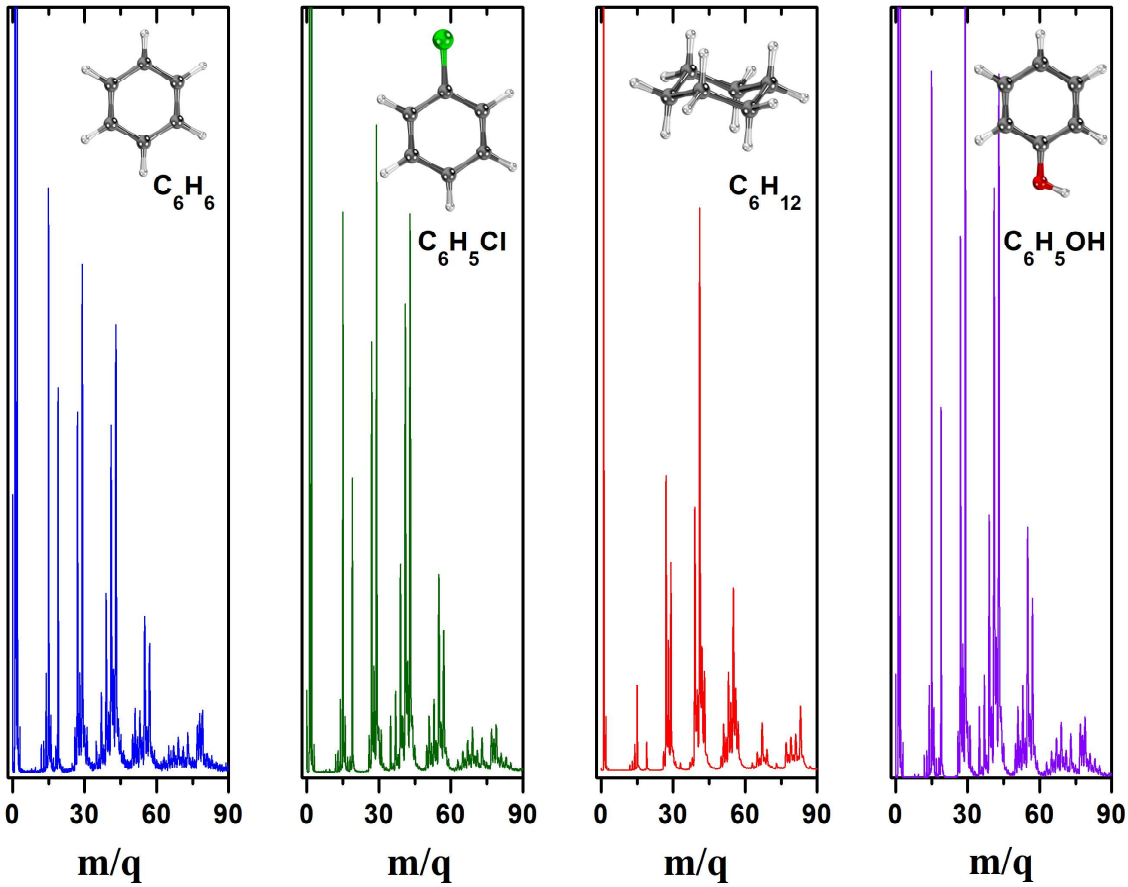

Figure 7.2: Overview of the mass spectrum (0-90 m/q) of fragments desorbed to the gas phase from benzene (blue), chlorobenzene (green), cyclohexane (red) and phenol (purple) condensed at a temperature of 125 K, and subjected to an electron beam impact of 2.3 keV.

tion after electron beam impact of 2.3 keV using the Electron-Stimulated-Ion-Desorption technique (ESID, Ramsier and Yates 1991). The desorbed fragments were analyzed by TOF-Mass spectroscopy. All condensed phase experiments with astrophysical ice analogues were carried out at the Laboratório de Química de Superfícies (LaQuiS) of the Federal University of Rio de Janeiro.

7.1 Hydrogenation and Deprotonation of Substituted Benzene Rings in Astrophysical Ice Analogs

Figure 7.2 shows an overview of the mass spectrum (0-90 m/q) of cations desorbed to the gas phase of pure samples of benzene (C_6H_6), cyclohexane (C_6H_{12}), chlorobenzene (C_6H_5Cl) and a solution of phenol (C_6H_5OH) in methanol (CH_3OH) at 89%. The fragmentation pattern is dependent on the nature of the substituents. However, in all cases it is possible to identify the H_n^+ ($n = 1-3$)

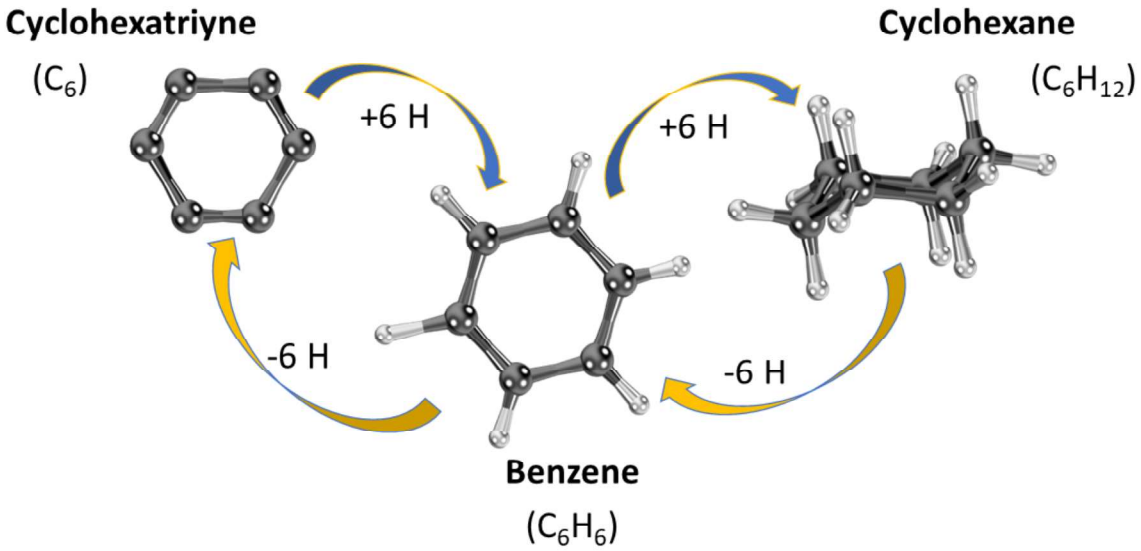

Figure 7.3: Schematic diagram of the complete protonation and deprotonation reaction of benzene molecule.

ions, as well the C*n* family groups C_1 (12 – 15 a.m.u.), C_2 (24 – 30 a.m.u.), C_3 (36 – 44 a.m.u.), C_4 (48 – 58 a.m.u.), C_5 (60 – 72 a.m.u.) and C_6 (72 – 86 a.m.u.).

From now on, we will focus on the identification of fragments with masses around 72 to 86 a.m.u. By analyzing this m/q range for the mentioned compounds, it is possible to verify the influence of the substituent group on the loss and gain of hydrogen by the aromatic ring. Figure 7.3 shows a schematic diagram of the process of deprotonation or dehydrogenation (loss of H) and protonation or hydrogenation (gain of H) of the benzene ring. The experimental results reveal that both reaction pathways are active in the experimental conditions, as C_6Hn^+ ionic fragments featuring partial or complete loss of hydrogenation, as well as featuring partial or complete saturation, were detected.

Fig.7.4 shows the 72 to 86 a.m.u. region of the mass spectrum of all samples obtained herein. For benzene (top-left panel), the protonated benzene ion, $C_6H_7^+$ (or $C_6H_6H^+$) is predominantly formed. Moreover, as introduced in the previous paragraphs, it is possible to see that both hydrogenation and dehydrogenation processes are active. The most produced ions after C_6H_6 dehydrogenation are the benzyl cation, $C_6H_5^+$, and the C_6H^+ species. The formation of $C_6H_4^+$, $C_6H_3^+$, $C_6H_2^+$ and the cyclohexatriyne cation, C_6^+, is also observed. On the other hand, hydrogenation was observed until the complete loss of aromaticity, with the formation of the cyclohexane cation $C_6H_{12}^+$ and protonated cyclohexane ($C_6H_{12}H^+$) species. It is worth mentioning that such remarkable hydrogenation process is not observed in gas phase experiments. We suggest that cyclohexane, as well as other alkanes and cycloalkanes, could be formed as a desorption product of benzene-rich astrophysical ices. The

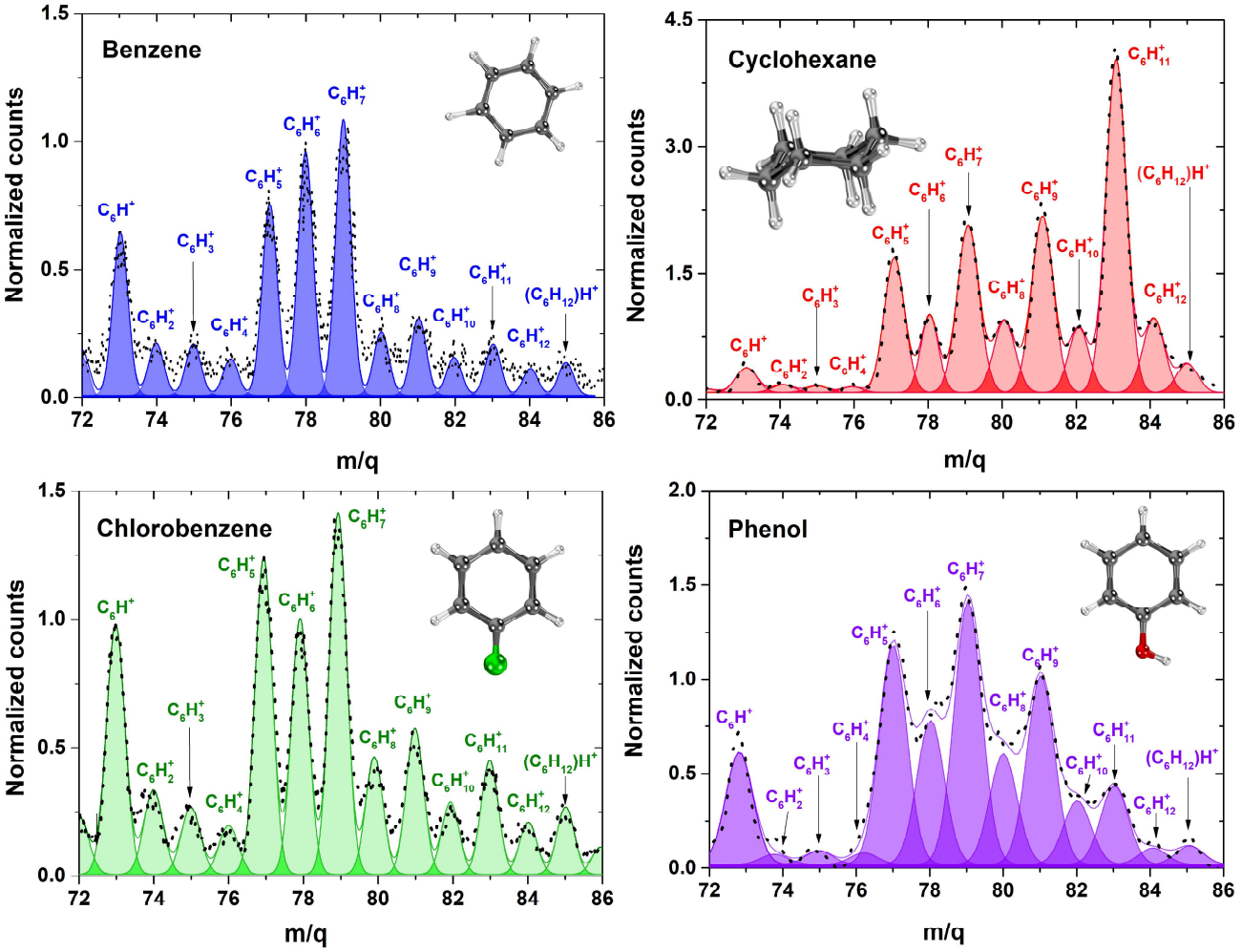

Figure 7.4: Production of fragments from m/q = 72−86 desorbed to the gas phase from condensed samples of benzene (top-left panel), chlorobenzene (bottom-left panel), cyclohexane (top-right panel) and phenol (bottom-right).

relative ionic desorption yields, normalized with the mass of the benzene molecule (78) are shown in Fig. 7.5.

Figure 7.4 (bottom-left panel) shows the region of the mass spectrum of chlorobenzene with masses from 72 to 86 a.m.u. This region particularly shows the result of the ejection of the Cl atom (possibly as $Cl^{\cdot}$ or HCl) from the parent molecule. The profile of the mono-substituted benzene with a chlorine atom shows a noteworthy resemblance to the one of benzene. As in the previous case, $C_6H_7^+$ is predominantly formed and the benzyl cation ($C_6H_5^+$) is one of the most abundant moieties of the C_6 family group. The latter species is formed directly by the loss of the halogen atom of chlorobenzene. The formation of dehydrogenated products is active up to the cyclohexatriyne cation (C_6^+), and the C_6H^+ species is predominantly formed by such process. The formation of protonated $C_6H_n^+$ species on the surface of frozen chlorobenzene is active from $n = 6$ to $n = 13$. The formation

of species with odd number of hydrogens is preferential, which is related to the closed-shell nature of their electronic configurations, in contrast to the ions with even number of hydrogens.

In the bottom-right panel of Figure 7.4, we show the formation of protonated and deprotonated species after ejection of OH (possibly as OH^- or H_2O) from the parent molecule of phenol (C_6H_5OH). The results reveal that the protonation and deprotonation processes are both active. Similarly to the previous cases, the fragments mostly produced from dehydrogenation are $C_6H_5^+$ and C_6H^+. The formation of $C_6H_2^+$, $C_6H_3^+$ and $C_6H_4^+$ are also observed, but not as significant as the ones observed for benzene and chlorobenzene. Again, hydrogenation of the aromatic ring up to the saturation limit is also observed, being the fragments with odd number of hydrogens more produced than the ones with an even number of hydrogens.

Taking into account that protonation is active up to the saturation limit, it is quite reasonable to suggest that such highly hidrogenated species would be formed after the breakage of the carbon ring backbone, leading to the formation of acyclic structures. Such ring opening mechanism would facilitate the formation of tertiary carbocations, which could aid in the charge stabilization of the monopositive species. It is worth mentioning that the production of dehydrogenated and hydrogenated species of the type $C_6H_nCl^+$ (for chlorobenzene) and $C_6H_nOH^+$ (for phenol) are also produced in our experiments. However, their intensities are significantly smaller than the ones of $C_6H_n^+$. This reveals that both hydrogenation and dehydrogenation are more active after nucleofuge (Cl and OH) elimination, suggesting that dissociation of these groups is probably the first step of both pathways.

The top-right panel of Figure 7.4 shows the production of $C_6H_n^+$ species from the cyclohexane parent molecule. The loss of one hydrogen atom, leading to the formation of $C_6H_{11}^+$, is the main fragmentation pathway toward this series. Other closed-shell species, such as $C_6H_9^+$, $C_6H_7^+$ and $C_6H_5^+$, are also substantially produced. The abundance of the cyclohexane parent ion and the $C_6H_6^+$ species are quite similar, which suggests that the production of neutral benzene from a cyclohexane ice is more feasible from the deprotonation of a benzyl ($C_6H_7^+$) ion than from the electron attachment into a desorbed $C_6H_6^+$ species.

Finally, Figure 7.6 shows the formation of highly hydrogenated $C_6H_n^+$ ($n = 13-15$) species from the cyclohexane experiments. We show that the hydrogenation process in cyclohexane ices is effective up to the formation of $C_6H_{15}^+$. This is a clear evidence that after the electron impact the cyclohexane ring is cleaved, which leads to the formation of an acyclic ionic structure. In fact, in a recent publication we have shown that such open chain structures are among the most stable $C_6H_{12}^+$ isomers,

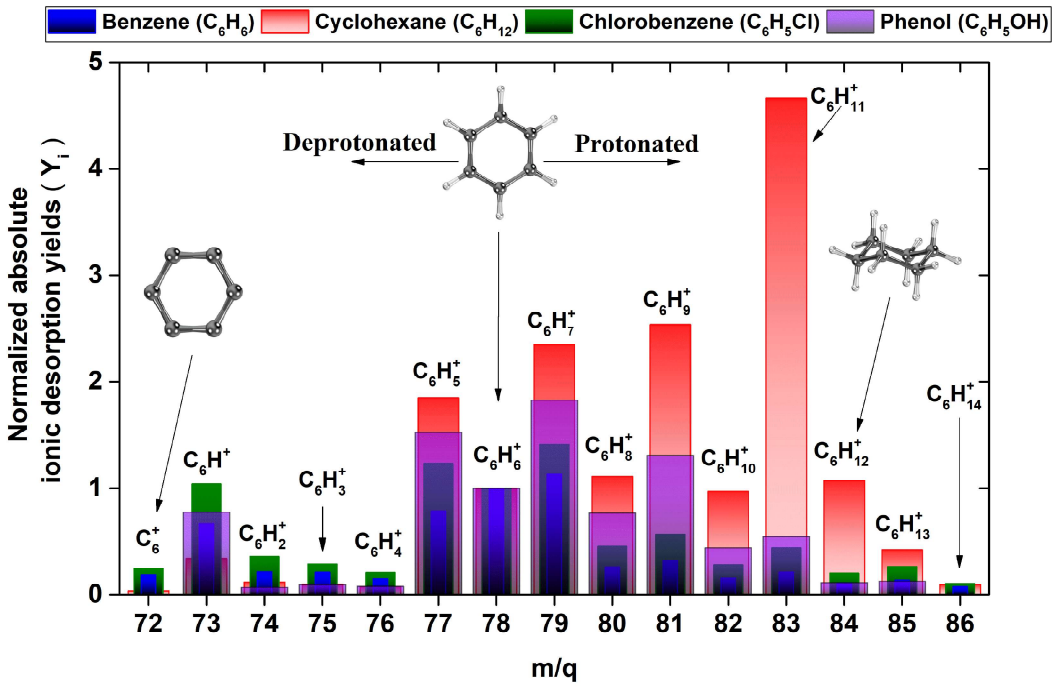

Figure 7.5: Absolute ionic desorption yields, normalized with the mass of the benzene molecule (78 a.m.u). Benzene (blue), chlorobenzene (green), cyclohexane (red) and phenol (purple).

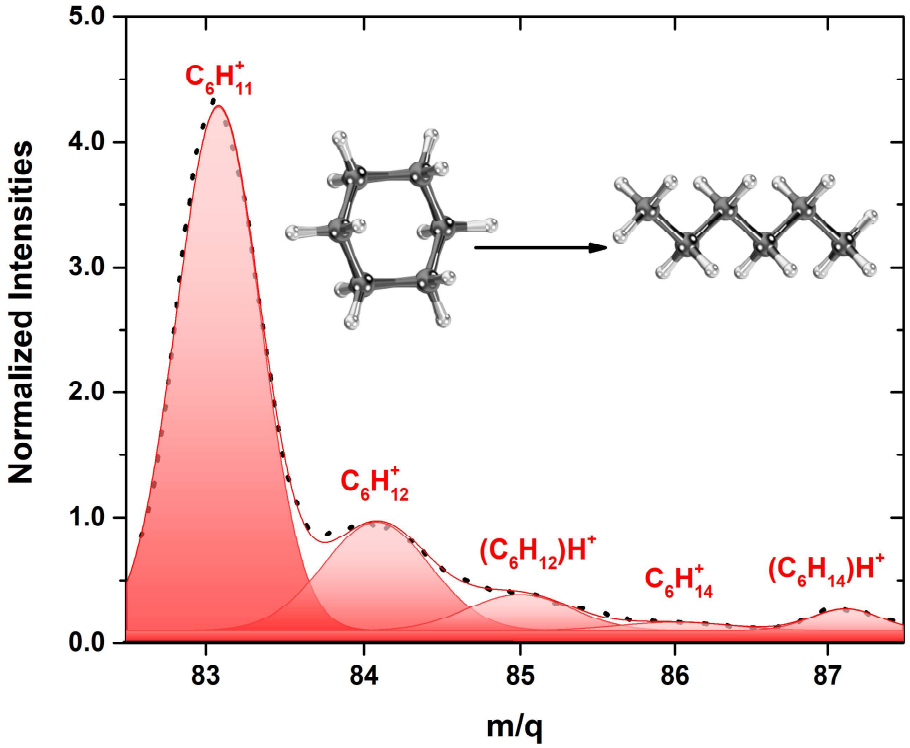

Figure 7.6: Formation of highly hydrogenated $C_6H_n^+$ $(n = 13-15)$ species from the cyclohexane experiments. Adapted from Quitián-Lara et al. (2018).

and the global minimum is attributed to the 2,3-dimethyl-2-butene (or tetramethyl-ethylene) radical cation (Quitián-Lara et al., 2018; Fantuzzi et al., 2019), a highly branched structure. In fact, the first alkyl branched molecule detected in the interstellar medium was the isopropyl-cyanide (C_3H_7CN) species, in a recent study developed by Belloche et al. (2014). We suggest, therefore, that the desorption of fragments produced from hydrogenation processes in cyclohexane-rich astrophysical ices could enhance the abundance of branched molecules in the ISM and CSM.

Chapter 8

Observational Results: The Protostellar Core IRAS 4A

There is convincing observational evidence, based on e.g. isotopic studies, that the small objects of our Solar system (comets and asteroids) have retained, at least partially, the chemical composition of the early phases of the protosolar nebula (Pizzarello and Huang, 2005; Cleeves et al., 2014), possibly in its prestellar phase, before the onset of the gravitational collapse. Recently, the study of the composition of Comet 67P by the Rosetta space mission has revealed the presence of numerous complex organic molecules, including glycine, the simplest amino-acid, with relative abundances similar to those observed in the interstellar medium (Altwegg et al., 2016). These and many other examples illustrate unambiguously that chemistry in space is efficient and leads to the formation of complex organics, which may have been inherited by the small bodies of our Solar System from the earliest stages of star formation. Therefore, it is important to characterize the chemical composition of protostellar environments and to understand its evolution with the formation of stars similar to our own sun (Lefloch et al., 2018).

The data described herein were obtained using the IRAM 30m radio telescope from a highly sensitive survey of the Class 0 protostellar core IRAS 4A, in the spectral windows 72-115 GHz, 130-172 GHz, 205-272 GHz, as part of the Large Program ASAI. The goal of ASAI was to investigate the emergence and the evolution of molecular complexity along the formation of solar-type protostars. This was achieved through unbiased spectral surveys of a carefully selected sample of ten template sources, which cover the full formation process of solar-type stars, from the prestellar phase to the late protostellar phase, including jets and outflows. In this chapter, we present the results of the molecular

survey of IRAS 4A (see Chapter 1), the brightest protostar of the ASAI sample and a template for astrochemical studies of solar-type star formation.

8.1 Identification of the Molecular Species in IRAS 4A

The final line spectra of IRAS 4A in the 3mm, 2mm and 1mm bands display a large number of emission lines, as shown in Figs. 8.1, 8.2, 8.3. The complete spectrum of the source can be seen in Appendices A, B and C.

Molecular lines were identified and analyzed using the version 5.1 of the software CASSIS developed at IRAP (Toulouse, France) for that purpose (Vastel et al., 2015). For the lines identification, we used the Cologne Database for Molecular Spectroscopy (CDMS; Müller et al. (2005)) and the Jet Propulsion Laboratory (JPL) catalogues (Pickett et al., 1998). In this survey we consider only the lines detected with an intensity equal or greater than 3σ.

8.1.1 CASSIS

The CASSIS (Centre d'Analyse Scientifique de Spectres Instrumentaux et Synthétiques) software (CESR and IRAP, 2019), developed by CESR/IRAP since 2005, allows the analysis of single disk spectra, with four main tools (Fig.8.4):

1. Line identification tool. This module allows spectral exploration and identification of chemical species through local spectroscopic databases (mainly CDMS, JPL, NIST, Vastel).

2. Prediction of spectra tool. This module allows spectra prediction from any single disk telescope using local spectroscopic databases and integrated model information.

3. Data comparison tool. This module allows comparison of telescope (or laboratory) data with a variety of models.

4. Rotational diagram tool. This module allows the determination of the physical parameters of the source after generation of the rotational diagram plot. These diagrams are used for obtaining estimated values of column densities and excitation temperatures of molecular species (both with error bars).

In order to adjust the line profiles, the internal formalism of CASSIS defines the opacity of the line as a function of the column density and the excitation temperature (Vastel, 2016). Assuming the latter as a constant along the line of sight, we have :

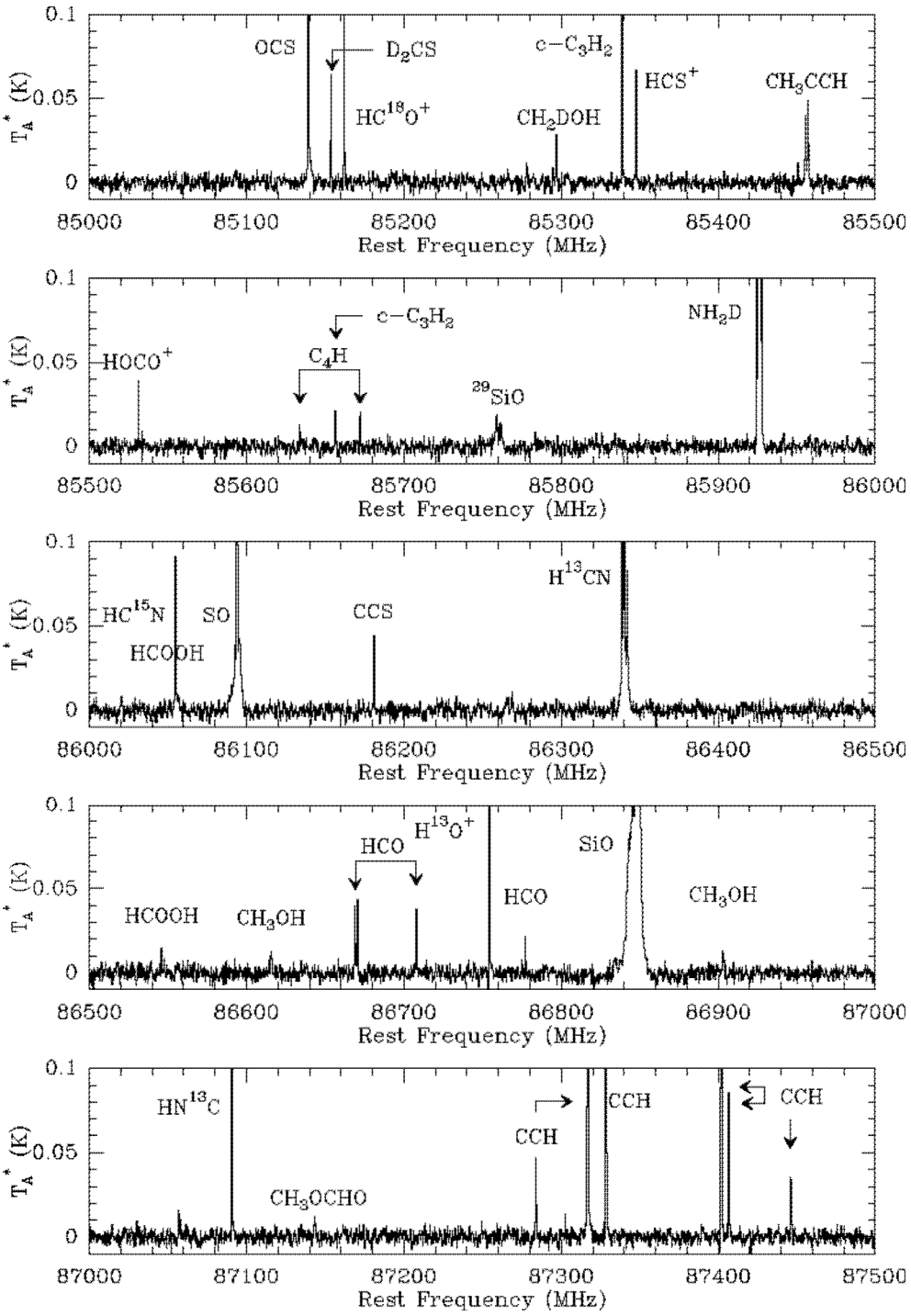

Figure 8.1: Final line spectrum detected between 85000 and 87500 MHz towards IRAS 4A in the 3mm band. The main lines, with intensities higher than 3σ, are identified. Intensities are expressed in units of Antenna temperature T_A^*.

$$\int \tau d\upsilon = \int \frac{h\nu\Phi_\nu}{c}\left(B_{lu}n_l - B_{ul}n_u\right)d\upsilon = \frac{g_u}{g_l}\frac{A_{ul}c^3 n_l}{8\pi\nu^3}\left(1-exp\left(\frac{-h\nu}{k_B T_{ex}}\right)\right) \tag{8.1}$$

where Φ_ν is the line profile with $\int \Phi_\nu d\nu = 1$, B_{lu} is the probability of the absorption of a photon,

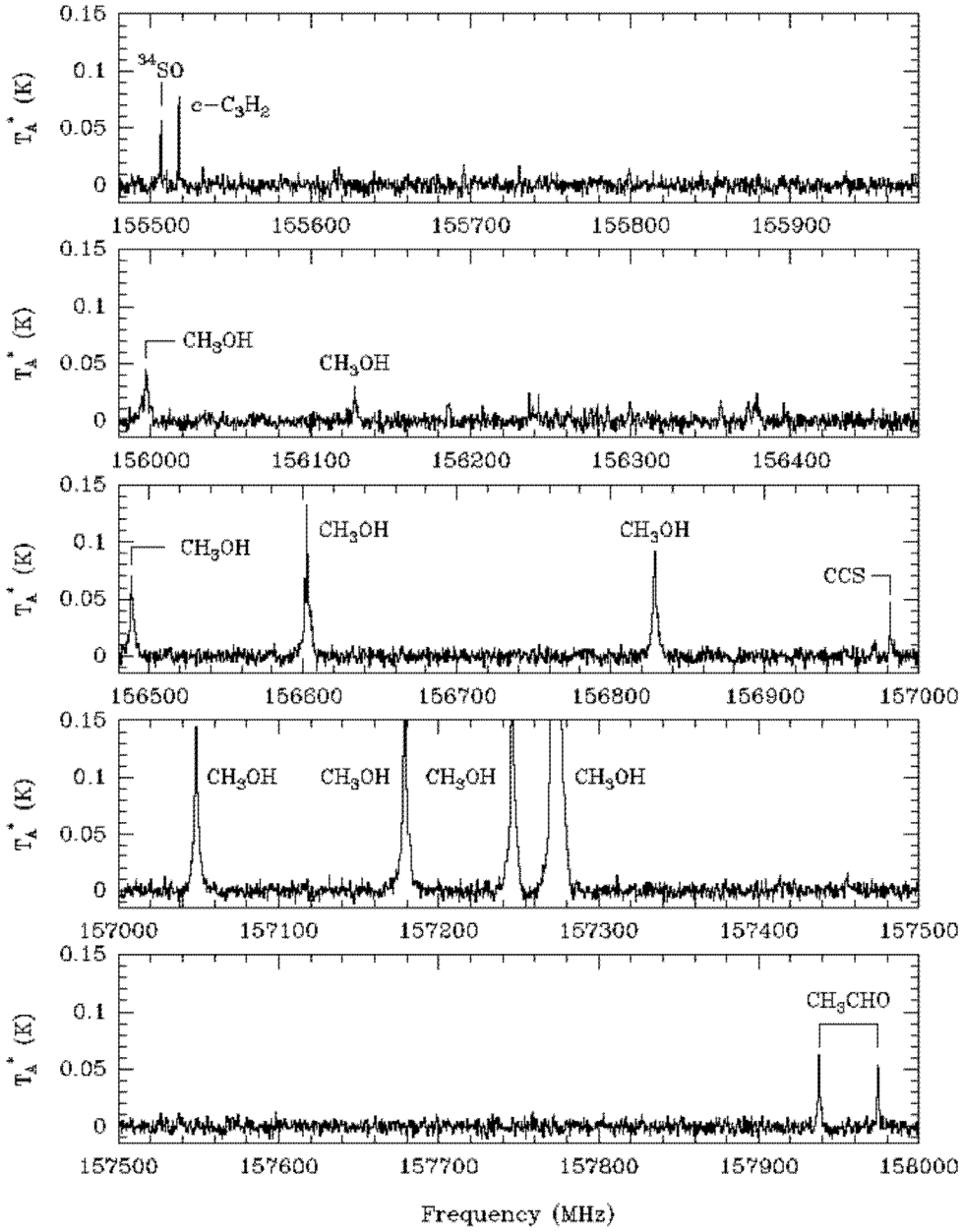

Figure 8.2: Final line spectrum detected between 156500 and 158000 MHz towards IRAS 4A in the 2mm band. The main lines, with intensities higher than 3σ, are identified. Intensities are expressed in units of Antenna temperature T_A^*.

B_{ul} is the probability of stimulated emission of a photon, and n_l (n_u) is the density of the state l (u). For more details, see Chapter 2).

For a Gaussian line fit, we can express the opacity τ_{ul} as a function of the cloud depth z by the following equation:

$$\tau_{ul}(z) = \frac{A_{ul}c^3}{8\pi\nu^3\Delta\upsilon\sqrt{\pi}/2\sqrt{ln2}} \int_0^z n_u \left(\frac{n_l g_u}{n_u g_l} - 1\right) dz' \tag{8.2}$$

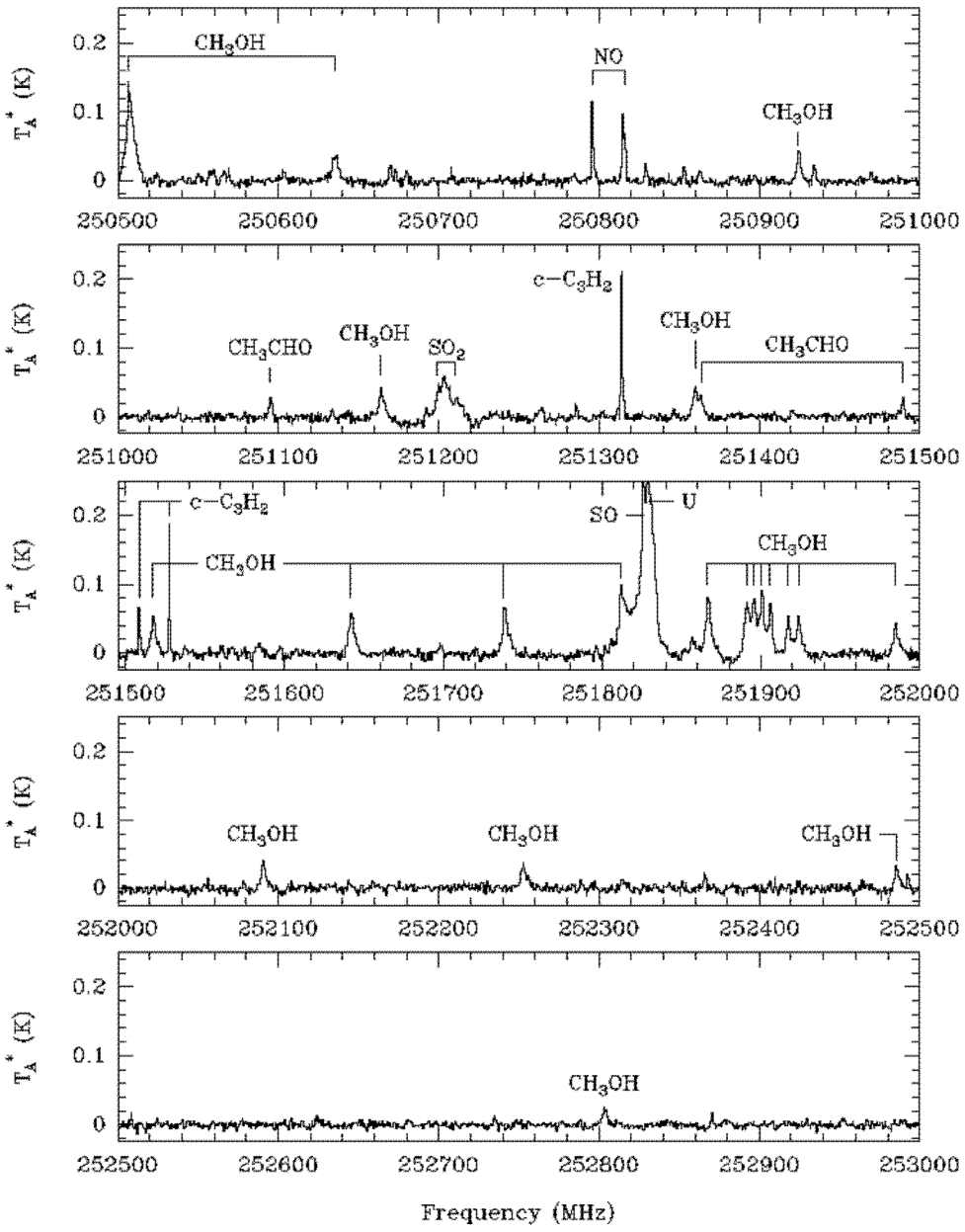

Figure 8.3: Final line spectrum detected between 250500 and 253000 MHz towards IRAS 4A in the 1mm band. The main lines, with intensities higher than 3σ, are identified. Intensities are expressed in units of Antenna temperature T_A^*.

where Δv, in velocity units, is the FWHM of the observed line. Integrating on the line of sight, we have the opacity at the line center, τ_0:

$$\tau_0 = \frac{g_u}{g_l} \frac{c^2}{8\pi\nu^2\Delta\nu\sqrt{\pi}/2\sqrt{ln2}} A_{ul} N_l \left(1 - exp^{-h\nu/k_B T_{ex}}\right) \tag{8.3}$$

where $\Delta\nu$, in frequency units, is the FWHM of the observed line, and N_l is the column density of

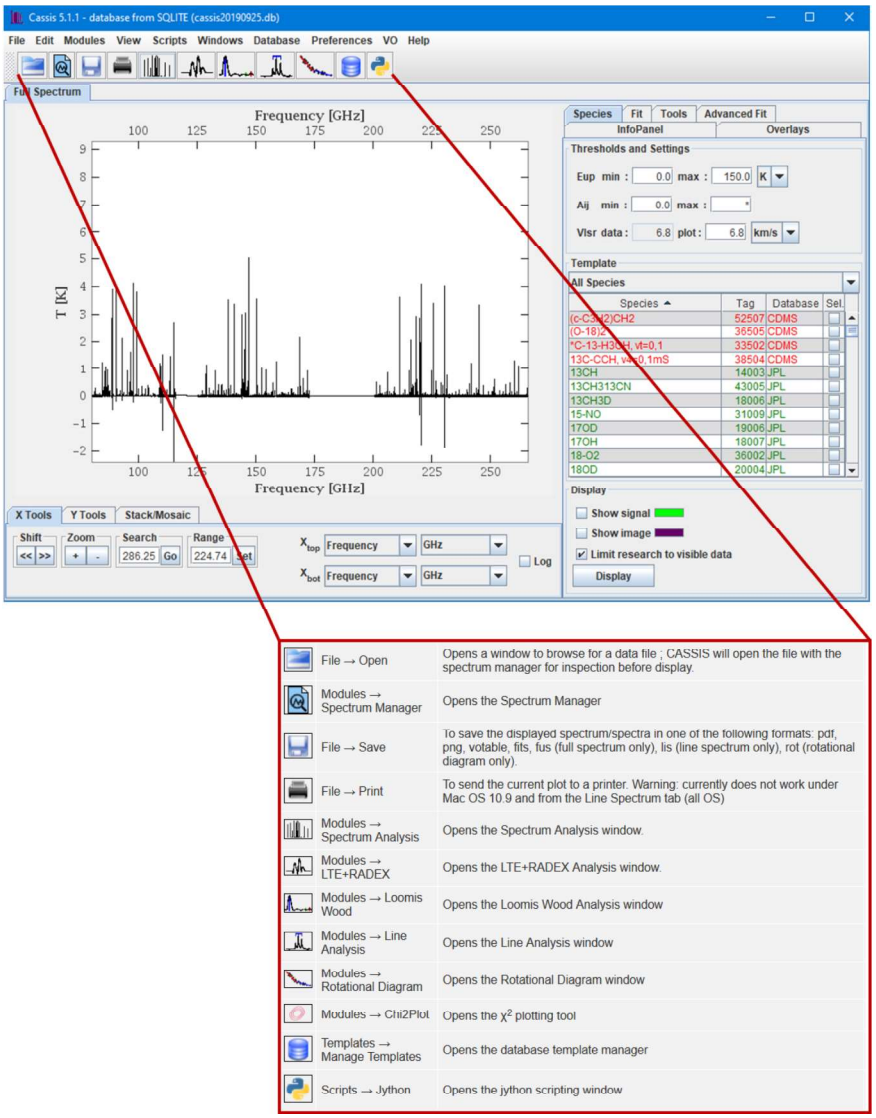

Figure 8.4: Image of the graphical framework of CASSIS 5.1.1 software. The spectral analysis tools is highlighted. Adapted from CESR and IRAP (2019).

the lower state.

We used Gaussian profiles to fit all the emission lines detected in IRAS 4A spectra. For the chemical identification of the emission line we use the CDMS and JPL catalogues.

8.1.2 Line profile fitting

Inspection of individual profiles in the line survey leads to identification of three types of profiles, as can be seen in Figs. 8.1, 8.2 and 8.3: narrow line component (N), double narrow plus wide (N + W) components, and multi-component, hyperfine profiles (hfp). This is illustrated in Figs. 8.5, 8.6 and 8.7. The physical interpretation of these kinematical components is presented in the next section.

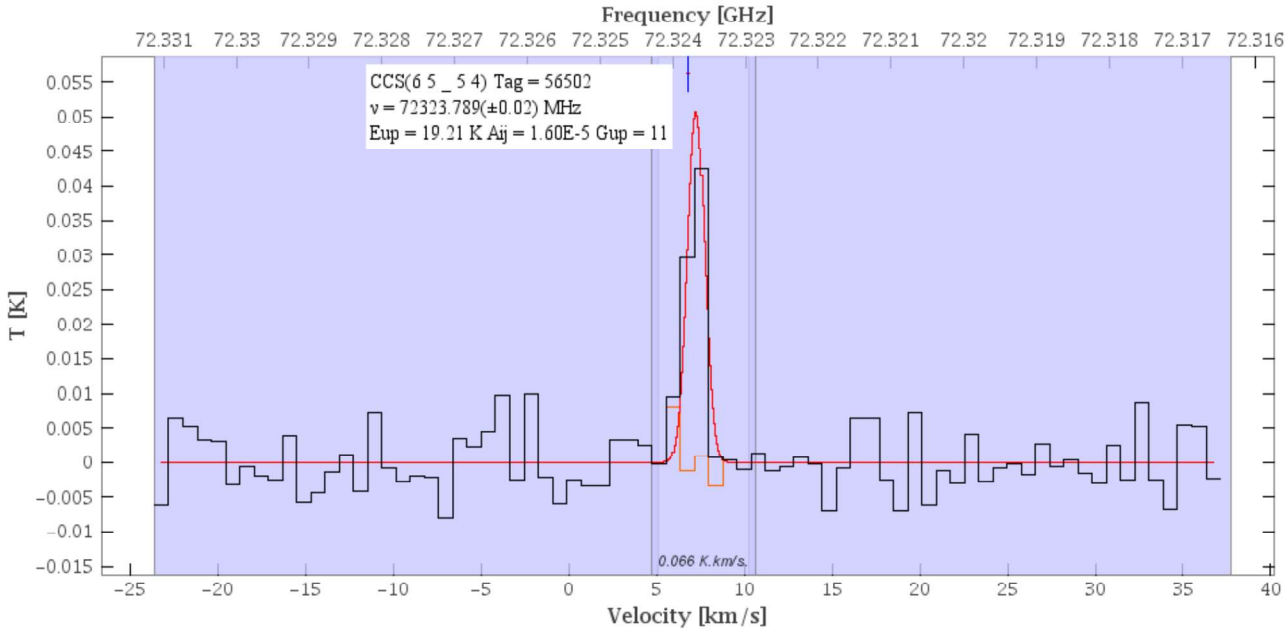

Figure 8.5: Example line profile fit (N type) with a single narrow emission.

We also encountered a few special cases, like e.g. CO and ^{13}CO, in which a strong absorption feature was detected (Fig. 8.8). As discussed in Chapter 3, these features are caused by contamination from the reference position during the data acquisition in Wobbler Switching mode. In those few cases, we discarded the contaminated spectral line profiles and made use of the "clean" spectra obtained in Position-Switching mode for the subsequent analysis. The determination of the physical parameters of the different chemical species identified in the source is strongly linked to the type of line profile. Emission lines with a single component, such as those in Fig. 8.5, allow a proper fitting.

The presence of multiple components generates a greater dispersion in the rotational diagram. Since they are actually tracing physically different components, the analysis was performed separately for each component.

8.1.3 Rotational Diagram Analysis

The rotational diagram draws the distribution of the column densities of the different energy levels of a chemical species as a function of the energy levels (Goldsmith and Langer, 1999; Vastel, 2016). Under the conditions of local thermodynamical equilibrium (LTE), the distribution follows a Boltzmann distribution (see eq. 8.8), i.e. the natural log of the statistically weighted column density (N_u/g_u) is a linear function of the level energy (E_u/k). The slope of the line is inversely proportional to the excitation temperature of the transition. Under LTE conditions, all transitions have the same

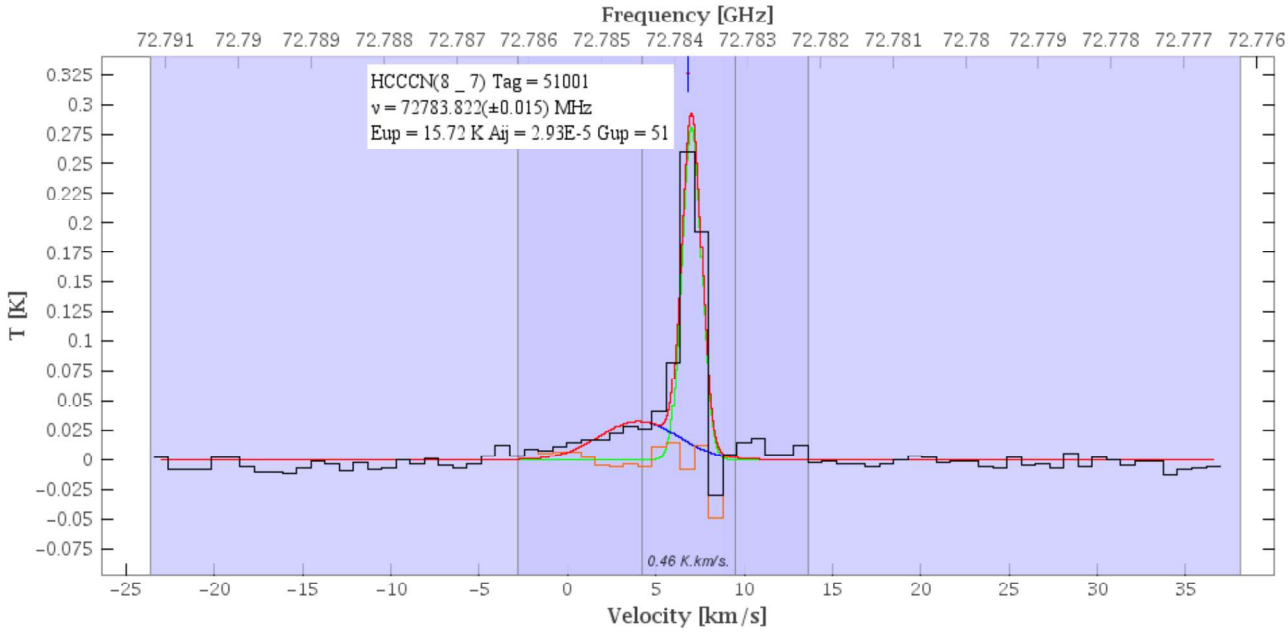

Figure 8.6: Example line profile fit (N+W type) with a double component emission.

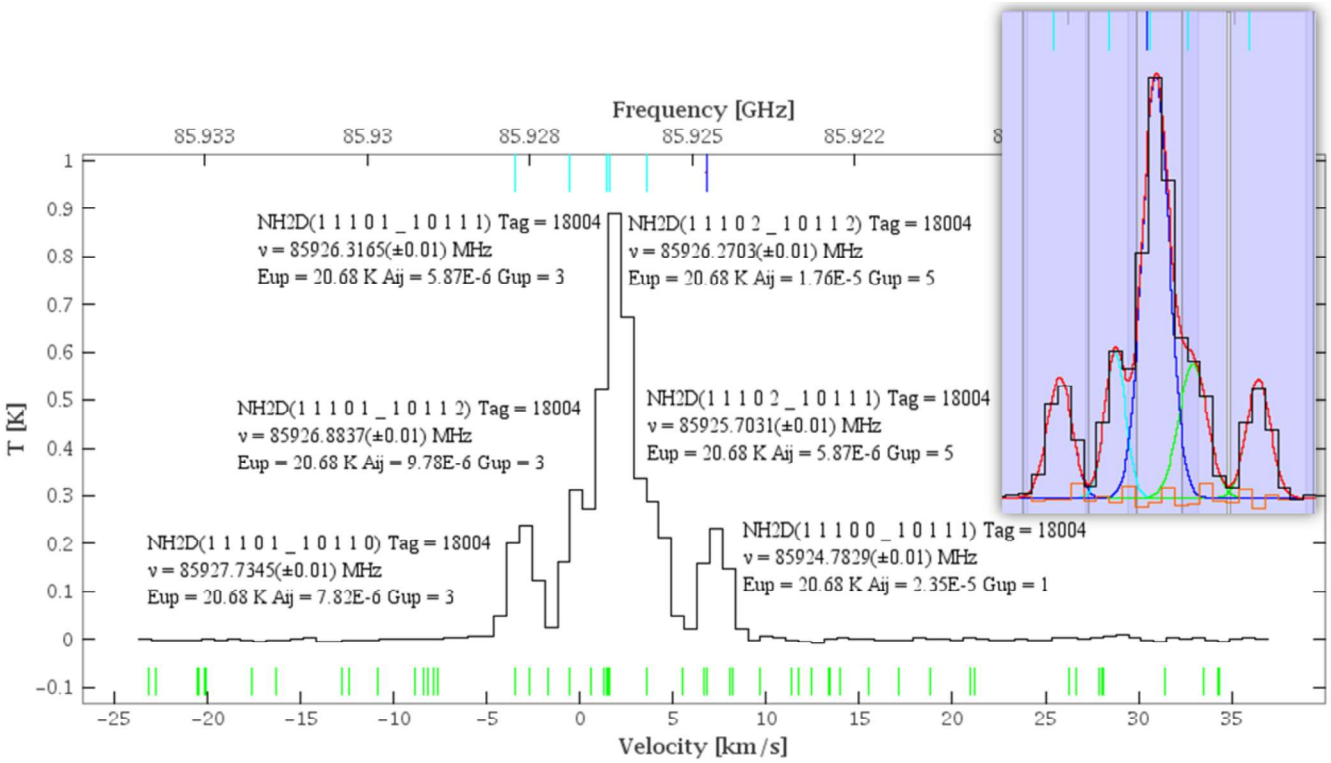

Figure 8.7: Example of line profile adjustment (hfp type) with an emission of hyper-fine components.

excitation temperature, which is then referred to as the rotational temperature.

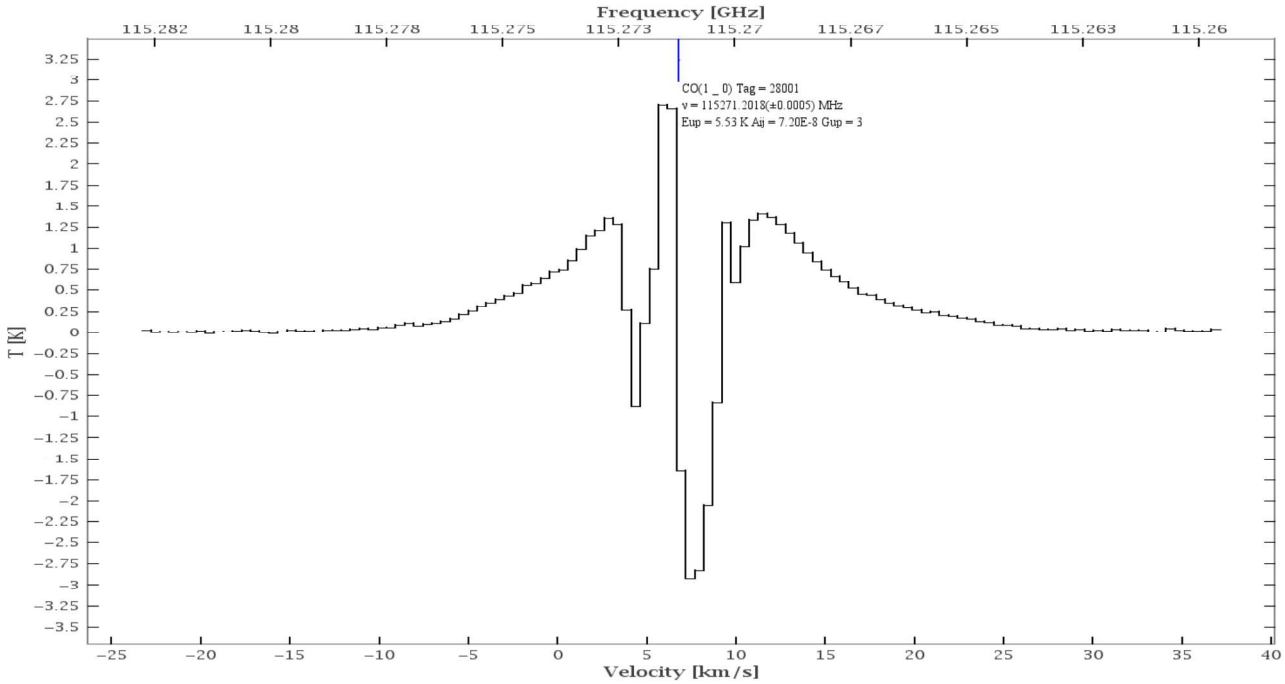

Figure 8.8: Example of the CO emission line with the presence of strong absorption profiles.

For the rotational diagram, CASSIS estimates the column density in the upper state as:

$$N_u = \int T_b d\upsilon \times \frac{8\pi k\nu^2}{hc^3 A_{ul}} \times \frac{\tau}{1-e^{-\tau}} \tag{8.4a}$$

$$N_u = W \times \frac{8\pi k\nu^2}{hc^3 A_{ul}} \times C_\tau \tag{8.4b}$$

where W is the integrated area, C_τ is the optical depth correction factor, and T_b is the brightness temperature of the molecular transition. With $C_\tau = 1$ when the line is optically thin, τ, which is the optical depth of the transition, can be written as:

$$\tau = \frac{c^3 A_{ul} N_u}{8\pi\nu^3 \Delta\upsilon\sqrt{\pi}/2\sqrt{ln2}} \left[exp\left(\frac{h\nu}{k_B T_{rot}}\right) - 1 \right] \tag{8.5}$$

where T_{rot} is the rotational temperature of the molecular transition. Assuming that $h\nu/k_B \gg 2.7$ K, T_b is given by:

$$T_b = \frac{h\nu}{k_B} \frac{1}{\left[exp\left(\frac{h\nu}{k_B T_{rot}}\right) - 1 \right]} \frac{1-e^{-\tau}}{\tau} \times \tau \tag{8.6}$$

For a molecule at LTE, the excitation temperatures of all the rotational transitions are identical,

equal to the rotational temperature and thus the population of each level is given by:

$$N_u = \frac{N_{tot}}{Q(T_{rot})} g_u exp\left(\frac{-E_u}{k_B T_{rot}}\right) \tag{8.7}$$

Rewriting equation 8.7, one retrieves the Boltzmann Distribution law:

$$ln\frac{N_u}{g_u} = ln\frac{N_{tot}}{Q(T_{rot})} - \frac{E_u}{k_B T_{rot}} \tag{8.8}$$

In order to obtain a reliable estimate of the physical parameters of a molecular species from a rotational diagram analysis, the first step is therefore to measure the line parameters (velocity-integrated flux, main-beam brightness temperature, linewidth) of all the molecular transitions identified in the line survey. Once done, CASSIS produces a detailed .rotd file with the integrated area and the rms values of all the transitions.

Then, a non-negligible difficulty consists in estimating properly the brightness temperature of the molecular transitions, from the main-beam brightness temperature T_{MB}. The latter is obtained from the spectra delivered by IRAM 30m, which are expressed in antenna temperature T_A^*, corrected for atmospheric attenuation and sky coupling. The intensities are easily converted to main-beam antenna temperature units T_{MB} by applying the values of the forward efficiency F_{eff} (sky coupling) and the beam efficiency B_{eff}, which are calibrated and monitored by the IRAM 30m staff.

The source brightness temperature, which is the "real" astrophysical quantity of interest, can be rigorously obtained only though the deconvolution of the source intensity distribution from the instrumental response, as is the case in interferometry. For single dish telescope observations, only an approximate deconvolution is performed, which consists in adopting an idealized (simple) geometry for the source distribution, usually uniform or gaussian-like. In the case of IRAS 4A, and based on the previous observations of the cold molecular gas and dust in the source, we have adopted a uniform source size of 100 arcs for all molecular transitions of low excitation ($T_{rot} \leq 30$K). This point is further discussed in the next section. The value for the uncertainty of instrumental calibration is given by the user. In this case, the instrumental uncertainties of IRAM 30m are typically 10%, 15% and 20% for spectral bands at 3mm, 2mm and 1mm, respectively (Lefloch et al., 2018). Then, the uncertainty of the integrated area is calculated using the following formula:

$$\Delta W = \sqrt{(cal/100 \times W)^2 + (rms\sqrt{2 \times FWHM \times \Delta v})^2} \tag{8.9}$$

where *cal* (%) is the calibration value, W (K km s^{-1}) is the integrated area, *rms* (K) is the noise around the selected species, FWHM (km s^{-1}) is the full width at half maximum and Δv (km s^{-1}) is the bin size. For more details see Vastel (2016).

8.2 Molecular Content

In this spectral survey, using the CDMS and JPL catalogues, a total of 92 molecular species was detected, including main and rare isotopologues. A grand total of 1456 rotational transitions was detected, where 1254 correspond to the narrow emission and 202 to the emission of the wide component. The summary of the spectroscopic properties and observational parameters of all detected lines are shown in Table D (also Appendix D).

Based on a careful analysis and fitting of the multi-component line profiles in the survey, we found that line profiles can usually be divided as follows: a narrow (N) component with an FWHM of 2-3 km s^{-1}, and a wide (W) with an FWHM ranging between 5 and 30 km s^{-1}, arising from the molecular outflow (see Lefloch et al. (2018)).

Of the 92 molecular species identified and analyzed in this survey, more than 80% display a component with an excitation temperature below 30K. On the other hand, we observe that several species, like e.g. CH_3OH, H_2CS, HCCCN, H_2CO and OCS display a second, higher excitation temperature, of lower extent. However, it should be noted that some species, like SO and SO_2, also trace components of high-excitation, associated with the widest profiles (FWHM of 12-17 km s^{-1}).

The different molecular species identified in the survey were classified into five distinct groups depending on the elemental content, following the classification proposed by Lefloch et al. (2018) for the analysis of the 3mm ASAI data. The groups are C-bearing, O-bearing, N-bearing, S-bearing, and X-bearing, where X represents either phosphorus or silicon (see Table 8.1). Each molecule was assigned to a specific group:

- C-bearing: C_xH_y
- O-bearing: $C_xH_yO_z$
- N-bearing: $C_xH_yO_zN_t$
- S-bearing: $C_xH_yO_zN_tS_u$
- X-bearing: P-, Si-

Table 8.1: Summary of the molecular content of the ASAI line survey of IRAS 4A. Total number of species and lines detected (all isotopes included) per each elemental group.

Group	No. species	No. lines	D	^{13}C	^{15}N	^{17}O	^{18}O	^{33}S	^{34}S	^{29}Si
S-bearing	26	228	4	2			1	2	6	
N-bearing	25	218	6	3	4					
O-bearing	31	701	7	6		3	5			
C-bearing	7	99	1							
X[a]-bearing	3	6								1

[a] P- and Si-bearing species

The detection of rare isotopologues depends on the instrumental sensitivity and the emitting gas column density. Therefore, the number of main isotopologues and molecular lines detected is an excellent indicator of the molecular complexity. The number of rare isotopologues is high for some elemental groups, like S-bearing and O-bearing species, for which the total number of detected species is 26 and 31, with a number of rare isotopologues species of 15 and 19, respectively. The deuterated isotopologues are also commonly found in both molecular families (see Table 8.1).

In the framework of this thesis, and due to the limited amount of time, we have analysed only the gas properties associated with the narrow line component, using the rotational diagram technique. In a first step, we have assumed a size of 100 arcs for the emitting region, in other words, that the emission arises from an extended molecular gas layer. In practice, it means that the main-beam brightness temperature of the molecular transitions is equal to the brightness temperature, which is the true astrophysical parameter. However, complementary to the catalog, the lines with medium and wide profiles are also included in Table D (see Appendix D).

8.2.1 O-Bearing Molecules

The line survey of IRAS 4A shows a remarkable dominance of O-bearing species, among which Complex Organic Molecules (COMs) such as CH_3OH, CH_3CHO, CH_3OCHO and chemically related species such as H_2CO, H_2CCO, with a total of 701 identified rotational frequency lines. Table 8.2 lists the physical parameters obtained for each of the identified O-bearing species. Among the 31 distinct species identified, 21 have rare isotopologues. Deuterium is the most commonly found isotopologue with 7 molecular species, followed by ^{13}C and ^{18}O with 6 and 5, respectively. In fact, a high content of O-bearing species is a characteristic feature of hot corinos (Bottinelli et al., 2007; López-Sepulcre et al., 2017). The number of deuterated species is also an important piece of information as it reveals

the past history of the protostellar material frozen onto the dust grains and subsequently released in the gas phase as a consequence of the gas warm-up around the protostar and/or protostellar shocks between the ejected material (jets and outflows) and the parental envelope.

CO lines and its isotopologues are commonly used to trace the low-density gas distribution in envelopes and outflows of low-mass protostars. Conversely, a molecule such as CH_3OH, with a large dipole moment, allows to probe a wide range of physical conditions. For example, low excitation transitions of CH_3OH are sensitive to the gas density, while highly excited lines are sensitive to both the kinetic temperature and the gas density (Parise et al., 2006). This is because of the spectroscopic properties of the molecule. The rotational transitions are characterized by two quantum numbers (J,K) and the transitions obey the selection rules, $\Delta J, \Delta K = 0, \pm 1$. The rotational transitions span a wide range of spontaneous emission Einstein coefficient A_{ij}, with the consequence that their optical depths may vary considerably (Goldsmith and Langer, 1999). In the IRAS 4A line survey, we have detected CH_3OH transitions with upper energy levels ranging between 5K and 600K.

Fig. 8.9 shows the rotational diagram of CH_3OH and its ^{13}C- and D-isotopologues. After elimination of lines blended with transitions of other molecular species, scatter remains in the distribution of CH_3OH fluxes. The population distribution in the CH_3OH rotational diagram shows three regimes of excitation, each of them can be fitted in a first approximation by a straight line. Each regime is associated with a physical component of "low", "warm", and "high" excitation.

- The cold component is detected in the E_{up} range between 5 and 40K. It has a column density N_{CH_3OH} = 1.2 ($\pm$ 0.5)$\times 10^{14}$ cm^{-2} and an excitation temperature T_{ex} = 16.9 ($\pm$ 4.3)K.
- The warm component is detected in the E_{up} range between 40 and 80K. It has a column density N_{CH_3OH} = 1.2 ($\pm$ 1.3)$\times 10^{14}$ cm^{-2} and an excitation temperature T_{ex} = 40.7 ($\pm$ 25.5) K.
- The hot component is detected at E_{up} higher than 80 K. It has a column density N_{CH_3OH} = 2.2 ($\pm$ 0.4)$\times 10^{14}$ cm^{-2} and an excitation temperature T_{ex} = 185.5 ($\pm$ 26.1) K.

The parameters of the warm and hot components are merely indicative as an accurate determination must take into account the actual size of their respective emitting region. In this survey we use a standard source size of 100 arcs, therefore hot regions are expected to be more compact, with sizes around 2 arcs. The identification of these regimes of excitation is actually revealing the presence of a radial gradient of excitation inside the protostellar envelope of IRAS 4A. Molecular emission maps at high angular resolution are necessary to address this point.

The detected transitions of the rare ^{13}C- and D- isotopologues cover a narrower range of excita-

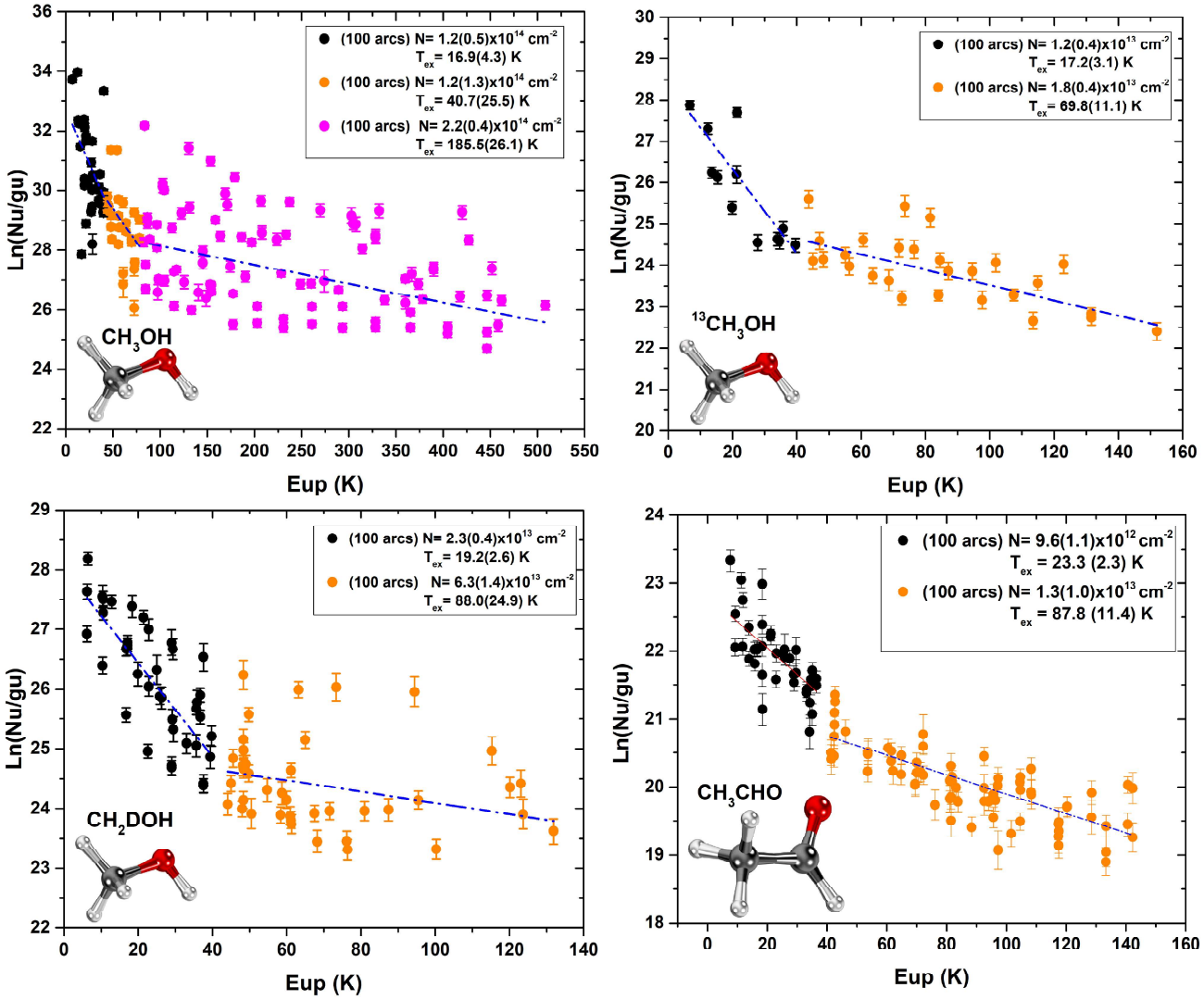

Figure 8.9: Rotational diagram of CH_3OH, $^{13}CH_3OH$, CH_2DOH and CH_3CHO identified in IRAS 4A with a source size of 100 arcs.

tion, with E_{up} between 5 and 160 K. In this range of E_{up}, we also detect two excitation components in their respective rotational diagrams (Fig.8.9). The excitation temperature of the cold and warm components of CH_3OH and its isotopologues are in rather good agreement. The column density of the main isotope of CH_3OH is in good agreement with the reported value, which is $\chi_{(CH_3OH)} = 1.1\times10^{-8}$ (Koumpia et al., 2017), for $N_{H_2} = 1.6\times10^{24}$ cm^{-2} (Moret et al., 2013; Bottinelli et al., 2007). We note that these excitation temperatures are also similar to those measured in CH_3CHO and H_2CCO.

The case of methyl formate CH_3OCHO is very illustrative of the difficulties inherent to this kind of analysis, without information on the exact spatial distribution of the emission. As can be seen in Fig. 8.10, a simple rotational diagram analysis with a source size of 100 arcsec yields two excitation components of about 40K and 800K, respectively. The presence of an extended (100 arcsec !) gas

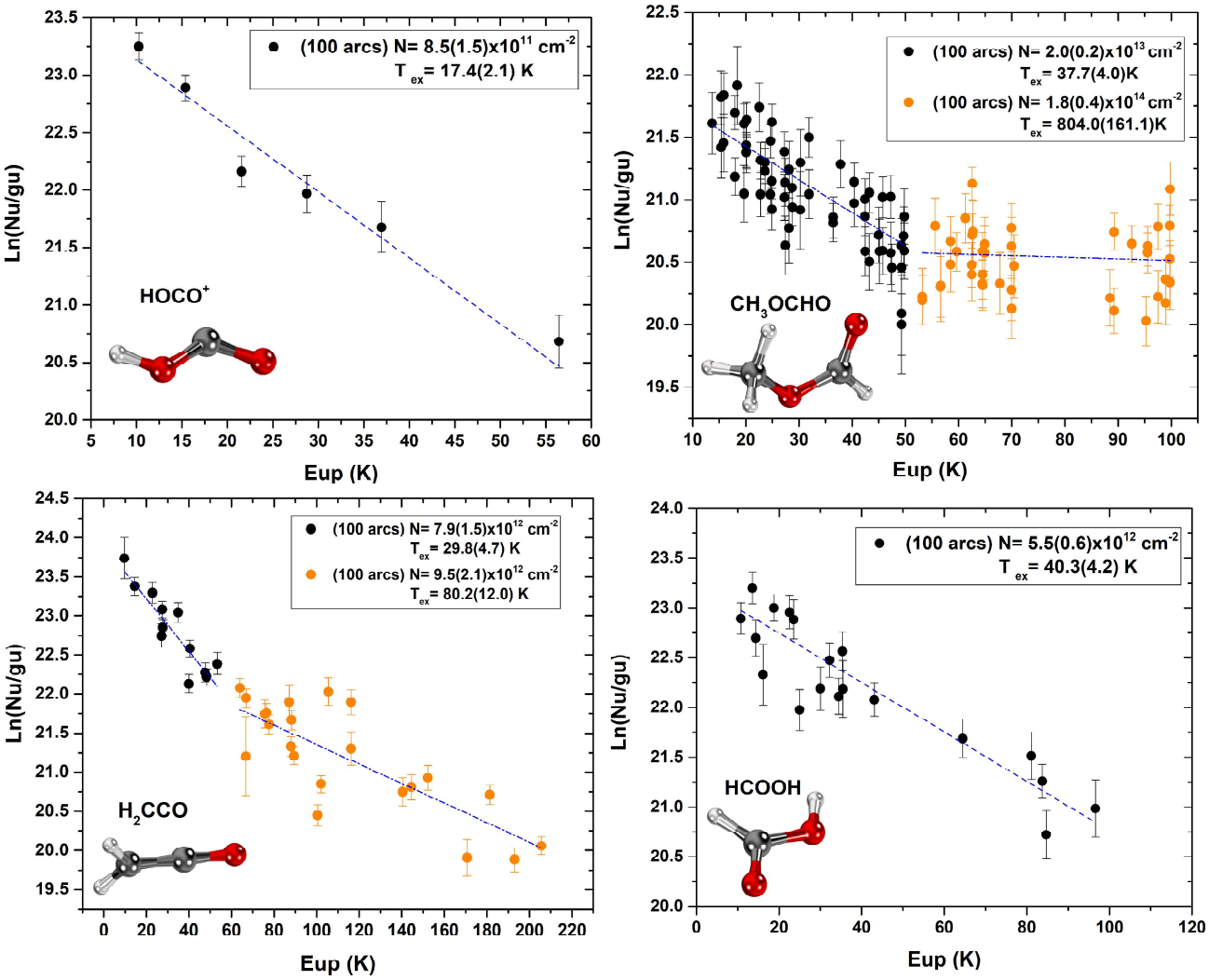

Figure 8.10: Rotational diagram of $HOCO^+$, CH_3OCHO, H_2CCO and HCOOH identified in IRAS 4A with a source size of 100 arcs.

layer of 800K is absurd, obviously, not to mention that no other species in the survey, in particular CH_3OH, displays any similar high-excitation component. The most simple explanation is that the size of the CH_3OCHO emitting region is actually smaller. Indeed, repeating the population diagram analysis with a size of 20 arcsec, we obtain an excitation temperature of about 150K for the high-excitation component, which is physically much more reasonable and in reasonable agreement with the results of the other O-bearing tracers, like CH_3OH.

8.2.2 S-Bearing Molecules

Sulfur-bearing molecules are the second most abundant species in IRAS 4A, after O-bearing species. The list of detected S-bearing species is given in Table 8.3 with a total of 228 molecular

Table 8.2: O-bearing species (including rare isotopologues) identified in IRAS 4A with a source size of 100 arcs.

		< 30K		< 70K		> 70K	
id	Species	T_{ex} (K)	N (cm^{-2})	T_{ex} (K)	N (cm^{-2})	T_{ex} (K)	N (cm^{-2})
19002	HDO	154.1	1.1×10^{13}				
28503	CO	4.4	1.1×10^{16}				
29004	HCO	—	—				
29501	^{13}CO	9.6	4.3×10^{12}				
29503	C^{17}O	28.8(12.0)	$1.4(0.2)\times10^{15}$				
29507	HCO	7.1	6.6×10^{12}				
30001	C^{18}O	17.3	2.9×10^{15}				
30002	H^{13}CO	9.7	2.1×10^{12}				
30505	HC^{13}O	—	—				
30004	H_2CO	10.8(1.0)	$2.8(0.6)\times10^{13}$			171.2(72.8)	$1.0(0.3)\times10^{14}$
30510	DCO	7.5(1.0)	$5.0(1.2)\times10^{12}$				
31001	HC^{18}O	9.9(3.4)	$2.7(1.5)\times10^{11}$				
31002	H$^{13}_2$CO	15.6(3.5)	$1.6(0.7)\times10^{12}$				
31003	HDCO	12.6(2.0)	$2.2(1.1)\times10^{13}$				
30503	^{13}C^{17}O	—	—				
31502	^{13}C^{18}O			69.9	1.8×10^{14}		
31504	H_2COH	29.4	7.1×10^{11}				
32003	CH_3OH	16.9(4.3)	$1.2(0.5)\times10^{14}$	40.7(25.5)	$1.2(1.3)\times10^{14}$	185.5(26.1)	$2.2(0.4)\times10^{14}$
32004	$H_2C^{18}O$	18.3(4.2)	$4.0(1.7)\times10^{11}$				
32006	D_2CO	14.2(1.8)	$3.3(0.8)\times10^{12}$			91.9(19.6)	$5.6(0.7)\times10^{12}$
33004	CH_2DOH	19.9(2.6)	$2.3(0.4)\times10^{13}$			88.0(24.9)	$6.3(1.4)\times10^{13}$
33502	$^{13}CH_3OH$	17.2(3.1)	$1.2(0.4)\times10^{13}$	69.8(11.1)	$1.8(0.4)\times10^{13}$		
42501	H_2CCO	29.8(4.7)	$7.9(1.5)\times10^{12}$			80.2(12.0)	$9.5(2.1)\times10^{12}$
44003	CH_3CHO	21.0(1.6)	$9.5(1.0)\times10^{12}$			85.5(9.1)	$1.2(0.1)\times10^{13}$
45010	HOCO	17.4(2.1)	$8.5(1.5)\times10^{11}$				
46004	C_2H_5OH			40.2(12.4)	$1.8(0.5)\times10^{13}$		
46005	HCOOH			40.3(4.2)	$5.5(0.6)\times10^{12}$		
46008	CH_3OCH_3			54.1(15.4)	$4.5(1.2)\times10^{13}$		
58003	CH_3COCH_3	—	—				
60003	CH_3OCHO			37.7(4.0)	$2.0(0.2)\times10^{13}$	804.0(161.1)	$1.8(0.4)\times10^{14}$
60501	$CH_2(OH)CHO$	—	—				

lines. Among the 26 species identified, 15 are rare isotopologues. In the S-bearing group, ^{34}S is the most commonly found rare isotope, being found in 6 molecular species. The second most abundant is deuterium, which is found in 4 S-bearing molecular species.

Simple S-bearing molecules are detected in different astrophysical objects (Pineau des Forets et al., 1993; Fuente et al., 2016; Gorai, 2018; Lefloch et al., 2018; Jacobsen et al., 2019). These species are widely used to trace shocks in star forming regions in dense clouds (Pineau des Forets et al.,

1993; Gorai, 2018). Usually the abundance of SO_2 and SO molecules increases significantly with the presence of shocks (Gorai, 2018). S-bearing species are often used to date chemical evolutionary timescales (CCS/NH_3) and to constrain various physical processes: temperature (SO, SO_2, OCS), X-ray irradiation (SO), grain processing (SO/H_2S, SO/SO_2), and turbulent transport (CCS/CO). Thus, these species can be considered as excellent multi-tracers (Pineau des Forets et al., 1993; Gorai, 2018; Semenov et al., 2018).

On the other hand, the abundance and the nature of the main sulfur carriers on the grains is still very debated. Recent models of dark cloud chemistry by Vidal et al. (2017) show that depending on the age of the cloud, the main reservoir of sulfur could either be atomic sulfur in the gas phase or HS and H_2S in icy grain bulks. In the gas phase, H_2S participates as a precursor in the formation of SO and S_2O through sputtering or thermal evaporation (Pineau des Forets et al., 1993; Fuente et al., 2016). So far, only two molecules were identified in solid phase: OCS and SO_2, with OCS being the only unambiguous identification in the infrared (Fuente et al., 2016). Observations of the protostellar ice by the James Webb Space Telescope (JWST) will hopefully bring some strong constraints on the grain mantle composition.

Fig. 8.11 shows the rotational diagrams of SO, ^{33}SO, ^{34}SO, and the S^{18}O with a source size of 100 arcs and the Fig. 8.12 shows the rotational diagrams of the SO_2, OCS and CCS molecules with a source size of 100 arcs and 20 arcs. The detected transitions of all the molecular species in 100 arcs probe a similar range of E_{up}, between 5 and 100K, except for the OCS and OC^{34}S with transitions detected from the energy levels higher E_{up} to 150K.

In Figs. 8.11 and 8.12, we can see that the rotational diagrams of the isotopologues of SO, CCS and SO_2 can be fitted by a single component in the range of excitation considered. The estimated SO column density is $1.1(\pm0.2)\times10^{14}$ cm^{-2}, while that of CCS is $2.8(\pm0.6)\times10^{12}$ cm^{-2}. The latter has column density values comparable in magnitude to the ^{33}S and ^{34}S isotopes of SO. From Fig. 8.11, we can see that the excitation temperatures of SO, ^{34}SO and S^{18}O are around 10K, while for ^{33}SO this value is around 20K.

The cases of OCS and the isotopologue OC^{34}S are more complex. As can be seen in Table 8.3, assuming a source size of 100 arcs was considered, OCS and OC^{34}S do not present any low excitation component.

At 100 arcs, in the OCS population diagram we detect two components (Fig. 8.12). The low-excitation component has a column density of $4.3(\pm0.2)\times10^{13}$ cm^{-2} and a T_{ex} of 30.4 (±1.0)K.

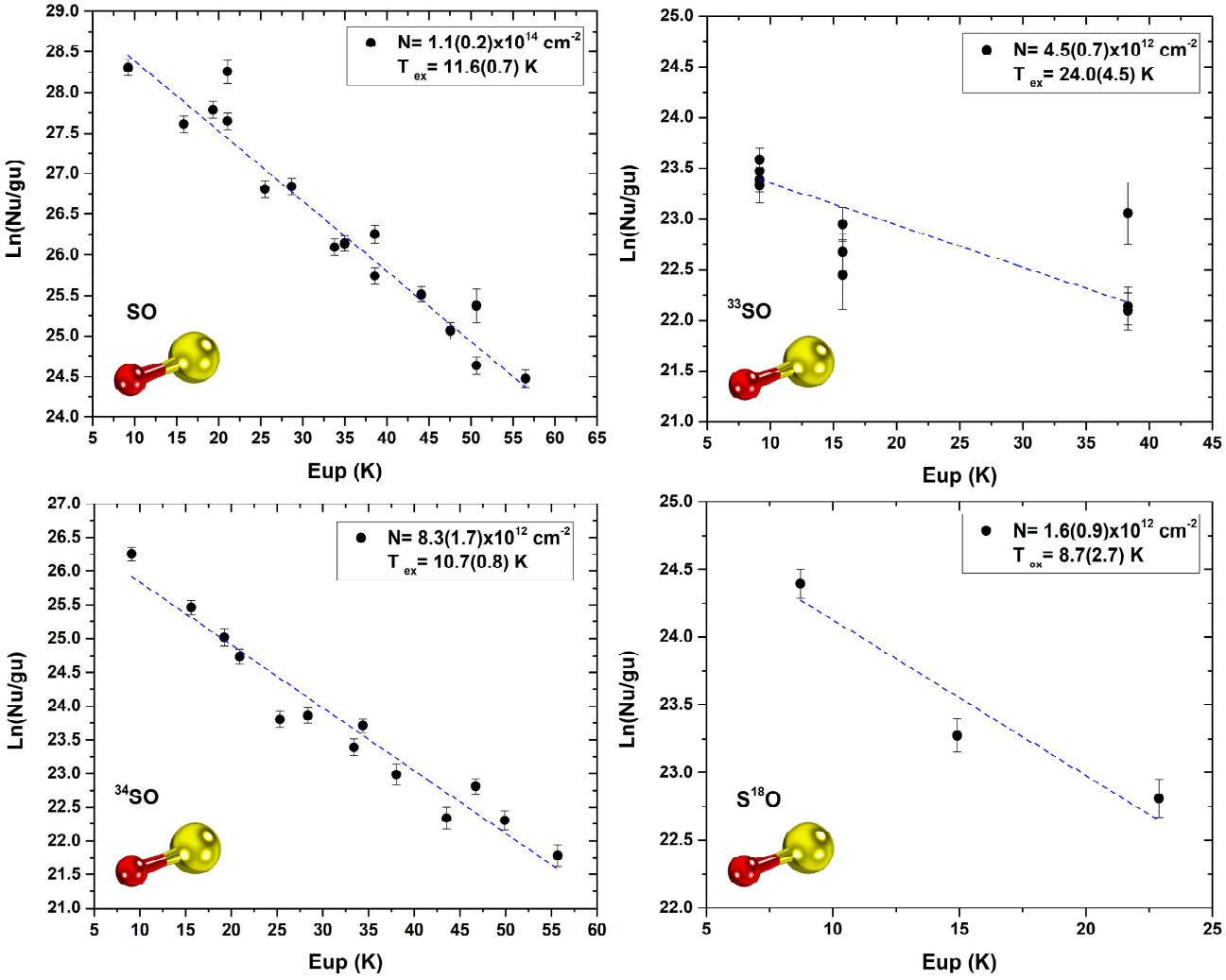

Figure 8.11: Rotational diagrams for different SO isotopologues with a source size of 100 arcs.

These values are in the same range of E_{up} as the SO isotopologues. On the other hand, the second, high-excitation component has a column density of $4.7(\pm 1.7) \times 10^{13}$ cm^{-2} and excitation temperature of 60.0($\pm$ 11.4)K, which is detected in a higher range of E_{up}, above 80K. The analysis of OC^{34}S at 100 arcs also reveals two component. The first, with an excitation temperature of around 47K, is determined in the range of $E_{up} = 15-50$K. This result is not consistent at all with OCS nor with the other S-bearing species.

If the lower excitation components derived for OCS and OC^{34}S are in rough agreement (30K and 47K, respectively), the high-excitation temperatures fully disagree (60K and 340K, respectively). The second component of OC^{34}S at 100 arcs shows a high excitation temperature much greater than the warm component of the OCS and the hot component of the CH_3OH. However, the excitation conditions are expected to be the same in the same range of E_{up}. Again, like for CH_3OCHO, we

Table 8.3: S-bearing species (including rare isotopologues) identified in IRAS 4A with a source size of 100 arcs.

		< 30K		< 70K		> 70K	
id	Species	T_{ex} (K)	N (cm^{-2})	T_{ex} (K)	N (cm^{-2})	T_{ex} (K)	N (cm^{-2})
34502	H_2S			47.2	4×10^{13}		
35502	HDS	10.8	1.1×10^{13}				
36504	H^{34}_2S			56.2	1.1×10^{13}		
36503	D_2S						
44001	CS	12.9(1.7)	$2.3(0.5)\times10^{13}$				
45501	^{13}CS	5.8	2.9×10^{12}				
45005	HCS	14.4(2.3)	$6.9(1.9)\times10^{11}$				
45502	$C^{33}S$	12.6(2.7)	$8.3(3.0)\times10^{11}$				
46001	$C^{34}S$	29.3(9.0)	$4.7(1.1)\times10^{12}$				
46509	H_2CS	17.0(1.1)	$1.2(0.2)\times10^{13}$	46.8(7.6)	$1.5(0.7)\times10^{13}$		
47504	HDCS	15.7(0.7)	$3.5(0.3)\times10^{12}$				
48001	SO	11.6(0.7)	$1.1(0.2)\times10^{14}$				
48010	SO^+	9.8(0.6)	$5.4(0.7)\times10^{12}$				
48507	D_2CS	14.1(1.8)	$2.5(0.5)\times10^{12}$				
48508	$H_2C^{34}S$	9.3(2.4)	1×10^{12}				
48510	CH_3SH	20.3(6.3)	$4.8(1.7)\times10^{12}$				
49501	^{33}SO	24.0(4.5)	$4.5(0.7)\times10^{12}$				
50001	^{34}SO	10.7(0.8)	$8.3(1.7)\times10^{12}$				
50002	$S^{18}O$	8.7(2.7)	$1.6(0.9)\times10^{12}$				
56007	CCS	15.5(1.5)	$2.8(0.6)\times10^{12}$				
60001	OCS			30.4(1.0)	$4.3(0.2)\times10^{13}$	60.0(11.4)	$4.7(1.7)\times10^{13}$
61502	$O^{13}CS$			62.8(7.9)	$5.1(1.0)\times10^{12}$		
62001	$OC^{34}S$			46.7(8.6)	$4.6(0.6)\times10^{12}$	338.7(256.1)	$1.2(0.3)\times10^{13}$
64002	SO_2	13.1(1.2)	$1.4(0.3)\times10^{13}$	54.7(24.0)	$1.4(0.8)\times10^{13}$		
66002	$^{34}SO_2$	9.4(0.9)	$1.1(0.1)\times10^{12}$				
68001	CCCS	12.7(3.4)	$1.0(0.8)\times10^{12}$				

propose that the OCS emission arises from a smaller region than the 100 arcsec initially assumed.

If we adopt a typical source size of 20 arcs, the excitation temperatures in the E_{up} range of 5-100K are now 23.8 ($\pm$2.0)K for OCS and 26.8 ($\pm$2.5)K for $OC^{34}S$. When we adjust the font size to 20 arcs we get a more consistent result, with excitation temperatures of 71.3 ($\pm$60.3)K and 96.6 ($\pm$57.5)K for OCS and $OC^{34}S$, respectively, in the E_{up} range of 80-120K. These results are now consistent between different isotopologues and they are also consistent with the results obtained for other S-bearing species and for CH_3OH. These results are much more realistic and show that the high excitation components in IRAS 4A are more compact and need to be studied in more detail.

To summarize, the population diagram analysis OCS has revealed features similar to those of

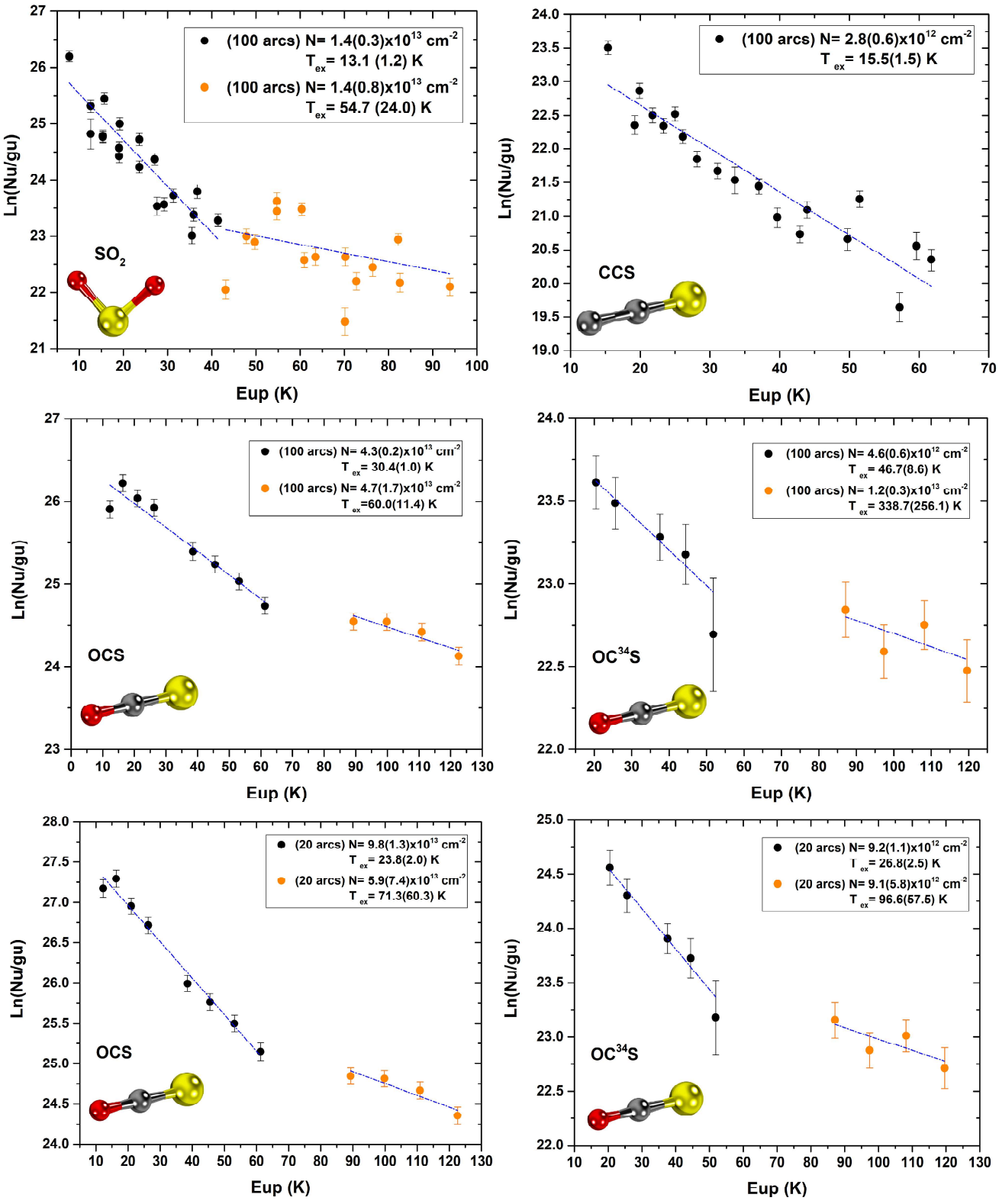

Figure 8.12: Rotational diagram of selected S-bearing molecules identified in IRAS 4A with a source size at 100 arcs (top and middle panels) and 20 arcs (bottom panels).

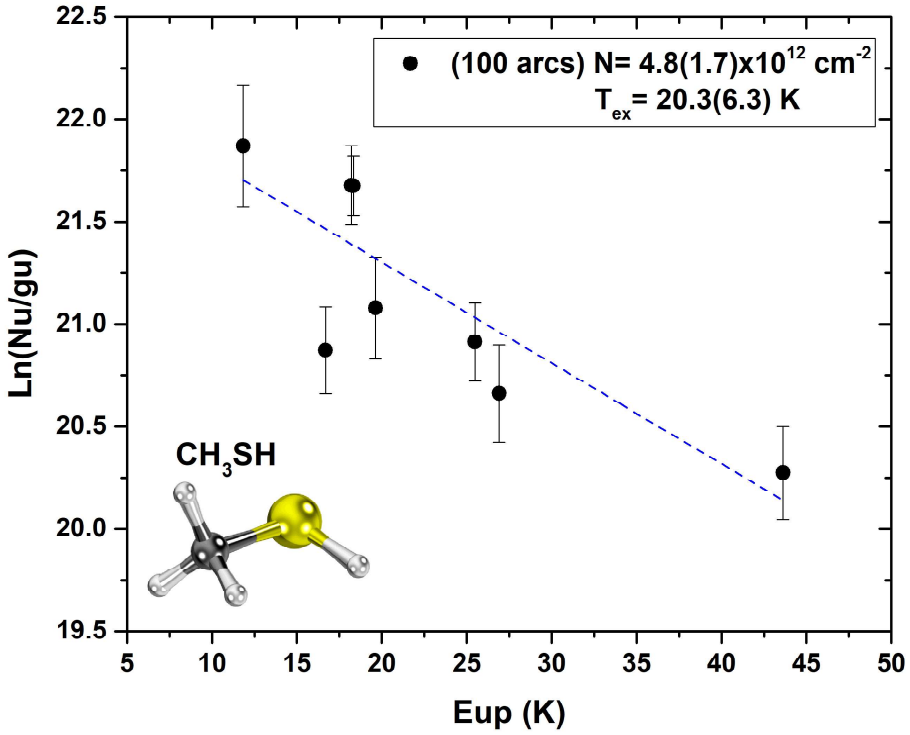

Figure 8.13: Rotational diagram of the complex organic molecule CH_3SH identified in IRAS 4A.

CH_3OH. As it probes a wide range of excitation, we can detect two physical components with different T_{ex}. We note that the other S-bearing species cover a narrower range of excitation conditions, with E_{up} less than 55K. For this reason, the second OCS component is missed by the other S-bearing species. The first OCS component is of low excitation with T= 20-30 K. The second OCS component is of higher excitation with $T \simeq 70-90$K. More precisely, OCS may reveal or the presence of a temperature gradient across the protostellar envelope. A crude estimate of the low-excitation region size of 20 arcs is provided by the condition of consistency between the OCS and $OC^{34}S$ analysis. This implies that the emission at an excitation temperature of 70-90K most likely arises from a region smaller than 20 arcs in size. We speculate that the difference of size in the emission of OCS with respect to SO could reflect radial variations of the envelope chemical composition as one gets closer to the protostar. Emission maps of the S-bearing species at 10 arcs resolution with the IRAM 30m telescope and higher angular resolution with the NOEMA interferometer would help confirm our interpretation.

Finally in this section, we present the result of the rotational diagram of the methyl mercaptan molecule (CH_3SH, see Fig. 8.13). This is the only S-bearing complex organic molecule detected in the spectral survey. The estimated column density of CH_3SH is $4.8(\pm1.7)\times 10^{12}$ cm^{-2}, with an

excitation temperature of 20.3(±6.3)K. This species was observed in other star-forming regions, from low-mass (IRAS16293-2422) to intermediate-mass (Cep E-mm) and high-mass (Sgr B2, G327.3-0.6) (Linke et al., 1979; Gorai, 2018; Jacobsen et al., 2019; Lefloch et al., 2018; Sahu et al., 2019).

8.2.3 N-Bearing Molecules

In the cold and dense regions of protostellar and prestellar cores, the freeze out of molecular species onto dust grains is commonly observed (see Bergin and Tafalla 2007; Ceccarelli et al. 2007 for a review). This is the case of CO, CS, HCO^+, H_2CO, H_2O for instance (Bergin and Langer, 1997). In these objects, however, other species such as ammonia (NH_3) and nitrenium (N_2H^+) remain in the gas phase for a longer time and their abundance may increase with the increase of the local density (Roueff et al., 2005), following an opposite trend with respect to that observed for CO (Bergin and Langer, 1997; Belloche and André, 2004; Flower et al., 2006). It is now well established that the depletion of heavy elements and the increase in the abundance of deuterated species are closely related, since the adsorption of CO and other gas phase molecules in the grains surface facilitates the deuterium redistribution by decreasing the destruction rate of deuterated molecular ions (Bacmann et al., 2003; Ceccarelli et al., 2007; Roueff et al., 2005; Flower et al., 2006; Emprechtinger et al., 2009). An interesting property of N-bearing species is that they have adsorption energies similar to the one of CO. Therefore, one might expect them to freeze out in a similar way to CO (Flower et al., 2006; Emprechtinger et al., 2009). The observed difference of behaviour remains to be understood.

We could identify a total of 218 rotational transitions from N-bearing species in the IRAS 4A spectral line survey. In total, 25 molecular species were identified, of which 13 have rare isotopologues. The list of identified N-bearing molecular species is presented in Table 8.4. Deuterium is the rare isotopologue most commonly found, with 6 molecular species, followed by ^{15}N and ^{13}C with 4 and 3, respectively.

Fig. 8.14 shows the rotational diagrams of HC_3N, NS and CH_3CN. Similarly to CH_3OH, the rotational levels of CH_3CN are characterized by the two quantum numbers (J,K). The dipole moment of CH_3CN is however much larger than of CH_3OH, which implies that a much higher H_2 gas density is needed for LTE conditions to be met. As a consequence, the rotational diagram of CH_3CN presents a structure more complex than that of CH_3OH, further away from LTE, and which can be described as series of the type K_J. Each series can be fitted by a straight line of slope $1/T_{ex}$. It appears that 7 series K_J can be fitted by a gas component of similar excitation temperature T_{ex}, in the range of $33-55$K.

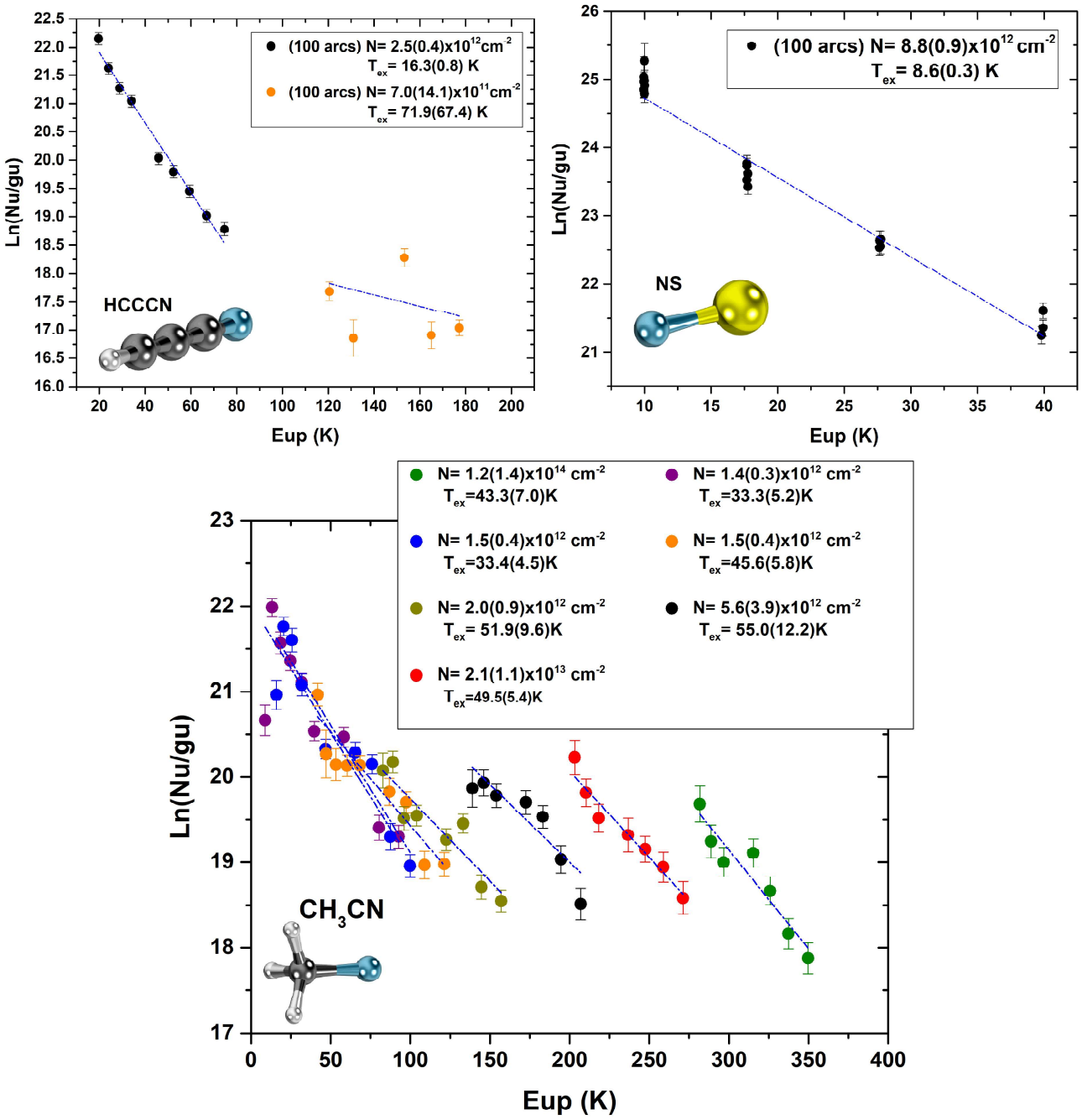

Figure 8.14: Rotational diagrams of HC_3N, NS and CH_3CN.

Hence, we conclude that the CH_3CN emission arises from one single gas component of moderately high excitation, in the range of $T_{ex} = 33-55$K.

The rotational diagrams of HCCCN and NS (Fig.8.14) both show a low scatter in the data points in the low excitation components, indicating that these species are close to local thermodynamic equilibrium. The detected emission traces a region with T_{ex} close to 10K, of lower excitation than CH_3CN, similar to the low-excitation component already reported in other molecular species. It

Table 8.4: N-bearing species (including rare isotopologues) identified in IRAS 4A with a source size of 100 arcs.

		< 30K		< 70K		> 70K	
id	Species	T_{ex} (K)	N (cm^{-2})	T_{ex} (K)	N (cm^{-2})	T_{ex} (K)	N (cm^{-2})
18004	NH_2D	9.4(4.1)	$2.4(2.5)\times10^{13}$	79.7	7.3×10^{12}		
26504	CN	4.7(0.4)	$4.9(1.0)\times10^{13}$				
27001	HCN	—	—				
27002	HNC	7.2	1.0×10^{13}				
27505	^{13}CN	—	—				
28002	H^{13}CN	4.8(0.6)	$4.7(1.7)\times10^{12}$				
28003	HC^{15}N	6.6(1.4)	$3.8(1.8)\times10^{11}$				
28004	DCN	5.1(0.3)	4.5×10^{12}				
28005	HN^{13}C	6.3	2.1×10^{12}				
28006	H^{15}NC	6.3	4.4×10^{11}				
28508	DNC	6.2(0.3)	$5.0(0.6)\times10^{12}$				
29005	N_2H	—	—				
30008	NO	13.4(1.4)	$4.5(0.5)\times10^{14}$				
30009	N_2D	7.3(0.7)	$3.5(0.5)\times10^{12}$				
30507	^{15}NNH	14.2	3.3×10^{10}				
30508	N^{15}NH	18	3.5×10^{10}				
41001	CH_3CN			44.6(7.1)	$2.2(1.2)\times10^{13}$		
43002	HNCO	22.1(1.7)	$5.0(0.7)\times10^{12}$				
43509	HCNO	11.8	9.8×10^{10}				
43510	HOCN	4.6	1.2×10^{11}				
44006	DNCO	3.5	3.5×10^{12}				
45003	NH_2CHO	21.6(6.2)	$3.5(1.1)\times10^{11}$	42.2(37.8)	$2.2(2.9)\times10^{12}$		
46010	NS	8.6(0.3)	$8.8(0.9)\times10^{12}$				
51001	HC_3N	16.3(0.8)	$2.5(0.4)\times10^{12}$			71.9(67.4)	$7.0(14.1)\times10^{11}$
52005	DC_3N			37.9(26.0)	$6.7(3.4)\times10^{10}$		

is clear that the low excitation component of HCCCN can not account for the flux detected in the transitions of high E_{up} (> 100K). We find direct evidence for the presence of a second, high-excitation HCCCN component towards IRAS4A. Unfortunately, the data suffers some scatter, and the fit to this second component is rather poor, though compatible with the warm components of the $^{13}CH_3OH$ and CH_2DOH.

8.2.4 C-Bearing Molecules

The IRAS 4A content in C-bearing species is considerably less rich in terms of identified lines and molecules than in O- and S-bearing species. In total, only 99 rotational frequencies attributed

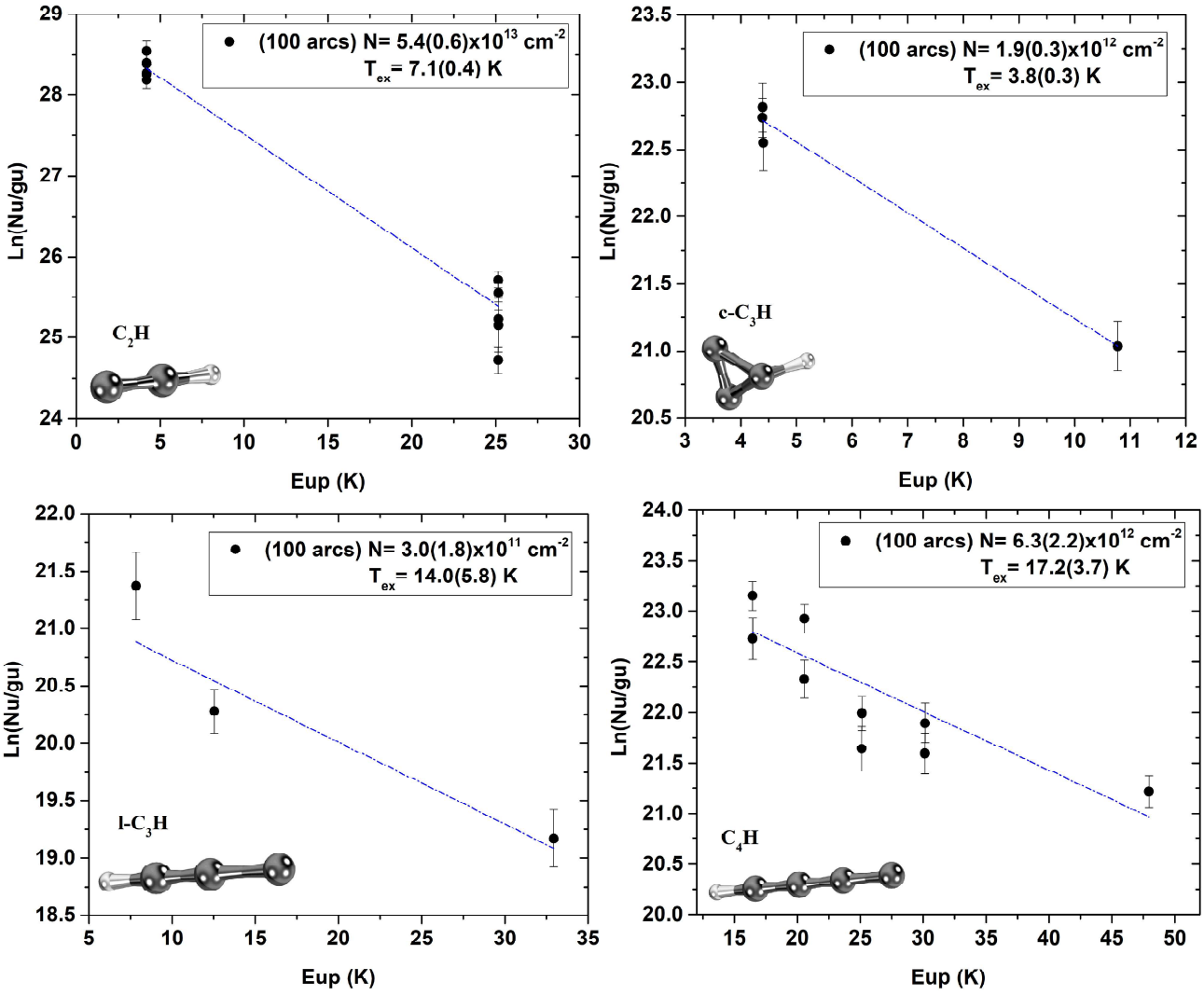

Figure 8.15: Rotational diagram of polyyne molecules identified in IRAS 4A at 100 arcs.

to 7 different species – of which 6 are main isotopologues and the last one contains deuterium – are observed. Table 8.5 shows that most of the C-bearing molecules identified in IRAS 4A are of the polyyne type. These molecules are highly unsaturated, and therefore present a high C/H ratio. The linear molecules CCH, l-C_3H and C_4H were identified in the source. Higher-order polyynes, the ones containing five or more carbon atoms, were not detected in our survey. We also observe the presence of the cyclic C-bearing molecules c-C_3H and c-C_3H_2, the former being a structural isomer of l-C_3H. The presence of the unsaturated hydrocarbon propyne (CH_3CCH), or methyl acetylene, is also identified. The signature(s) of deuterated isotopologue(s) were detected in several C-bearing species. Since these species form preferentially in the gas phase, the detection of the deuterated counterparts indicate that they are tracing cold gas material, probably associated with the external protostellar envelope of IRAS4A.

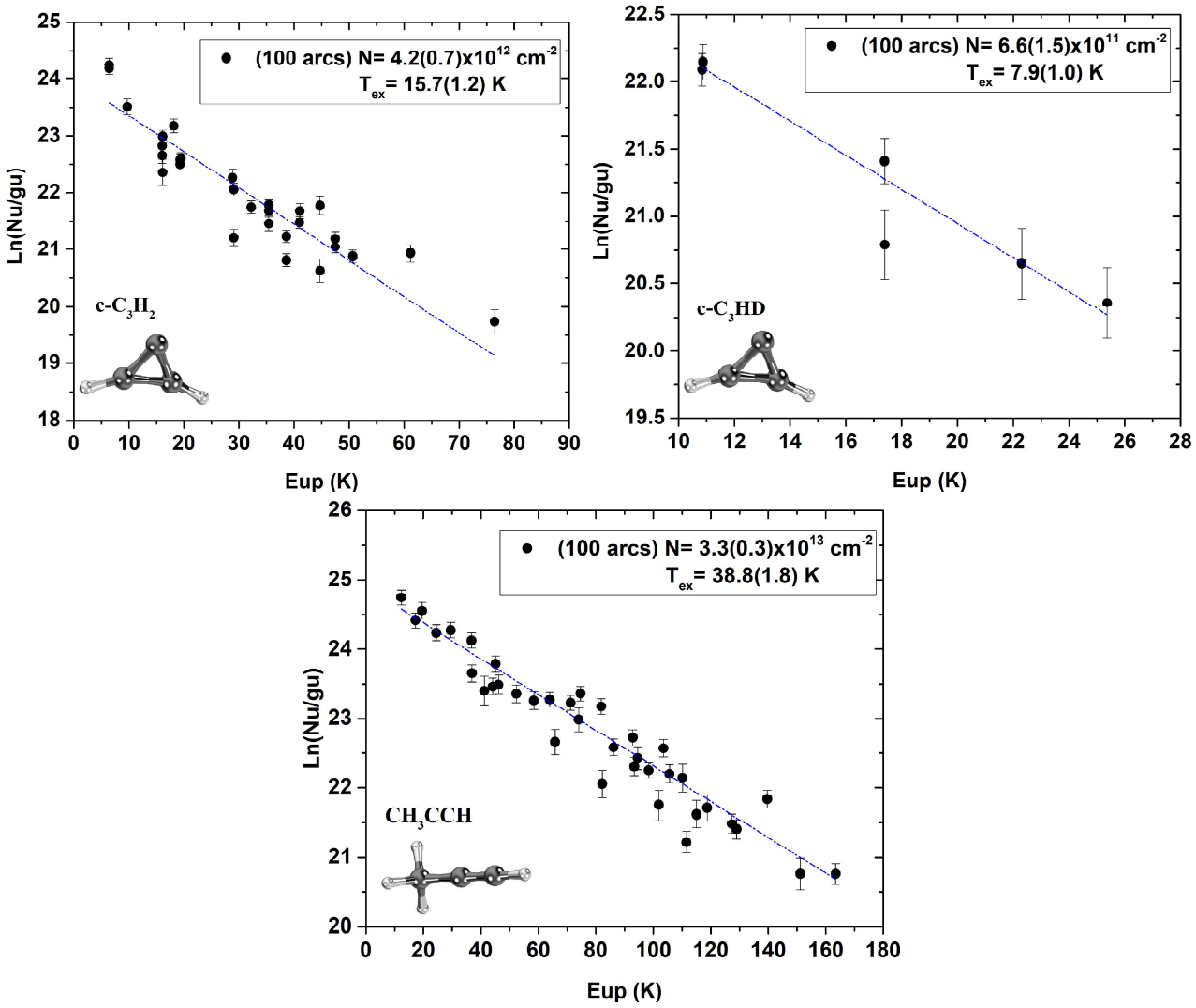

Figure 8.16: Rotational diagram of hydrocarbon molecules identified in IRAS 4A at 100 arcs.

Table 8.5: C-bearing species (including rare isotopologues) identified in IRAS 4A with a source size of 100 arcs.

		< 30K		< 70K	
id	Species	T_{ex} (K)	N (cm^{-2})	T_{ex} (K)	N (cm^{-2})
25001	CCH	7.1(0.4)	$5.4(0.6)\times10^{13}$		
37002	l-C_3H	14.0(5.8)	$3.0(1.8)\times10^{11}$		
37003	c-C_3H	3.8(0.3)	$1.9(0.3)\times10^{12}$		
38002	c-C_3H_2	15.7(1.2)	$4.2(0.7)\times10^{12}$		
39003	c-C_3HD	7.9(1.0)	$6.6(1.5)\times10^{11}$		
40502	CH_3CCH			38.8(1.8)	$3.3(0.3)\times10^{13}$
49003	C_4H	17.2(3.7)	$6.3(2.2)\times10^{12}$		

Figs. 8.15 and 8.16 show the rotational diagram of all C-bearing molecules identified in IRAS 4A. The highest relative abundances with respect to N_{H_2} are: CCH ($\chi = 3.4\times10^{-9}$); methyl acetylene,

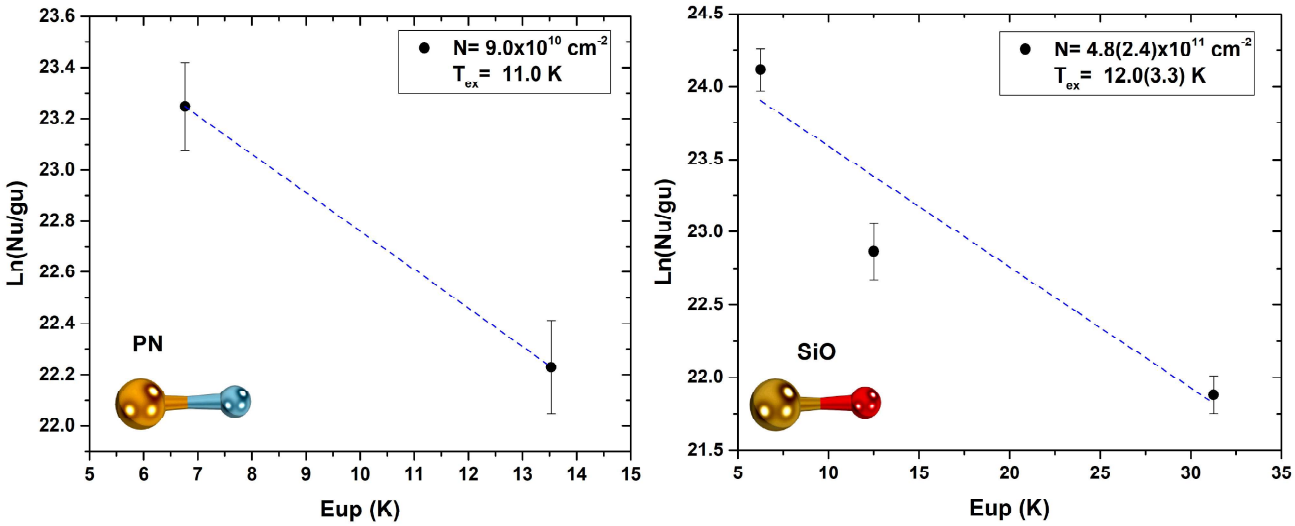

Figure 8.17: Rotational diagram of P-bearing and Si-bearing molecules identified in the protostellar object NGC 1333 IRAS 4A.

CH_3CCH ($\chi = 2.0\times10^{-9}$) and C_4H ($\chi = 3.9\times10^{-10}$). The cyclic C-bearing molecules c-C_3H_2 ($\chi = 2.6\times10^{-10}$) and c-C_3H ($\chi = 1.2\times10^{-10}$) have relatively lower abundances in comparison. This result evidences that polyyne chains are the most common carbon reservoir among the C-bearing molecules in the protostellar object NGC 1333 IRAS 4A.

8.2.5 X-Bearing Molecules: P and Si

In this section we report the identification of phosphorus- and silicon-bearing molecules. Phosphorus is a crucial element for prebiotic chemistry and for the development of life on Earth, Therefore, the study of phosphorus in low-mass protostar regions such as IRAS 4A is important to understand its role and properties in the early phases of the proto-Solar nebula.

Phosphorus-bearing species, such as HCP, PH_3, CP, CCP, PO and PN have been identified around evolved stars and it was proposed that these last structures (PN and PO) are the main phosphorus reservoirs in the gas phase (Agúndez et al., 2007; Milam et al., 2008; Lefloch et al., 2016; Ziurys et al., 2018).

Lefloch et al. (2016) conducted a systematic search for P-bearing molecules in star forming regions of solar type. The authors detected both PO and PN. This was the first identification of PO in a solar-type star forming region. The authors showed that both PO and PN were associated with a shock region in the outflow powered by the low-mass class 0 protostar L1157-mm.

PN is the only P-bearing species which was detected towards IRAS 4A. Two weak PN emission

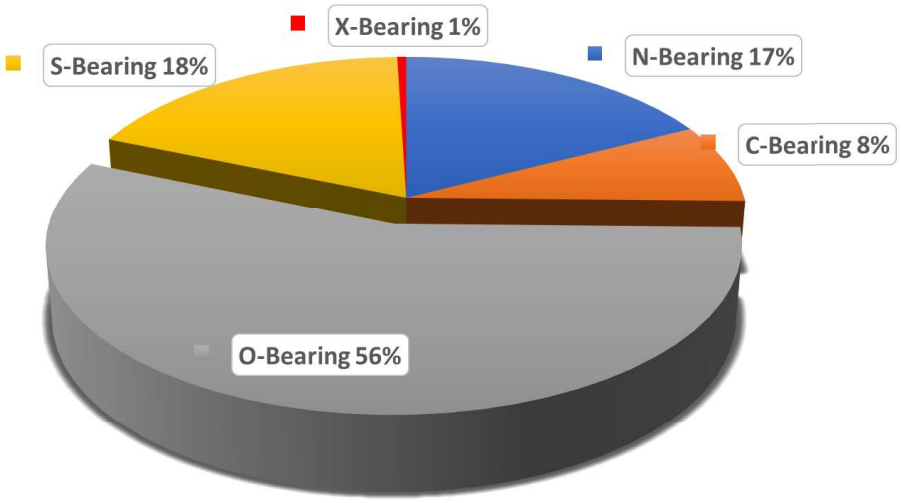

Figure 8.18: Percentage of identified rotational lines per molecular group in IRAS 4A.

lines were identified, both with narrow line widths and low excitation (T_{rot}= 11 K). (Fig.8.17). Unlike L1157-mm, the narrow line widths of the line profiles exclude a shock origin for the PN material in the envelope. The origin of this emission and the formation pathway of PN requires some work both from modellers and observers.

For the sake of completeness, we mention the detection of SiO and its two are ^{29}Si and ^{30}Si isotopologues, towards IRAS 4A (Fig.8.17). The presence of SiO in the IRAS 4A outflows had been reported by several groups using both single-dish (Lefloch et al., 1998) and interferometric observations (Santangelo et al., 2015). The line profiles are very broad (up to 20 km s^{-1}) and coincide very well with those of CO, showing that SiO emission arises from the protostellar outflow. As explained in the introduction of this Chapter, we concentrated our analysis on the chemical composition of the protostellar envelope, and, for this reason, we did not model the SiO emission, as it arises from shocks in the outflowing gas.

Tables 8.2, 8.3 8.4 and 8.5 shows a list of all O-, S-, N-, C-, P- and Si-bearing species identified in IRAS 4A, including information of main isotopologues, rare isotopologues and isomeric structures. The physical parameters such as excitation temperature and column densities are also in these tables. The rotational frequencies identified per molecule are found in Table D (see Appendix D).

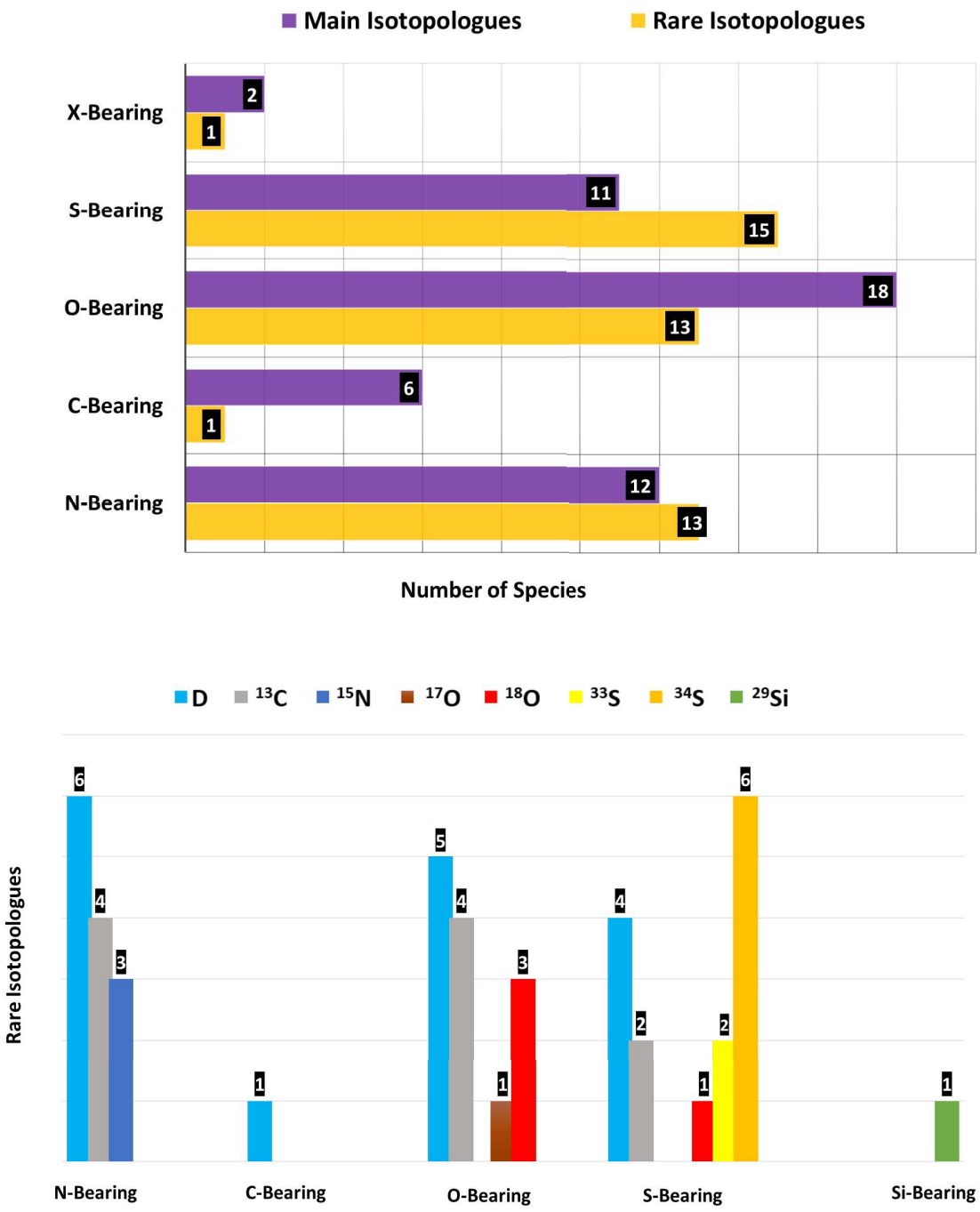

Figure 8.19: Number of species identified per molecular group. Top panel: number of main and rare isotopologues identified per group. Bottom panel: identification of rare isotopologue type per molecular species

8.3 Summary

In summary, the analysis of the ASAI survey of IRAS 4A has allowed us to obtain a chemical and physical description of the protostellar envelope. The molecular species identified at the source show

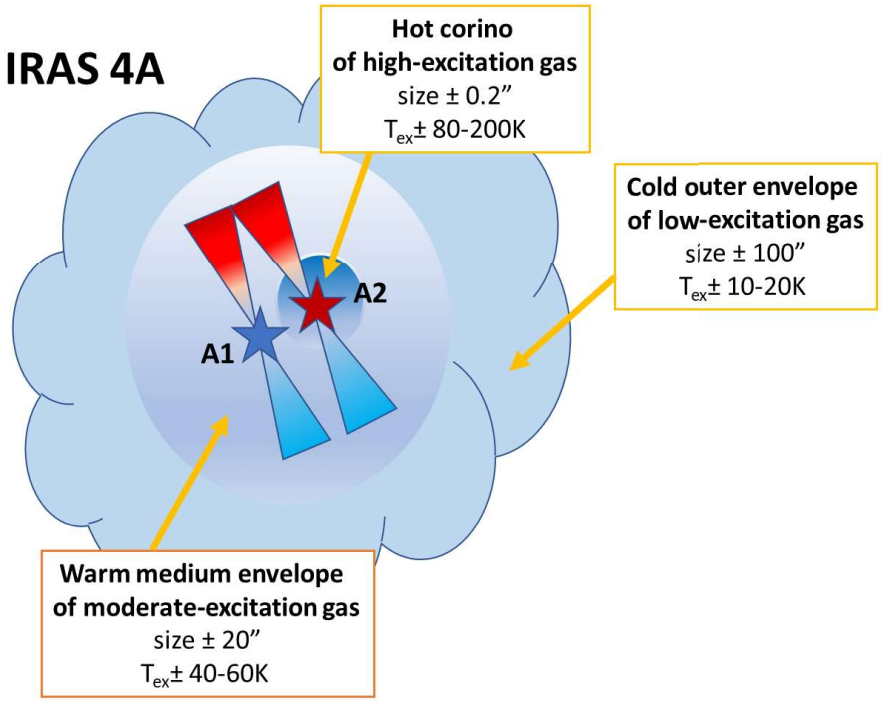

Figure 8.20: Representative diagram of the morphology of IRAS 4A.

a clear dominance of the oxygen-bearing species, representing 56% of the total number of molecules identified. Other important groups, such as sulfur- and nitrogen-bearing molecules, constitute 18% and 17%, respectively (Fig. 8.18). Carbon-bearing molecules are responsible for 8% of the total number of species that we identified, while X-bearing (X = P, Si) molecules account for merely 1%.

The analysis of species with rare isotopologues shows that deuterium is present in 4 of the 5 groups characterized in IRAS 4A. Similarly, we can see that the group of sulfur-bearing species has the highest content of rare isotopologues species, with 15 in total, followed by the O-bearing and N-bearing groups with a total of 13 each (Fig. 8.19)

The high number of rotational frequencies attributed to 92 different molecular species clearly indicates that IRAS 4A is a chemically rich source. By using rotational diagram analysis, we show that the object presents three distinct physical components (Fig. 8.20). The cold outer envelope, with a size of $\sim$ 100 arcs, is rich in simple molecular species with excitation temperatures below 30K. The warm medium excitation component, with temperatures ranging from 40 to 60K, is the one where complex organic molecules are identified. We estimate that such component has an approximate size of 20 arcs, as described by the OCS molecule. Finally, we show the presence of a third component, with excitation temperatures between 80 and 200K. This component is consistent with a dense and hot compact region of the hot corino. Based on our analysis, we propose that the hot envelope has a

size of ~ 0.2 arcs, as traced by the CH_3OH molecule. Further interferometric observations would aid in the morphological characterization of the hot and warm regions of IRAS 4A.

Chapter 9

Summary

9.1 Experimental Results

9.1.1 The Cyclohexane Molecule (C_6H_{12})

In Chapter 4, we probed the stability of the fully hydrogenated benzene molecule, cyclohexane, in circumstellar photodissociation regions. We obtained the fragmentation pattern of the C_6H_{12} under interaction with UV and X-ray photons. The production of the radical parent cation, as well as its photodissociation products, were evaluated from 10.8 eV to 307.0 eV photon energy, and their production was directly compared with the previous data of benzene, the basic unit of a PAH molecule. The main geometrical features of the most stable structures of the parent ion $C_6H_{12}{}^{+\cdot}$) were described. We determined the absolute photoionization and photodissociation cross sections of cyclohexane, and their values were compared to those of benzene. The astrochemical implications of the experimental data and computational results were discussed in the context of the PDR region of the carbon-rich planetary nebula NGC 7027, which provided insights into the photostability of super-hydrogenated PAHs in such photon-rich environments.

A decreasing exponential profile is observed for the production of the parent ion of cyclohexane in the range of energies from 10.8 eV to 200.0 eV, and its production is approximately half of benzene's parent ion around 16 eV. From 10.8 eV to 20.0 eV, ions from the $C_4H_n^+$ and $C_5H_n^+$ families are the ones most produced, while in the UV range from 20.0 eV to 100.0 eV families with less amount of carbon atoms are preferentially formed. For higher UV energies, the production of $C_3H_3^+$ becomes significant, a trend which is also observed in the soft X-ray region. The astrochemically relevant H_3^+

and CH_3^+ ions were also observed with reasonable abundances, likely formed from H^+ migration to a CH_2 unit followed by dissociation. Stable C_6H_n ions, on the other hand, are not efficiently formed after the molecular rearrangements that follow the X-ray ionization process of neutral cyclohexane.

The smaller photoabsorption of cyclohexane in comparison to that of benzene is responsible for its lower photoionization and photodissociation cross sections. By obtaining these absolute values and combining them with the X-ray photon flux in the PDR of NGC 7027, it was possible to evaluate the photoionization and photodissociation rates of cyclohexane, as well as its half-life time, in the mentioned astrophysical object. We estimate that cyclohexane has a half-life time of 3.5×10^3 years in the C1s resonance energy of 287.7 eV. In the C1s edge, the survival of cyclohexane is $\sim$ 20% higher than that of benzene. Since the strong C1s$\rightarrow \pi^*$ aromatic transition of PAHs is expected to be suppressed as the number of peripheral H atoms increases, such process will ultimately result in an enhancement of the X-ray stability of H_n-PAHs to photodissociation processes, which is described herein as an auxiliary protection mechanism of super-hydrogenated PAHs. A damping out process of the strong absorption feature of aromatic molecules is, thus, related to the protective effect of additional hydrogen atoms in H_n-PAHs. Finally, as the most stable $C_6H_{12}^{+\cdot}$ structures are acyclic branched species, we propose that the single photoionization of cyclohexane and other saturated hydrocarbons could enhance the abundance of branched molecules in PDR regions.

9.1.2 The Biphenyl Molecule

In Chapter 5, we make use of mass spectrometry measurements, coincidence techniques and astrochemical modeling to study the photoionization and photodissociation of biphenyl ($C_{12}H_{10}$) upon its interaction with soft X-ray photons in the edge of the inner-shell C1s resonance energy. The molecule is composed of two phenyl rings connected by a C–C sigma bond in a non-planar fashion, with a torsional angle ϕ between the C_6H_5 rings of around 44^o. Biphenyl is pointed as an important building block of polycyclic aromatic hydrocarbons (PAHs), such as phenanthrene ($C_{14}H_{10}$) and pyrene ($C_{16}H_{10}$), and could be produced in planetary nebulae by both radical-neutral and radical-radical reactions in the gas phase. All measurements were performed using synchrotron radiation at the Brazilian Synchrotron Light Laboratory, National Center for Energy and Materials Research (LNLS/CNPEM), Campinas. Our results are compared with the ones previously obtained by our group for benzene (C_6H_6) and naphthalene ($C_{10}H_8$), and discussed in the context of four planetary nebulae featuring PAH infrared emission: BD+30°3639, NGC 7027, NGC 5315 and NGC 40.

We show that the most produced singly-charged ion for a photon energy below the C1s resonance is $C_6H_5^+$. Such species is obtained by breaking the central C–C bond of biphenyl after the photoionization process, and retains the six-membered ring aromatic structure. The second most prominent ion is $C_{12}H_{10}^{+\cdot}$, whose global minimum energy geometry is related to the singly-charged acenaphthene molecule, composed of a C_2-bridged naphthalene. Since this structure (**A.1**$^{+\cdot}$) is almost 20 kcal mol^{-1} more stable than the biphenyl-like structure (**A.3**$^{+\cdot}$) as revealed by DFT and coupled-cluster calculations obtained by collaborators, we expect that the measured $C_{12}H_{10}^{+\cdot}$ ion isomerizes to **A.1**$^{+\cdot}$. For a photon energy above the C1s resonance, these species are further dissociated into smaller fragments, especially the open-chain species $C_4H_2^{+\cdot}$ and $C_4H_3^+$. This result suggests that ring-opening photoionization pathways are more active for photon energies above the C1s resonance.

The doubly-charged ions $C_6H_3^{2+}$ and $C_6H_5^{2+}$ were also unambiguously identified in our mass spectrometry measurements. The detection of $C_6H_5^{2+}$ indicates that heterolytic charge separation after cleavage of the central carbon-carbon bond in the doubly-charged parent ion is also active. By using photoelectron photoion photoion coincidence (PEPIPICO) techniques, we were able to identify that the main fragmentation processes after double ionization of biphenyl are related to the production of a C_6-containing neutral species and singly-charged fragments containing 2 and 4 carbon atoms in a three-body decay fashion.

By combining our mass spectrometry experiments with the absolute photoabsorption cross sections (σ_{ph-abs}) measurements by the group of Hitchcock, we were able to determine the photoionization (σ_{ph-i}) and photodissociation (σ_{ph-d}) cross sections of biphenyl at 275 eV and 310 eV. The σ_{ph-d} values were calculated as 8.67×10^{-20} cm^{-2} and 1.17×10^{-17} cm^{-2} at 275 eV and 310 eV, respectively. We used these values in combination to X-ray attenuation models due to the presence of interstellar grains to obtain the photodissociation rates (k_{ph-d}) of biphenyl in distinct planetary nebulae at several distances from the central star. These quantities were employed for the estimation of the half-lives ($t_{1/2}$) of biphenyl at 275 eV and 310 eV in planetary nebulae featuring PAH emission. For a photon energy of 275 eV, the half-lives of biphenyl span from 2.46×10^7 yr to 4.34×10^8 yr, while for 310 eV they span from 1.07×10^5 yr to 1.99×10^6 yr. These values are, at best, similar to the ones estimated for amorphous hydrocarbons and PAHs in the ISM ($2-6 \times 10^8$ yr), but at least one order of magnitude smaller than the injection timescales of carbonaceous materials into the ISM by AGB stars and carbon-rich planetary nebulae (2.5×10^9 yr). These values suggest that other processes, such as density inhomogeneities, should be considered to account for the presence of biphenyl and

small-sized PAHs in such hostile environments.

9.1.3 PAHs in AGNs

In Chapter 6, we examined the photoionization and photodissociation profiles of selected polycyclic aromatic hydrocarbons (PAHs) upon their interaction with 2500 eV photons. The results are discussed in the context of the chemistry of the circumnuclear regions of AGNs, which is the focus of our study. The measurements were performed by Dr. Thiago Monfredini as part of his PhD thesis (Monfredini, 2015). The following molecules were studied: naphthalene ($C_{10}H_8$), anthracene ($C_{14}H_{10}$), 2-methyl-anthracene ($C_{14}H_9CH_3$, or $C_{15}H_{12}$) and pyrene ($C_{16}H_{10}$).

By using the *PIY* results obtained by Monfredini (2015), we could determine the photoionization and photodissociation cross sections of the PAH molecules at 2500 eV. These values were used to estimate the photoionization and photodissociation rates of PAHs in the circumnuclear regions (20-80 pc) of six AGN sources with distinct X-ray fluxes. From the photodissociation rates, we could estimate the half-lives of those molecules for different optical depth values of the X-ray photon flux. These values were compared to the PAH injection timescale (2.5×10^9 yr) described by Jones et al. (1994) assuming that the main sources of PAHs are carbon-rich AGB stars.

In spite of considering attenuation of the X-ray radiation field by a dusty torus associated with an H_2 column density of 2×10^{23} cm^{-2} ($\tau = 4.45$), the lifetime of PAHs spanned values from 10^8 yr to merely 10^2 yr. These results may indicate that, in order to circumvent molecular destruction, a more sophisticated interplay between PAHs and dust grains should be considered. In this perspective, we briefly describe two possible scenarios in which grains could assist in the survival of PAHs.

We could not see any significant difference in the half-life values by increasing the size of the carbon backbone. This is probably due to the fact that we spanned only small-size PAH molecules ($10 \leq N_C \leq 16$). In addition, we show that the multiple photoionization rates are significantly greater than the single ones, irrespective of the AGN source. These results suggest that an enrichment of multiply charged ions caused by X-ray photoselection can occur in AGNs. The precise determination of the charge state of PAHs based on specific spectral signatures should be developed in order to confirm this photoselectivity mechanism.

9.1.4 Condensed Phase

In Chapter 7, we show preliminary results of protonation and deprotonation processes in condensed phase of benzene and substituted benzene rings, such as chlorobenzene (C_6H_5Cl), cyclohexane and phenol (C_6H_5OH). Our results indicate that for benzene, chlorobenzene and phenol the protonated benzene ion ($C_6H_7^+$) is predominantly formed, and dehydrogenation is observed as far as the formation of the cyclohexatriyne cation, C_6^+. Apart from dehydrogenation, we also observe that these molecules are capable of forming hydrogenated products up to the complete loss of aromaticity on the carbon ring, resulting in the production of the cyclohexane cation ($C_6H_{12}^+$) and the protonated cyclohexane ($C_6H_{12}H^+$) species. For cyclohexane ices, we show that the hydrogenation process is effective up to the formation of $C_6H_{15}^+$, evidencing a ring opening mechanism activation after electron impact. We suggest that highly hydrogenated molecules, such as alkanes and cycloalkanes, could be formed in the ISM and CSM as desorption products of benzene- and substituted benzene-rich astrophysical ices.

9.2 Observational Results

We have analyzed the full ASAI spectral line survey of IRAS 4A, carried out between 72 and 276 GHz with the IRAM 30m telescope. We have detected 92 molecular species, including the rare isotopologues, and identified a grand total of 1456 rotational transitions including narrow and wide components. We confirm the molecular richness previously reported by the ASAI team (Lefloch et al., 2018). The spectrum is dominated by the emission of O-bearing molecular species. S-bearing species are also found very abundant.

We could discriminate the signature of the protostellar core, characterized by narrow to moderately narrow linewidths (2-5 km s^{-1}) from the signature of the outflow powered by the protostar, which display broader linewidths, up to 25-30 km s^{-1}.

The molecular gas column densities and the rotational temperature of molecular species were derived using the method of population diagram analysis (i.e. taking into account and correcting for the line opacity effects in the rotational diagram).

When gathering the results of the population diagram analysis for the different elemental groups, we see that the molecular line emission can be roughly classified into three components, each of them with specific physical properties:

- A component of low-excitation, with typical T_{ex}= 10-30K. We interpret this component as the external, cold and extended protostellar envelope.
- A component of moderate excitation, with typical T_{ex}= 40-60K. This component is best detected in the high-excitation lines of molecular species $E_{up} \geq$ 50K. This component is less extended that the cold envelope. A crude estimate based on a multi-isotopologue OCS analysis suggests a size of the order of 20 arcs.
- A component of high excitation, with typical T_{ex}= 80-200K. We could not constrain the size of this component. We propose that this component arises from the inner protostellar region, of hot and dense gas. Taquet et al. (2015) estimated a size of 0.2 arcs for the hot corino of IRAS 4A, from PdBI observations. Their observations of CH_3OH in the 2mm band yields an excitation temperature in the range 150-250K, in rough agreement with the ASAI results. Given the similarity of excitation temperature, the size estimated by Taquet et al. (2015) is probably a reasonable estimate for the size of the ASAI emission.

This decomposition is somewhat arbitrary: variations are observed in the excitation temperatures of molecular species, even within each group. It merely reflects the presence of a thermal and density gradients inside the protostellar envelope of IRAS 4A. Observationally, it appears as a break in the slope of rotational diagram best fits near E_{up}= 50 K and E_{up}= 100 K.

A strong chemical differentiation is observed between the three excitation components:

- The high excitation component is detected only in lines of CH_3OH, CH_2DOH CH_3CHO and OCS. For many molecular species, only transitions with E_{up} less than 50-60 K were detected. The IRAS 4A study by Taquet et al. (2015) suggests that the lack of detection of more species is essentially an observational bias due to our limited (though excellent single-dish) sensitivity. The similarity of the CH_3OH excitation conditions indicates that we have detected the signature of the hot corino of IRAS 4A, i.e. the region with a rich content in complex organic molecules where the icy mantles evaporates of the dust grain. Due to the limited sensitivity of the IRAM 30m, the hot corino is detected only in a few molecular species.
- Carbon-bearing species are mainly detected in the cold outer envelope of low-excitation gas (10K). The only species detected in the warm component is CH_3CCH. We can exclude an observational bias as the range of E_{up} is broad enough. Hence, some C-species disappear from the gas phase towards the inner protostellar regions.

9.3 Published Papers

[1] Lefloch, B.; Bachiller, R.;...; Quitián-Lara H. M.; et al. Astrochemical Evolution Along Star Formation: Overview of the IRAM Large Program ASAI. *Monthly Notices of the Royal Astronomical Society*, **2018**, *477*, 4792-4809.

[2] Quitián-Lara, H. M.; Fantuzzi, F.; Nascimento, M. A. C.; Wolff, W.; Boechat-Roberty, H. M. Hydrogenated Benzene in Circumstellar Environments: Insights into the Photostability of Super-hydrogenated PAHs. *The Astrophysical Journal*, **2018**, *854(1)*, 61.

[3] Monfredini T.; Quitián-Lara H. M.; Fantuzzi F.; Wolff W.; Mendoza E.; Lago A. F.; Sales D. A.;Pastoriza M. G.; Boechat-Roberty H. M. Destruction and multiple ionization of PAHs by X-rays in circumnuclear regions of AGNs. *Monthly Notices of the Royal Astronomical Society*, **2019**, *488*, 451-469.

[4] Fantuzzi F.; Wolff W.; Quitián-Lara H. M.; Boechat-Roberty H. M.; Hilgers G.; Rudek B.; Nascimento M. A. C. Unexpected reversal of stability in strained systems containing one-electron bonds. *Physical Chemistry Chemical Physics*, **2019**, *21(45)*, 24984-24992.

9.4 Conference Papers

[5] Quitián-Lara, H. M.; Ribeiro, F.; Andrade, D. P.; Rocco, M. L.; Wolff, W.; Boechat-Roberty, H. M. Protonation and hydrogenation of benzene molecule on a surface grain. *Boletim da Sociedade Astronômica Brasileira*, **2018**, *29*, n/a.

[6] Quitián-Lara, H. M.; Lefloch, B.; Boechat-Roberty, H. M. Identification of organic molecules in the protostellar region NGC 1333-IRAS 4A. *Boletim da Sociedade Astronômica Brasileira*, **2018**, *29*, n/a.

[7] Quitián-Lara, H. M.; Wolff, W.; Boechat-Roberty, H. M. Stability of the hydrogenated benzene in the PDR of the planetary nebula NGC 7027. *Revista Mexicana de Astronomía y Astrofísica (Serie de Conferencias)*, **2017**, *49*, 172.

9.5 Papers in Preparation

[8] Molecular survey of the Protostellar Object NGC 1333-IRAS 4A as part of the Large Program ASAI. *In preparation*.

[9] Dissociative Single and Double Photoionization of Biphenyl by Soft X-rays in Planetary Nebulae. *In preparation*.

Bibliography

Abplanalp, M. J., Frigge, R., and Kaiser, R. I. (2019). Low-temperature synthesis of polycyclic aromatic hydrocarbons in Titan's surface ices and on airless bodies. Science Advances, 5(10):eaaw5841.

Agúndez, M., Cernicharo, J., and Guélin, M. (2007). Discovery of Phosphaethyne (HCP) in Space: Phosphorus Chemistry in Circumstellar Envelopes. Astrophys. J., 662(2):L91–L94.

Agúndez, M., Goicoechea, J. R., Cernicharo, J., Faure, A., and Roueff, E. (2010). THE CHEMISTRY OF VIBRATIONALLY EXCITED H ₂ IN THE INTERSTELLAR MEDIUM. Astrophys. J., 713(1):662–670.

Agúndez, M. and Wakelam, V. (2013). Chemistry of Dark Clouds: Databases, Networks, and Models. Chem. Rev., 113(12):8710–8737.

Ali, A., Ismail, H. A., and Alsolami, Z. (2015). A new statistical distance scale for planetary nebulae. Astrophys. Space Sci., 357(1).

Allamandola, L. J., Hudgins, D. M., and Sandford, S. A. (1999). Modeling the Unidentified Infrared Emission with Combinations of Polycyclic Aromatic Hydrocarbons. Astrophys. J., 511(2):L115–L119.

Allamandola, L. J., Tielens, G. G. M., and Barker, J. R. (1989). Interstellar polycyclic aromatic hydrocarbons - The infrared emission bands, the excitation/emission mechanism, and the astrophysical implications. Astrophys. J. Suppl. Ser., 71:733.

Almenningen, A., Bastiansen, O., Fernholt, L., Cyvin, B. N., Cyvin, S. J., and Samdal, S. (1985). Structure and barrier of internal rotation of biphenyl derivatives in the gaseous state. J. Mol. Struct., 128(1-3):59–76.

Alonso-Herrero, A., Esquej, P., Roche, P. F., Ramos Almeida, C., González-Martín, O., Packham, C., Levenson, N. A., Mason, R. E., Hernán-Caballero, A., Pereira-Santaella, M., Alvarez, C., Aretxaga, I., López-Rodríguez, E., Colina, L., Díaz-Santos, T., Imanishi, M., Rodríguez Espinosa, J. M., and Perlman, E. (2016). A mid-infrared spectroscopic atlas of local active galactic nuclei on sub-arcsecond resolution using GTC/CanariCam. Mon. Not. R. Astron. Soc., 455(1):563–583.

Alonso-Herrero, A., Ramos Almeida, C., Esquej, P., Roche, P. F., Hernán-Caballero, A., Hönig, S. F., González-Martín, O., Aretxaga, I., Mason, R. E., Packham, C., Levenson, N. A., Rodríguez Espinosa, J. M., Siebenmorgen, R., Pereira-Santaella, M., Díaz-Santos, T., Colina, L., Alvarez, C., and Telesco, C. M. (2014). Nuclear 11.3 μm PAH emission in local active galactic nuclei. Mon. Not. R. Astron. Soc., 443(3):2766–2782.

Altwegg, K., Balsiger, H., Bar-Nun, A., Berthelier, J.-J., Bieler, A., Bochsler, P., Briois, C., Calmonte, U., Combi, M. R., Cottin, H., De Keyser, J., Dhooghe, F., Fiethe, B., Fuselier, S. A., Gasc, S., Gombosi, T. I., Hansen, K. C., Haessig, M., Jäckel, A., Kopp, E., Korth, A., Le Roy, L., Mall, U., Marty, B., Mousis, O., Owen, T., Rème, H., Rubin, M., Sémon, T., Tzou, C.-Y., Hunter Waite, J., and Wurz, P. (2016). Prebiotic chemicals—amino acid and phosphorus—in the coma of comet 67P/Churyumov-Gerasimenko. Science Advances, 2(5):e1600285.

Andrade, D. P. P., Rocco, M. L. M., and Boechat-Roberty, H. M. (2010). X-ray photodesorption from methanol ice. Mon. Not. R. Astron. Soc., 409(3):1289–1296.

Andre, P., Ward-Thompson, D., and Barsony, M. (1993). Submillimeter continuum observations of Rho Ophiuchi A - The candidate protostar VLA 1623 and prestellar clumps. Astrophys. J., 406:122.

André, P., Ward-Thompson, G., and Barsony, M. (2000). From Prestellar Cores to Protostars: the Initial Conditions of Star Formation. In Mannings, V., Boss, A. P., and Russell, S. S., editors, Protostars Planets IV, pages 59–96. The University of Arizona Press, Tucson.

Antonucci, R. (1993). Unified Models for Active Galactic Nuclei and Quasars. Annu. Rev. Astron. Astrophys., 31(1):473–521.

Arion, T. B. (2008). Ionization and fragmentation of chalcogene clusters by highly charged ions and synchrotron radiation. PhD Thesis, Freie Universität Berlin, pages 1–144.

Arnoult, K. M., Wdowiak, T. J., and Beegle, L. W. (2000). Laboratory investigation of the contribution of complex aromatic/aliphatic polycyclic hybrid molecular structures to interstellar ultraviolet extinction and infrared emission. Astrophys. J., 535:815–822.

Arulmozhiraja, S. and Fujii, T. (2001). Torsional barrier, ionization potential, and electron affinity of biphenyl—A theoretical study. J. Chem. Phys., 115(23):10589–10594.

Atkins, P. and Friedman, R. (2005). Molecular Quantum Mechanics. Oxford University Press, Oxford, 4th edition.

Baars, J., Greve, A., Hein, H., Morris, D., Penalver, J., and Thum, C. (1994). Design parameters and measured performance of the IRAM 30-m Millimeter Radio Telescope. Proceedings of the IEEE, 82(5):687–696.

Bacmann, A., Lefloch, B., Ceccarelli, C., Steinacker, J., Castets, A., and Loinard, L. (2003). CO Depletion and Deuterium Fractionation in Prestellar Cores. Astrophys. J., 585(1):L55–L58.

Baldo, M. A., Lamansky, S., Burrows, P. E., Thompson, M. E., and Forrest, S. R. (1999). Very high-efficiency green organic light-emitting devices based on electrophosphorescence. Appl. Phys. Lett., 75(1):4–6.

Ballantyne, D. R. (2008). Obscuring Active Galactic Nuclei with Nuclear Starburst Disks. Astrophys. J., 685(2):787–800.

Bally, J., Walawender, J., Johnstone, D., Kirk, H., and Goodman, A. (2008). The Perseus Cloud, volume 4, page 308.

Banisaukas, J., Szczepanski, J., Eyler, J., Vala, M., Hirata, S., Head-Gordon, M., Oomens, J., Meijer, G., and von Helden, G. (2003). Vibrational and Electronic Spectroscopy of Acenaphthylene and Its Cation. J. Phys. Chem. A, 107(6):782–793.

Barai, P., Proga, D., and Nagamine, K. (2012). Multiphase, non-spherical gas accretion on to a black hole. Mon. Not. R. Astron. Soc., 424(1):728–746.

Basile, B. P., Middleditch, B. S., and Oró, J. (1984). Polycyclic aromatic hydrocarbons in the Murchison meteorite. Org. Geochem., 5(4):211–216.

Bastiansen, O. and Samdal, S. (1985). Structure and barrier of internal rotation of biphenyl derivatives in the gaseous state. J. Mol. Struct., 128(1-3):115–125.

Belloche, A. and André, P. (2004). Disappearance of N 2Hˆ+ from the gas phase in the class 0 protostar IRAM 04191. Astron. Astrophys., 419(3):L35–L38.

Belloche, A., Garrod, R. T., Muller, H. S. P., and Menten, K. M. (2014). Detection of a branched alkyl molecule in the interstellar medium: iso-propyl cyanide. Science (80-.)., 345(6204):1584–1587.

Benz, R. C. and Dunbar, R. C. (1979). Photodissociation spectroscopy of alkane radical cations. J. Am. Chem. Soc., 101(21):6363–6366.

Bergin, E. A. and Langer, W. D. (1997). Chemical Evolution in Preprotostellar and Protostellar Cores. Astrophys. J., 486(1):316–328.

Bergin, E. A. and Tafalla, M. (2007). Cold Dark Clouds: The Initial Conditions for Star Formation. Annual Review of Astronomy and Astrophysics, 45(1):339–396.

Berkowitz, J. (2002). Atomic and Molecular Photoabsorption Absolute Total Cross Sections. Academic Press, 2002. ISBN: 0-12-091841-2.

Bernard, J. P., Giard, M., Normand, P., and Tiphene, D. (1994). PAH distribution in BD+30^{o}3639. 289:524–538.

Bernard-Salas, J., Pottasch, S. R., Beintema, D. A., and Wesselius, P. R. (2001). The ISO-SWS spectrum of planetary nebula NGC 7027. Astron. Astrophys., 367(3):949–958.

Bernard-Salas, J. and Tielens, a. G. G. M. (2005). Physical conditions in Photo-Dissociation Regions around Planetary Nebulae. Astron. Astrophys., 431:523–538.

Bernatowicz, T. J., Cowsik, R., Gibbons, P. C., Lodders, K., Fegley, B., Amari, S., and Lewis, R. S. (1996). Constraints on Stellar Grain Formation from Presolar Graphite in the Murchison Meteorite. Astrophys. J., 472(2):760–782.

Berresheim, A. J., Müller, M., and Müllen, K. (1999). Polyphenylene Nanostructures. Chem. Rev., 99(7):1747–1786.

Bertoldi, F. and McKee, C. F. (1992). Pressure-confined clumps in magnetized molecular clouds. Astrophys. J., 395:140.

Biczysko, M., Bloino, J., and Puzzarini, C. (2018). Computational challenges in Astrochemistry. WIREs Comput. Mol. Sci., 8(3).

Boechat-Roberty, H. M., Neves, R., Pilling, S., Lago, A. F., and De Souza, G. G. B. (2009a). Dissociation of the benzene molecule by ultraviolet and soft X-rays in circumstellar environment. Mon. Not. R. Astron. Soc., 394(2):810–817.

Boechat-Roberty, H. M., Neves, R., Pilling, S., Lago, A. F., and de Souza, G. G. B. (2009b). Dissociation of the benzene molecule by ultraviolet and soft X-rays in circumstellar environment. Mon. Not. R. Astron. Soc., 394(2):810–817.

Boersma, C., Bregman, J., and Allamandola, L. J. (2014). Properties of Polycyclic Aromatic Hydrocarbons in the Northwest Photon Dominated Region of NGC 7023. II. Traditional PAH Analysis Using k-means as a Visualization Tool. Astrophys. J., 795:110.

Boersma, C., Mattioda, a. L., Bauschlicher, C. W., Peeters, E., Tielens, a. G. G. M., and Allamandola, L. J. (2009). THE 5.25 AND 5.7 μm ASTRONOMICAL POLYCYCLIC AROMATIC HYDROCARBON EMISSION FEATURES. Astrophys. J., 690(2):1208–1221.

Boese, R., Niederprüm, N., and Bläser, D. (1992). Comparative study by single crystal X-ray structure determinations of tetramethylaminoborane and tetramethylethene at 110 K. Structural Chemistry, 3(6):399–406.

Bonnar, W. B. (1956). Boyle's Law and Gravitational Instability. Mon. Not. R. Astron. Soc., 116(3):351–359.

Bonnell, I. A., Bate, M. R., and Vine, S. G. (2003). The hierarchical formation of a stellar cluster. Mon. Not. R. Astron. Soc., 343(2):413–418.

Borchers, F., Levsen, K., Schwarz, H., Wesdemiotis, C., and Wolfschuetz, R. (1977). Isomerization of hydrocarbon ions. 7. Ring opening reactions in cycloalkane molecular ions. A collisional activation and field ionization kinetic study. J. Am. Chem. Soc., 99(6):1716–1721.

Bottinelli, S., Ceccarelli, C., Lefloch, B., Williams, J. P., Castets, A., Caux, E., Cazaux, S., Maret, S., Parise, B., and Tielens, A. G. G. M. (2004). Complex Molecules in the Hot Core of the Low-Mass Protostar NGC 1333 IRAS 4A. Astrophys. J., 615(1):354–358.

Bottinelli, S., Ceccarelli, C., Williams, J. P., and Lefloch, B. (2007). Hot corinos in NGC1333-IRAS4B and IRAS2A. Astron. Astrophys., 463:601–610.

Brandl, B. R., Bernard-Salas, J., Spoon, H. W. W., Devost, D., Sloan, G. C., Guilles, S., Wu, Y., Houck, J. R., Weedman, D. W., Armus, L., Appleton, P. N., Soifer, B. T., Charmandaris, V., Hao, L., Higdon, J. A. Marshall, S. J., and Herter, T. L. (2006). The Mid-Infrared Properties of Starburst Galaxies from Spitzer -IRS Spectroscopy. Astrophys. J., 653(2):1129–1144.

Buchanan, A. C., Livingston, R., Dworkin, A. S., and Smith, G. P. (1980). Electron spin resonance study of the generation of stable arene radical cations in molten antimony trichloride. The Journal of Physical Chemistry, 84(4):423–427.

Buntinx, G. and Poizat, O. (1989). Triplet (T 1) state and radical cation resonance Raman investigation of biphenyl derivatives. J. Chem. Phys., 91(4):2153–2162.

Burdick, G., Shields, G., Appling, J., and Moran, T. (1985). Structures, energetics and fragmentation pathways of CnH22+ carbodications. Int. J. Mass Spectrom. Ion Process., 64(3):315–333.

Burke, D. J. and Brown, W. A. (2010). Ice in space: surface science investigations of the thermal desorption of model interstellar ices on dust grain analogue surfaces. Phys. Chem. Chem. Phys., 12(23):5947.

Burkhart, B. (2018). The Star Formation Rate in the Gravoturbulent Interstellar Medium. Astrophys. J., 863(2):118.

Candian, A., Bouwman, J., Hemberger, P., Bodi, A., and Tielens, A. G. G. M. (2018). Dissociative ionisation of adamantane: a combined theoretical and experimental study. Phys. Chem. Chem. Phys.

Cardozo, T. M., Fantuzzi, F., and Nascimento, M. A. C. (2014). The non-covalent nature of the molecular structure of the benzene molecule. Phys. Chem. Chem. Phys., 16(22):11024.

Carelli, F., Sebastianelli, F., Satta, M., and Gianturco, F. A. (2011). Gas-phase route to polycyclic aromatic hydrocarbon formation in protoplanetary atmospheres: Role of stabilized benzyne anions. Mon. Not. R. Astron. Soc., 415(1):425–430.

Carey, F. A. and Sundberg, R. J. (2007). Advanced Organic Chemistry. Advanced Organic Chemistry. Springer US, Boston, MA.

Carravetta, V., Ågren, H., and Cesar, A. (1988). Discrete-continuum interaction for the core-hole state of water. Chem. Phys. Lett., 148(2-3):210–214.

Carroll, B. and Ostlie, D. (2007). An Introduction to Modern Astrophysics. Pearson Addison-Wesley.

Cazaux, S., Boschman, L., Rougeau, N., Reitsma, G., Hoekstra, R., Teillet-Billy, D., Morisset, S., Spaans, M., and Schlathölter, T. (2016). The sequence to hydrogenate coronene cations: A journey guided by magic numbers. Sci. Rep., 6(November 2015):19835.

Cazaux, S., Tielens, A. G. G. M., Ceccarelli, C., Castets, A., Wakelam, V., Caux, E., Parise, B., and Teyssier, D. (2003). The Hot Core around the Low-mass Protostar IRAS 16293-2422: Scoundrels Rule! Astrophys. J. Lett., 593(1):L51–L55.

Ceccarelli, C., Caselli, P., Bockelée-Morvan, D., Mousis, O., Pizzarello, S., Robert, F., and Semenov, D. (2014). Deuterium Fractionation: The Ariadne's Thread from the Precollapse Phase to Meteorites and Comets Today. In Protostars Planets VI. University of Arizona Press.

Ceccarelli, C., Caselli, P., Fontani, F., Neri, R., López-Sepulcre, A., Codella, C., Feng, S., Jiménez-Serra, I., Lefloch, B., Pineda, J. E., Vastel, C., Alves, F., Bachiller, R., Balucani, N., Bianchi, E., Bizzocchi, L., Bottinelli, S., Caux, E., Chacón-Tanarro, A., Choudhury, R., Coutens, A., Dulieu, F., Favre, C., Hily-Blant, P., Holdship, J., Kahane, C., Al-Edhari, A. J., Laas, J., Ospina, J., Oya, Y., Podio, L., Pon, A., Punanova, A., Quenard, D., Rimola, A., Sakai, N., Sims, I. R., Spezzano, S., Taquet, V., Testi, L., Theulé, P., Ugliengo, P., Vasyunin, A. I., Viti, S., Wiesenfeld, L., and Yamamoto, S. (2017). Seeds Of Life In Space (SOLIS): The Organic Composition Diversity at 300–1000 au Scale in Solar-type Star-forming Regions. Astrophys. J., 850(2):176.

Ceccarelli, C., Caselli, P., Herbst, E., Tielens, A. G. G. M., and Caux, E. (2007). Extreme Deuteration and Hot Corinos: The Earliest Chemical Signatures of Low-Mass Star Formation. In Reipurth, B., Jewitt, D., and Keil, K., editors, Protostars and Planets V, page 47.

CESR and IRAP (2019). Centre d'Analyse Scientifique de Spectres Instrumentaux et Synthétiques - CASSIS- software.

Chakraborty, A., Fulara, J., Dietsche, R., and Maier, J. P. (2014). Spectroscopic characterization of $C_7H_3^+$ and $C_7H_3^{\cdot}$: electronic absorption and fluorescence in 6 K neon matrices. Phys. Chem. Chem. Phys., 16(15):7023–7030.

Chen, M., Crasemann, B., and Mark, H. (1981). Widths and fluorescence yields of atomic L-shell vacancy states. Phys. Rev. A, 24(1):177–182.

Cheng, C. L., Murthy, D. S. N., and Ritchie, G. L. D. (1972). Molecular conformations from magnetic anisotropies. J. Chem. Soc. Faraday Trans. 2, 68:1679.

Cherchneff, I., Barker, J. R., and Tielens, A. G. G. M. (1992). Polycyclic Aromatic Hydrocarbon Formation in Carbon-rich Stellar Envelopes. Astrophys. J., 401:269–287.

Chuang, K. J., Fedoseev, G., Ioppolo, S., van Dishoeck, E. F., and Linnartz, H. (2016). H-atom addition and abstraction reactions in mixed CO, H_2CO and CH_3OH ices - an extended view on complex organic molecule formation. Mon. Not. R. Astron. Soc., 455(2):1702–1712.

Chyba, C. F. and Hand, K. P. (2005). Astrobiology: The Study of the Living Universe. Annu. Rev. Astron. Astrophys., 43(1):31–74.

Cleeves, L. I., Bergin, E. A., Alexander, C. M. O., Du, F., Graninger, D., Oberg, K. I., and Harries, T. J. (2014). The ancient heritage of water ice in the solar system. Science, 345(6204):1590–1593.

Codella, C., Ceccarelli, C., Cabrit, S., Gueth, F., Podio, L., Bachiller, R., Fontani, F., Gusdorf, A., Lefloch, B., Leurini, S., and Tafalla, M. (2016). Water and acetaldehyde in HH212: The first hot corino in Orion. Astron. Astrophys., 586:L3.

Codella, C., Ceccarelli, C., Lefloch, B., Fontani, F., Busquet, G., Caselli, P., Kahane, C., Lis, D., Taquet, V., Vasta, M., Viti, S., and Wiesenfeld, L. (2012). THE HERSCHEL AND IRAM CHESS SPECTRAL SURVEYS OF THE PROTOSTELLAR SHOCK L1157-B1: FOSSIL DEUTERATION. Astrophys. J., 757(1):L9.

Cohen, M. and Barlow, M. J. (2005). Polycyclic aromatic hydrocarbon emission bands in selected planetary nebulae: A study of the behaviour with gas phase C/O ratio. Mon. Not. R. Astron. Soc., 362(4):1199–1207.

Cohen, Y., Klein, J., and Rabinovitz, M. (1988). The charge alternation concept. Application to cyclic conjugated doubly charged systems. J. Am. Chem. Soc., 110(14):4634–4640.

Comastri, A., Setti, G., Zamorani, G., and Hasinger, G. (1995). The contribution of AGNs to the X-ray background. Astron. Astrophys., 296:1–12.

Congiu, E., Fedoseev, G., Ioppolo, S., Dulieu, F., Chaabouni, H., Baouche, S., Lemaire, J. L., Laffon, C., Parent, P., Lamberts, T., Cuppen, H. M., and Linnartz, H. (2012). NO ICE HYDROGENATION: A SOLID PATHWAY TO NH_2OH FORMATION IN SPACE. Astrophys. J., 750(1):L12.

Constantinidis, P., Schmitt, H.-C., Fischer, I., Yan, B., and Rijs, A. M. (2015). Formation of polycyclic aromatic hydrocarbons from bimolecular reactions of phenyl radicals at high temperatures. Phys. Chem. Chem. Phys., 17(43):29064–29071.

Cottin, H., Moore, M. H., and Benilan, Y. (2003). Photodestruction of Relevant Interstellar Molecules in Ice Mixtures. Astrophys. J., 590(2):874–881.

Cox, P., Maillard, J., Huggins, P. J., Forveille, T., Simons, D., Guilloteau, S., Rigaut, F., Bachiller, R., and Omont, A. (1997). Molecular hydrogen morphology, kinematics and excitation in AFGL 2688 and NGC 7027. Astron. Astrophys., 321:907–920.

Cruz-Diaz, G. A., Erickson, S. E., da Silveira, E. F., Ricca, A., de Barros, A. L. F., da Costa, C. A. P., Pereira, R. C., and Mattioda, A. L. (2019). PAH Products and Processing by Different Energy Sources. Astrophys. J., 882(1):44.

Cuppen, H. M., Walsh, C., Lamberts, T., Semenov, D., Garrod, R. T., Penteado, E. M., and Ioppolo, S. (2017). Grain Surface Models and Data for Astrochemistry. Space Sci. Rev., 212(1-2):1–58.

Deguchi, S., Izumiura, H., Kaifu, N., Mao, X., Nguyen-Q-Rieu, and Ukita, N. (1990). Molecular envelope of the planetary nebula NGC 7027. Astrophys. J., 351:522.

Delgado-Inglada, G. and Rodríguez, M. (2014). C/O abundance ratios, iron depletions, and infrared dust features in galactic planetary nebulae. Astrophys. J., 784(2).

Deo, R. P., Crenshaw, D. M., Kraemer, S. B., Dietrich, M., Elitzur, M., Teplitz, H., and Turner, T. J. (2007). Spitzer IRS Observations of Seyfert 1.8 and 1.9 Galaxies: A Comparison with Seyfert 1 and Seyfert 2. Astrophys. J., 671(1):124–135.

Desai, V., Armus, L., Spoon, H. W. W., Charmandaris, V., Bernard-Salas, J., Brandl, B. R., Farrah, D., Soifer, B. T., Teplitz, H. I., Ogle, P. M., Devost, D., Higdon, S. J. U., Marshall, J. A., and Houck, J. R. (2007). PAH Emission from Ultraluminous Infrared Galaxies. Astrophys. J., 669:810–820.

Dewar, M. J. S. and Worley, S. D. (1969). Photoelectron Spectra of Molecules. I. Ionization Potentials of Some Organic Molecules and Their Interpretation. J. Chem. Phys., 50(2):654–667.

Di Francesco, J., Evans II, N. J., Caselli, P., Myers, P. C., Shirley, Y., Aikawa, Y., and Tafalla, M. (2006). An Observational Perspective of Low-Mass Dense Cores I:Internal Physical and Chemical Properties. In Reipurth, B., Jewitt, D., and Keil, K., editors, Protostars Planets V, pages 17–32. University of Arizona Press.

Di Matteo, T., Springel, V., and Hernquist, L. (2005). Energy input from quasars regulates the growth and activity of black holes and their host galaxies. Nature, 433(7026):604–607.

Diamond-Stanic, A. M. and Rieke, G. H. (2010). The Effect of Active Galactic Nuclei on the Mid-infrared Aromatic Features. Astrophys. J., 724:140–153.

Doering, J. P., Gedanken, A., Hitchock, A. P., Fischer, P., Moore, J., Olthoff, J. K., Tossell, J., Raghavachari, K., and Robin, M. B. (1986). Electronic excitation and .pi.-electron interaction in borazine. J. Am. Chem. Soc., 108(13):3602–3608.

Draine, B. T. (2011). Physics of the Interstellar and Intergalactic Medium. Princeton University Press, New Jersey.

Draine, B. T. and Li, A. (2001). Infrared Emission from Interstellar Dust. I. Stochastic Heating of Small Grains. Astrophys. J., 551:807–824.

Draine, B. T. and Li, A. (2007). Infrared Emission from Interstellar Dust. IV. The Silicate-Graphite-PAH Model in the Post-Spitzer Era. Astrophys. J., 657:810–837.

Drescher, M., Hentschel, M., Kienberger, R., Uiberacker, M., Yakovlev, V., Scrinzi, A., Westerwalbesloh, T., Kleineberg, U., Heinzmann, U., and Krausz, F. (2002). Time-resolved atomic inner-shell spectroscopy. Nature, 419(6909):803–807.

Duley, W. W. and Hu, A. (2012). THE 217.5 nm BAND, INFRARED ABSORPTION, AND INFRARED EMISSION FEATURES IN HYDROGENATED AMORPHOUS CARBON NANOPARTICLES. Astrophys. J., 761(2):115.

Dunbar, R. C. (1976). Identification of characteristic chromophores in gas-phase ions by photodissociation spectroscopy. Anal. Chem., 48(4):723–726.

Dunbar, R. C. (1984). Photodissociation in the icr ion trap. In Bowers, M. T., editor, Gas Phase Ion Chemistry, Volume 3: Ions and Light, pages 130–167. Academic Press.

Ebert, R. (1955). Über die Verdichtung von H I-Gebieten. Mit 5 Textabbildungen. Z. Astrophys., 37:217–232.

Ebrero, J., Costantini, E., Kaastra, J. S., Detmers, R. G., Arav, N., Kriss, G. A., Korista, K. T., and Steenbrugge, K. C. (2010). XMM- Newton RGS observation of the warm absorber in Mrk 279. Astron. Astrophys., 520:A36.

Ekern, S. P., Marshall, A. G., Szczepanski, J., and Vala, M. (1998). Photodissociation of Gas-Phase Polycylic Aromatic Hydrocarbon Cations. J. Phys. Chem. A, 102(20):3498–3504.

Eland, J. (1987). The dynamics of three-body dissociations of dications studied by the triple coincidence technique PEPIPICO. Mol. Phys., 61(3):725–745.

Elitzur, M. (1992). Astronomical Masers. Annu. Rev. Astron. Astrophys., 30(1):75–112.

Emprechtinger, M., Caselli, P., Volgenau, N. H., Stutzki, J., and Wiedner, M. C. (2009). The N_2D^+/N_2H^+ ratio as an evolutionary tracer of Class 0 protostars. Astron. Astrophys., 493(1):89–105.

Erickson, R., Lund, A., and Lindgren, M. (1995). Analysis of powder EPR and ENDOR spectra of the biphenyl radical cation on H-ZSM-5 zeolite, silica gel and in CFCl3 matrix. Chem. Phys., 193(1-2):89–99.

Esparza-Arredondo, D., González-Martín, O., Dultzin, D., Alonso-Herrero, A., Almeida, C. R., Díaz-Santos, T., García-Bernete, I., Martinez-Paredes, M., and Rodríguez-Espinosa, J. M. (2018). Circumnuclear Star Formation and AGN Activity: Clues from Surface Brightness Radial Profile of PAHs and [S IV]. Astrophys. J., 859(2):124.

Esquej, P., Alonso-Herrero, A., González-Martín, O., Hönig, S. F., Hernán-Caballero, A., Roche, P., Ramos Almeida, C., Mason, R. E., Díaz-Santos, T., Levenson, N. A., Aretxaga, I., Rodríguez Espinosa, J. M., and Packham, C. (2013). NUCLEAR STAR FORMATION ACTIVITY AND BLACK HOLE ACCRETION IN NEARBY SEYFERT GALAXIES. Astrophys. J., 780(1):86.

Esquej, P., Alonso-Herrero, A., González-Martín, O., Hönig, S. F., Hernán-Caballero, A., Roche, P., Ramos Almeida, C., Mason, R. E., Díaz-Santos, T., Levenson, N. A., Aretxaga, I., Rodríguez Espinosa, J. M., and Packham, C. (2014). Nuclear Star Formation Activity and Black Hole Accretion in Nearby Seyfert Galaxies. Astrophys. J., 780:86.

Fantuzzi, F., de Sousa, D. W. O., and Chaer Nascimento, M. A. (2017a). Chemical bonding in the pentagonal-pyramidal benzene dication and analogous isoelectronic hexa-coordinate species. Comput. Theor. Chem., 1116:225–233.

Fantuzzi, F., de Sousa, D. W. O., and Nascimento, M. A. C. (2017b). The Nature of the Chemical Bond from a Quantum Mechanical Interference Perspective. ChemistrySelect, 2(2):604–619.

Fantuzzi, F., Pilling, S., Santos, A. C. F., Baptista, L., Rocha, A. B., and Boechat-Roberty, H. M. (2011). Photodissociation of methyl formate in circumstellar environment: Stability under soft X-rays. Mon. Not. R. Astron. Soc., 417(4):2631–2641.

Fantuzzi, F., Wolff, W., Quitián-Lara, H. M., Boechat-Roberty, H. M., Hilgers, G., Rudek, B., and Nascimento, M. A. C. (2019). Unexpected reversal of stability in strained systems containing one-electron bonds. Phys. Chem. Chem. Phys., 21(45):24984–24992.

Faroon, O. and Ruiz, P. (2016). Polychlorinated biphenyls: New evidence from the last decade. Toxicol. Ind. Health, 32(11):1825–1847.

Federrath, C. (2015). Inefficient star formation through turbulence, magnetic fields and feedback. Mon. Not. R. Astron. Soc., 450(4):4035–4042.

Fedoseev, G., Ioppolo, S., Lamberts, T., Zhen, J. F., Cuppen, H. M., and Linnartz, H. (2012). Efficient surface formation route of interstellar hydroxylamine through NO hydrogenation. II. The multilayer regime in interstellar relevant ices. J. Chem. Phys., 137(5):054714.

Ferrarese, L. and Ford, H. (2005). Supermassive Black Holes in Galactic Nuclei: Past, Present and Future Research. Space Sci. Rev., 116(3-4):523–624.

Flower, D. R., Pineau des Forêts, G., and Walmsley, C. M. (2006). The abundances of nitrogen-containing molecules during pre-protostellar collapse. Astron. Astrophys., 456(1):215–223.

Foppa, L. and Dupont, J. (2015). Benzene partial hydrogenation: advances and perspectives. Chem. Soc. Rev., 44(7):1886–1897.

Freeman, M. J. and Kastner, J. H. (2016). A MULTI-WAVELENGTH 3D MODEL OF BD+30^{o}3639. Astrophys. J. Suppl. Ser., 226(2):15.

Frenklach, M. and Feigelson, E. (1989). Formation of polycyclic aromatic hydrocarbons in circumstellar envelopes. Astrophys. J., 341:372–384.

Fuente, A., Cernicharo, J., Roueff, E., Gerin, M., Pety, J., Marcelino, N., Bachiller, R., Lefloch, B., Roncero, O., and Aguado, A. (2016). Ionization fraction and the enhanced sulfur chemistry in Barnard 1. Astron. Astrophys., 593:A94.

Fuente, A., Martın-Pintado, J., Bachiller, R., Rodrıguez-Franco, A., and Palla, F. (2002). The history of mass dispersal around Herbig Ae/Be stars. Astron. Astrophys., 387(3):977–992.

Fulara, J., Freivogel, P., Forney, D., and Maier, J. P. (1995). Electronic absorption spectra of linear carbon chains in neon matrices. III. HC 2 n +1 H. J. Chem. Phys., 103(20):8805–8810.

Furuya, K., Torii, H., Furukawa, Y., and Tasumi, M. (1998). Density functional study on the structures and vibrational spectra of the radical anion and cation of biphenyl. J. Mol. Struct. THEOCHEM, 424(3):225–235.

Gallart, C., Zoccali, M., and Aparicio, A. (2005). The Adequacy of Stellar Evolution Models for the Interpretation of the Color-Magnitude Diagrams of Resolved Stellar Populations. Annu. Rev. Astron. Astrophys., 43(1):387–434.

Garrod, R. T., Weaver, S. L. W., and Herbst, E. (2008). Complex Chemistry in Star-forming Regions: An Expanded Gas-Grain Warm-up Chemical Model. Astrophys. J., 682(1):283–302.

Gatchell, M., Stockett, M. H., de Ruette, N., Chen, T., Giacomozzi, L., Nascimento, R. F., Wolf, M., Anderson, E. K., Delaunay, R., Vizcaino, V., Rousseau, P., Adoui, L., Huber, B. A., Schmidt, H. T., Zettergren, H., and Cederquist, H. (2015). Failure of hydrogenation in protecting polycyclic aromatic hydrocarbons from fragmentation. Phys. Rev. A, 92(5):050702.

Glassgold, A. E., Omont, A., and Guelin, M. (1992). Protonated acetylene - an important circumstellar and interstellar ion. Astrophys. J., 396:115.

Goicoechea, J. R., Cernicharo, J., Masso, H., and Senent, M. L. (2004). A New Unidentified Far-Infrared Band in NGC 7027. Astrophys. J., 609(1):225–230.

Goldsmith, P. F. and Langer, W. D. (1999). Population Diagram Analysis of Molecular Line Emission. Astrophys. J., 517(1):209–225.

Goodman, A. A., Rosolowsky, E. W., Borkin, M. A., Foster, J. B., Halle, M., Kauffmann, J., and Pineda, J. E. (2009). A role for self-gravity at multiple length scales in the process of star formation. Nature, 457(7225):63–66.

Gorai, P. (2018). Explaining Major Sources of Sulfur-Bearing Molecules in the Interstellar Medium. pages 467–475.

Górny, S. K., Stasińska, G., Szczerba, R., and Tylenda, R. (2001). Infrared properties of planetary nebulae with [WR] central stars. Astron. Astrophys., 377(3):1007–1015.

Gorti, U. and Hollenbach, D. (2004). Models of Chemistry, Thermal Balance, and Infrared Spectra from Intermediate-Aged Disks around G and K Stars. Astrophys. J., 613:424–447.

Gu, Q. and Huang, J. (2002). Seyfert 2 Galaxies with Spectropolarimetric Observations. Astrophys. J., 579(1):205–213.

Guerrero, M. A., Chu, Y., and Gruendl, R. A. (2000). ROSAT Observations of X-Ray Emission from Planetary Nebulae. Astrophys. J. Suppl. Ser., 129(1):295–313.

Guilhaus, M. (1995). Special feature: Tutorial. Principles and instrumentation in time-of-flight mass spectrometry. Physical and instrumental concepts. J. Mass Spectrom., 30(11):1519–1532.

Guzman-Ramirez, L., Lagadec, E., Jones, D., Zijlstra, A. A., and Gesicki, K. (2014). PAH formation in O-rich planetary nebulae. Mon. Not. R. Astron. Soc., 441(1):364–377.

Guzman-Ramirez, L., Lagadec, E., Jones, D., Zijlstra, A. A., and Gesicki, K. (2015). PAH Formation in O-rich Evolved Stars, volume 497 of Astron. Soc. Pacific Conf. Ser., page 155.

Häfelinger, G. and Regelmann, C. (1987). Refined ab initio 6-31G split-valence basis set optimization of the molecular structures of biphenyl in twisted, planar, and perpendicular conformations. J. Comput. Chem., 8(7):1057–1065.

Hasegawa, T. and Kwok, S. (2001). Molecular Line Emissions from the Photodissociation Region of NGC 7027. Astron. Astrophys., 562:824–841.

Hasegawa, T., Volk, K., and Kwok, S. (2000). A Chemical Model of the Neutral Envelope of the Planetary Nebula NGC 7027. Astrophys. J., 532(2):994–1005.

Hasegawa, T. I. and Kwok, S. (2003). Neutral Carbon in Post–Asymptotic Giant Branch Stars and Planetary Nebulae. Astrophys. J., 585(1):475–481.

Hayatsu, R., Matsuoka, S., Scott, R. G., Studier, M. H., and Anders, E. (1977). Origin of organic matter in the early solar system—VII. The organic polymer in carbonaceous chondrites. Geochim. Cosmochim. Acta, 41(9):1325–1339.

Henke, B. L., Gullikson, E. M., and Davis, J. C. (1993). X-ray interactions: photoabsorption, scattering, transmission and reflection at E= 50-30000 eV, Z=1-92. Atomic Data and Nuclear Data Tables, 54:181–342.

Henke, B. L., Lee, P., Tanaka, T. J., Shimabukuro, R. L., and Fujikawa, B. K. (1982). Low-Energy X-Ray Interaction Coefficients: Photoabsorption, Scattering and Reflection, E = 100-2000 eV, Z = 1-94. Atomic Data and Nuclear Data Tables, 27:1.

Hennebelle, P. and Falgarone, E. (2012). Turbulent molecular clouds. Astron. Astrophys. Rev., 20(1):55.

Henning, T. (2010). Astromineralogy, volume 815 of Lect. Notes Phys. Springer Berlin Heidelberg, Berlin, Heidelberg.

Herbst, E. and van Dishoeck, E. F. (2009). Complex Organic Interstellar Molecules. Annu. Rev. Astron. Astrophys., 47(1):427–480.

Hernández-Trujillo, J. and Matta, C. F. (2007). Hydrogen–hydrogen bonding in biphenyl revisited. Struct. Chem., 18(6):849–857.

Hickox, R. C. and Alexander, D. M. (2018). Obscured Active Galactic Nuclei. Annu. Rev. Astron. Astrophys., 56(1):625–671.

Higuchi, A. E., Sakai, N., Watanabe, Y., López-Sepulcre, A., Yoshida, K., Oya, Y., Imai, M., Zhang, Y., Ceccarelli, C., Lefloch, B., Codella, C., Bachiller, R., Hirota, T., Sakai, T., and Yamamoto, S. (2018). Chemical Survey toward Young Stellar Objects in the Perseus Molecular Cloud Complex. Astrophys. J. Suppl. Ser., 236(2):52.

Hitchcock, A. and Brion, C. (1980a). Inner-shell excitation of formaldehyde, acetaldehyde and acetone studied by electron impact. J. Electron Spectros. Relat. Phenomen., 19(2):231–250.

Hitchcock, A. and Brion, C. (1980b). K-shell excitation spectra of CO, N2 and O2. J. Electron Spectros. Relat. Phenomen., 18(1):1–21.

Hitchcock, A. and Mancini, D. (1994). Bibliography and database of inner shell excitation spectra of gas phase atoms and molecules. J. Electron Spectros. Relat. Phenomen., 67(1):vii.

Hitchcock, A. and Rühl, E. (1989). Near edge spectroscopy of free molecules. Phys. B Condens. Matter, 158(1-3):403–404.

Hitchcock, A. P., Fischer, P., Gedanken, A., and Robin, M. B. (1987). Antibonding .sigma.* valence MOs in the inner-shell and outer-shell spectra of the fluorobenzenes. J. Phys. Chem., 91(3):531–540.

Hitchcock, A. P., Newbury, D. C., Ishii, I., Stöhr, J., Horsley, J. A., Redwing, R. D., Johnson, A. L., and Sette, F. (1986). Carbon K -shell excitation of gaseous and condensed cyclic hydrocarbons: C_3H_6, C_4H_8, C_5H_8, C_5H_{10}, C_6H_{10}, C_6H_{12}, and C_8H_8. J. Chem. Phys., 85(9):4849–4862.

Hogeveen, H. and Kwant, P. (1973). Direct observation of a remarkably stable dication of unusual structure: $(CCH_3)_6^{2+}$. Tetrahedron Lett., 14(19):1665–1670.

Holman, M. W., Yan, P., Ching, K.-C., Liu, R., Ishak, F. I., and Adams, D. M. (2005). A conformational switch of intramolecular electron transfer. Chem. Phys. Lett., 413(4-6):501–505.

Horsley, J. A., Stöhr, J., Hitchcock, A. P., Newbury, D. C., Johnson, A. L., and Sette, F. (1985). Resonances in the K shell excitation spectra of benzene and pyridine: Gas phase, solid, and chemisorbed states. J. Chem. Phys., 83(12):6099–6107.

Hrušák, J., Schröder, D., and Iwata, S. (1997). The ground state (1A1) and the lowest triplet state (3B1) of the phenyl cation C6H5+ revisited. J. Chem. Phys., 106(18):7541–7549.

Hsia, C.-H., Sadjadi, S., Zhang, Y., and Kwok, S. (2016). THE 6 μ m FEATURE AS A TRACER OF ALIPHATIC COMPONENTS OF INTERSTELLAR CARBONACEOUS GRAINS. Astrophys. J., 832(2):213.

Huang, Y., Aponte, J. C., Zhao, J., Tarozo, R., and Hallmann, C. (2015). Hydrogen and carbon isotopic ratios of polycyclic aromatic compounds in two CM2 carbonaceous chondrites and implications for prebiotic organic synthesis. Earth Planet. Sci. Lett., 426:101–108.

Izumi, T., Wada, K., Fukushige, R., Hamamura, S., and Kohno, K. (2018). Circumnuclear Multiphase Gas in the Circinus Galaxy. II. The Molecular and Atomic Obscuring Structures Revealed with ALMA. Astrophys. J., 867(1):48.

Jacobsen, S. K., Jørgensen, J. K., Di Francesco, J., Evans, N. J., Choi, M., and Lee, J.-E. (2019). Organic chemistry in the innermost, infalling envelope of the Class 0 protostar L483. Astron. Astrophys., 629:A29.

Jašík, J., Gerlich, D., and Roithová, J. (2014). Probing Isomers of the Benzene Dication in a Low-Temperature Trap. J. Am. Chem. Soc., 136(8):2960–2962.

Jeans, J. H. (1902). The Stability of a Spherical Nebula. Philos. T. R. Soc. A Royal Society A: Mathematical, Physical and Engineering Sciences, 199(312-320):1–53.

Jenkins, S., Maza, J. R., Xu, T., Jiajun, D., and Kirk, S. R. (2015). Biphenyl: A stress tensor and vector-based perspective explored within the quantum theory of atoms in molecules. Int. J. Quantum Chem., 115(23):1678–1690.

Jensen, J. J., Hönig, S. F., Rakshit, S., Alonso-Herrero, A., Asmus, D., Gandhi, P., Kishimoto, M., Smette, A., and Tristram, K. R. W. (2017). PAH features within few hundred parsecs of active galactic nuclei. Mon. Not. R. Astron. Soc., 470:3071–3094.

Jia, W. L., Feng, X. D., Bai, D. R., Lu, Z. H., Wang, S., and Vamvounis, G. (2005). Mes 2 B(p- 4,4‘-biphenyl-NPh(1-naphthyl)): A Multifunctional Molecule for Electroluminescent Devices. Chem. Mater., 17(1):164–170.

Jochims, H., Rühl, E., Baumgärtel, H., Tobita, S., and Leach, S. (1997). VUV peaks in absorption spectra and photoion yield curves of polycyclic aromatic hydrocarbons and related compounds. Int. J. Mass Spectrom. Ion Process., 167-168:35–53.

Jochims, H. W., Baumgaertel, H., and Leach, S. (1996). Photoionization quantum yields of polycyclic aromatic hydrocarbons. Astron. Astrophys., 314:1003–1009.

Jochims, H. W., Baumgärtel, H., and Leach, S. (1999). Structure-dependent Photostability of Polycyclic Aromatic Hydrocarbon Cations: Laboratory Studies and Astrophysical Implications. Astrophys. J., 512:500–510.

Jochims, H. W., Ruhl, E., Baumgartel, H., Tobita, S., and Leach, S. (1994). Size effects on dissociation rates of polycyclic aromatic hydrocarbon cations: Laboratory studies and astophysical implications. Astrophys. J., 420:307–317.

Johansson, K. O., Head-Gordon, M. P., Schrader, P. E., Wilson, K. R., and Michelsen, H. A. (2018). Resonance-stabilized hydrocarbon-radical chain reactions may explain soot inception and growth. Science (80-.)., 361(6406):997–1000.

Johansson, M. P. and Olsen, J. (2008). Torsional Barriers and Equilibrium Angle of Biphenyl: Reconciling Theory with Experiment. J. Chem. Theory Comput., 4(9):1460–1471.

Johnson III, R. D. (2013). NIST Computational Chemistry Comparison and Benchmark Database.

Jones, A. P., Tielens, A. G. G. M., and Hollenbach, D. J. (1996). Grain Shattering in Shocks: The Interstellar Grain Size Distribution. Astrophys. J., 469:740.

Jones, A. P., Tielens, A. G. G. M., Hollenbach, D. J., and McKee, C. F. (1994). Grain destruction in shocks in the interstellar medium. Astrophys. J., 433:797.

Jones, B. M., Zhang, F., Kaiser, R. I., Jamal, A., Mebel, A. M., Cordiner, M. A., and Charnley, S. B. (2011). Formation of benzene in the interstellar medium. Proc. Natl. Acad. Sci., 108(2):452–457.

Kaiser, D., Reusch, E., Hemberger, P., Bodi, A., Welz, E., Engels, B., and Fischer, I. (2018). The ortho -benzyne cation is not planar. Phys. Chem. Chem. Phys., 20(6):3988–3996.

Kaiser, R. I., Parker, D. S., and Mebel, A. M. (2015). Reaction Dynamics in Astrochemistry: Low-Temperature Pathways to Polycyclic Aromatic Hydrocarbons in the Interstellar Medium. Annu. Rev. Phys. Chem., 66(1):43–67.

Kakhiani, K., Lourderaj, U., Hu, W., Birney, D., and Hase, W. L. (2009). Cyclohexane Isomerization. Unimolecular Dynamics of the Twist-Boat Intermediate †. J. Phys. Chem. A, 113(16):4570–4580.

Kamraj, N., Harrison, F. A., Baloković, M., Lohfink, A., and Brightman, M. (2018). Coronal Properties of Swift /BAT-selected Seyfert 1 AGNs Observed with NuSTAR. Astrophys. J., 866(2):124.

Kaneda, H., Onaka, T., Sakon, I., Kitayama, T., Okada, Y., and Suzuki, T. (2008). Properties of Polycyclic Aromatic Hydrocarbons in Local Elliptical Galaxies Revealed by the Infrared Spectrograph on Spitzer. Astrophys. J., 684:270–281.

Kania-Korwel, I., Parkin, S., Robertson, L. W., and Lehmler, H.-J. (2004). Synthesis of polychlorinated biphenyls and their metabolites with a modified Suzuki-coupling. Chemosphere, 56(8):735–744.

Kara, E., García, J. A., Lohfink, A., Fabian, A. C., Reynolds, C. S., Tombesi, F., and Wilkins, D. R. (2017). The high-Eddington NLS1 Ark 564 has the coolest corona. Mon. Not. R. Astron. Soc., 468(3):3489–3498.

Karska, A., Herczeg, G. J., van Dishoeck, E. F., Wampfler, S. F., Kristensen, L. E., Goicoechea, J. R., Visser, R., Nisini, B., San José-García, I., Bruderer, S., Śniady, P., Doty, S., Fedele, D., Yıldız, U. A., Benz, A. O., Bergin, E., Caselli, P., Herpin, F., Hogerheijde, M. R., Johnstone, D., Jørgensen, J. K., Liseau, R., Tafalla, M., van der Tak, F., and Wyrowski, F. (2013). Water in star-forming regions with Herschel (WISH). Astron. Astrophys., 552:A141.

Karttunen, H., Kröger, P., Oja, H., Poutanen, M., and Donner, K. J., editors (2003). Fundamental Astronomy. Springer Berlin Heidelberg, Berlin, Heidelberg.

Kastner, J. H., Montez, Jr, R., Balick, B., and De Marco, O. (2008). Serendipitous Chandra X-Ray Detection of a Hot Bubble within the Planetary Nebula NGC 5315. Astrophys. J., 672(2):957–961.

Kastner, J. H., Vrtilek, S. D., and Soker, N. (2001). Discovery of Extended X-Ray Emission from the Planetary Nebula NGC 7027 by the [ITAL]Chandra X-Ray Observatory[/ITAL]. Astrophys. J., 550(2):L189–L192.

Kawakatu, N. and Wada, K. (2008). Coevolution of Supermassive Black Holes and Circumnuclear Disks. Astrophys. J., 681(1):73–83.

Kirk, J. M., Ward-Thompson, D., and André, P. (2005). The initial conditions of isolated star formation - VI. SCUBA mapping of pre-stellar cores. Mon. Not. R. Astron. Soc., 360(4):1506–1526.

Klein, J. E. M. N., Havenith, R. W. A., and Knizia, G. (2018). The Pentagonal-Pyramidal Hexamethylbenzene Dication: Many Shades of Coordination Chemistry at Carbon. Chem. - A Eur. J., 24(47):12340–12345.

Kolczewski, C., Püttner, R., Martins, M., Schlachter, A. S., Snell, G., Sant'Anna, M. M., Hermann, K., and Kaindl, G. (2006). Spectroscopic analysis of small organic molecules: A comprehensive

near-edge x-ray-absorption fine-structure study of C 6 -ring-containing molecules. J. Chem. Phys., 124(3).

Korich, A. L., McBee, I. A., Bennion, J. C., Gifford, J. I., and Hughes, T. S. (2014). Synthesis and Photophysical Properties of Biphenyl and Terphenyl Arylene–Ethynylene Macrocycles. J. Org. Chem., 79(4):1594–1610.

Koumpia, E., Semenov, D. A., van der Tak, F. F. S., Boogert, A. C. A., and Caux, E. (2017). The chemical structure of the Class 0 protostellar envelope NGC 1333 IRAS 4A. Astron. Astrophys., 603:A88.

Kramer, C. (1997). Calibration of spectral line data at the IRAM 30m radio telescope. Technical report.

Kramer, C. (2018). IRAM 30-meter Telescope: Observing Capabilities and Organisation. Technical report.

Krumholz, M. R. (2014). The big problems in star formation: The star formation rate, stellar clustering, and the initial mass function. Phys. Rep., 539(2):49–134.

Kutner, M. L. and Ulich, B. L. (1981). Recommendations for calibration of millimeter-wavelength spectral line data. Astrophys. J., 250:341.

Lada, C. J. (1987). Star Formation: From OB Associations to Protostars. In Star Form. Reg., pages 1–18. Springer Netherlands, Dordrecht.

Lada, E. A., Strom, K. M., and Myers, P. C. (1993). Environments of Star Formation - Relationship Between Molecular Clouds Dense Cores and Young Stars. In Levy, E. H. and Lunine, J. I., editors, Protostars and Planets III, page 245.

Lagache, G., Dole, H., Puget, J.-L., Pérez-González, P. G., Le Floc'h, E., Rieke, G. H., Papovich, C., Egami, E., Alonso-Herrero, A., Engelbracht, C. W., Gordon, K. D., Misselt, K. A., and Morrison, J. E. (2004). Polycyclic Aromatic Hydrocarbon Contribution to the Infrared Output Energy of the Universe at z $\simeq$ 2. Astrophys. J. Suppl. Ser., 154:112–117.

Lammertsma, K. and Schleyer, P. v. R. (1988). Structures and energies of isomeric carbodications (C5H42+ and C6H42+). J. Phys. Chem., 92(4):881–886.

Langer, W. D., Castets, A., and Lefloch, B. (1996). The IRAS 2 and IRAS 4 Outflows and Star Formation in NGC 1333. Astrophys. J., 471(2):L111–L114.

Lattelais, M., Pauzat, F., Ellinger, Y., and Ceccarelli, C. (2009). INTERSTELLAR COMPLEX ORGANIC MOLECULES AND THE MINIMUM ENERGY PRINCIPLE. Astrophys. J., 696(2):L133–L136.

Latter, W. B., Dayal, A., Bieging, J. H., Meakin, C., Hora, J. L., Kelly, D. M., and Tielens, A. G. G. M. (2000). Revealing the Photodissociation Region: HST/NICMOS Imaging of NGC 7027. Astrophys. J., 539(2):783.

Lau, R. M., Werner, M., Sahai, R., and Ressler, M. E. (2016). EVIDENCE FROM SOFIA IMAGING OF POLYCYCLIC AROMATIC HYDROCARBON FORMATION ALONG A RECENT OUTFLOW IN NGC 7027. Astrophys. J., 833(1):115.

Le Page, V., Snow, T. P., and Bierbaum, V. M. (2003). Hydrogenation and Charge States of Polycyclic Aromatic Hydrocarbons in Diffuse Clouds. II. Results. Astrophys. J., 584:316–330.

Leach, S., Eland, J. H. D., and Price, S. D. (1989a). Formation and Dissociation of Dications of Naphthalene, Azulene, and Related Heterocyclic Compounds. J. Phys. Chem, 93:7575–7583.

Leach, S., Eland, J. H. D., and Price, S. D. (1989b). Formation and dissociation of dications of naphthalene-d8. J. Phys. Chem, 93:7583–7593.

Lee, K. L. K., McGuire, B. A., and McCarthy, M. C. (2019). Gas-phase synthetic pathways to benzene and benzonitrile: a combined microwave and thermochemical investigation. Physical Chemistry Chemical Physics, 21(6):2946–2956.

Lefloch, B., Bachiller, R., Ceccarelli, C., Cernicharo, J., Codella, C., Fuente, A., Kahane, C., López-Sepulcre, A., Tafalla, M., Vastel, C., Caux, E., González-García, M., Bianchi, E., Gómez-Ruiz, A., Holdship, J., Mendoza, E., Ospina-Zamudio, J., Podio, L., Quénard, D., Roueff, E., Sakai, N., Viti, S., Yamamoto, S., Yoshida, K., Favre, C., Monfredini, T., Quitián-Lara, H. M., Marcelino, N., Boechat-Roberty, H. M., and Cabrit, S. (2018). Astrochemical evolution along star formation: overview of the IRAM Large Program ASAI. Mon. Not. R. Astron. Soc., 477(4):4792–4809.

Lefloch, B., Castets, A., Cernicharo, J., Langer, W. D., and Zylka, R. (1998). Cores and cavities in NGC 1333. Astron. Astrophys., 334:269–279.

Lefloch, B., Castets, A., Cernicharo, J., and Loinard, L. (1998). Widespread s[CLC]i[/CLC]o emission in NGC 1333. Astrophys. J., 504(2):L109–L112.

Lefloch, B., Vastel, C., Viti, S., Jimenez-Serra, I., Codella, C., Podio, L., Ceccarelli, C., Mendoza, E., Lepine, J. R. D., and Bachiller, R. (2016). Phosphorus-bearing molecules in solar-type star-forming regions: first PO detection. Mon. Not. R. Astron. Soc., 462(4):3937–3944.

Leventis, N., Hanna, S. B., and Sotiriou-Leventis, C. (1997). A Three-Dimensional Energy Surface for the Conformational Inversion of Cyclohexane. J. Chem. Educ., 74(7):813.

Li, A. and Draine, B. T. (2002). Infrared Emission from Interstellar Dust. III. The Small Magellanic Cloud. Astrophys. J., 576(2):762–772.

Li, A. and Draine, B. T. (2012). the Carriers of the Interstellar Unidentified Infrared Emission Features: Aromatic or Aliphatic? Astrophys. J., 760(2):L35.

Li, J., Harrington, J. P., and Borkowski, K. J. (2002). The Angular Expansion and Distance of the Planetary Nebula BD $+30^o$3639. Astron. J., 123(5):2676–2688.

Li, J., Huang, W., Xu, T., Kirk, S. R., and Jenkins, S. (2018). A vector-based representation of the chemical bond for the substituted torsion of biphenyl. Chem. Phys. Lett., 702:32–37.

Li, J., Shen, Z., Wang, J., Chen, X., Li, D., Wu, Y., Dong, J., Zhao, R., Gou, W., Wang, J., Li, S., Wang, B., and Zheng, X. (2017). Widespread Presence of Glycolaldehyde and Ethylene Glycol around Sagittarius B2. Astrophys. J., 849(2):115.

Li, W., Evans II, N. J., and Lada, E. A. (1997). Looking for Distributed Star Formation in L1630: A Near-Infrared (J , H , K) Survey. Astrophys. J., 488(1):277–285.

Lindon, J., Tranter, G. E., and Koppenaal, D. (2016). Encyclopedia of Spectroscopy and Spectrometry. Academic Press.

Linke, R. A., Frerking, M. A., and Thaddeus, P. (1979). Interstellar methyl mercaptan. Astrophys. J., 234:L139.

Linnartz, H., Bossa, J.-B., Bouwman, J., Cuppen, H. M., Cuylle, S. H., van Dishoeck, E. F., Fayolle, E. C., Fedoseev, G., Fuchs, G. W., Ioppolo, S., Isokoski, K., Lamberts, T., Öberg, K. I., Romanzin,

C., Tenenbaum, E., and Zhen, J. (2011). Solid State Pathways towards Molecular Complexity in Space. Proc. IAU, 7(S280):390–404.

Lo, S.-C., Bera, R. N., Harding, R. E., Burn, P. L., and Samuel, I. D. W. (2008). Solution-Processible Phosphorescent Blue Dendrimers Based on Biphenyl-Dendrons and Fac - tris(phenyltriazolyl)iridium(III) Cores. Adv. Funct. Mater., 18(19):3080–3090.

Lo, S.-C., Namdas, E. B., Burn, P. L., and Samuel, I. D. W. (2003). Synthesis and Properties of Highly Efficient Electroluminescent Green Phosphorescent Iridium Cored Dendrimers. Macromolecules, 36(26):9721–9730.

Longair, M. S. (1994). Classical Cosmology. pages 369–379.

López-Sepulcre, A., Sakai, N., Neri, R., Imai, M., Oya, Y., Ceccarelli, C., Higuchi, A. E., Aikawa, Y., Bottinelli, S., Caux, E., Hirota, T., Kahane, C., Lefloch, B., Vastel, C., Watanabe, Y., and Yamamoto, S. (2017). Complex organics in IRAS 4A revisited with ALMA and PdBI: Striking contrast between two neighbouring protostellar cores. Astron. Astrophys., 606:A121.

Lubiński, P., Beckmann, V., Gibaud, L., Paltani, S., Papadakis, I. E., Ricci, C., Soldi, S., Türler, M., Walter, R., and Zdziarski, A. A. (2016). A comprehensive analysis of the hard X-ray spectra of bright Seyfert galaxies. Mon. Not. R. Astron. Soc., 458(3):2454–2475.

Lutz, D., Spoon, H. W. W., Rigopoulou, D., Moorwood, A. F. M., and Genzel, R. (1998). The Nature and Evolution of Ultraluminous Infrared Galaxies:A Mid-Infrared Spectroscopic Survey. Astrophys. J., 505(2):L103–L107.

Maaskant, K. M., Min, M., Waters, L. B. F. M., and Tielens, A. G. G. M. (2014). Polycyclic aromatic hydrocarbon ionization as a tracer of gas flows through protoplanetary disk gaps. Astron. Astrophys., 563:A78.

Mac Low, M.-M. and Klessen, R. S. (2004). Control of star formation by supersonic turbulence. Rev. Mod. Phys., 76(1):125–194.

Maciel, J. B., Morikawa, E., and de Souza, G. G. B. (1997). A new time-of-flight mass spectrometer for electron-ion and ion-ion coincidence experiments (PEPICO, PIPICO and PEPIPICO). AIP Conf. Proc., (417):22–25.

Malischewski, M. and Seppelt, K. (2017). Crystal Structure Determination of the Pentagonal-Pyramidal Hexamethylbenzene Dication C 6 (CH 3) 6 2+. Angew. Chemie Int. Ed., 56(1):368–370.

Maness, H. L., Vrtilek, S. D., Kastner, J. H., and Soker, N. (2003). Abundance anomalies in the X-ray spectra of planetary nebulae NGC 7027 and BD +30 degrees 3639. Astrophys. J., 589(1):439–443.

Marcelino, N., Cernicharo, J., Roueff, E., Gerin, M., and Mauersberger, R. (2005). Deuterated Thioformaldehyde in the Barnard 1 Cloud. Astrophys. J., 620(1):308–320.

Marciniak, A., Despré, V., Barillot, T., Rouzée, A., Galbraith, M., Klei, J., Yang, C.-H., Smeenk, C., Loriot, V., Reddy, S. N., Tielens, A., Mahapatra, S., Kuleff, A. I., Vrakking, M., and Lépine, F. (2015). XUV excitation followed by ultrafast non-adiabatic relaxation in PAH molecules as a femto-astrochemistry experiment. Nat. Commun., 6:7909.

Marcolino, W. L. F., Hillier, D. J., de Araujo, F. X., and Pereira, C. B. (2007). Detailed Far-Ultraviolet to Optical Analysis of Four [WR] Stars. Astrophys. J., 654(2):1068–1086.

Martín, N. and Scott, L. T. (2015). Challenges in aromaticity: 150 years after Kekulé's benzene. Chem. Soc. Rev., 44(18):2013–2016.

Martin-Drumel, M. A., Pirali, O., Falvo, C., Parneix, P., Gamboa, A., Calvo, F., and Bréchignac, P. (2014). Low-energy vibrational spectra of flexible diphenyl molecules: biphenyl, diphenylmethane, bibenzyl and 2-, 3- and 4-phenyltoluene. Phys. Chem. Chem. Phys., 16(40):22062–22072.

Martinez-Sansigre, A., Lacy, M., Sajina, A., and Rawlings, S. (2008). Mid-Infrared Spectroscopy of High-Redshift Obscured Quasars. Astrophys. J., 674(2):676–685.

Masson, C. R. (1986). Angular expansion measurement with the VLA - The distance to NGC 7027. Astrophys. J., 302:L27.

Materese, C. K., Nuevo, M., and Sandford, S. A. (2015). N - AND O -HETEROCYCLES PRODUCED FROM THE IRRADIATION OF BENZENE AND NAPHTHALENE IN H 2 O/NH 3 -CONTAINING ICES. Astrophys. J., 800(2):116.

Matsumoto, H., Sakon, I., Onaka, T., Sako, S., Miyata, T., Kataza, H., Okada, Y., Okamoto, Y. K., Honda, M., Yamashita, T., Takahashi, H., and Fujiyoshi, T. (2008). Mid-Infrared Observations of Planetary Nebula BD +30 3639: Evolution and Distribution of Unidentified IR Band Carriers. Astrophys. J., 677(2):1120–1131.

Matta, C. F., Hernández-Trujillo, J., Tang, T.-H., and Bader, R. F. W. (2003). Hydrogen–Hydrogen Bonding: A Stabilizing Interaction in Molecules and Crystals. Chem. - A Eur. J., 9(9):1940–1951.

Matthewman, R., Martins, Z., and Sephton, M. A. (2013). Type IV Kerogens as Analogues for Organic Macromolecular Materials in Aqueously Altered Carbonaceous Chondrites. Astrobiology, 13(4):324–333.

Mazzarella, J. M., Voit, G. M., Soifer, B. T., Matthews, K., Graham, J. R., Armus, L., and Shupe, D. (1994). Near-infrared continuum and 3.3 micrometer(s) polycyclic aromatic hydrocarbon imaging of the starburst ring in the type 1 Seyfert galaxy NGC 7469. Astron. J., 107:1274.

McKee, C., Zweibel, E., Goodman, A., and Heiles, C. (1993). Magnetic Fields in Star-Forming Regions - Theory. In Levy, E. H. and Lunine, J. I., editors, Protostars and Planets III, pages 327–366. University of Arizona Press, Tucson.

McKee, C. F. and Ostriker, E. C. (2007). Theory of Star Formation. Annu. Rev. Astron. Astrophys., 45(1):565–687.

Mendoza, E. (2014). Estudo experimental e observacional de moléculas prebióticas em ambientes circunstelares. PhD thesis, Observatório do Valongo-UFRJ.

Menéndez-Delmestre, K., Blain, A. W., Smail, I., Alexander, D. M., Chapman, S. C., Armus, L., Frayer, D., Ivison, R. J., and Teplitz, H. (2009). Mid-Infrared Spectroscopy of Submillimeter Galaxies: Extended Star Formation in Massive High-redshift Galaxies. Astrophys. J., 699:667–685.

Menor-Salván, C., Ruiz-Bermejo, M., Osuna-Esteban, S., Muñoz-Caro, G., and Veintemillas-Verdaguer, S. (2008). Synthesis of Polycyclic Aromatic Hydrocarbons and Acetylene Polymers in Ice: A Prebiotic Scenario. Chem. Biodivers., 5(12):2729–2739.

Merino, P., Švec, M., Martinez, J., Jelinek, P., Lacovig, P., Dalmiglio, M., Lizzit, S., Soukiassian, P., Cernicharo, J., and Martin-Gago, J. (2014). Graphene etching on SiC grains as a path to interstellar polycyclic aromatic hydrocarbons formation. Nature Communications, 5(1):3054.

Messenger, S., Amari, S., Gao, X., Walker, R. M., Clemett, S. J., Chillier, X. D. F., Zare, R. N., and Lewis, R. S. (1998). Indigenous Polycyclic Aromatic Hydrocarbons in Circumstellar Graphite Grains from Primitive Meteorites. Astrophys. J., 502(1):284–295.

Micelotta, E. R., Jones, A. P., and Tielens, A. G. G. M. (2010a). Polycyclic aromatic hydrocarbon processing in a hot gas. Astron. Astrophys., 510:A37.

Micelotta, E. R., Jones, A. P., and Tielens, A. G. G. M. (2010b). Polycyclic aromatic hydrocarbon processing in interstellar shocks. Astron. Astrophys., 510:A36.

Micelotta, E. R., Jones, A. P., and Tielens, A. G. G. M. (2011). Polycyclic aromatic hydrocarbon processing by cosmic rays. Astron. Astrophys., 526:A52.

Milam, S. N., Halfen, D. T., Tenenbaum, E. D., Apponi, A. J., Woolf, N. J., and Ziurys, L. M. (2008). Constraining Phosphorus Chemistry in Carbon- and Oxygen-Rich Circumstellar Envelopes: Observations of PN, HCP, and CP. Astrophys. J., 684(1):618–625.

Miller, J. M., Bachetti, M., Barret, D., Harrison, F. A., Fabian, A. C., Webb, N. A., Walton, D. J., and Rana, V. (2014). PATCHY ACCRETION DISKS IN ULTRA-LUMINOUS X-RAY SOURCES. Astrophys. J., 785(1):L7.

Mimura, K. (1995). Synthesis of polycyclic aromatic hydrocarbons from benzene by impact shock: Its reaction mechanism and cosmochemical significance. Geochim. Cosmochim. Acta, 59(3):579–591.

Minkov, I., Gel'mukhano, F., Ågren, H., Friedlein, R., Suess, C., and Salaneck, W. R. (2005). Core Excitations of Biphenyl. J. Phys. Chem. A, 109(7):1330–1336.

Monfredini, T. (2015). PRODUÇÃO DE ÍONS VIA DESTRUIÇÃO DEHIDROCARBONETOS AROMÁTICOS POLICÍCLICOS PORRAIOS X E A DETECÇÃO DE ÍONS MOLECULARES EM OBJETOS ESTELARES JOVENS. PhD thesis, Observatório do Valongo - Universidade Federal do Rio de Janeiro.

Monfredini, T., Fantuzzi, F., Nascimento, M. A. C., Wolff, W., and Boechat-Roberty, H. M. (2016). Single and Double Photoionization and Photodissociation of Toluene By Soft X-Rays in a Circumstellar Environment. Astrophys. J., 821(1):4.

Monfredini, T., Quitián-Lara, H. M., Fantuzzi, F., Wolff, W., Mendoza, E., Lago, A. F., Sales, D. A., Pastoriza, M. G., and Boechat-Roberty, H. M. (2019). Destruction and multiple ionization of PAHs by X-rays in circumnuclear regions of AGNs. Mon. Not. R. Astron. Soc., 488(1):451–469.

Monteiro, H. and Falceta-Gonçalves, D. (2011). THREE-DIMENSIONAL PHOTOIONIZATION STRUCTURE AND DISTANCES OF PLANETARY NEBULAE. IV. NGC 40. Astrophys. J., 738(2):174.

Montez, R. and Kastner, J. H. (2018). Dissecting the X-Ray Emission in the Young Planetary Nebula NGC 7027. Astrophys. J., 861(1):45.

Montez Jr., R., Kastner, J. H., Balick, B., Behar, E., Blackman, E., Bujarrabal, V., Chu, Y.-H., Corradi, R. L. M., De Marco, O., Frank, A., Freeman, M., Frew, D. J., Guerrero, M. A., Jones, D., Lopez, J. A., Miszalski, B., Nordhaus, J., Parker, Q. A., Sahai, R., Sandin, C., Schonberner, D., Soker, N., Sokoloski, J. L., Steffen, M., Toalá, J. A., Ueta, T., Villaver, E., and Zijlstra, A. (2015). THE CHANDRA PLANETARY NEBULA SURVEY (ChanPlaNS). III. X-RAY EMISSION FROM THE CENTRAL STARS OF PLANETARY NEBULAE. Astrophys. J., 800(1):8.

Montillaud, J., Joblin, C., and Toublanc, D. (2013). Evolution of polycyclic aromatic hydrocarbons in photodissociation regions. Hydrogenation and charge states. Astron. Astrophys., 552:15.

Moret, M.-E., Zhang, L., and Peters, J. C. (2013). A Polar Copper–Boron One-Electron σ-Bond. J. Am. Chem. Soc., 135(10):3792–3795.

Morris, M. and Jura, M. (1983). Molecular self-shielding in the outflows from late-type stars. Astrophys. J., 264:546.

Motte, F. and André, P. (2001). The circumstellar environment of low-mass protostars: A millimeter continuum mapping survey. Astron. Astrophys., 365(3):440–464.

Mouschovias, T. C. (1991). Magnetic braking, ambipolar diffusion, cloud cores, and star formation - Natural length scales and protostellar masses. Astrophys. J., 373:169.

Müller, H. S., Schlöder, F., Stutzki, J., and Winnewisser, G. (2005). The Cologne Database for Molecular Spectroscopy, CDMS: a useful tool for astronomers and spectroscopists. J. Mol. Struc., 742(1-3):215–227.

Müller, H. S. P., Endres, C. P., Stutzki, J., and Schlemmer, S. (2018). Molecules in space. Website: https://www.astro.uni-koeln.de/cdms/molecules.

Murashima, M., Kokubun, M., Makishima, K., Kotoku, J., Murakami, H., Matsushita, K., Hayashida, K., Arnaud, K., Hamaguchi, K., and Matsumoto, H. (2006). Suzaku Reveals Helium-burning Products in the X-Ray-emitting Planetary Nebula BD +30 3639. Astrophys. J., 647(2):L131–L134.

Mushotzky, R. F., Cowie, L. L., Barger, A. J., and Arnaud, K. A. (2000). Resolving the extragalactic hard X-ray background. Nature, 404(6777):459–464.

Mühlhauser, M., Haubrich, J., Mpourmpakis, G., Mavrandonakis, A., and Froudakis, G. E. (2003). Ab initio MR-CI investigation of linear HC_5H^+ and HC_7H^+. Internet Electron. J. Mol. Des., 2(9):578–588.

Nejad-Asghar, M. (2007). Formation of fluctuations in a molecular slab via isobaric thermal instability. Mon. Not. R. Astron. Soc., 379(1):222–228.

Netzer, H. (2015). Revisiting the Unified Model of Active Galactic Nuclei. Annu. Rev. Astron. Astrophys., 53(1):365–408.

Nicolaides, A., Smith, D. M., Jensen, F., and Radom, L. (1997). Phenyl Radical, Cation, and Anion. The Triplet–Singlet Gap and Higher Excited States of the Phenyl Cation. J. Am. Chem. Soc., 119(34):8083–8088.

Öberg, K. I. (2016). Photochemistry and Astrochemistry: Photochemical Pathways to Interstellar Complex Organic Molecules. Chem. Rev., 116(17):9631–9663.

Öberg, K. I., van der Marel, N., Kristensen, L. E., and van Dishoeck, E. F. (2011). Complex Molecules toward Low-mass Protostars: The Serpens Core. Astrophys. J., 740(1):14.

O'Dowd, M. J., Schiminovich, D., Johnson, B. D., Treyer, M. A., Martin, C. D., Wyder, T. K., Charlot, S., Heckman, T. M., Martins, L. P., Seibert, M., and van der Hulst, J. M. (2009). POLYCYCLIC AROMATIC HYDROCARBONS IN GALAXIES AT $z \simeq 0.1$: THE EFFECT OF STAR FORMATION AND ACTIVE GALACTIC NUCLEI. Astrophys. J., 705(1):885–898.

Oey, M. S., López-Hernández, J., Kellar, J. A., Pellegrini, E. W., Gordon, K. D., Jameson, K. E., Li, A., Madden, S. C., Meixner, M., Roman-Duval, J., Bot, C., Rubio, M., and Tielens, A. G. G. M. (2017). Dust Emission at 8 and 24 μm as Diagnostics of H ii Region Radiative Transfer. Astrophys. J., 844:63.

Ohsawa, R., Onaka, T., Sakon, I., Mori, T. I., Miyata, T., Asano, K., Matsuura, M., and Kaneda, H. (2012). Unusual Carbonaceous Dust Distribution in PN G095.2+00.7. Astrophys. J. Lett., 760:L34.

Onishi, T., Mizuno, A., Kawamura, A., Ogawa, H., and Fukui, Y. (1998). A C 18 O Survey of Dense Cloud Cores in Taurus: Star Formation. Astrophys. J., 502(1):296–314.

Ospina-Zamudio, J., Lefloch, B., Ceccarelli, C., Kahane, C., Favre, C., López-Sepulcre, A., and Montarges, M. (2018). First hot corino detected around an isolated intermediate-mass protostar: Cep E-mm. Astron. Astrophys., 618:A145.

Ospina-Zamudio, J., Lefloch, B., Favre, C., López-Sepulcre, A., Bianchi, E., Ceccarelli, C., De Simone, M., Bouvier, M., and Kahane, C. (2019). Molecules in the Cep E-mm jet: evidence for shock-driven photochemistry? Mon. Not. R. Astron. Soc., 490(2):2679–2691.

Oya, Y., Sakai, N., Watanabe, Y., Higuchi, A. E., Hirota, T., López-Sepulcre, A., Sakai, T., Aikawa, Y., Ceccarelli, C., Lefloch, B., Caux, E., Vastel, C., Kahane, C., and Yamamoto, S. (2017). L483: Warm Carbon-chain Chemistry Source Harboring Hot Corino Activity. Astrophys. J., 837(2):174.

Pacios, L. F. and Gómez, L. (2006). Conformational changes of the electrostatic potential of biphenyl: A theoretical study. Chem. Phys. Lett., 432(4-6):414–420.

Padoan, P. and Nordlund, A. (2002). The Stellar Initial Mass Function from Turbulent Fragmentation. Astrophys. J., 576(2):870–879.

Padoan, P. and Nordlund, Å. (2011). THE STAR FORMATION RATE OF SUPERSONIC MAGNETOHYDRODYNAMIC TURBULENCE. Astrophys. J., 730(1):40.

Palla, F. (1996). The quest for evolutionary diagrams of young stellar objects. In Disk. Outflows Around Young Stars, pages 143–168. Springer Berlin Heidelberg.

Papadakis, R., Li, H., Bergman, J., Lundstedt, A., Jorner, K., Ayub, R., Haldar, S., Jahn, B. O., Denisova, A., Zietz, B., Lindh, R., Sanyal, B., Grennberg, H., Leifer, K., and Ottosson, H. (2016).

Metal-free photochemical silylations and transfer hydrogenations of benzenoid hydrocarbons and graphene. Nat. Commun., 7:12962.

Papadakis, R. and Ottosson, H. (2015). The excited state antiaromatic benzene ring: a molecular Mr Hyde? Chem. Soc. Rev., 44(18):6472–6493.

Parise, B., Belloche, A., Leurini, S., Schilke, P., Wyrowski, F., and Güsten, R. (2006). CO and CH 3 OH observations of the BHR71 outflows with APEX. Astron. Astrophys., 454(2):L79–L82.

Park, J., Burova, S., Rodgers, A. S., and Lin, M. C. (1999). Experimental and Theoretical Studies of the C 6 H 5 + C 6 H 6 Reaction. J. Phys. Chem. A, 103(45):9036–9041.

Park, J. and Lin, M. C. (1997). Kinetics for the Recombination of Phenyl Radicals. J. Phys. Chem. A, 101(1):14–18.

Parker, D. S. N., Zhang, F., Kim, Y. S., Kaiser, R. I., Landera, A., Kislov, V. V., Mebel, A. M., and Tielens, A. G. G. M. (2012). Low temperature formation of naphthalene and its role in the synthesis of PAHs (Polycyclic Aromatic Hydrocarbons) in the interstellar medium. Proc. Nat. Acad. Sci., 109(1):53–58.

Patzer, A., Chakraborty, S., Solcà, N., and Dopfer, O. (2010). IR Spectrum and Structure of the Phenyl Cation. Angew. Chemie Int. Ed., 49(52):10145–10148.

Peeters, E., Hony, S., Van Kerckhoven, C., Tielens, A. G. G. M., Allamandola, L. J., Hudgins, D. M., and Bauschlicher, C. W. (2002). The rich 6 to 9 μm spectrum of interstellar PAHs. Astron. Astrophys., 390(3):1089–1113.

Peeters, E., Spoon, H. W. W., and Tielens, A. G. G. M. (2004). Polycyclic Aromatic Hydrocarbons as a Tracer of Star Formation? Astrophys. J., 613(2):986–1003.

Peeters, E., Tielens, A. G. G. M., van Kerckhoven, C., Hony, S., Allamandola, L. J., Hudgins, D. M., and Bauschlicher, C. W. (2002). ISO Spectroscopy of PAH Features. In Crowther, P., editor, Hot Star Workshop III: The Earliest Phases of Massive Star Birth, volume 267 of Astron. Soc. Pacific Conf. Ser., page 403.

Persi, P., Cesarsky, D., Marenzi, A. R., Preite-Martinez, A., Rouan, D., Siebenmorgen, R., Lacombe, F., and Tiphene, D. (1999). Mid-infrared spectral images of planetary nebulae with ISOCAM. Astron. Astrophys., 351:201–211.

Persson, M. V. (2014). Current view of protostellar evolution (ENG).

Petrucci, P. O., Haardt, F., Maraschi, L., Grandi, P., Malzac, J., Matt, G., Nicastro, F., Piro, L., Perola, G. C., and De Rosa, A. (2001). Testing Comptonization Models Using Beppo SAX Observations of Seyfert 1 Galaxies. Astrophys. J., 556(2):716–726.

Peverati, R., Bera, P. P., Lee, T. J., and Head-Gordon, M. (2016). INSIGHTS INTO HYDROCARBON CHAIN AND AROMATIC RING FORMATION IN THE INTERSTELLAR MEDIUM: COMPUTATIONAL STUDY OF THE ISOMERS OF C+4H+3$^+$, $C_6H_3^+$ AND $C_6H_5^+$ AND THEIR FORMATION PATHWAYS. Astrophys. J., 830(2):128.

Pickett, H., Poynter, R., Cohen, E., Delitsky, M., Pearson, J., and Müller, H. (1998). SUBMILLIMETER, MILLIMETER, AND MICROWAVE SPECTRAL LINE CATALOG. Journal of Quantitative Spectroscopy and Radiative Transfer, 60(5):883–890.

Pilling, S., Santos, A. C. F., and Boechat-Roberty, H. M. (2006). Photodissociation of organic molecules in star-forming regions. Astron. Astrophys., 449(3):1289–1296.

Pineau des Forets, G., Roueff, E., Schilke, P., and Flower, D. R. (1993). Sulphur-bearing molecules as tracers of shocks in interstellar clouds. Mon. Not. R. Astron. Soc., 262(4):915–928.

Pino, T., Chabot, M., Béroff, K., Godard, M., Fernandez-Villoria, F., Le, K. C., Breuer, L., Herder, M., Wucher, A., Bender, M., Severin, D., Trautmann, C., and Dartois, E. (2019). Release of large polycyclic aromatic hydrocarbons and fullerenes by cosmic rays from interstellar dust. Swift heavy ion irradiations of interstellar carbonaceous dust analogue. Astron. Astrophys., 623:A134.

Pizzarello, S. and Huang, Y. (2005). The deuterium enrichment of individual amino acids in carbonaceous meteorites: A case for the presolar distribution of biomolecule precursors. Geochimica et Cosmochimica Acta, 69(3):599–605.

Plunkett, A. L., Arce, H. G., Corder, S. A., Mardones, D., Sargent, A. I., and Schnee, S. L. (2013). CARMA Observations of Protostellar Outflows in NGC 1333. Astrophys. J., 774(1):22.

Poater, J., Solà, M., and Bickelhaupt, F. M. (2006). Hydrogen–Hydrogen Bonding in Planar Biphenyl, Predicted by Atoms-In-Molecules Theory, Does Not Exist. Chem. - A Eur. J., 12(10):2889–2895.

Popelier, P. L. A., Maxwell, P. I., Thacker, J. C. R., and Alkorta, I. (2019). A relative energy gradient (REG) study of the planar and perpendicular torsional energy barriers in biphenyl. Theor. Chem. Acc., 138(1):12.

Postma, J., Bari, S., Hoekstra, R., Tielens, A. G. G. M., and Schlathölter, T. (2010). IONIZATION AND FRAGMENTATION OF ANTHRACENE UPON INTERACTION WITH keV PROTONS AND α PARTICLES. Astrophys. J., 708(1):435–444.

Puzzarini, C., Stanton, J. F., and Gauss, J. (2010). Quantum-chemical calculation of spectroscopic parameters for rotational spectroscopy. Int. Rev. Phys. Chem., 29(2):273–367.

Quitián-Lara, H. M., Fantuzzi, F., Nascimento, M. A. C., Wolff, W., and Boechat-Roberty, H. M. (2018). Hydrogenated Benzene in Circumstellar Environments: Insights into the Photostability of Super-hydrogenated PAHs. Astrophys. J., 854(1):61.

Quitián-Lara, H. M. (2016). A estabilidade de pahs hidrogenados em ambientes circunstelares. Master's thesis, Observatório do Valongo - Universidade Federal do Rio de Janeiro.

Ramsier, R. and Yates, J. (1991). Electron-stimulated desorption: Principles and applications. Surf. Sci. Rep., 12(6-8):246–378.

Reichertz, L. A., Weferling, B., Esch, W., and Kreysa, E. (2001). The fastscanning observing technique for millimeter and submillimeter astronomy. Astron. Astrophys., 379(2):735–739.

Reitsma, G., Boschman, L., Deuzeman, M. J., González-Magaña, O., Hoekstra, S., Cazaux, S., Hoekstra, R., and Schlathölter, T. (2014). Deexcitation dynamics of superhydrogenated polycyclic aromatic hydrocarbon cations after soft-x-ray absorption. Phys. Rev. Lett., 113(5):1–5.

Reitsma, G., Boschman, L., Deuzeman, M. J., Hoekstra, S., Hoekstra, R., and Schlathölter, T. (2015). Near edge X-ray absorption mass spectrometry on coronene. J. Chem. Phys., 142(2):024308.

Rennie, E. E., Kempgens, B., KÖPpe, H. M., Hergenhahn, U., Feldhaus, J., Itchkawitz, B. S., Kilcoyne, A. L. D., KivimÄKi, A., Maier, K., Piancastelli, M. N., Polcik, M., A., R., and Bradshaw, A. M. (2000). A comprehensive photoabsorption, photoionization, and shake-up excitation study of the C1s cross section of benzene. Journal of Chemical Physics, 113:17.

Ressler, M. E. and Barsony, M. (2003). Structure of the Mid-Infrared–emitting Disk around WL 16. Astrophys. J., 584(2):832–842.

Ribeiro, F. d. A., Almeida, G. C., Garcia-Basabe, Y., Wolff, W., Boechat-Roberty, H. M., and Rocco, M. L. M. (2015). Non-thermal ion desorption from an acetonitrile (CH 3 CN) astrophysical ice analogue studied by electron stimulated ion desorption. Phys. Chem. Chem. Phys., 17(41):27473–27480.

Ribeiro, F. d. A., Almeida, G. C., Wolff, W., Boechat-Roberty, H. M., and Rocco, M. L. M. (2014). Fragmentation and Ion Desorption from Condensed Pyrimidine by Electron Impact: Implications for Cometary and Interstellar Heterocyclic Chemistry. J. Phys. Chem. C, 118:25978–25986.

Ricca, A., Bauschlicher, C. W., Roser, J. E., and Peeters, E. (2018). Polycyclic Aromatic Hydrocarbons with Straight Edges and the 7.6/6.2 and 8.6/6.2 Intensity Ratios in Reflection Nebulae. Astrophys. J., 854(2):115.

Robertson, G. B. (1961). Crystal and Molecular Structure of Diphenyl. Nature, 191(4788):593–594.

Roelfsema, P. R., Cox, P., Tielens, A. G. G. M., Allamandola, L. J., Baluteau, J.-P., Barlow, M. J., Beintema, D., Boxhoorn, D. R., Cassinelli, J. P., Caux, E., Churchwell, E., Clegg, P. E., de Graauw, T., Heras, A. M., Huygen, R., van der Hucht, K. A., Hudgins, D. M., Kessler, M. F., Lim, T., and Sandford, S. A. (1996). SWS observations of IR emission features towards compact HII regions. Astron. Astrophys., 315:L289–L292.

Roth, H. D. (1987). Organic Radical Cations in Fluid Solution: Unusual Structures and Rearrangements. Acc. Chem. Res., 20(9):343–350.

Roth, H. D. (1992). Structure and reactivity of organic radical cations. In Mattay, J., editor, Photoinduced Electron Transf. IV, pages 131–245. Springer, Heidelberg.

Roueff, E., Lis, D. C., van der Tak, F. F. S., Gerin, M., and Goldsmith, P. F. (2005). Interstellar deuterated ammonia: from NH 3 to ND 3. Astron. Astrophys., 438(2):585–598.

Rubio, M., Merchan, M., Orti, E., and Roos, B. O. (1995). A Theoretical Study of the Electronic Spectra of the Biphenyl Cation and Anion. J. Phys. Chem., 99(41):14980–14987.

Ruffert, M. and Arnett, D. (1994). Three-dimensional hydrodynamic Bondi-Hoyle accretion. 2: Homogeneous medium at Mach 3 with gamma = 5/3. Astrophys. J., 427:351.

Rybicki, G. B. and Lightman, A. P. (1985). Radiative Processes in Astrophysics. Wiley-VCH Verlag GmbH & Co. KGaA, Weinheim, Germany.

Rzepa, H. (2012). Ring-flipping in cyclohexane in a different light.

Sadavoy, S. I., Di Francesco, J., André, P., Pezzuto, S., Bernard, J. P., Maury, A., Men'shchikov, A., Motte, F., Nguyen-Lu'o'ng, Q., Schneider, N., Arzoumanian, D., Benedettini, M., Bontemps, S., Elia, D., Hennemann, M., Hill, T., Könyves, V., Louvet, F., Peretto, N., Roy, A., and White, G. J. (2014). Class 0 Protostars in the Perseus Molecular Cloud: A Correlation Between the Youngest Protostars and the Dense Gas Distribution. Astrophys. J. Lett., 787(2):L18.

Safe, S. H. (1994). Polychlorinated Biphenyls (PCBs): Environmental Impact, Biochemical and Toxic Responses, and Implications for Risk Assessment. Crit. Rev. Toxicol., 24(2):87–149.

Sahu, D., Liu, S.-Y., Su, Y.-N., Li, Z.-Y., Lee, C.-F., Hirano, N., and Takakuwa, S. (2019). Implications of a Hot Atmosphere/Corino from ALMA Observations toward NGC 1333 IRAS 4A1. Astrophys. J., 872(2):196.

Saito, M. and Kimura, Y. (2009). ORIGIN OF ORGANIC GLOBULES IN METEORITES: LABORATORY SIMULATION USING AROMATIC HYDROCARBONS. Astrophys. J., 703(2):L147–L151.

Sakai, N., Sakai, T., Hirota, T., Burton, M., and Yamamoto, S. (2009). DISCOVERY OF THE SECOND WARM CARBON-CHAIN-CHEMISTRY SOURCE, IRAS15398 – 3359 IN LUPUS. Astrophys. J., 697(1):769–786.

Sakai, N., Sakai, T., Hirota, T., Watanabe, Y., Ceccarelli, C., Kahane, C., Bottinelli, S., Caux, E., Demyk, K., Vastel, C., Coutens, A., Taquet, V., Ohashi, N., Takakuwa, S., Yen, H.-W., Aikawa, Y., and Yamamoto, S. (2014). Change in the chemical composition of infalling gas forming a disk around a protostar. Nature, 507(7490):78–80.

Sakai, N., Sakai, T., and Yamamoto, S. (2006). Detection of $HCOOCH_3$ toward a Low-Mass Protostar, NGC 1333 IRAS 4B. Publ. Astron. Soc. Jpn., 58:L15–L18.

Sakai, T., Sakai, N., Kamegai, K., Hirota, T., Yamaguchi, N., Shiba, S., and Yamamoto, S. (2008). A Molecular Line Observation toward Massive Clumps Associated with Infrared Dark Clouds. Astrophys. J., 678(2):1049–1069.

Sakamoto, N., Tsuchida, H., Kato, T., Kamakura, S., Ogawa, H., Ishii, K., Marakami, I., Kato, D., Sakaue, H., Kato, M., Berkowitz, J., and Inokuti, M. (2010). Oscillator strength spectra and related quantities of 9 atoms and 23 molecules over the entire energy region. Technical report, Toki, Japan.

Salak, D., Nakai, N., Hatakeyama, T., and Miyamoto, Y. (2016). Gas Dynamics and Outflow in the Barred Starburst Galaxy NGC 1808 Revealed with ALMA. Astrophys. J., 823:68.

Salak, D., Tomiyasu, Y., Nakai, N., Kuno, N., Miyamoto, Y., and Kaneko, H. (2017). Evolution of Molecular Clouds in the Superwind Galaxy NGC 1808 Probed by ALMA Observations. Astrophys. J., 849(2):90.

Salak, D., Tomiyasu, Y., Nakai, N., Kuno, N., Miyamoto, Y., and Kaneko, H. (2018). Dense Molecular Gas in the Starburst Nucleus of NGC 1808. Astrophys. J., 856(2):97.

Sales, D. A., Pastoriza, M. G., and Riffel, R. (2010). POLYCYCLIC AROMATIC HYDROCARBON AND EMISSION LINE RATIOS IN ACTIVE GALACTIC NUCLEI AND STARBURST GALAXIES. Astrophys. J., 725(1):605–614.

Sales, D. A., Pastoriza, M. G., Riffel, R., and Winge, C. (2013). Polycyclic aromatic hydrocarbon in the central region of the Seyfert 2 galaxy NGC 1808. Mon. Not. R. Astron. Soc., 429(3):2634–2642.

Sandell, G. and Knee, L. (2001). NGC1333 - Protostars and Outflows, volume 235 of Astron. Soc. Pacific Conf. Ser., page 154.

Sandford, S. A., Bernstein, M. P., and Materese, C. K. (2013). THE INFRARED SPECTRA OF POLYCYCLIC AROMATIC HYDROCARBONS WITH EXCESS PERIPHERAL H ATOMS (H n -PAHs) AND THEIR RELATION TO THE 3.4 AND 6.9 μm PAH EMISSION FEATURES. Astrophys. J. Suppl. Ser., 205(1):8.

Santander-García, M., Bujarrabal, V., and Alcolea, J. (2012). Modeling the physical and excitation conditions of the molecular envelope of NGC7027. Astron. Astrophys., 545:A114.

Santangelo, G., Codella, C., Cabrit, S., Maury, A. J., Gueth, F., Maret, S., Lefloch, B., Belloche, A., André, P., Hennebelle, P., Anderl, S., Podio, L., and Testi, L. (2015). Jet multiplicity in the proto-binary system NGC 1333-IRAS4A. Astron. Astrophys., 584:A126.

Santangelo, G., Nisini, B., Codella, C., Lorenzani, A., Yıldız, U. A., Antoniucci, S., Bjerkeli, P., Cabrit, S., Giannini, T., Kristensen, L. E., Liseau, R., Mottram, J. C., Tafalla, M., and van Dishoeck, E. F. (2014). Water distribution in shocked regions of the NGC 1333-IRAS 4A protostellar outflow. Astron. Astrophys., 568:A125.

Santos-Lleó, M., Clavel, J., Schulz, B., Altieri, B., Barr, P., Alloin, D., Berlind, P., Bertram, R., Crenshaw, D. M., Edelson, R. A., Giveon, U., Horne, K., Huchra, J. P., Kaspi, S., Kriss, G. A., Krolik, J. H., Malkan, M. A., Malkov, Y. F., Netzer, H., O'Brien, P. T., Peterson, B. M., Pogge, R. W., Pronik, V. I., Qian, B.-C., Reichert, G. A., Rodríguez-Pascual, P. M., Sergeev, S. G., Tao, J., Tokarz, S., Wagner, R. M., Wamsteker, W., and Wilkes, B. J. (2001). Monitoring of the optical and 2.5-11.7 μ m spectrum and mid-IR imaging of the Seyfert 1 galaxy Mrk 279 with ISO. Astron. Astrophys., 369(1):57–64.

Sasaki, Y. and Hamaguchi, H.-o. (1994). Raman spectra and structure of biphenyl isoatomers (the S0, S1, T1 states and the cation and anion radicals). Spectrochim. Acta Part A Mol. Spectrosc., 50(8-9):1475–1485.

Scaiano, J. C. and Stewart, L. C. (1983). Phenyl radical kinetics. J. Am. Chem. Soc., 105(11):3609–3614.

Schlafly, E. F., Green, G., Finkbeiner, D. P., Rix, H.-W., Bell, E. F., Burgett, W. S., Chambers, K. C., Draper, P. W., Hodapp, K. W., Kaiser, N., Magnier, E. A., Martin, N. F., Metcalfe, N., Price, P. A., and Tonry, J. L. (2014). A LARGE CATALOG OF ACCURATE DISTANCES TO MOLECULAR CLOUDS FROM PS1 PHOTOMETRY. Astrophys. J., 786(1):29.

Schworer, G., Lacour, S., Huélamo, N., Pinte, C., Chauvin, G., Coudé du Foresto, V., Ehrenreich, D., Girard, J., and Tuthill, P. (2017). A Resolved and Asymmetric Ring of PAHs within the Young Circumstellar Disk of IRS 48. Astrophys. J., 842:77.

Scott, J. E., Kriss, G. A., Lee, J. C., Arav, N., Ogle, P., Roraback, K., Weaver, K., Alexander, T., Brotherton, M., Green, R. F., Hutchings, J., Kaiser, M. E., Marshall, H., Oegerle, W., and Zheng, W. (2004). Intrinsic Absorption in the Spectrum of Markarian 279: Simultaneous Chandra , FUSE , and STIS Observations. Astrophys. J. Suppl. Ser., 152(1):1–27.

Scott, L. T. (2015). Chemistry at the interior atoms of polycyclic aromatic hydrocarbons. Chem. Soc. Rev., 44(18):6464–6471.

Semenov, D., Favre, C., Fedele, D., Guilloteau, S., Teague, R., Henning, T., Dutrey, A., Chapillon, E., Hersant, F., and Piétu, V. (2018). Chemistry in disks. Astron. Astrophys., 617:A28.

Seok, J. Y. and Li, A. (2017). Polycyclic Aromatic Hydrocarbons in Protoplanetary Disks around Herbig Ae/Be and T Tauri Stars. Astrophys. J., 835(2):291.

Sephton, M. A. (2002). Organic compounds in carbonaceous meteorites. Nat. Prod. Rep., 19(3):292–311.

Sephton, M. A., Waite, J. H., and Brockwell, T. G. (2018). How to Detect Life on Icy Moons. Astrobiology, 18(7):843–855.

Shaw, A. M. (2007). Astrochemistry: From Astronomy to Astrobiology. John Wiley & Sons Ltd.

Shiotani, M., Lindgren, M., Ohta, N., and Ichikawa, T. (1991). Radical cations of Cyclohexanes Alkyl-Substituted on One Carbon: an ESR Study of the Jahn–Teller Distorted HOMO of Cyclohexane. J. Chem. Soc., Perkin Trans. 2, (5):711–719.

Shu, F. H. (1977). Self-similar collapse of isothermal spheres and star formation. Astrophys. J., 214:488.

Shu, F. H., Adams, F. C., and Lizano, S. (1987a). Star Formation in Molecular Clouds: Observation and Theory. Annu. Rev. Astron. Astrophys., 25(1):23–81.

Shu, F. H., Lizano, S., and Adams, F. C. (1987b). Star Formation in Molecular Cloud Cores. Symp. - Int. Astron. Union, 115:417–434.

Shu, X. W., Wang, J. X., Jiang, P., Fan, L. L., and Wang, T. G. (2007). Investigating the Nuclear Obscuration in Two Types of Seyfert 2 Galaxies. Astrophys. J., 657(1):167–176.

Shukla, B., Susa, A., Miyoshi, A., and Koshi, M. (2008). Role of Phenyl Radicals in the Growth of Polycyclic Aromatic Hydrocarbons. J. Phys. Chem. A, 112(11):2362–2369.

Shukla, B., Tsuchiya, K., and Koshi, M. (2011). Novel Products from C 6 H 5 + C 6 H 6 /C 6 H 5 Reactions. J. Phys. Chem. A, 115(21):5284–5293.

Simonian, G. V. and Martini, P. (2017). Circumstellar dust, PAHs and stellar populations in early-type galaxies: insights from GALEX and WISE. Mon. Not. R. Astron. Soc., 464(4):3920–3936.

Smith, I. W. (2011). Laboratory Astrochemistry: Gas-Phase Processes. Annu. Rev. Astron. Astrophys., 49(1):29–66.

Sorrell, W. H. (2001). Origin of Amino Acids and Organic Sugars in Interstellar Clouds. Astrophys. J., 555(2):L129–L132.

Steglich, M., Jäger, C., Huisken, F., Friedrich, M., Plass, W., Räder, H.-J., Müllen, K., and Henning, T. (2013). THE ABUNDANCES OF HYDROCARBON FUNCTIONAL GROUPS IN THE INTERSTELLAR MEDIUM INFERRED FROM LABORATORY SPECTRA OF HYDROGENATED AND METHYLATED POLYCYCLIC AROMATIC HYDROCARBONS. Astrophys. J. Suppl. Ser., 208(2):26.

Steinicke, W. (2016). WILLIAM HERSCHEL'S 'HOLE IN THE SKY'AND THE DISCOVERY OF DARK NEBULAE. Journal of Astronomical History and Heritage, 19(3):305–326.

Stierwalt, S., Armus, L., Charmandaris, V., Diaz-Santos, T., Marshall, J., Evans, A. S., Haan, S., Howell, J., Iwasawa, K., Kim, D. C., Murphy, E. J., Rich, J. A., Spoon, H. W. W., Inami, H., Petric, A. O., and U, V. (2014). MID-INFRARED PROPERTIES OF LUMINOUS INFRARED GALAXIES. II. PROBING THE DUST AND GAS PHYSICS OF THE GOALS SAMPLE. Astrophys. J., 790(2):124.

Stöhr, J. (1992). NEXAFS Spectroscopy, volume 25 of Springer Series in Surface Sciences. Springer Berlin Heidelberg, Berlin, Heidelberg.

Stoltzfus, D. M., Jiang, W., Brewer, A. M., and Burn, P. L. (2018). Twisted dendrons for highly luminescent green emissive phosphorescent dendrimers. J. Mater. Chem. C, 6(38):10315–10326.

Strom, K. M., Strom, S. E., and Kinman, T. D. (1974). Optical Polarization of Selected Herbig-Haro Objects. Astrophys. J. Lett., 191:L93.

Sturm, E., Rupke, D., Contursi, A., Kim, D.-C., Lutz, D., Netzer, H., Veilleux, S., Genzel, R., Lehnert, M., Tacconi, L. J., Maoz, D., Mazzarella, J., Lord, S., Sanders, D., and Sternberg, A. (2006). Mid-Infrared Diagnostics of LINERs. Astrophys. J., 653(1):L13–L16.

Sun, Y.-L., Huang, W.-J., and Lee, S.-H. (2015). Formation of Polyynes C 4 H 2 , C 6 H 2 , C 8 H 2 , and C 10 H 2 from Reactions of C 2 H, C 4 H, C 6 H, and C 8 H Radicals with C 2 H 2. The J. Phys. Chem. Lett., 6(20):4117–4122.

Suzuki, H. (1959). Relations between Electronic Absorption Spectra and Spatial Configurations of Conjugated Systems. I. Biphenyl. Bull. Chem. Soc. Jpn., 32(12):1340–1350.

Swings, P. and Rosenfeld, L. (1937). Considerations Regarding Interstellar Molecules. Astrophys. J., 86:483.

Szczerba, R., Górny, S. K., Stasińska, G., Siódmiak, N., and Tylenda, R. (2001). PAH features in the ISO SWS01 spectra of [WR] planetary nebulae. Astrophys. Space Sci., 275(1-2):113–120.

Tachikawa, H. and Kawabata, H. (2003). Dynamics of the Hole-Capture Processes in Biphenyl and Poly(4-vinylbiphenyl): A Direct ab Initio Trajectory Study. J. Phys. Chem. B, 107(5):1113–1119.

Taha, A. S., Labadie, L., Pantin, E., Matter, A., Alvarez, C., Esquej, P., Grellmann, R., Rebolo, R., Telesco, C., and Wolf, S. (2018). The spatial extent of polycyclic aromatic hydrocarbons emission in the Herbig star HD 179218. Astron. Astrophys., 612:A15.

Talbi, D. and Chandler, G. S. (2012). Theoretical infrared spectra of biphenyl, terphenyls and tetraphenyls for astrophysical purposes. J. Mol. Spectrosc., 275:21–27.

Taquet, V., López-Sepulcre, A., Ceccarelli, C., Neri, R., Kahane, C., and Charnley, S. B. (2015). CONSTRAINING THE ABUNDANCES OF COMPLEX ORGANICS IN THE INNER REGIONS OF SOLAR-TYPE PROTOSTARS. Astrophys. J., 804(2):81.

Thompson, T. A., Quataert, E., and Murray, N. (2005). Radiation Pressure-supported Starburst Disks and Active Galactic Nucleus Fueling. Astrophys. J., 630:167–185.

Tielens, A. (2008). Interstellar Polycyclic Aromatic Hydrocarbon Molecules. Annu. Rev. Astron. Astrophys., 46(1):289–337.

Tielens, A. G. G. M. (2005). The Physics and Chemistry of the Interstellar Medium. Cambridge University Press.

Tielens, A. G. G. M. (2013). The molecular universe. Rev. Mod. Phys., 85(3):1021–1081.

Tommasin, S., Spinoglio, L., Malkan, M. A., and Fazio, G. (2010). SPITZER -IRS HIGH-RESOLUTION SPECTROSCOPY OF THE 12 μm SEYFERT GALAXIES. II. RESULTS FOR THE COMPLETE DATA SET. Astrophys. J., 709(2):1257–1283.

Tranter, R. S., Klippenstein, S. J., Harding, L. B., Giri, B. R., Yang, X., and Kiefer, J. H. (2010). Experimental and Theoretical Investigation of the Self-Reaction of Phenyl Radicals. J. Phys. Chem. A, 114(32):8240–8261.

Tsuzuki, S. and Tanabe, K. (1991). Ab initio molecular orbital calculations of the internal rotational potential of biphenyl using polarized basis sets with electron correlation correction. J. Phys. Chem., 95(1):139–144.

Tully, R. B. (1988). Nearby galaxies catalog. Cambridge University Press, Cambridge.

Ueda, Y., Yamaoka, K., and Remillard, R. (2009). GRS 1915+105 IN "SOFT STATE": NATURE OF ACCRETION DISK WIND AND ORIGIN OF X-RAY EMISSION. Astrophys. J., 695(2):888–899.

Urry, C. M. and Padovani, P. (1995). Unified Schemes for Radio-Loud Active Galactic Nuclei. Publ. Astron. Soc. Pacific, 107:803.

Usero, A., García-Burillo, S., Fuente, A., Martín-Pintado, J., and Rodríguez-Fernández, N. J. (2004). Molecular gas chemistry in AGN. Astron. Astrophys., 419(3):897–912.

van der Hart, W. (2001). Ab initio calculations on the isomerization of alkene radical cations. 2. Ring opening of cycloalkane radical cations. Int. J. Mass Spectrom., 210-211:13–20.

Vastel, C. (2016). Formalism of the CASSIS software.

Vastel, C., Bottinelli, S., Caux, E., Glorian, J.-M., and Boiziot, M. (2015). Cassis: a tool to visualize and analyse instrumental and synthetic spectra. In Martins, F., Boissier, S., Buat, V., Cambrésy, L., and Petit, P., editors, SF2A-2015: Proceedings of the Annual meeting of the French Society of Astronomy and Astrophysics, pages 313–316.

Vastel, C., Ceccarelli, C., Lefloch, B., and Bachiller, R. (2014). the Origin of Complex Organic Molecules in Prestellar Cores. Astrophys. J., 795(1):L2.

Vasudevan, R. V. and Fabian, A. C. (2009). Simultaneous X-ray/optical/UV snapshots of active galactic nuclei from XMM-Newton: Spectral energy distributions for the reverberation mapped sample. Mon. Not. R. Astron. Soc., 392(3):1124–1140.

Venkataraman, L., Klare, J. E., Nuckolls, C., Hybertsen, M. S., and Steigerwald, M. L. (2006). Dependence of single-molecule junction conductance on molecular conformation. Nature, 442(7105):904–907.

Vermeij, R., Peeters, E., Tielens, A. G. G. M., and van der Hulst, J. M. (2002). The PAH emission spectra of Large Magellanic Cloud H II regions. Astron. Astrophys., 382(3):1042–1051.

Vidal, T. H. G., Loison, J.-C., Jaziri, A. Y., Ruaud, M., Gratier, P., and Wakelam, V. (2017). On the reservoir of sulphur in dark clouds: chemistry and elemental abundance reconciled. Mon. Not. R. Astron. Soc., 469(1):435–447.

Voit, G. M. (1992). Destruction and survival of polycyclic aromatic hydrocarbons in active galaxies. Mon. Not. R. Astron. Soc., 258(4):841–848.

Wada, K. (2012). RADIATION-DRIVEN FOUNTAIN AND ORIGIN OF TORUS AROUND ACTIVE GALACTIC NUCLEI. Astrophys. J., 758(1):66.

Wada, K., Schartmann, M., and Meijerink, R. (2016). MULTI-PHASE NATURE OF A RADIATION-DRIVEN FOUNTAIN WITH NUCLEAR STARBURST IN A LOW-MASS ACTIVE GALACTIC NUCLEUS. Astrophys. J., 828(2):L19.

Wakelam, V., Smith, I. W. M., Herbst, E., Troe, J., Geppert, W., Linnartz, H., Öberg, K., Roueff, E., Agúndez, M., Pernot, P., Cuppen, H. M., Loison, J. C., and Talbi, D. (2010). Reaction Networks for Interstellar Chemical Modelling: Improvements and Challenges. Space Sci. Rev., 156(1-4):13–72.

Walawender, J., Bally, J., Francesco, J., Jørgensen, J., and Getman, K. . (2008). NGC 1333: A Nearby Burst of Star Formation. In Reipurth, B., editor, Handb. Star Form. Reg. Vol. I, volume 4, page 346.

Wallace, W. E. (2011). "Mass Spectra", NIST Mass Spectrometry Data Center. National Institute of Standards and Technology, Gaithersburg MD, 20899.

Wang, J., Cooper, G., Tulumello, D., and Hitchcock, A. P. (2005). Inner Shell Excitation Spectroscopy of Biphenyl and Substituted Biphenyls: Probing Ring–Ring Delocalization. J. Phys. Chem. A, 109(48):10886–10896.

Waters, L. B. F. M., Beintema, D. A., Zijlstra, A. A., de Koter, A., Molster, F. J., Bouwman, J., de Jong, T., Pottasch, S. R., and de Graauw, T. (1998). Crystalline silicates in planetary nebulae with [WC] central stars. Astron. Astrophys., 331:L61–L64.

Wesson, R., Cernicharo, J., Barlow, M. J., Matsuura, M., Decin, L., Groenewegen, M. A. T., Polehampton, E. T., Agundez, M., Cohen, M., Daniel, F., Exter, K. M., Gear, W. K., Gomez, H. L., Hargrave, P. C., Imhof, P., Ivison, R. J., Leeks, S. J., Lim, T. L., Olofsson, G., Savini, G., Sibthorpe, B., Swinyard, B. M., Ueta, T., Witherick, D. K., and Yates, J. A. (2010). Special feature Herschel -SPIRE FTS spectroscopy of the carbon-rich objects. Astron. Astrophys., 144:1–8.

Wiley, W. C. and McLaren, I. H. (1955). Time-of-Flight Mass Spectrometer with Improved Resolution. Rev. Sci. Instrum., 26(12):1150–1157.

Wilking, B. A., Lada, C. J., and Young, E. T. (1989). IRAS observations of the Rho Ophiuchi infrared cluster - Spectral energy distributions and luminosity function. Astrophys. J., 340:823.

Wilms, J., Allen, A., and McCray, R. (2000). On the Absorption of X-Rays in the Interstellar Medium. Astrophys. J., 542(2):914–924.

Wilson, T. L. (2013). Techniques of Radio Astronomy. In Planets, Stars and Stellar Systems, pages 283–323. Springer Netherlands, Dordrecht.

Wilson, T. L., Rohlfs, K., and Hüttemeister, S. (2009). Tools of Radio Astronomy. Astronomy and Astrophysics Library. Springer Berlin Heidelberg, Berlin, Heidelberg.

Wolf, M., Kiefer, H. V., Langeland, J., Andersen, L. H., Zettergren, H., Schmidt, H. T., Cederquist, H., and Stockett, M. H. (2016). PHOTO-STABILITY OF SUPER-HYDROGENATED PAHs DETERMINED BY ACTION SPECTROSCOPY EXPERIMENTS. Astrophys. J., 832(1):24.

Woods, P. M., Millar, T. J., Herbst, E., and Zijlstra, A. A. (2003). The chemistry of protoplanetary nebulae. Astron. Astrophys., 402(1):189–199.

Yabuta, H., Williams, L. B., Cody, G. D., Alexander, C. M. O., and Pizzarello, S. (2007). The insoluble carbonaceous material of CM chondrites: A possible source of discrete organic compounds under hydrothermal conditions. Meteorit. Planet. Sci., 42(1):37–48.

Yang, X., Glaser, R., Li, A., and Zhong, J. (2017a). The carriers of the unidentified infrared emission features: Clues from polycyclic aromatic hydrocarbons with aliphatic sidegroups. New Astron. Rev., 77:1–22.

Yang, X. J., Li, A., Glaser, R., and Zhong, J. X. (2017b). Polycyclic Aromatic Hydrocarbons with Aliphatic Sidegroups: Intensity Scaling for the C–H Stretching Modes and Astrophysical Implications. Astrophys. J., 837(2):171.

Yu, Y. S., Nordon, R., Kastner, J. H., Houck, J., Behar, E., and Soker, N. (2009). The X-ray spectrum of a planetary nebula at high resolution: Chandra gratings spectroscopy of BD $+30^o3639$. Astrophys. J., 690(1):440–452.

Zhang, F., Gu, X., and Kaiser, R. I. (2008). Formation of the diphenyl molecule in the crossed beam reaction of phenyl radicals with benzene. J. Chem. Phys., 128(8):084315.

Zhang, S. N. (2005). A Single Intrinsic Luminosity Function for Both Type I and Type II Active Galactic Nuclei. Astrophys. J., 618(2):L79–L82.

Zhang, Y. and Kwok, S. (2014). on the Viability of the Pah Model As an Explanation of the Unidentified Infrared Emission Features. Astrophys. J., 798(1):37.

Zhao, D., Doney, K. D., and Linnartz, H. (2014). LABORATORY GAS-PHASE DETECTION OF THE CYCLOPROPENYL CATION (c-$C_3H_3^+$). Astrophys. J., 791(2):L28.

Zhao, L., Kaiser, R. I., Xu, B., Ablikim, U., Ahmed, M., Joshi, D., Veber, G., Fischer, F. R., and Mebel, A. M. (2018). Pyrene synthesis in circumstellar envelopes and its role in the formation of 2D nanostructures. Nat. Astron., 2(5):413–419.

Zhao, T. Q., Li, Q., Liu, B. S., Gover, R. K. E., Sarre, P. J., and Cheung, A. S.-C. (2016). Laboratory astrochemistry: catalytic conversion of acetylene to polycyclic aromatic hydrocarbons over SiC grains. Phys. Chem. Chem. Phys., 18(5):3489–3496.

Zhen, J., Castellanos, P., Bouwman, J., Linnartz, H., and Tielens, A. G. G. M. (2017). Infrared Spectra of Hexa-peri-hexabenzocoronene Cations: HBC + and HBC 2+. Astrophys. J., 836(1):28.

Zhen, J., Castillo, S. R., Joblin, C., Mulas, G., Sabbah, H., Giuliani, A., Nahon, L., Martin, S., Champeaux, J.-P., and Mayer, P. M. (2016). VUV Photo-Processing of PAH Cations: Quantitative Study on the Ionization Versus Fragmentation Processes. Astrophys. J., 822(2):113.

Ziurys, L. M., Schmidt, D. R., and Bernal, J. J. (2018). New Circumstellar Sources of PO and PN: The Increasing Role of Phosphorus Chemistry in Oxygen-rich Stars. Astrophys. J., 856(2):169.

Zyubina, T., Kim, G.-S., Lin, S., Mebel, A., and Bandrauk, A. (2002). Dissociation pathways of benzene trication. Chem. Phys. Lett., 359(3-4):253–261.

Appendix A

IRAS 4A: Spectral Bands (3mm)

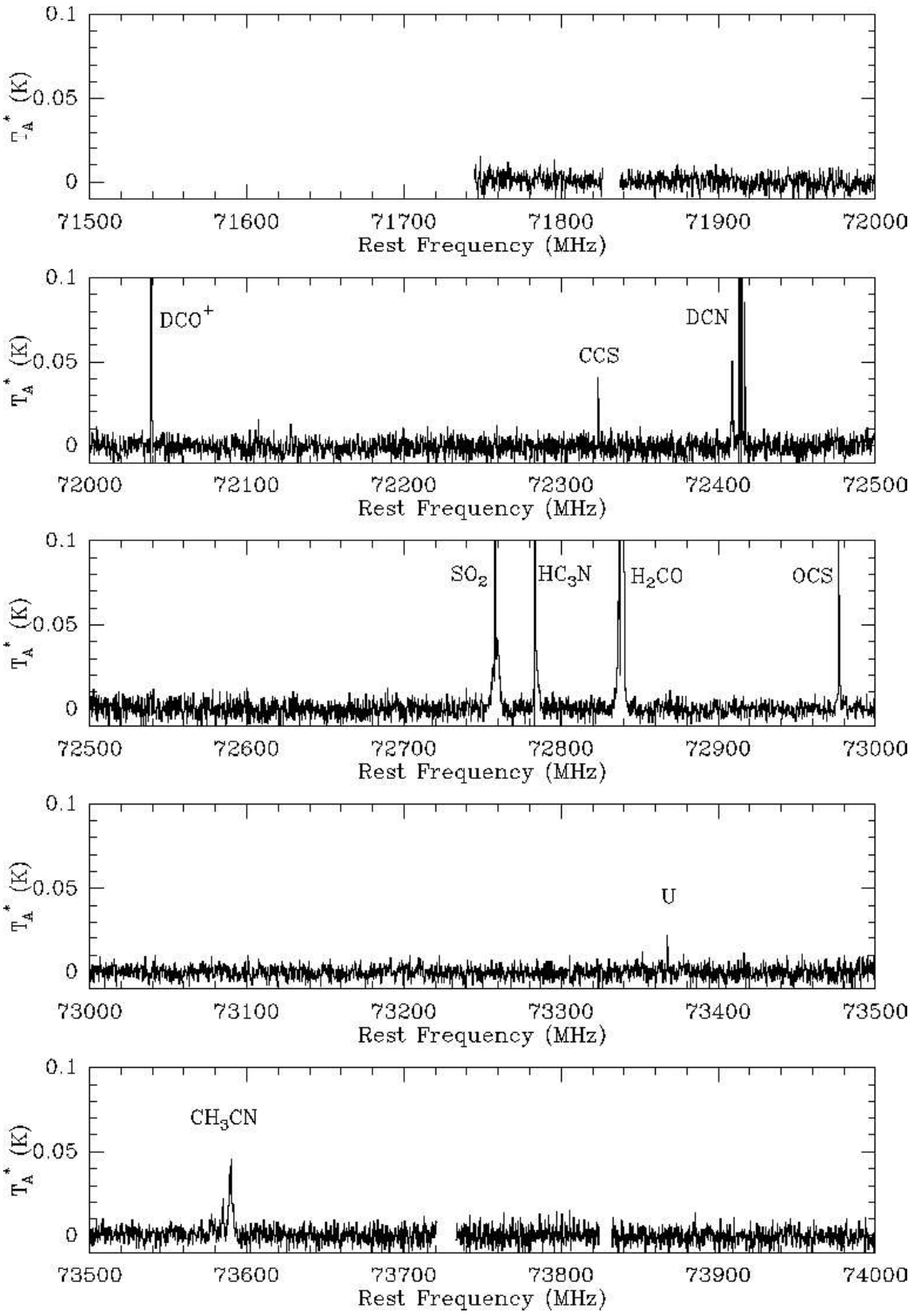

Figure A.1: The images of the total spectrum, including the three spectral bands (72-115GHz, 130-172GHz, 205-272GHz) of the protostar region of class 0 IRAS 4A.

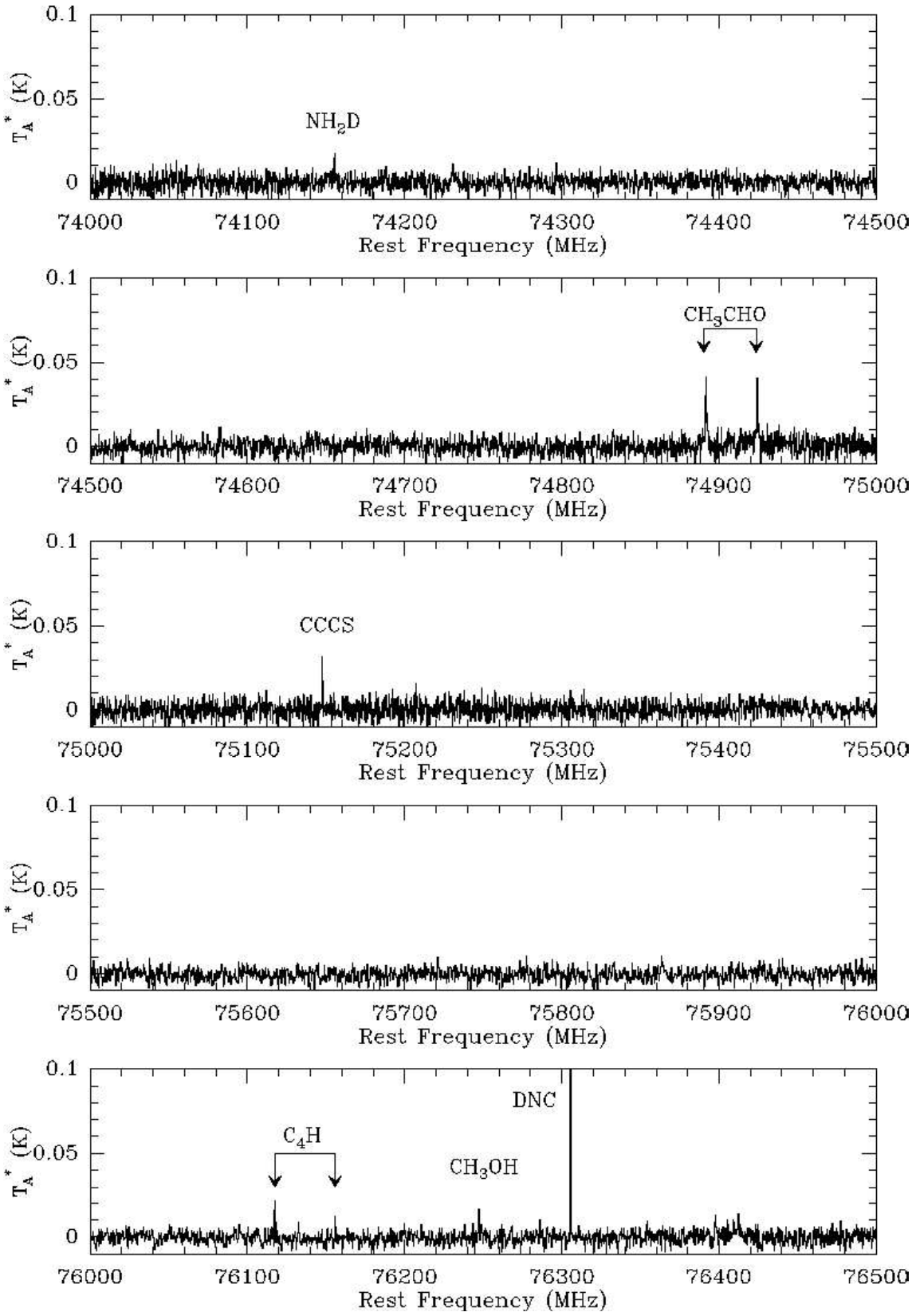
0.1
0.05
0
T_A^* (K)
NH_2D
74000
74100
74200
74300
74400
74500
Rest Frequency (MHz)
CH_3CHO
74500
74600
74700
74800
74900
75000
CCCS
75000
75100
75200
75300
75400
75500
75500
75600
75700
75800
75900
76000
DNC
C_4H
CH_3OH
76000
76100
76200
76300
76400
76500

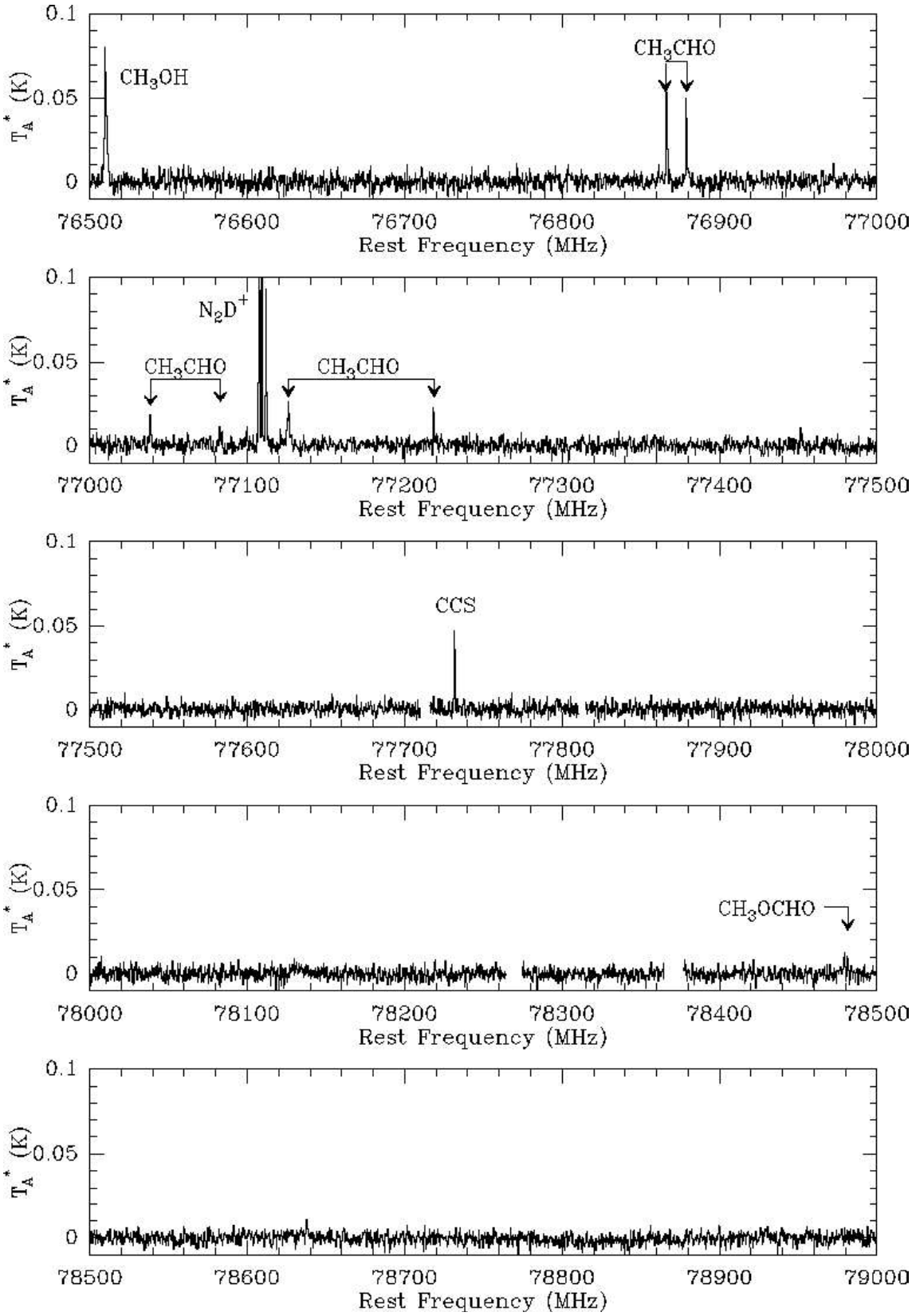
0.1
0.05
0
T_A^* (K)
CH_3OH
CH_3CHO
76500
76600
76700
76800
76900
77000
Rest Frequency (MHz)
N_2D^+
CH_3CHO
CH_3CHO
77000
77100
77200
77300
77400
77500
CCS
77500
77600
77700
77800
77900
78000
CH_3OCHO
78000
78100
78200
78300
78400
78500
78500
78600
78700
78800
78900
79000

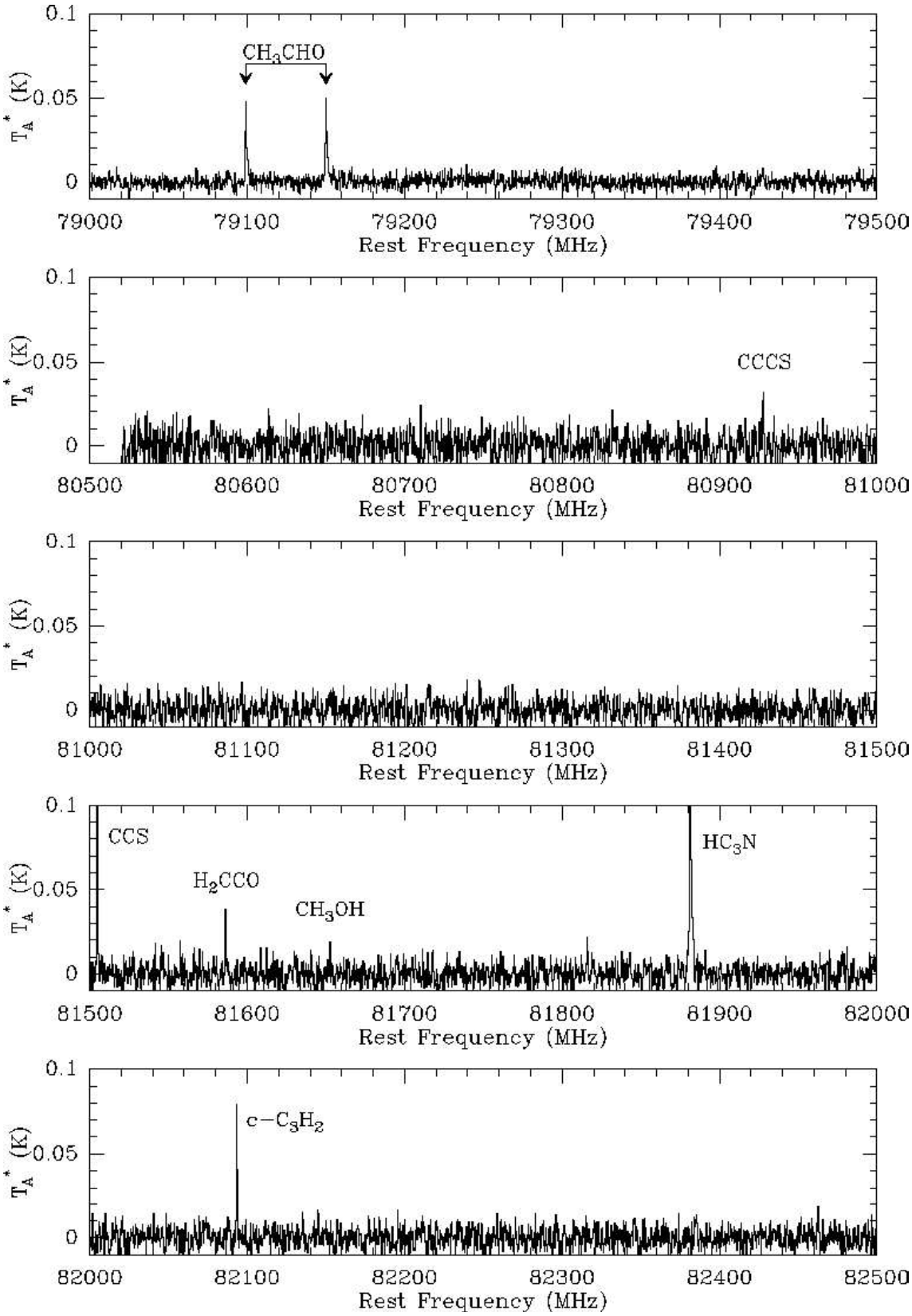
0.1
0.05
0
T_A^* (K)
CH_3CHO
79000
79100
79200
79300
79400
79500
Rest Frequency (MHz)
CCCS
80500
80600
80700
80800
80900
81000
81000
81100
81200
81300
81400
81500
CCS
H_2CCO
CH_3OH
HC_3N
81500
81600
81700
81800
81900
82000
$c-C_3H_2$
82000
82100
82200
82300
82400
82500

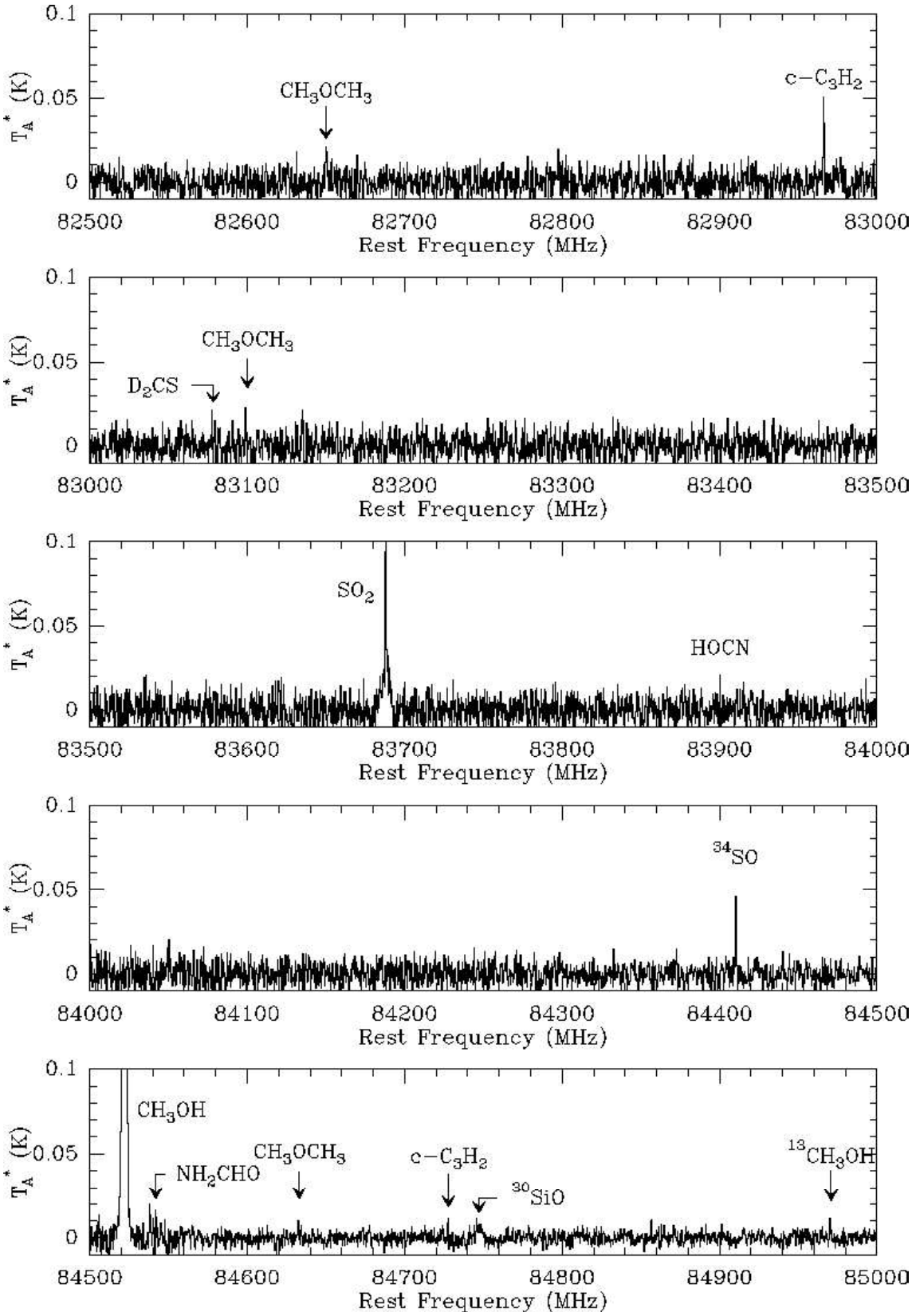
0.1
0.05
0
T_A^* (K)
CH_3OCH_3
c−C_3H_2
82500
82600
82700
82800
82900
83000
Rest Frequency (MHz)
CH_3OCH_3
D_2CS
83000
83100
83200
83300
83400
83500
Rest Frequency (MHz)
SO_2
HOCN
83500
83600
83700
83800
83900
84000
Rest Frequency (MHz)
^{34}SO
84000
84100
84200
84300
84400
84500
Rest Frequency (MHz)
CH_3OH
NH_2CHO
CH_3OCH_3
c−C_3H_2
^{30}SiO
$^{13}CH_3OH$
84500
84600
84700
84800
84900
85000
Rest Frequency (MHz)

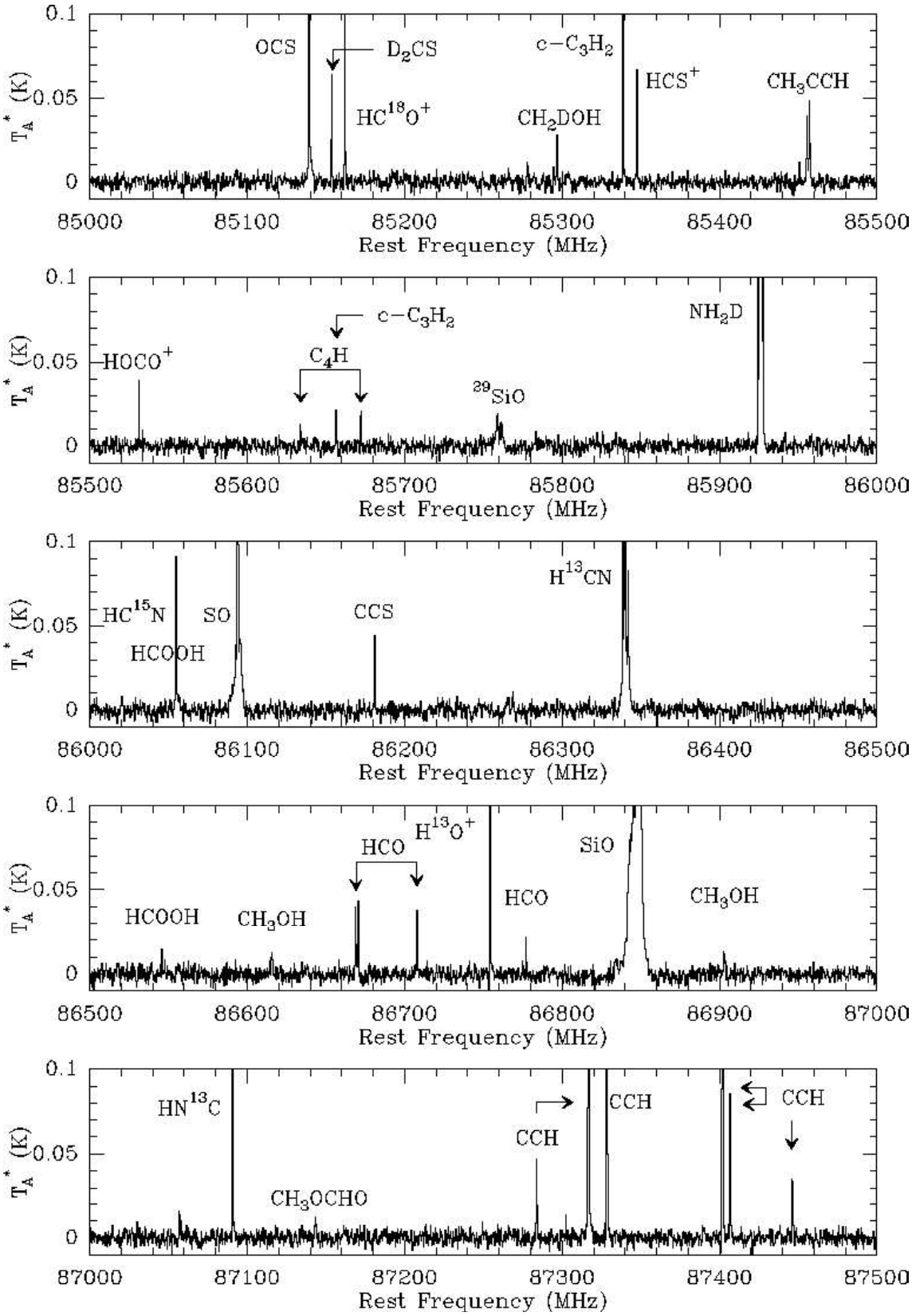
0.1
0.05
0
T_A^* (K)
OCS
D_2CS
$c-C_3H_2$
HCS^+
CH_3CCH
$HC^{18}O^+$
CH_2DOH
85000
85100
85200
85300
85400
85500
Rest Frequency (MHz)
$HOCO^+$
$c-C_3H_2$
C_4H
^{29}SiO
NH_2D
85500
85600
85700
85800
85900
86000
Rest Frequency (MHz)
$HC^{15}N$
SO
HCOOH
CCS
$H^{13}CN$
86000
86100
86200
86300
86400
86500
Rest Frequency (MHz)
HCOOH
CH_3OH
HCO
$H^{13}O^+$
HCO
SiO
CH_3OH
86500
86600
86700
86800
86900
87000
Rest Frequency (MHz)
$HN^{13}C$
CH_3OCHO
CCH
CCH
CCH
87000
87100
87200
87300
87400
87500
Rest Frequency (MHz)

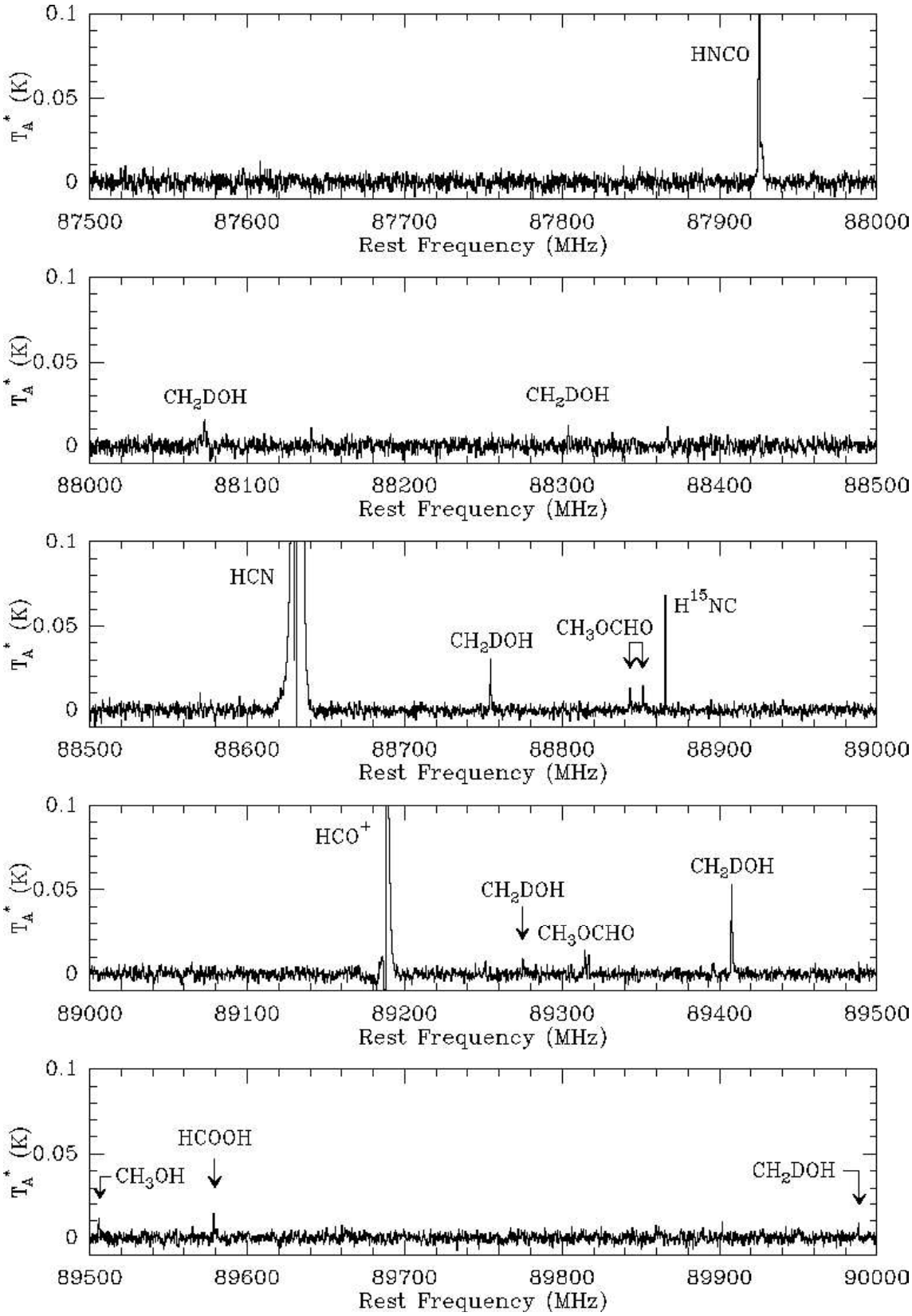
0.1
0.05
0
T_A^* (K)
HNCO
87500
87600
87700
87800
87900
88000
Rest Frequency (MHz)
CH_2DOH
CH_2DOH
88000
88100
88200
88300
88400
88500
Rest Frequency (MHz)
HCN
CH_2DOH
CH_3OCHO
$H^{15}NC$
88500
88600
88700
88800
88900
89000
Rest Frequency (MHz)
HCO^+
CH_2DOH
CH_3OCHO
CH_2DOH
89000
89100
89200
89300
89400
89500
Rest Frequency (MHz)
HCOOH
CH_3OH
CH_2DOH
89500
89600
89700
89800
89900
90000
Rest Frequency (MHz)

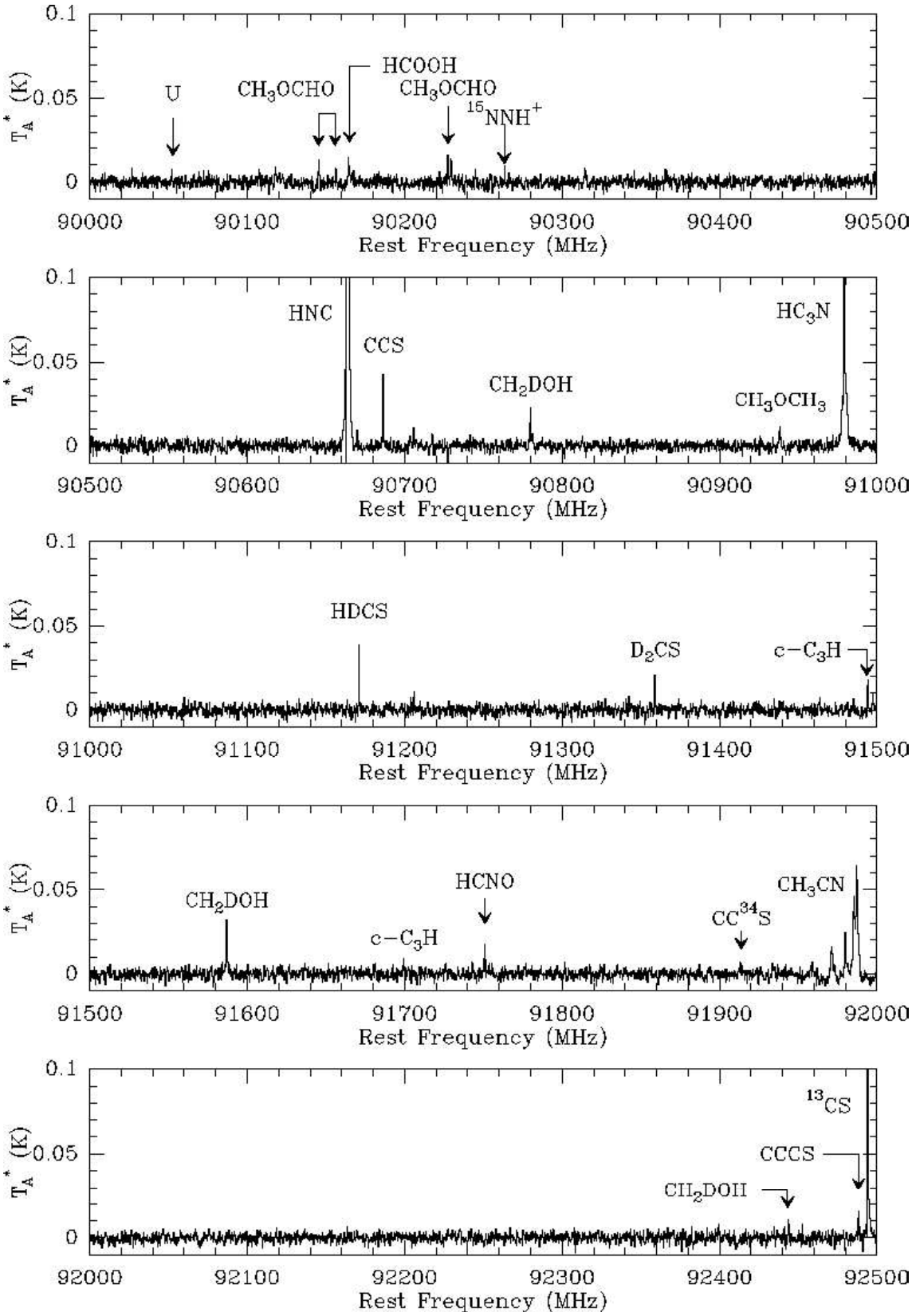
0.1
0.05
0
T_A^* (K)
U
CH_3OCHO
HCOOH
CH_3OCHO
$^{15}NNH^+$
90000
90100
90200
90300
90400
90500
Rest Frequency (MHz)
HNC
CCS
CH_2DOH
CH_3OCH_3
HC_3N
90500
90600
90700
90800
90900
91000
Rest Frequency (MHz)
HDCS
D_2CS
$c-C_3H$
91000
91100
91200
91300
91400
91500
Rest Frequency (MHz)
CH_2DOH
$c-C_3H$
HCNO
$CC^{34}S$
CH_3CN
91500
91600
91700
91800
91900
92000
Rest Frequency (MHz)
^{13}CS
CCCS
CH_2DOH
92000
92100
92200
92300
92400
92500
Rest Frequency (MHz)

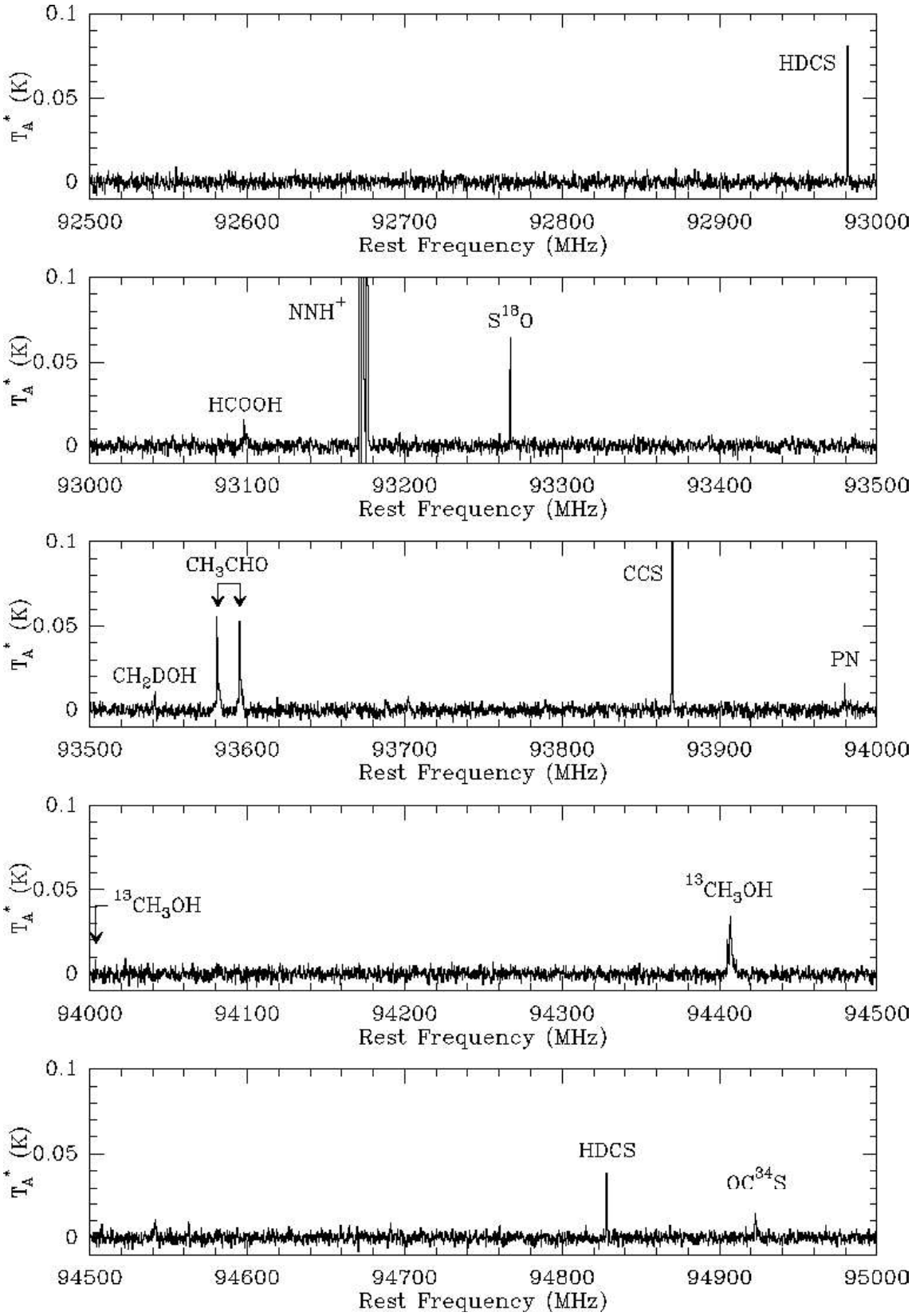
0.1
0.05
0
T_A^* (K)
HDCS
92500
92600
92700
92800
92900
93000
Rest Frequency (MHz)
NNH$^+$
S^{18}O
HCOOH
93000
93100
93200
93300
93400
93500
Rest Frequency (MHz)
CH$_3$CHO
CCS
CH$_2$DOH
PN
93500
93600
93700
93800
93900
94000
Rest Frequency (MHz)
^{13}CH$_3$OH
^{13}CH$_3$OH
94000
94100
94200
94300
94400
94500
Rest Frequency (MHz)
HDCS
OC^{34}S
94500
94600
94700
94800
94900
95000
Rest Frequency (MHz)

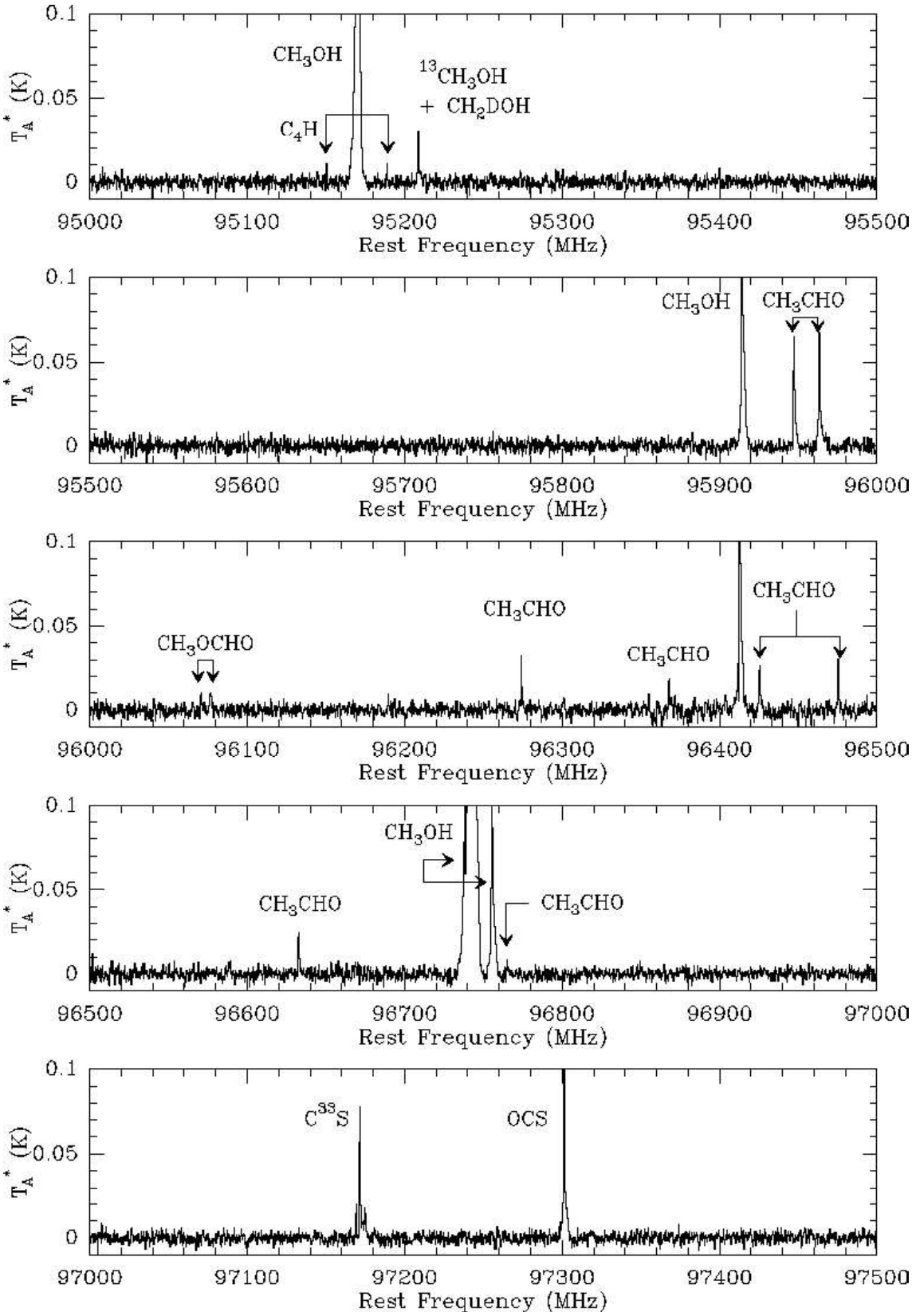
0.1
0.05
0
T_A^* (K)
CH_3OH
$^{13}CH_3OH$
+ CH_2DOH
C_4H
95000
95100
95200
95300
95400
95500
Rest Frequency (MHz)
CH_3OH
CH_3CHO
95500
95600
95700
95800
95900
96000
CH_3OCHO
CH_3CHO
CH_3CHO
CH_3CHO
96000
96100
96200
96300
96400
96500
CH_3OH
CH_3CHO
CH_3CHO
96500
96600
96700
96800
96900
97000
$C^{33}S$
OCS
97000
97100
97200
97300
97400
97500

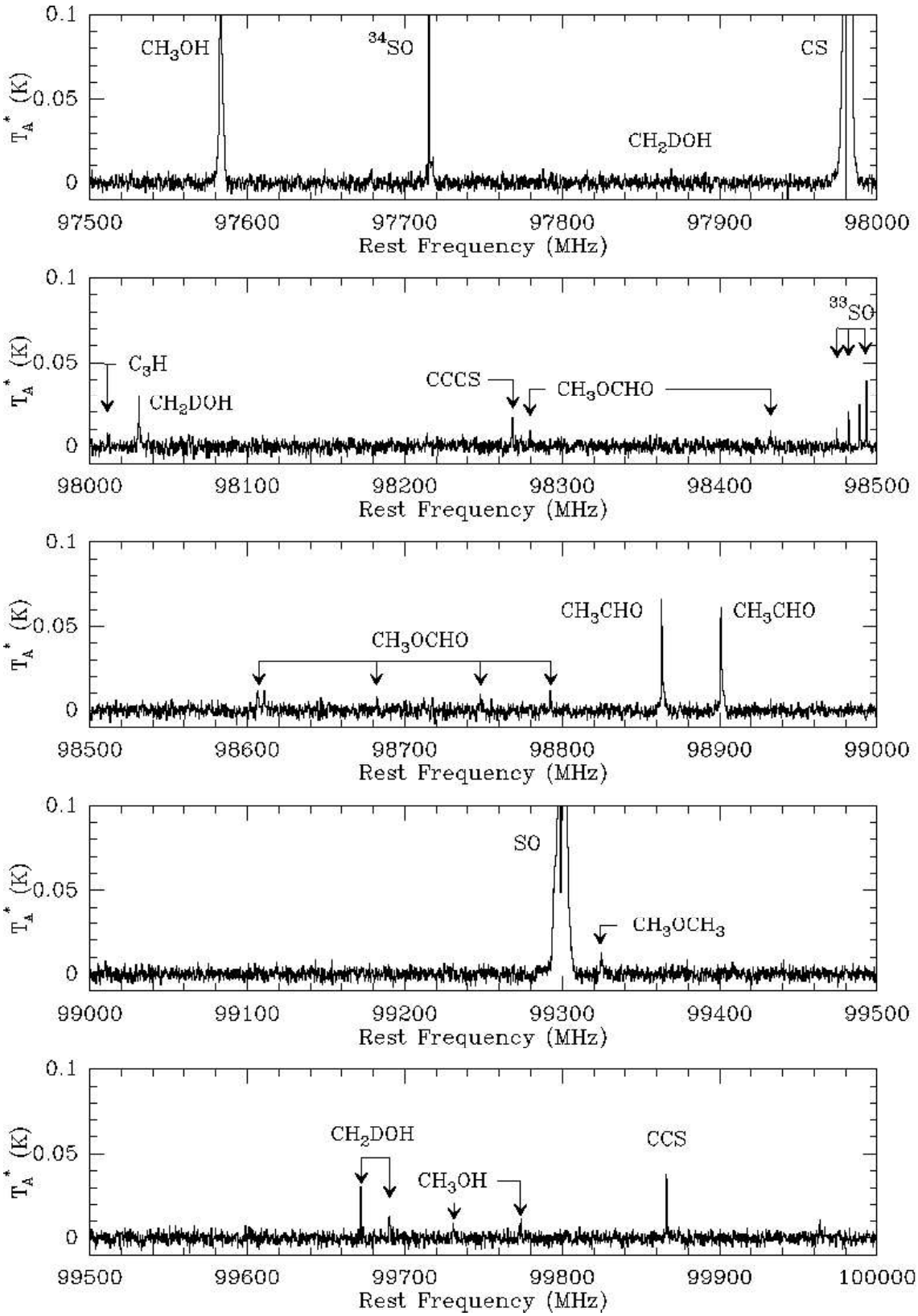
0.1
0.05
0
T_A^* (K)
CH_3OH
^{34}SO
CS
CH_2DOH
97500
97600
97700
97800
97900
98000
Rest Frequency (MHz)
^{33}SO
C_3H
CH_2DOH
CCCS
CH_3OCHO
98000
98100
98200
98300
98400
98500
Rest Frequency (MHz)
CH_3CHO
CH_3CHO
CH_3OCHO
98500
98600
98700
98800
98900
99000
Rest Frequency (MHz)
SO
CH_3OCH_3
99000
99100
99200
99300
99400
99500
Rest Frequency (MHz)
CH_2DOH
CCS
CH_3OH
99500
99600
99700
99800
99900
100000
Rest Frequency (MHz)

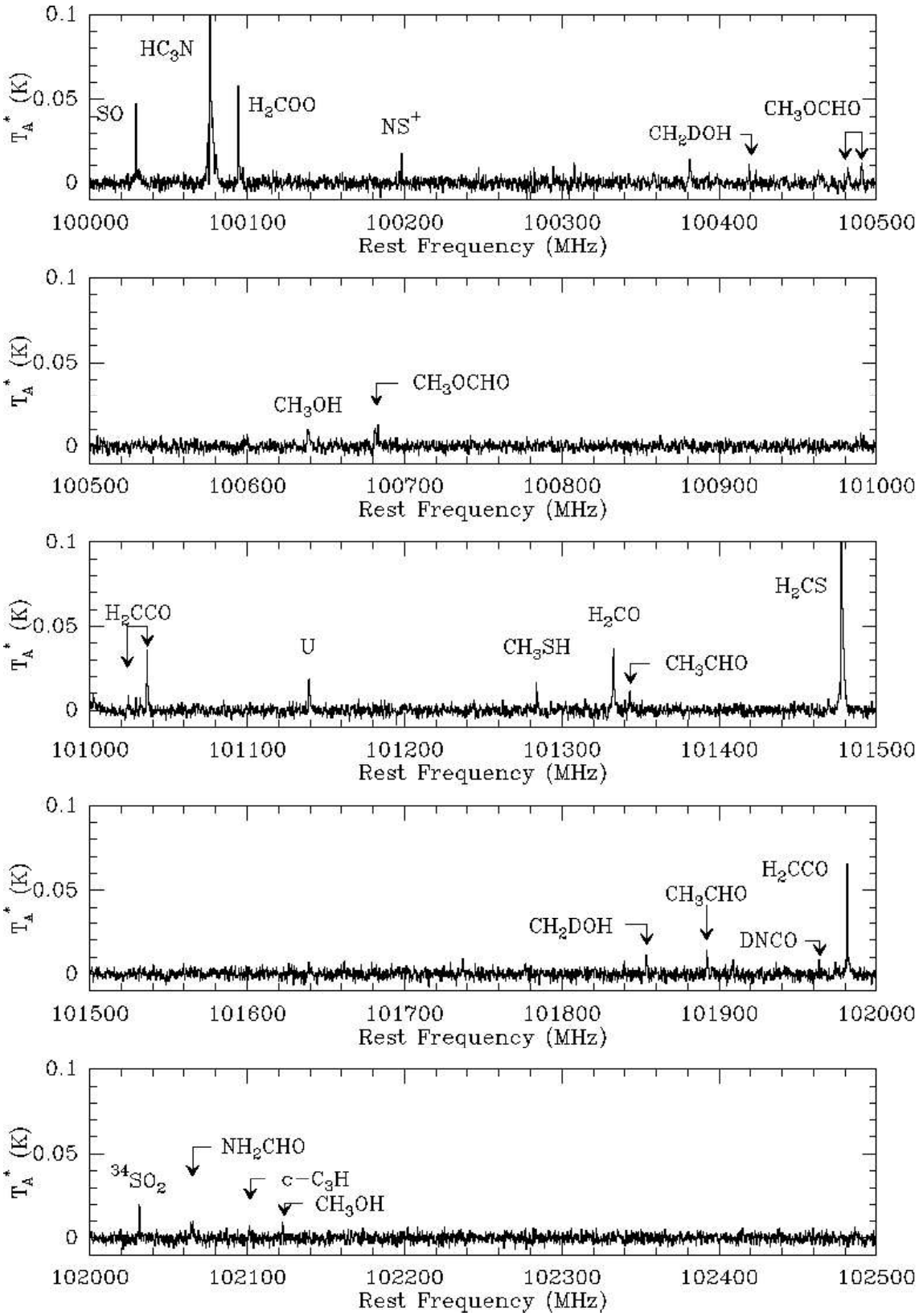
0.1
0.05
0
T_A^* (K)
HC_3N
SO
H_2COO
NS^+
CH_2DOH
CH_3OCHO
100000
100100
100200
100300
100400
100500
Rest Frequency (MHz)
CH_3OH
CH_3OCHO
100500
100600
100700
100800
100900
101000
H_2CCO
U
CH_3SH
H_2CO
CH_3CHO
H_2CS
101000
101100
101200
101300
101400
101500
CH_2DOH
CH_3CHO
H_2CCO
DNCO
101500
101600
101700
101800
101900
102000
$^{34}SO_2$
NH_2CHO
c$-C_3H$
CH_3OH
102000
102100
102200
102300
102400
102500

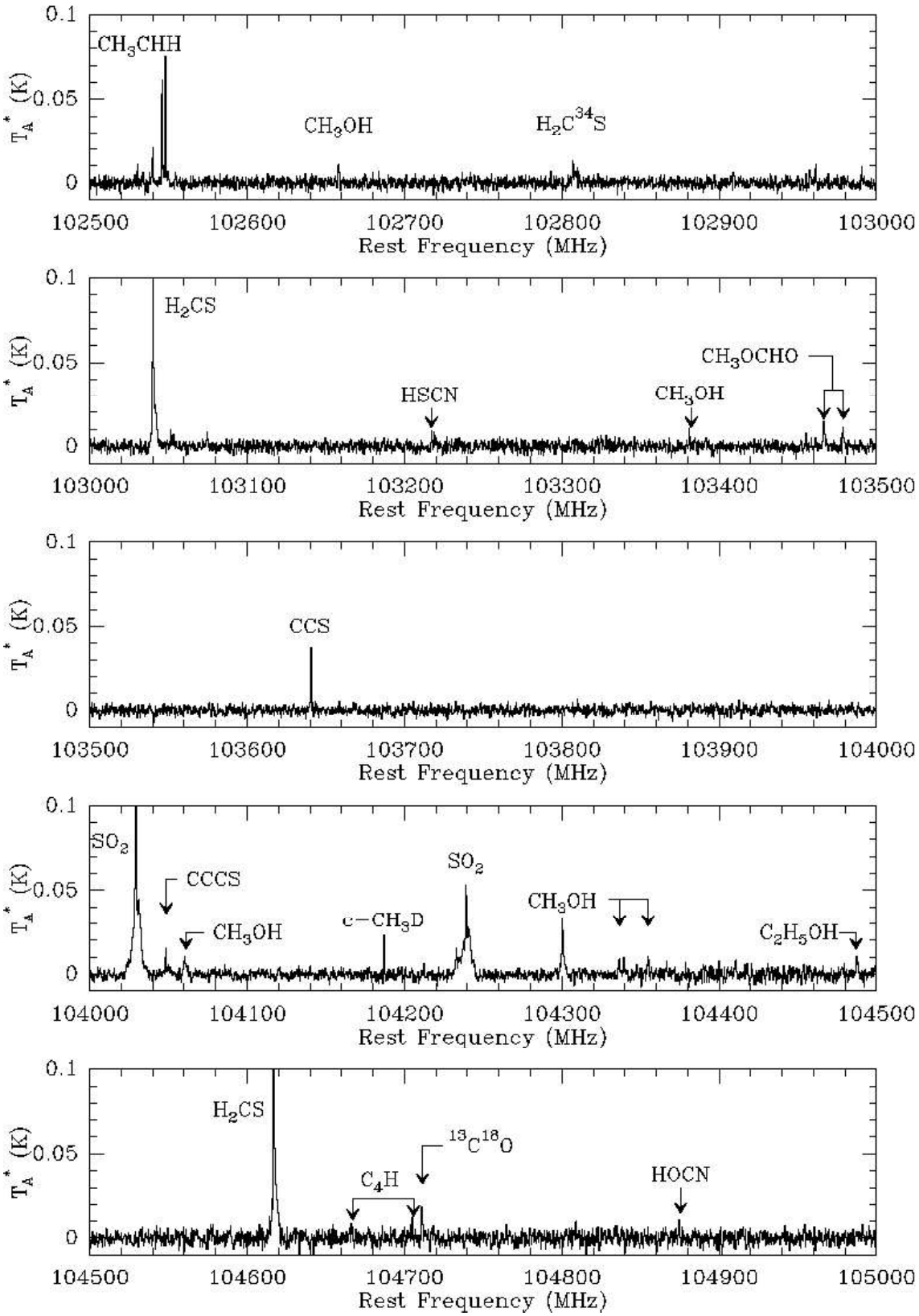
0.1
0.05
0
T_A^* (K)
CH_3CHH
CH_3OH
$H_2C^{34}S$
102500
102600
102700
102800
102900
103000
Rest Frequency (MHz)
H_2CS
HSCN
CH_3OH
CH_3OCHO
103000
103100
103200
103300
103400
103500
Rest Frequency (MHz)
CCS
103500
103600
103700
103800
103900
104000
Rest Frequency (MHz)
SO_2
CCCS
CH_3OH
c−CH_3D
SO_2
CH_3OH
C_2H_5OH
104000
104100
104200
104300
104400
104500
Rest Frequency (MHz)
H_2CS
$^{13}C^{18}O$
C_4H
HOCN
104500
104600
104700
104800
104900
105000
Rest Frequency (MHz)

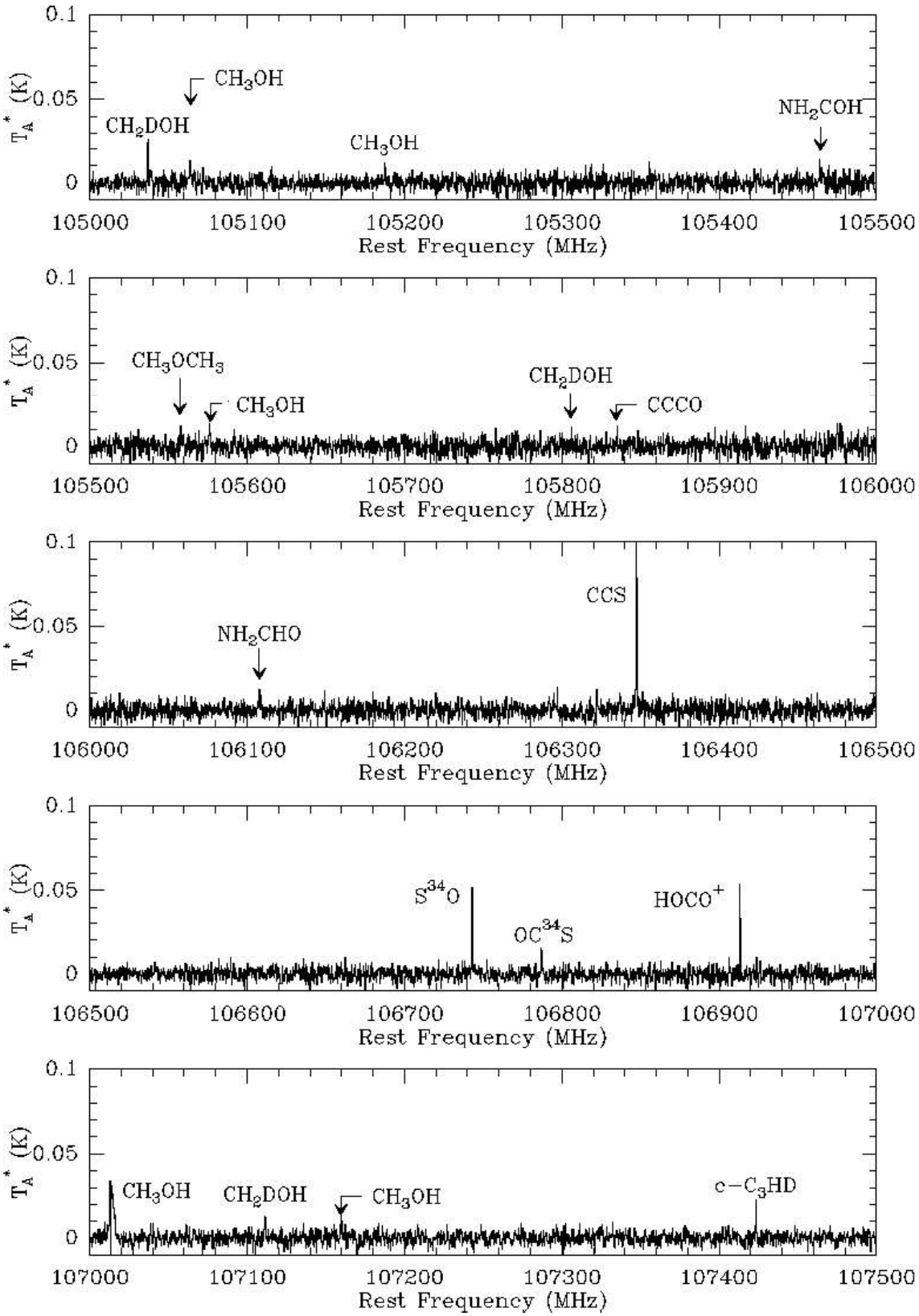
0.1
0.05
0
T_A^* (K)
CH_3OH
CH_2DOH
CH_3OH
NH_2COH
105000
105100
105200
105300
105400
105500
Rest Frequency (MHz)
CH_3OCH_3
CH_3OH
CH_2DOH
CCCO
105500
105600
105700
105800
105900
106000
Rest Frequency (MHz)
NH_2CHO
CCS
106000
106100
106200
106300
106400
106500
Rest Frequency (MHz)
$S^{34}O$
$OC^{34}S$
$HOCO^+$
106500
106600
106700
106800
106900
107000
Rest Frequency (MHz)
CH_3OH
CH_2DOH
CH_3OH
$c-C_3HD$
107000
107100
107200
107300
107400
107500
Rest Frequency (MHz)

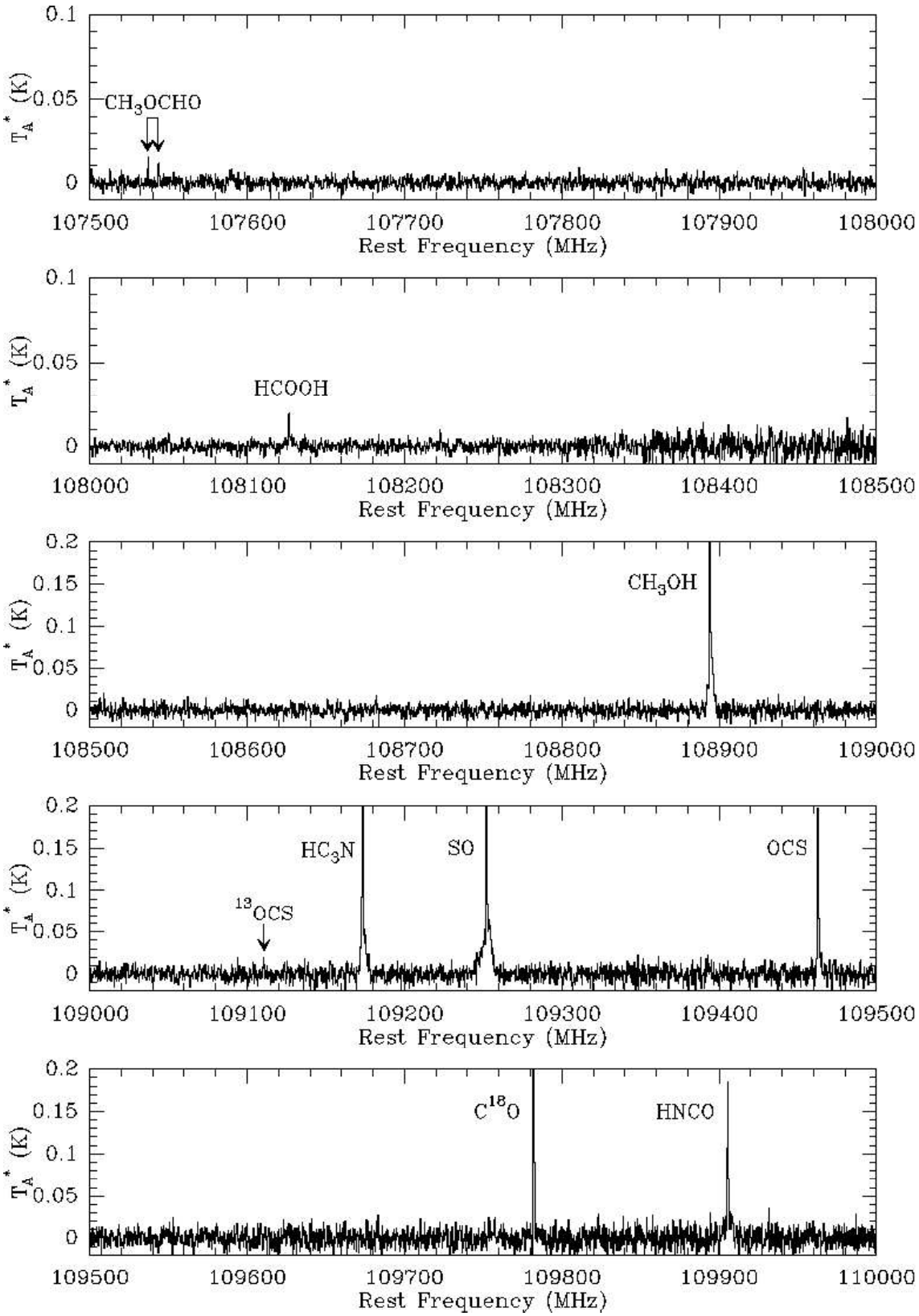
0.1
0.05
0
T_A^* (K)
CH_3OCHO
107500
107600
107700
107800
107900
108000
Rest Frequency (MHz)
HCOOH
108000
108100
108200
108300
108400
108500
CH_3OH
0.2
0.15
108500
108600
108700
108800
108900
109000
HC_3N
SO
OCS
^{13}OCS
109000
109100
109200
109300
109400
109500
$C^{18}O$
HNCO
109500
109600
109700
109800
109900
110000

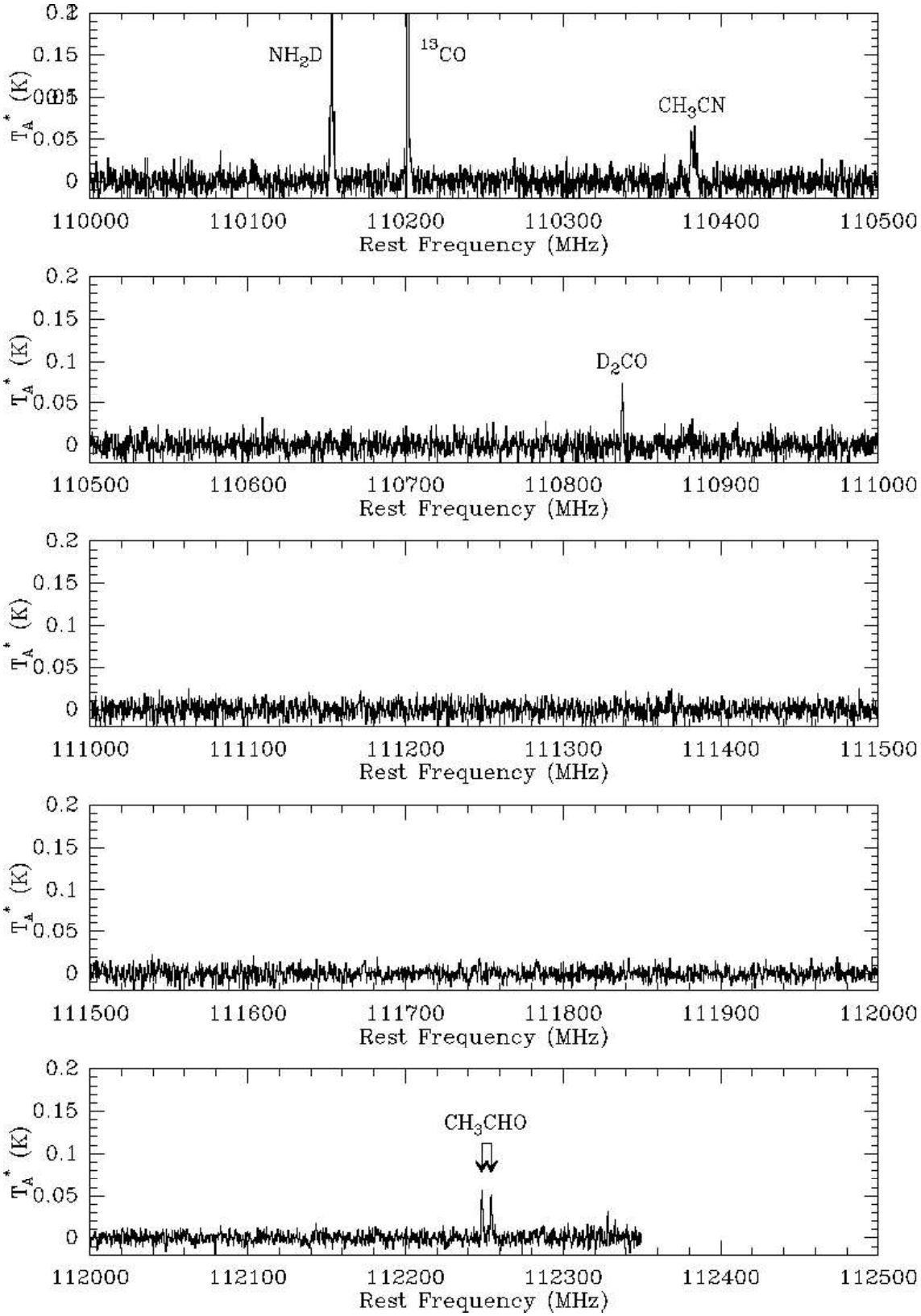
NH2D
13CO
CH3CN
D2CO
CH3CHO
T*A (K)
Rest Frequency (MHz)
110000
110100
110200
110300
110400
110500
110500
110600
110700
110800
110900
111000
111000
111100
111200
111300
111400
111500
111500
111600
111700
111800
111900
112000
112000
112100
112200
112300
112400
112500

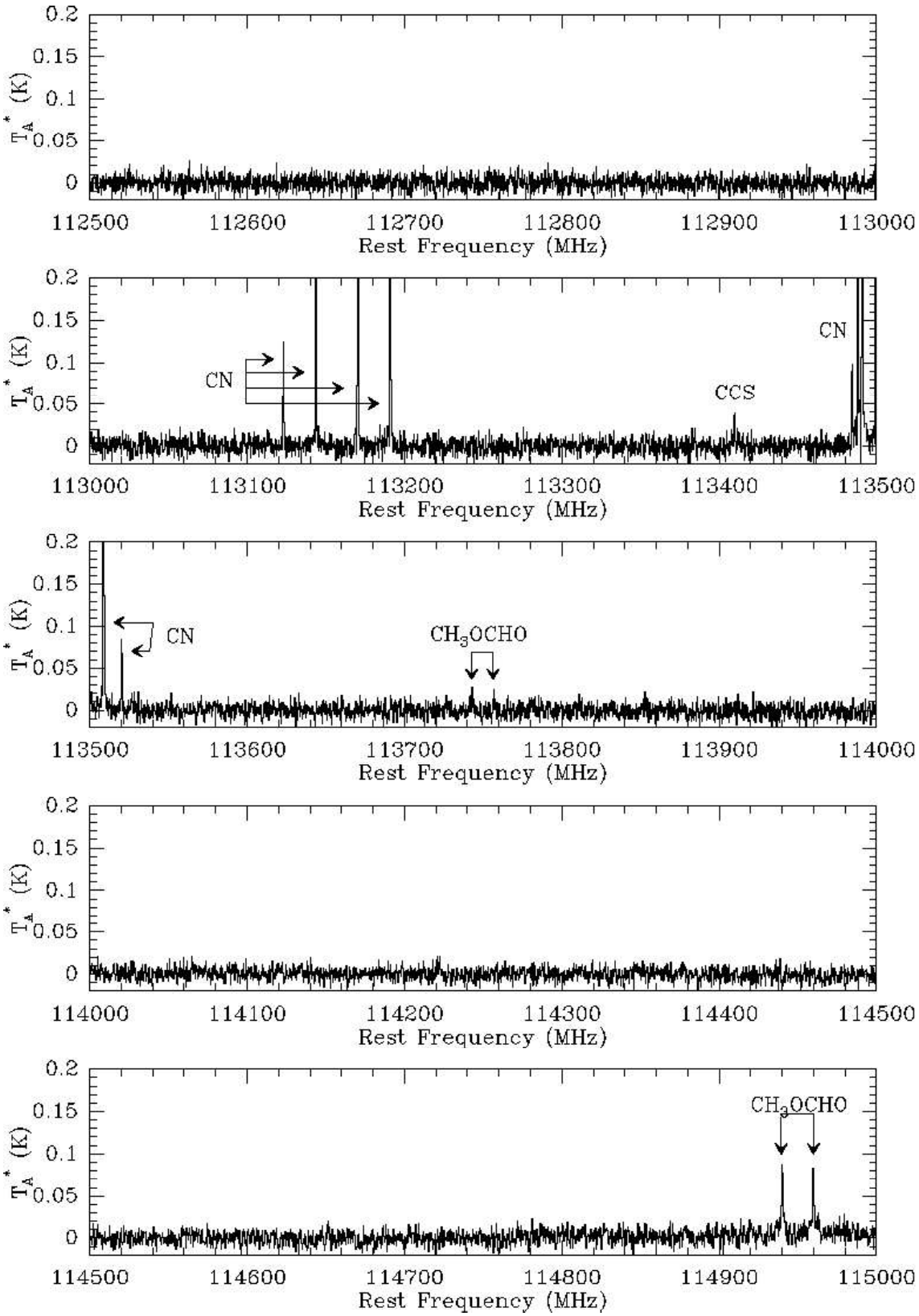
0.2
0.15
0.1
0.05
0
T_A^* (K)
112500
112600
112700
112800
112900
113000
Rest Frequency (MHz)
CN
CN
CCS
113000
113100
113200
113300
113400
113500
Rest Frequency (MHz)
CN
CH_3OCHO
113500
113600
113700
113800
113900
114000
Rest Frequency (MHz)
114000
114100
114200
114300
114400
114500
Rest Frequency (MHz)
CH_3OCHO
114500
114600
114700
114800
114900
115000
Rest Frequency (MHz)

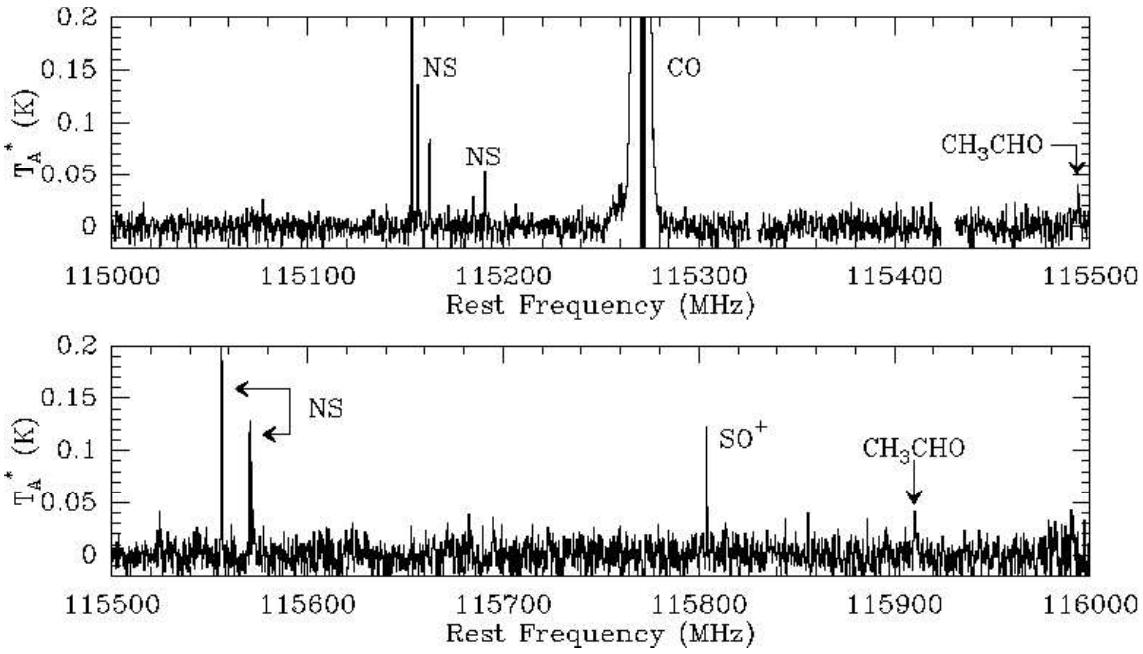
0.2
0.15
0.1
0.05
0
T_A^* (K)
NS
NS
CO
CH_3CHO
115000
115100
115200
115300
115400
115500
Rest Frequency (MHz)
0.2
0.15
0.1
0.05
0
T_A^* (K)
NS
SO^+
CH_3CHO
115500
115600
115700
115800
115900
116000
Rest Frequency (MHz)

Appendix B

IRAS 4A: Spectral Bands (2mm)

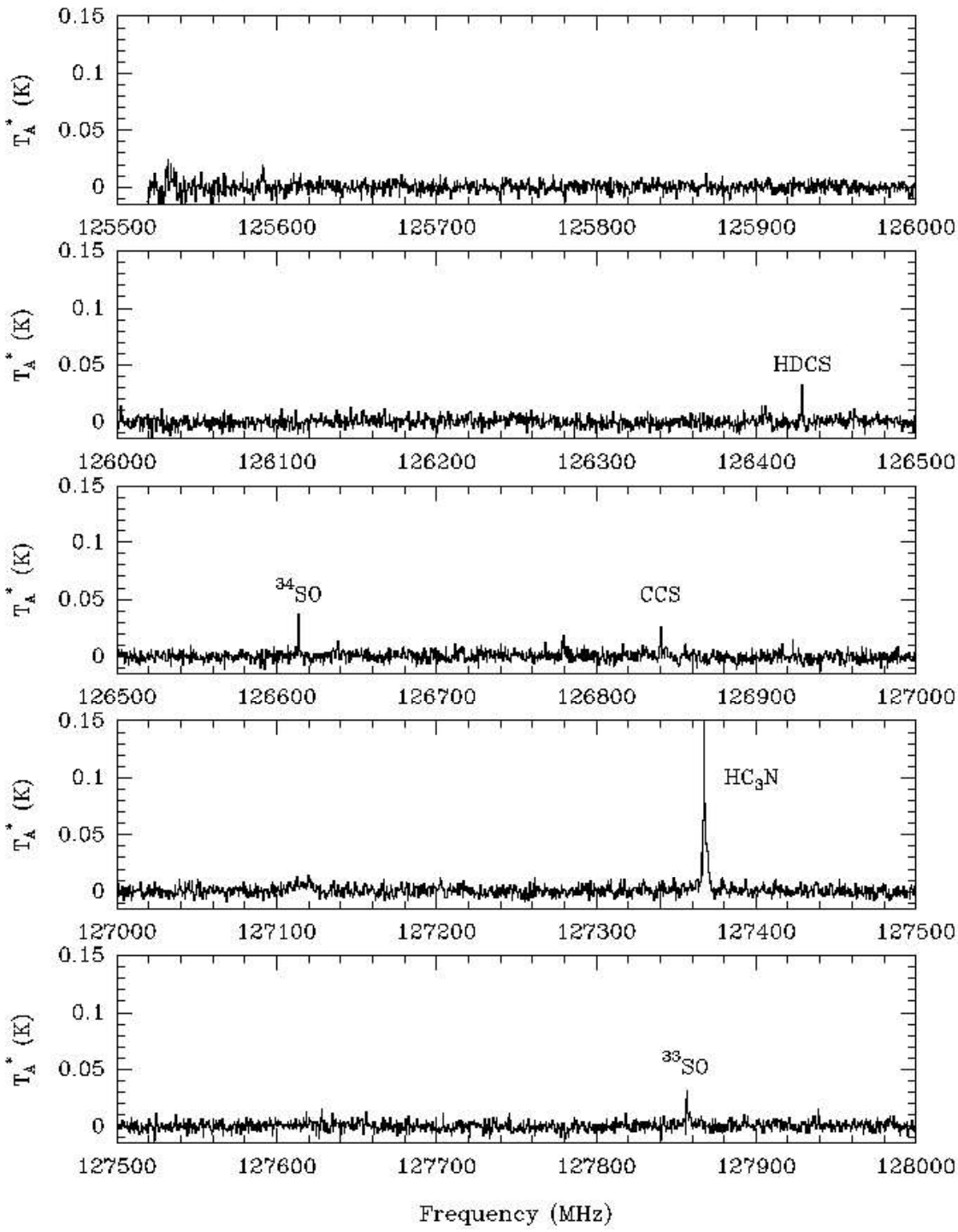
0.15
0.1
0.05
0
T_A^* (K)
125500
125600
125700
125800
125900
126000
HDCS
126000
126100
126200
126300
126400
126500
^{34}SO
CCS
126500
126600
126700
126800
126900
127000
HC_3N
127000
127100
127200
127300
127400
127500
^{33}SO
127500
127600
127700
127800
127900
128000
Frequency (MHz)

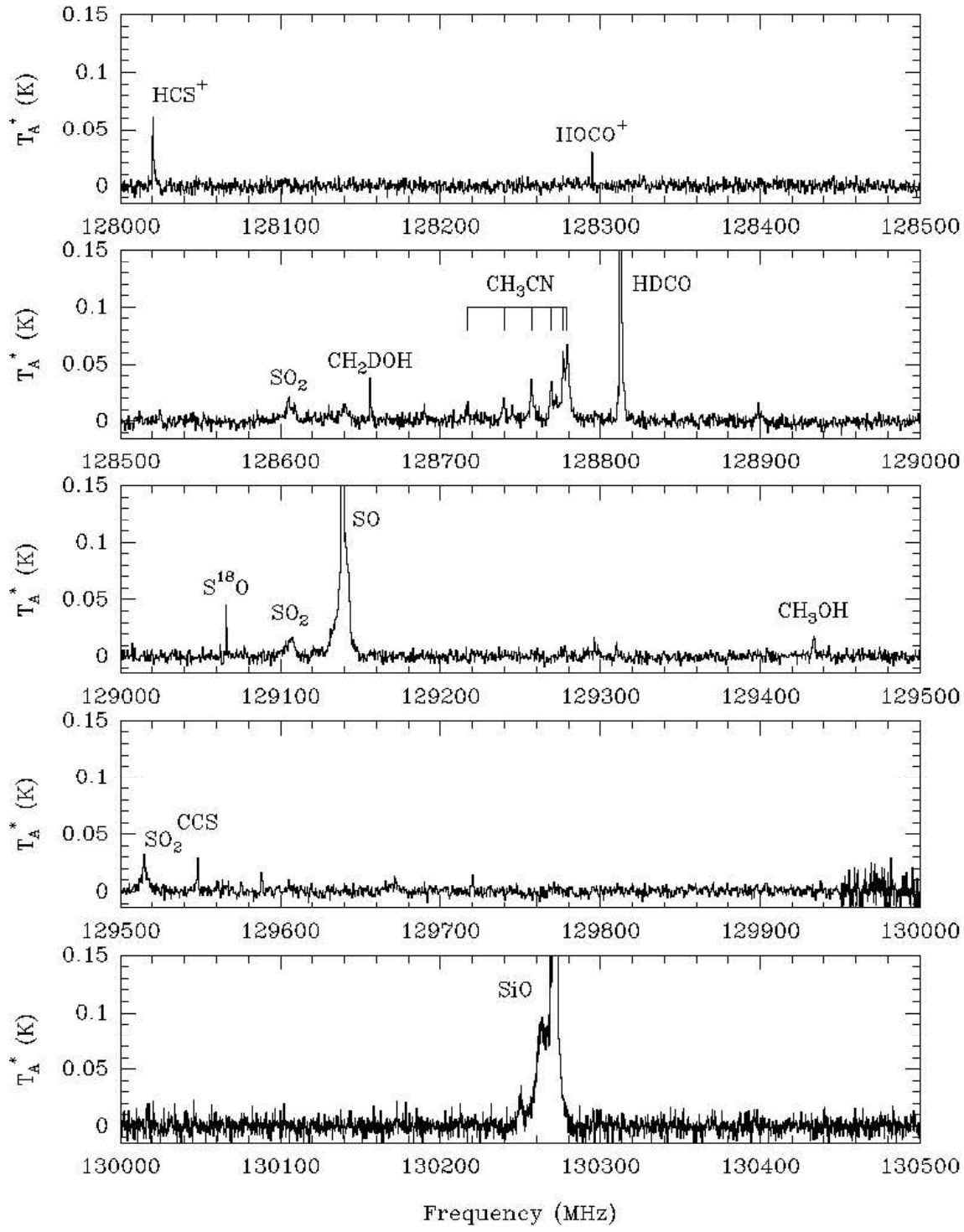
0.15
0.1
0.05
0
T_A^* (K)
HCS^+
$HOCO^+$
128000
128100
128200
128300
128400
128500
CH_3CN
HDCO
CH_2DOH
SO_2
128500
128600
128700
128800
128900
129000
SO
$S^{18}O$
SO_2
CH_3OH
129000
129100
129200
129300
129400
129500
CCS
SO_2
129500
129600
129700
129800
129900
130000
SiO
130000
130100
130200
130300
130400
130500
Frequency (MHz)

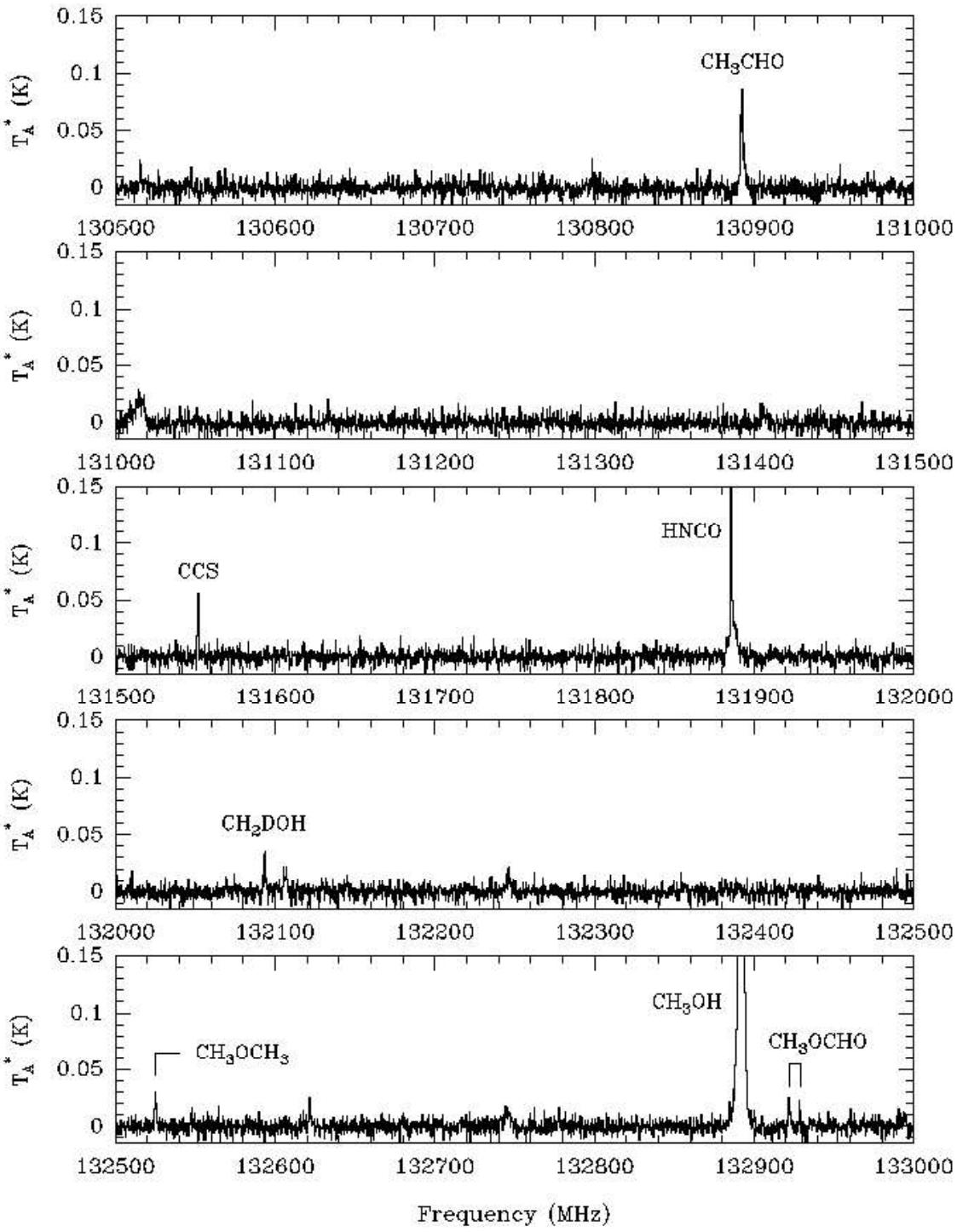
0.15
0.1
0.05
0
T_A^* (K)
CH_3CHO
130500
130600
130700
130800
130900
131000
131100
131200
131300
131400
131500
CCS
HNCO
131500
131600
131700
131800
131900
132000
CH_2DOH
132000
132100
132200
132300
132400
132500
CH_3OH
CH_3OCHO
CH_3OCH_3
132500
132600
132700
132800
132900
133000
Frequency (MHz)

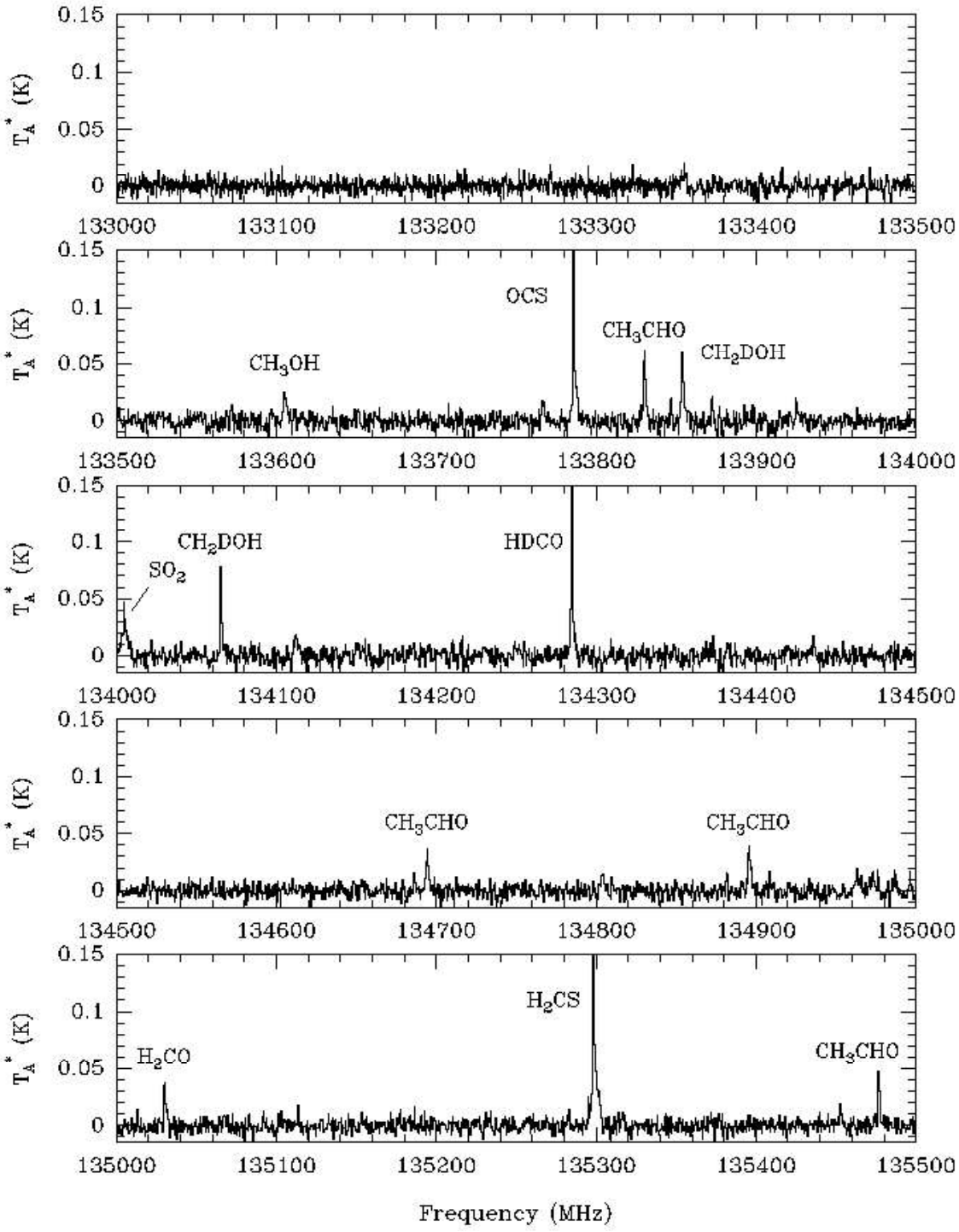
0.15
0.1
0.05
0
T_A^* (K)
133000
133100
133200
133300
133400
133500
OCS
CH_3CHO
CH_2DOH
CH_3OH
133500
133600
133700
133800
133900
134000
CH_2DOH
SO_2
HDCO
134000
134100
134200
134300
134400
134500
CH_3CHO
CH_3CHO
134500
134600
134700
134800
134900
135000
H_2CS
H_2CO
CH_3CHO
135000
135100
135200
135300
135400
135500
Frequency (MHz)

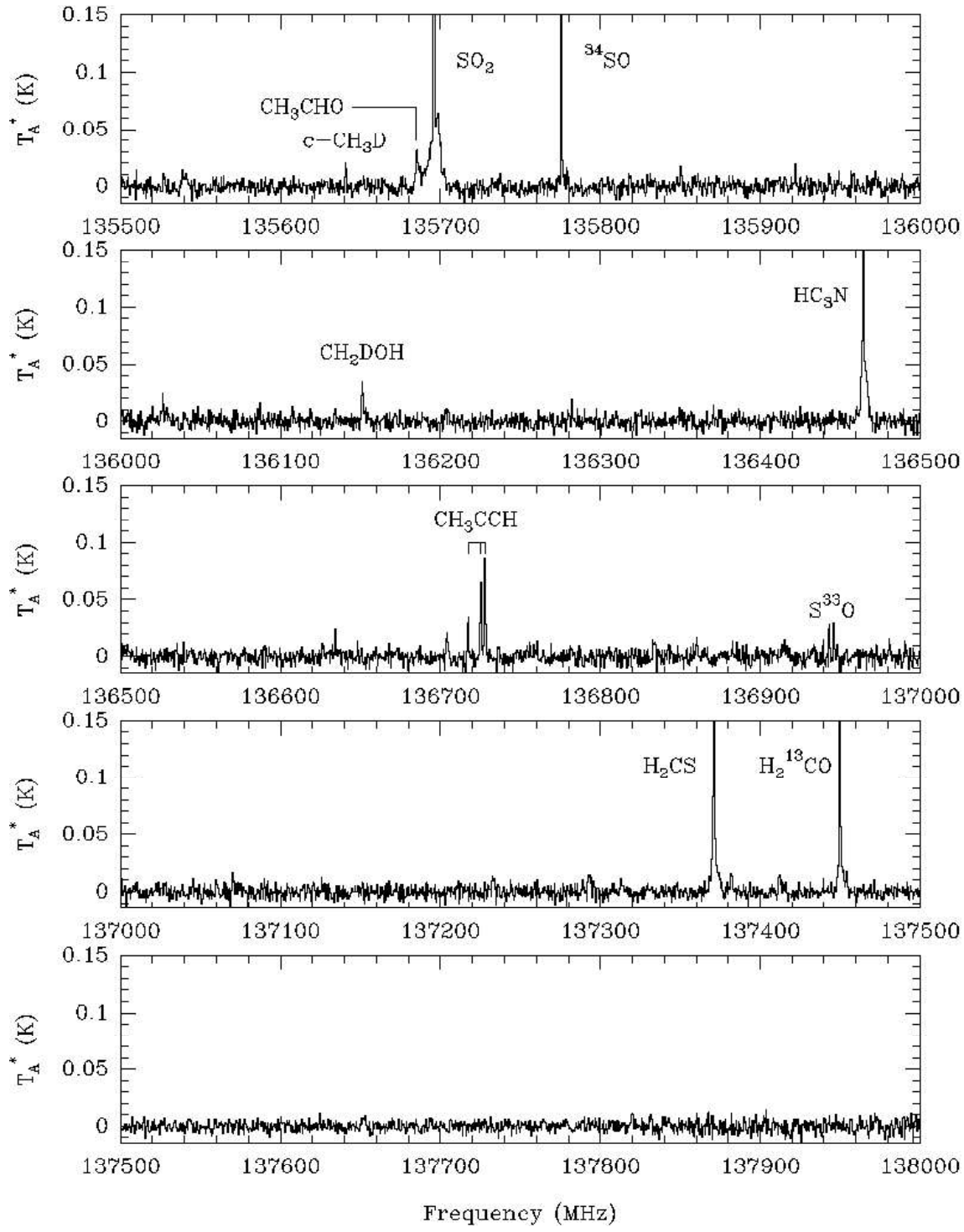
0.15
0.1
0.05
0
T_A^* (K)
SO_2
^{34}SO
CH_3CHO
c−CH_3D
135500
135600
135700
135800
135900
136000
HC_3N
CH_2DOH
136000
136100
136200
136300
136400
136500
CH_3CCH
$S^{33}O$
136500
136600
136700
136800
136900
137000
H_2CS
$H_2{}^{13}CO$
137000
137100
137200
137300
137400
137500
137500
137600
137700
137800
137900
138000
Frequency (MHz)

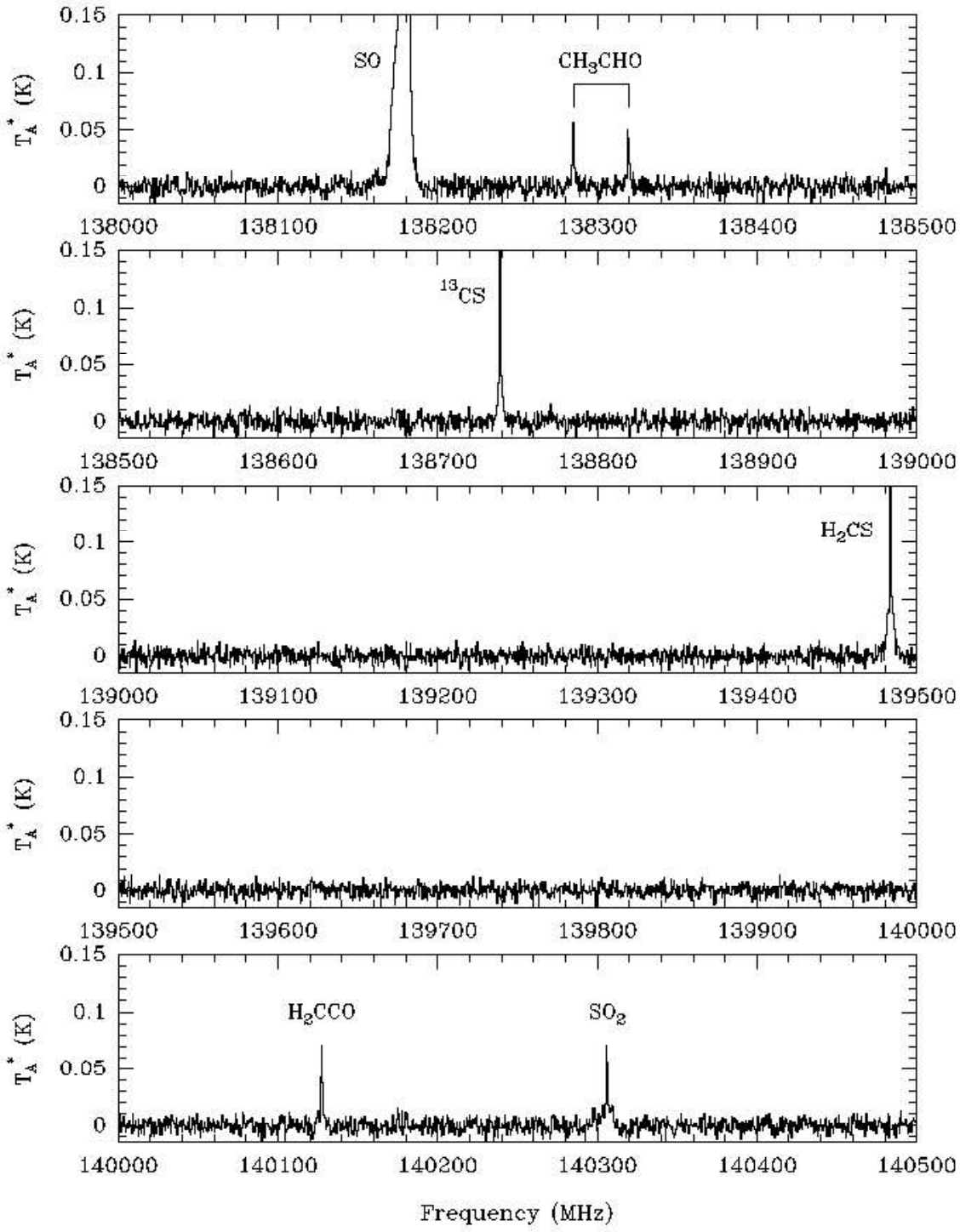
SO
CH3CHO
13CS
H2CS
H2CCO
SO2
TA* (K)
Frequency (MHz)

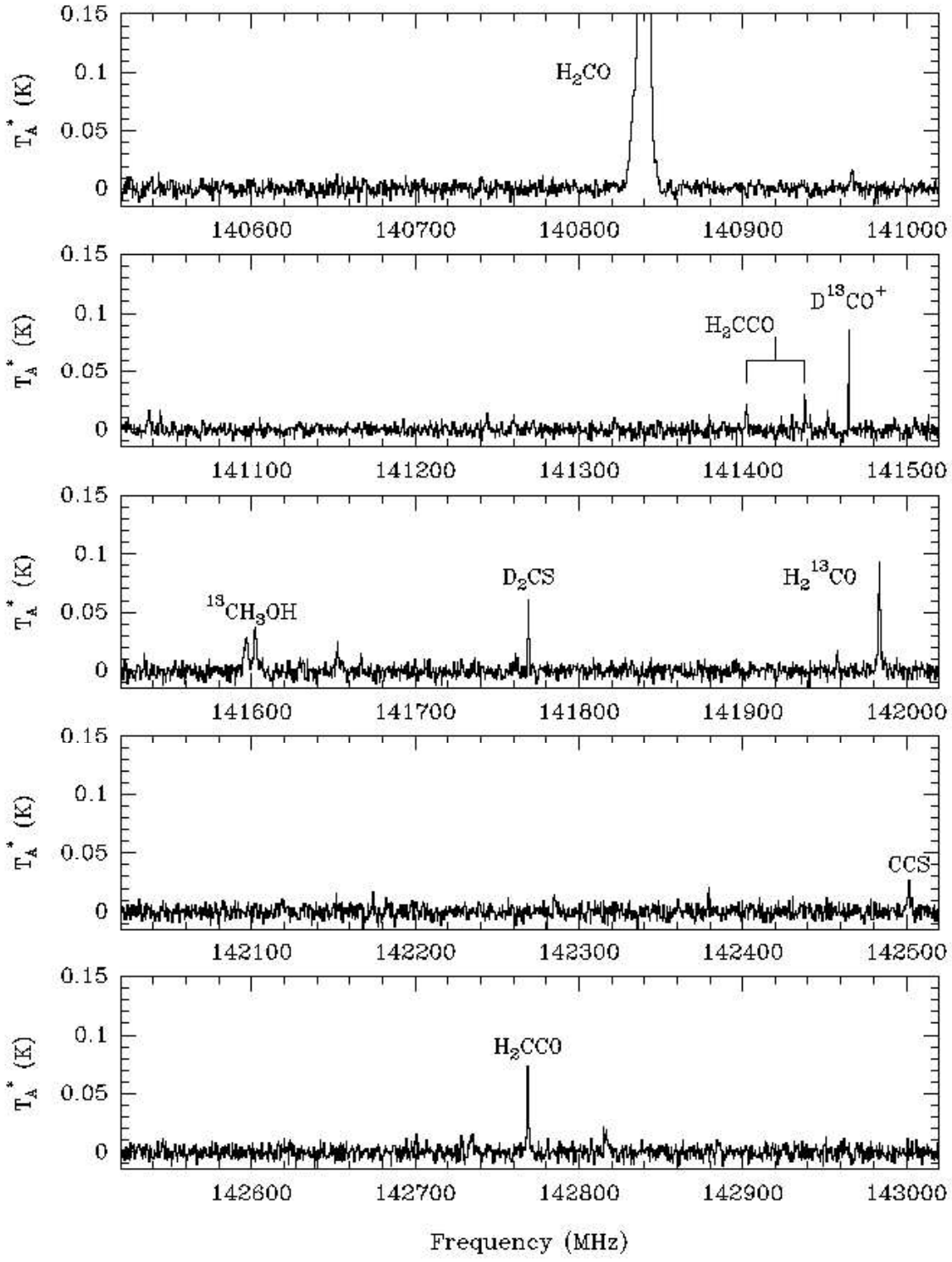
0.15
0.1
0.05
0
T_A^* (K)
H_2CO
140600
140700
140800
140900
141000
H_2CCO
$D^{13}CO^+$
141100
141200
141300
141400
141500
$^{13}CH_3OH$
D_2CS
$H_2{}^{13}CO$
141600
141700
141800
141900
142000
CCS
142100
142200
142300
142400
142500
H_2CCO
142600
142700
142800
142900
143000
Frequency (MHz)

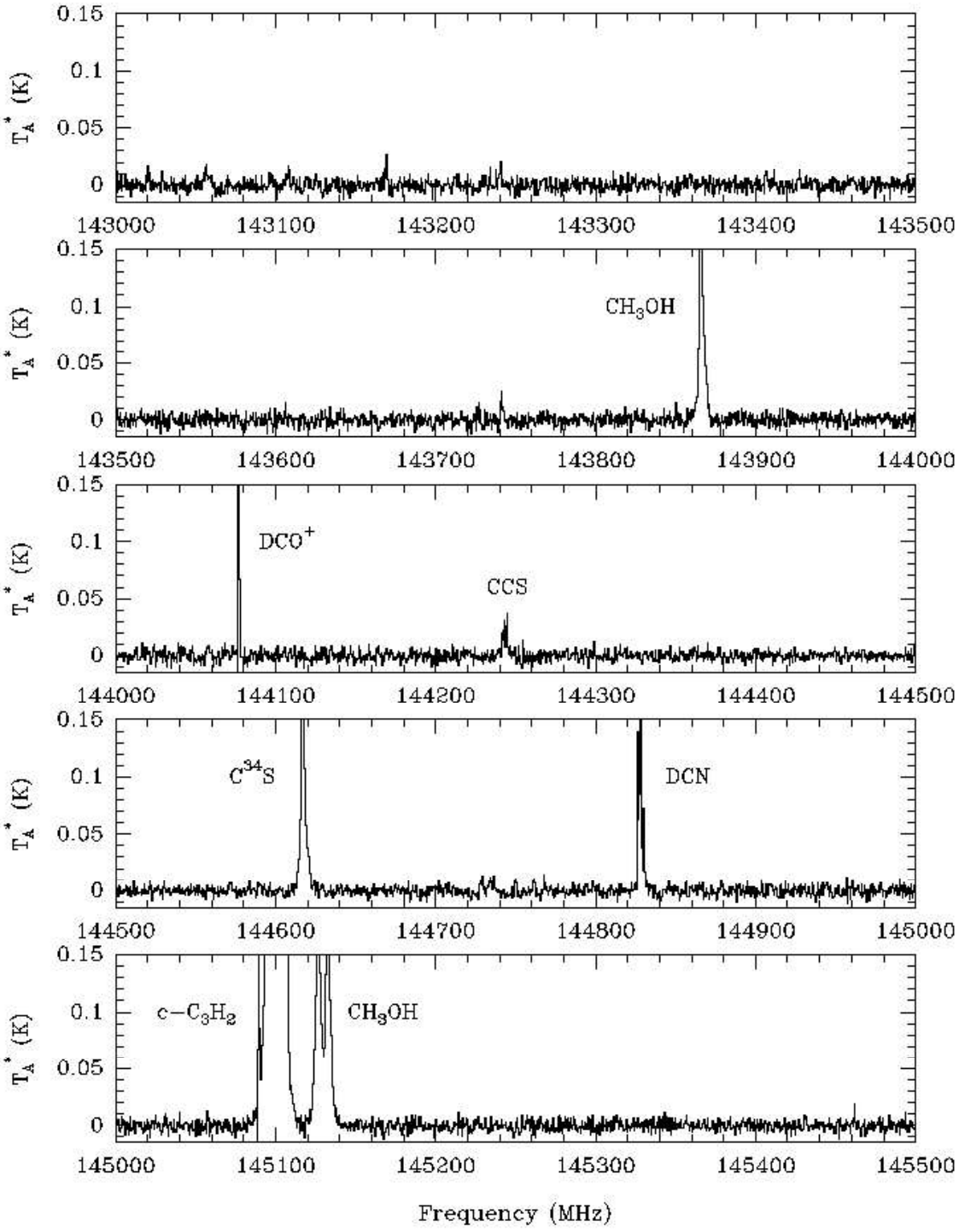
0.15
0.1
0.05
0
T_A^* (K)
143000
143100
143200
143300
143400
143500
CH_3OH
143500
143600
143700
143800
143900
144000
DCO^+
CCS
144000
144100
144200
144300
144400
144500
$C^{34}S$
DCN
144500
144600
144700
144800
144900
145000
$c-C_3H_2$
CH_3OH
145000
145100
145200
145300
145400
145500
Frequency (MHz)

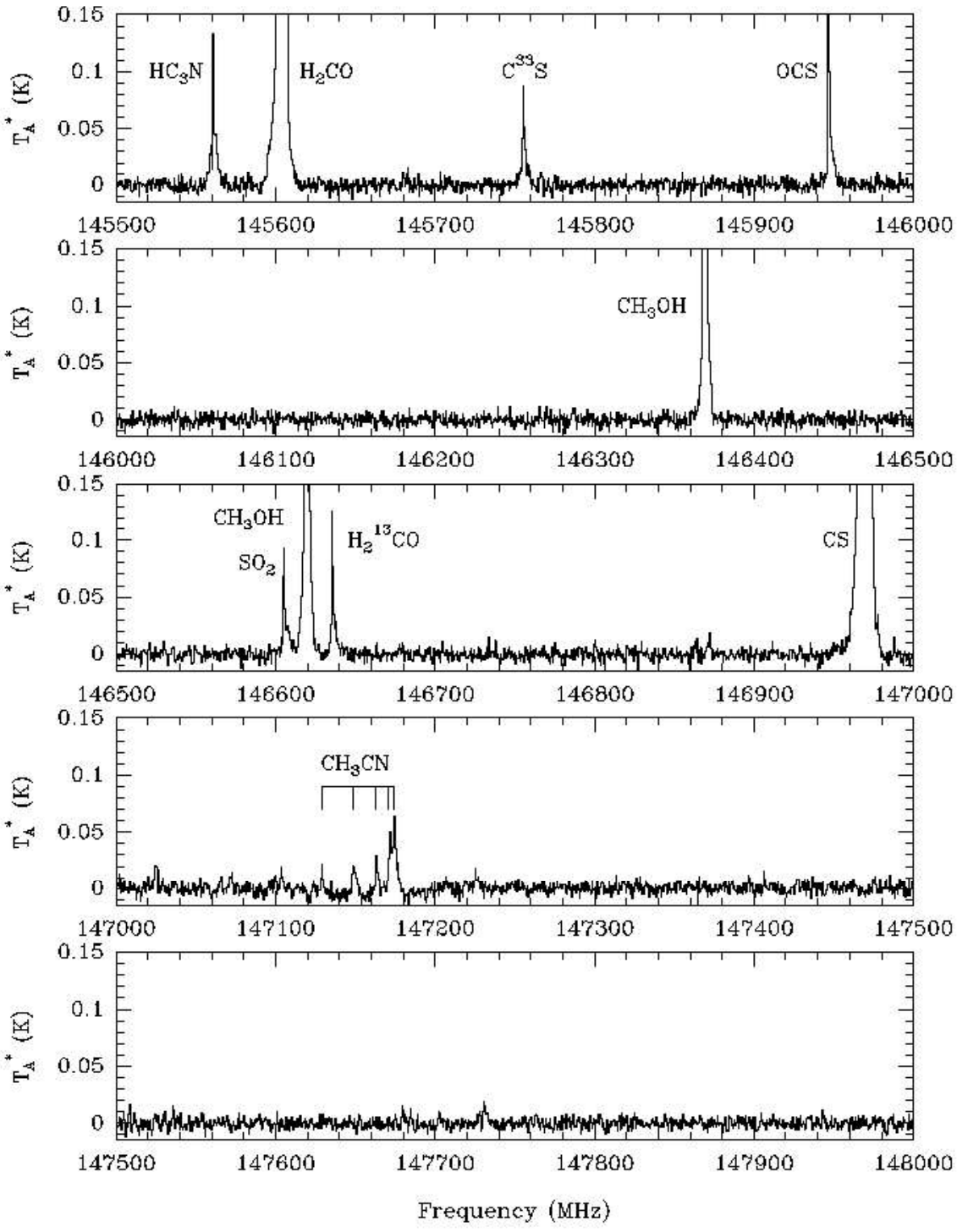
HC3N
H2CO
C33S
OCS
CH3OH
CH3OH
SO2
H2 13CO
CS
CH3CN
T*A (K)
Frequency (MHz)

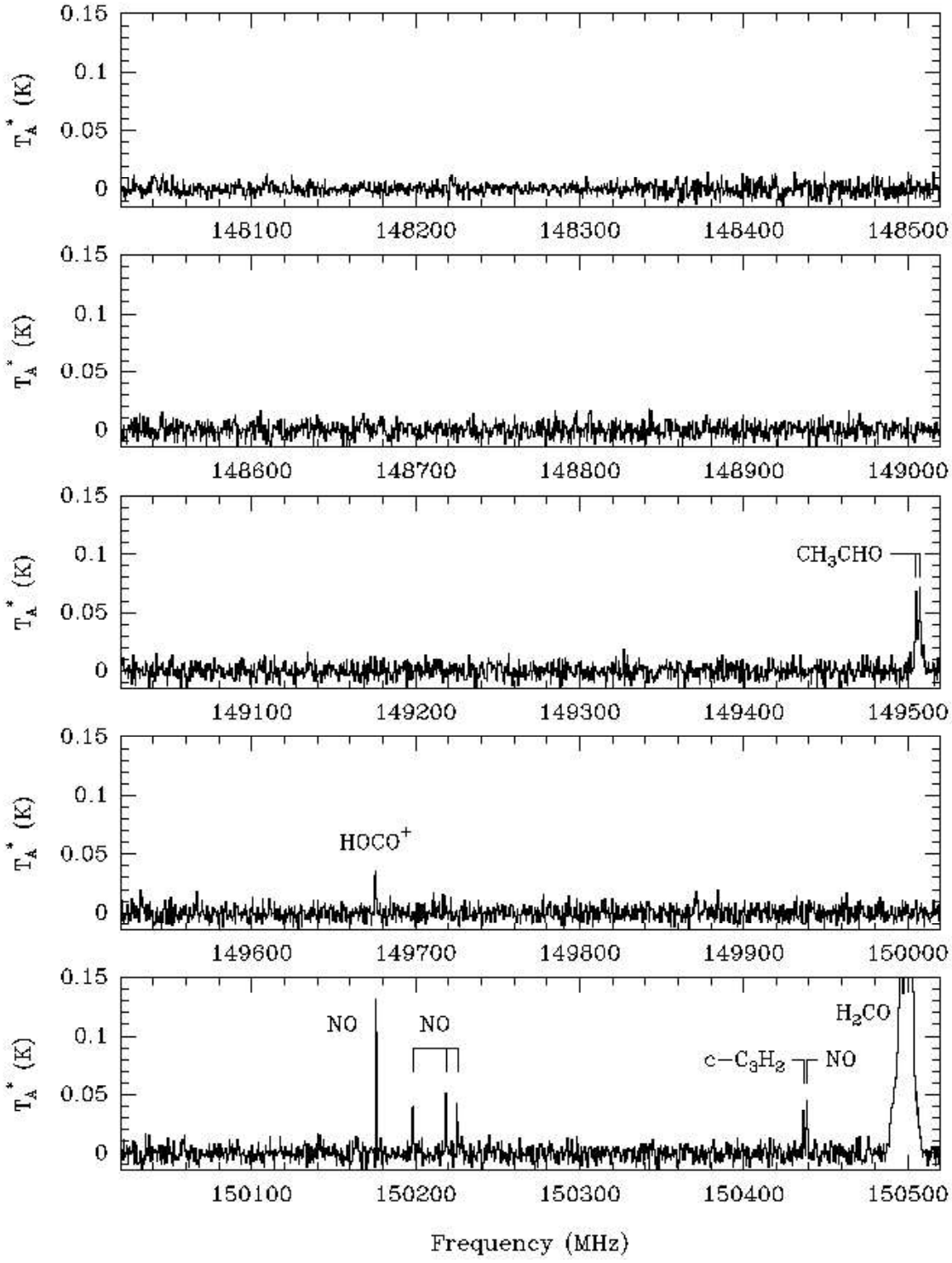
0.15
0.1
0.05
0
T_A^* (K)
148100
148200
148300
148400
148500
148600
148700
148800
148900
149000
CH_3CHO
149100
149200
149300
149400
149500
$HOCO^+$
149600
149700
149800
149900
150000
NO
NO
$c-C_3H_2$
NO
H_2CO
150100
150200
150300
150400
150500
Frequency (MHz)

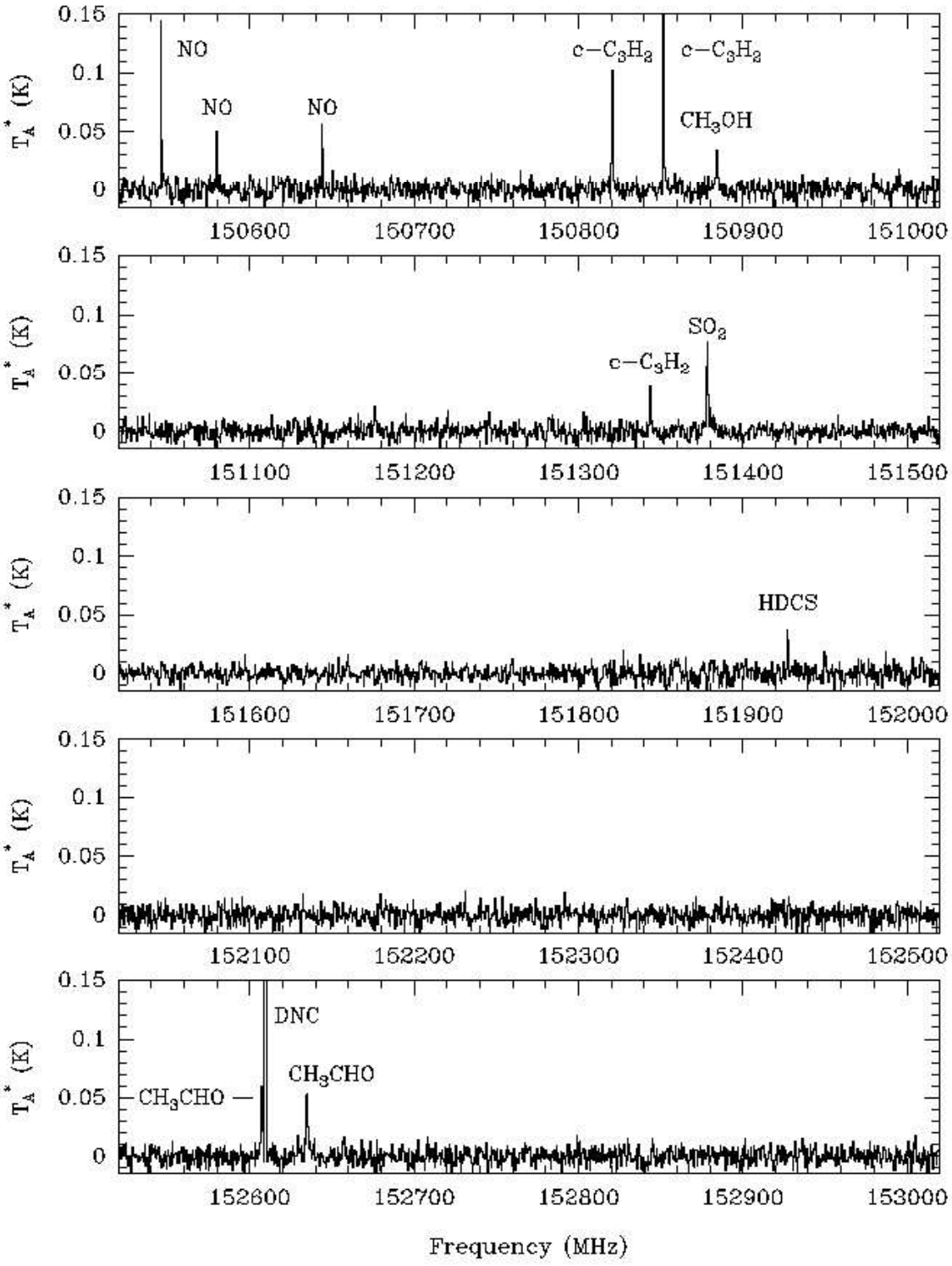
NO
NO
NO
c−C3H2
c−C3H2
CH3OH
SO2
c−C3H2
HDCS
DNC
CH3CHO
CH3CHO
TA* (K)
Frequency (MHz)

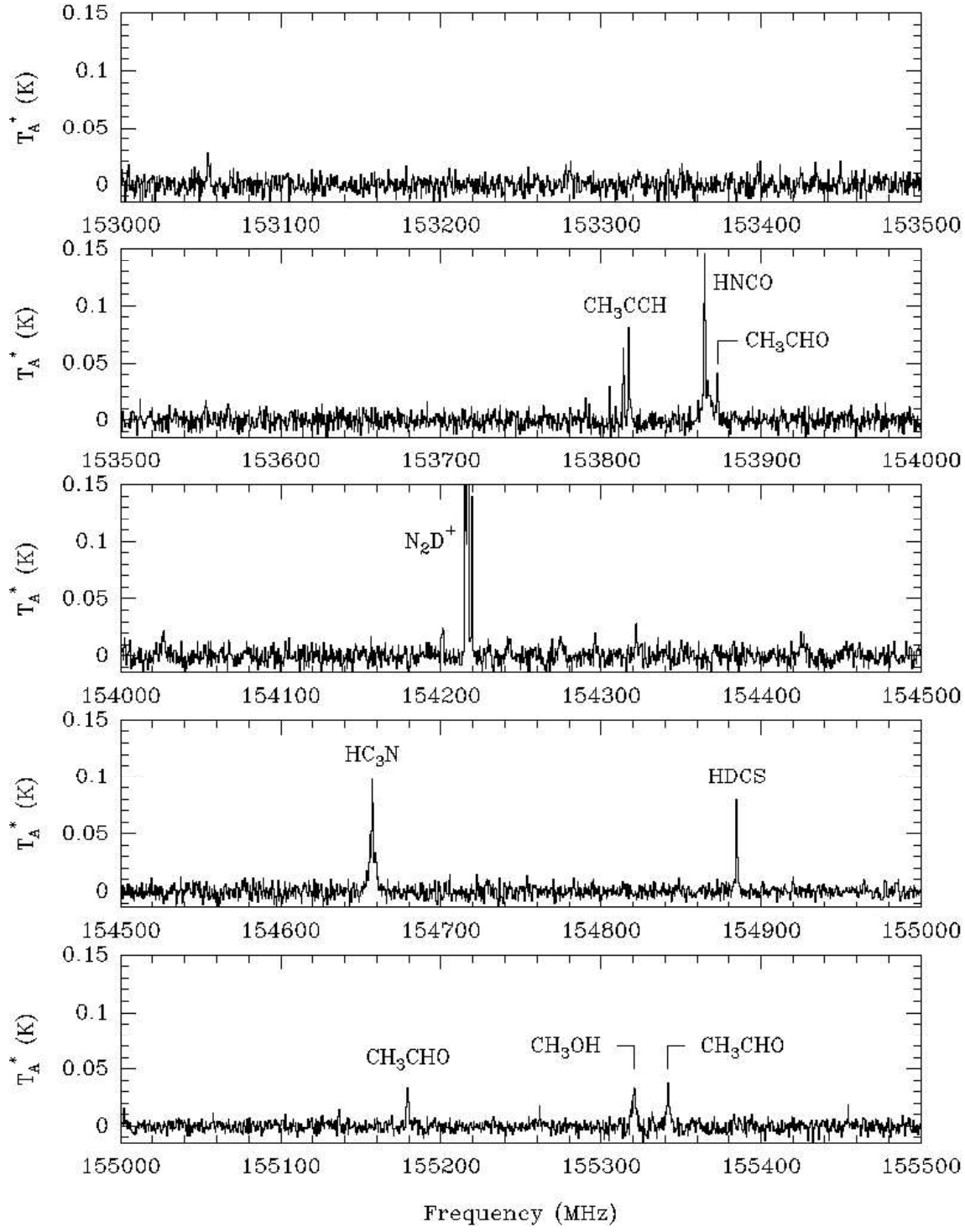
0.15
0.1
0.05
0
T_A^* (K)
153000
153100
153200
153300
153400
153500
CH_3CCH
HNCO
CH_3CHO
153500
153600
153700
153800
153900
154000
N_2D^+
154000
154100
154200
154300
154400
154500
HC_3N
HDCS
154500
154600
154700
154800
154900
155000
CH_3CHO
CH_3OH
CH_3CHO
155000
155100
155200
155300
155400
155500
Frequency (MHz)

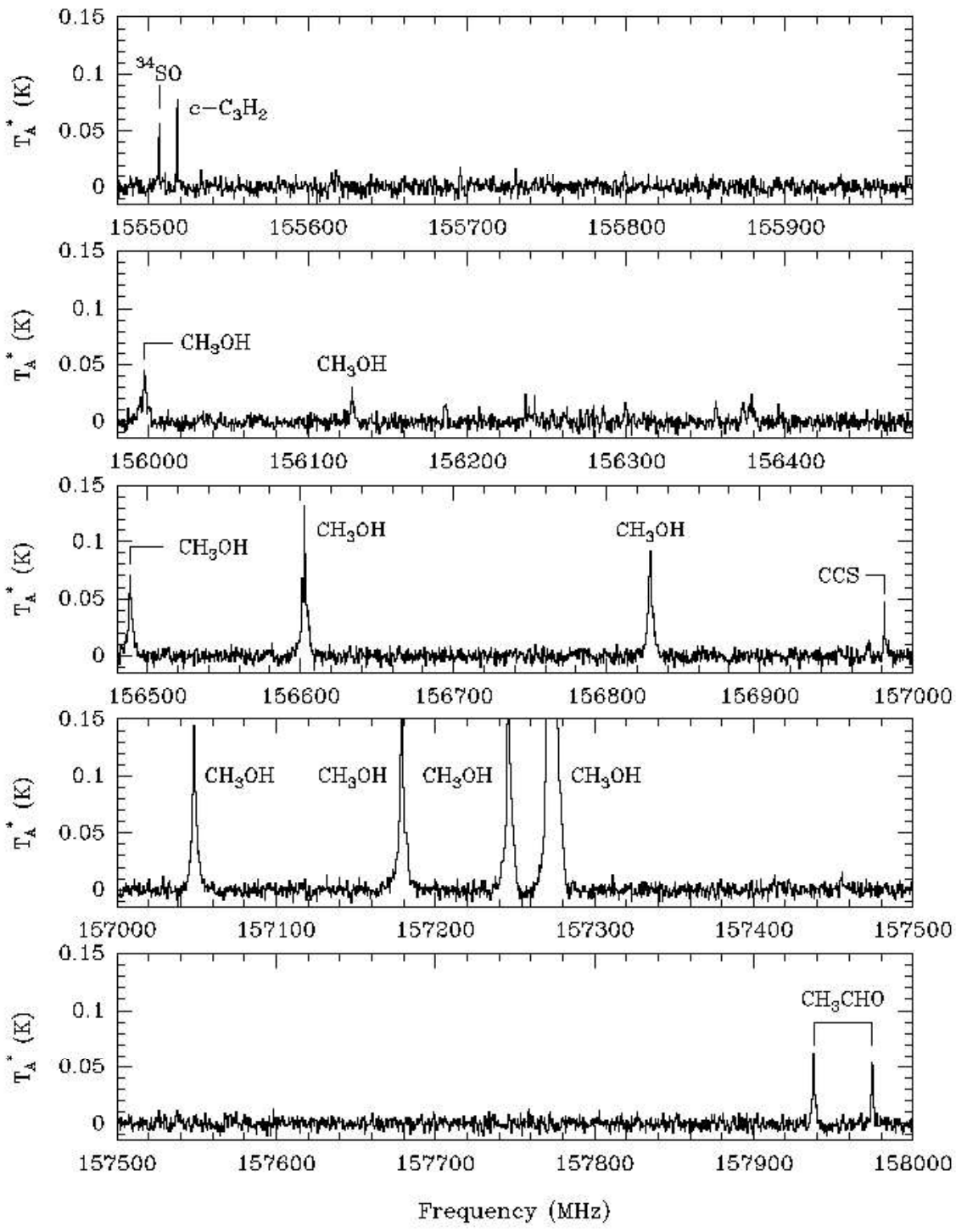
0.15
0.1
0.05
0
T_A^* (K)
^{34}SO
$c-C_3H_2$
155500
155600
155700
155800
155900
CH$_3$OH
CH$_3$OH
156000
156100
156200
156300
156400
CH$_3$OH
CH$_3$OH
CH$_3$OH
CCS
156500
156600
156700
156800
156900
157000
CH$_3$OH
CH$_3$OH
CH$_3$OH
CH$_3$OH
157000
157100
157200
157300
157400
157500
CH$_3$CHO
157500
157600
157700
157800
157900
158000
Frequency (MHz)

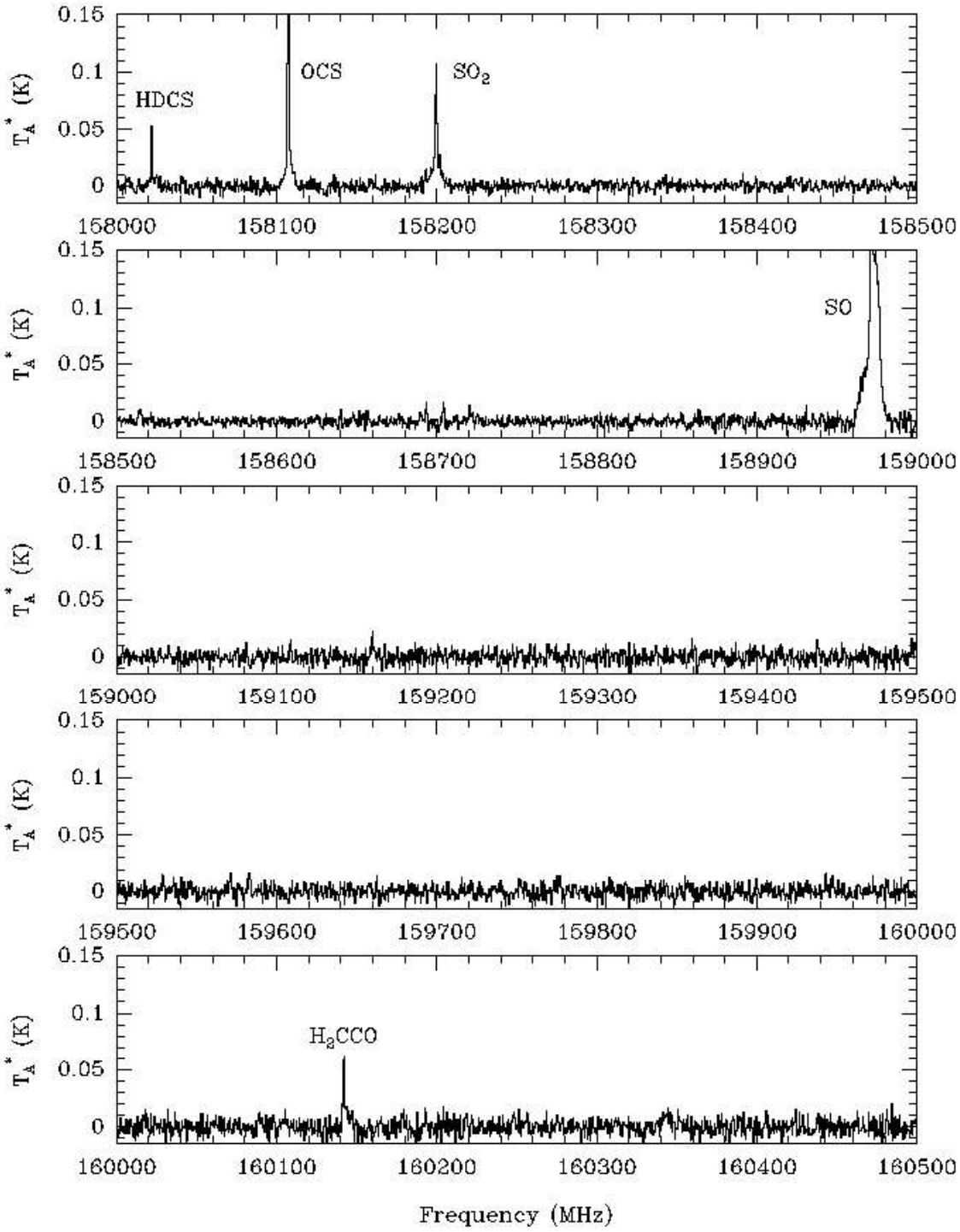
HDCS
OCS
SO2
SO
H2CCO
T_A* (K)
0.15
0.1
0.05
0
158000
158100
158200
158300
158400
158500
158600
158700
158800
158900
159000
159100
159200
159300
159400
159500
159600
159700
159800
159900
160000
160100
160200
160300
160400
160500
Frequency (MHz)

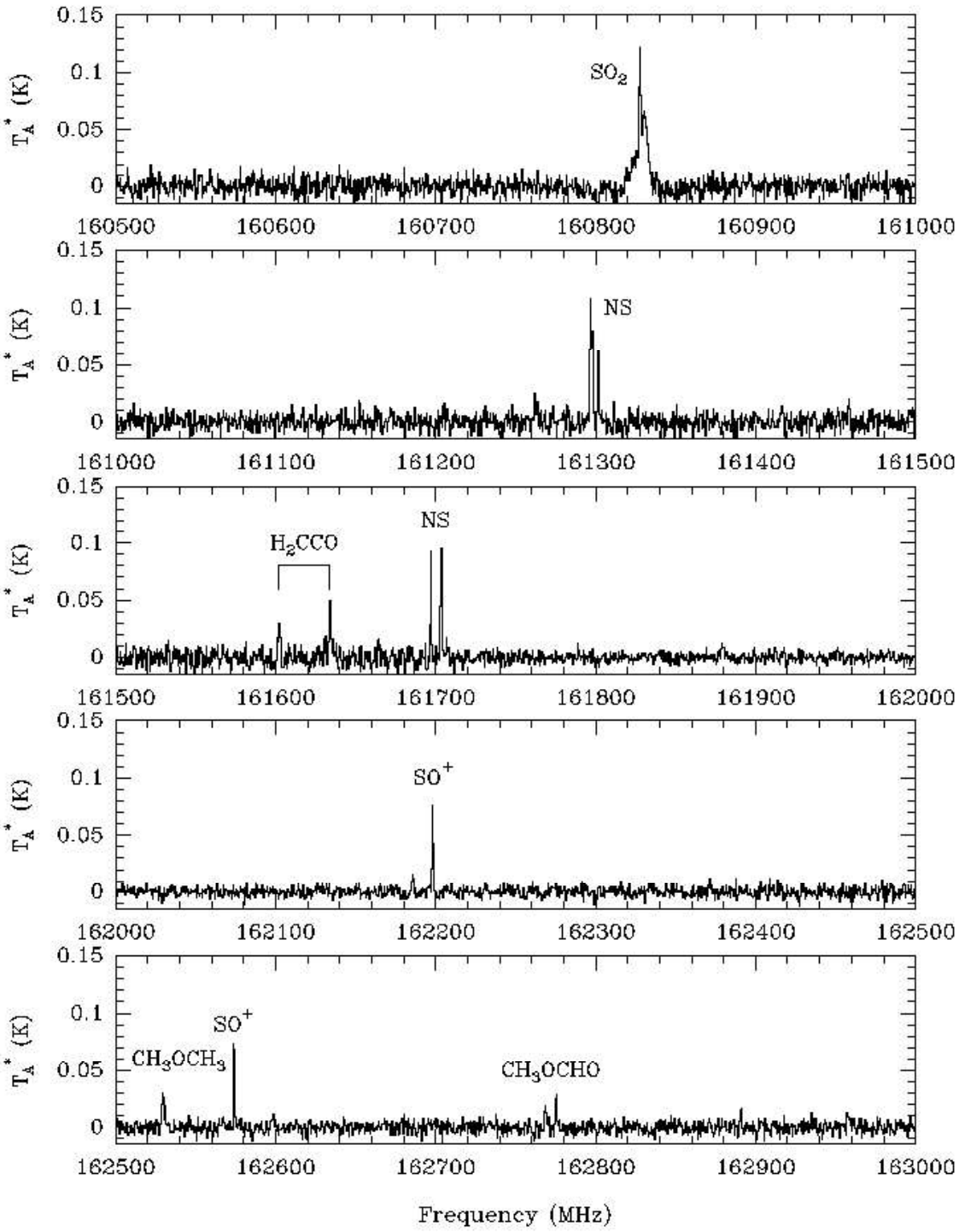
0.15
0.1
0.05
0
T_A^* (K)
SO_2
160500
160600
160700
160800
160900
161000
NS
161000
161100
161200
161300
161400
161500
H_2CCO
NS
161500
161600
161700
161800
161900
162000
SO^+
162000
162100
162200
162300
162400
162500
SO^+
CH_3OCH_3
CH_3OCHO
162500
162600
162700
162800
162900
163000
Frequency (MHz)

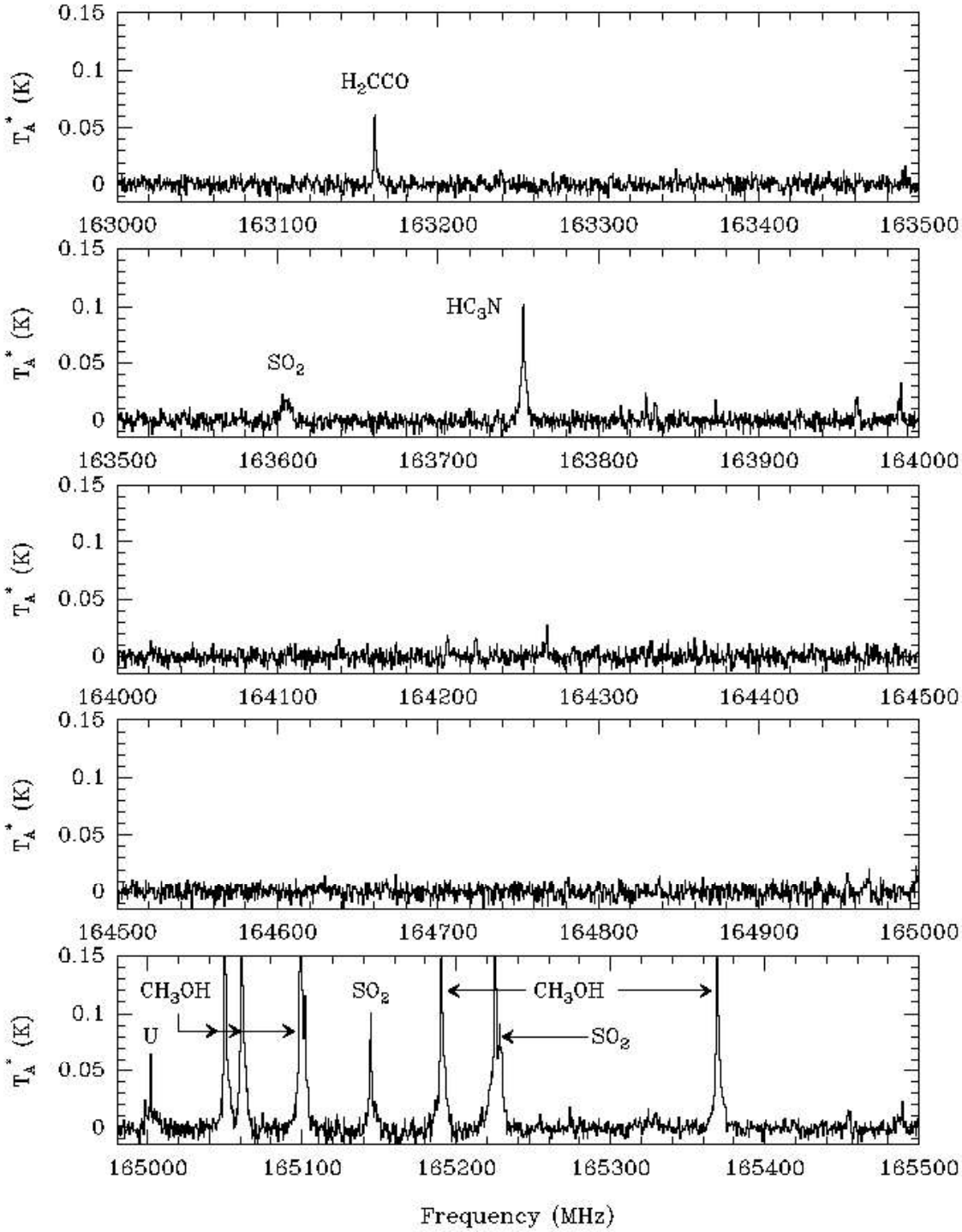
H2CCO
HC3N
SO2
CH3OH
U
SO2
CH3OH
SO2
TA* (K)
Frequency (MHz)

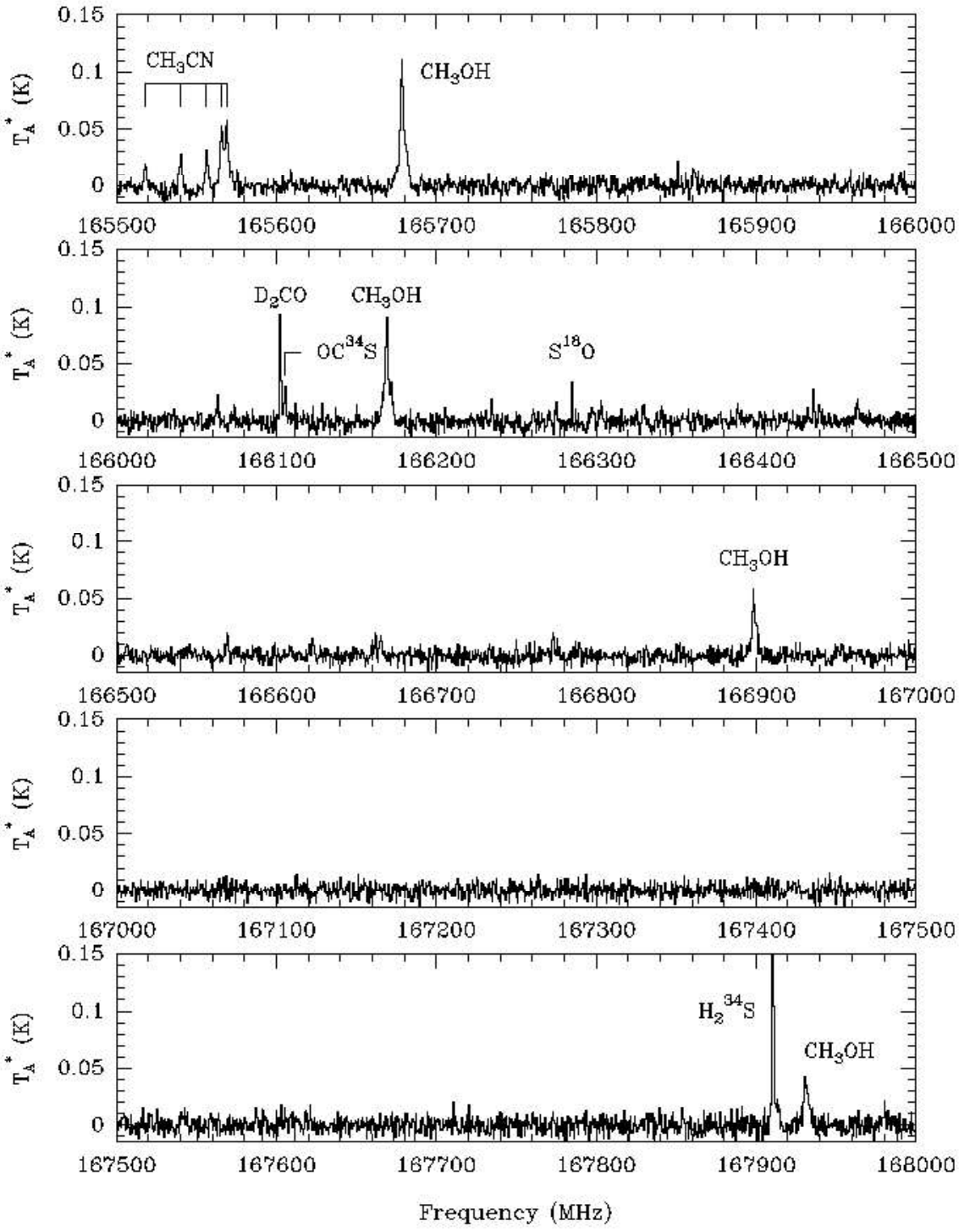
CH3CN
CH3OH
D2CO
CH3OH
OC34S
S18O
CH3OH
H2 34S
CH3OH
TA* (K)
0.15
0.1
0.05
0
165500
165600
165700
165800
165900
166000
166100
166200
166300
166400
166500
166600
166700
166800
166900
167000
167100
167200
167300
167400
167500
167600
167700
167800
167900
168000
Frequency (MHz)

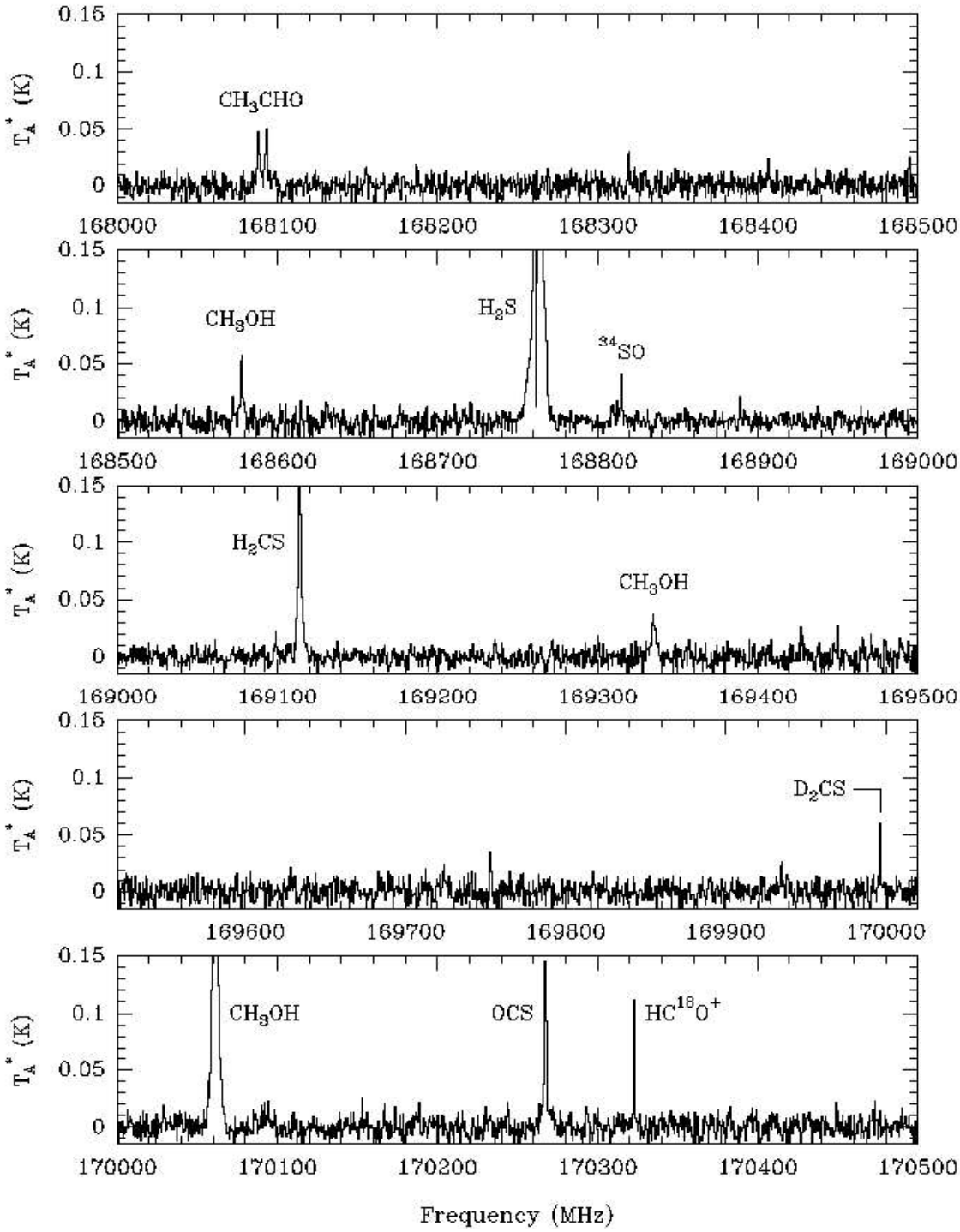
0.15
0.1
0.05
0
T_A^* (K)
CH_3CHO
168000
168100
168200
168300
168400
168500
CH_3OH
H_2S
^{34}SO
168500
168600
168700
168800
168900
169000
H_2CS
CH_3OH
169000
169100
169200
169300
169400
169500
D_2CS
169600
169700
169800
169900
170000
CH_3OH
OCS
$HC^{18}O^+$
170000
170100
170200
170300
170400
170500
Frequency (MHz)

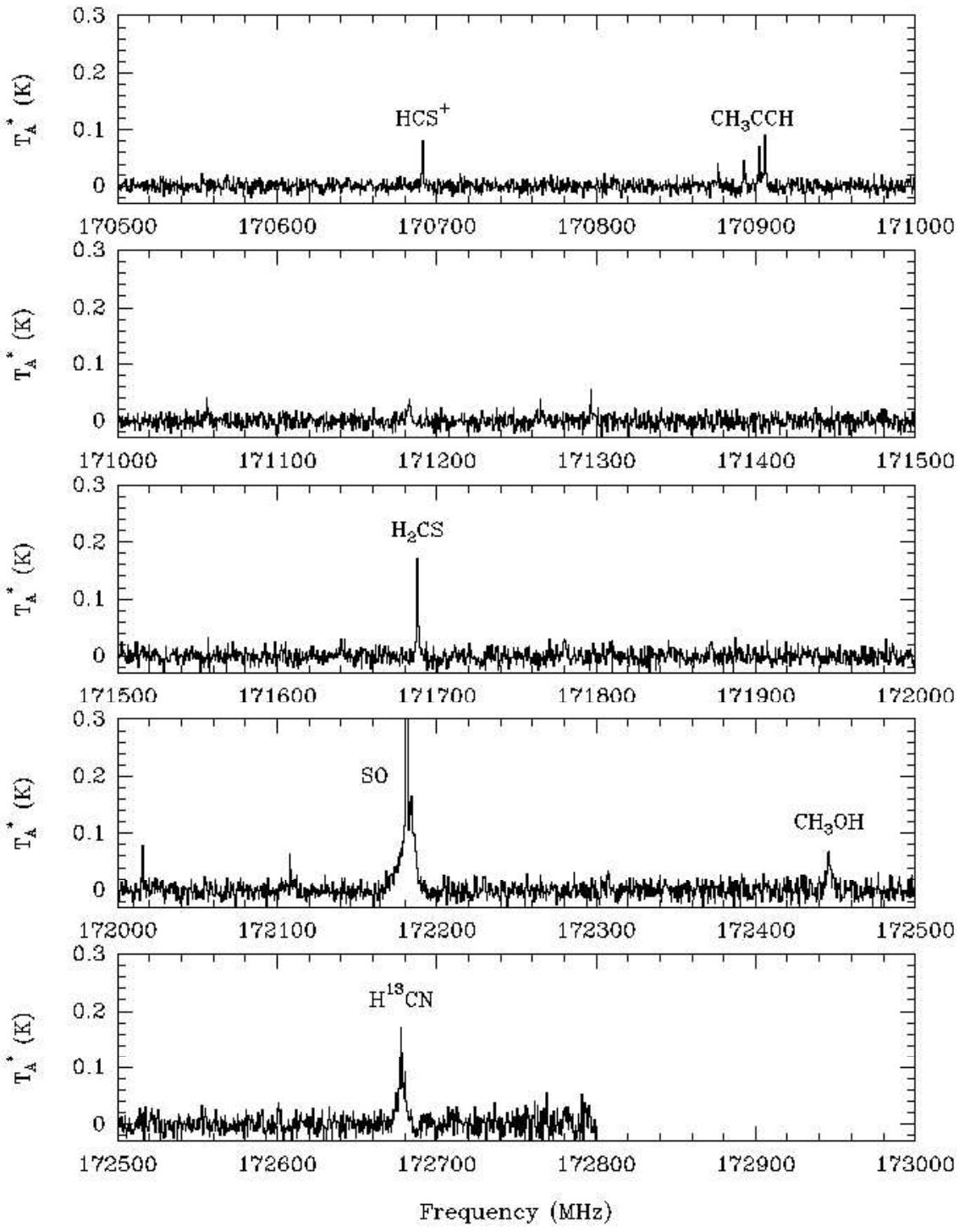
HCS+
CH3CCH
H2CS
SO
CH3OH
H13CN
T*A (K)
Frequency (MHz)

Appendix C

IRAS 4A: Spectral Bands (1mm)

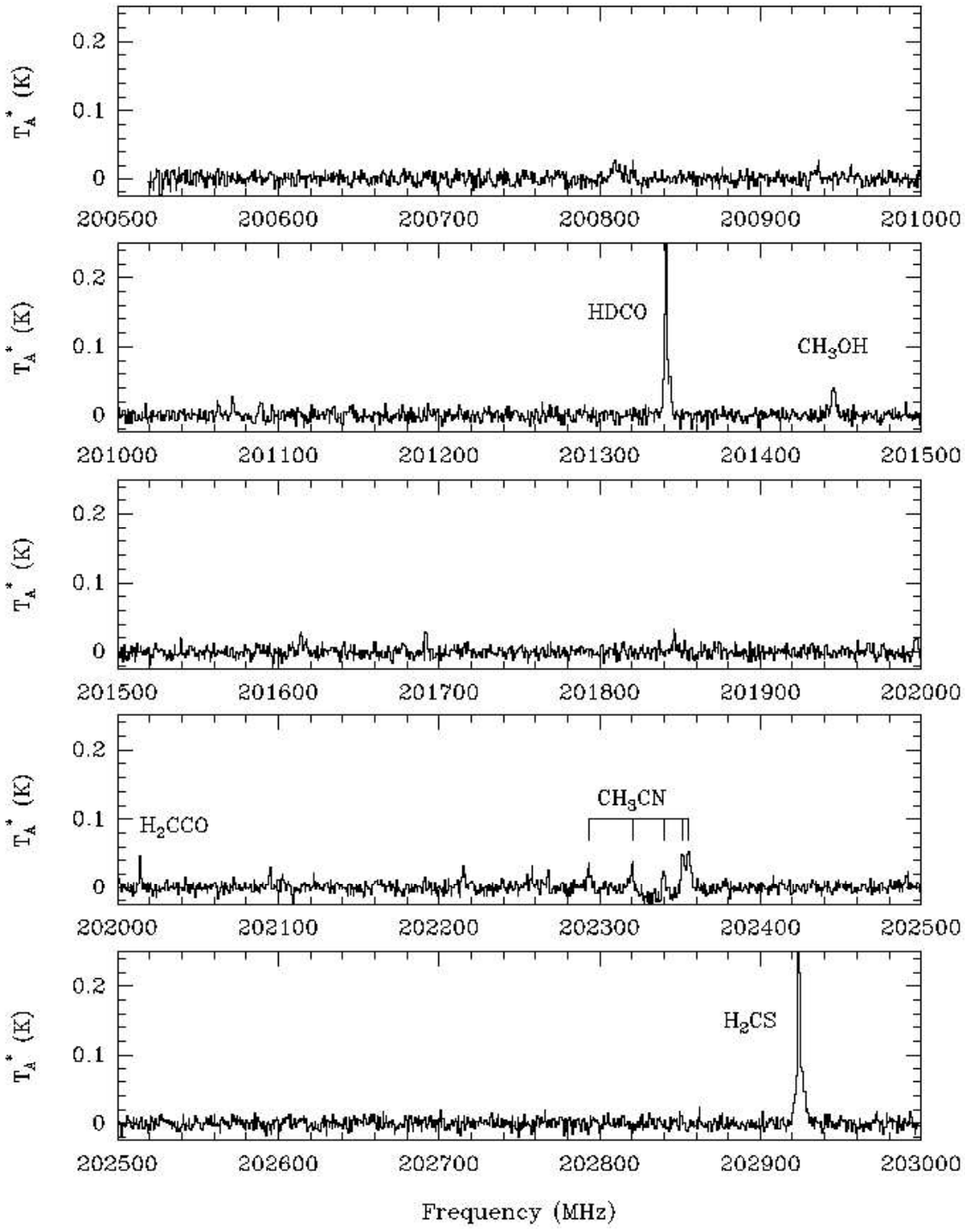
T_A^* (K)
0.2
0.1
0
200500
200600
200700
200800
200900
201000
HDCO
CH_3OH
201000
201100
201200
201300
201400
201500
201500
201600
201700
201800
201900
202000
H_2CCO
CH_3CN
202000
202100
202200
202300
202400
202500
H_2CS
202500
202600
202700
202800
202900
203000
Frequency (MHz)

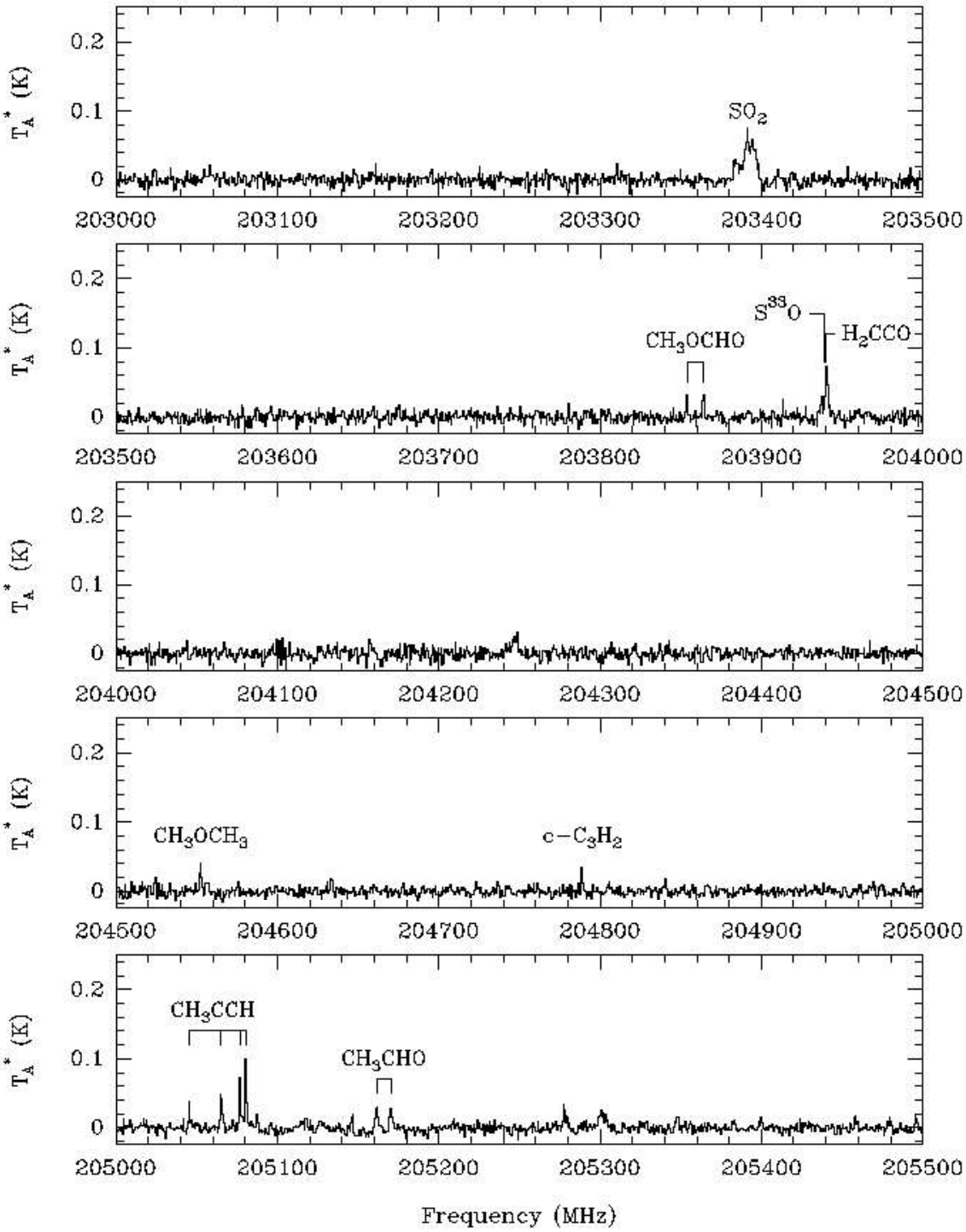
T_A^* (K)
0.2
0.1
0
SO_2
203000
203100
203200
203300
203400
203500
CH_3OCHO
$S^{33}O$
H_2CCO
203500
203600
203700
203800
203900
204000
204000
204100
204200
204300
204400
204500
CH_3OCH_3
$c-C_3H_2$
204500
204600
204700
204800
204900
205000
CH_3CCH
CH_3CHO
205000
205100
205200
205300
205400
205500
Frequency (MHz)

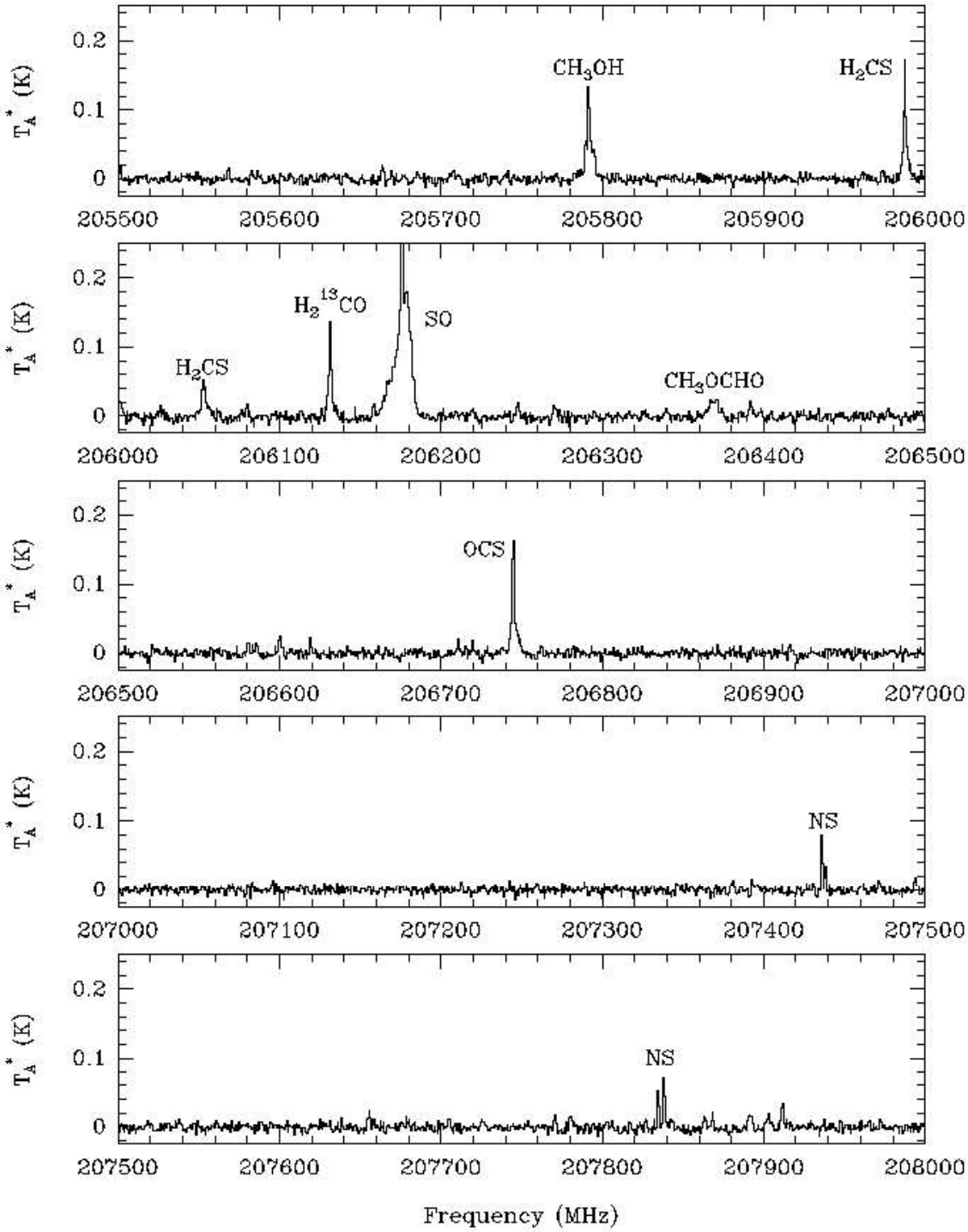
T_A^* (K)
0.2
0.1
0
CH_3OH
H_2CS
205500
205600
205700
205800
205900
206000
H_2CS
$H_2{}^{13}CO$
SO
CH_3OCHO
206000
206100
206200
206300
206400
206500
OCS
206500
206600
206700
206800
206900
207000
NS
207000
207100
207200
207300
207400
207500
NS
207500
207600
207700
207800
207900
208000
Frequency (MHz)

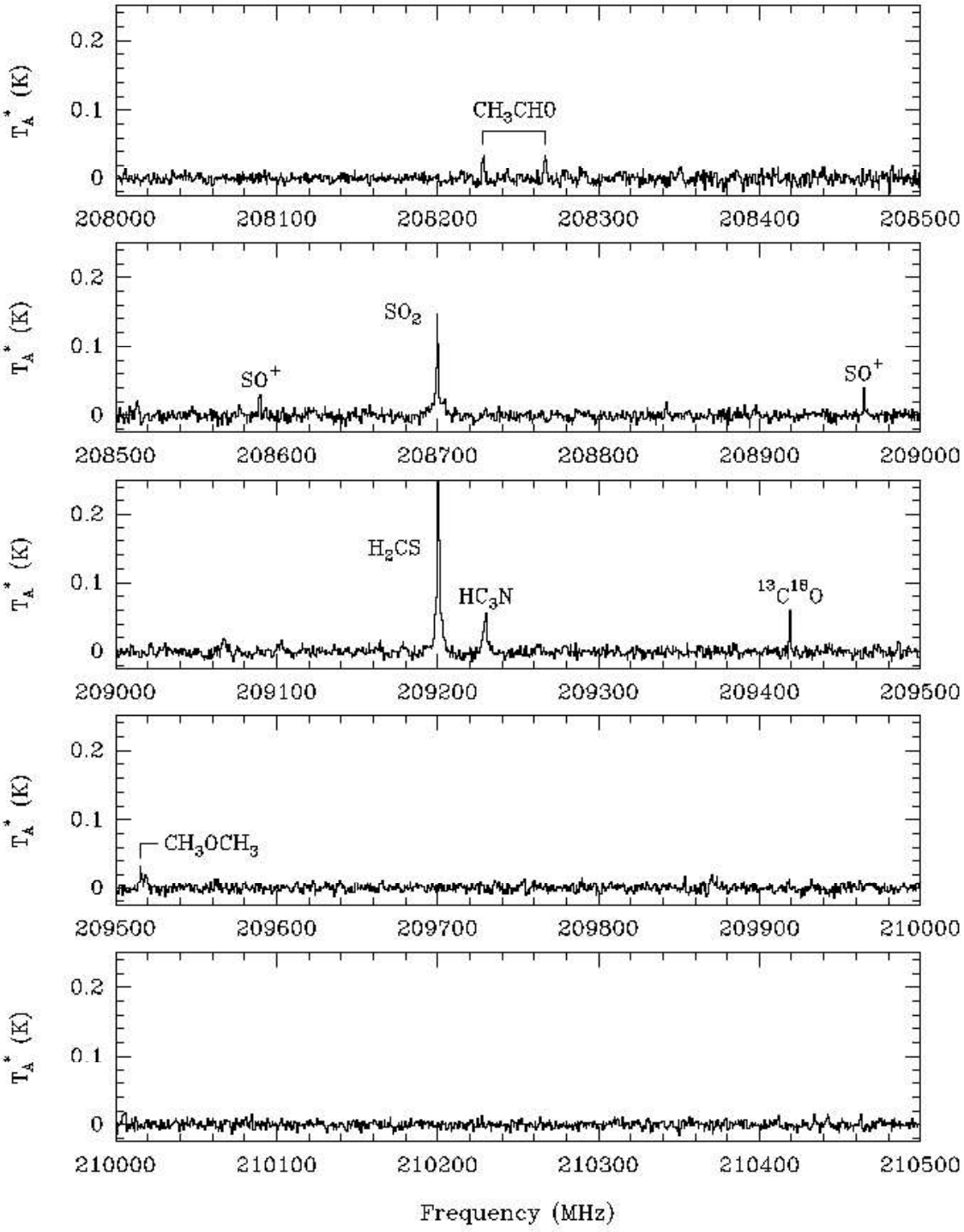
T_A^* (K)
0.2
0.1
0
CH_3CHO
208000
208100
208200
208300
208400
208500
SO_2
SO^+
SO^+
208500
208600
208700
208800
208900
209000
H_2CS
HC_3N
$^{13}C^{18}O$
209000
209100
209200
209300
209400
209500
CH_3OCH_3
209500
209600
209700
209800
209900
210000
210000
210100
210200
210300
210400
210500
Frequency (MHz)

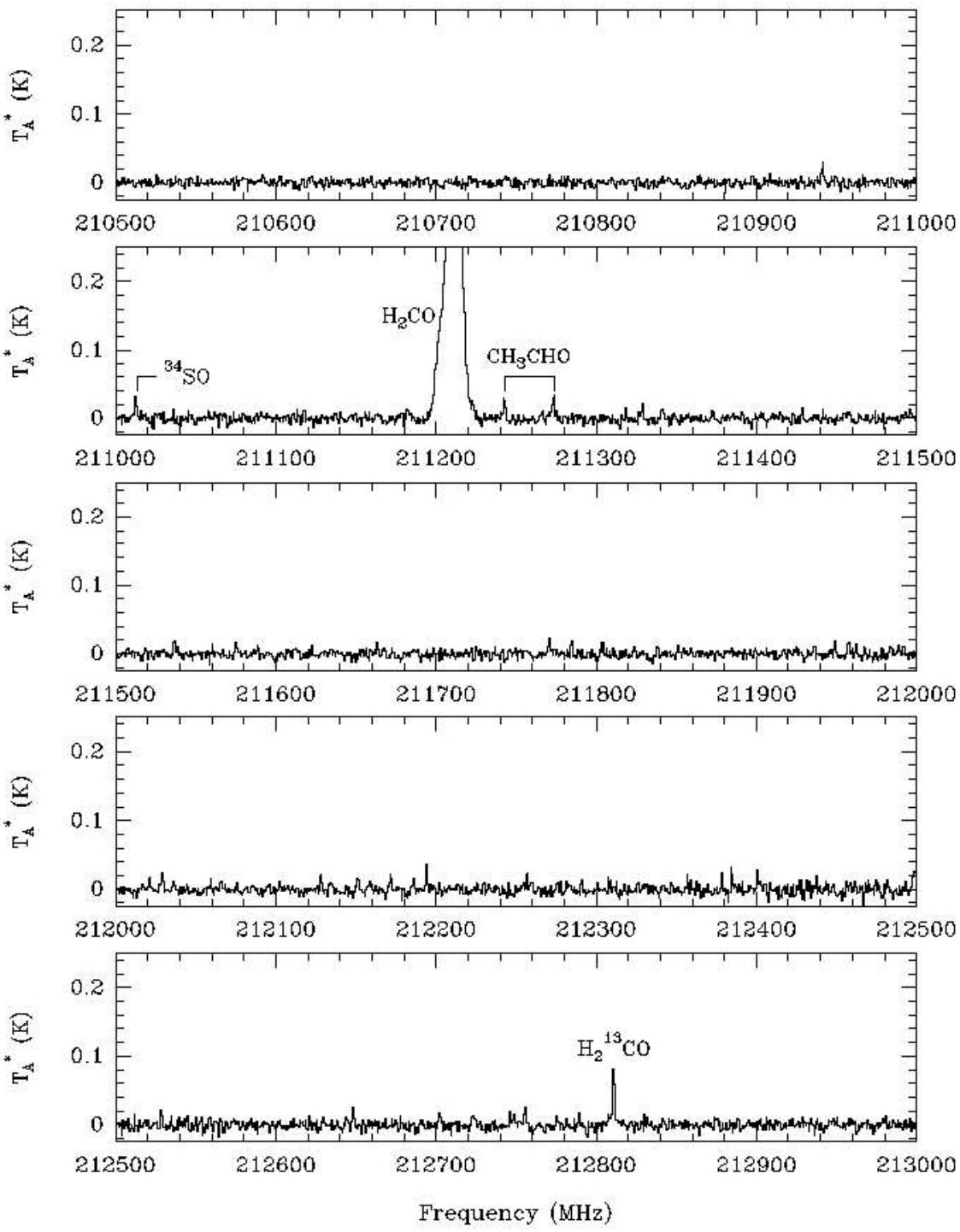
0.2
0.1
0
T_A^* (K)
210500
210600
210700
210800
210900
211000
H_2CO
CH_3CHO
^{34}SO
211000
211100
211200
211300
211400
211500
211500
211600
211700
211800
211900
212000
212000
212100
212200
212300
212400
212500
$H_2{}^{13}CO$
212500
212600
212700
212800
212900
213000
Frequency (MHz)

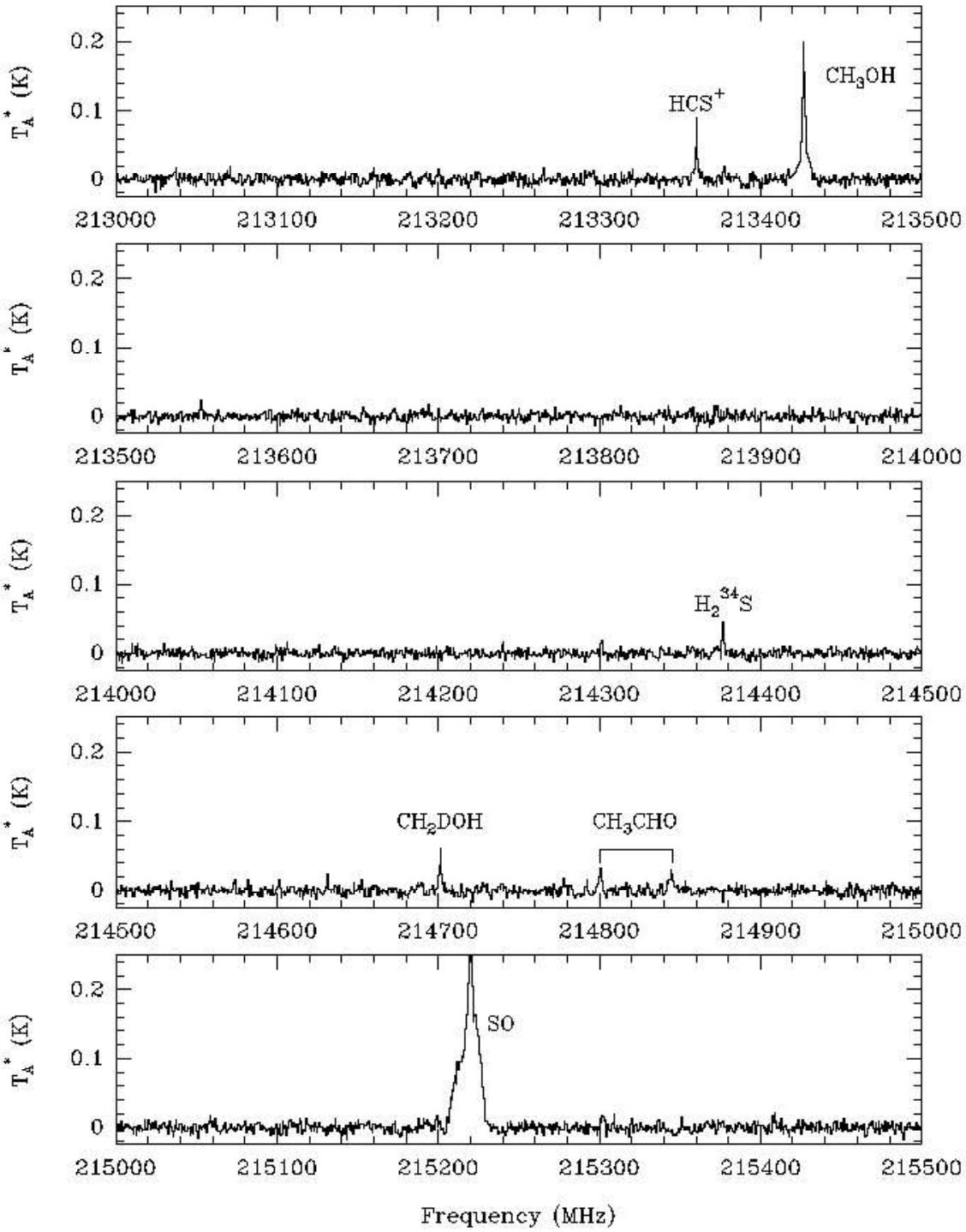
HCS+
CH3OH
H2 34S
CH2DOH
CH3CHO
SO
T*A (K)
Frequency (MHz)

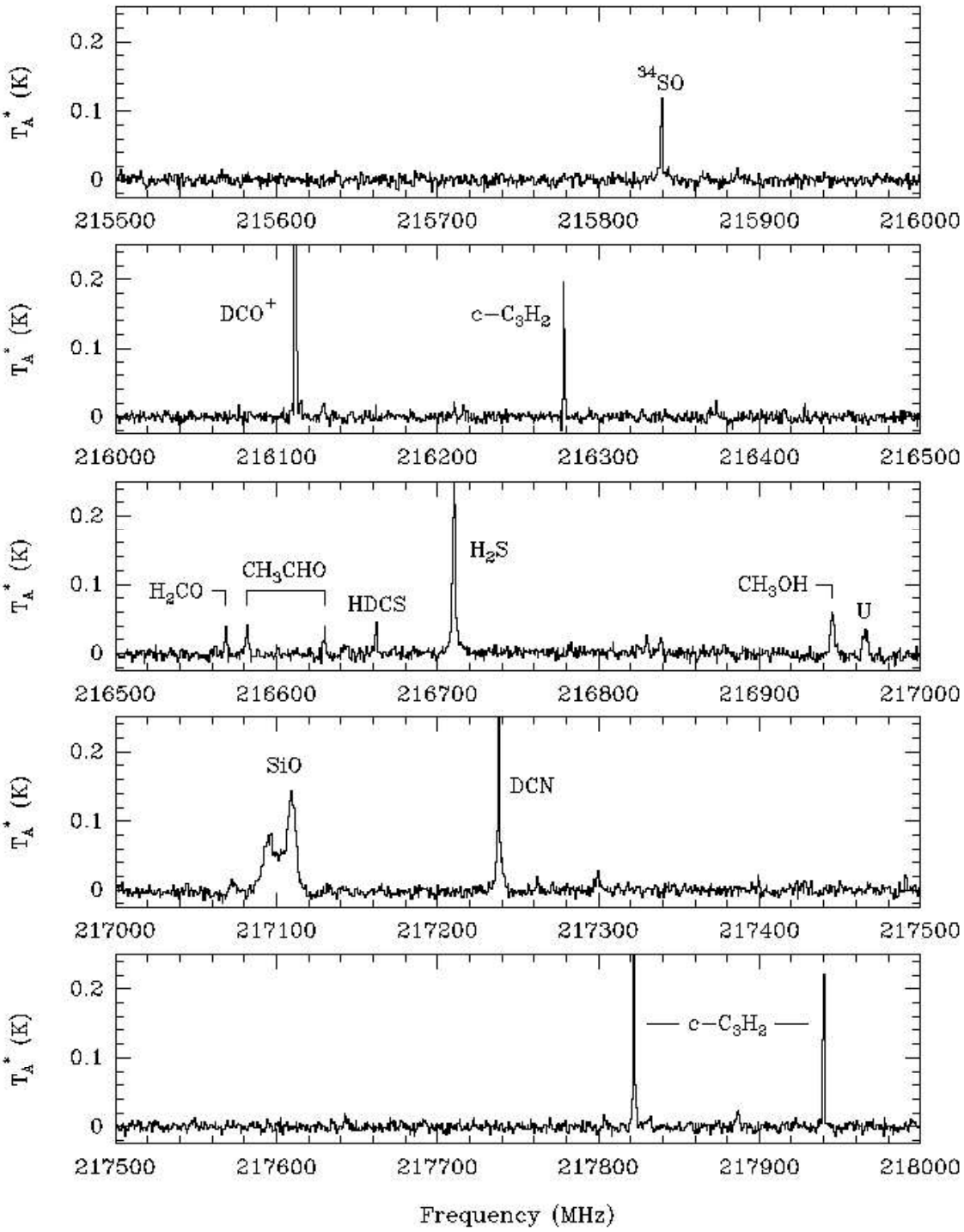
^{34}SO
DCO$^+$
c−C$_3$H$_2$
H$_2$CO
CH$_3$CHO
HDCS
H$_2$S
CH$_3$OH
U
SiO
DCN
c−C$_3$H$_2$
T$_A^*$ (K)
Frequency (MHz)

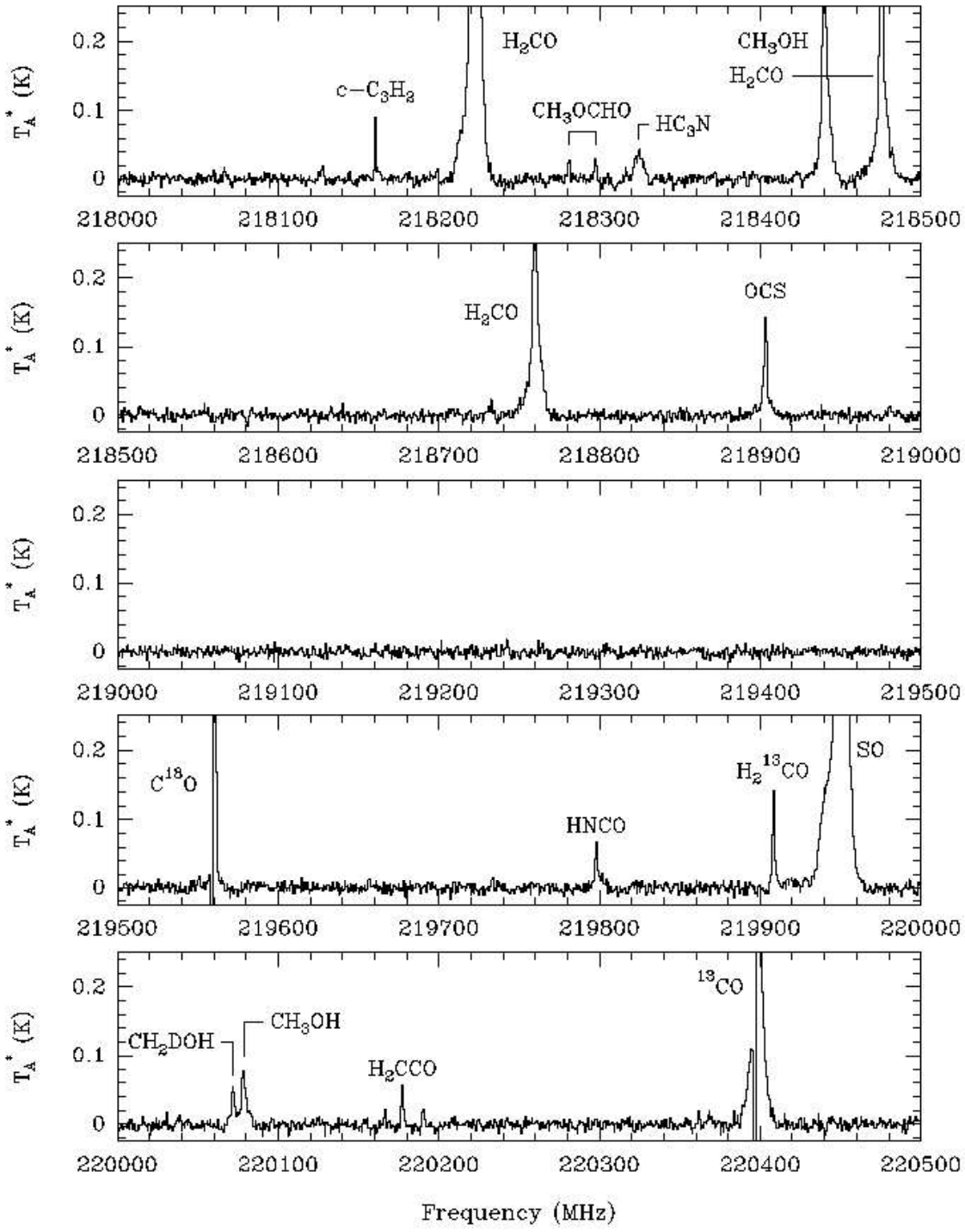
T_A^* (K)
0.2
0.1
0
$c-C_3H_2$
H_2CO
CH_3OCHO
HC_3N
CH_3OH
H_2CO
218000
218100
218200
218300
218400
218500
H_2CO
OCS
218500
218600
218700
218800
218900
219000
219000
219100
219200
219300
219400
219500
$C^{18}O$
HNCO
$H_2{}^{13}CO$
SO
219500
219600
219700
219800
219900
220000
CH_2DOH
CH_3OH
H_2CCO
^{13}CO
220000
220100
220200
220300
220400
220500
Frequency (MHz)

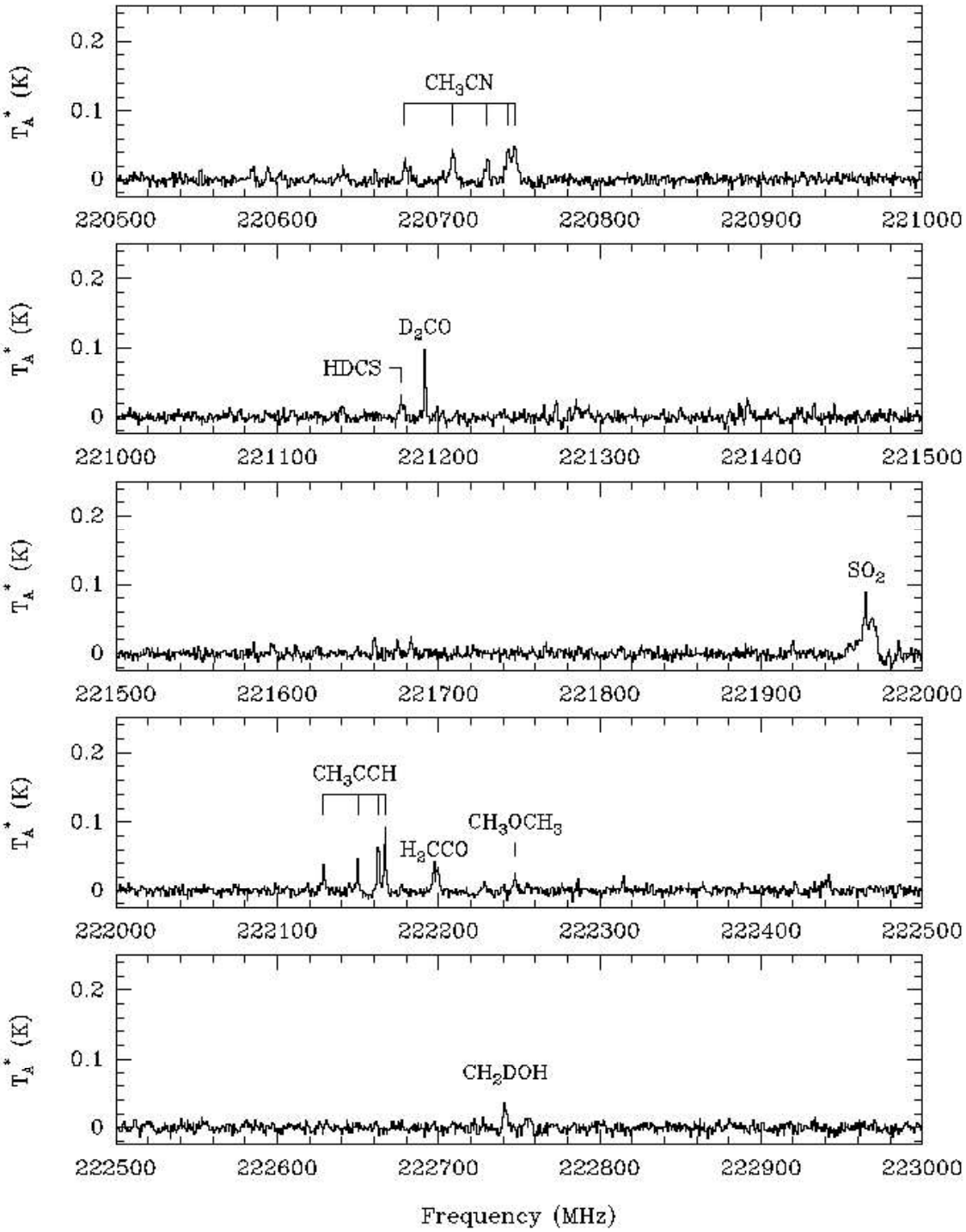
T_A^* (K)
0.2
0.1
0
CH_3CN
220500
220600
220700
220800
220900
221000
D_2CO
HDCS
221000
221100
221200
221300
221400
221500
SO_2
221500
221600
221700
221800
221900
222000
CH_3CCH
CH_3OCH_3
H_2CCO
222000
222100
222200
222300
222400
222500
CH_2DOH
222500
222600
222700
222800
222900
223000
Frequency (MHz)

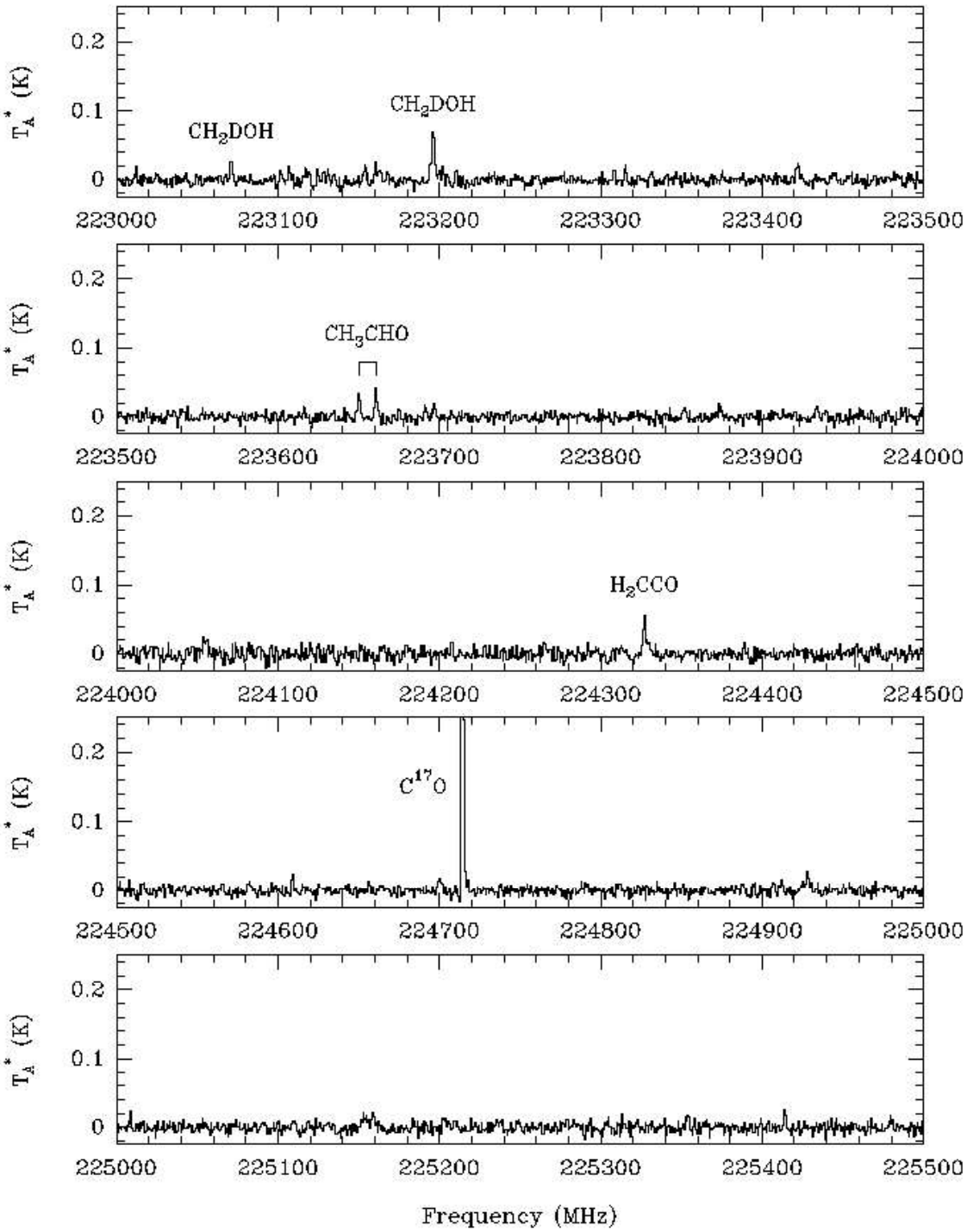
T_A^* (K)
0.2
0.1
0
CH_2DOH
CH_2DOH
223000
223100
223200
223300
223400
223500
CH_3CHO
223500
223600
223700
223800
223900
224000
H_2CCO
224000
224100
224200
224300
224400
224500
$C^{17}O$
224500
224600
224700
224800
224900
225000
225000
225100
225200
225300
225400
225500
Frequency (MHz)

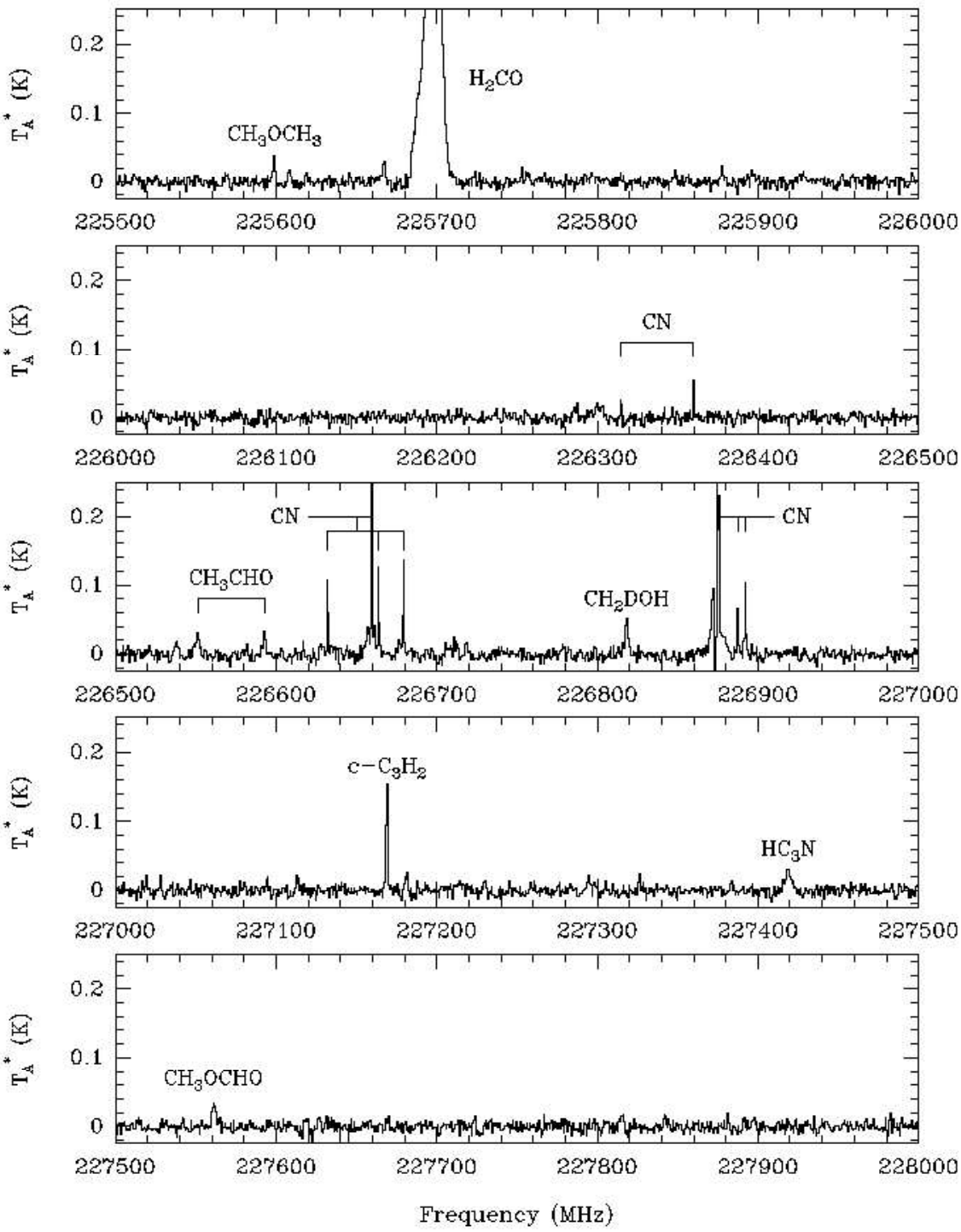
T_A^* (K)
0.2
0.1
0
H_2CO
CH_3OCH_3
225500
225600
225700
225800
225900
226000
CN
226000
226100
226200
226300
226400
226500
CN
CN
CH_3CHO
CH_2DOH
226500
226600
226700
226800
226900
227000
$c-C_3H_2$
HC_3N
227000
227100
227200
227300
227400
227500
CH_3OCHO
227500
227600
227700
227800
227900
228000
Frequency (MHz)

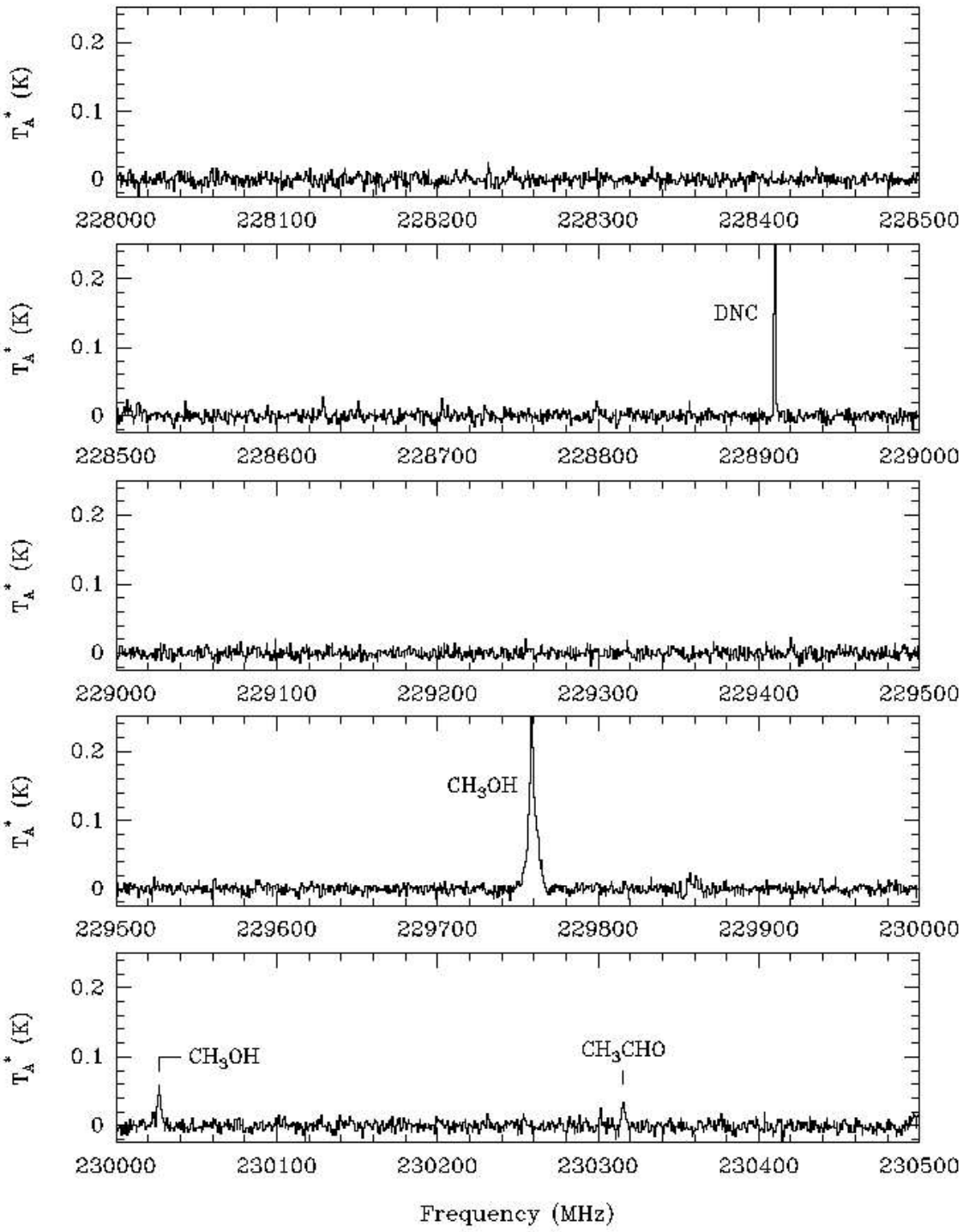
0.2
0.1
0
T_A^* (K)
228000
228100
228200
228300
228400
228500
DNC
228500
228600
228700
228800
228900
229000
229000
229100
229200
229300
229400
229500
CH_3OH
229500
229600
229700
229800
229900
230000
CH_3OH
CH_3CHO
230000
230100
230200
230300
230400
230500
Frequency (MHz)

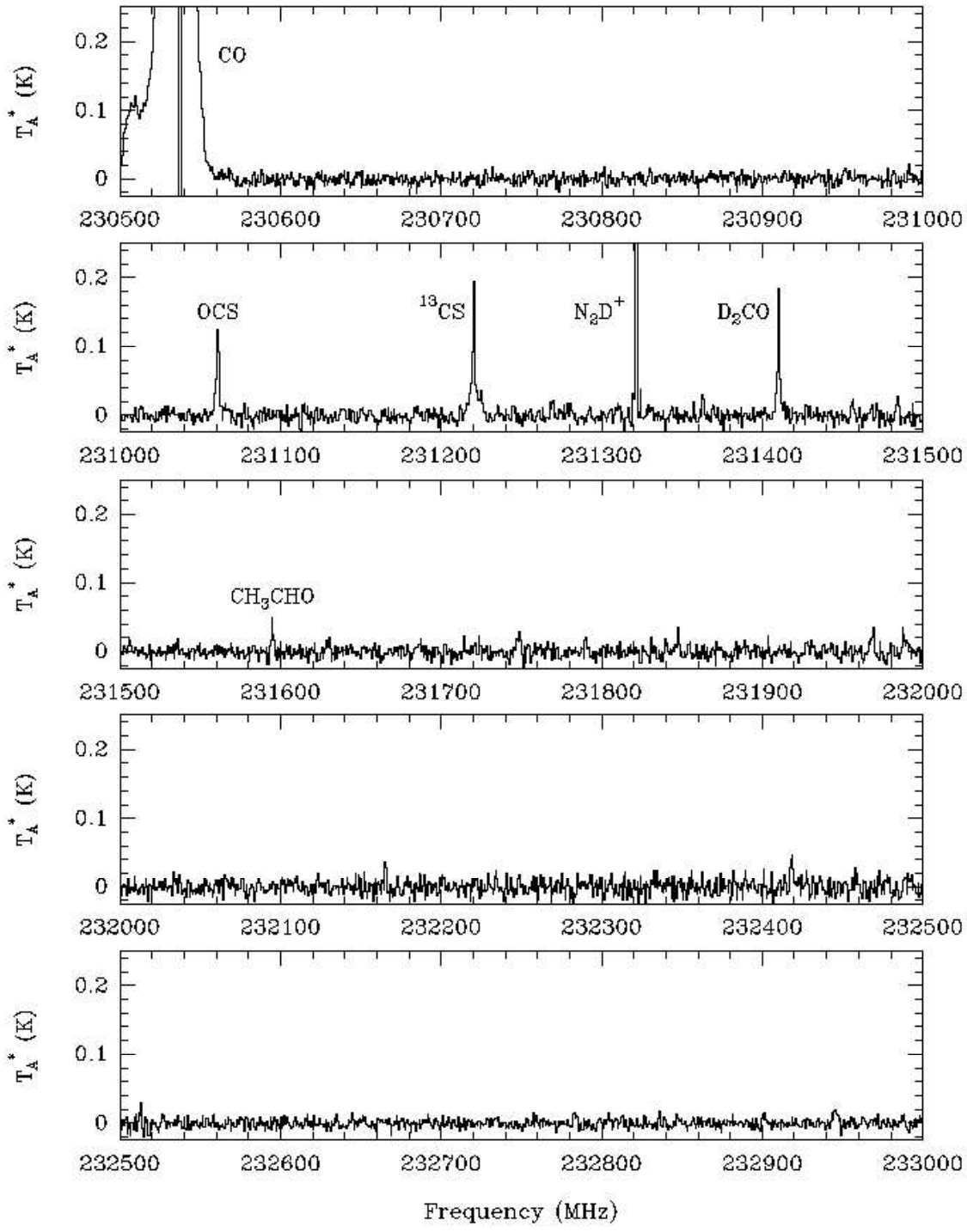
CO
OCS
^{13}CS
N_2D^+
D_2CO
CH_3CHO
T_A^* (K)
0.2
0.1
0
230500
230600
230700
230800
230900
231000
231100
231200
231300
231400
231500
231600
231700
231800
231900
232000
232100
232200
232300
232400
232500
232600
232700
232800
232900
233000
Frequency (MHz)

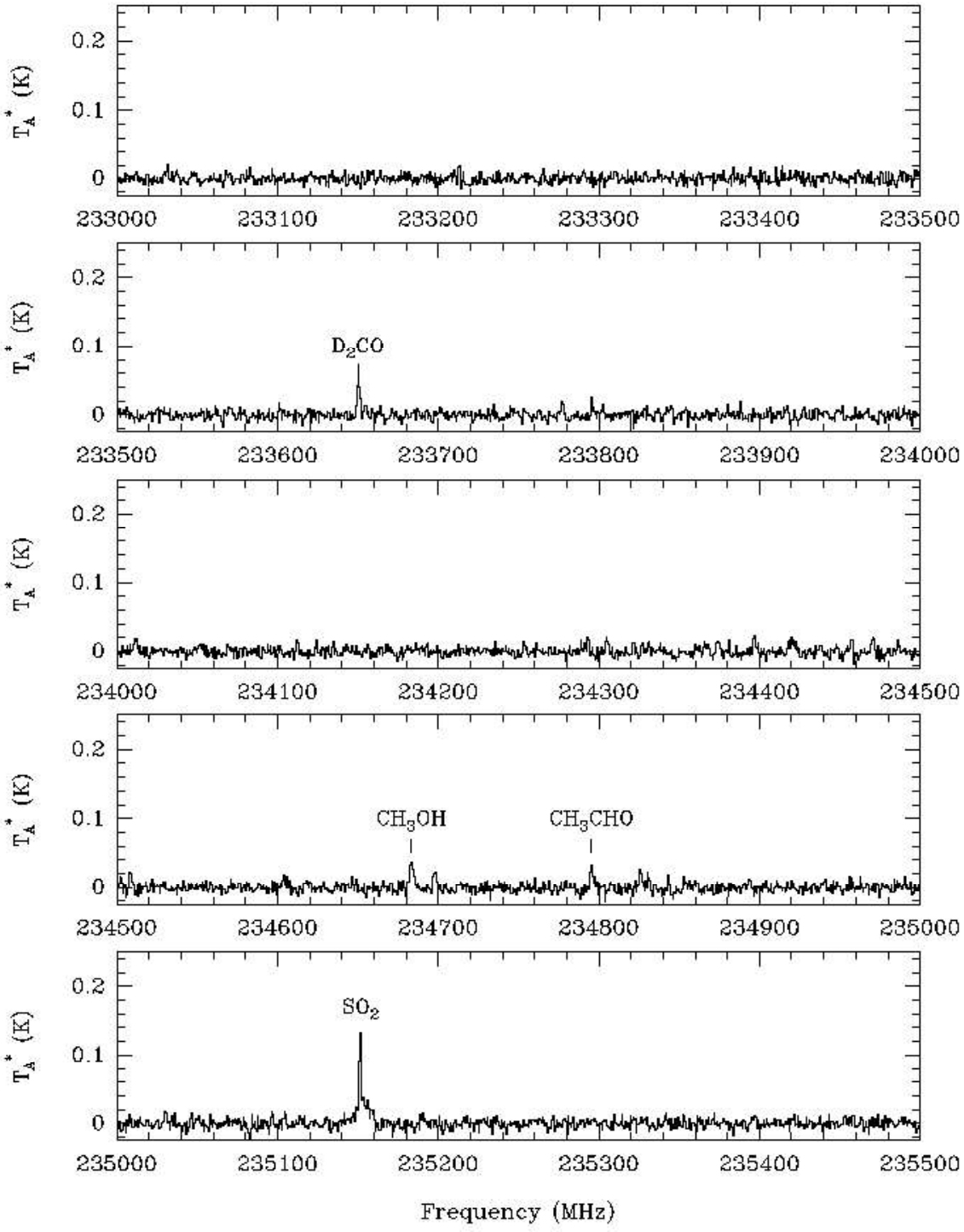
0.2
0.1
0
T_A^* (K)
233000
233100
233200
233300
233400
233500
D_2CO
233500
233600
233700
233800
233900
234000
234000
234100
234200
234300
234400
234500
CH_3OH
CH_3CHO
234500
234600
234700
234800
234900
235000
SO_2
235000
235100
235200
235300
235400
235500
Frequency (MHz)

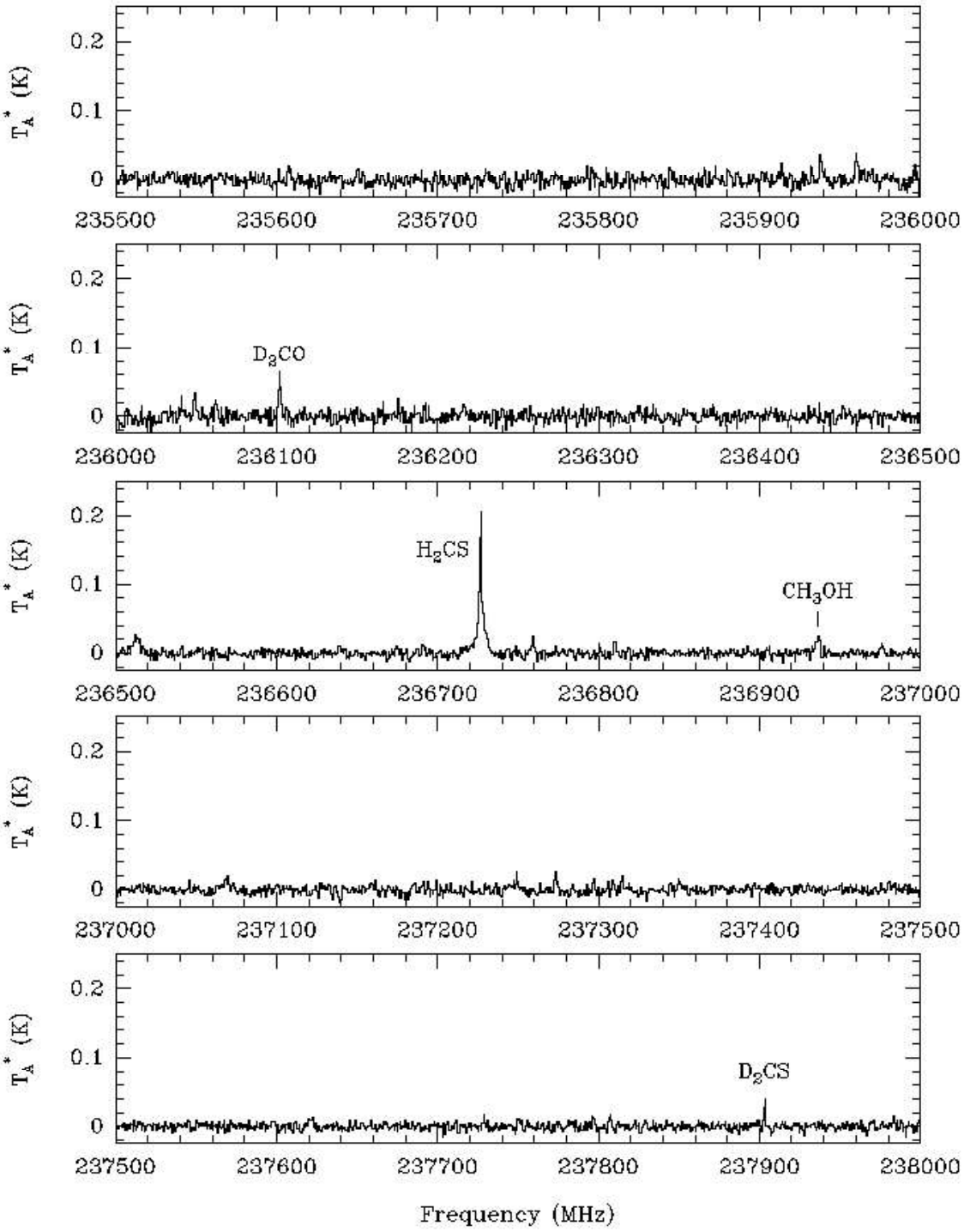
0.2
0.1
0
T_A^* (K)
235500
235600
235700
235800
235900
236000
D_2CO
236000
236100
236200
236300
236400
236500
H_2CS
CH_3OH
236500
236600
236700
236800
236900
237000
237000
237100
237200
237300
237400
237500
D_2CS
237500
237600
237700
237800
237900
238000
Frequency (MHz)

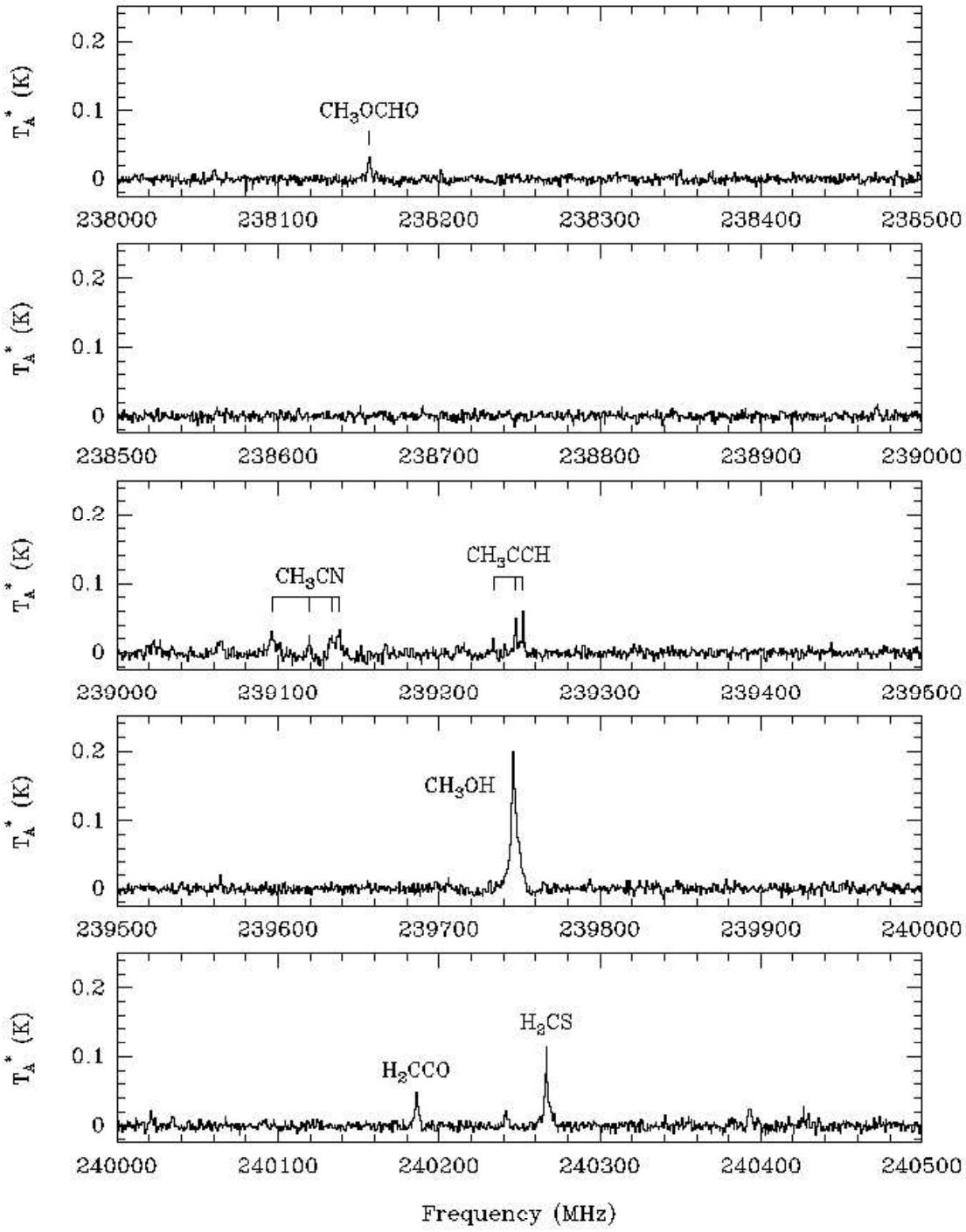
T_A^* (K)
0.2
0.1
0
CH_3OCHO
238000
238100
238200
238300
238400
238500
238500
238600
238700
238800
238900
239000
CH_3CN
CH_3CCH
239000
239100
239200
239300
239400
239500
CH_3OH
239500
239600
239700
239800
239900
240000
H_2CS
H_2CCO
240000
240100
240200
240300
240400
240500
Frequency (MHz)

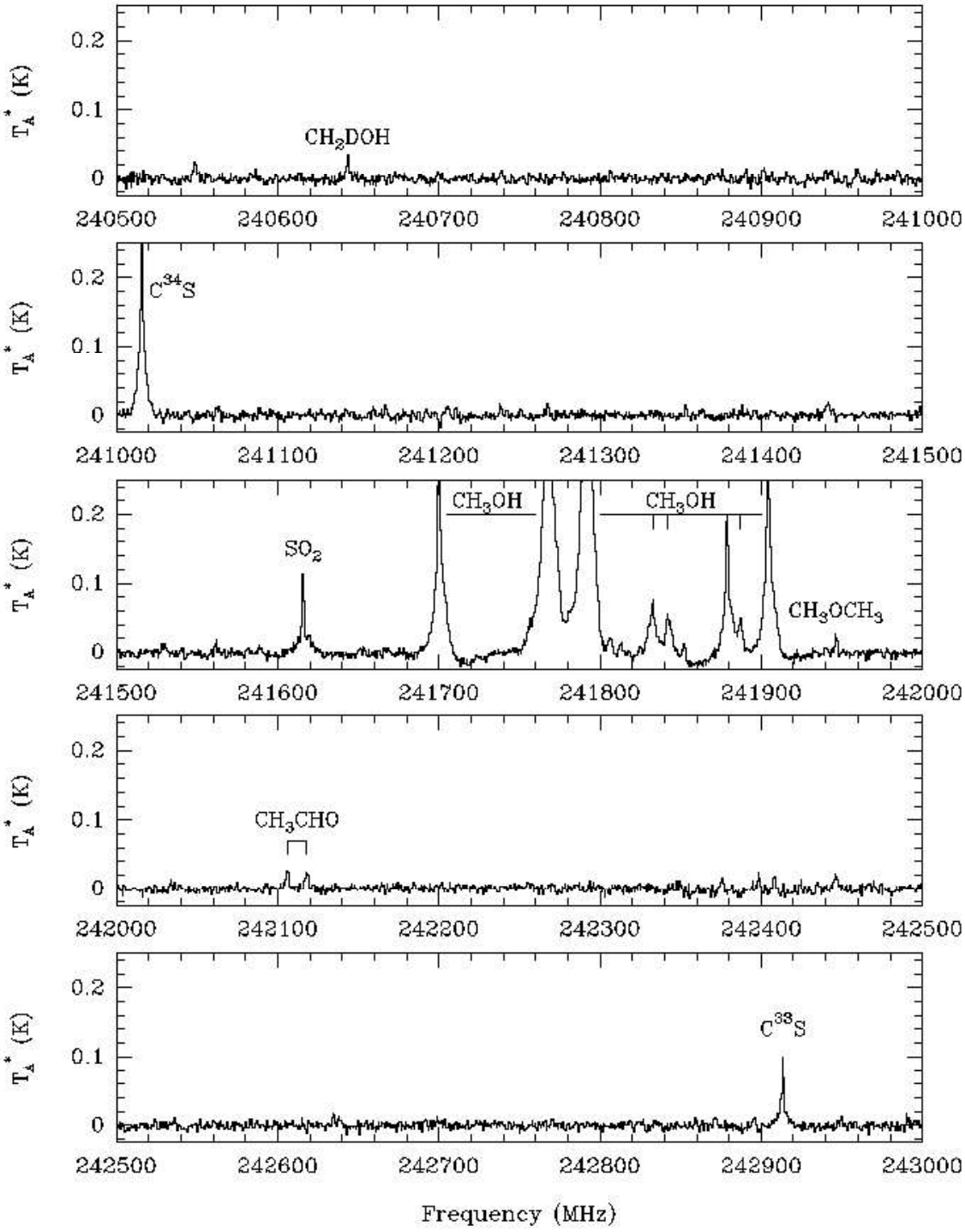
T_A^* (K)
0.2
0.1
0
CH_2DOH
240500
240600
240700
240800
240900
241000
$C^{34}S$
241000
241100
241200
241300
241400
241500
SO_2
CH_3OH
CH_3OH
CH_3OCH_3
241500
241600
241700
241800
241900
242000
CH_3CHO
242000
242100
242200
242300
242400
242500
$C^{33}S$
242500
242600
242700
242800
242900
243000
Frequency (MHz)

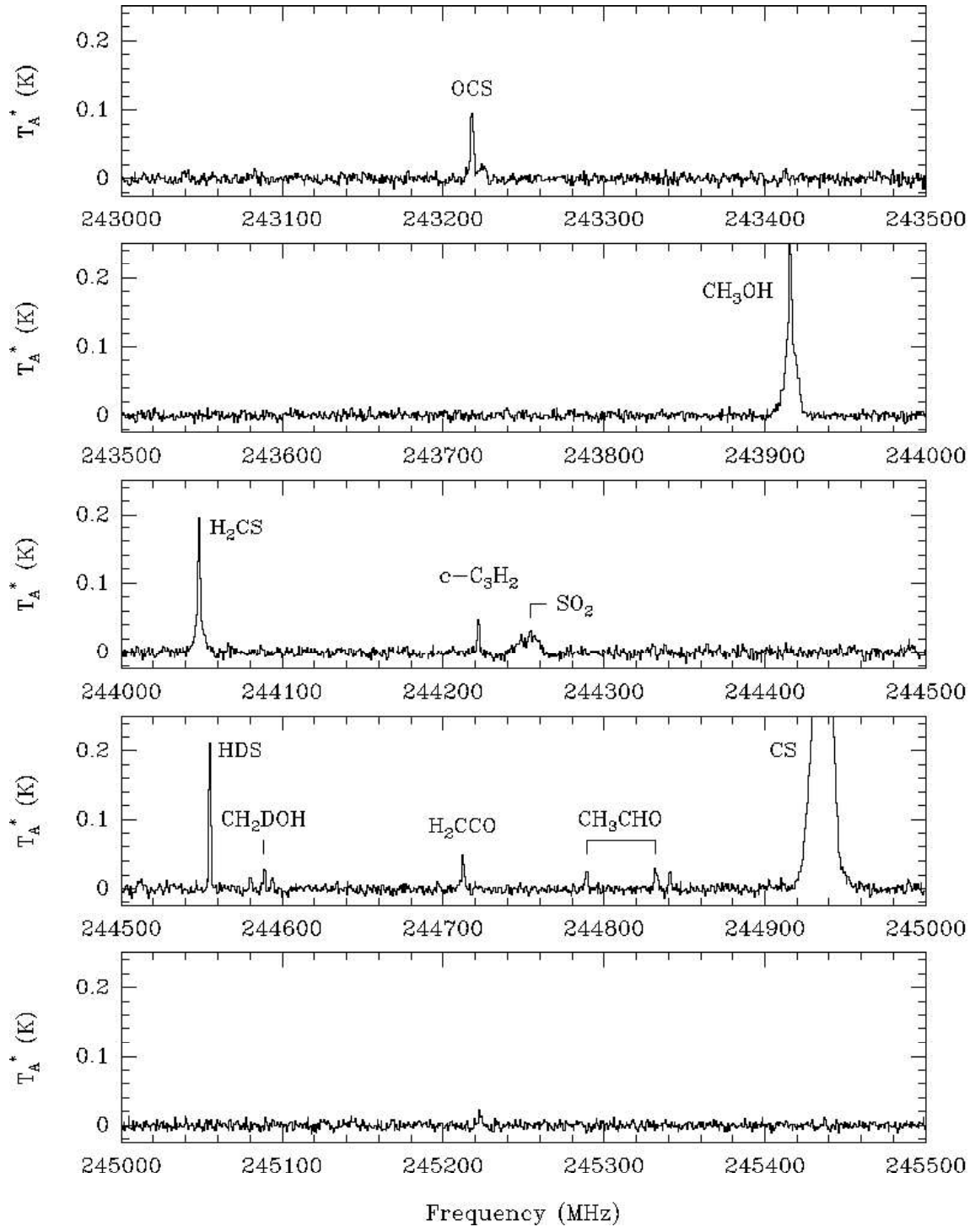
OCS
CH3OH
H2CS
c−C3H2
SO2
HDS
CH2DOH
H2CCO
CH3CHO
CS
TA* (K)
Frequency (MHz)

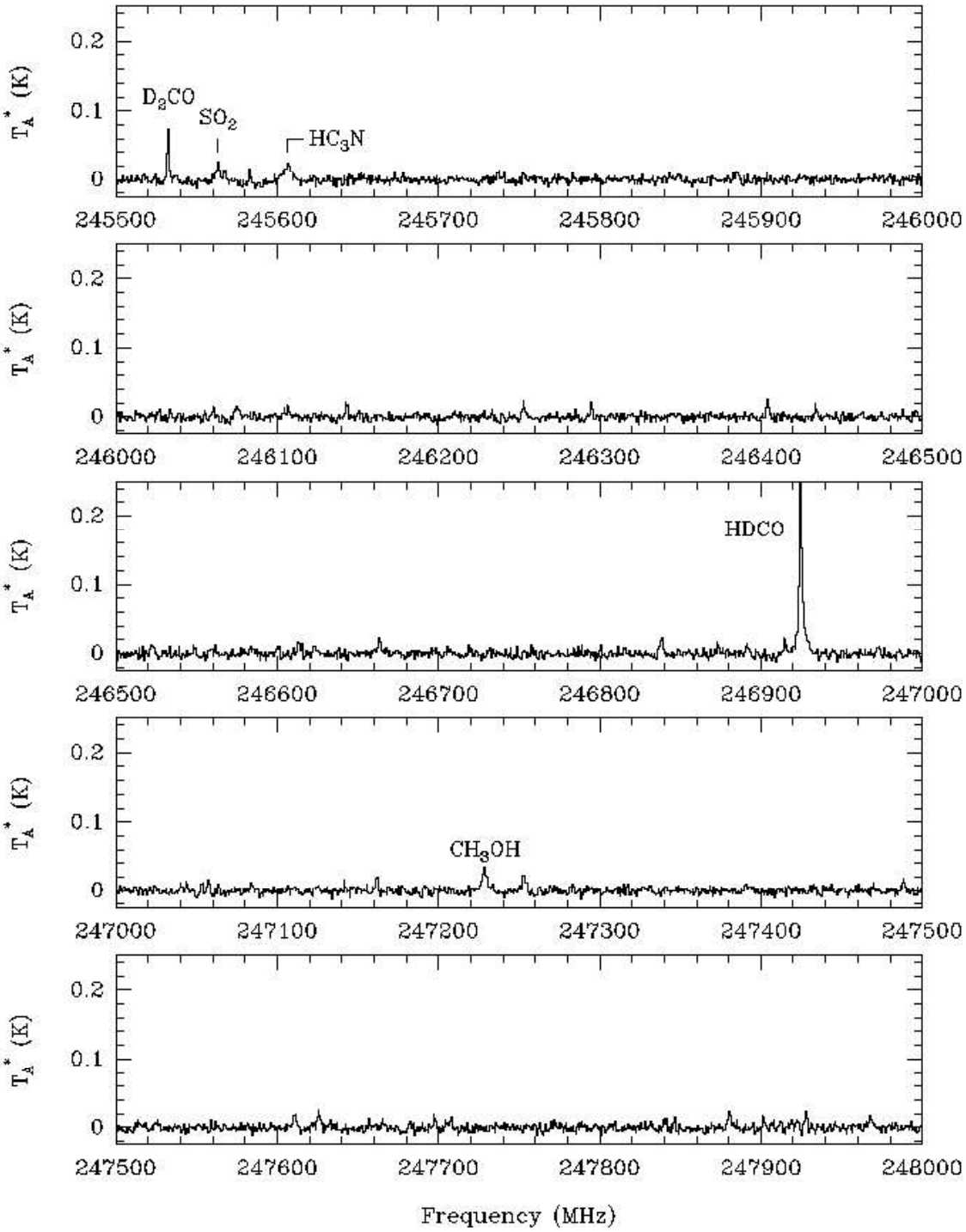
D_2CO
SO_2
HC_3N
HDCO
CH_3OH
T_A^* (K)
0.2
0.1
0
245500
245600
245700
245800
245900
246000
246100
246200
246300
246400
246500
246600
246700
246800
246900
247000
247100
247200
247300
247400
247500
247600
247700
247800
247900
248000
Frequency (MHz)

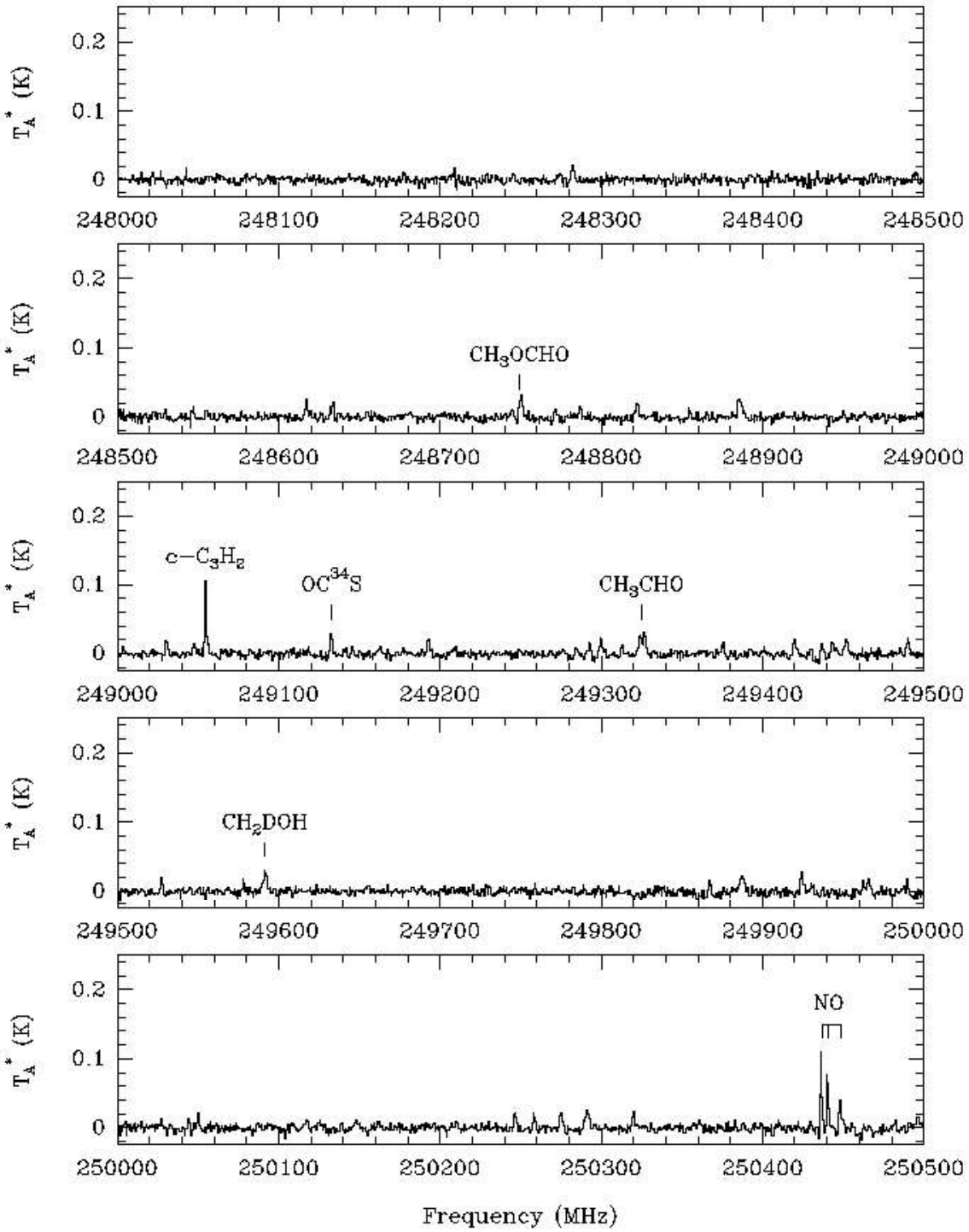
0.2
0.1
0
T_A^* (K)
248000
248100
248200
248300
248400
248500
CH_3OCHO
248500
248600
248700
248800
248900
249000
$c-C_3H_2$
$OC^{34}S$
CH_3CHO
249000
249100
249200
249300
249400
249500
CH_2DOH
249500
249600
249700
249800
249900
250000
NO
250000
250100
250200
250300
250400
250500
Frequency (MHz)

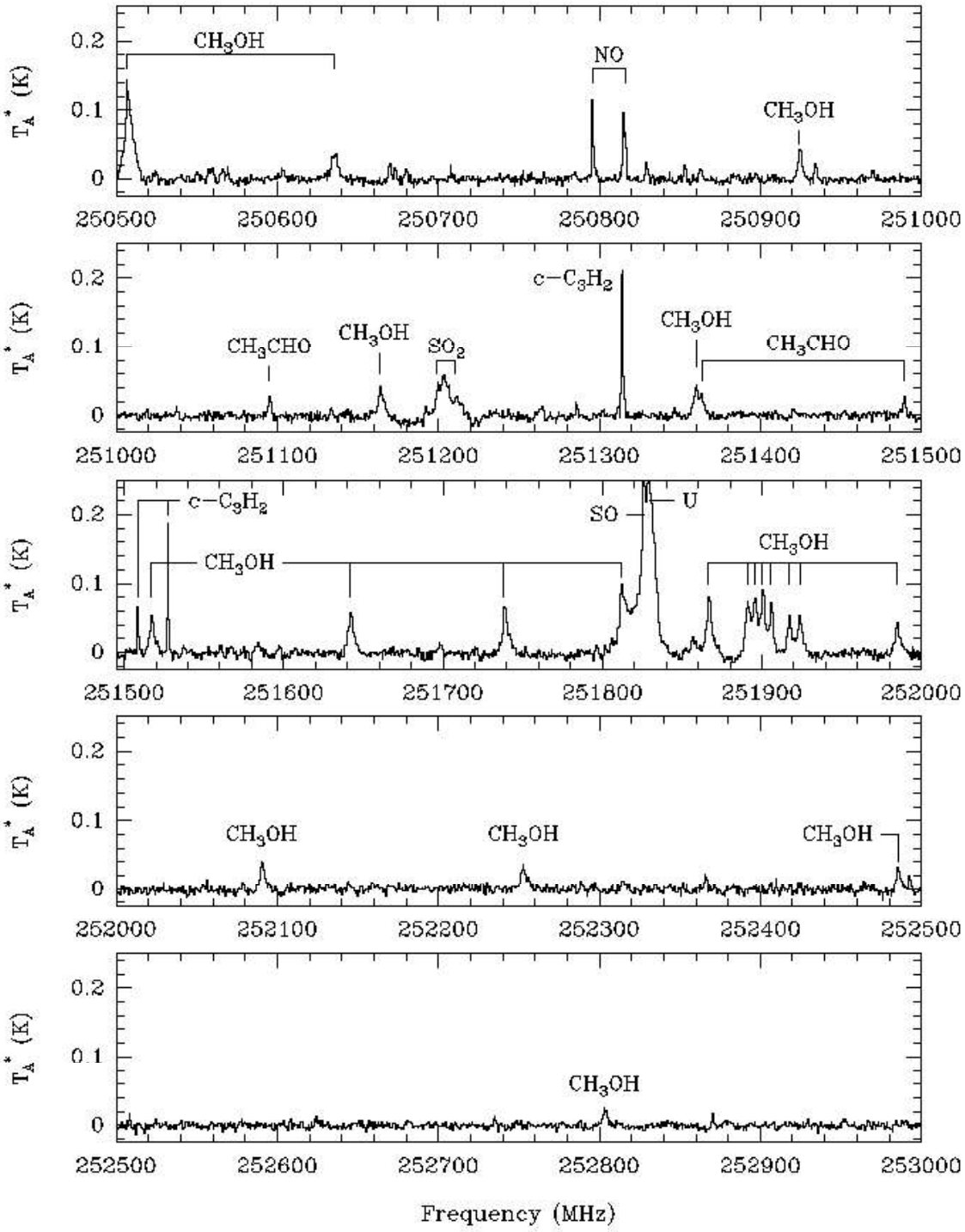
CH3OH
NO
CH3OH
CH3CHO
CH3OH
SO2
c−C3H2
CH3OH
CH3CHO
c−C3H2
CH3OH
SO
U
CH3OH
CH3OH
CH3OH
CH3OH
CH3OH
0.2
0.1
0
T_A* (K)
250500
250600
250700
250800
250900
251000
251000
251100
251200
251300
251400
251500
251500
251600
251700
251800
251900
252000
252000
252100
252200
252300
252400
252500
252500
252600
252700
252800
252900
253000
Frequency (MHz)

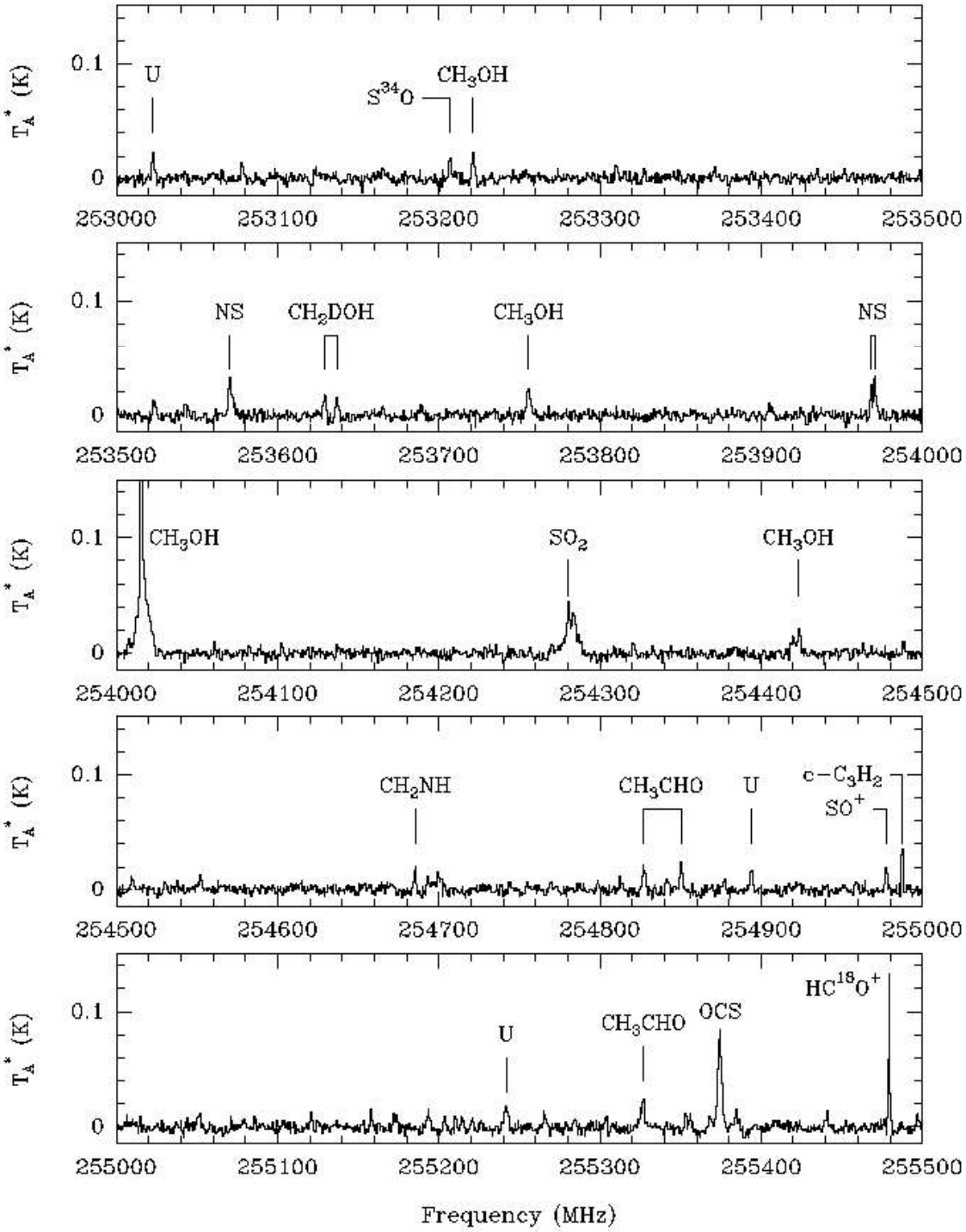
U
S34O
CH3OH
NS
CH2DOH
CH3OH
NS
CH3OH
SO2
CH3OH
CH2NH
CH3CHO
U
c-C3H2
SO+
U
CH3CHO
OCS
HC18O+
TA* (K)
0.1
0
253000
253100
253200
253300
253400
253500
253500
253600
253700
253800
253900
254000
254000
254100
254200
254300
254400
254500
254500
254600
254700
254800
254900
255000
255000
255100
255200
255300
255400
255500
Frequency (MHz)

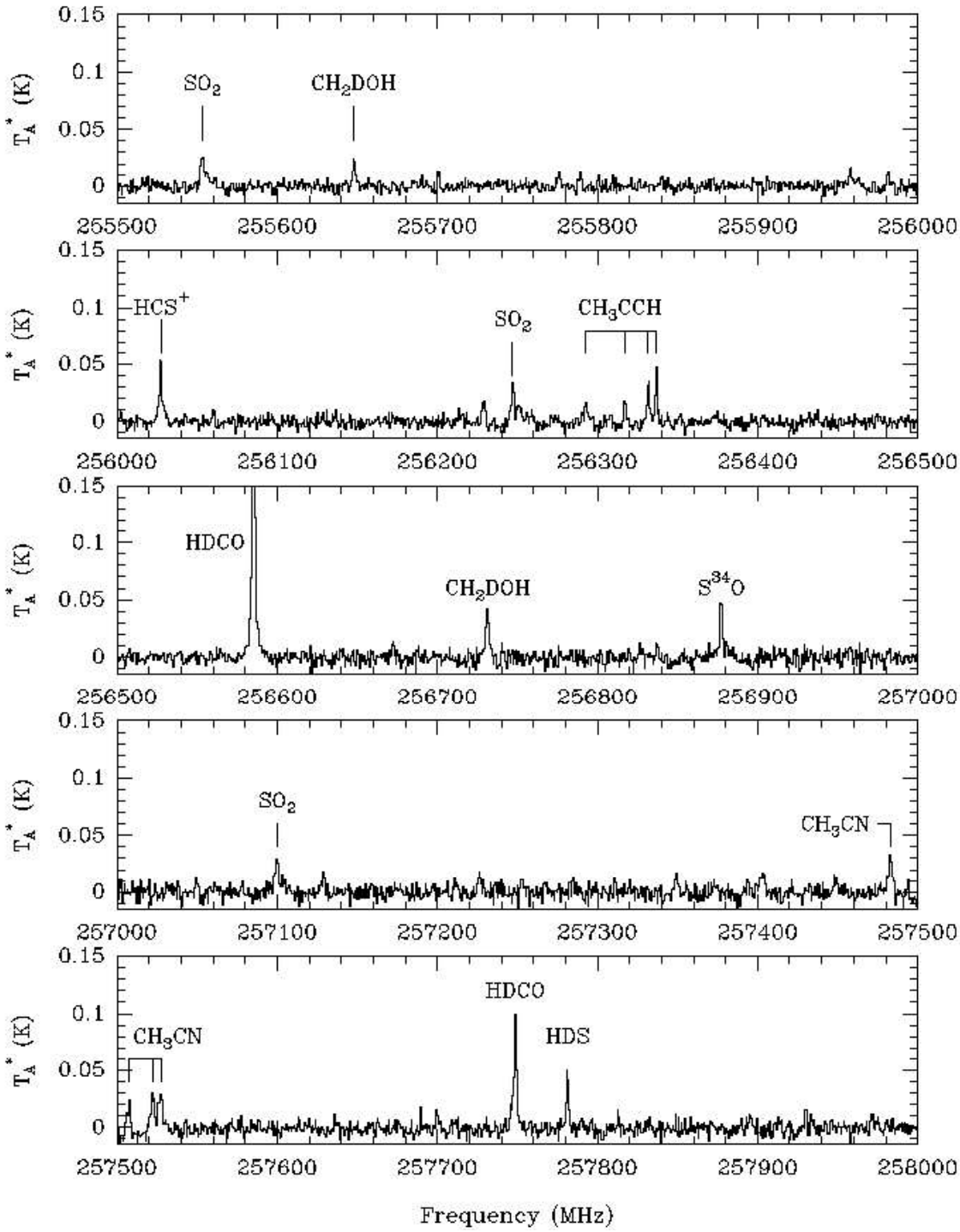
0.15
0.1
0.05
0
T_A^* (K)
SO_2
CH_2DOH
255500
255600
255700
255800
255900
256000
HCS^+
SO_2
CH_3CCH
256000
256100
256200
256300
256400
256500
HDCO
CH_2DOH
$S^{34}O$
256500
256600
256700
256800
256900
257000
SO_2
CH_3CN
257000
257100
257200
257300
257400
257500
CH_3CN
HDCO
HDS
257500
257600
257700
257800
257900
258000
Frequency (MHz)

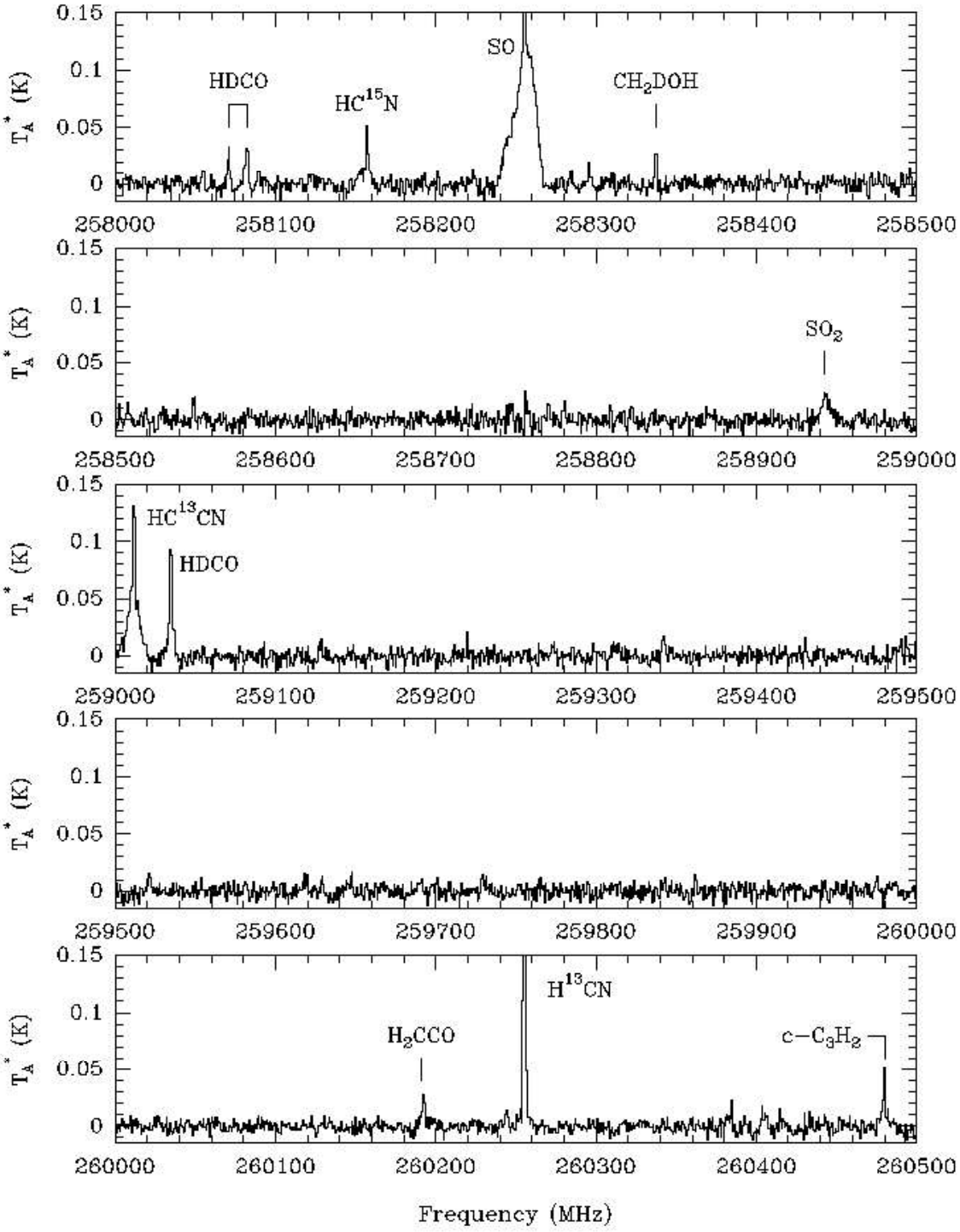
HDCO
HC15N
SO
CH2DOH
SO2
HC13CN
HDCO
H2CCO
H13CN
c−C3H2
TA* (K)
Frequency (MHz)

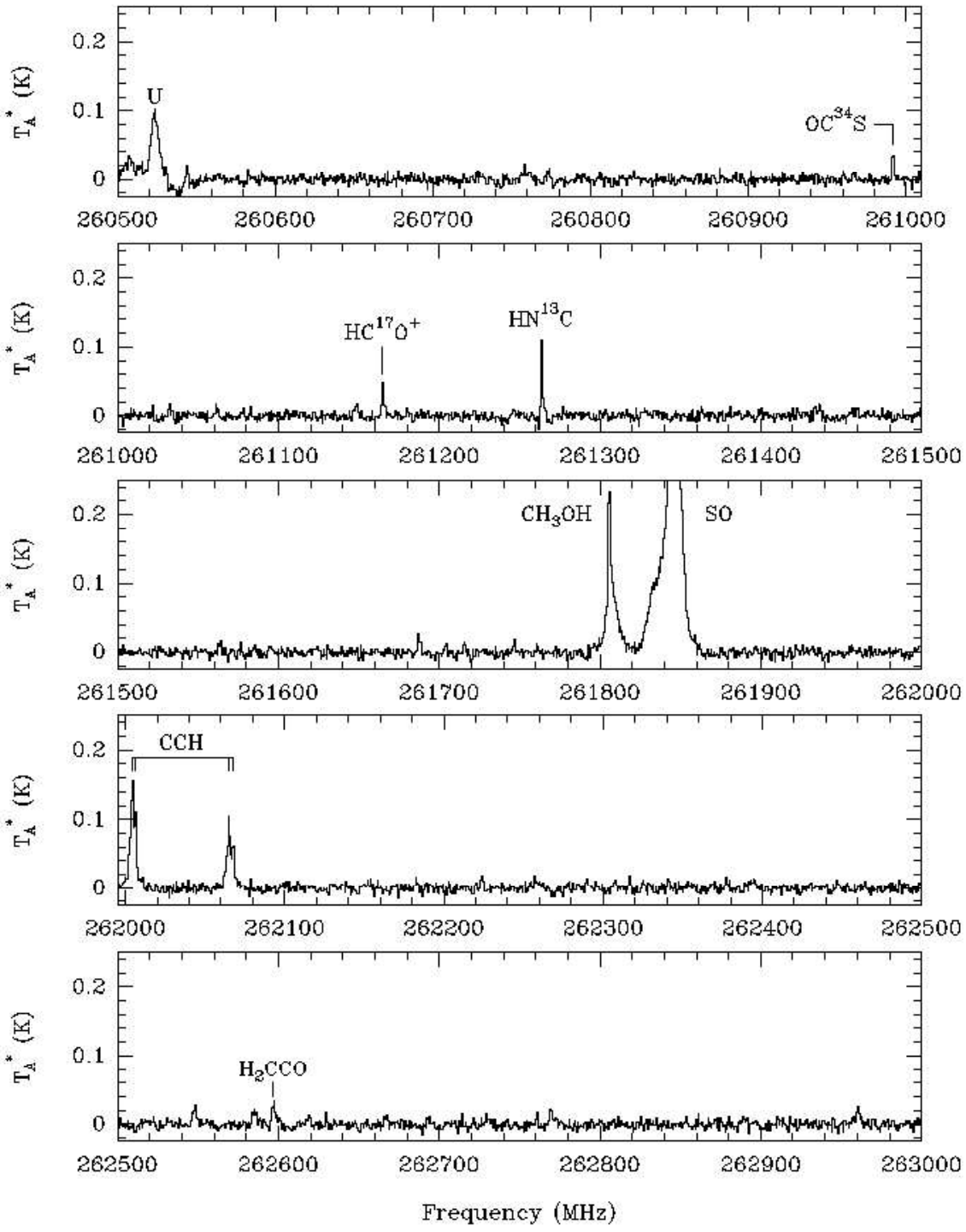
U
OC34S
HC17O+
HN13C
CH3OH
SO
CCH
H2CCO
T*A (K)
0.2
0.1
0
260500
260600
260700
260800
260900
261000
261100
261200
261300
261400
261500
261600
261700
261800
261900
262000
262100
262200
262300
262400
262500
262600
262700
262800
262900
263000
Frequency (MHz)

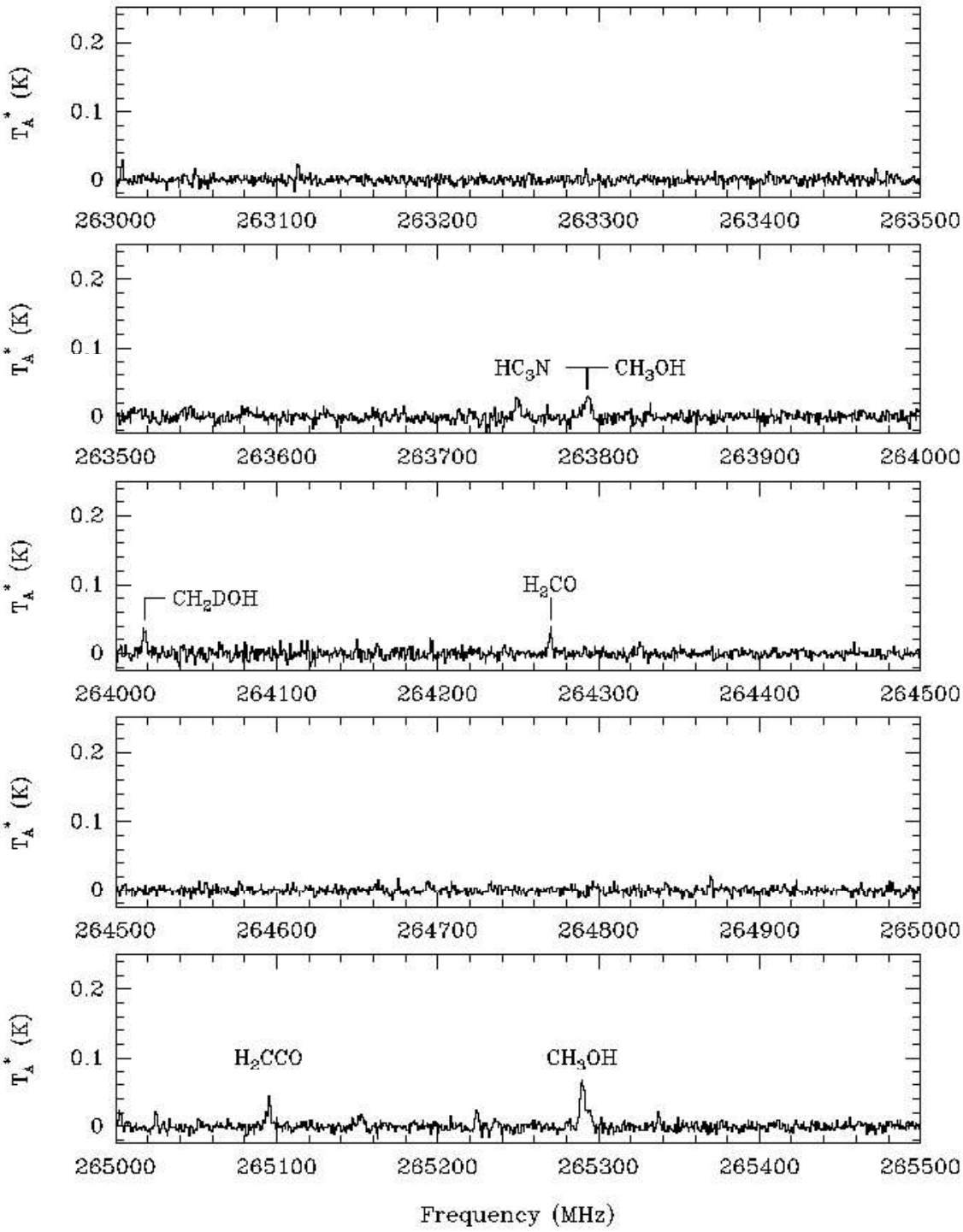
0.2
0.1
0
T_A^* (K)
263000
263100
263200
263300
263400
263500
HC_3N
CH_3OH
263500
263600
263700
263800
263900
264000
CH_2DOH
H_2CO
264000
264100
264200
264300
264400
264500
264500
264600
264700
264800
264900
265000
H_2CCO
CH_3OH
265000
265100
265200
265300
265400
265500
Frequency (MHz)

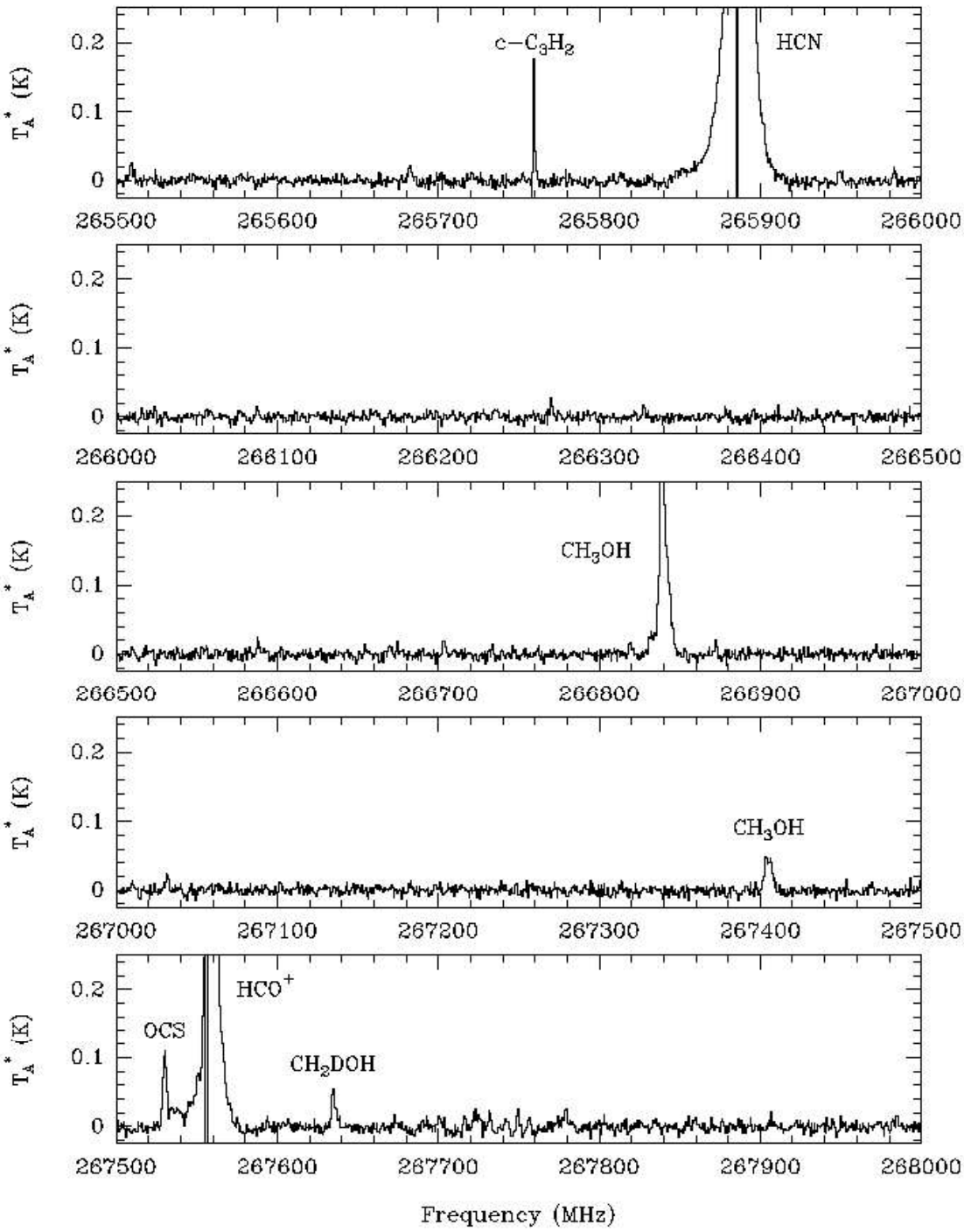
c−C3H2
HCN
CH3OH
CH3OH
OCS
HCO+
CH2DOH
T_A* (K)
Frequency (MHz)

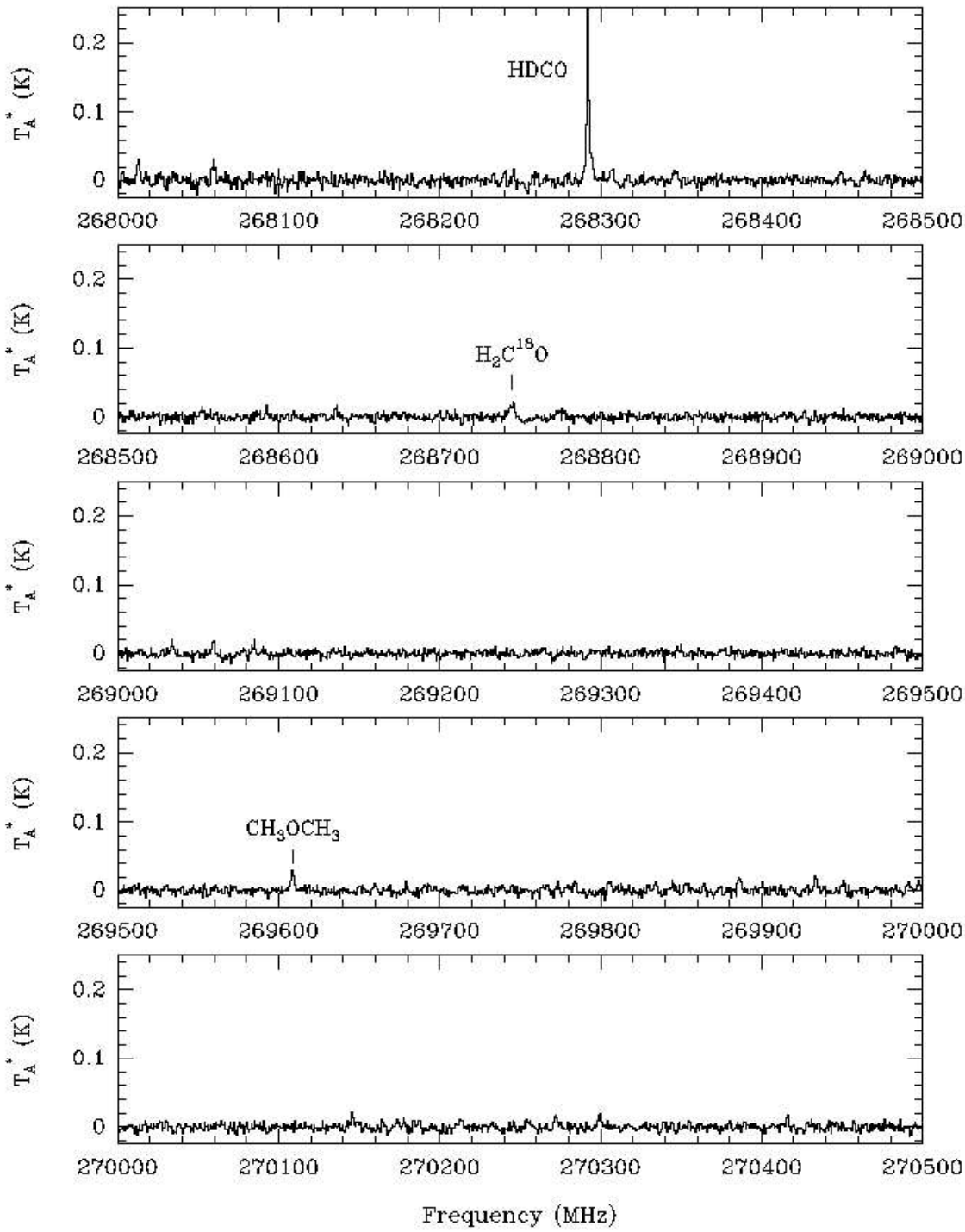
HDCO
$H_2C^{18}O$
CH_3OCH_3
T_A^* (K)
0.2
0.1
0
268000
268100
268200
268300
268400
268500
268600
268700
268800
268900
269000
269100
269200
269300
269400
269500
269600
269700
269800
269900
270000
270100
270200
270300
270400
270500
Frequency (MHz)

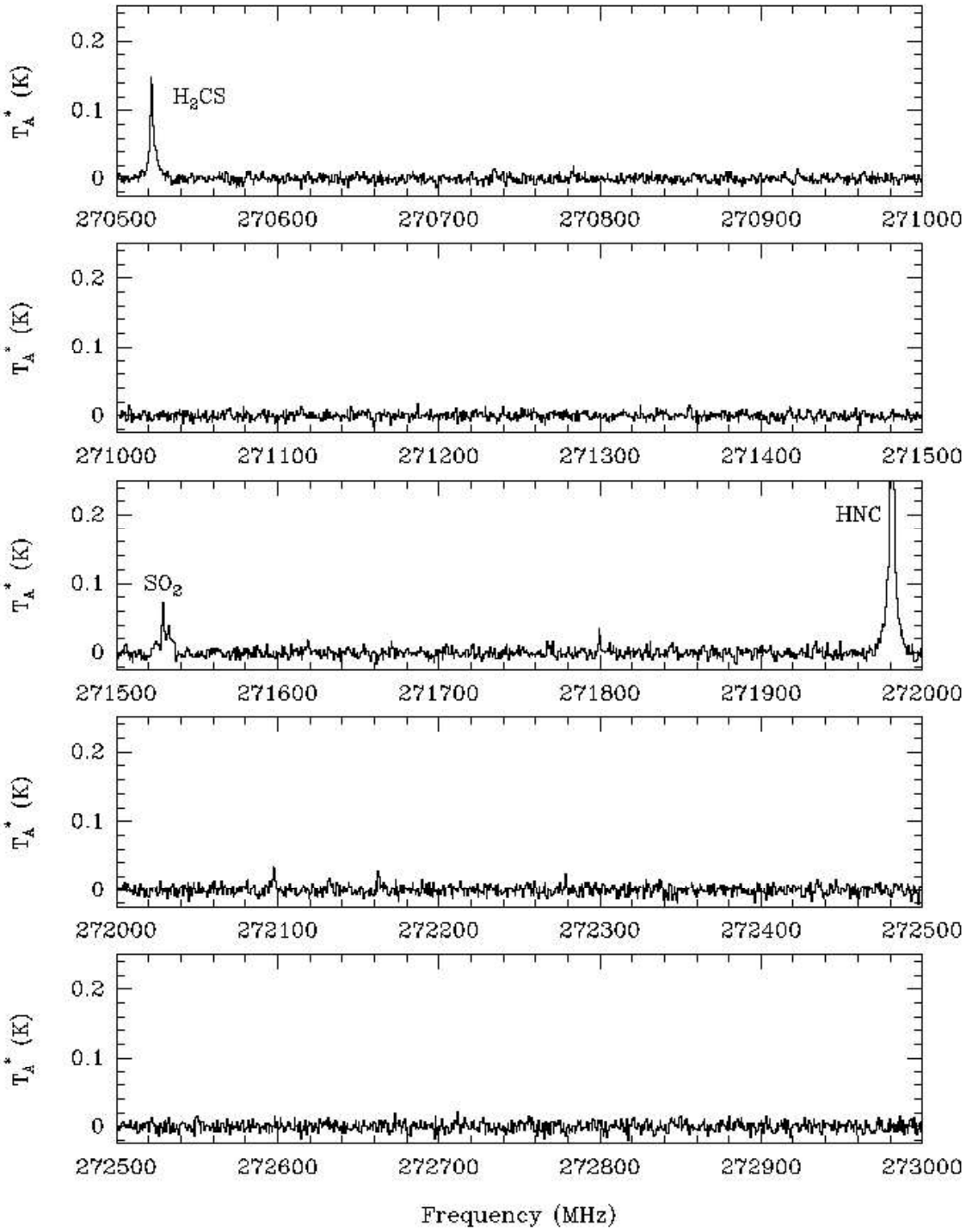
H_2CS
SO_2
HNC
T_A^* (K)
0.2
0.1
0
270500
270600
270700
270800
270900
271000
271100
271200
271300
271400
271500
271600
271700
271800
271900
272000
272100
272200
272300
272400
272500
272600
272700
272800
272900
273000
Frequency (MHz)

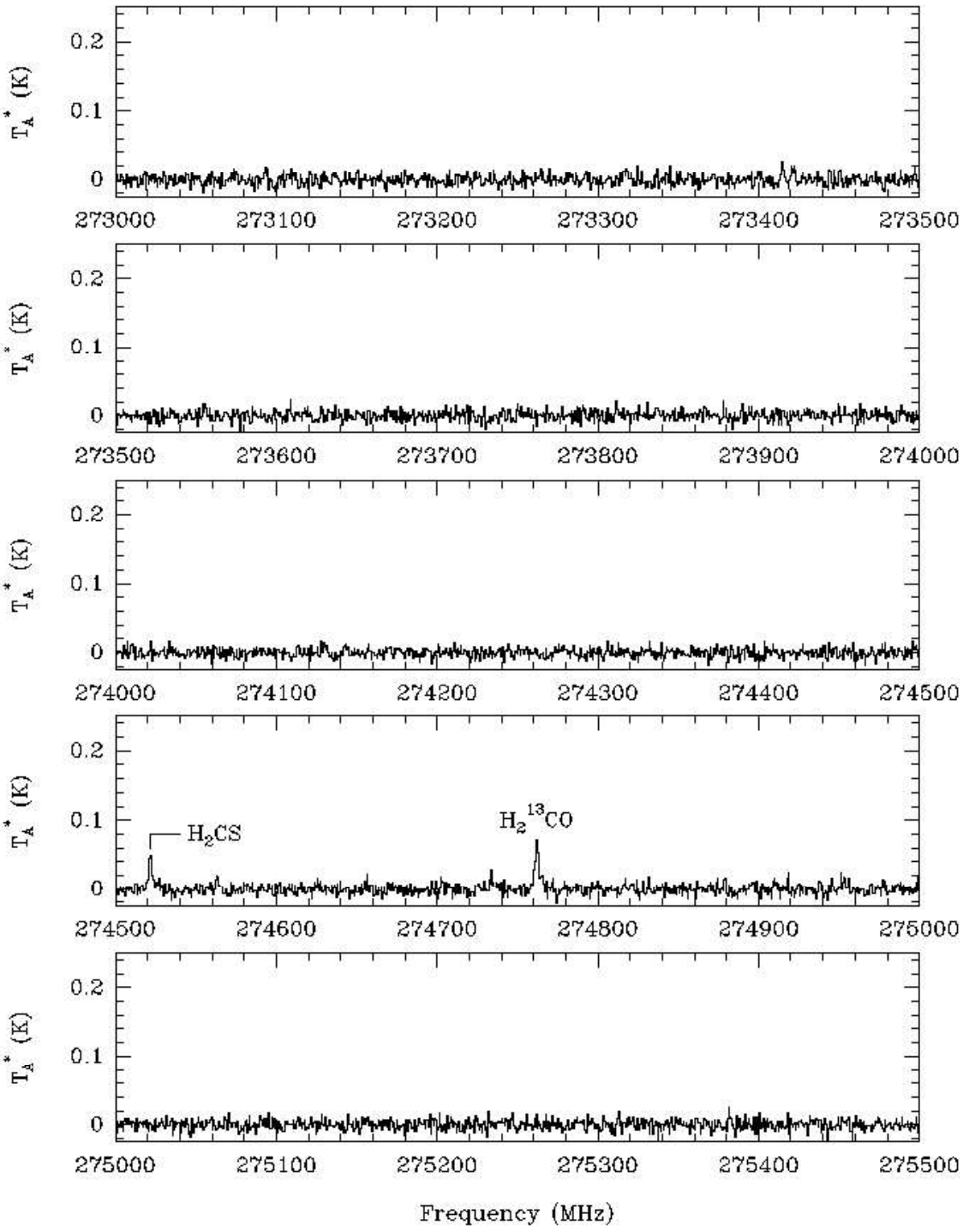
0.2
0.1
0
T_A^* (K)
273000
273100
273200
273300
273400
273500
273500
273600
273700
273800
273900
274000
274000
274100
274200
274300
274400
274500
H_2CS
$H_2{}^{13}CO$
274500
274600
274700
274800
274900
275000
275000
275100
275200
275300
275400
275500
Frequency (MHz)

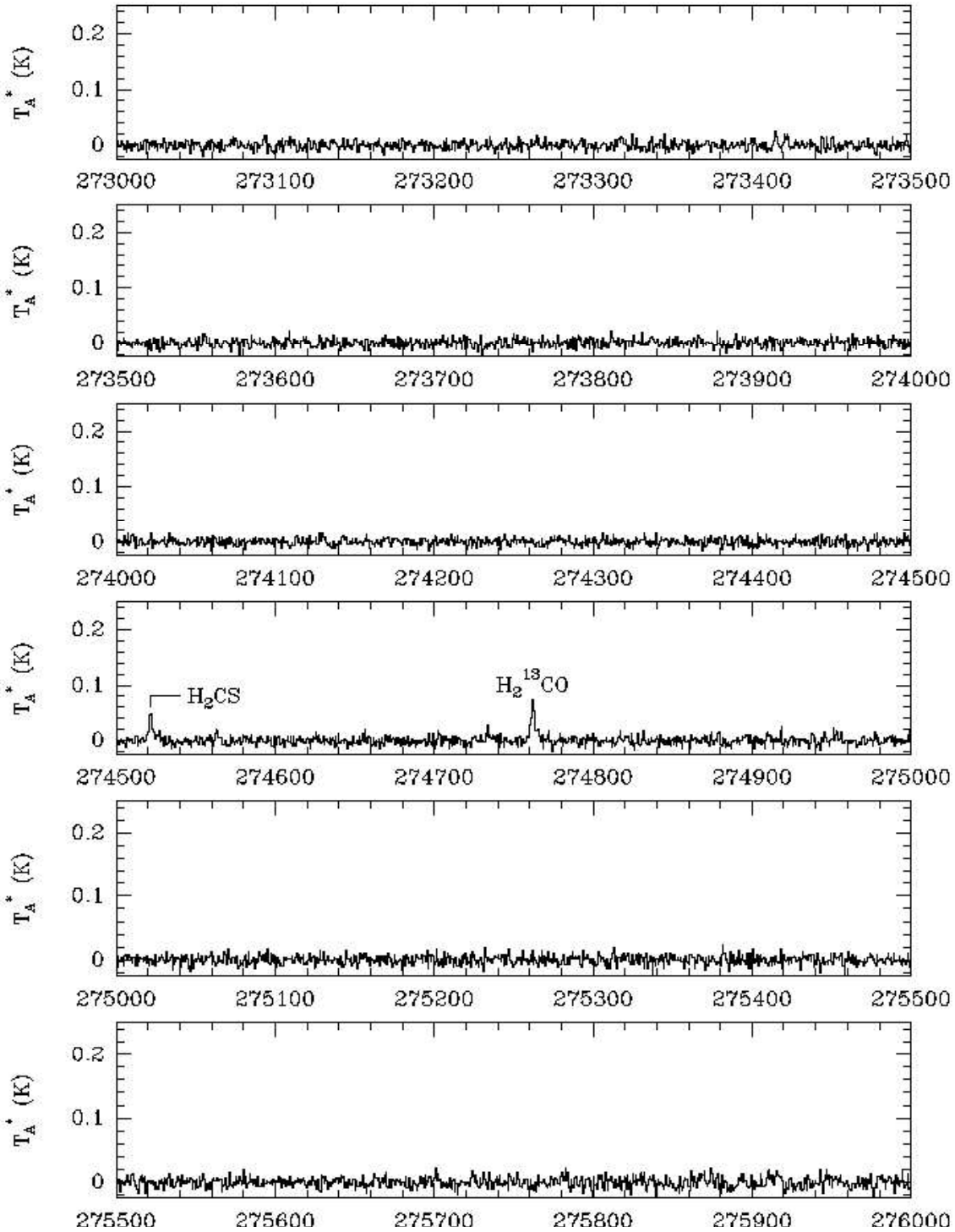
T_A^* (K)
0.2
0.1
0
273000
273100
273200
273300
273400
273500
273500
273600
273700
273800
273900
274000
274000
274100
274200
274300
274400
274500
H_2CS
$H_2{}^{13}CO$
274500
274600
274700
274800
274900
275000
275000
275100
275200
275300
275400
275500
275500
275600
275700
275800
275900
276000
Frequency (MHz)

Appendix D

IRAS 4A: Rotational Frequencies Catalogue

Table D.1: Identification of rotational frequencies in IRAS 4A.

id	Species	Frequency (MHz)	E_{up} (K)	A_{ij} (s^{-1})	V_0 (km s^{-1})	FWHM (km s^{-1})	Intensity (K)	FitFlux (K km s^{-1})	rms (mK)
28006	HN-15-C	266587.800	25.589	6.890E-04	6.562	0.681	0.044	0.032	6.836
25001	CCH	262078.776	25.160	6.492E-06	6.562	0.710	0.016	0.012	6.919
51001	HCCCN	218324.788	130.983	8.229E-04	6.677	0.719	0.024	0.018	9.178
30008	NO	251509.438	19.278	1.568E-09	7.600	0.756	0.085	0.068	6.612
38002	c-C3H2	218160.442	35.418	4.443E-04	6.838	0.764	0.114	0.093	7.410
28001	CO	230538.000	16.596	6.910E-07	5.988	0.771	3.310	2.715	1009.243
38002	c-C3H2	217822.148	38.608	5.933E-04	6.885	0.783	0.446	0.371	7.031
30008	NO	250753.140	19.275	4.437E-07	7.406	0.813	0.015	0.013	5.361
45005	HCS+	256027.800	43.007	4.130E-04	7.647	0.814	0.058	0.050	5.200
26504	CN, v=0,1	226874.781	16.335	1.143E-04	6.911	0.822	0.554	0.485	10.366
26504	CN, v=0,1	226659.558	16.310	9.466E-05	6.783	0.864	0.422	0.388	11.333
38002	c-C3H2	265759.438	32.221	7.992E-04	6.673	0.873	0.277	0.258	17.106
26504	CN, v=0,1	226359.871	16.310	1.608E-05	6.747	0.878	0.082	0.077	8.471
38002	c-C3H2	251527.302	47.489	7.422E-04	6.723	0.886	0.211	0.199	10.358
38002	c-C3H2	252409.831	76.451	1.340E-04	6.738	0.891	0.018	0.017	4.938
38002	c-C3H2	251508.691	47.489	7.421E-04	6.718	0.892	0.081	0.077	7.951
26504	CN, v=0,1	226632.190	16.309	4.259E-05	6.785	0.893	0.144	0.136	9.708
51001	HCCCN	163753.389	74.663	3.448E-04	6.661	0.894	0.082	0.078	5.789
26504	CN, v=0,1	226679.311	16.309	5.268E-05	6.787	0.904	0.173	0.166	8.240
32003	CH3OH	156602.395	21.445	8.926E-06	6.674	0.906	0.081	0.078	8.566
26504	CN, v=0,1	226887.420	16.336	2.731E-05	6.920	0.917	0.077	0.076	10.076
44003	CH3CHO	212400.924	81.484	3.000E-04	7.129	0.920	0.032	0.032	9.745

Continued on next page

Table D.1 – continued from previous page

id	Species	Frequency (MHz)	E_{up} (K)	A_{ij} (s^{-1})	V_0 (km s^{-1})	FWHM (km s^{-1})	Intensity (K)	FitFlux (K km s^{-1})	rms (mK)
31504	H2COH+	126923.380	9.140	1.830E-05	7.543	0.937	0.019	0.019	4.443
52005	DCCCN	92872.387	26.743	6.133E-05	6.877	0.938	0.011	0.011	2.416
44001	CS	244935.644	35.266	2.998E-04	6.696	0.940	2.431	2.433	66.885
44003	CH3CHO	212059.563	117.439	2.560E-04	6.627	0.942	0.021	0.021	6.541
31001	HCO-18+	255480.210	24.523	9.130E-04	7.717	0.943	0.154	0.154	4.999
44003	CH3CHO	250814.720	120.392	4.880E-04	6.564	0.948	0.104	0.105	5.099
27002	HNC	271981.142	26.106	9.337E-04	6.618	0.953	1.948	1.976	22.164
38002	c-C3H2	216278.756	19.466	2.812E-04	6.908	0.968	0.278	0.287	7.221
30004	H2CO	225697.775	33.450	2.770E-04	6.699	0.972	2.639	2.731	68.604
48507	D2CS	166073.855	34.248	6.583E-05	7.053	0.972	0.023	0.024	5.254
46008	CH3OCH3	241530.972	26.309	5.443E-05	7.718	0.977	0.018	0.018	5.433
38002	c-C3H2	251314.343	50.669	9.347E-04	6.729	0.977	0.316	0.329	8.435
40502	CH3CCH	205045.501	129.002	2.775E-05	6.898	0.977	0.045	0.046	6.268
30008	NO	150198.760	7.209	1.839E-07	7.629	0.977	0.065	0.067	5.638
26504	CN, v=0,1	113490.970	5.447	1.192E-05	6.775	0.978	1.384	1.441	34.769
45502	CS-33, v=0,1	242913.610	34.975	2.907E-04	6.760	0.980	0.084	0.088	6.070
51001	HCCCN	127367.666	45.846	1.610E-04	6.824	0.989	0.165	0.174	7.453
44003	CH3CHO	171296.985	41.324	1.680E-04	6.891	0.992	0.063	0.066	12.741
32003	CH3OH	146618.697	104.412	8.041E-06	6.887	0.995	0.392	0.415	10.711
38002	c-C3H2	217940.046	35.417	4.426E-04	6.883	0.996	0.289	0.306	9.064
30004	H2CO	211211.468	32.059	2.270E-04	6.760	0.997	2.830	3.004	68.642
39003	c-C3HD	158420.819	22.304	9.705E-05	6.527	0.999	0.012	0.012	3.539
43510	HOCN	83900.570	10.067	4.220E-05	7.259	0.999	0.028	0.030	6.721

Continued on next page

Table D.1 – continued from previous page

id	Species	Frequency (MHz)	E_{up} (K)	A_{ij} (s^{-1})	V_0 (km s^{-1})	FWHM (km s^{-1})	Intensity (K)	FitFlux (K km s^{-1})	rms (mK)
46001	CS-34	241016.194	34.702	2.857E-04	6.969	1.000	0.298	0.317	7.873
56502	CCS	155454.488	57.203	1.729E-04	6.901	1.012	0.022	0.024	5.221
30002	HC-13-O+	260255.340	24.981	1.330E-03	6.770	1.014	1.237	1.334	11.497
38002	c-C3H2	145089.595	16.050	7.441E-05	6.804	1.015	0.185	0.200	20.549
44001	CS	146969.033	14.107	6.108E-05	6.572	1.016	4.093	4.425	106.088
31002	H2C-13-O	219908.525	32.938	2.564E-04	6.988	1.023	0.082	0.089	7.793
46004	C2H5OH	148304.057	58.146	7.217E-06	7.183	1.033	0.013	0.015	3.892
26504	CN, v=0,1	226663.693	16.308	8.465E-05	6.769	1.033	0.138	0.152	9.081
48507	D2CS	221321.781	54.166	1.609E-04	6.647	1.043	0.020	0.023	6.824
34502	H2S	168762.762	27.877	2.677E-05	6.435	1.047	1.856	2.069	45.053
25001	CCH	262006.403	25.148	5.524E-05	6.553	1.049	0.084	0.094	17.691
29501	C-13-O	220398.680	15.866	6.070E-07	6.480	1.051	3.946	4.413	103.132
30004	H2CO	218222.192	20.957	2.816E-04	6.788	1.051	2.332	2.608	47.416
45003	NH2CHO	142701.514	30.407	1.973E-04	7.907	1.051	0.019	0.021	5.908
31001	HCO-18+	170322.750	12.261	2.530E-04	6.977	1.054	0.140	0.157	8.288
51001	HCCCN	145560.946	59.381	2.414E-04	6.794	1.054	0.111	0.124	5.980
38002	c-C3H2	249054.368	41.021	4.572E-04	6.677	1.057	0.146	0.165	7.260
51001	HCCCN	209230.234	120.505	7.236E-04	7.108	1.063	0.035	0.039	6.738
26504	CN, v=0,1	226616.571	16.308	1.073E-05	6.586	1.063	0.023	0.026	8.264
66002	S-34-O2	203225.140	14.986	6.204E-05	6.619	1.064	0.024	0.027	8.680
30507	N-15-NH+	270783.590	25.992	1.140E-03	6.869	1.068	0.022	0.025	6.135
28002	HC-13-N	259011.820	24.862	1.200E-04	6.785	1.068	0.108	0.122	7.128
32003	CH3OH	205791.270	16.840	6.277E-05	6.724	1.069	0.091	0.103	10.375

Continued on next page

Table D.1 – continued from previous page

id	Species	Frequency (MHz)	E_{up} (K)	A_{ij} (s^{-1})	V_0 (km s^{-1})	FWHM (km s^{-1})	Intensity (K)	FitFlux (K km s^{-1})	rms (mK)
44003	CH3CHO	212134.140	97.246	2.810E-04	7.059	1.070	0.017	0.019	6.689
44003	CH3CHO	153872.682	42.326	1.140E-04	6.776	1.075	0.042	0.048	6.736
64002	SO2	203391.550	70.123	8.804E-05	7.084	1.077	0.035	0.040	11.398
26504	CN, v=0,1	226892.128	16.336	1.810E-05	6.743	1.081	0.111	0.127	9.318
28004	DCN	217238.400	20.852	3.826E-04	6.660	1.082	0.305	0.352	7.439
32003	CH3OH	157272.338	27.053	2.146E-05	6.796	1.085	0.168	0.194	9.108
46004	C2H5OH	231220.812	118.418	4.122E-05	7.013	1.085	0.176	0.204	10.819
28003	HCN-15	258157.100	24.779	7.647E-04	6.755	1.086	0.046	0.053	6.481
27505	C-13-N	108636.923	5.214	9.611E-06	7.372	1.088	0.011	0.013	5.243
26504	CN, v=0,1	226314.540	16.309	9.904E-06	6.703	1.092	0.036	0.042	7.987
64002	SO2	134004.860	43.146	2.501E-05	6.847	1.101	0.030	0.035	5.143
44003	CH3CHO	236049.131	76.135	4.440E-04	6.922	1.103	0.042	0.049	13.218
36503	D2S	237903.800	11.418	4.990E-05	7.234	1.105	0.050	0.059	6.443
32003	CH3OH	104060.634	273.900	1.588E-06	6.744	1.109	0.005	0.006	1.822
35502	HDS	257781.410	47.038	4.990E-05	7.013	1.110	0.039	0.046	6.666
28005	HNC-13	261263.310	25.078	6.480E-04	6.402	1.118	0.143	0.171	6.858
60003	CH3OCHO	153399.352	56.632	5.336E-05	6.520	1.138	0.028	0.033	7.892
30508	NN-15-H+	273608.985	26.263	1.181E-03	6.663	1.140	0.026	0.031	10.356
26504	CN, v=0,1	226875.896	16.336	8.587E-05	6.842	1.143	0.256	0.311	12.074
60003	CH3OCHO	111682.189	28.122	1.980E-05	6.786	1.145	0.021	0.026	6.191
38002	c-C3H2	227169.127	29.069	3.425E-04	6.819	1.148	0.187	0.228	10.313
46004	C2H5OH	129665.731	23.894	1.085E-05	6.903	1.148	0.011	0.013	3.111
33502	*C-13-H3OH, vt=0,1	163872.900	76.499	9.910E-06	6.528	1.151	0.020	0.025	5.487

Continued on next page

Table D.1 – continued from previous page

id	Species	Frequency (MHz)	E_{up} (K)	A_{ij} (s^{-1})	V_0 (km s^{-1})	FWHM (km s^{-1})	Intensity (K)	FitFlux (K km s^{-1})	rms (mK)
39003	c-C3HD	166112.362	25.366	2.128E-04	6.927	1.153	0.018	0.022	6.019
38002	c-C3H2	204788.926	28.822	1.365E-04	6.873	1.158	0.039	0.048	7.250
30004	H2CO	145602.949	10.483	7.808E-05	6.699	1.160	2.378	2.936	89.595
31003	HDCO	268292.020	40.166	5.081E-04	6.826	1.161	0.231	0.286	7.788
42501	H2CCO	262760.857	140.455	2.007E-04	6.760	1.162	0.020	0.025	5.240
30008	NO	250815.594	19.278	1.554E-06	7.539	1.163	0.103	0.127	7.110
46010	NS	253968.393	39.933	2.840E-04	6.947	1.164	0.030	0.037	2.906
30004	H2CO	140839.502	21.923	5.300E-05	6.574	1.170	2.790	3.475	72.922
30008	NO	150176.480	7.207	3.310E-07	7.608	1.171	0.172	0.215	8.537
33004	CH2DOH	168812.161	37.590	1.945E-06	6.819	1.171	0.020	0.025	5.766
48508	H2CS-34	133026.910	29.145	3.104E-05	7.120	1.172	0.017	0.022	4.678
30008	NO	250436.848	19.226	1.841E-06	7.442	1.175	0.126	0.158	7.617
42501	H2CCO	79180.141	218.558	2.786E-08	7.035	1.177	0.009	0.011	2.607
52005	DCCCN	84429.825	22.286	4.626E-05	6.959	1.179	0.007	0.009	4.438
38002	c-C3H2	155518.295	16.136	1.226E-04	6.856	1.181	0.106	0.133	5.932
30008	NO	150546.520	7.246	3.334E-07	7.669	1.183	0.175	0.221	7.952
38002	c-C3H2	244222.133	18.166	6.491E-05	6.824	1.185	0.068	0.086	7.512
44003	CH3CHO	231363.284	128.542	3.480E-04	7.002	1.194	0.038	0.048	8.962
51001	HCCCN	136464.401	52.395	1.985E-04	6.845	1.196	0.121	0.154	6.647
33004	CH2DOH	247846.432	131.908	2.754E-05	6.875	1.197	0.019	0.024	6.066
27505	C-13-N	216710.144	15.642	5.681E-08	6.512	1.198	0.242	0.309	8.784
33004	CH2DOH	269034.330	44.119	5.299E-05	7.210	1.202	0.024	0.030	6.330
39003	c-C3HD	136370.910	17.394	1.106E-04	7.146	1.202	0.018	0.023	5.232

Continued on next page

Table D.1 – continued from previous page

id	Species	Frequency (MHz)	E_{up} (K)	A_{ij} (s^{-1})	V_0 (km s^{-1})	FWHM (km s^{-1})	Intensity (K)	FitFlux (K km s^{-1})	rms (mK)
30008	NO	250708.245	19.278	2.958E-07	7.472	1.203	0.023	0.029	4.863
51001	HCCCN	154657.284	66.804	2.900E-04	6.886	1.208	0.069	0.089	6.176
33004	CH2DOH	268464.024	80.977	4.465E-05	6.434	1.208	0.020	0.026	3.384
58003	CH3COCH3	110148.838	29.945	4.260E-05	6.918	1.210	0.032	0.041	9.566
38002	c-C3H2	151343.873	35.417	4.350E-05	6.865	1.210	0.039	0.051	5.023
48507	D2CS	113484.714	13.622	2.081E-05	7.328	1.225	0.092	0.120	10.166
37002	C3H	163491.557	32.936	2.244E-04	6.877	1.227	0.017	0.022	5.407
40502	CH3CCH	239234.034	115.023	4.631E-05	6.774	1.228	0.029	0.038	8.179
27505	C-13-N	108426.889	5.231	6.266E-06	7.124	1.230	0.011	0.015	4.082
44003	CH3CHO	231847.579	92.611	3.940E-04	6.895	1.230	0.037	0.048	10.641
30004	H2CO	150498.334	22.618	6.467E-05	6.507	1.231	2.794	3.661	78.637
60003	CH3OCHO	200956.372	97.508	1.100E-04	6.612	1.233	0.030	0.039	8.527
48010	SO+	162574.058	16.745	2.144E-05	7.351	1.234	0.092	0.121	5.105
44001	CS	97980.950	7.054	1.689E-05	6.618	1.237	3.628	4.778	82.894
46005	HCOOH	111746.790	16.125	1.438E-05	7.259	1.237	0.019	0.026	6.491
33502	*C-13-H3OH, vt=0,1	155262.012	114.935	1.670E-05	7.160	1.238	0.019	0.025	3.905
31003	HDCO	256585.430	30.848	4.736E-04	6.721	1.245	0.340	0.451	5.939
48507	D2CS	145461.965	27.291	4.302E-05	7.257	1.248	0.022	0.029	4.966
27001	HCN	88631.847	4.254	2.426E-05	6.451	1.248	2.751	3.655	59.453
31502	C-13-O-18	209419.098	15.076	8.722E-08	6.820	1.249	0.083	0.110	7.603
29004	HCO	86777.460	4.183	4.610E-06	7.682	1.252	0.026	0.034	2.731
30508	NN-15-H+	91205.695	4.377	3.403E-05	6.246	1.254	0.012	0.016	2.525
31003	HDCO	246924.600	37.602	3.961E-04	6.731	1.256	0.309	0.413	7.696

Continued on next page

Table D.1 – continued from previous page

id	Species	Frequency (MHz)	E_{up} (K)	A_{ij} (s^{-1})	V_0 (km s^{-1})	FWHM (km s^{-1})	Intensity (K)	FitFlux (K km s^{-1})	rms (mK)
48508	H2CS-34	166275.426	37.125	6.349E-05	7.104	1.256	0.023	0.031	6.064
28003	HCN-15	172107.956	12.390	2.115E-04	6.494	1.256	0.065	0.087	13.543
46509	H2CS	236727.020	58.620	1.920E-04	6.941	1.264	0.169	0.227	7.583
60003	CH3OCHO	148028.088	69.978	3.618E-05	6.747	1.270	0.013	0.018	3.855
64002	SO2	271529.015	35.496	1.107E-04	6.780	1.271	0.049	0.066	8.707
30510	DCO+	216112.582	20.744	7.660E-04	7.252	1.273	2.126	2.880	16.330
45001	C-13-S	138739.335	13.317	5.107E-05	7.168	1.275	0.185	0.251	7.354
64002	SO2	72758.243	19.155	2.769E-06	7.330	1.281	0.143	0.195	5.509
30001	CO-18	219560.360	15.806	6.010E-07	6.887	1.286	2.643	3.617	98.038
41001	CH3CN	128690.111	281.788	4.724E-05	7.088	1.289	0.018	0.024	4.192
48010	SO+	115804.405	8.889	7.232E-06	7.432	1.289	0.126	0.173	13.149
32003	CH3OH	250506.853	153.099	4.228E-05	6.828	1.291	0.064	0.087	6.891
25001	CCH	262067.331	25.160	4.827E-05	6.605	1.292	0.071	0.098	3.344
47504	HDCS	252735.009	63.582	2.380E-04	6.958	1.294	0.014	0.020	3.309
33502	*C-13-H3OH, vt=0,1	165575.639	27.852	2.365E-05	6.783	1.297	0.017	0.023	3.937
40502	CH3CCH	239247.728	93.348	4.705E-05	6.863	1.297	0.055	0.076	8.041
43509	HCNO	91751.320	11.009	3.840E-05	7.544	1.298	0.021	0.030	2.875
40502	CH3CCH	273419.906	111.547	7.089E-05	6.154	1.299	0.022	0.030	5.032
44006	DNCO	101963.505	14.681	7.110E-09	7.150	1.301	0.010	0.013	2.141
44003	CH3CHO	270212.786	133.259	6.190E-04	6.970	1.302	0.017	0.024	5.578
32003	CH3OH	241842.284	72.530	5.115E-05	7.487	1.302	0.017	0.023	6.736
31003	HDCO	201341.350	27.290	1.963E-04	6.995	1.303	0.440	0.610	12.471
50001	S-34-O	211013.673	43.539	1.147E-04	8.077	1.311	0.036	0.050	7.591

Continued on next page

Table D.1 – continued from previous page

id	Species	Frequency (MHz)	E_{up} (K)	A_{ij} (s^{-1})	V_0 (km s^{-1})	FWHM (km s^{-1})	Intensity (K)	FitFlux (K km s^{-1})	rms (mK)
40502	CH3CCH	239252.294	86.123	4.729E-05	6.813	1.312	0.072	0.101	8.096
56502	CCS	72783.541	46.396	2.631E-07	5.866	1.315	0.275	0.384	8.475
32003	CH3OH	229758.756	89.103	4.192E-05	7.150	1.315	0.217	0.303	10.895
60003	CH3OCHO	148039.433	69.960	3.620E-05	6.985	1.318	0.015	0.021	4.604
48001	SO	251825.770	50.661	1.963E-04	6.796	1.318	0.384	0.539	23.477
46001	CS-34	144617.109	13.881	5.820E-05	6.925	1.320	0.514	0.722	8.289
46008	CH3OCH3	241528.306	26.310	4.504E-05	7.061	1.321	0.016	0.022	5.197
30009	NND+	231321.665	22.204	7.139E-04	6.954	1.322	0.758	1.067	13.757
48010	SO+	208965.420	26.774	4.721E-05	7.564	1.324	0.045	0.064	6.854
34502	H2S	216710.437	83.980	4.872E-05	6.921	1.325	0.250	0.353	8.970
40502	CH3CCH	205065.070	92.880	2.879E-05	6.889	1.326	0.064	0.090	6.301
32003	CH3OH	96501.713	420.324	2.531E-06	7.012	1.326	0.013	0.018	2.723
33004	CH2DOH	135452.934	29.489	8.577E-06	7.334	1.331	0.021	0.030	5.104
61502	OC-13-S	230317.527	110.543	3.545E-05	7.155	1.333	0.016	0.023	7.980
33004	CH2DOH	212185.540	48.338	4.810E-06	6.083	1.334	0.019	0.027	7.006
32006	D2CO	234293.720	76.624	1.580E-04	7.289	1.336	0.023	0.033	8.324
30008	NO	150580.560	7.238	2.964E-07	7.564	1.337	0.048	0.068	6.743
44003	CH3CHO	212066.069	117.408	2.560E-04	6.771	1.338	0.018	0.026	6.498
31003	HDCO	257748.760	62.775	3.604E-04	6.914	1.338	0.077	0.109	5.483
44003	CH3CHO	212257.139	81.465	3.000E-04	7.141	1.339	0.032	0.045	7.899
46005	HCOOH	268240.356	96.615	2.042E-04	6.198	1.341	0.019	0.028	9.826
38002	c-C3H2	150820.665	19.307	1.799E-04	6.858	1.342	0.124	0.177	7.059
44003	CH3CHO	212029.131	117.511	2.560E-04	6.661	1.342	0.026	0.037	6.422

Continued on next page

Table D.1 – continued from previous page

id	Species	Frequency (MHz)	E_{up} (K)	A_{ij} (s^{-1})	V_0 (km s^{-1})	FWHM (km s^{-1})	Intensity (K)	FitFlux (K km s^{-1})	rms (mK)
46509	H2CS	270521.931	71.603	2.903E-04	6.765	1.342	0.107	0.152	7.880
44003	CH3CHO	212021.554	142.161	2.270E-04	7.071	1.343	0.025	0.035	6.334
30008	NO	150225.660	7.211	2.943E-07	7.557	1.343	0.049	0.070	7.300
31003	HDCO	128812.860	9.276	5.397E-05	7.040	1.347	0.772	1.107	9.717
30510	DCO+	144077.289	10.372	2.120E-04	7.276	1.348	3.139	4.503	20.492
52005	DCCCN	75987.153	18.234	3.309E-05	6.766	1.348	0.008	0.012	3.962
28007	DNC	228910.489	21.972	5.566E-04	7.077	1.349	0.472	0.679	10.384
32003	CH3OH	234683.370	60.924	1.845E-05	7.280	1.350	0.011	0.016	8.233
44003	CH3CHO	212384.736	81.389	2.990E-04	7.162	1.351	0.038	0.054	8.797
46010	NS	115570.763	10.007	1.977E-05	7.088	1.354	0.145	0.209	14.240
49501	S-33-O	98482.302	9.156	8.201E-06	7.515	1.357	0.022	0.032	1.770
38002	c-C3H2	150851.908	19.307	1.801E-04	6.880	1.357	0.340	0.491	9.952
46509	H2CS	209200.620	48.313	1.300E-04	7.151	1.359	0.205	0.297	8.600
46010	NS	161297.246	17.690	6.859E-05	7.363	1.360	0.115	0.167	7.617
60003	CH3OCHO	147684.903	47.467	4.846E-06	6.905	1.362	0.014	0.020	4.375
30008	NO	250796.436	19.282	1.849E-06	7.440	1.363	0.142	0.206	7.172
42501	H2CCO	161631.673	87.104	4.385E-05	7.049	1.364	0.024	0.035	7.017
30008	NO	250448.530	19.230	1.381E-06	7.378	1.370	0.044	0.064	7.220
40502	CH3CCH	170902.518	52.340	1.683E-05	6.599	1.371	0.087	0.127	10.398
40502	CH3CCH	205076.816	71.204	2.941E-05	6.897	1.373	0.103	0.151	7.428
46010	NS	115156.812	9.951	1.957E-05	7.593	1.373	0.153	0.223	10.665
60003	CH3OCHO	170244.089	67.797	6.994E-05	7.100	1.373	0.024	0.036	8.186
46509	H2CS	244048.504	60.026	2.103E-04	6.957	1.375	0.137	0.200	7.587

Continued on next page

Table D.1 – continued from previous page

id	Species	Frequency (MHz)	E_{up} (K)	A_{ij} (s^{-1})	V_0 (km s^{-1})	FWHM (km s^{-1})	Intensity (K)	FitFlux (K km s^{-1})	rms (mK)
29507	HCO+, v=0	89188.530	4.280	4.190E-05	6.437	1.375	4.317	6.321	106.790
30008	NO	150644.340	7.241	1.853E-07	7.504	1.376	0.062	0.090	7.155
62505	OCS-34	201691.979	87.122	2.374E-05	6.972	1.377	0.041	0.061	9.048
46010	NS	115153.935	9.949	2.329E-05	7.584	1.378	0.238	0.349	11.464
60003	CH3OCHO	163829.677	62.499	6.374E-05	6.934	1.382	0.028	0.041	6.057
44003	CH3CHO	250934.559	104.623	5.100E-04	6.740	1.385	0.028	0.041	4.266
32003	CH3OH	95169.391	83.539	2.131E-06	6.721	1.387	0.636	0.939	20.936
35502	HDS	244555.580	11.737	2.060E-05	7.244	1.392	0.231	0.343	6.621
44003	CH3CHO	77082.462	29.635	6.310E-06	7.161	1.392	0.013	0.020	2.375
29005	NNH+	93176.130	4.472	3.628E-05	6.779	1.394	0.875	1.298	24.750
33502	*C-13-H3OH, vt=0,1	166128.782	68.635	2.321E-05	6.895	1.396	0.016	0.024	5.476
48010	SO+	162198.598	16.673	2.129E-05	7.419	1.399	0.078	0.116	4.092
48010	SO+	208590.016	26.684	4.696E-05	7.469	1.399	0.043	0.064	7.753
40502	CH3CCH	205080.732	63.978	2.961E-05	6.966	1.399	0.107	0.159	8.151
46005	HCOOH	246106.087	83.741	1.563E-04	6.245	1.400	0.022	0.033	5.557
43510	HOCN	104874.680	15.100	8.420E-05	6.892	1.401	0.010	0.015	2.903
60003	CH3OCHO	111171.634	30.229	1.995E-05	6.171	1.402	0.022	0.033	8.056
32006	D2CO	234331.400	76.627	1.580E-04	7.162	1.404	0.019	0.029	7.373
38002	c-C3H2	260479.746	44.722	1.770E-04	6.822	1.405	0.051	0.076	11.805
33502	*C-13-H3OH, vt=0,1	161789.215	43.713	3.875E-06	6.636	1.407	0.013	0.020	3.814
64002	SO2	83688.093	36.715	6.825E-06	7.079	1.407	0.096	0.144	7.840
46010	NS	115162.982	9.952	1.747E-05	7.723	1.410	0.099	0.149	11.749
27002	HNC	90663.593	4.351	2.690E-05	6.781	1.411	4.077	6.125	61.349

Continued on next page

Table D.1 – continued from previous page

id	Species	Frequency (MHz)	E_{up} (K)	A_{ij} (s^{-1})	V_0 (km s^{-1})	FWHM (km s^{-1})	Intensity (K)	FitFlux (K km s^{-1})	rms (mK)
30008	NO	250440.659	19.229	1.547E-06	7.408	1.412	0.087	0.131	6.557
18004	NH2D	85926.270	20.679	1.760E-05	4.988	1.415	0.303	0.457	3.701
30008	NO	150218.730	7.209	1.471E-07	7.435	1.418	0.056	0.084	6.599
38002	c-C3H2	218732.732	61.166	9.815E-05	6.909	1.418	0.035	0.052	7.037
40502	CH3CCH	153814.276	44.138	1.218E-05	6.868	1.420	0.077	0.117	7.434
31003	HDCO	259034.910	62.867	3.658E-04	7.058	1.421	0.064	0.097	5.891
64002	SO2	160827.880	49.709	3.953E-05	6.955	1.423	0.071	0.108	9.645
40502	CH3CCH	153805.461	65.816	1.172E-05	6.672	1.424	0.033	0.051	7.612
46010	NS	115571.954	10.004	1.766E-05	7.240	1.425	0.099	0.151	14.308
48001	SO	129138.923	25.512	2.294E-05	7.318	1.427	1.111	1.687	16.998
49501	S-33-O	98474.602	9.155	7.687E-06	7.262	1.428	0.012	0.018	1.946
46509	H2CS	205987.858	34.609	1.277E-04	7.163	1.429	0.133	0.203	8.925
48507	D2CS	169996.857	28.584	7.261E-05	7.239	1.431	0.060	0.092	8.420
38002	c-C3H2	254987.640	41.060	5.170E-04	6.728	1.434	0.047	0.071	7.050
46005	HCOOH	90164.628	23.527	5.542E-06	7.267	1.436	0.014	0.022	2.689
50001	S-34-O	97715.390	9.093	1.094E-05	7.445	1.436	0.539	0.823	10.947
40502	CH3CCH	222150.010	103.542	3.686E-05	6.882	1.437	0.057	0.087	7.362
33004	CH2DOH	260543.628	48.338	2.223E-05	6.389	1.437	0.020	0.031	5.283
43509	HCNO	137624.960	23.118	1.350E-04	7.786	1.441	0.015	0.023	3.806
30004	H2CO	89565.060	368.668	9.298E-07	6.276	1.441	0.007	0.011	2.169
45003	NH2CHO	84888.741	37.005	1.132E-06	6.375	1.442	0.007	0.010	2.596
46509	H2CS	202924.054	47.259	1.187E-04	7.134	1.446	0.272	0.419	9.975
46509	H2CS	240266.872	46.140	2.049E-04	6.986	1.449	0.084	0.129	6.190

Continued on next page

Table D.1 – continued from previous page

id	Species	Frequency (MHz)	E_{up} (K)	A_{ij} (s^{-1})	V_0 (km s^{-1})	FWHM (km s^{-1})	Intensity (K)	FitFlux (K km s^{-1})	rms (mK)
46010	NS	115556.253	10.010	2.354E-05	7.124	1.450	0.243	0.375	14.299
44003	CH3CHO	171265.471	41.417	1.680E-04	7.051	1.451	0.039	0.060	11.478
28004	DCN	144827.991	10.426	1.259E-04	6.706	1.452	0.468	0.724	6.738
44003	CH3CHO	96765.371	25.778	2.780E-06	6.709	1.453	0.009	0.013	2.091
60003	CH3OCHO	206619.476	89.245	1.276E-04	7.244	1.454	0.024	0.038	6.293
30008	NO	150439.120	7.241	1.480E-07	7.592	1.454	0.050	0.078	6.570
32003	CH3OH	252803.388	230.825	8.457E-05	7.224	1.456	0.028	0.044	5.856
26504	CN, v=0,1	226303.037	16.309	4.169E-06	6.999	1.458	0.024	0.037	8.212
46509	H2CS	206054.165	87.280	1.136E-04	6.676	1.463	0.048	0.075	7.044
46005	HCOOH	93098.355	14.354	7.626E-06	7.628	1.466	0.015	0.023	2.523
60003	CH3OCHO	132010.774	34.458	2.998E-06	7.464	1.467	0.020	0.031	5.854
60003	CH3OCHO	147406.369	99.766	2.086E-05	6.782	1.468	0.016	0.025	4.481
60003	CH3OCHO	163988.912	64.503	6.539E-05	7.009	1.468	0.032	0.050	5.654
46010	NS	161697.257	17.770	6.910E-05	7.125	1.468	0.097	0.151	7.226
48001	SO	261843.684	47.551	2.327E-04	6.839	1.471	0.766	1.199	32.432
44003	CH3CHO	230315.792	81.056	4.040E-04	6.903	1.471	0.043	0.068	8.445
30004	H2CO	72837.948	3.496	8.145E-06	6.895	1.472	1.666	2.612	35.416
46008	CH3OCH3	204549.475	82.601	3.240E-05	6.804	1.473	0.021	0.032	7.524
44003	CH3CHO	263003.981	95.678	6.200E-04	6.699	1.477	0.031	0.049	6.970
28004	DCN	72413.484	3.475	1.312E-05	7.004	1.480	0.267	0.420	8.092
27505	C-13-N	108780.201	5.248	1.050E-05	7.608	1.481	0.017	0.027	5.368
45502	CS-33, v=0,1	145755.732	13.991	5.922E-05	7.037	1.481	0.090	0.142	6.595
48001	SO	109252.220	21.051	1.101E-05	7.536	1.485	1.199	1.896	22.600

Continued on next page

Table D.1 – continued from previous page

id	Species	Frequency (MHz)	E_{up} (K)	A_{ij} (s^{-1})	V_0 (km s^{-1})	FWHM (km s^{-1})	Intensity (K)	FitFlux (K km s^{-1})	rms (mK)
46509	H2CS	169114.079	37.520	6.681E-05	6.992	1.486	0.264	0.417	7.217
44003	CH3CHO	231369.829	128.512	3.480E-04	7.227	1.493	0.021	0.034	8.813
50001	S-34-O	135775.314	15.609	3.063E-05	6.613	1.494	0.427	0.678	10.657
33502	*C-13-H3OH, vt=0,1	255220.865	63.642	4.534E-05	6.668	1.495	0.010	0.016	2.928
44003	CH3CHO	234795.456	81.865	4.280E-04	6.660	1.495	0.042	0.068	9.648
60003	CH3OCHO	147535.539	88.489	2.655E-05	6.358	1.497	0.018	0.029	5.357
33004	CH2DOH	237249.907	76.401	8.126E-05	7.499	1.499	0.028	0.045	7.413
30510	DCO+	72039.310	3.457	2.210E-05	7.289	1.501	2.404	3.840	18.761
30507	N-15-NH+	90263.840	4.332	3.300E-05	7.276	1.501	0.011	0.017	2.460
60003	CH3OCHO	161152.501	70.465	5.320E-05	7.069	1.502	0.021	0.033	7.304
64002	SO2	208700.320	15.336	6.717E-05	7.193	1.503	0.138	0.220	7.983
66002	S-34-O2	133471.470	15.536	2.107E-05	7.652	1.504	0.019	0.031	5.375
37002	C3H	98011.611	12.539	4.662E-05	7.540	1.506	0.009	0.014	1.712
32003	CH3OH	107013.831	28.349	3.066E-06	5.809	1.506	0.013	0.020	4.930
45003	NH2CHO	161900.079	58.098	1.205E-05	8.154	1.506	0.009	0.014	3.684
42501	H2CCO	222197.635	63.997	1.235E-04	6.995	1.509	0.047	0.076	6.041
60003	CH3OCHO	135921.949	55.603	2.952E-05	6.992	1.511	0.019	0.031	5.398
40502	CH3CCH	136717.562	58.434	8.064E-06	6.995	1.512	0.045	0.073	5.565
60003	CH3OCHO	142815.476	49.289	4.290E-05	6.923	1.513	0.021	0.034	5.672
60003	CH3OCHO	141667.012	43.232	4.059E-05	6.812	1.519	0.018	0.029	5.341
30505	HCO-17+	261164.920	25.068	1.352E-03	6.575	1.519	0.052	0.083	4.935
51001	HCCCN	254699.500	177.259	1.310E-03	6.439	1.520	0.017	0.027	3.260
60003	CH3OCHO	136282.597	49.701	3.253E-05	7.097	1.521	0.019	0.031	5.842

Continued on next page

Table D.1 – continued from previous page

id	Species	Frequency (MHz)	E_{up} (K)	A_{ij} (s^{-1})	V_0 (km s^{-1})	FWHM (km s^{-1})	Intensity (K)	FitFlux (K km s^{-1})	rms (mK)
31002	H2C-13-O	206131.626	31.616	2.112E-04	7.007	1.522	0.124	0.201	7.101
45003	NH2CHO	84891.566	37.005	1.697E-05	7.640	1.523	0.009	0.014	2.630
56502	CCS	72323.789	19.209	1.596E-05	7.253	1.524	0.042	0.069	4.259
39003	c-C3HD	135640.900	17.388	1.085E-04	7.055	1.524	0.026	0.042	4.961
47504	HDCS	154885.030	22.308	5.375E-05	7.257	1.525	0.085	0.139	4.716
46010	NS	207438.692	27.649	1.418E-04	7.341	1.525	0.039	0.063	6.203
32003	CH3OH	157276.019	20.090	2.182E-05	6.823	1.525	0.264	0.428	9.677
60001	OCS	72976.779	12.258	1.068E-06	7.278	1.526	0.119	0.193	4.324
33502	*C-13-H3OH, vt=0,1	236049.520	71.785	4.756E-05	7.351	1.527	0.036	0.059	13.438
26504	CN, v=0,1	113499.644	5.448	1.063E-05	7.025	1.527	0.432	0.701	19.319
48001	SO	86093.950	19.314	5.354E-06	7.296	1.528	1.049	1.707	11.665
33502	*C-13-H3OH, vt=0,1	95273.440	73.585	1.560E-06	6.960	1.528	0.008	0.013	2.369
33502	*C-13-H3OH, vt=0,1	155695.809	94.590	1.772E-05	6.869	1.528	0.019	0.031	5.040
28002	HC-13-N	172677.960	12.431	1.600E-04	6.656	1.529	0.179	0.292	17.609
50002	SO-18	129065.999	14.910	2.633E-05	6.809	1.530	0.045	0.073	4.484
33004	CH2DOH	172015.919	10.401	2.210E-05	6.824	1.532	0.082	0.133	12.651
46010	NS	115185.307	9.952	5.592E-06	7.367	1.532	0.031	0.051	11.447
28004	DCN	72417.030	3.475	1.312E-05	7.169	1.533	0.091	0.149	7.467
27001	HCN	88633.936	4.254	2.427E-05	6.572	1.533	0.870	1.420	46.982
46509	H2CS	139483.682	29.906	3.580E-05	7.399	1.533	0.327	0.535	8.783
44003	CH3CHO	216630.234	64.807	3.410E-04	7.150	1.534	0.041	0.067	8.435
60003	CH3OCHO	141044.354	47.467	4.016E-05	6.853	1.534	0.019	0.030	4.310
44003	CH3CHO	274563.412	101.628	7.040E-04	7.100	1.539	0.024	0.039	8.182

Continued on next page

Table D.1 – continued from previous page

id	Species	Frequency (MHz)	E_{up} (K)	A_{ij} (s^{-1})	V_0 (km s^{-1})	FWHM (km s^{-1})	Intensity (K)	FitFlux (K km s^{-1})	rms (mK)
28007	DNC	152609.774	10.986	1.539E-04	7.288	1.540	1.102	1.806	16.195
48507	D2CS	141769.445	20.425	4.148E-05	7.336	1.540	0.065	0.107	5.767
43002	HNCO	153864.992	29.538	6.133E-09	6.925	1.543	0.135	0.222	6.800
29503	CO-17	112358.982	5.392	6.697E-08	7.240	1.544	0.250	0.411	9.646
46010	NS	161301.747	17.693	6.097E-05	7.169	1.544	0.069	0.113	7.748
60003	CH3OCHO	203864.211	95.550	1.223E-04	7.127	1.547	0.038	0.063	8.399
33502	*C-13-H3OH, vt=0,1	165851.224	55.041	2.332E-05	6.877	1.549	0.023	0.037	5.459
47504	HDCS	158022.076	31.738	5.479E-05	7.042	1.551	0.054	0.089	4.237
46010	NS	161298.411	17.692	6.299E-05	7.444	1.552	0.091	0.151	7.429
28004	DCN	72414.905	3.475	1.312E-05	6.871	1.553	0.421	0.696	7.885
26504	CN, v=0,1	113488.120	5.448	6.736E-06	6.979	1.553	0.569	0.942	24.020
64002	SO2	140306.170	29.199	2.527E-05	7.081	1.555	0.068	0.112	6.226
41001	CH3CN	73590.218	8.829	3.171E-05	6.981	1.555	0.024	0.040	3.755
64002	SO2	104029.418	7.744	1.006E-05	7.386	1.555	0.380	0.629	5.064
48010	SO+	255353.237	39.029	8.811E-05	7.208	1.555	0.013	0.022	4.664
30008	NO	250816.954	19.275	1.387E-06	7.775	1.555	0.068	0.112	7.000
48510	CH3SH,v=0-2	101029.707	16.690	8.615E-06	7.158	1.556	0.009	0.014	1.994
32003	CH3OH	241832.718	84.618	3.867E-05	6.703	1.556	0.041	0.068	6.600
40502	CH3CCH	256336.629	98.425	5.829E-05	6.687	1.558	0.048	0.079	5.001
48001	SO	99299.870	9.226	1.148E-05	7.246	1.558	3.920	6.504	58.418
48001	SO	206176.005	38.576	1.030E-04	7.168	1.559	0.702	1.165	15.352
19002	HDO	241561.550	95.225	1.187E-05	6.319	1.560	0.021	0.034	5.476
31001	HCO-18+	85162.160	4.087	2.630E-05	7.016	1.560	0.114	0.189	3.174

Continued on next page

Table D.1 – continued from previous page

id	Species	Frequency (MHz)	E_{up} (K)	A_{ij} (s^{-1})	V_0 (km s^{-1})	FWHM (km s^{-1})	Intensity (K)	FitFlux (K km s^{-1})	rms (mK)
49501	S-33-O	203937.422	38.309	8.416E-05	7.091	1.561	0.032	0.052	8.558
33004	CH2DOH	240643.524	59.974	4.680E-05	6.736	1.561	0.035	0.059	6.660
28004	DCN	144826.573	10.426	3.148E-05	6.632	1.564	0.143	0.237	4.728
30004	H2CO	218760.066	68.111	1.576E-04	6.973	1.565	0.381	0.634	10.894
49501	S-33-O	136943.672	15.730	2.826E-05	7.737	1.568	0.033	0.055	6.556
49003	C4H	133213.647	47.945	1.073E-05	7.044	1.570	0.014	0.024	4.555
48507	D2CS	87302.662	14.724	8.120E-06	7.373	1.573	0.014	0.024	3.081
26504	CN, v=0,1	113144.157	5.430	1.053E-05	7.077	1.574	0.466	0.780	18.391
47504	HDCS	216662.476	41.622	1.510E-04	7.199	1.576	0.048	0.081	8.093
46010	NS	115524.603	10.004	5.647E-06	7.151	1.576	0.039	0.065	11.386
40502	CH3CCH	170892.726	74.017	1.632E-05	6.774	1.577	0.051	0.085	10.828
44003	CH3CHO	226551.622	71.392	3.940E-04	7.008	1.577	0.039	0.065	8.329
31504	H2COH+	252870.339	30.398	1.610E-04	6.653	1.578	0.017	0.028	4.726
33502	*C-13-H3OH, vt=0,1	255355.930	151.978	8.457E-05	6.844	1.578	0.013	0.021	4.687
26504	CN, v=0,1	113191.279	5.432	6.682E-06	6.985	1.578	0.523	0.878	21.017
44003	CH3CHO	79150.166	11.767	1.460E-05	7.185	1.579	0.038	0.064	2.768
42501	H2CCO	265095.049	102.120	2.099E-04	6.679	1.579	0.050	0.083	4.526
32003	CH3OH	254015.377	20.090	1.902E-05	6.696	1.582	0.137	0.230	5.762
32003	CH3OH	166898.566	104.624	2.277E-05	7.045	1.584	0.029	0.048	6.166
43002	HNCO	87925.044	10.549	1.151E-08	6.610	1.585	0.170	0.287	3.960
60003	CH3OCHO	100294.604	27.414	1.261E-05	6.645	1.586	0.009	0.016	2.461
30009	NND+	154217.096	11.102	1.975E-04	7.232	1.587	0.977	1.649	10.748
48001	SO	172181.460	33.775	5.948E-05	7.140	1.587	0.863	1.458	19.204

Continued on next page

Table D.1 – continued from previous page

id	Species	Frequency (MHz)	E_{up} (K)	A_{ij} (s^{-1})	V_0 (km s^{-1})	FWHM (km s^{-1})	Intensity (K)	FitFlux (K km s^{-1})	rms (mK)
31002	H2C-13-O	213037.340	67.751	1.457E-04	6.664	1.588	0.020	0.034	7.895
48001	SO	215220.653	44.104	1.216E-04	7.178	1.588	0.713	1.206	19.453
42501	H2CCO	140127.474	39.953	2.961E-05	7.002	1.590	0.065	0.109	5.456
48001	SO	138178.600	15.857	3.228E-05	7.205	1.590	3.482	5.894	56.057
33502	*C-13-H3OH, vt=0,1	221285.241	87.118	3.720E-05	6.793	1.591	0.027	0.045	8.877
31002	H2C-13-O	146635.672	22.384	5.987E-05	6.935	1.591	0.098	0.167	5.426
50001	S-34-O	155506.461	28.370	4.039E-05	6.449	1.591	0.061	0.104	5.258
46004	C2H5OH	217803.689	23.893	6.544E-05	6.680	1.593	0.018	0.031	5.947
46509	H2CS	101477.805	22.910	1.260E-05	7.330	1.594	0.330	0.559	6.116
64002	SO2	165225.452	27.085	4.134E-05	7.102	1.595	0.195	0.331	7.882
37003	c-C3H	132993.978	10.774	6.056E-05	6.834	1.595	0.017	0.029	5.397
32006	D2CO	221191.790	31.961	2.850E-04	7.139	1.597	0.098	0.166	9.539
30009	NND+	77112.035	3.701	2.058E-05	6.922	1.597	0.120	0.204	3.644
48001	SO	258255.813	56.498	2.161E-04	6.956	1.598	0.328	0.559	14.603
49501	S-33-O	98489.232	9.157	9.416E-06	7.394	1.599	0.027	0.045	1.782
46509	H2CS	103040.447	9.891	1.484E-05	7.394	1.599	0.242	0.411	4.292
40502	CH3CCH	153817.215	36.911	1.233E-05	6.873	1.600	0.084	0.143	8.796
48010	SO+	254977.935	38.921	8.771E-05	7.382	1.600	0.020	0.034	4.539
32003	CH3OH	143169.517	112.709	4.128E-06	7.086	1.601	0.028	0.047	5.213
30002	HC-13-O+	86754.290	4.164	3.830E-05	7.230	1.601	0.979	1.668	13.972
40502	CH3CCH	153790.772	101.940	1.095E-05	7.210	1.601	0.022	0.038	6.506
36504	H2S-34	167910.516	27.825	2.636E-05	6.831	1.603	0.285	0.486	9.415
45010	HOCO+	149675.871	28.734	7.284E-05	7.082	1.605	0.039	0.066	7.527

Continued on next page

Table D.1 – continued from previous page

id	Species	Frequency (MHz)	E_{up} (K)	A_{ij} (s^{-1})	V_0 (km s^{-1})	FWHM (km s^{-1})	Intensity (K)	FitFlux (K km s^{-1})	rms (mK)
19002	HDO	225896.720	167.562	1.319E-05	7.361	1.606	0.023	0.040	8.195
33004	CH2DOH	269886.317	68.218	7.855E-05	6.416	1.608	0.020	0.035	6.354
64002	SO2	135696.020	15.663	2.208E-05	7.221	1.609	0.344	0.589	9.198
33004	CH2DOH	244841.135	37.592	4.821E-05	6.948	1.611	0.027	0.046	6.111
33004	CH2DOH	133872.705	31.207	9.009E-06	7.040	1.612	0.026	0.045	7.320
41001	CH3CN	202258.154	236.811	5.620E-04	7.016	1.612	0.032	0.055	9.812
61502	OC-13-S	254552.731	134.395	4.798E-05	7.289	1.614	0.018	0.031	3.002
60003	CH3OCHO	206719.916	95.261	1.279E-04	7.254	1.615	0.022	0.037	6.592
64002	SO2	235151.720	19.029	7.690E-05	6.964	1.616	0.113	0.194	9.241
56502	CCS	129548.446	42.903	9.896E-05	6.941	1.617	0.029	0.050	3.288
29005	NNH+	93171.880	4.472	3.627E-05	6.904	1.617	1.803	3.104	9.117
51001	HCCCN	100076.392	28.818	7.739E-05	6.931	1.619	0.218	0.375	6.104
46004	C2H5OH	205458.472	64.039	5.610E-05	7.063	1.623	0.022	0.038	6.255
48001	SO	158971.800	28.681	4.317E-05	7.111	1.624	1.207	2.086	17.166
62505	OCS-34	260991.808	144.059	5.177E-05	6.769	1.625	0.041	0.070	6.661
64002	SO2	158199.740	15.336	2.532E-05	6.993	1.626	0.090	0.155	4.360
32003	CH3OH	250635.200	230.829	8.241E-05	7.562	1.627	0.033	0.058	5.087
47504	HDCS	221177.103	51.453	1.574E-04	7.177	1.628	0.034	0.059	7.134
60003	CH3OCHO	155002.320	53.193	5.209E-05	7.156	1.629	0.014	0.025	3.859
33004	CH2DOH	268059.704	71.589	7.085E-05	6.989	1.632	0.030	0.053	6.657
48001	SO	219949.442	34.985	1.361E-04	7.201	1.632	1.627	2.827	36.505
32006	D2CO	231410.270	27.883	3.470E-04	7.088	1.634	0.206	0.358	10.157
44003	CH3CHO	95947.437	13.934	2.840E-05	7.176	1.634	0.051	0.088	2.810

Continued on next page

Table D.1 – continued from previous page

id	Species	Frequency (MHz)	E_{up} (K)	A_{ij} (s^{-1})	V_0 (km s^{-1})	FWHM (km s^{-1})	Intensity (K)	FitFlux (K km s^{-1})	rms (mK)
46004	C2H5OH	100990.102	35.173	6.229E-06	6.836	1.635	0.008	0.015	1.855
18004	NH2D	85924.783	20.679	2.346E-05	7.292	1.636	0.238	0.414	4.076
68001	CCCS	92488.490	37.730	5.787E-05	7.489	1.640	0.017	0.029	3.041
44003	CH3CHO	245168.591	72.197	6.240E-05	6.791	1.641	0.010	0.018	5.359
64002	SO2	255958.045	27.620	6.626E-05	6.867	1.642	0.021	0.037	5.223
26504	CN, v=0,1	113170.492	5.432	5.145E-06	7.028	1.642	0.452	0.791	18.590
61502	OC-13-S	206079.955	89.018	2.532E-05	6.859	1.643	0.022	0.038	7.084
32006	D2CO	166102.750	21.346	1.100E-04	6.962	1.644	0.109	0.191	6.046
18004	NH2D	85926.270	20.679	1.760E-05	9.222	1.645	0.276	0.483	3.701
33502	*C-13-H3OH, vt=0,1	235938.220	39.579	5.397E-05	7.002	1.647	0.041	0.072	10.661
44003	CH3CHO	76878.952	9.231	1.430E-05	7.361	1.650	0.038	0.066	2.774
30004	H2CO	218475.632	68.094	1.570E-04	6.970	1.650	0.387	0.680	12.554
49501	S-33-O	203936.815	38.307	8.962E-05	6.207	1.650	0.031	0.055	8.758
33004	CH2DOH	132489.637	29.201	8.644E-06	7.343	1.651	0.021	0.036	4.957
32003	CH3OH	241852.299	97.531	3.895E-05	7.035	1.651	0.017	0.030	8.066
47504	HDCS	92981.601	8.926	1.096E-05	7.320	1.651	0.087	0.153	2.781
44003	CH3CHO	223650.093	72.270	3.780E-04	6.893	1.652	0.042	0.074	7.288
46509	H2CS	103051.842	62.557	8.249E-06	7.173	1.654	0.010	0.017	1.889
40502	CH3CCH	256317.071	127.325	5.724E-05	6.757	1.655	0.020	0.036	3.960
38002	c-C3H2	150436.545	9.708	5.890E-05	6.811	1.655	0.047	0.083	6.582
45010	HOCO+	106913.563	15.393	2.586E-05	7.547	1.656	0.050	0.088	3.302
32003	CH3OH	247228.587	60.925	2.157E-05	7.221	1.657	0.014	0.025	5.582
49501	S-33-O	136939.357	15.728	2.655E-05	7.386	1.658	0.014	0.025	6.999

Continued on next page

Table D.1 – continued from previous page

id	Species	Frequency (MHz)	E_{up} (K)	A_{ij} (s^{-1})	V_0 (km s^{-1})	FWHM (km s^{-1})	Intensity (K)	FitFlux (K km s^{-1})	rms (mK)
41001	CH3CN	165413.015	389.527	1.516E-04	6.137	1.659	0.008	0.015	4.131
46008	CH3OCH3	146872.545	26.309	9.656E-06	7.254	1.659	0.019	0.033	5.277
40502	CH3CCH	273414.692	118.772	7.060E-05	6.675	1.660	0.028	0.049	8.815
60003	CH3OCHO	98279.762	45.133	6.057E-06	6.957	1.668	0.009	0.015	2.543
32003	CH3OH	96493.551	307.525	3.384E-06	6.489	1.668	0.009	0.016	2.513
33004	CH2DOH	166063.164	33.007	2.396E-05	6.370	1.670	0.023	0.040	5.067
44003	CH3CHO	250673.674	140.573	4.580E-04	6.979	1.672	0.020	0.035	5.489
46010	NS	207834.866	27.745	1.522E-04	7.198	1.672	0.058	0.103	6.750
64002	SO2	146605.520	19.029	2.469E-05	6.968	1.672	0.092	0.163	7.520
18004	NH2D	110152.096	21.259	1.651E-05	7.289	1.673	0.082	0.146	10.188
44003	CH3CHO	96425.614	22.911	2.410E-05	7.237	1.673	0.019	0.033	2.464
45010	HOCO+	128295.063	21.550	4.538E-05	7.099	1.674	0.034	0.060	4.231
38002	c-C3H2	84727.696	16.135	1.146E-05	7.149	1.674	0.013	0.023	3.198
43002	HNCO	131885.734	22.154	3.163E-05	7.092	1.675	0.141	0.251	7.709
33004	CH2DOH	223107.081	50.481	4.378E-05	6.985	1.676	0.020	0.036	8.922
32006	D2CO	245532.880	34.884	3.900E-04	7.030	1.677	0.075	0.134	5.403
33502	*C-13-H3OH, vt=0,1	255120.837	84.029	7.246E-05	6.928	1.677	0.014	0.025	2.284
40502	CH3CCH	170876.410	110.141	1.546E-05	6.928	1.677	0.039	0.069	10.890
40502	CH3CCH	256331.739	105.650	5.803E-05	6.715	1.678	0.042	0.075	7.268
32003	CH3OH	155320.895	140.603	1.550E-05	6.880	1.679	0.016	0.028	6.356
36503	D2S	91359.120	14.393	4.240E-06	7.095	1.682	0.022	0.040	2.509
41001	CH3CN	165489.391	218.280	2.657E-04	6.925	1.683	0.023	0.042	4.926
45005	HCS+	213360.530	30.720	2.354E-04	6.943	1.684	0.092	0.165	7.973

Continued on next page

Table D.1 – continued from previous page

id	Species	Frequency (MHz)	E_{up} (K)	A_{ij} (s^{-1})	V_0 (km s^{-1})	FWHM (km s^{-1})	Intensity (K)	FitFlux (K km s^{-1})	rms (mK)
33004	CH2DOH	221273.004	54.738	4.199E-05	6.644	1.685	0.029	0.051	8.938
46509	H2CS	171688.117	24.723	7.281E-05	6.999	1.685	0.138	0.248	12.902
29004	HCO	86670.760	4.178	4.690E-06	7.610	1.687	0.048	0.086	3.323
46509	H2CS	135298.261	29.404	3.267E-05	7.082	1.687	0.327	0.587	9.402
46509	H2CS	137371.210	16.484	3.647E-05	7.452	1.688	0.198	0.355	5.935
50002	SO-18	93267.270	8.716	9.525E-06	7.042	1.689	0.068	0.122	2.907
46005	HCOOH	252078.606	84.715	1.680E-04	6.989	1.689	0.011	0.019	4.812
44003	CH3CHO	130892.749	27.491	7.270E-05	6.879	1.691	0.091	0.163	8.547
44003	CH3CHO	154274.686	53.689	1.050E-04	6.307	1.695	0.025	0.046	6.656
49501	S-33-O	127856.548	25.407	3.120E-06	6.437	1.695	0.036	0.065	5.022
44003	CH3CHO	77125.695	18.396	1.080E-05	7.283	1.695	0.011	0.020	2.597
28002	HC-13-N	172680.210	12.431	8.900E-05	6.594	1.696	0.093	0.168	5.360
40502	CH3CCH	102530.348	82.258	2.669E-06	6.921	1.697	0.011	0.020	2.587
60003	CH3OCHO	163961.884	64.504	6.535E-05	7.721	1.697	0.021	0.039	5.790
18004	NH2D	85927.735	20.679	7.822E-06	7.234	1.698	0.247	0.447	3.373
46010	NS	207838.365	27.742	1.446E-04	7.181	1.699	0.073	0.132	6.555
50001	S-34-O	201846.573	38.057	9.660E-05	7.124	1.700	0.040	0.073	8.651
46509	H2CS	240549.066	98.834	1.888E-04	7.137	1.700	0.030	0.054	6.403
49501	S-33-O	136946.194	15.732	3.083E-05	7.533	1.702	0.030	0.055	6.810
46008	CH3OCH3	153054.441	40.395	1.735E-05	6.461	1.703	0.033	0.059	8.141
32003	CH3OH	218440.063	45.460	4.686E-05	7.120	1.704	0.312	0.566	10.265
26504	CN, v=0,1	113508.907	5.448	5.190E-06	7.071	1.704	0.469	0.850	23.946
32004	H2CO-18	138770.900	9.991	6.761E-05	7.390	1.706	0.016	0.028	6.568

Continued on next page

Table D.1 – continued from previous page

id	Species	Frequency (MHz)	E_{up} (K)	A_{ij} (s^{-1})	V_0 (km s^{-1})	FWHM (km s^{-1})	Intensity (K)	FitFlux (K km s^{-1})	rms (mK)
64002	SO2	241615.798	23.589	8.455E-05	7.093	1.709	0.095	0.173	5.845
32006	D2CO	110837.830	13.374	2.580E-05	7.442	1.710	0.077	0.140	9.387
28005	HNC-13	87090.850	4.180	1.870E-05	7.420	1.712	0.371	0.677	5.779
33502	*C-13-H3OH, vt=0,1	215886.963	45.011	4.528E-05	7.187	1.713	0.021	0.038	6.814
45005	HCS+	170691.723	20.480	1.178E-04	7.190	1.714	0.078	0.142	9.745
60003	CH3OCHO	163960.387	64.522	6.534E-05	6.603	1.715	0.021	0.038	6.008
40502	CH3CCH	239211.215	151.143	4.510E-05	6.737	1.716	0.017	0.031	7.093
18004	NH2D	85926.270	20.679	1.760E-05	7.147	1.717	0.889	1.624	3.701
46010	NS	207436.246	27.647	1.438E-04	7.189	1.717	0.089	0.163	6.360
60003	CH3OCHO	110788.664	30.274	1.972E-05	6.251	1.718	0.026	0.048	8.797
30001	CO-18	109782.170	5.269	6.270E-08	7.296	1.719	1.072	1.960	40.632
43002	HNCO	109905.601	15.824	8.902E-09	6.877	1.723	0.171	0.313	10.032
60003	CH3OCHO	107537.258	28.770	1.722E-05	7.008	1.723	0.016	0.028	2.192
66002	S-34-O2	102031.878	7.642	9.495E-06	7.381	1.723	0.020	0.038	2.263
60003	CH3OCHO	238161.536	40.436	2.644E-05	7.514	1.725	0.015	0.027	5.858
39003	c-C3HD	104187.108	10.849	4.333E-05	6.957	1.725	0.024	0.044	2.318
49003	C4H	95150.391	25.112	3.848E-06	6.916	1.727	0.010	0.019	2.613
47504	HDCS	91171.067	17.735	9.188E-06	7.306	1.727	0.042	0.077	2.880
44003	CH3CHO	270145.407	133.355	6.200E-04	6.513	1.727	0.022	0.040	5.863
32003	CH3OH	145093.754	27.053	1.231E-05	6.787	1.728	0.323	0.594	44.030
60003	CH3OCHO	129296.357	36.448	3.059E-05	7.187	1.729	0.019	0.035	3.689
60003	CH3OCHO	147397.073	99.778	2.085E-05	7.560	1.732	0.015	0.027	4.339
60003	CH3OCHO	142735.139	49.276	4.283E-05	6.772	1.733	0.013	0.024	6.335

Continued on next page

Table D.1 – continued from previous page

id	Species	Frequency (MHz)	E_{up} (K)	A_{ij} (s^{-1})	V_0 (km s^{-1})	FWHM (km s^{-1})	Intensity (K)	FitFlux (K km s^{-1})	rms (mK)
44003	CH3CHO	231456.744	108.353	3.750E-04	7.102	1.734	0.028	0.051	10.027
45010	HOCO+	171055.968	36.943	1.097E-04	6.682	1.737	0.034	0.062	11.568
51001	HCCCN	109173.634	34.057	1.008E-04	7.041	1.737	0.192	0.355	9.563
60003	CH3OCHO	203853.774	95.562	1.222E-04	6.818	1.737	0.036	0.067	8.202
44003	CH3CHO	250829.159	120.329	4.880E-04	6.603	1.740	0.026	0.048	5.321
46509	H2CS	104617.027	23.212	1.381E-05	7.327	1.740	0.301	0.557	7.412
32003	CH3OH	136915.288	451.937	4.448E-06	7.209	1.741	0.019	0.035	5.464
32004	H2CO-18	214778.490	32.485	2.387E-04	7.372	1.742	0.022	0.042	7.563
45005	HCS+	85347.900	6.144	1.326E-05	7.559	1.745	0.072	0.134	2.984
60003	CH3OCHO	153397.844	56.651	5.335E-05	6.958	1.746	0.018	0.034	7.938
44003	CH3CHO	96384.409	34.161	1.850E-05	6.931	1.748	0.010	0.019	3.002
51001	HCCCN	90979.023	24.015	5.788E-05	7.013	1.750	0.236	0.439	8.921
42501	H2CCO	202014.311	53.333	9.240E-05	6.880	1.754	0.048	0.090	8.946
46010	NS	253970.581	39.930	2.745E-04	6.915	1.754	0.038	0.071	4.334
32003	CH3OH	96741.371	6.965	3.408E-06	7.181	1.756	1.105	2.066	39.568
45005	HCS+	128020.670	12.288	4.795E-05	7.478	1.756	0.066	0.124	5.154
45010	HOCO+	213813.385	56.440	2.167E-04	7.015	1.756	0.018	0.033	7.122
32003	CH3OH	241791.352	34.817	6.047E-05	7.015	1.763	0.774	1.452	16.158
32003	CH3OH	254419.419	289.225	1.789E-05	6.362	1.763	0.016	0.030	2.630
40502	CH3CCH	222128.815	139.663	3.573E-05	6.705	1.764	0.043	0.081	6.982
32003	CH3OH	145126.191	36.172	6.772E-06	6.860	1.764	0.148	0.278	49.165
44003	CH3CHO	214800.824	70.596	3.240E-04	7.039	1.765	0.036	0.068	7.673
32003	CH3OH	165050.175	23.368	2.349E-05	6.998	1.767	0.137	0.258	6.422

Continued on next page

Table D.1 – continued from previous page

id	Species	Frequency (MHz)	E_{up} (K)	A_{ij} (s^{-1})	V_0 (km s^{-1})	FWHM (km s^{-1})	Intensity (K)	FitFlux (K km s^{-1})	rms (mK)
31002	H2C-13-O	141983.740	10.223	7.246E-05	7.044	1.768	0.083	0.157	5.780
50002	SO-18	166285.240	22.891	5.782E-05	7.038	1.768	0.037	0.070	6.301
44003	CH3CHO	211243.043	69.990	3.090E-04	7.349	1.770	0.035	0.067	6.613
33004	CH2DOH	225878.232	35.623	3.230E-05	7.088	1.770	0.027	0.051	8.542
29503	CO-17	112360.007	5.392	6.697E-08	7.033	1.772	0.131	0.246	6.686
62505	OCS-34	130515.730	37.584	6.334E-06	7.016	1.774	0.023	0.044	5.760
28006	HN-15-C	88865.720	4.265	1.980E-05	7.310	1.774	0.076	0.143	2.324
38002	c-C3H2	85656.431	29.069	1.673E-05	6.767	1.775	0.021	0.041	2.703
50001	S-34-O	126613.930	25.310	2.163E-05	6.991	1.776	0.043	0.082	4.575
31002	H2C-13-O	137449.950	21.723	4.930E-05	7.150	1.777	0.137	0.260	5.177
44003	CH3CHO	93595.235	15.822	2.530E-05	7.089	1.781	0.040	0.077	2.172
60003	CH3OCHO	76701.827	15.357	5.738E-06	7.075	1.782	0.011	0.020	2.719
42501	H2CCO	101981.429	27.735	1.089E-05	7.107	1.783	0.062	0.117	3.005
33004	CH2DOH	253077.615	95.473	2.653E-05	6.458	1.784	0.016	0.030	3.760
44003	CH3CHO	154201.472	69.484	9.180E-05	6.760	1.784	0.027	0.052	5.276
60003	CH3OCHO	88843.187	17.957	9.817E-06	7.071	1.784	0.013	0.024	1.720
48507	D2CS	85153.920	8.175	8.476E-06	7.302	1.786	0.069	0.132	3.110
60003	CH3OCHO	218280.900	99.730	1.508E-04	6.775	1.787	0.033	0.063	6.858
64002	SO2	200809.180	130.665	4.695E-05	6.396	1.787	0.033	0.063	10.023
40502	CH3CCH	222166.971	74.640	3.777E-05	6.852	1.791	0.103	0.197	6.859
32003	CH3OH	213377.528	389.918	1.066E-05	6.576	1.792	0.024	0.046	8.032
48510	CH3SH,v=0-2	126403.806	19.628	1.844E-05	7.483	1.793	0.015	0.029	5.083
60003	CH3OCHO	164968.638	58.519	6.460E-05	6.494	1.793	0.020	0.038	6.633

Continued on next page

Table D.1 – continued from previous page

id	Species	Frequency (MHz)	E_{up} (K)	A_{ij} (s^{-1})	V_0 (km s^{-1})	FWHM (km s^{-1})	Intensity (K)	FitFlux (K km s^{-1})	rms (mK)
32003	CH3OH	96744.545	20.090	3.407E-06	6.867	1.793	0.218	0.417	20.707
32003	CH3OH	145103.185	13.928	1.232E-05	7.031	1.794	1.167	2.229	44.635
28002	HC-13-N	172676.570	12.431	5.340E-05	6.391	1.795	0.123	0.234	14.650
45001	C-13-S	92494.308	6.659	1.421E-05	7.251	1.798	0.188	0.359	4.732
45003	NH2CHO	127393.710	48.213	1.053E-04	7.509	1.798	0.010	0.019	4.468
44003	CH3CHO	251363.729	104.674	5.070E-04	7.055	1.801	0.040	0.077	5.597
56502	CCS	126840.481	39.669	9.233E-05	7.009	1.801	0.029	0.056	4.762
44003	CH3CHO	98863.314	16.589	2.990E-05	6.999	1.804	0.052	0.100	2.298
33004	CH2DOH	138455.879	25.002	8.686E-06	7.098	1.804	0.018	0.035	6.235
32003	CH3OH	213427.061	23.367	3.370E-05	7.113	1.804	0.151	0.290	7.049
46001	CS-34	96412.940	6.941	1.610E-05	7.084	1.804	0.491	0.943	9.044
32003	CH3OH	169335.219	148.730	2.280E-05	7.359	1.804	0.017	0.034	7.389
46005	HCOOH	89579.172	10.762	7.242E-06	7.242	1.805	0.015	0.029	2.329
32003	CH3OH	170060.592	36.173	2.552E-05	6.872	1.808	0.416	0.801	11.878
32003	CH3OH	241767.234	40.391	5.806E-05	7.013	1.808	0.666	1.282	13.959
28007	DNC	76305.727	3.662	1.604E-05	7.180	1.811	0.924	1.781	4.485
33502	*C-13-H3OH, vt=0,1	255203.728	72.702	6.345E-05	7.081	1.812	0.009	0.017	2.445
44003	CH3CHO	230301.923	81.043	4.040E-04	6.966	1.813	0.027	0.052	8.958
29004	HCO	86708.360	4.161	4.600E-06	7.541	1.813	0.043	0.083	3.060
44003	CH3CHO	79099.313	11.844	1.460E-05	7.044	1.813	0.038	0.128	3.157
50001	S-34-O	106742.920	20.907	1.027E-05	6.189	1.815	0.052	0.100	3.216
27001	HCN	88630.416	4.254	2.427E-05	6.309	1.817	1.876	3.628	93.520
28003	HCN-15	86054.961	4.130	2.203E-05	7.010	1.818	0.089	0.172	3.021

Continued on next page

Table D.1 – continued from previous page

id	Species	Frequency (MHz)	E_{up} (K)	A_{ij} (s^{-1})	V_0 (km s^{-1})	FWHM (km s^{-1})	Intensity (K)	FitFlux (K km s^{-1})	rms (mK)
33004	CH2DOH	89275.302	19.897	2.452E-06	6.911	1.820	0.010	0.019	2.111
44003	CH3CHO	270177.716	133.358	6.200E-04	6.458	1.822	0.014	0.027	5.922
32003	CH3OH	103381.258	207.078	3.985E-07	7.301	1.823	0.011	0.020	2.016
60003	CH3OCHO	205495.754	98.969	1.275E-04	6.914	1.825	0.024	0.046	6.575
60003	CH3OCHO	148516.039	62.731	4.026E-05	6.445	1.825	0.019	0.036	6.803
48001	SO	136634.799	50.661	1.784E-06	7.412	1.828	0.022	0.043	6.257
46008	CH3OCH3	204552.564	55.267	1.913E-05	6.856	1.828	0.044	0.086	7.196
33004	CH2DOH	90779.841	10.596	1.573E-06	6.591	1.829	0.022	0.042	2.425
42501	H2CCO	202095.367	105.535	8.882E-05	7.154	1.830	0.031	0.060	8.420
32003	CH3OH	261805.675	28.011	5.573E-05	6.736	1.832	0.168	0.327	8.717
62505	OCS-34	142379.430	44.417	8.253E-06	7.147	1.832	0.024	0.047	5.751
33004	CH2DOH	241852.554	115.282	1.318E-05	7.341	1.832	0.019	0.037	8.433
46005	HCOOH	231505.705	64.467	1.326E-04	6.426	1.833	0.023	0.046	7.736
44003	CH3CHO	96274.252	22.934	2.410E-05	7.031	1.834	0.028	0.055	2.566
44003	CH3CHO	214845.041	70.573	3.250E-04	7.157	1.834	0.035	0.068	6.928
26504	CN, v=0,1	113123.370	5.430	1.286E-06	7.376	1.838	0.107	0.210	9.333
40502	CH3CCH	170905.783	45.113	1.700E-05	6.772	1.838	0.101	0.198	11.169
33004	CH2DOH	223315.468	58.724	3.812E-05	6.945	1.838	0.022	0.044	7.058
44003	CH3CHO	250680.123	140.542	4.580E-04	6.734	1.842	0.018	0.035	4.998
31003	HDCO	134284.830	17.628	4.587E-05	6.854	1.843	0.411	0.806	9.139
32003	CH3OH	165190.475	44.263	2.321E-05	6.978	1.843	0.144	0.283	7.086
44003	CH3CHO	270187.741	133.295	6.190E-04	7.137	1.843	0.014	0.027	5.866
44003	CH3CHO	149505.128	34.666	1.100E-04	6.898	1.845	0.070	0.138	8.721

Continued on next page

Table D.1 – continued from previous page

id	Species	Frequency (MHz)	E_{up} (K)	A_{ij} (s^{-1})	V_0 (km s^{-1})	FWHM (km s^{-1})	Intensity (K)	FitFlux (K km s^{-1})	rms (mK)
50001	S-34-O	215839.436	34.384	1.287E-04	6.509	1.845	0.125	0.246	7.736
32003	CH3OH	241879.025	55.871	5.961E-05	7.043	1.846	0.117	0.229	5.913
42501	H2CCO	101036.630	14.548	1.104E-05	7.242	1.846	0.035	0.069	2.597
46008	CH3OCH3	265150.830	65.449	5.452E-05	6.212	1.846	0.014	0.027	5.841
37003	c-C3H	91699.471	4.405	1.374E-05	6.862	1.847	0.010	0.021	2.445
56502	CCS	131551.962	37.016	1.049E-04	7.071	1.849	0.058	0.114	6.041
41001	CH3CN	239119.504	108.919	1.151E-03	6.795	1.849	0.031	0.061	8.131
32003	CH3OH	241700.159	47.935	6.037E-05	6.960	1.850	0.213	0.420	7.067
33004	CH2DOH	91586.845	25.841	5.285E-06	6.581	1.851	0.025	0.050	2.819
40502	CH3CCH	102546.024	24.452	3.461E-06	6.913	1.852	0.059	0.116	3.997
52005	DCCCN	101314.830	31.606	8.059E-05	6.804	1.853	0.007	0.013	2.227
33004	CH2DOH	214300.665	39.773	1.711E-05	5.824	1.854	0.022	0.044	6.076
31003	HDCO	258071.000	102.608	2.111E-04	6.714	1.855	0.033	0.065	6.784
33004	CH2DOH	267778.995	100.289	5.946E-05	6.261	1.858	0.024	0.047	6.780
33004	CH2DOH	128656.035	6.175	1.027E-05	6.787	1.858	0.040	0.079	4.871
45010	HOCO+	85531.512	10.262	1.295E-05	7.494	1.858	0.041	0.081	2.931
33004	CH2DOH	214701.730	16.741	4.111E-05	7.094	1.863	0.059	0.118	8.167
48510	CH3SH,v=0-2	75816.443	11.841	3.333E-06	6.918	1.863	0.010	0.020	3.384
46008	CH3OCH3	143020.764	11.083	1.087E-05	7.458	1.866	0.018	0.036	5.240
32003	CH3OH	233795.666	446.583	2.196E-05	6.721	1.866	0.027	0.053	7.778
49003	C4H	95188.948	25.131	3.829E-06	7.108	1.867	0.012	0.025	2.215
32003	CH3OH	157270.832	15.447	2.206E-05	7.082	1.868	0.385	0.765	17.334
32003	CH3OH	165061.130	28.011	2.343E-05	6.907	1.868	0.157	0.312	7.513

Continued on next page

Table D.1 – continued from previous page

id	Species	Frequency (MHz)	E_{up} (K)	A_{ij} (s^{-1})	V_0 (km s^{-1})	FWHM (km s^{-1})	Intensity (K)	FitFlux (K km s^{-1})	rms (mK)
33004	CH2DOH	265509.198	67.481	7.461E-05	6.707	1.869	0.027	0.054	5.216
44003	CH3CHO	231595.273	92.580	3.960E-04	7.200	1.869	0.047	0.094	9.079
64002	SO2	151378.630	12.585	1.875E-05	7.042	1.869	0.079	0.157	6.040
44003	CH3CHO	212498.646	81.493	3.010E-04	6.312	1.869	0.036	0.071	10.095
33004	CH2DOH	89407.817	6.437	2.021E-06	6.704	1.873	0.054	0.108	2.655
33004	CH2DOH	267634.613	45.002	6.260E-05	6.853	1.874	0.037	0.074	7.757
44003	CH3CHO	234825.872	81.843	4.280E-04	7.041	1.875	0.036	0.073	9.410
45511	PN	140967.690	13.531	1.050E-04	7.007	1.876	0.019	0.038	4.611
36504	H2S-34	214376.924	83.805	4.736E-05	7.045	1.877	0.050	0.101	6.990
60003	CH3OCHO	161458.217	70.492	5.350E-05	6.672	1.879	0.021	0.042	7.217
60003	CH3OCHO	168495.069	61.292	6.780E-05	7.299	1.880	0.028	0.056	8.286
51001	HCCCN	245606.308	165.035	1.174E-03	6.158	1.880	0.011	0.023	5.176
44003	CH3CHO	231748.719	92.511	3.940E-04	6.484	1.881	0.029	0.059	10.490
32003	CH3OH	165099.240	34.977	2.333E-05	6.890	1.881	0.152	0.305	8.751
60001	OCS	97301.209	21.014	2.580E-06	7.229	1.882	0.175	0.350	4.775
33502	*C-13-H3OH, vt=0,1	93619.460	21.295	2.320E-06	7.364	1.883	0.008	0.017	2.115
46005	HCOOH	129671.750	24.981	2.219E-05	7.261	1.883	0.012	0.024	3.299
48510	CH3SH,v=0-2	101284.348	18.333	8.694E-06	7.288	1.884	0.016	0.032	2.316
33004	CH2DOH	224928.016	55.265	4.417E-05	6.841	1.884	0.031	0.063	8.619
41001	CH3CN	147103.738	210.337	1.634E-04	6.900	1.886	0.020	0.040	4.161
32003	CH3OH	251984.837	133.361	7.994E-05	6.707	1.886	0.026	0.052	5.549
40502	CH3CCH	102547.984	17.226	3.560E-06	6.956	1.887	0.071	0.143	4.079
44003	CH3CHO	212128.388	97.245	2.810E-04	7.216	1.892	0.027	0.055	6.856

Continued on next page

Table D.1 – continued from previous page

id	Species	Frequency (MHz)	E_{up} (K)	A_{ij} (s^{-1})	V_0 (km s^{-1})	FWHM (km s^{-1})	Intensity (K)	FitFlux (K km s^{-1})	rms (mK)
60003	CH3OCHO	141652.995	43.246	4.057E-05	7.135	1.894	0.025	0.051	5.205
33004	CH2DOH	269059.272	61.312	6.696E-05	6.477	1.894	0.020	0.040	5.601
32003	CH3OH	157178.987	47.936	2.038E-05	6.991	1.895	0.126	0.254	6.363
32003	CH3OH	108893.945	13.125	1.471E-05	7.007	1.896	0.222	0.449	6.848
60003	CH3OCHO	90227.659	20.080	1.051E-05	7.094	1.896	0.017	0.034	2.732
30004	H2CO	216568.651	173.990	7.216E-06	6.508	1.896	0.045	0.090	7.523
44003	CH3CHO	242118.136	83.817	4.810E-04	6.652	1.897	0.028	0.056	5.970
32003	CH3OH	93196.672	302.894	4.194E-06	7.023	1.897	0.008	0.016	2.465
41001	CH3CN	147072.602	288.847	1.172E-04	6.793	1.897	0.016	0.033	4.370
50001	S-34-O	253208.020	55.691	2.037E-04	7.938	1.898	0.019	0.037	5.078
33004	CH2DOH	225667.710	48.985	4.434E-05	7.254	1.901	0.040	0.081	8.545
29503	CO-17	224714.187	16.177	3.916E-07	6.684	1.902	0.769	1.557	23.824
32006	D2CO	233650.700	49.626	2.690E-04	7.222	1.904	0.072	0.145	8.315
32003	CH3OH	247161.950	338.141	2.572E-05	6.897	1.907	0.023	0.046	6.057
25001	CCH	262064.843	25.159	5.275E-05	6.619	1.907	0.102	0.206	12.032
32003	CH3OH	217299.205	373.927	4.292E-05	6.456	1.908	0.028	0.056	7.248
44003	CH3CHO	270415.845	117.540	6.370E-04	6.563	1.908	0.019	0.038	6.245
33004	CH2DOH	105036.951	65.015	7.217E-06	6.682	1.910	0.026	0.052	3.476
33502	*C-13-H3OH, vt=0,1	255265.637	131.595	8.304E-05	7.127	1.910	0.014	0.029	3.261
37002	C3H	76199.925	7.834	2.019E-05	6.831	1.912	0.009	0.019	2.987
32003	CH3OH	241904.147	60.725	5.093E-05	6.543	1.913	0.186	0.379	7.012
66002	S-34-O2	229857.630	18.673	7.141E-05	7.379	1.913	0.026	0.054	8.989
61502	OC-13-S	133355.416	38.401	6.756E-06	7.214	1.913	0.021	0.043	5.523

Continued on next page

Table D.1 – continued from previous page

id	Species	Frequency (MHz)	E_{up} (K)	A_{ij} (s^{-1})	V_0 (km s^{-1})	FWHM (km s^{-1})	Intensity (K)	FitFlux (K km s^{-1})	rms (mK)
60003	CH3OCHO	141260.421	45.754	3.874E-05	6.944	1.914	0.015	0.031	3.894
60003	CH3OCHO	163987.455	64.521	6.538E-05	6.706	1.915	0.020	0.042	5.844
41001	CH3CN	110364.354	82.842	8.330E-05	6.934	1.916	0.037	0.075	9.327
33004	CH2DOH	221683.458	48.231	2.976E-05	7.338	1.916	0.027	0.055	7.443
33502	*C-13-H3OH, vt=0,1	135113.796	101.896	1.255E-05	6.846	1.920	0.017	0.034	5.159
42501	H2CCO	222228.618	116.191	1.195E-04	6.780	1.921	0.017	0.034	6.468
46008	CH3OCH3	145682.643	26.310	1.006E-05	6.541	1.921	0.016	0.032	4.849
44003	CH3CHO	93580.909	15.747	2.530E-05	6.995	1.922	0.046	0.094	2.118
62505	OCS-34	225413.638	108.189	3.324E-05	6.722	1.926	0.032	0.066	7.182
33004	CH2DOH	258337.113	37.590	7.000E-05	6.673	1.927	0.029	0.059	3.891
31502	C-13-O-18	104711.404	5.025	5.454E-08	7.179	1.927	0.018	0.037	2.978
47504	HDCS	126429.120	24.154	2.680E-05	7.142	1.930	0.037	0.077	5.285
42501	H2CCO	141438.067	27.154	3.108E-05	6.863	1.930	0.034	0.069	6.114
44003	CH3CHO	211273.792	70.003	3.090E-04	7.013	1.930	0.038	0.077	7.053
33502	*C-13-H3OH, vt=0,1	156379.367	19.906	2.146E-05	7.301	1.930	0.025	0.052	4.880
32003	CH3OH	251164.108	177.456	8.161E-05	6.724	1.931	0.020	0.040	5.279
62505	OCS-34	249133.029	131.533	4.498E-05	7.032	1.932	0.031	0.065	5.556
49501	S-33-O	98493.642	9.160	1.099E-05	7.527	1.932	0.039	0.080	2.193
48508	H2CS-34	101284.314	9.722	1.409E-05	7.164	1.932	0.016	0.033	2.321
60003	CH3OCHO	132105.508	42.444	3.381E-05	7.046	1.933	0.016	0.034	6.417
38002	c-C3H2	82966.200	16.049	1.091E-05	6.753	1.933	0.053	0.109	6.121
46008	CH3OCH3	212756.195	69.520	5.399E-05	7.306	1.933	0.028	0.058	8.558
60001	OCS	85139.121	16.344	1.714E-06	7.222	1.935	0.172	0.354	4.716

Continued on next page

Table D.1 – continued from previous page

id	Species	Frequency (MHz)	E_{up} (K)	A_{ij} (s^{-1})	V_0 (km s^{-1})	FWHM (km s^{-1})	Intensity (K)	FitFlux (K km s^{-1})	rms (mK)
40502	CH3CCH	256292.630	163.443	5.593E-05	6.626	1.935	0.017	0.034	4.046
47504	HDCS	94828.488	18.086	1.034E-05	7.282	1.939	0.039	0.080	2.508
42501	H2CCO	242398.451	193.008	1.509E-04	6.827	1.940	0.026	0.054	6.501
48001	SO	246404.687	21.051	1.027E-06	7.519	1.940	0.025	0.051	5.277
44003	CH3CHO	226592.725	71.305	3.940E-04	6.917	1.940	0.038	0.079	7.642
42501	H2CCO	260191.982	100.473	1.984E-04	6.321	1.942	0.027	0.056	5.092
32003	CH3OH	104300.337	158.637	1.960E-06	6.811	1.942	0.023	0.049	2.106
56502	CCS	142501.695	49.742	1.325E-04	7.046	1.942	0.027	0.055	5.423
60003	CH3OCHO	132928.736	40.379	3.364E-05	7.254	1.942	0.022	0.045	5.507
32003	CH3OH	146368.328	28.589	1.125E-05	6.678	1.943	0.171	0.353	7.480
33502	*C-13-H3OH, vt=0,1	255214.891	113.475	8.087E-05	7.265	1.943	0.010	0.021	4.019
42501	H2CCO	244712.269	89.398	1.644E-04	6.591	1.944	0.052	0.108	6.713
33004	CH2DOH	223153.515	87.438	2.892E-05	6.111	1.950	0.024	0.050	7.703
47504	HDCS	151927.543	30.860	4.869E-05	6.957	1.950	0.041	0.086	6.936
56502	CCS	93870.107	19.892	3.744E-05	7.417	1.952	0.120	0.249	7.037
44003	CH3CHO	77038.601	18.314	1.080E-05	6.993	1.953	0.016	0.033	2.696
41001	CH3CN	257349.179	349.721	1.202E-03	6.652	1.956	0.018	0.038	6.089
56502	CCS	86181.391	23.345	2.778E-05	7.262	1.956	0.048	0.100	2.941
50001	S-34-O	246663.638	49.895	1.845E-04	7.109	1.957	0.025	0.052	5.388
45511	PN	93979.770	6.766	2.920E-05	7.277	1.958	0.015	0.032	2.862
38002	c-C3H2	85338.893	6.445	2.553E-05	7.224	1.959	0.325	0.678	6.674
44003	CH3CHO	242106.020	83.889	4.810E-04	6.720	1.959	0.029	0.061	5.698
32003	CH3OH	168577.831	44.263	4.381E-06	6.878	1.961	0.039	0.082	8.108

Continued on next page

Table D.1 – continued from previous page

id	Species	Frequency (MHz)	E_{up} (K)	A_{ij} (s^{-1})	V_0 (km s^{-1})	FWHM (km s^{-1})	Intensity (K)	FitFlux (K km s^{-1})	rms (mK)
33502	*C-13-H3OH, vt=0,1	263113.343	56.339	7.428E-05	6.137	1.962	0.023	0.049	9.197
30004	H2CO	72409.090	65.928	8.010E-07	6.994	1.964	0.037	0.077	3.573
60003	CH3OCHO	137313.330	49.797	3.327E-05	7.214	1.965	0.013	0.028	4.385
32003	CH3OH	268743.954	228.444	1.763E-05	6.776	1.965	0.019	0.041	3.164
68001	CCCS	104048.454	47.440	8.267E-05	7.040	1.968	0.014	0.030	2.148
30004	H2CO	101332.991	87.565	1.570E-06	6.876	1.968	0.027	0.057	2.486
32003	CH3OH	89505.853	171.459	7.639E-07	6.665	1.968	0.011	0.024	2.305
29507	HCO+, v=0	267557.630	25.682	1.450E-03	5.130	1.970	1.002	2.101	160.909
44003	CH3CHO	154296.489	53.694	1.050E-04	6.905	1.971	0.023	0.047	6.117
32003	CH3OH	157246.062	36.335	2.099E-05	6.900	1.973	0.151	0.317	6.982
48001	SO	100029.640	38.576	1.104E-06	7.402	1.974	0.048	0.101	3.057
32003	CH3OH	249192.836	378.278	2.537E-05	6.700	1.975	0.022	0.047	5.155
33004	CH2DOH	132093.628	16.741	6.150E-06	6.740	1.976	0.040	0.084	6.015
33004	CH2DOH	267031.234	58.385	7.540E-05	6.481	1.977	0.025	0.053	4.988
47504	HDCS	212648.357	49.815	1.399E-04	7.145	1.978	0.027	0.057	8.591
41001	CH3CN	110374.989	47.122	9.875E-05	7.383	1.980	0.026	0.054	9.618
40502	CH3CCH	222162.730	81.866	3.754E-05	6.843	1.984	0.077	0.162	7.785
60003	CH3OCHO	164955.703	58.532	6.457E-05	7.412	1.987	0.022	0.046	6.585
33004	CH2DOH	133847.377	26.321	8.849E-06	7.394	1.987	0.025	0.053	6.098
44003	CH3CHO	212171.487	97.142	2.810E-04	6.586	1.988	0.024	0.050	7.125
62505	OCS-34	213553.061	97.371	2.822E-05	7.177	1.989	0.024	0.052	6.327
32003	CH3OH	243915.788	49.660	5.966E-05	7.004	1.990	0.143	0.303	6.646
33004	CH2DOH	253629.097	22.574	4.870E-05	6.587	1.990	0.020	0.042	2.516

Continued on next page

Table D.1 – continued from previous page

id	Species	Frequency (MHz)	E_{up} (K)	A_{ij} (s^{-1})	V_0 (km s^{-1})	FWHM (km s^{-1})	Intensity (K)	FitFlux (K km s^{-1})	rms (mK)
25001	CCH	87407.165	4.197	1.658E-06	7.542	1.991	0.090	0.190	6.624
56502	CCS	99866.521	28.138	4.404E-05	7.367	1.992	0.039	0.083	2.708
41001	CH3CN	73588.799	15.975	2.972E-05	6.776	1.995	0.024	0.050	3.945
30009	NND+	77107.860	3.701	2.057E-05	7.469	1.999	0.266	0.565	4.923
28002	HC-13-N	86338.770	4.144	2.220E-05	7.007	2.002	0.192	0.409	15.983
28002	HC-13-N	86342.270	4.144	2.220E-05	7.371	2.002	0.091	0.193	4.291
29501	C-13-O	110201.350	5.289	6.330E-08	6.874	2.002	1.846	3.934	85.696
44006	DNCO	81571.696	9.787	9.190E-09	7.072	2.002	0.016	0.035	4.833
60003	CH3OCHO	164205.978	64.918	5.977E-05	6.893	2.002	0.020	0.042	6.679
37003	c-C3H	91494.349	4.391	1.588E-05	7.031	2.003	0.019	0.040	2.705
44003	CH3CHO	155342.088	42.504	1.170E-04	6.819	2.003	0.043	0.092	5.859
45002	Si-29-O	85759.000	6.174	2.820E-05	7.132	2.005	0.017	0.035	4.325
44003	CH3CHO	98900.944	16.513	2.990E-05	6.978	2.007	0.047	0.101	2.530
32003	CH3OH	241887.674	72.534	5.119E-05	7.328	2.008	0.040	0.086	17.516
44003	CH3CHO	167980.548	27.416	1.750E-05	6.891	2.011	0.022	0.046	7.727
44003	CH3CHO	138284.995	28.917	8.570E-05	7.284	2.012	0.056	0.119	6.498
44003	CH3CHO	134908.454	62.084	5.470E-05	6.928	2.012	0.021	0.044	5.438
18004	NH2D	110155.056	21.260	5.503E-06	7.377	2.014	0.083	0.177	12.306
46008	CH3OCH3	241946.497	81.131	8.288E-05	6.971	2.015	0.029	0.061	6.006
32003	CH3OH	167931.056	125.517	2.275E-05	7.364	2.016	0.024	0.052	8.027
46005	HCOOH	135737.700	35.459	2.327E-05	6.486	2.018	0.013	0.028	5.689
60003	CH3OCHO	158693.722	59.640	5.612E-05	6.995	2.019	0.019	0.040	3.887
33004	CH2DOH	255647.816	29.010	6.251E-05	6.737	2.020	0.026	0.056	3.386

Continued on next page

Table D.1 – continued from previous page

id	Species	Frequency (MHz)	E_{up} (K)	A_{ij} (s^{-1})	V_0 (km s^{-1})	FWHM (km s^{-1})	Intensity (K)	FitFlux (K km s^{-1})	rms (mK)
37003	c-C3H	91497.608	4.392	1.376E-05	7.502	2.021	0.012	0.027	2.569
44003	CH3CHO	76866.436	9.329	1.430E-05	7.249	2.022	0.050	0.108	3.187
33004	CH2DOH	268449.125	80.976	4.465E-05	6.862	2.022	0.015	0.033	4.408
44002	SiO	86846.960	6.252	2.940E-05	7.162	2.023	0.109	0.234	14.686
60003	CH3OCHO	143240.505	47.253	4.225E-05	6.912	2.029	0.025	0.055	6.052
32003	CH3OH	144736.349	314.471	1.223E-05	6.629	2.031	0.015	0.033	3.055
44003	CH3CHO	152635.194	33.104	1.180E-04	7.079	2.032	0.060	0.130	7.379
64002	SO2	131014.860	76.411	1.855E-05	7.258	2.032	0.028	0.060	7.331
39003	c-C3HD	107423.653	10.879	4.886E-05	7.082	2.034	0.023	0.050	2.762
25001	CCH	87402.004	4.197	1.376E-06	7.234	2.035	0.190	0.411	6.727
60003	CH3OCHO	132921.937	40.395	3.362E-05	6.569	2.036	0.024	0.053	5.870
44003	CH3CHO	216581.930	64.871	3.410E-04	6.896	2.037	0.041	0.089	7.437
32003	CH3OH	145097.435	19.505	1.096E-05	7.014	2.039	1.035	2.246	46.654
33502	*C-13-H3OH, vt=0,1	268635.444	107.483	6.856E-05	6.193	2.041	0.017	0.038	3.560
32003	CH3OH	132890.759	54.312	7.748E-06	6.666	2.042	0.496	1.077	37.237
41001	CH3CN	202293.183	172.556	6.151E-04	6.976	2.043	0.041	0.089	7.976
33004	CH2DOH	99672.139	49.785	6.410E-06	6.422	2.043	0.029	0.063	2.609
48510	CH3SH,v=0-2	151659.989	25.481	3.217E-05	7.168	2.043	0.016	0.034	4.376
56502	CCS	77731.711	21.764	2.035E-05	7.072	2.045	0.048	0.104	2.793
32003	CH3OH	241267.862	458.387	6.605E-05	7.209	2.046	0.016	0.034	5.522
46005	HCOOH	86546.185	13.568	6.126E-06	7.253	2.047	0.016	0.036	2.601
32003	CH3OH	95914.310	21.444	2.494E-06	6.694	2.047	0.088	0.193	3.272
41001	CH3CN	220641.084	247.400	7.627E-04	7.053	2.048	0.026	0.056	6.007

Continued on next page

Table D.1 – continued from previous page

id	Species	Frequency (MHz)	E_{up} (K)	A_{ij} (s^{-1})	V_0 (km s^{-1})	FWHM (km s^{-1})	Intensity (K)	FitFlux (K km s^{-1})	rms (mK)
60003	CH3OCHO	98747.906	31.911	1.018E-05	6.684	2.049	0.009	0.020	2.152
44003	CH3CHO	74891.677	11.256	1.240E-05	7.004	2.050	0.031	0.163	4.911
60003	CH3OCHO	205501.702	98.955	1.276E-04	6.716	2.051	0.025	0.054	5.586
42501	H2CCO	203940.225	66.887	9.413E-05	6.852	2.052	0.079	0.172	9.940
64002	SO2	254280.536	41.402	1.136E-04	6.779	2.054	0.042	0.093	5.586
33502	*C-13-H3OH, vt=0,1	254841.818	131.594	8.277E-05	6.702	2.054	0.012	0.026	3.837
33004	CH2DOH	268012.863	61.175	5.381E-05	6.704	2.055	0.036	0.079	4.837
32004	H2CO-18	268745.789	44.120	5.115E-04	6.878	2.056	0.020	0.043	4.829
32003	CH3OH	239746.219	49.060	5.665E-05	6.837	2.058	0.119	0.260	7.274
33004	CH2DOH	249591.472	22.575	4.818E-05	6.574	2.060	0.030	0.065	5.012
49003	C4H	85634.006	20.546	2.787E-06	7.641	2.063	0.014	0.031	2.853
60003	CH3OCHO	100308.179	27.398	1.264E-05	7.102	2.065	0.012	0.026	2.765
46008	CH3OCH3	209515.609	59.309	5.065E-05	6.570	2.067	0.035	0.077	6.574
32003	CH3OH	250924.398	202.983	8.212E-05	6.385	2.070	0.021	0.046	4.464
60003	CH3OCHO	98611.163	27.244	1.200E-05	7.233	2.071	0.010	0.023	2.270
45003	NH2CHO	127412.285	48.214	1.054E-04	7.185	2.072	0.011	0.025	4.459
33004	CH2DOH	261687.366	48.313	7.596E-05	6.611	2.074	0.027	0.060	6.295
32003	CH3OH	96739.358	12.542	2.558E-06	7.062	2.074	0.897	1.980	60.856
32006	D2CO	236102.370	49.803	2.770E-04	7.255	2.074	0.063	0.139	11.889
60003	CH3OCHO	164223.815	64.907	5.982E-05	7.323	2.075	0.018	0.039	6.250
32003	CH3OH	143865.795	28.348	1.069E-05	6.943	2.076	0.140	0.309	5.738
46004	C2H5OH	142285.054	37.155	1.509E-05	6.617	2.077	0.016	0.036	5.732
25001	CCH	87328.624	4.191	1.373E-06	7.338	2.078	0.188	0.415	7.552

Continued on next page

Table D.1 – continued from previous page

id	Species	Frequency (MHz)	E_{up} (K)	A_{ij} (s^{-1})	V_0 (km s^{-1})	FWHM (km s^{-1})	Intensity (K)	FitFlux (K km s^{-1})	rms (mK)
33004	CH2DOH	253637.057	48.007	6.024E-05	6.818	2.082	0.016	0.036	3.066
44003	CH3CHO	254827.152	94.094	5.510E-04	6.766	2.082	0.026	0.057	4.730
42501	H2CCO	202000.958	170.711	8.407E-05	7.122	2.082	0.018	0.041	7.921
64002	SO2	100878.105	12.585	1.026E-06	6.797	2.082	0.006	0.012	1.962
60003	CH3OCHO	163835.525	62.484	6.375E-05	6.736	2.082	0.017	0.038	5.922
45003	NH2CHO	106541.562	27.234	3.436E-06	7.106	2.086	0.008	0.018	2.253
32003	CH3OH	104354.831	207.991	1.563E-06	6.842	2.088	0.010	0.022	2.336
32003	CH3OH	266838.148	57.069	7.736E-05	6.537	2.089	0.219	0.487	11.683
26504	CN, v=0,1	113520.432	5.448	1.299E-06	7.487	2.089	0.080	0.179	10.246
28002	HC-13-N	86340.180	4.144	2.220E-05	7.118	2.091	0.316	0.704	15.449
32003	CH3OH	145131.864	34.977	1.125E-05	6.464	2.092	0.109	0.243	10.818
25001	CCH	87316.925	4.193	1.653E-06	7.279	2.094	0.343	0.765	16.145
49003	C4H	76117.432	16.436	1.941E-06	6.964	2.095	0.025	0.055	3.341
44003	CH3CHO	251489.286	104.695	5.140E-04	6.560	2.095	0.029	0.064	5.633
56502	CCS	106347.726	24.996	5.484E-05	7.447	2.096	0.101	0.225	5.092
60001	OCS	133785.900	38.525	6.816E-06	7.097	2.099	0.163	0.364	5.887
45003	NH2CHO	211329.457	67.802	6.564E-04	7.407	2.101	0.022	0.050	6.813
18004	NH2D	110153.587	21.260	1.238E-05	7.353	2.101	0.318	0.712	12.076
31002	H2C-13-O	212811.184	20.436	2.614E-04	7.086	2.102	0.086	0.192	8.892
44003	CH3CHO	149507.462	34.591	1.100E-04	6.664	2.103	0.069	0.153	8.746
44003	CH3CHO	155179.571	42.538	1.150E-04	6.800	2.103	0.034	0.076	4.599
44003	CH3CHO	270271.692	117.594	6.440E-04	6.466	2.107	0.020	0.044	5.948
46004	C2H5OH	91485.140	22.627	4.536E-06	6.784	2.107	0.008	0.017	2.305

Continued on next page

Table D.1 – continued from previous page

id	Species	Frequency (MHz)	E_{up} (K)	A_{ij} (s^{-1})	V_0 (km s^{-1})	FWHM (km s^{-1})	Intensity (K)	FitFlux (K km s^{-1})	rms (mK)
32003	CH3OH	97582.798	21.564	2.626E-06	6.681	2.107	0.107	0.239	3.602
33004	CH2DOH	264869.977	60.942	7.212E-05	6.910	2.109	0.022	0.050	6.308
42501	H2CCO	163160.881	48.291	4.736E-05	6.761	2.110	0.069	0.154	5.470
60003	CH3OCHO	142733.524	49.294	4.282E-05	6.955	2.111	0.010	0.022	6.261
50001	S-34-O	84410.690	19.234	5.046E-06	7.292	2.114	0.047	0.105	5.358
60003	CH3OCHO	135091.835	44.970	3.369E-05	6.104	2.114	0.015	0.033	4.944
46509	H2CS	206052.602	153.059	9.587E-05	6.619	2.115	0.053	0.120	7.198
27505	C-13-N	108657.646	5.242	7.227E-06	7.820	2.115	0.015	0.034	4.972
32003	CH3OH	84521.172	40.391	1.970E-06	6.373	2.116	0.799	1.799	16.875
41001	CH3CN	257403.584	271.225	1.286E-03	6.786	2.116	0.018	0.041	6.823
32003	CH3OH	249443.301	145.333	1.484E-05	6.543	2.119	0.018	0.041	7.518
60003	CH3OCHO	137293.183	49.810	3.312E-05	6.692	2.120	0.016	0.037	5.406
44003	CH3CHO	154322.197	53.598	1.050E-04	6.940	2.121	0.031	0.071	6.680
50001	S-34-O	168815.514	33.412	5.607E-05	7.780	2.122	0.043	0.097	5.804
60001	OCS	206745.161	89.305	2.554E-05	6.976	2.122	0.133	0.300	6.982
45003	NH2CHO	102064.380	17.684	6.712E-05	6.729	2.126	0.010	0.022	2.237
60003	CH3OCHO	142817.021	49.270	4.290E-05	7.061	2.129	0.018	0.041	5.835
32003	CH3OH	265224.426	360.022	8.345E-05	6.307	2.132	0.018	0.042	7.769
29005	NNH+	93173.700	4.472	3.627E-05	7.021	2.132	2.192	4.973	32.185
56502	CCS	81505.170	15.387	2.429E-05	7.129	2.133	0.158	0.358	5.486
41001	CH3CN	128739.669	139.017	1.200E-04	6.238	2.134	0.016	0.037	5.150
56502	CCS	144244.824	43.939	1.388E-04	6.973	2.134	0.042	0.095	5.420
33004	CH2DOH	252492.641	18.357	2.182E-05	7.124	2.135	0.019	0.043	6.621

Continued on next page

Table D.1 – continued from previous page

id	Species	Frequency (MHz)	E_{up} (K)	A_{ij} (s^{-1})	V_0 (km s^{-1})	FWHM (km s^{-1})	Intensity (K)	FitFlux (K km s^{-1})	rms (mK)
44003	CH3CHO	231506.291	108.252	3.750E-04	6.989	2.135	0.023	0.053	7.667
42501	H2CCO	141402.470	144.536	2.535E-05	6.831	2.136	0.022	0.049	4.743
56502	CCS	103640.759	31.090	4.979E-05	7.134	2.141	0.036	0.083	2.397
60003	CH3OCHO	132246.730	42.416	3.393E-05	7.290	2.145	0.019	0.044	5.607
48508	H2CS-34	135030.655	16.203	3.463E-05	7.443	2.145	0.040	0.092	5.760
44003	CH3CHO	231484.374	108.291	3.750E-04	6.884	2.145	0.032	0.074	8.750
25001	CCH	87284.156	4.191	2.806E-07	7.611	2.145	0.049	0.112	4.238
30004	H2CO	135030.440	112.793	2.792E-06	7.004	2.145	0.040	0.091	5.874
44003	CH3CHO	254850.487	94.074	5.510E-04	6.773	2.147	0.025	0.056	4.573
60001	OCS	158107.360	53.117	1.132E-05	6.958	2.148	0.158	0.362	4.417
64002	SO2	256246.946	35.887	1.074E-04	6.714	2.150	0.035	0.080	3.983
49003	C4H	76156.028	16.451	1.925E-06	7.259	2.154	0.014	0.032	3.183
32003	CH3OH	144728.359	312.568	6.776E-06	6.815	2.154	0.012	0.027	3.236
32003	CH3OH	253221.376	260.986	8.544E-05	6.739	2.158	0.023	0.054	2.696
46509	H2CS	274521.931	59.315	3.082E-04	7.127	2.158	0.044	0.102	6.996
42501	H2CCO	142768.945	40.460	3.132E-05	6.889	2.159	0.076	0.174	5.745
56502	CCS	113410.186	33.581	6.535E-05	6.933	2.161	0.034	0.079	8.888
46010	NS	161703.404	17.767	6.346E-05	6.582	2.161	0.101	0.232	6.828
33502	*C-13-H3OH, vt=0,1	84970.220	81.524	3.027E-06	6.474	2.163	0.012	0.027	3.046
44003	CH3CHO	205170.686	61.463	2.900E-04	7.038	2.163	0.034	0.079	6.482
44003	CH3CHO	135685.474	35.049	7.590E-05	6.799	2.169	0.030	0.069	6.035
32003	CH3OH	132621.824	86.457	4.133E-06	6.453	2.170	0.022	0.050	5.387
44003	CH3CHO	154200.916	69.484	9.170E-05	7.003	2.171	0.022	0.051	5.547

Continued on next page

Table D.1 – continued from previous page

id	Species	Frequency (MHz)	E_{up} (K)	A_{ij} (s^{-1})	V_0 (km s^{-1})	FWHM (km s^{-1})	Intensity (K)	FitFlux (K km s^{-1})	rms (mK)
68001	CCCS	86708.377	33.291	4.758E-05	7.672	2.172	0.040	0.093	3.204
60001	OCS	145946.812	45.529	8.880E-06	6.903	2.172	0.165	0.381	6.413
41001	CH3CN	128717.359	203.278	8.727E-05	6.655	2.175	0.017	0.038	4.676
64002	SO2	245563.423	72.713	1.191E-04	6.665	2.175	0.025	0.058	6.826
32003	CH3OH	230027.047	39.828	1.486E-05	6.964	2.177	0.048	0.110	7.965
60003	CH3OCHO	74296.741	18.401	4.395E-06	6.887	2.178	0.012	0.027	4.376
46008	CH3OCH3	111783.010	25.250	5.840E-06	7.392	2.178	0.016	0.038	5.288
33502	*C-13-H3OH, vt=0,1	166569.486	84.492	2.310E-05	7.013	2.181	0.019	0.044	5.204
44003	CH3CHO	255384.754	88.392	5.640E-04	6.882	2.182	0.017	0.039	4.513
60003	CH3OCHO	98432.760	37.838	8.473E-06	6.824	2.183	0.009	0.021	2.102
32003	CH3OH	96755.501	28.011	2.624E-06	6.784	2.184	0.086	0.200	3.112
44003	CH3CHO	95963.459	13.837	2.840E-05	7.078	2.187	0.060	0.139	3.015
46008	CH3OCH3	100463.040	24.707	3.455E-06	6.556	2.187	0.009	0.021	1.520
44003	CH3CHO	154026.697	42.330	1.120E-04	6.450	2.193	0.027	0.064	6.885
30004	H2CO	264270.140	209.940	1.079E-05	6.535	2.195	0.037	0.087	4.123
41001	CH3CN	202215.371	315.315	4.973E-04	7.017	2.196	0.034	0.079	9.277
41001	CH3CN	165454.370	296.787	2.134E-04	7.308	2.197	0.017	0.040	4.548
48510	CH3SH,v=0-2	151654.184	26.907	3.248E-05	6.417	2.198	0.011	0.027	4.429
33004	CH2DOH	265682.508	61.176	8.173E-05	6.847	2.201	0.023	0.053	5.499
60003	CH3OCHO	158704.392	59.627	5.614E-05	6.928	2.201	0.017	0.041	3.724
44003	CH3CHO	251095.451	104.562	5.050E-04	6.914	2.202	0.031	0.072	4.854
32003	CH3OH	143108.385	366.788	6.439E-06	7.260	2.205	0.016	0.037	5.818
33004	CH2DOH	132777.830	35.623	7.918E-06	6.909	2.208	0.017	0.040	5.199

Continued on next page

Table D.1 – continued from previous page

id	Species	Frequency (MHz)	E_{up} (K)	A_{ij} (s^{-1})	V_0 (km s^{-1})	FWHM (km s^{-1})	Intensity (K)	FitFlux (K km s^{-1})	rms (mK)
44003	CH3CHO	101892.414	7.662	3.890E-06	7.201	2.210	0.012	0.029	2.265
33502	*C-13-H3OH, vt=0,1	235960.370	33.976	5.620E-05	6.887	2.211	0.037	0.086	10.337
46008	CH3OCH3	222247.600	21.758	3.382E-05	7.125	2.211	0.027	0.064	7.100
32003	CH3OH	251641.787	114.793	7.756E-05	6.444	2.213	0.021	0.050	4.936
32003	CH3OH	257402.086	446.535	9.106E-05	6.711	2.214	0.015	0.035	3.039
61502	OC-13-S	109110.845	26.183	3.665E-06	7.293	2.215	0.019	0.044	6.372
60003	CH3OCHO	129310.166	36.433	3.061E-05	6.322	2.217	0.014	0.034	2.781
44003	CH3CHO	260544.019	96.321	6.010E-04	6.756	2.218	0.027	0.063	7.358
51001	HCCCN	81881.461	19.649	4.198E-05	7.056	2.222	0.253	0.599	7.205
44003	CH3CHO	208267.045	60.430	3.050E-04	6.928	2.225	0.041	0.098	7.554
49003	C4H	104705.112	30.157	5.154E-06	7.208	2.225	0.011	0.027	2.860
44003	CH3CHO	205161.898	61.537	2.900E-04	6.862	2.225	0.039	0.092	5.781
68001	CCCS	75147.913	25.246	3.082E-05	7.568	2.226	0.028	0.066	4.725
48508	H2CS-34	99774.075	22.761	1.198E-05	7.493	2.227	0.012	0.029	2.430
32003	CH3OH	150884.543	186.432	5.863E-06	6.889	2.228	0.035	0.083	6.256
60003	CH3OCHO	132245.128	42.435	3.392E-05	6.938	2.229	0.015	0.036	5.399
62505	OCS-34	94922.799	20.500	2.397E-06	6.774	2.231	0.014	0.033	2.504
60003	CH3OCHO	162768.855	62.587	6.244E-05	7.123	2.233	0.022	0.052	5.337
33004	CH2DOH	134976.337	35.834	8.321E-06	6.783	2.236	0.019	0.046	6.101
32003	CH3OH	251866.524	73.013	6.101E-05	6.561	2.236	0.043	0.102	5.834
46008	CH3OCH3	258548.775	93.332	1.037E-04	6.222	2.237	0.020	0.047	8.288
60003	CH3OCHO	143234.201	47.269	4.224E-05	6.677	2.241	0.015	0.035	5.885
44003	CH3CHO	250853.152	120.291	4.870E-04	6.854	2.243	0.020	0.048	5.375

Continued on next page

Table D.1 – continued from previous page

id	Species	Frequency (MHz)	E_{up} (K)	A_{ij} (s^{-1})	V_0 (km s^{-1})	FWHM (km s^{-1})	Intensity (K)	FitFlux (K km s^{-1})	rms (mK)
45502	CS-33, v=0,1	97172.064	6.995	1.638E-05	7.832	2.243	0.076	0.182	3.819
46004	C2H5OH	104487.260	23.251	5.676E-06	6.688	2.243	0.010	0.023	2.359
60003	CH3OCHO	103478.663	24.633	1.518E-05	6.762	2.245	0.011	0.027	2.025
18004	NH2D	76397.864	260.914	1.263E-07	7.464	2.245	0.012	0.029	3.368
40502	CH3CCH	136728.012	29.529	8.604E-06	7.107	2.248	0.090	0.215	6.316
60003	CH3OCHO	162775.275	62.571	6.245E-05	6.606	2.248	0.033	0.079	5.065
32003	CH3OH	165678.649	69.801	2.295E-05	6.879	2.253	0.062	0.149	4.774
40502	CH3CCH	136725.400	36.756	8.470E-06	7.131	2.255	0.076	0.183	6.485
49003	C4H	85672.581	20.563	2.769E-06	6.926	2.260	0.021	0.050	2.972
33004	CH2DOH	95208.692	36.727	5.775E-06	6.439	2.261	0.028	0.067	2.805
42501	H2CCO	262596.587	205.611	1.943E-04	5.690	2.262	0.030	0.072	4.083
49003	C4H	104666.575	30.135	5.170E-06	7.371	2.263	0.009	0.022	2.429
44003	CH3CHO	77126.413	18.284	1.080E-05	6.950	2.263	0.021	0.050	2.830
41001	CH3CN	238972.390	337.370	9.256E-04	7.118	2.263	0.018	0.044	6.248
32003	CH3OH	86902.916	102.717	6.915E-07	7.231	2.266	0.014	0.035	3.232
48508	H2CS-34	102807.338	23.052	1.310E-05	7.345	2.266	0.012	0.029	2.091
46005	HCOOH	108126.700	18.757	1.251E-05	6.804	2.267	0.019	0.047	2.691
25001	CCH	87446.512	4.197	2.822E-07	7.565	2.270	0.039	0.095	4.457
33502	*C-13-H3OH, vt=0,1	168155.444	123.005	2.300E-05	6.926	2.270	0.021	0.050	7.715
44003	CH3CHO	152607.614	33.197	1.180E-04	6.920	2.271	0.056	0.136	5.587
28001	CO	115271.202	5.532	7.200E-08	5.009	2.272	4.143	10.021	584.659
42501	H2CCO	262548.207	88.229	2.051E-04	6.819	2.273	0.026	0.063	4.830
60003	CH3OCHO	148045.822	69.961	3.621E-05	6.919	2.273	0.014	0.034	4.275

Continued on next page

Table D.1 – continued from previous page

id	Species	Frequency (MHz)	E_{up} (K)	A_{ij} (s^{-1})	V_0 (km s^{-1})	FWHM (km s^{-1})	Intensity (K)	FitFlux (K km s^{-1})	rms (mK)
33502	*C-13-H3OH, vt=0,1	255193.509	97.620	7.766E-05	6.850	2.277	0.015	0.036	3.998
32003	CH3OH	166169.098	86.052	2.285E-05	6.748	2.278	0.058	0.142	5.328
60003	CH3OCHO	90156.473	19.667	9.749E-06	7.235	2.280	0.008	0.020	2.369
43002	HNCO	263748.646	82.281	3.453E-09	6.325	2.280	0.028	0.069	5.659
32003	CH3OH	172445.839	78.077	1.161E-05	6.900	2.283	0.069	0.168	15.009
41001	CH3CN	257522.428	99.846	1.468E-03	7.097	2.285	0.028	0.068	5.963
60003	CH3OCHO	76803.994	13.675	6.249E-06	6.779	2.288	0.011	0.027	3.252
44003	CH3CHO	74924.134	11.330	1.240E-05	7.008	2.290	0.043	0.104	4.743
32003	CH3OH	267403.471	117.457	4.671E-05	6.870	2.290	0.050	0.123	6.680
33004	CH2DOH	223071.131	48.400	3.975E-05	6.866	2.291	0.028	0.069	6.750
32003	CH3OH	157048.617	61.850	1.964E-05	6.981	2.292	0.078	0.191	4.971
56502	CCS	90686.381	26.116	3.292E-05	7.100	2.295	0.043	0.105	2.465
42501	H2CCO	160142.242	47.639	4.478E-05	6.989	2.300	0.066	0.162	8.703
60003	CH3OCHO	200936.163	97.516	1.099E-04	7.010	2.302	0.028	0.068	8.812
44003	CH3CHO	147065.731	18.314	8.980E-06	6.567	2.309	0.011	0.028	4.187
46008	CH3OCH3	133271.309	72.875	1.041E-05	6.468	2.309	0.015	0.037	4.725
44003	CH3CHO	223660.603	72.197	3.780E-04	6.988	2.310	0.046	0.113	7.500
18004	NH2D	74155.310	50.725	4.440E-06	6.063	2.310	0.016	0.040	4.413
42501	H2CCO	224327.250	77.653	1.260E-04	6.893	2.311	0.058	0.143	8.036
46005	HCOOH	151176.281	32.236	3.582E-05	6.571	2.311	0.021	0.053	5.567
62505	OCS-34	106787.390	25.625	3.436E-06	7.186	2.312	0.015	0.037	2.767
32003	CH3OH	252090.409	154.248	8.146E-05	6.588	2.312	0.043	0.107	3.718
50001	S-34-O	256877.456	46.712	2.198E-04	6.692	2.313	0.051	0.126	6.459

Continued on next page

Table D.1 – continued from previous page

id	Species	Frequency (MHz)	E_{up} (K)	A_{ij} (s^{-1})	V_0 (km s^{-1})	FWHM (km s^{-1})	Intensity (K)	FitFlux (K km s^{-1})	rms (mK)
43002	HNCO	219798.320	58.020	1.511E-04	7.073	2.317	0.064	0.158	8.205
33004	CH2DOH	89988.240	29.356	1.941E-06	6.577	2.320	0.009	0.023	1.879
33502	*C-13-H3OH, vt=0,1	246143.897	122.327	7.313E-06	7.595	2.320	0.021	0.051	5.756
32003	CH3OH	232945.797	190.371	2.127E-05	7.305	2.321	0.022	0.054	6.732
44003	CH3CHO	208228.560	60.519	3.050E-04	7.002	2.321	0.040	0.098	7.392
32003	CH3OH	251738.437	98.546	7.457E-05	6.670	2.323	0.042	0.103	5.695
42501	H2CCO	161602.244	152.291	4.018E-05	6.286	2.325	0.030	0.074	6.863
30009	NND+	77109.610	3.701	2.057E-05	7.391	2.329	0.364	0.901	4.002
33004	CH2DOH	226818.248	36.727	3.578E-05	6.792	2.329	0.058	0.144	8.235
46005	HCOOH	134686.370	35.358	2.274E-05	7.241	2.330	0.016	0.041	4.693
32004	H2CO-18	134435.900	21.546	4.610E-05	6.790	2.331	0.018	0.044	5.580
32003	CH3OH	251811.956	84.618	6.966E-05	6.758	2.334	0.052	0.130	11.422
45003	NH2CHO	127330.123	95.863	4.285E-05	7.554	2.336	0.009	0.023	4.625
32003	CH3OH	76509.684	47.934	8.979E-07	6.681	2.337	0.047	0.116	3.255
40502	CH3CCH	136704.504	94.559	7.390E-06	7.271	2.345	0.023	0.058	5.208
56502	CCS	169753.449	59.620	2.277E-04	7.563	2.347	0.029	0.073	9.882
27505	C-13-N	108651.297	5.214	9.783E-06	7.395	2.348	0.012	0.031	4.708
18004	NH2D	216562.487	119.559	5.444E-05	6.900	2.348	0.013	0.031	7.451
25001	CCH	262004.227	25.149	5.742E-05	6.824	2.352	0.136	0.341	11.620
46008	CH3OCH3	132525.239	32.392	1.052E-05	7.058	2.353	0.027	0.066	4.871
44003	CH3CHO	255326.968	88.451	5.640E-04	6.922	2.354	0.024	0.061	4.174
33004	CH2DOH	221391.766	120.161	2.846E-05	6.782	2.355	0.028	0.070	8.474
46008	CH3OCH3	225598.731	69.790	6.531E-05	6.526	2.356	0.037	0.093	8.323

Continued on next page

Table D.1 – continued from previous page

id	Species	Frequency (MHz)	E_{up} (K)	A_{ij} (s^{-1})	V_0 (km s^{-1})	FWHM (km s^{-1})	Intensity (K)	FitFlux (K km s^{-1})	rms (mK)
41001	CH3CN	220679.287	183.147	8.209E-04	6.808	2.356	0.035	0.088	6.631
41001	CH3CN	147129.230	146.078	2.012E-04	6.489	2.358	0.022	0.056	4.782
60003	CH3OCHO	90145.723	19.684	9.742E-06	6.942	2.358	0.014	0.035	2.529
60003	CH3OCHO	141037.702	47.483	4.014E-05	6.999	2.358	0.015	0.039	4.145
33502	*C-13-H3OH, vt=0,1	165609.427	34.649	2.356E-05	7.115	2.359	0.013	0.034	4.152
32003	CH3OH	252485.675	202.981	8.366E-05	6.788	2.360	0.033	0.082	6.180
60003	CH3OCHO	148040.699	69.962	3.619E-05	6.853	2.361	0.012	0.029	4.474
33004	CH2DOH	96864.806	123.091	3.474E-06	7.509	2.366	0.006	0.016	1.900
41001	CH3CN	165565.891	46.877	3.801E-04	6.825	2.368	0.054	0.135	5.504
44003	CH3CHO	244789.251	83.140	4.990E-04	6.649	2.370	0.028	0.070	5.721
32003	CH3OH	88594.787	328.260	1.097E-06	5.919	2.372	0.008	0.021	2.197
60003	CH3OCHO	206601.165	89.254	1.276E-04	7.443	2.380	0.028	0.071	6.551
44003	CH3CHO	211984.409	142.256	2.270E-04	7.181	2.380	0.015	0.037	6.145
42501	H2CCO	220177.569	76.458	1.192E-04	6.881	2.387	0.065	0.165	6.843
38002	c-C3H2	82093.559	6.428	2.073E-05	7.350	2.392	0.083	0.211	6.396
32003	CH3OH	166773.281	390.018	1.846E-05	6.941	2.394	0.021	0.053	6.221
33004	CH2DOH	223196.401	32.157	3.575E-05	6.986	2.396	0.073	0.186	8.730
60003	CH3OCHO	90229.624	20.062	1.051E-05	7.172	2.397	0.014	0.036	3.006
46005	HCOOH	155617.882	30.014	3.982E-05	7.658	2.398	0.016	0.041	5.965
32004	H2CO-18	201614.257	31.222	1.975E-04	7.020	2.400	0.033	0.084	10.492
60001	OCS	109463.063	26.267	3.697E-06	7.141	2.402	0.194	0.495	8.993
48510	CH3SH,v=0-2	151759.927	43.622	2.879E-05	7.204	2.402	0.013	0.032	4.820
41001	CH3CN	128769.436	53.302	1.638E-04	6.803	2.406	0.026	0.066	6.895

Continued on next page

Table D.1 – continued from previous page

id	Species	Frequency (MHz)	E_{up} (K)	A_{ij} (s^{-1})	V_0 (km s^{-1})	FWHM (km s^{-1})	Intensity (K)	FitFlux (K km s^{-1})	rms (mK)
60003	CH3OCHO	218297.890	99.722	1.509E-04	7.100	2.407	0.032	0.082	9.141
44003	CH3CHO	96475.524	23.026	2.420E-05	6.746	2.412	0.031	0.080	3.274
42501	H2CCO	100094.514	27.464	1.030E-05	7.105	2.412	0.057	0.145	3.171
64002	SO2	205300.570	70.214	5.317E-05	6.314	2.416	0.027	0.069	7.381
60003	CH3OCHO	205663.741	98.957	1.278E-04	6.991	2.416	0.021	0.055	5.884
40502	CH3CCH	102540.145	46.132	3.164E-06	7.031	2.416	0.020	0.050	2.770
45003	NH2CHO	105464.258	15.219	8.107E-05	7.242	2.418	0.011	0.029	3.708
46005	HCOOH	157455.166	81.087	2.783E-05	7.078	2.419	0.011	0.029	4.573
33004	CH2DOH	136151.142	17.131	6.743E-06	6.570	2.421	0.036	0.092	4.731
33502	*C-13-H3OH, vt=0,1	94405.163	12.401	2.377E-06	6.759	2.426	0.020	0.051	3.085
41001	CH3CN	202320.443	122.566	6.563E-04	6.793	2.429	0.047	0.122	8.670
41001	CH3CN	239022.924	258.872	1.003E-03	6.534	2.432	0.020	0.052	6.861
32003	CH3OH	254423.520	328.261	8.731E-05	6.517	2.439	0.022	0.056	4.144
40502	CH3CCH	85450.766	41.210	1.704E-06	6.759	2.442	0.012	0.030	3.011
60003	CH3OCHO	100683.368	24.893	1.472E-05	7.044	2.444	0.013	0.034	2.103
32003	CH3OH	217886.504	508.379	3.379E-05	6.519	2.445	0.026	0.067	6.977
33004	CH2DOH	270299.931	76.175	8.783E-05	7.318	2.446	0.017	0.045	5.523
32003	CH3OH	265289.562	69.801	2.584E-05	6.643	2.449	0.044	0.116	7.223
46005	HCOOH	158720.562	43.077	3.887E-05	6.792	2.451	0.013	0.035	3.359
30503	C-13-O-17	214573.873	15.447	3.615E-07	7.333	2.452	0.015	0.038	6.541
62505	OCS-34	237273.635	119.577	3.882E-05	7.063	2.457	0.020	0.054	7.737
60003	CH3OCHO	111674.131	28.139	1.979E-05	7.251	2.464	0.016	0.041	5.186
33004	CH2DOH	222741.460	45.570	4.317E-05	7.284	2.467	0.034	0.089	8.707

Continued on next page

Table D.1 – continued from previous page

id	Species	Frequency (MHz)	E_{up} (K)	A_{ij} (s^{-1})	V_0 (km s^{-1})	FWHM (km s^{-1})	Intensity (K)	FitFlux (K km s^{-1})	rms (mK)
42501	H2CCO	161634.073	34.911	4.678E-05	6.598	2.469	0.045	0.118	7.150
33502	*C-13-H3OH, vt=0,1	95208.660	21.410	2.440E-06	6.363	2.471	0.030	0.078	2.546
46010	NS	253570.476	39.817	2.733E-04	6.549	2.477	0.031	0.082	5.027
41001	CH3CN	257507.561	121.277	1.445E-03	6.520	2.482	0.026	0.069	5.931
32003	CH3OH	249419.924	328.277	8.227E-05	6.855	2.486	0.025	0.066	6.239
44003	CH3CHO	77084.096	29.631	6.310E-06	6.936	2.487	0.011	0.028	2.413
33004	CH2DOH	223422.058	48.313	2.887E-05	6.928	2.489	0.026	0.068	6.304
44003	CH3CHO	262960.097	95.760	6.200E-04	6.393	2.492	0.026	0.070	6.842
44003	CH3CHO	133830.492	25.873	7.920E-05	6.887	2.494	0.065	0.171	6.623
46004	C2H5OH	144734.098	13.410	1.571E-05	6.869	2.497	0.014	0.037	3.337
32003	CH3OH	247610.918	446.583	8.106E-05	6.378	2.497	0.021	0.055	5.827
33004	CH2DOH	134065.381	12.871	7.300E-06	6.490	2.499	0.082	0.218	7.402
45003	NH2CHO	146871.604	28.326	2.246E-04	8.212	2.509	0.010	0.026	5.369
56502	CCS	166662.346	61.759	2.133E-04	6.895	2.510	0.019	0.050	4.815
46509	H2CS	171780.167	77.396	6.126E-05	6.827	2.511	0.033	0.087	13.325
44003	CH3CHO	157974.590	36.427	1.290E-04	6.877	2.514	0.055	0.146	4.330
41001	CH3CN	147163.244	60.365	2.517E-04	6.402	2.515	0.032	0.086	4.586
60003	CH3OCHO	100681.545	24.912	1.472E-05	7.005	2.516	0.010	0.027	2.095
32003	CH3OH	253755.809	293.465	8.635E-05	6.278	2.519	0.019	0.051	4.537
33502	*C-13-H3OH, vt=0,1	141602.528	13.593	1.145E-05	7.395	2.525	0.036	0.097	6.303
32003	CH3OH	249451.842	145.332	1.484E-05	6.596	2.527	0.022	0.060	7.253
32003	CH3OH	240241.490	82.532	1.440E-05	6.834	2.528	0.022	0.060	6.032
60001	OCS	170267.494	61.289	1.418E-05	6.818	2.529	0.145	0.391	9.096

Continued on next page

Table D.1 – continued from previous page

id	Species	Frequency (MHz)	E_{up} (K)	A_{ij} (s^{-1})	V_0 (km s^{-1})	FWHM (km s^{-1})	Intensity (K)	FitFlux (K km s^{-1})	rms (mK)
44003	CH3CHO	157937.697	36.497	1.290E-04	6.927	2.530	0.060	0.162	4.640
33004	CH2DOH	127202.590	123.699	1.106E-05	7.193	2.536	0.011	0.029	4.429
60003	CH3OCHO	206247.919	92.586	1.239E-04	6.968	2.538	0.023	0.063	5.717
32003	CH3OH	248282.424	404.830	8.155E-05	6.910	2.547	0.023	0.061	6.368
31003	HDCO	258082.640	102.609	2.111E-04	7.118	2.549	0.032	0.088	5.057
49501	S-33-O	203941.543	38.312	8.380E-05	6.484	2.553	0.016	0.044	10.556
31002	H2C-13-O	274762.112	44.802	5.470E-04	6.795	2.554	0.070	0.190	6.890
44003	CH3CHO	138319.628	28.845	8.570E-05	7.094	2.561	0.049	0.135	6.195
33502	*C-13-H3OH, vt=0,1	255050.965	97.619	7.757E-05	6.251	2.565	0.010	0.028	4.799
60003	CH3OCHO	107543.711	28.754	1.723E-05	6.480	2.568	0.012	0.033	2.295
40502	CH3CCH	85457.300	12.304	2.029E-06	6.957	2.569	0.050	0.138	3.007
32003	CH3OH	201071.847	163.898	9.114E-06	7.129	2.570	0.029	0.080	8.312
42501	H2CCO	240185.794	87.985	1.555E-04	6.431	2.571	0.044	0.121	7.300
33004	CH2DOH	207780.441	22.843	1.745E-05	6.328	2.573	0.022	0.060	6.398
60003	CH3OCHO	78481.388	15.849	6.809E-06	6.813	2.590	0.010	0.028	2.907
68001	CCCS	98268.518	42.446	6.952E-05	7.181	2.592	0.015	0.043	2.727
44003	CH3CHO	96371.791	34.257	1.850E-05	6.528	2.593	0.011	0.030	3.455
44003	CH3CHO	211992.280	142.249	2.270E-04	7.063	2.599	0.014	0.039	6.673
33502	*C-13-H3OH, vt=0,1	234011.580	48.251	5.269E-05	7.036	2.600	0.018	0.050	7.102
33004	CH2DOH	88304.126	22.843	1.947E-06	6.801	2.602	0.011	0.032	2.567
33004	CH2DOH	256731.552	25.192	6.896E-05	7.003	2.604	0.046	0.126	5.486
32003	CH3OH	241441.270	360.023	5.795E-05	6.277	2.607	0.020	0.055	5.123
56502	CCS	141602.294	100.057	7.007E-07	7.043	2.609	0.036	0.099	6.467

Continued on next page

Table D.1 – continued from previous page

id	Species	Frequency (MHz)	E_{up} (K)	A_{ij} (s^{-1})	V_0 (km s^{-1})	FWHM (km s^{-1})	Intensity (K)	FitFlux (K km s^{-1})	rms (mK)
41001	CH3CN	220594.423	325.902	6.917E-04	7.127	2.616	0.022	0.062	6.787
33004	CH2DOH	86668.751	10.596	4.653E-06	6.532	2.618	0.036	0.101	3.364
44003	CH3CHO	249326.638	93.022	5.160E-04	6.573	2.620	0.029	0.080	5.214
33004	CH2DOH	247625.746	29.015	5.957E-05	7.158	2.621	0.021	0.058	5.977
41001	CH3CN	147149.068	96.084	2.307E-04	6.409	2.628	0.030	0.085	5.564
44003	CH3CHO	168088.618	42.733	1.570E-04	6.719	2.637	0.049	0.137	8.255
32003	CH3OH	165369.341	55.871	2.308E-05	6.843	2.638	0.100	0.281	5.042
60003	CH3OCHO	98792.289	31.893	1.054E-05	6.739	2.639	0.012	0.032	2.268
32003	CH3OH	107159.906	304.734	1.203E-06	7.298	2.642	0.013	0.035	3.449
40502	CH3CCH	85455.667	19.531	1.948E-06	7.132	2.642	0.039	0.109	3.746
33004	CH2DOH	106336.754	73.321	1.366E-06	6.241	2.645	0.008	0.024	2.952
42501	H2CCO	80832.117	9.699	5.525E-06	7.279	2.647	0.022	0.063	7.717
32003	CH3OH	242446.084	248.933	2.290E-05	6.898	2.648	0.022	0.062	6.236
68001	CCCS	80928.182	29.130	3.860E-05	8.169	2.652	0.032	0.090	8.872
44003	CH3CHO	134996.063	46.192	6.640E-05	6.415	2.655	0.017	0.047	4.519
64002	SO2	165144.651	23.589	3.122E-05	6.944	2.658	0.092	0.261	7.917
46005	HCOOH	162598.480	34.434	4.456E-05	7.030	2.658	0.014	0.039	4.219
33004	CH2DOH	88754.512	17.130	4.916E-06	6.594	2.659	0.031	0.087	2.476
60003	CH3OCHO	88851.607	17.940	9.821E-06	6.953	2.664	0.014	0.040	1.970
42501	H2CCO	81586.230	22.841	5.326E-06	6.906	2.664	0.040	0.114	5.330
60003	CH3OCHO	98682.615	31.885	1.051E-05	7.295	2.665	0.008	0.024	2.045
41001	CH3CN	257482.792	156.990	1.407E-03	6.584	2.667	0.031	0.087	6.257
60003	CH3OCHO	132107.205	42.425	3.382E-05	7.027	2.667	0.018	0.051	6.144

Continued on next page

Table D.1 – continued from previous page

id	Species	Frequency (MHz)	E_{up} (K)	A_{ij} (s^{-1})	V_0 (km s^{-1})	FWHM (km s^{-1})	Intensity (K)	FitFlux (K km s^{-1})	rms (mK)
44003	CH3CHO	250637.020	140.641	4.580E-04	7.264	2.668	0.044	0.125	7.237
44003	CH3CHO	244832.176	83.055	4.990E-04	6.632	2.669	0.029	0.081	6.131
62505	OCS-34	166105.721	59.791	1.318E-05	6.934	2.669	0.031	0.088	6.043
33004	CH2DOH	210005.257	39.435	3.872E-05	6.258	2.671	0.020	0.056	7.686
60001	OCS	231060.983	110.900	3.577E-05	6.840	2.671	0.127	0.361	10.437
32003	CH3OH	251923.701	114.793	7.783E-05	6.609	2.672	0.056	0.159	5.553
44003	CH3CHO	168093.444	42.658	1.570E-04	6.918	2.674	0.053	0.151	8.154
48507	D2CS	83077.759	14.319	6.996E-06	7.765	2.677	0.020	0.057	5.573
33004	CH2DOH	98031.213	21.446	2.421E-06	6.602	2.679	0.030	0.084	2.573
32003	CH3OH	201996.513	417.920	2.923E-05	6.834	2.679	0.026	0.074	8.571
62505	OCS-34	154242.780	51.819	1.053E-05	6.798	2.680	0.012	0.033	7.636
46008	CH3OCH3	162529.572	33.050	2.117E-05	6.858	2.680	0.030	0.086	4.477
33004	CH2DOH	272098.060	49.785	6.359E-05	6.796	2.682	0.030	0.086	7.908
32003	CH3OH	171182.450	174.263	2.296E-05	5.989	2.692	0.036	0.105	12.390
64002	SO2	129514.810	60.927	2.502E-05	7.065	2.693	0.028	0.079	4.829
64002	SO2	255553.303	31.294	9.283E-05	6.860	2.694	0.028	0.080	4.440
60001	OCS	255374.461	134.829	4.841E-05	6.701	2.702	0.085	0.245	4.753
60001	OCS	243218.040	122.573	4.177E-05	6.907	2.703	0.099	0.285	7.920
44003	CH3CHO	249323.932	93.008	5.160E-04	6.404	2.705	0.028	0.082	5.127
32003	CH3OH	104410.457	207.992	1.565E-06	6.758	2.706	0.008	0.023	2.703
60001	OCS	267530.239	147.668	5.571E-05	6.687	2.708	0.100	0.289	8.815
32003	CH3OH	96588.596	332.212	2.551E-06	6.925	2.715	0.007	0.019	2.152
46008	CH3OCH3	147731.357	38.147	1.178E-05	7.513	2.718	0.019	0.054	4.153

Continued on next page

Table D.1 – continued from previous page

id	Species	Frequency (MHz)	E_{up} (K)	A_{ij} (s^{-1})	V_0 (km s^{-1})	FWHM (km s^{-1})	Intensity (K)	FitFlux (K km s^{-1})	rms (mK)
38002	c-C3H2	77100.034	44.722	1.540E-05	7.123	2.719	0.011	0.031	2.772
44003	CH3CHO	135476.752	35.090	7.400E-05	6.546	2.720	0.044	0.129	5.710
32003	CH3OH	263793.875	359.954	8.211E-05	6.958	2.723	0.032	0.092	6.144
33004	CH2DOH	85296.727	6.240	4.484E-06	6.490	2.728	0.029	0.084	3.286
32003	CH3OH	129433.338	197.076	4.317E-06	6.409	2.738	0.018	0.052	3.032
33004	CH2DOH	88073.074	10.401	1.436E-06	6.992	2.744	0.014	0.041	3.427
41001	CH3CN	165569.082	39.732	3.849E-04	6.737	2.745	0.058	0.168	5.731
32003	CH3OH	102658.160	179.190	2.653E-07	6.504	2.752	0.009	0.027	1.798
42501	H2CCO	222199.883	181.375	1.143E-04	6.713	2.753	0.037	0.108	6.496
60003	CH3OCHO	96070.725	23.609	1.205E-05	6.531	2.759	0.011	0.032	2.288
32003	CH3OH	105063.816	223.843	2.373E-06	7.320	2.763	0.012	0.035	3.615
44003	CH3CHO	77218.291	18.327	1.090E-05	6.424	2.765	0.024	0.070	3.064
42501	H2CCO	222314.404	116.205	1.196E-04	6.528	2.766	0.021	0.061	6.278
32003	CH3OH	102122.776	153.632	1.721E-07	7.206	2.766	0.010	0.028	2.033
32003	CH3OH	156828.517	78.077	1.878E-05	6.932	2.766	0.050	0.148	4.903
33004	CH2DOH	134112.347	29.010	3.863E-06	6.290	2.770	0.020	0.058	7.022
33502	*C-13-H3OH, vt=0,1	156356.390	35.760	2.068E-05	7.030	2.770	0.018	0.054	4.869
64002	SO2	257099.966	47.835	1.223E-04	6.543	2.771	0.029	0.084	5.738
32003	CH3OH	156488.902	96.614	1.780E-05	7.223	2.785	0.040	0.117	5.170
60003	CH3OCHO	154984.538	53.206	5.206E-05	6.444	2.799	0.009	0.025	3.587
32003	CH3OH	251917.065	63.728	4.360E-05	6.422	2.799	0.053	0.159	4.415
60003	CH3OCHO	100490.682	22.762	1.434E-05	6.827	2.801	0.012	0.035	2.058
33502	*C-13-H3OH, vt=0,1	156299.396	47.081	2.012E-05	6.791	2.804	0.016	0.048	5.794

Continued on next page

Table D.1 – continued from previous page

id	Species	Frequency (MHz)	E_{up} (K)	A_{ij} (s^{-1})	V_0 (km s^{-1})	FWHM (km s^{-1})	Intensity (K)	FitFlux (K km s^{-1})	rms (mK)
56502	CCS	156981.653	51.473	1.795E-04	6.853	2.819	0.043	0.129	6.208
33004	CH2DOH	88754.512	17.130	4.916E-06	6.594	2.825	0.030	0.091	2.532
60003	CH3OCHO	86268.739	22.527	7.502E-06	7.028	2.827	0.011	0.034	2.884
32003	CH3OH	86615.574	102.703	6.846E-07	6.196	2.833	0.013	0.039	2.734
60003	CH3OCHO	100482.241	22.779	1.433E-05	7.503	2.838	0.009	0.027	2.202
33004	CH2DOH	100381.445	63.203	2.393E-06	6.749	2.843	0.013	0.041	2.064
32003	CH3OH	251359.888	154.249	8.077E-05	6.281	2.856	0.044	0.134	5.470
33502	*C-13-H3OH, vt=0,1	156186.559	60.661	1.944E-05	7.024	2.860	0.018	0.056	4.867
32003	CH3OH	251905.729	63.727	4.360E-05	6.771	2.862	0.070	0.214	7.273
60003	CH3OCHO	73885.081	18.371	4.323E-06	6.792	2.863	0.014	0.041	4.153
60003	CH3OCHO	89314.657	20.154	1.016E-05	7.218	2.864	0.014	0.044	2.088
41001	CH3CN	239133.313	87.487	1.172E-03	6.552	2.865	0.029	0.087	8.693
32003	CH3OH	256228.714	404.796	8.964E-05	6.420	2.869	0.017	0.053	4.079
60003	CH3OCHO	141244.026	45.768	3.872E-05	6.786	2.880	0.015	0.047	4.037
32003	CH3OH	144750.264	427.271	1.085E-05	7.110	2.887	0.012	0.038	3.220
32003	CH3OH	100638.872	233.608	1.687E-06	7.496	2.898	0.010	0.030	1.712
41001	CH3CN	165518.064	154.022	3.085E-04	6.586	2.910	0.021	0.064	4.320
60003	CH3OCHO	89316.642	20.136	1.017E-05	6.176	2.928	0.011	0.034	1.581
32003	CH3OH	236936.089	260.205	2.787E-05	6.307	2.930	0.025	0.078	6.046
60003	CH3OCHO	103466.572	24.649	1.517E-05	7.042	2.935	0.013	0.041	2.014
60003	CH3OCHO	96076.845	23.592	1.205E-05	6.988	2.941	0.010	0.030	2.398
52005	DCCCN	109757.143	36.873	1.028E-04	6.502	2.947	0.019	0.061	8.163
32003	CH3OH	101737.293	130.400	1.081E-07	6.990	2.964	0.008	0.025	2.189

Continued on next page

Table D.1 – continued from previous page

id	Species	Frequency (MHz)	E_{up} (K)	A_{ij} (s^{-1})	V_0 (km s^{-1})	FWHM (km s^{-1})	Intensity (K)	FitFlux (K km s^{-1})	rms (mK)
44003	CH3CHO	134694.446	34.942	7.420E-05	6.723	2.966	0.036	0.113	5.085
64002	SO2	104239.295	54.712	1.122E-05	6.882	2.969	0.042	0.133	7.693
44002	SiO	130268.610	12.504	1.062E-04	6.846	2.979	0.057	0.181	25.912
44003	CH3CHO	112248.716	21.134	4.500E-05	6.789	2.992	0.052	0.164	5.698
32003	CH3OH	105576.396	269.848	8.462E-07	7.110	2.994	0.011	0.036	3.808
41001	CH3CN	239137.916	80.343	1.179E-03	6.598	2.998	0.033	0.098	8.773
32003	CH3OH	104336.667	237.297	5.859E-07	7.008	3.005	0.010	0.031	1.727
60003	CH3OCHO	98606.856	27.260	1.198E-05	6.778	3.006	0.010	0.033	2.140
41001	CH3CN	257448.128	206.976	1.354E-03	5.716	3.009	0.013	0.040	5.351
32003	CH3OH	234698.519	122.722	6.339E-06	7.097	3.012	0.022	0.071	8.581
32003	CH3OH	76247.258	169.008	8.544E-07	7.080	3.019	0.016	0.053	3.578
64002	SO2	258942.199	63.472	1.318E-04	6.035	3.019	0.024	0.078	7.350
64002	SO2	76412.165	54.712	1.585E-06	6.413	3.028	0.013	0.041	2.380
46004	C2H5OH	152656.891	13.440	1.844E-05	6.628	3.033	0.015	0.048	6.891
41001	CH3CN	202351.612	65.417	7.035E-04	6.824	3.042	0.056	0.182	9.544
46008	CH3OCH3	99325.250	10.214	4.378E-06	7.806	3.043	0.011	0.036	2.642
41001	CH3CN	91979.994	41.825	5.318E-05	6.471	3.046	0.022	0.071	3.069
32003	CH3OH	252252.849	177.455	8.265E-05	6.797	3.049	0.035	0.113	4.126
32003	CH3OH	249887.467	293.477	8.246E-05	6.567	3.054	0.003	0.102	6.531
32003	CH3OH	255241.888	365.372	8.841E-05	6.479	3.063	0.018	0.060	3.439
60003	CH3OCHO	87143.282	22.601	7.735E-06	6.821	3.076	0.010	0.033	3.103
41001	CH3CN	239096.497	144.633	1.115E-03	6.809	3.083	0.028	0.092	7.445
46008	CH3OCH3	147024.897	26.032	1.512E-05	6.979	3.090	0.018	0.059	5.415

Continued on next page

Table D.1 – continued from previous page

id	Species	Frequency (MHz)	E_{up} (K)	A_{ij} (s^{-1})	V_0 (km s^{-1})	FWHM (km s^{-1})	Intensity (K)	FitFlux (K km s^{-1})	rms (mK)
32003	CH3OH	209518.804	461.993	3.130E-05	6.828	3.092	0.022	0.072	6.604
44003	CH3CHO	112254.508	21.209	4.500E-05	6.848	3.099	0.053	0.174	5.606
33004	CH2DOH	264017.721	48.425	5.780E-05	6.424	3.104	0.037	0.122	8.229
60003	CH3OCHO	147730.751	78.551	3.165E-05	6.327	3.113	0.019	0.062	4.043
42501	H2CCO	101024.416	66.741	9.266E-06	6.868	3.117	0.008	0.007	1.705
64002	SO2	244254.218	93.901	1.639E-04	6.774	3.118	0.031	0.102	9.716
46509	H2CS	240393.762	164.596	1.675E-04	6.921	3.122	0.021	0.071	7.974
32003	CH3OH	88939.971	328.277	1.110E-06	5.915	3.137	0.007	0.022	2.115
33004	CH2DOH	84856.816	94.445	1.643E-06	7.499	3.170	0.010	0.033	3.480
41001	CH3CN	128757.030	89.022	1.456E-04	6.953	3.175	0.036	0.121	5.371
43002	HNCO	87597.342	53.786	8.367E-06	6.423	3.183	0.008	0.027	3.035
60501	CH2(OH)CHO	85288.347	29.742	9.360E-06	7.517	3.185	0.006	0.021	2.655
46008	CH3OCH3	90938.099	18.976	2.871E-06	6.369	3.196	0.011	0.038	2.211
60003	CH3OCHO	78479.392	15.868	6.808E-06	7.277	3.209	0.012	0.041	2.813
41001	CH3CN	128776.882	31.868	1.748E-04	6.559	3.231	0.052	0.180	8.480
41001	CH3CN	202339.922	86.850	6.857E-04	7.173	3.235	0.032	0.112	10.053
41001	CH3CN	165556.322	68.311	3.658E-04	6.650	3.263	0.031	0.107	4.062
60001	OCS	218903.357	99.811	3.037E-05	6.801	3.265	0.144	0.500	7.644
41001	CH3CN	110383.500	18.542	1.111E-04	6.710	3.267	0.064	0.223	10.175
64002	SO2	128605.130	82.583	2.615E-05	6.778	3.276	0.019	0.067	5.142
41001	CH3CN	165540.377	104.028	3.420E-04	6.607	3.282	0.032	0.111	4.909
41001	CH3CN	239064.299	194.621	1.066E-03	6.657	3.292	0.017	0.061	6.149
32003	CH3OH	250291.181	260.994	8.252E-05	6.356	3.298	0.027	0.094	4.599

Continued on next page

Table D.1 – continued from previous page

id	Species	Frequency (MHz)	E_{up} (K)	A_{ij} (s^{-1})	V_0 (km s^{-1})	FWHM (km s^{-1})	Intensity (K)	FitFlux (K km s^{-1})	rms (mK)
32003	CH3OH	156127.544	86.465	6.742E-06	6.119	3.301	0.027	0.094	5.749
32003	CH3OH	216945.521	55.871	1.214E-05	6.771	3.320	0.065	0.229	7.602
46005	HCOOH	133767.070	22.545	2.503E-05	7.488	3.324	0.019	0.067	5.100
41001	CH3CN	220730.261	97.443	8.985E-04	6.846	3.331	0.032	0.114	6.415
32003	CH3OH	133605.439	60.724	4.011E-06	7.649	3.360	0.022	0.080	6.353
41001	CH3CN	147174.588	31.785	2.686E-04	6.691	3.379	0.067	0.242	4.863
60003	CH3OCHO	100080.542	24.939	1.444E-05	7.355	3.381	0.015	0.055	2.741
41001	CH3CN	257527.384	92.702	1.476E-03	7.045	3.388	0.027	0.097	6.605
51001	HCCCN	236512.777	153.248	1.048E-03	7.300	3.399	0.024	0.085	8.057
60003	CH3OCHO	76711.146	15.340	5.741E-06	7.073	3.407	0.008	0.030	2.572
64002	SO2	221965.210	60.362	1.138E-04	7.027	3.412	0.079	0.285	11.065
18004	NH2D	99118.679	261.462	2.863E-05	6.543	3.431	0.006	0.023	2.237
46008	CH3OCH3	82650.180	6.693	2.545E-06	6.895	3.432	0.020	0.075	5.773
41001	CH3CN	220709.017	133.158	8.661E-04	6.943	3.442	0.047	0.171	6.517
42501	H2CCO	101002.361	131.933	7.056E-06	6.315	3.484	0.010	-0.001	1.992
32003	CH3OH	248885.468	365.395	8.196E-05	6.223	3.500	0.026	0.095	5.315
32003	CH3OH	267406.071	366.284	4.242E-05	6.592	3.548	0.043	0.163	5.953
33502	*C-13-H3OH, vt=0,1	94407.129	6.797	3.168E-06	6.611	3.557	0.032	0.122	2.885
48510	CH3SH,v=0-2	126405.627	18.202	1.842E-05	6.470	3.587	0.014	0.053	4.824
32003	CH3OH	220078.561	96.614	2.516E-05	6.937	3.602	0.081	0.311	7.088
41001	CH3CN	220743.011	76.011	9.177E-04	6.059	3.641	0.047	0.182	6.520
41001	CH3CN	202355.509	58.272	7.094E-04	6.948	3.644	0.057	0.220	9.567
31002	H2C-13-O	219908.525	32.938	2.564E-04	7.049	3.662	0.073	0.283	7.793

Continued on next page

Table D.1 – continued from previous page

id	Species	Frequency (MHz)	E_{up} (K)	A_{ij} (s^{-1})	V_0 (km s^{-1})	FWHM (km s^{-1})	Intensity (K)	FitFlux (K km s^{-1})	rms (mK)
41001	CH3CN	91987.088	13.244	6.333E-05	6.581	3.719	0.060	0.237	3.603
38002	c-C3H2	217822.148	38.608	5.933E-04	6.491	3.730	0.062	0.245	7.031
51001	HCCCN	263792.308	189.919	1.456E-03	5.034	3.743	0.031	0.124	7.921
46509	H2CS	240393.037	164.596	1.675E-04	6.106	3.764	0.022	0.088	7.939
41001	CH3CN	110381.372	25.687	1.080E-04	6.714	3.776	0.056	0.224	10.754
32003	CH3OH	201445.493	72.534	1.329E-05	6.725	3.867	0.041	0.168	9.806
33502	*C-13-H3OH, vt=0,1	156373.659	15.375	2.168E-05	6.873	3.869	0.016	0.065	4.650
42501	H2CCO	242375.735	75.629	1.609E-04	7.344	3.877	0.015	0.062	6.576
41001	CH3CN	91985.314	20.390	6.079E-05	6.480	3.887	0.044	0.181	3.552
41001	CH3CN	128779.364	24.722	1.784E-04	7.002	3.937	0.058	0.242	5.421
32003	CH3OH	94541.785	131.281	1.293E-06	6.483	3.940	0.009	0.036	2.461
44002	SiO	217104.980	31.259	5.210E-04	9.274	3.948	0.032	0.134	7.634
64002	SO2	251199.675	82.179	1.756E-04	6.336	3.997	0.051	0.218	6.959
32003	CH3OH	155997.524	117.457	1.670E-05	6.925	4.004	0.042	0.179	6.978
32003	CH3OH	234683.370	60.924	1.845E-05	6.567	4.045	0.033	0.144	8.233
32003	CH3OH	251890.886	84.619	6.972E-05	6.144	4.059	0.071	0.307	5.843
46010	NS	253572.148	39.819	2.713E-04	7.311	4.108	0.013	0.058	4.251
41001	CH3CN	147171.752	38.931	2.643E-04	6.251	4.126	0.053	0.234	5.289
31003	HDCO	268292.020	40.166	5.081E-04	6.096	4.146	0.074	0.328	7.788
31003	HDCO	259034.910	62.867	3.658E-04	7.085	4.230	0.041	0.185	5.891
32003	CH3OH	251517.309	133.361	7.950E-05	6.514	4.233	0.048	0.216	5.711
45005	HCS+	256027.800	43.007	4.130E-04	7.391	4.280	0.024	0.111	5.200
33004	CH2DOH	267634.613	45.002	6.260E-05	5.438	4.283	0.027	0.121	7.757

Continued on next page

Table D.1 – continued from previous page

id	Species	Frequency (MHz)	E_{up} (K)	A_{ij} (s^{-1})	V_0 (km s^{-1})	FWHM (km s^{-1})	Intensity (K)	FitFlux (K km s^{-1})	rms (mK)
32003	CH3OH	251811.956	84.618	6.966E-05	4.370	4.371	0.028	0.132	11.422
27505	C-13-N	216710.144	15.642	5.681E-08	6.592	4.410	0.143	0.673	8.784
27002	HNC	271981.142	26.106	9.337E-04	6.917	4.643	0.341	1.684	22.164
32003	CH3OH	251900.452	73.013	6.103E-05	6.618	4.650	0.081	0.402	8.447
41001	CH3CN	91971.130	77.546	4.051E-05	5.975	4.670	0.017	0.085	2.108
41001	CH3CN	220747.261	68.866	9.244E-04	7.075	4.683	0.049	0.243	6.859
34502	H2S	216710.437	83.980	4.872E-05	6.993	4.721	0.126	0.634	8.970
31003	HDCO	257748.760	62.775	3.604E-04	7.274	4.734	0.036	0.183	5.483
33502	*C-13-H3OH, vt=0,1	141597.059	19.196	1.019E-05	7.460	4.737	0.024	0.123	6.024
32003	CH3OH	251895.728	98.545	7.470E-05	6.795	4.780	0.075	0.384	6.116
32003	CH3OH	250924.398	202.983	8.212E-05	6.498	4.869	0.027	0.142	4.464
32003	CH3OH	145093.754	27.053	1.231E-05	3.475	5.121	0.162	0.882	44.030
27001	HCN	88631.847	4.254	2.426E-05	4.331	5.222	0.793	4.406	59.453
32003	CH3OH	247228.587	60.925	2.157E-05	6.709	5.230	0.025	0.138	5.582
46509	H2CS	171688.117	24.723	7.281E-05	6.771	5.273	0.039	0.219	12.902
31003	HDCO	256585.430	30.848	4.736E-04	6.952	5.288	0.081	0.457	5.939
30004	H2CO	145602.949	10.483	7.808E-05	4.837	5.459	0.673	3.914	89.595
32003	CH3OH	145126.191	36.172	6.772E-06	5.194	5.539	0.106	0.628	49.165
31002	H2C-13-O	206131.626	31.616	2.112E-04	6.727	5.782	0.045	0.276	7.101
32003	CH3OH	168577.831	44.263	4.381E-06	6.517	5.854	0.026	0.161	8.108
60001	OCS	72976.779	12.258	1.068E-06	6.345	5.881	0.028	0.178	4.324
48510	CH3SH,v=0-2	75816.443	11.841	3.333E-06	3.881	5.940	0.003	0.021	3.384
32003	CH3OH	251641.787	114.793	7.756E-05	5.982	6.070	0.042	0.271	4.936

Continued on next page

Table D.1 – continued from previous page

id	Species	Frequency (MHz)	E_{up} (K)	A_{ij} (s^{-1})	V_0 (km s^{-1})	FWHM (km s^{-1})	Intensity (K)	FitFlux (K km s^{-1})	rms (mK)
45005	HCS+	213360.530	30.720	2.354E-04	6.962	6.133	0.021	0.098	7.785
42501	H2CCO	101036.630	14.548	1.104E-05	6.133	6.273	0.007	0.048	2.597
27002	HNC	90663.593	4.351	2.690E-05	5.768	6.425	0.155	1.059	61.349
31003	HDCO	246924.600	37.602	3.961E-04	6.324	6.430	0.073	0.502	7.696
46509	H2CS	169114.079	37.520	6.681E-05	6.197	6.496	0.079	0.545	7.217
31003	HDCO	201341.350	27.290	1.963E-04	5.886	6.533	0.073	0.507	12.471
32003	CH3OH	166898.566	104.624	2.277E-05	6.381	6.578	0.039	0.273	6.166
45502	CS-33, v=0,1	242913.610	34.975	2.907E-04	7.339	6.594	0.035	0.243	6.070
30004	H2CO	72409.090	65.928	8.010E-07	7.687	6.629	0.015	0.103	3.573
46509	H2CS	205987.858	34.609	1.277E-04	6.697	6.718	0.047	0.339	8.925
31003	HDCO	128812.860	9.276	5.397E-05	5.635	6.719	0.060	0.426	9.717
32003	CH3OH	251984.837	133.361	7.994E-05	6.069	6.730	0.024	0.171	5.549
51001	HCCCN	227418.906	141.897	9.308E-04	6.992	6.733	0.029	0.209	7.950
28004	DCN	217238.400	20.852	3.826E-04	6.729	6.756	0.068	0.486	7.439
32003	CH3OH	155320.895	140.603	1.550E-05	7.066	6.758	0.025	0.176	6.356
32003	CH3OH	241842.284	72.530	5.115E-05	6.325	6.778	0.053	0.381	6.736
46509	H2CS	209200.620	48.313	1.300E-04	7.059	6.806	0.084	0.609	8.600
51001	HCCCN	209230.234	120.505	7.236E-04	7.510	6.865	0.035	0.255	6.738
46509	H2CS	270521.931	71.603	2.903E-04	6.090	6.907	0.062	0.455	7.880
46509	H2CS	244048.504	60.026	2.103E-04	6.936	6.955	0.063	0.463	7.587
33004	CH2DOH	91586.845	25.841	5.285E-06	6.113	7.254	0.011	0.082	2.819
46001	CS-34	241016.194	34.702	2.857E-04	7.416	7.267	0.123	0.950	7.873
45001	C-13-S	138739.335	13.317	5.107E-05	7.282	7.288	0.045	0.346	7.354

Continued on next page

Table D.1 – continued from previous page

id	Species	Frequency (MHz)	E_{up} (K)	A_{ij} (s^{-1})	V_0 (km s^{-1})	FWHM (km s^{-1})	Intensity (K)	FitFlux (K km s^{-1})	rms (mK)
31002	H2C-13-O	146635.672	22.384	5.987E-05	5.513	7.296	0.036	0.283	5.426
32003	CH3OH	265289.562	69.801	2.584E-05	4.606	7.305	0.031	0.243	7.223
32003	CH3OH	165050.175	23.368	2.349E-05	5.560	7.375	0.065	0.507	6.422
30004	H2CO	101332.991	87.565	1.570E-06	6.704	7.447	0.014	0.109	2.486
60001	OCS	85139.121	16.344	1.714E-06	3.812	7.450	0.017	0.132	4.716
30004	H2CO	72837.948	3.496	8.145E-06	4.170	7.478	0.305	2.431	35.416
32003	CH3OH	104060.634	273.900	1.588E-06	6.609	7.512	0.006	0.044	1.822
32003	CH3OH	251866.524	73.013	6.101E-05	5.953	7.593	0.042	0.340	5.834
32003	CH3OH	266838.148	57.069	7.736E-05	4.555	7.649	0.187	1.524	11.683
31002	H2C-13-O	141983.740	10.223	7.246E-05	6.823	7.692	0.017	0.139	5.780
45001	C-13-S	92494.308	6.659	1.421E-05	5.498	7.699	0.016	0.132	4.732
60001	OCS	133785.900	38.525	6.816E-06	4.681	7.722	0.038	0.309	5.887
46509	H2CS	236727.020	58.620	1.920E-04	6.916	7.745	0.063	0.516	7.583
32003	CH3OH	167931.056	125.517	2.275E-05	5.647	7.753	0.026	0.212	8.027
32003	CH3OH	84521.172	40.391	1.970E-06	3.707	7.862	0.615	5.145	16.875
60001	OCS	145946.812	45.529	8.880E-06	3.896	7.913	0.038	0.319	6.413
31002	H2C-13-O	137449.950	21.723	4.930E-05	6.282	7.966	0.031	0.260	5.177
46509	H2CS	103040.447	9.891	1.484E-05	5.058	8.005	0.030	0.255	4.292
32003	CH3OH	169335.219	148.730	2.280E-05	6.882	8.017	0.024	0.204	7.389
60001	OCS	158107.360	53.117	1.132E-05	5.810	8.056	0.030	0.257	4.417
28003	HCN-15	258157.100	24.779	7.647E-04	7.721	8.061	0.016	0.141	6.481
46509	H2CS	101477.805	22.910	1.260E-05	4.682	8.070	0.043	0.369	6.116
32003	CH3OH	165061.130	28.011	2.343E-05	5.967	8.114	0.087	0.751	7.513

Continued on next page

Table D.1 – continued from previous page

id	Species	Frequency (MHz)	E_{up} (K)	A_{ij} (s^{-1})	V_0 (km s^{-1})	FWHM (km s^{-1})	Intensity (K)	FitFlux (K km s^{-1})	rms (mK)
32003	CH3OH	218440.063	45.460	4.686E-05	5.895	8.131	0.189	1.632	10.265
46509	H2CS	202924.054	47.259	1.187E-04	6.023	8.137	0.091	0.788	9.975
32003	CH3OH	251164.108	177.456	8.161E-05	5.913	8.177	0.027	0.233	5.279
32003	CH3OH	170060.592	36.173	2.552E-05	5.308	8.202	0.214	1.872	11.878
46509	H2CS	240266.872	46.140	2.049E-04	6.437	8.245	0.036	0.319	6.190
32003	CH3OH	205791.270	16.840	6.277E-05	5.722	8.277	0.063	0.559	10.375
32003	CH3OH	241832.718	84.618	3.867E-05	7.226	8.295	0.043	0.377	6.600
32003	CH3OH	251738.437	98.546	7.457E-05	5.357	8.299	0.034	0.301	5.695
32003	CH3OH	250506.853	153.099	4.228E-05	5.196	8.306	0.095	0.838	6.891
30004	H2CO	150498.334	22.618	6.467E-05	4.144	8.394	0.818	7.308	78.637
32003	CH3OH	230027.047	39.828	1.486E-05	7.788	8.436	0.016	0.140	7.965
60001	OCS	206745.161	89.305	2.554E-05	6.165	8.444	0.040	0.358	6.982
32003	CH3OH	146618.697	104.412	8.041E-06	4.830	8.489	0.220	1.984	10.711
32003	CH3OH	146368.328	28.589	1.125E-05	4.352	8.490	0.174	1.571	7.480
32003	CH3OH	132890.759	54.312	7.748E-06	4.252	8.494	0.371	3.352	37.237
46001	CS-34	96412.940	6.941	1.610E-05	4.410	8.532	0.048	0.433	9.044
32003	CH3OH	213427.061	23.367	3.370E-05	6.739	8.610	0.060	0.549	7.049
44002	SiO	130268.610	12.504	1.062E-04	-0.149	8.639	0.209	1.923	25.912
46509	H2CS	137371.210	16.484	3.647E-05	6.779	8.641	0.042	0.384	5.935
46004	C2H5OH	231220.812	118.418	4.122E-05	7.224	8.710	0.053	0.488	10.819
51001	HCCCN	163753.389	74.663	3.448E-04	6.884	8.714	0.054	0.504	5.789
32003	CH3OH	108893.945	13.125	1.471E-05	4.652	8.737	0.080	0.743	6.848
32003	CH3OH	95169.391	83.539	2.131E-06	4.644	8.744	0.285	2.648	20.936

Continued on next page

Table D.1 – continued from previous page

id	Species	Frequency (MHz)	E_{up} (K)	A_{ij} (s^{-1})	V_0 (km s^{-1})	FWHM (km s^{-1})	Intensity (K)	FitFlux (K km s^{-1})	rms (mK)
51001	HCCCN	218324.788	130.983	8.229E-04	7.090	8.759	0.038	0.359	9.178
42501	H2CCO	140127.474	39.953	2.961E-05	7.069	8.763	0.014	0.126	5.456
32003	CH3OH	95914.310	21.444	2.494E-06	4.657	8.814	0.068	0.639	3.272
30004	H2CO	218222.192	20.957	2.816E-04	6.197	8.873	0.654	6.179	47.416
42501	H2CCO	101981.429	27.735	1.089E-05	5.754	8.901	0.012	0.112	3.005
44001	CS	97980.950	7.054	1.689E-05	4.252	8.968	0.672	6.415	82.894
51001	HCCCN	245606.308	165.035	1.174E-03	6.707	8.974	0.018	0.173	5.176
60001	OCS	97301.209	21.014	2.580E-06	5.326	8.975	0.030	0.289	4.775
32003	CH3OH	97582.798	21.564	2.626E-06	4.747	9.057	0.083	0.796	3.602
32003	CH3OH	96739.358	12.542	2.558E-06	0.037	9.075	0.507	4.902	60.856
32003	CH3OH	241904.147	60.725	5.093E-05	6.032	9.100	0.131	1.272	7.012
32003	CH3OH	254015.377	20.090	1.902E-05	5.253	9.142	0.065	0.631	5.762
32003	CH3OH	96755.501	28.011	2.624E-06	4.699	9.146	0.043	0.420	3.112
32003	CH3OH	156602.395	21.445	8.926E-06	6.391	9.148	0.063	0.616	8.566
32003	CH3OH	157272.338	27.053	2.146E-05	7.181	9.215	0.248	2.429	9.108
51001	HCCCN	127367.666	45.846	1.610E-04	5.646	9.237	0.049	0.485	7.453
32003	CH3OH	241879.025	55.871	5.961E-05	6.248	9.238	0.080	0.786	5.913
51001	HCCCN	136464.401	52.395	1.985E-04	5.939	9.264	0.061	0.597	6.647
46001	CS-34	144617.109	13.881	5.820E-05	6.021	9.282	0.102	1.008	8.289
51001	HCCCN	145560.946	59.381	2.414E-04	5.124	9.295	0.044	0.433	5.980
32003	CH3OH	229758.756	89.103	4.192E-05	6.184	9.302	0.143	1.416	10.895
36504	H2S-34	167910.516	27.825	2.636E-05	5.158	9.304	0.023	0.229	9.415
32003	CH3OH	104300.337	158.637	1.960E-06	6.043	9.357	0.015	0.145	2.106

Continued on next page

Table D.1 – continued from previous page

id	Species	Frequency (MHz)	E_{up} (K)	A_{ij} (s^{-1})	V_0 (km s^{-1})	FWHM (km s^{-1})	Intensity (K)	FitFlux (K km s^{-1})	rms (mK)
32003	CH3OH	76509.684	47.934	8.979E-07	4.680	9.370	0.044	0.441	3.255
46509	H2CS	139483.682	29.906	3.580E-05	6.903	9.389	0.051	0.511	8.783
30004	H2CO	218760.066	68.111	1.576E-04	6.533	9.389	0.175	1.747	10.894
51001	HCCCN	81881.461	19.649	4.198E-05	4.849	9.391	0.047	0.469	7.205
32003	CH3OH	143865.795	28.348	1.069E-05	5.376	9.438	0.108	1.082	5.738
56502	CCS	72783.541	46.396	2.631E-07	3.068	9.477	0.028	0.281	8.475
30004	H2CO	218475.632	68.094	1.570E-04	6.529	9.495	0.168	1.694	12.554
32003	CH3OH	239746.219	49.060	5.665E-05	5.738	9.502	0.092	0.931	7.274
32003	CH3OH	145103.185	13.928	1.232E-05	4.559	9.615	0.711	7.276	44.635
51001	HCCCN	109173.634	34.057	1.008E-04	5.696	9.676	0.053	0.547	9.563
32003	CH3OH	165190.475	44.263	2.321E-05	5.954	9.693	0.069	0.712	7.086
32003	CH3OH	156488.902	96.614	1.780E-05	6.808	9.707	0.031	0.316	5.170
32003	CH3OH	241791.352	34.817	6.047E-05	6.014	9.742	0.351	3.641	16.158
46509	H2CS	274521.931	59.315	3.082E-04	6.213	9.803	0.009	0.089	6.996
51001	HCCCN	154657.284	66.804	2.900E-04	7.022	9.883	0.041	0.435	6.176
32003	CH3OH	165678.649	69.801	2.295E-05	5.974	9.891	0.052	0.544	4.774
46509	H2CS	135298.261	29.404	3.267E-05	4.668	9.894	0.057	0.605	9.402
64002	SO2	134004.860	43.146	2.501E-05	5.958	9.915	0.025	0.268	5.143
32003	CH3OH	261805.675	28.011	5.573E-05	4.657	9.945	0.089	0.940	8.717
46509	H2CS	104617.027	23.212	1.381E-05	5.037	9.996	0.038	0.404	7.412
51001	HCCCN	90979.023	24.015	5.788E-05	5.110	10.065	0.046	0.492	8.921
32003	CH3OH	165099.240	34.977	2.333E-05	5.149	10.099	0.103	1.112	8.751
43002	HNCO	87925.044	10.549	1.151E-08	4.317	10.108	0.028	0.299	3.960

Continued on next page

Table D.1 – continued from previous page

id	Species	Frequency (MHz)	E_{up} (K)	A_{ij} (s^{-1})	V_0 (km s^{-1})	FWHM (km s^{-1})	Intensity (K)	FitFlux (K km s^{-1})	rms (mK)
32003	CH3OH	243915.788	49.660	5.966E-05	6.394	10.119	0.121	1.307	6.646
41001	CH3CN	73590.218	8.829	3.171E-05	7.341	10.169	0.026	0.280	3.755
32003	CH3OH	157048.617	61.850	1.964E-05	6.288	10.226	0.066	0.718	4.971
44001	CS	146969.033	14.107	6.108E-05	4.685	10.245	1.055	11.505	106.088
32003	CH3OH	166169.098	86.052	2.285E-05	5.991	10.292	0.037	0.408	5.328
32003	CH3OH	156828.517	78.077	1.878E-05	6.420	10.376	0.045	0.501	4.903
32003	CH3OH	145131.864	34.977	1.125E-05	5.266	10.500	0.138	1.537	10.818
32003	CH3OH	157246.062	36.335	2.099E-05	6.157	10.553	0.099	1.110	6.982
32003	CH3OH	241767.234	40.391	5.806E-05	6.253	10.570	0.287	3.234	13.959
32003	CH3OH	241700.159	47.935	6.037E-05	6.135	10.615	0.136	1.532	7.067
48001	SO	251825.770	50.661	1.963E-04	3.294	10.622	0.224	2.527	23.477
64002	SO2	271529.015	35.496	1.107E-04	4.930	10.675	0.027	0.310	8.707
32003	CH3OH	157178.987	47.936	2.038E-05	6.175	10.680	0.083	0.939	6.363
30004	H2CO	225697.775	33.450	2.770E-04	6.911	10.720	0.794	9.057	68.604
51001	HCCCN	100076.392	28.818	7.739E-05	4.930	10.772	0.044	0.506	6.104
32003	CH3OH	96741.371	6.965	3.408E-06	5.644	10.801	0.532	6.121	39.568
41001	CH3CN	73588.799	15.975	2.972E-05	1.736	10.862	0.026	0.052	3.945
43002	HNCO	131885.734	22.154	3.163E-05	4.673	10.910	0.032	0.372	7.709
30004	H2CO	211211.468	32.059	2.270E-04	7.175	10.941	0.788	9.178	68.642
28003	HCN-15	86054.961	4.130	2.203E-05	5.335	11.017	0.011	0.126	3.021
34502	H2S	168762.762	27.877	2.677E-05	5.347	11.023	0.275	3.232	45.053
32003	CH3OH	145097.435	19.505	1.096E-05	3.642	11.132	0.599	7.103	46.654
32003	CH3OH	107013.831	28.349	3.066E-06	6.546	11.147	0.021	0.246	4.930

Continued on next page

Table D.1 – continued from previous page

id	Species	Frequency (MHz)	E_{up} (K)	A_{ij} (s^{-1})	V_0 (km s^{-1})	FWHM (km s^{-1})	Intensity (K)	FitFlux (K km s^{-1})	rms (mK)
32003	CH3OH	165369.341	55.871	2.308E-05	5.669	11.235	0.055	0.655	5.042
44001	CS	244935.644	35.266	2.998E-04	6.419	11.338	1.023	12.340	66.885
30004	H2CO	140839.502	21.923	5.300E-05	5.462	11.548	0.617	7.584	72.922
43002	HNCO	153864.992	29.538	6.133E-09	5.137	11.616	0.025	0.305	6.800
64002	SO2	208700.320	15.336	6.717E-05	7.012	12.115	0.026	0.333	7.983
64002	SO2	235151.720	19.029	7.690E-05	4.923	12.487	0.033	0.433	9.241
43002	HNCO	109905.601	15.824	8.902E-09	4.405	12.506	0.025	0.332	10.032
64002	SO2	241615.798	23.589	8.455E-05	6.025	12.597	0.026	0.344	5.845
64002	SO2	135696.020	15.663	2.208E-05	4.273	12.749	0.053	0.716	9.198
64002	SO2	158199.740	15.336	2.532E-05	6.686	12.849	0.022	0.298	4.360
64002	SO2	140306.170	29.199	2.527E-05	6.244	12.896	0.017	0.227	6.226
48001	SO	109252.220	21.051	1.101E-05	4.988	12.968	0.056	0.771	22.600
48001	SO	158971.800	28.681	4.317E-05	3.871	13.009	0.133	1.840	17.166
48001	SO	99299.870	9.226	1.148E-05	4.605	13.452	0.243	3.476	58.418
48001	SO	86093.950	19.314	5.354E-06	4.639	13.654	0.040	0.577	11.665
48001	SO	206176.005	38.576	1.030E-04	5.137	13.806	0.167	2.454	15.352
64002	SO2	203391.550	70.123	8.804E-05	5.434	13.831	0.051	0.748	11.398
48001	SO	261843.684	47.551	2.327E-04	4.466	13.936	0.343	5.087	32.432
48001	SO	129138.923	25.512	2.294E-05	4.814	13.982	0.099	1.477	16.998
64002	SO2	104029.418	7.744	1.006E-05	5.022	14.008	0.041	0.604	5.064
48001	SO	138178.600	15.857	3.228E-05	6.310	14.185	0.243	3.672	56.057
64002	SO2	165225.452	27.085	4.134E-05	5.331	14.545	0.077	1.190	7.882
64002	SO2	160827.880	49.709	3.953E-05	4.466	14.664	0.055	0.856	9.645

Continued on next page

Table D.1 – continued from previous page

id	Species	Frequency (MHz)	E_{up} (K)	A_{ij} (s^{-1})	V_0 (km s^{-1})	FWHM (km s^{-1})	Intensity (K)	FitFlux (K km s^{-1})	rms (mK)
48001	SO	172181.460	33.775	5.948E-05	4.986	14.934	0.125	1.993	19.204
32003	CH3OH	157276.019	20.090	2.182E-05	10.572	15.046	0.193	3.097	9.677
48001	SO	219949.442	34.985	1.361E-04	5.749	15.328	0.360	5.868	36.505
64002	SO2	83688.093	36.715	6.825E-06	6.141	15.385	0.025	0.404	7.840
32003	CH3OH	96744.545	20.090	3.407E-06	14.120	15.463	0.378	6.222	20.707
48001	SO	215220.653	44.104	1.216E-04	7.355	16.165	0.162	2.789	19.453
64002	SO2	72758.243	19.155	2.769E-06	4.770	16.694	0.036	0.634	5.509
48001	SO	258255.813	56.498	2.161E-04	6.687	17.310	0.116	2.135	14.603
27001	HCN	88633.936	4.254	2.427E-05	11.561	19.098	0.231	4.688	46.982